

STRATOSPHERIC PROCESSES  
AND THEIR ROLE IN  
CLIMATE

# SPARC

A project of the WMO/ICSU/IOC  
World Climate Research Programme



## SPARC Assessment of Upper Tropospheric and Stratospheric Water Vapour

December 2000

**WCRP - 113**  
**WMO/TD - No. 1043**  
**SPARC Report No.2.**



STRATOSPHERIC PROCESSES  
AND THEIR ROLE IN CLIMATE

SPARC

A project of the WMO/ICSU/IOC World Climate Research Programme

---

SPARC Assessment of  
Upper Tropospheric and Stratospheric Water Vapour

December 2000

Prepared by the SPARC Water Vapour Working Group under the auspices of the  
SPARC Scientific Steering Group

Edited by D. Kley, J.M. Russell III and C. Phillips

WCRP - 113  
WMO/TD - No. 1043  
SPARC Report No.2.



# SPARC ASSESSMENT OF UPPER TROPOSPHERIC AND STRATOSPHERIC WATER VAPOUR

## Table of Contents

Summary .....	vii
Foreword .....	xvii

Introduction .....	3
--------------------	---

### Chapter 1. Instrumentation and Data Sets

*Lead Authors: Ellis E. Remsberg and Cornelius Schiller*

1.1	Introduction .....	11
1.2	<i>In situ</i> hygrometers .....	15
	1.2.1 Frost point hygrometers .....	15
	1.2.2 Lyman- $\alpha$ hygrometers .....	21
	1.2.3 Tuneable diode laser spectrometers.....	29
	1.2.4 Radiosondes.....	33
	1.2.5 MOZAIC sensors .....	36
	1.2.6 Cryogenic samplers .....	39
1.3	Ground based, balloon-borne, and airborne remote sensing instruments .....	41
	1.3.1 Microwave instruments.....	41
	1.3.2 LIDAR .....	47
	1.3.3 Infrared and far-infrared measurements.....	52
1.4	Satellite sensors .....	56
	1.4.1 Operational satellite upper tropospheric humidity .....	58
	1.4.2 Limb Infrared Monitor of the Stratosphere (LIMS) .....	63
	1.4.3 Stratospheric Aerosol and Gas Experiment (SAGE) II.....	65
	1.4.4 Atmospheric Trace MOlecule Spectroscopy (ATMOS).....	67
	1.4.5 Halogen Occultation Experiment (HALOE) .....	69
	1.4.6 Microwave Limb Sounder (MLS) - lower stratosphere.....	75
	1.4.7 Microwave Limb Sounder (MLS) - upper troposphere .....	80
	1.4.8 Millimeter-wave atmospheric sounder (MAS) .....	82
	1.4.9 Improved Limb Atmospheric Spectrometer (ILAS).....	83
	1.4.10 Polar Ozone and Aerosol Measurement (POAM) III .....	86
1.5	Summary and conclusions.....	88

---

## Chapter 2. Data Quality

*Lead Authors: Samuel J. Oltmans and Karen H. Rosenlof*

---

2.1.	Introduction.....	95
2.2	Comparisons between aircraft-borne, balloon-borne, and ground-based sensors .....	98
2.2.1	Stratospheric measurements.....	98
2.2.2	Laboratory intercomparison of the NOAA-CMDL, NOAA-AL, and Harvard <i>in situ</i> instruments .....	103
2.2.3	Balloon infrared instrument comparisons.....	105
2.2.4	Tropospheric measurements.....	109
2.3	Comparisons made for the validation of satellite measurements .....	118
2.3.1	HALOE comparisons .....	118
2.3.2	MLS comparisons .....	126
2.3.3	SAGE II comparisons.....	129
2.3.4	ATMOS comparisons.....	131
2.3.5	ILAS comparisons .....	137
2.3.6	Upper stratosphere comparisons (WVMS and WASPAM).....	139
2.3.7	Comparisons with TOVS/HIRS .....	141
2.3.8	MLS tropospheric comparisons.....	144
2.4	Comparisons between satellite systems.....	149
2.4.1	ATMOS Comparisons.....	149
2.4.2	MLS with HALOE.....	153
2.4.3	POAM III with HALOE.....	155
2.4.4	ILAS with HALOE .....	158
2.4.5	TOVS/HIRS upper tropospheric comparisons .....	159
2.5	Comparisons of derived quantities.....	162
2.5.1	SAGE II and HALOE annual averages .....	162
2.5.2	Satellite seasonal climatology comparisons.....	164
2.5.3	Lowermost stratosphere <i>in situ</i> and satellite climatologies .....	167
2.5.4	Entry level [H <sub>2</sub> O] <sub>e</sub> and 2 CH <sub>4</sub> +H <sub>2</sub> O .....	168
2.5.5	Comparison of water vapour long-term changes and seasonal oscillations.....	173
2.6	Summary of comparisons .....	184
2.6.1	Stratospheric comparisons .....	184
2.6.2	Upper tropospheric humidity comparisons.....	191
2.6.3	Conclusions and recommendations.....	193

---

Chapter 3. Distribution and variability of water vapour in the upper troposphere  
and lower stratosphere

*Lead Authors: Andrew Gettelman, John E. Harries and Philip W. Mote*

---

3.1	Introduction.....	197
	3.1.1 Radiation .....	197
	3.1.2 Dynamics.....	199
	3.1.3 Chemistry .....	201
3.2	Mean Distribution of LS/UT Water Vapour.....	202
	3.2.1 Lower stratosphere .....	202
	3.2.2 Upper troposphere .....	206
3.3	Seasonal Cycle .....	208
	3.3.1 Lower stratosphere .....	208
	3.3.2 Upper troposphere .....	216
	3.3.3 The tropical tropopause region .....	224
3.4	Non-seasonal Variations.....	228
	3.4.1 Interannual variations.....	228
	3.4.2 Intraseasonal variations.....	232
	3.4.3 Transient variability.....	233
3.5	Long-term variations.....	241
	3.5.1 Stratospheric measurements .....	241
	3.5.2 Tropospheric measurements .....	247
	3.5.3 Causes of long-term variations.....	252
	3.5.4 Consequences of long-term variations.....	257
3.6	Conclusions.....	261
	3.6.1 Long-term variations.....	262
	3.6.2 Recommendations .....	263

---

References .....		265
------------------	--	-----

### Appendices

I	Co-chairs, Authors, Contributors and Reviewers .....	295
II	Acronyms and Abbreviations .....	301
III	WCRP Reports.....	305

---

## Summary

### Key findings

- A significant increase in the number and quality of stratospheric water vapour measurements has occurred over the past 25 years, particularly with the advent of satellite observations. Stated accuracy of most *in situ* and remote instruments as well as direct or indirect comparisons of coincident field measurements cluster within a  $\pm 10\%$  range.
- The concentration of stratospheric water vapour in the "overworld" ( $\Theta \geq \sim 380$  K) is determined by dry air upwelling through the tropical tropopause, methane oxidation in the stratosphere, and transport by the poleward-and-downward (Brewer-Dobson) mean circulation. At the tropical tropopause, air transported into the stratosphere is dried by a complex combination of processes that act on a variety of spatial and temporal scales. Water vapour in the upper troposphere is controlled by local and regional circulation patterns and seasonal changes of upper tropospheric temperature.
- There has been a 2 ppmv increase of stratospheric water vapour since the middle 1950s. This is substantial given typical current stratospheric values of 4-6 ppmv. Photochemical oxidation of methane in the stratosphere produces approximately two molecules of water vapour per molecule of methane. The increase in the concentration of tropospheric methane since the 1950s (0.55 ppmv) is responsible for at most one half of the increase in stratospheric water vapour over this time period. It is not clear what is responsible for the remainder of the observed increase in stratospheric water vapour.
- Upper tropospheric relative humidity (UTH) has been monitored for about 20 years by instruments on operational satellites. In the upper troposphere, no major inconsistencies were found between existing satellite-based measurements that would preclude their use in describing the long-term behaviour of upper tropospheric humidity. The data are also of sufficient quality for climatological and process studies.
- Assessing long-term changes in the UTH is difficult because of high variability during El Niño - Southern Oscillation events, other natural modes of variability in the large-scale circulation, and the competing effects of changes in water vapour concentration and temperature. Although both positive and negative statistically significant long-term changes can be found in different latitudinal bands, no striking global trend emerges from preliminary analyses.
- The operational radiosonde network does not produce water vapour data that can be used for either analyses of long-term change, process studies in the upper troposphere, or for validation of UTH measurements. However, emerging data sets from improved quality, quasi-operational aircraft and ground-based instrumentation show promise and should be used more extensively for process studies, climate analyses and validation of satellite data.

## Instrumentation, precision and accuracy

Tropospheric and stratospheric water vapour has been measured over the past 50 years by a large number of individuals and institutions using a variety of *in situ* and remote sensing measurement techniques. Measurement results are widely dispersed in the literature. Instrumentation has steadily evolved from a small number of manually operated *in situ* instruments to automatic devices deployed on balloon and aircraft platforms, and more recently to high precision sensors on satellites. Only a limited number of measurements of relative or specific humidity using a single instrument type have records longer than 10 years.

Operating principles and measurement specifications of most *in situ* research-type instruments currently in use are presented in Table 1 along with their estimated measurement accuracy. These instruments provide point measurements in time and space with high vertical resolution, typically in the range of a few hundred meters or better. Accuracy estimates range from 5 to 10% based on known or estimated random and systematic uncertainties inherent in the instrument system, calibration procedures and retrieval algorithms. Remote sensing instruments deployed on ground-based, balloon-borne and airborne platforms provide vertical profile measurements with stated accuracy similar to *in situ* instruments, although with coarser vertical resolution. Such vertical resolutions range from several hundred meters in the case of LIDAR, to a few kilometres for the infrared (IR) and far infrared (FIR) spectrometers, and approximately 10km for microwave instruments.

**Table 1.** *In situ* and remote sensing techniques for measurements of H<sub>2</sub>O from ground-based, balloon-borne and airborne platforms, along with their typical measurement range and overall accuracy, i.e. the sum of systematic and random errors. For details, see Table 1.29 and text in Section 1.2 and 1.3.

Technique	Range	Altitude range	Accuracy
Frost point hygrometry	10,000 – 0.5 ppmv	5 – 30 km	5 – 10%
Lyman- $\alpha$ fluorescence	500 – 0.2 ppmv	5 – 35 km	6 – 7%
Tunable diode laser spectrometry	> 0.1 ppmv	0 – 30 km	5 – 10%
MOZAIC sensor	> 20 ppmv	Troposphere	5 – 7% RH
Radiosonde	100 – $\approx$ 5%RH	middle and lower troposphere	not assessed
Micro wave spectrometry	20 – 0.2 ppmv	20 – 80 km	0.6 – 0.2 ppmv
LIDAR	> 4 ppmv	0 – 20 km	5 – 10%
IR and FIR spectrometry	> 1 ppmv	5 – 40 km	5 – 13%

Satellite and shuttle-based experiments for measuring stratospheric and upper tropospheric water vapour are listed in Table 2 along with random and systematic error estimates for single profile observations (as opposed to zonal or temporal averages). Accuracy estimates can be obtained from the root-sum-square of the random and systematic error components. Error estimates are given for ranges of vertical levels. Since some systematic error components vary randomly from profile to profile, these components are less important for daily, seasonal, or zonal means. Therefore, a zonal-average stratospheric error profile is dominated by the truly systematic error components, whose signs may be unknown and offsetting. The vertical resolution of satellite instruments, also given in Table 2, depends on the individual measurement concept (e.g. occultation or emission) and the specific instrument implementation. Horizontal resolution is typically on the order of 50 km to 300 km depending on whether the experiment is nadir or limb viewing.

**Table 2.** Estimates of random errors, systematic errors and vertical resolution of stratospheric H<sub>2</sub>O profiles derived from satellite instrumentation.

Instrument and data set	Random error	Systematic error	Vert. Res. (km)
LIMS (version 5) (Limb IR emission)	20-15% (1 – 5 hPa) 15-10% (5 – 10 hPa) 10% (10 – 50 hPa)	31-24% (1 - 5 hPa) 24-20% (5 – 10 hPa) 20-37% (10 – 50 hPa)	≈5
SAGE II (version 5.9) (IR solar occultation)	10-5% (3 – 10 hPa) 5-14% (10 – 25 hPa) 14% (25 – 300 hPa)	6-13% (3 - 7 hPa) 13% (7 - 25 hPa) 13-27% (25 – 100 hPa) 27% (100 – 300 hPa)	≈3
ATMOS (version 3) (IR solar occultation)	9-11% (1 – 300 hPa)	6% (1 – 300 hPa)	3 – 6
HALOE (version 19) (IR solar occultation)	9-7% (1 – 10 hPa) 7-13% (10 – 40 hPa) 13% (40 – 100 hPa)	10-14% (1 – 10 hPa) 14-19% (10 – 40 hPa) 19-24% (40 – 100 hPa)	2.3
MLS (version 0104) (Limb $\mu$ wave emission)	4% (1 – 10 hPa) 3% (10 – 50 hPa) 3-8% (50 – 100 hPa)	6-9% (1 – 10 hPa) 9-16% (10 – 50 hPa) 16-50% (50 – 100 hPa)	≈3
MAS (Limb $\mu$ wave emission)	5-10% (1 – 50 hPa)	10-15% (1 – 50 hPa)	≈5
ILAS (version 4.20) (IR Solar occultation)	More than 10% above 2 hPa 10-5% (2 – 300 hPa)	30% (1 - 2 hPa) 30-10% (2 - 7 hPa) 10% (7 – 300 hPa)	1 – 2
POAM III (version 2) (IR Solar occultation)	5% (3 – 100 hPa)	15% (3 – 100 hPa)	1 – 3

The Microwave Limb Sounder (MLS) and several generations of High Resolution Infrared Sounder (HIRS) instruments on the TIROS Operational Vertical Sounder (TOVS) suite of missions have provided measurements of upper tropospheric relative humidity from satellites. MLS relative humidity accuracy estimates for low to mid-latitudes range from 10 to 35% at 147 hPa and 20 to 50% at higher pressures. Accuracy estimates for individual relative humidity measurements made by TOVS are difficult to obtain but several generations of TOVS instruments span a temporal range of more than 20 years opening up the possibility of evaluating long-term changes. An issue for the use of TOVS is the availability of coincident accurate *in situ* profile data from one to the next generation of TOVS instruments to provide calibration across multiple spacecraft.

The data sets used in this assessment are available for independent verification of the results and conclusions of this Report at the SPARC Data Center (<http://www.sparc.sunysb.edu>) where they will also be preserved for future studies.

## Data quality assessment

### Stratosphere

Over 25 instruments representing several techniques were assessed for the quality of the data that they produce. For both the stratosphere and the troposphere there is no single technique or instrument platform that is recognised as a standard to which other techniques should be compared, and thus comparisons were made relative to one another.

The Halogen Occultation Experiment (HALOE) measurements on the Upper Atmosphere Research Satellite were selected as baseline data for stratospheric comparisons in this assessment. This was not meant to imply that HALOE is considered a standard, but rather that its spatial and temporal coverage allowed a maximum number of coincidences with other instruments. The layer between 60 and 100 hPa contains the best overlap of satellite, balloon-borne and aircraft measurements. Layers higher in the stratosphere, 10-50 hPa, and 1-10 hPa are also considered, but include only balloon-borne, satellite and ground-based microwave comparisons.

On average, measurements from the various instruments agree to within their stated levels of accuracy throughout the stratosphere. The mean of all the measurements compared was ~5% higher than HALOE, with a clustering of most of the instruments within a 10% range.

The differences between the stratospheric measurements are summarised in Figure 1 for three pressure layers previously mentioned. The mean differences are plotted as symbols and the bars represent differences estimated from indirect comparisons using one instrument as a transfer standard to compare with a second. A reasonable degree of consistency was found among measurements made from near the tropopause up to 50 km (~1 hPa). The majority of the instruments clustered within a 10% range, although direct comparisons among individual instruments showed larger differences sometimes exceeding 30%. Indirect intercomparisons show as much as 50% differences in some cases. Reasons for the differences were not revealed in this assessment process, although atmospheric variability is likely an important factor.

### Upper troposphere

The worldwide radiosonde network has provided tropospheric humidity measurements since the 1940's but sensor performance tends to be of poor quality at the cold temperatures and low pressures present in the upper troposphere. Comparisons between the widely used radiosonde Vaisala Humicap A sensor and the CMDL frostpoint instrument show, for example, that at temperatures of  $-60^{\circ}\text{C}$  the reported humidity from the radiosonde is only one half of the frostpoint instrument value. Additionally there have been numerous changes in radiosonde instrumentation over the period of the existing data record further complicating analysis of such data for long-term changes. Consequently, comparisons with *in situ* measurements of UTH from operational radiosondes should not be used to validate satellite data in this region.

The focus of the upper troposphere data quality assessment was TOVS because it has the most extensive record length, and hence is the most suitable for examining long term changes in UTH. The tropospheric MLS sensor provided the best data set for comparison with TOVS, and only small biases were found between them. Comparisons between satellite and direct water vapour measurements from *in situ* observations did not provide strong constraints on the performance of the TOVS satellite sensors. This was due mainly to problems with the *in situ* methods, especially the radiosondes and also because of difficulties in making comparisons in an inhomogeneous atmosphere when instruments have very different spatial coverage and altitude resolution. The assessment of the TOVS data did not reveal any major inconsistencies in this data set that would preclude its use in describing the long-term behaviour of upper tropospheric humidity. Overall measurements from these two very different techniques, TOVS and MLS, appear to produce comparable results on monthly averaged time scales. However, it was found that high spatial and temporal variability in the upper troposphere introduces major difficulties in validating satellite measurements. Judicious use of data from the MOZAIC (Measurement of Ozone and Water Vapour by Airbus In-Service Aircraft) project provided some information used in assessing

the quality of the MLS and TOVS measurements. To gauge their value in future correlative efforts, DIAL and Raman LIDAR systems were compared with radiosondes and frostpoint hygrometers. The LIDAR results in the troposphere agree to within about 10% with other correlative measurements, suggesting that such systems accurately measure water vapour. If deployed in sufficient numbers, such measurements could provide profile data valuable for validation of satellite measurements.

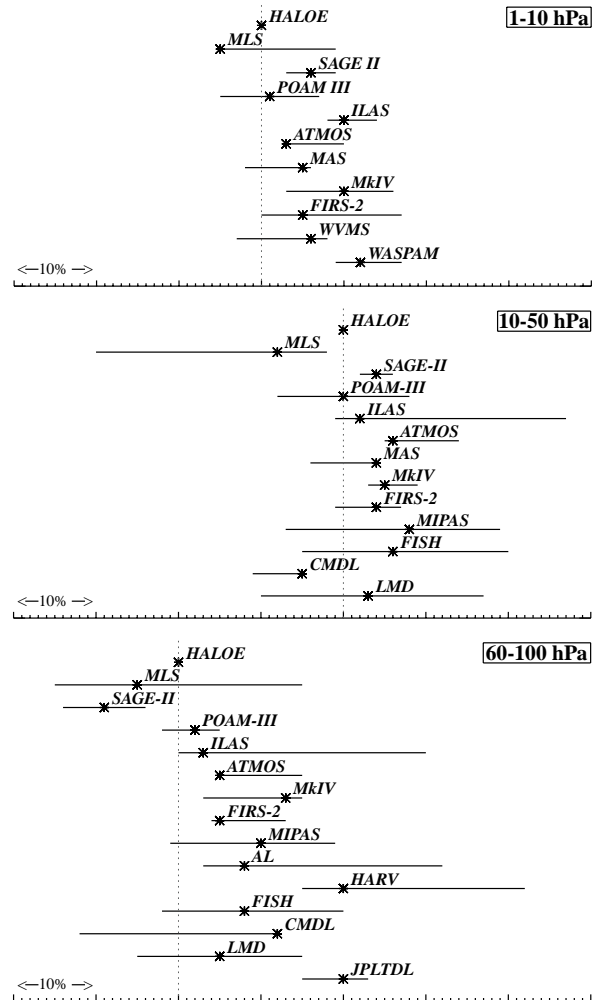


**Figure 1** Summary of the relationship between stratospheric measurements assessed in this report for 3 altitude ranges. The symbols give the direct percentage difference from HALOE, and the horizontal lines show the range of the indirect comparisons. Each tick mark is 1%, and the placement for HALOE is indicated by the dotted line. Where no direct comparison was available, the symbols give the average of the indirect comparisons.

## Spatial variability and seasonal changes

### Stratosphere, including the tropopause

The annual zonal mean water vapour distribution in the stratosphere is depicted in Figure 2. Key features are sharp vertical gradients at the tropopause and in the extratropical lower stratosphere, a minimum in the tropics at or just above the tropopause, and gradual increases upward and poleward. The water vapour distribution can be understood as a balance

between dry air entering via the tropical tropopause, a source of water vapour from methane oxidation in the upper stratosphere and return to the troposphere via the extratropical tropopause. The general features of the distribution are explained by Lagrangian-mean transport via the Brewer-Dobson circulation, wave-induced isentropic mixing, and upward extension of tropospheric circulations in the lowest few kilometres of the stratosphere. Nearly all air that reaches the stratosphere above 100 hPa passes through the tropical tropopause where freeze drying at low temperatures and other poorly understood processes produce annual mean mixing ratios of  $\sim 3.5\text{--}4$  ppmv. Some of this dry air rises slowly in the tropics, but most spreads poleward, primarily in the lowest few kilometres of the stratosphere. In addition, water vapour concentrations increase upward and away from the equator as methane is oxidised into water vapour. Below approximately 100 hPa, the extratropical lower stratosphere is moistened by air transported from the tropical upper troposphere horizontally across the subtropical tropopause at the location of the subtropical jet.

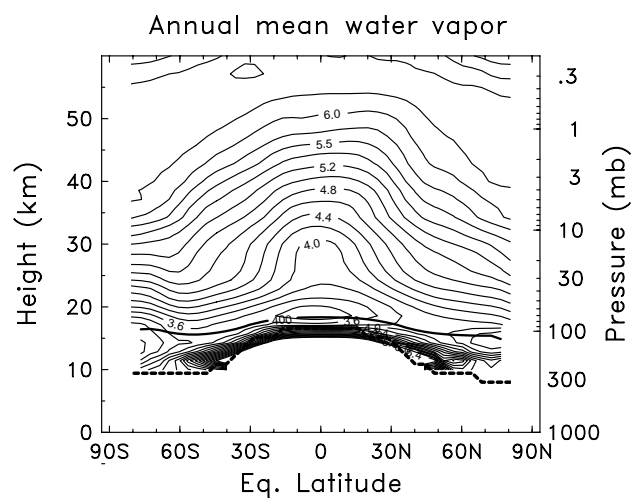


**Figure 2** Annual zonal mean water vapour from HALOE and MLS data by height and equivalent latitude. Contour interval of 0.2 ppmv. The thick dashed line is the tropopause, and the thick solid line is the 400K potential temperature surface.

The horizontal transport in the lower stratosphere has a strong seasonal component (Figure 3). An absolute minimum of the mixing ratio ( $\sim 2.8$  ppmv) is centred near  $20^\circ\text{N}$  during January-March, with the dry air propagating both towards the North pole and into the Southern Hemisphere. Relatively high water vapour values, centred near  $30^\circ\text{N}$ , are observed during the Northern Hemisphere summer coincident with the convective phases of the summer monsoons. Similar to the winter poleward propagation of the dry air masses, the higher summer values also appear to spread out to the pole of the summer hemisphere and into the winter hemisphere. The horizontal transport caused by the South Asian monsoon is stronger than other monsoon circulations, leading to more water vapour in the upper troposphere during boreal as opposed to austral summer.

At the tropical tropopause, a complex mix of processes act to remove water vapour from air as it enters the stratosphere from the troposphere below. Within the framework of large-scale mean ascent, the dehydration processes probably include smaller-scale (convective) ascent, radiative and microphysical processes within clouds, and wave-driven fluctuations in temperature. The location, strength, and relative importance of these processes vary seasonally. However, the observed seasonal variation in tropopause-level water vapour is influenced primarily by the annual variation in tropical tropopause

temperatures. Air rising through the tropopause is marked with seasonally varying mixing ratio, and retains these markings as it spreads rapidly poleward and more slowly upward into the stratosphere.

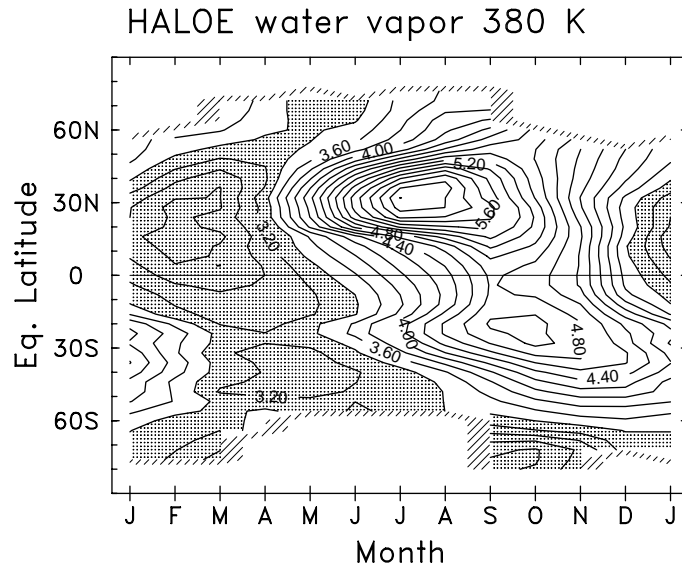


**Figure 3** Latitude-time evolution of water vapour mixing ratio near 380 K derived from seasonal cycle fits of the HALOE data.

### Upper troposphere

Upper tropospheric water vapour in the tropics and subtropics is strongly influenced by the Hadley Cell and the Walker Circulation. The predominant source for moisture in the tropical and subtropical upper troposphere is convection, producing, on average, moist regions in the convective areas over the western Pacific, South America and Africa (Figure 4). Moist areas also appear seasonally in the region of the Asian summer monsoon and along the intertropical and South Pacific convergence zones. The seasonality of surface temperature and of convection, which roughly follow the sun, as well as seasonal variations in monsoon circulation, produce concomitant seasonal changes in water vapour in the troposphere. This relationship between convection and upper tropospheric moisture changes sign near the tropical tropopause, somewhere between 150 hPa and 100 hPa, so that convection dries the tropopause region. Water vapour is also influenced by fluctuations at both shorter and longer time scales, including the quasi-biennial oscillation in the stratosphere and the El Niño-Southern Oscillation and the Tropical Intraseasonal Oscillation in the troposphere.

Upper tropospheric water vapour at middle and higher latitudes is highly variable and can be supplied by transport from the tropics, by mesoscale convection, or by extratropical cyclones. Dry air can be transported from the subtropics or from the extratropical lower stratosphere. These transport phenomena tend to be episodic rather than steady.

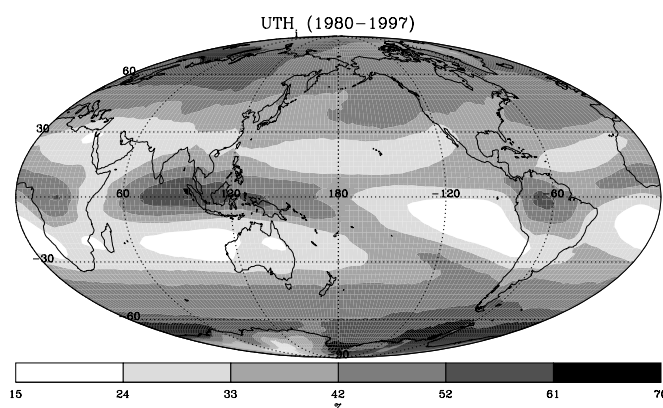


**Figure 4** Annual mean Upper Tropospheric Humidity over ice (UTHi) averaged for 1980-1987 from HIRS instruments, in percent.

### Long-term changes

#### Stratosphere

There is only one nearly continuous time series of stratospheric water vapour with a duration of 20 years, made using a single instrument type, and available for the determination of long-term change. Although differences between instrument systems were largely determined to fall within their stated uncertainty estimates, those differences are still too large to combine various instrument records to construct a longer time series. However, a number of data sets used in the assessment sampled the atmosphere periodically over a long period providing several time series of intermediate length (8-15 years). These were used in combination to estimate stratospheric changes. The observations are consistent in suggesting that water vapour has increased at a rate of about 1%/year over the past 45 years (Figure 5). The record also suggests that this increase has not been uniform but has varied over this period.

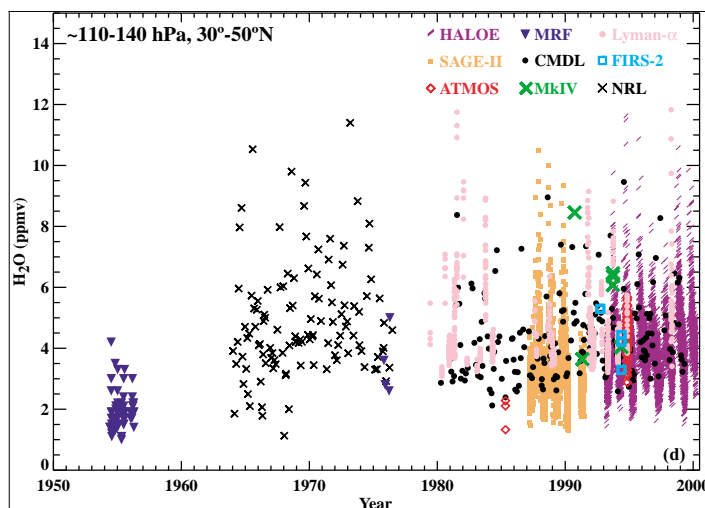


**Figure 5** Time series of Water vapour measurements made by several instruments between 30-50°N over the pressure range 110-140 hPa. Data plotted are individual measurements with the exception of NOAA-AL Lyman- $\alpha$  (1 minute averages). Data below 100 hPa have been screened to omit tropospheric measurements.

## Upper troposphere

The longest data set of upper tropospheric humidity is one that is derived from the HIRS instrumentation on different TOVS satellites. The HIRS instruments cover a time period of nearly twenty years. A linear fit of relative humidity from 1979 to present is shown in Figure 6. The trends for different latitudinal bands, and especially in the deep tropics, are slightly positive but insignificant at the 99% confidence level.

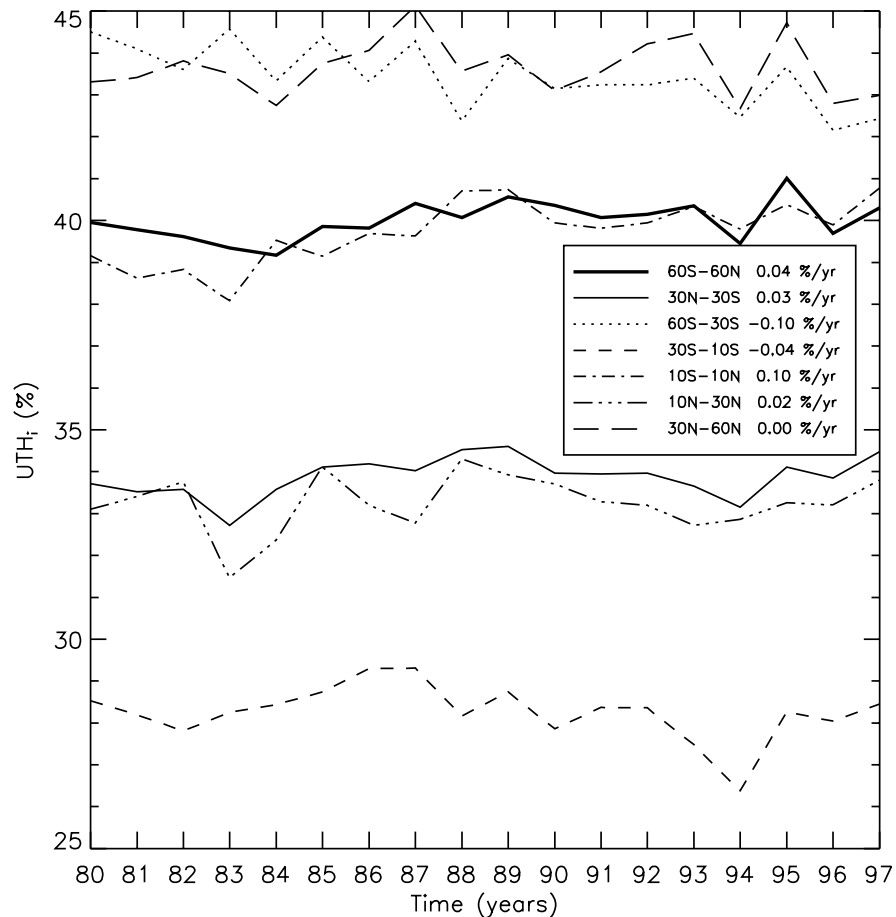


**Figure 6** Annual mean upper tropospheric humidity over ice from HIRS for various latitude bands and linear fit statistics from 1980 to 1997: 60°S-60°N (solid line), 60°S-30°S (dotted line), 30°S-10°S (dashed line), 10°S-10°N (dot-dash line), 10°N-30°N (dash-3dots line) and 30°N-60°N (long dashed line).

A shorter time series of UTH, 1992 to present, has been obtained using the MLS instrument. Figure 7 shows the MLS humidity for centre altitudes of 147 and 215 hPa over the latitude range 30°S-30°N. For the overlapping time period both data sets show a minimum in relative humidity that occurs in 1994 although the MLS minimum is shallower.

When combined with satellite-derived upper tropospheric temperature data which also show a small positive trend since 1979, the HIRS data imply a larger positive specific humidity trend, but the combination of uncertainties in these two types of measurements means that the uncertainty in specific humidity is large enough to hide trends that are significant to climate.

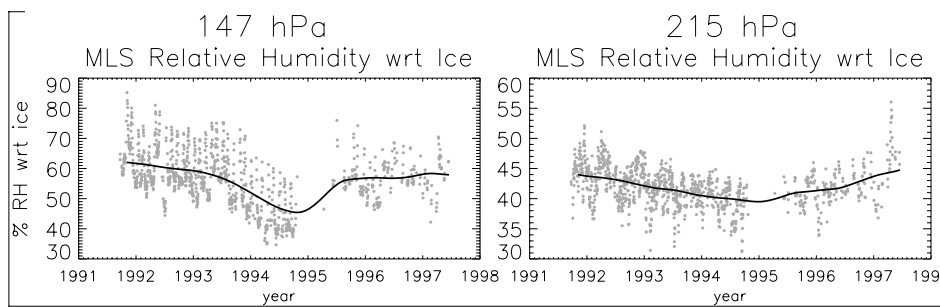


**Figure 7** MLS relative humidity over ice. Data were averaged between 30°S and 30°N. The figure on the left represents a 3 km layer around 147 hPa and that on the right a 3 km layer around 215 hPa. Dots are daily averages and the line is a 12-month running mean boxcar filter to remove the annual cycle.

## Recommendations

1. Further studies, including well designed intercomparison experiments and laboratory work, are required to quantify and understand the differences between stratospheric water vapour sensors. This is particularly important for *in situ* instruments. *In situ* instruments are critical for obtaining high-resolution data for use in process studies of water vapour transport between the troposphere and stratosphere. Strong validation programs including correlative measurements need to be a part of water vapour satellite measurement efforts. In the upper troposphere, such validation has not been a part of the measurement program. Improvement of radiosonde observations of water vapour and wider use of LIDAR would aid in such validation.
2. Greater attention needs to be paid to the continuity of measurements for determination of long-term changes in both the stratosphere and upper troposphere. It is important to have complementary observations, not relying solely on one instrument or approach. To better quantify dynamical effects that can impact long-term changes, all stratospheric measurements, whether satellite or *in situ*, should be combined with simultaneous methane measurements. Maintaining current long-term *in situ* measurement programs is necessary for any interpretation of long-term change. Stratospheric water vapour should be monitored *in situ* at various latitudes and in particular in the presently data sparse tropics and Southern Hemisphere. Satellite sensors with a history of high quality measurements should be included in future satellite missions in order to monitor long-term changes in stratospheric and upper tropospheric water vapour. Upper tropospheric specific humidity should be monitored with a view to determining long-term trends. To determine these trends effectively, the sequence of future satellite missions should be planned to provide overlap with existing instruments in orbit.
3. Process studies of upper tropospheric water vapour and convection should be undertaken. These would include joint measurements of water vapour, cloud microphysical properties, and chemical species that can provide a history of the air. More observations of the tropical tropopause region (15-20 km), by both *in situ* and remote sensing methods, are needed in order to improve our understanding of stratosphere-troposphere exchange there.
4. Data sets collected in the future should be added to those already archived for the purposes of this assessment at the SPARC Data Center: <http://www.sparc.sunysb.edu>. Valuable data from the 1940's, 1950's, and 1960's may already be lost, but some could and should be rescued.

---

## Foreword

This scientific assessment has been carried out by the WCRP project on Stratospheric Processes and their Role in Climate (SPARC). The objective of the report is to critically review measurements of water vapour in the stratosphere and upper troposphere, in order to consolidate our knowledge and understanding of the distribution of water vapour and its variability on time scales ranging from the seasonal to the long-term inter-annual.

Considering the fundamental role of water vapour in climate, and the scarcity of information concerning its distribution, variability and long-term evolution, the need for such an assessment was recognised by the SPARC Scientific Steering Group. The lack of knowledge on water vapour also leads to a large uncertainty in the prediction of climate change. One of the objectives of the assessment was therefore to support the Third IPCC Assessment Report on Climate Change due to be published in 2001.

Great effort has been made to prepare the best data sets possible, to retrieve historical data sets, and to make them all available to the assessment team. This report contains an extensive description of the measurements and their associated uncertainties, an assessment of data quality based on comparison studies of the various data sets, and a description of the understanding of the distribution and variability of water vapour in the stratosphere and upper troposphere which ensues from the data. Finally, recommendations are made to ensure that the difficulties met during this work are overcome in order that the remaining uncertainties in our knowledge and understanding can be resolved. The preceding summary also appears in SPARC Newsletter number 16 (January 2001).

The outline of the assessment was determined during an international workshop held at NCAR, Boulder, Colorado, USA, 26-28 August 1998. The drafts of the chapters were prepared in the following year and a number of new data sets were produced. The first draft report was examined by an international panel of reviewers both by mail peer review and at a meeting in Paris, France in January 2000. During the review meeting the responses to the mail review comments were proposed by the authors and discussed by the participants. This rigorous review greatly improved the report, the contribution of the reviewers being significant. A second draft report was reviewed by mail review in August 2000.

The success in producing the Report is the result of the intensive work and enthusiastic co-operation of a large number of scientists world-wide who have worked towards improving the quality of the measurements and our understanding of the observations. The work of the contributors and reviewers was generously supported by many organisations and agencies including WMO, WCRP, SPARC, DG Research of the European Commission, NASA, NOAA, NCAR, CNRS, CNES, Forschungszentrum Jülich, Imperial College and other national research programmes and institutions.

We take this opportunity to express our gratitude to all the scientists (authors, contributors and reviewers) who helped in the preparation of this assessment and to the SPARC scientific steering group who have been supportive since its inception. Our special gratitude is due to the lead authors of the chapters. Particular thanks must be given to: Petra Udelhofen at the SPARC Data Center for setting up the data archive, Sam Oltmans who organised the workshop at NCAR, Boulder, Colorado; Computational Physics Inc., for hosting the workshop in Washington D.C.; François Dulac from the CNES for hosting the review meeting in Paris, and Céline Phillips for her co-editorship. We also thank Marie-Christine Gaucher at the SPARC office for her help in the organisation of the review meeting in Paris and in the final editing of

the report and Catherine Michaut at the SPARC office for her help in editing the second peer-review draft and the final draft of the report.

Dieter Kley  
Forschungszentrum Jülich  
Germany  
Assessment Co-Chairs

James M. Russell III  
Hampton University  
USA

---

## Introduction

Water makes the Earth unique. Life, the climate and the weather all exist as they do because gaseous, liquid and solid forms of water can co-exist on the planet. The oceans, the ice masses, the clouds and the humidity of the atmosphere all play major roles in climate and weather [Peixoto and Oort, 1996]. The water vapour distribution in the upper troposphere (UT) and lower stratosphere (LS) is of central importance in several ways: it plays a major role in the balance of planetary radiation; it influences and responds to atmospheric motions; and it plays a key role in many aspects of UT/LS chemistry. Effects on the radiation balance are especially important because the water vapour molecule is strongly polar in shape giving it a strongly absorbing infrared spectrum. Consequently, it is the single most important “greenhouse gas” in the atmosphere, molecule-for-molecule. Harries [1997] pointed out that, because the effects of water vapour on the Earth radiative balance are so large, small errors in spectroscopic parameters and in radiative-dynamical models used to model the energy balance, can produce potentially large uncertainties in the prediction of climatic change. He presented evidence from sensitivity studies showing that the humidity concentration, particularly in the upper troposphere may need to be known with an accuracy in the range of 3-10% in order to avoid uncertainties in calculated radiative forcing that are of the order of the effect due to doubling CO<sub>2</sub> concentrations. Forster and Shine [1999], extending earlier work of Rind and Lonergan [1995], calculate that if the increase in the lower stratospheric H<sub>2</sub>O mixing ratio reported over Boulder, Colorado, from 1979 to present, by Oltmans and Hofmann [1995] is occurring globally, the contribution to surface warming would be 40% of that from the CO<sub>2</sub> increase over the same time period. Forster and Shine also emphasised that an increase of water vapour causes a cooling of the lower stratosphere that is comparable to the contribution due to ozone changes. These facts emphasise the urgent need to understand and assess the state of knowledge of atmospheric water vapour. In view of the potential effects on climate change, it is especially important to assess and attempt to understand long-term changes and decadal scale trends in water vapour.

Despite its abundance in the atmosphere and its importance for the climate system, many questions regarding H<sub>2</sub>O are presently unresolved. For example, the important question of feedback between water vapour mixing ratio in the upper troposphere and surface temperature is still unanswered. While increased temperature leads to increased moisture and further warming because of the “greenhouse” effect, it is unclear whether the warming produces more water due to further evaporation (positive feedback) or if the attendant increased upwelling causes a drying (negative feedback). Results of calculations by Manabe and Wetherald [1967] from a radiative-convective model with constant humidity suggested that the exponential increase of absolute humidity due to the sea surface temperature rise would exert a strong positive feedback. Other analyses from complex general circulation models are generally consistent with Manabe’s and Wetherald’s conclusions showing similarly large positive feedback. Ellsaesser [1984] on the other hand, argued that an increase in the strength of convection in the tropics would cause an increase in the Hadley Cell circulation. An increase in the strength of the circulation will lead to drying or negative feedback, rather than a moistening of the upper troposphere [Ellsaesser, 1984, Lindzen, 1990, and Sun and Lindzen, 1993]. In short, as far as the greenhouse effect and climatic change are concerned, it is still not clear whether thermodynamics or dynamics controls tropospheric water vapour.

Atmospheric water vapour is abundant in the atmosphere and possesses absorption features spread over a broad range of the electromagnetic spectrum. Therefore, it should be easy to measure. However, in practice, water vapour measurements have proved to be difficult. Water sticks to surfaces, thereby providing challenges for *in situ* techniques. Sharp vertical and

horizontal gradients present difficulties for remote sensing techniques. A lack of understanding of the fundamental physics behind the observed spectrum complicates the analysis of remote sensing measurements. The radiative effects of clouds are yet another complicating factor in making water vapour measurements. Consequently, our understanding of the distribution of upper tropospheric and lower stratospheric water vapour is not as thorough as it should be.

The importance of water vapour and the fact that an assessment of current knowledge has not been undertaken before, led the Scientific Steering Group of the international research project on Stratospheric Processes and their Role in Climate (SPARC), a project of the World Climate Research Programme (WCRP), to initiate and sponsor the study documented in this report. Four key points were noted:

- (1) The global, regional and seasonal distribution of water vapour in the UT/LS region of the atmosphere is not known with sufficient accuracy to validate climate models.
- (2) It is important to examine what can be said about long-term change of the water vapour concentration in the UT/LS by analysing existing *in situ* and satellite data sets from a common vantage point.
- (3) The various reports of the Intergovernmental Panel on Climate Change (IPCC) [IPCC, 1991, 1993, 1995] have all stressed the role of water vapour as a powerful greenhouse gas. However, the question of the magnitude and perhaps even the sign of the water vapour feedback still represents probably the single largest uncertainty in the quest for accurate prediction of global and regional warming caused by an increase of CO<sub>2</sub> concentration.
- (4) It is expected that new data requirements on both water vapour and related parameters (e.g. temperature) will come out of an assessment process, as has been the case for the SPARC Ozone Assessment [SPARC, 1998].

As an introduction to the report, we present a brief synopsis of the evolution of knowledge on the content and distribution water vapour. Key processes that influence these aspects of water vapour are only briefly discussed here, but more detail is provided in chapter 3.

## Water Vapour in the Stratosphere

The extreme dryness of the stratosphere was first discovered by Brewer and his colleagues using data collected in the British Meteorological Research Flight (MRF) program with a manually operated frost-point hygrometer taking measurements over Southern England [Brewer, 1949; Bannon *et al.*, 1952]. These flights started in 1943 and continued sporadically till the early 1980's. During the first flights in the 1940s, they found tropopause frost point temperatures of  $-58^{\circ}\text{C}$  ( $\sim 55$  ppmv near 250 hPa), and mixing ratios  $\sim 2$ km above the tropopause as low as 1.6 ppmv. The MRF flight series continued through the early 1960's, then resumed again in the 1970's and early 1980's [Murgatroyd *et al.*, 1955; Helliwell *et al.*, 1957; Cluley and Oliver, 1978; Foot, 1984]. Oliver and Cluley [1978] identified a  $-0.6^{\circ}\text{C}$  temperature error in the early MRF frost point measurements. After the application of an appropriate temperature correction, the mean "representative stratospheric humidity (r.s.h.)"<sup>1</sup> in the 1950's was  $\sim 3$  ppmv while that in the 1970's was  $\sim 5$  ppmv.

---

<sup>1</sup> Oliver and Cluley [1978] define r.s.h. as those values of mixing ratio that, having been measured above 187 hPa, were the least influenced by higher mixing ratios in the vicinity of the underlying tropopause.

The first balloon-borne *in situ* and remote observations of stratospheric water vapour were reported in the literature of the 1960's. Results were mixed with some measurements indicating a considerable increase of water vapour mixing ratio with altitude above the tropopause and others showing little or no change. The controversy was reviewed by Gutnik [1961]. It was later understood that out-gassing of water vapour from the balloon skin during ascent, when most of the measurements were made, caused water vapour contamination of the *in situ* sensors or the atmosphere in the vicinity of the rising or floating balloon.

Mastenbrook, from the U.S. Naval Research Laboratory, adapted the frost-point hygrometer for use on stratospheric balloons. He undertook a series of soundings from 1964 to 1979 over Washington, D.C. and conducted a two-year measurement series from 1964 to 1965 in tropical air over Trinidad, West Indies, [Mastenbrook, 1968, 1971, 1974, Mastenbrook and Daniels, 1980]. Mastenbrook's data showed that the aridity of the stratosphere extended vertically up to the maximum reachable levels of his balloons, about 28 km, thereby settling the question of whether the stratosphere was "wet" or "dry". Whether there was a small increase of the mixing ratio with altitude over and above the values found in the lower stratosphere was not so much a concern at that time. The question was whether or not there was a substantial increase of the water vapour mixing ratio with altitude. For example, Sissenwine *et al.* [1968] had reported water vapour mixing ratio increases at 32 km about 6 times higher than values in the lower stratosphere. The 1976 U.S. Standard Atmosphere [U.S. Standard Atmosphere, 1976] reflects the uncertainty that prevailed at the time on this issue and lists two alternative vertical profiles.

The U.S. Naval Research Laboratory series of balloon soundings lasted until 1979 when the measurement program was handed over to NOAA in Boulder, Colorado. It has continued since 1980 [Oltmans and Hofman, 1995, Oltmans *et al.*, 2000]. Just prior to the change from Washington to Boulder a switch to more modern electronics was also made which resulted in reduced scatter and improved time-height resolution of the instrument. Results from the Boulder soundings confirmed the principal earlier Mastenbrook results of a long-term strong seasonal change of water vapour mixing ratio in the lower stratosphere with maxima in summer. In addition, a positive trend of water vapour mixing ratio in the stratosphere of about 1% per year, which had been discovered by Mastenbrook over Washington D.C., was also found over Boulder.

The Lyman- $\alpha$  hygrometer, a new *in situ* instrument for the measurement of upper tropospheric and stratospheric water vapour, was introduced in 1978 [Kley and Stone, 1978, Bertaux and Dellanoy, 1978]. Using this technique Kley *et al.* [1979] showed that there is an increase of water vapour mixing ratio with altitude in the stratosphere. A tropical sounding over Brazil revealed the fact that an absolute minimum of water vapour mixing ratio, termed the hygropause, is located some 2-3 km above the tropical tropopause [Kley *et al.*, 1979]. The minimum mixing ratio of 2.6 ppmv was later corrected down to 2.3 ppmv [Kley *et al.*, 1983].

Global satellite measurements of water vapour commenced in 1978. The results from the Limb Infrared Monitor of the Stratosphere (LIMS) experiment on the Nimbus 7 satellite [Russell *et al.*, 1984; Remsberg *et al.*, 1984] extended the *in situ* measurements from 84°N to 64°S. The increase of the mixing ratio with altitude was confirmed and the measurements were extended to 55 km. LIMS also showed the hygropause to be a general feature of the tropical stratosphere. Work to combine the observations from different satellite instruments has proved valuable. For example the work by Jones *et al.* [1986] to merge water vapour from the LIMS experiment with CH<sub>4</sub> measurements provided by the Stratospheric And Mesospheric Sounder (SAMS) experiment on the same satellite resulted in the first global view of total hydrogen<sup>2</sup> variability

---

<sup>2</sup> A more correct definition of total hydrogen is  $2\text{CH}_4 + \text{H}_2\text{O} + \text{H}_2$ . However, the mixing ratio of molecular hydrogen (0.5 ppmv) is virtually constant and hydrogen is usually not included in the sum.

( $2 \times \text{CH}_4 + \text{H}_2\text{O}$ ). The Atmospheric Trace Molecule Spectroscopy (ATMOS) series of missions on several flights of the Space Shuttle [Farmer and Raper, 1986, Gunson *et al.*, 1990] confirmed the LIMS and SAMS findings.

Long-term satellite observations of stratospheric water vapour concentration began in 1986 with the Stratospheric Aerosol and Gas Experiment II (SAGE II) [McCormick *et al.*, 1993, Chiou *et al.*, 1997]. Due to a strong sensitivity of the SAGE II water vapour retrieval algorithm to aerosol interference and the Pinatubo volcanic eruption that put large amounts of aerosols into the stratosphere, the continuous record was interrupted in 1991. The Halogen Occultation Experiment (HALOE) was launched in 1991 and has provided nearly continuous measurements of water vapour over the pressure range from 0.01 down to 200 hPa [Russell *et al.*, 1993; Harries *et al.*, 1996]. Several other satellite, shuttle borne, and balloon instruments were operated during the 1980s and 1990s. These will be discussed in detail in subsequent chapters of this report.

## Water Vapour in the Upper Troposphere

Water in the troposphere occurs in all the possible aggregate states: liquid, gaseous and solid. The strong dependence of water vapour partial pressure on temperature, the fact that atmospheric temperatures from ground to tropopause span a range of some 60°C, and that transport in the troposphere is rapid, combine to cause large variability in tropospheric water vapour mixing ratios that are quantitatively difficult to understand. Moreover, very few methods exist to measure upper tropospheric water vapour mixing ratio (specific humidity) and relative humidity with high accuracy. Water vapour soundings by the operational national radiosonde networks do not produce high quality data in the upper troposphere. Research balloons and research aircraft have yielded a fair amount of information. However, compared to the large variability of upper tropospheric humidity on a variety of spatial and temporal scales, the database obtained by *in situ* techniques is inadequate. Satellite techniques, which are less influenced by spatial constraints, have begun to contribute to our knowledge.

Tropospheric water vapour concentrations are strongly coupled to dynamics and to temperature. Although the water vapour partial pressure of ascending air is not known to exceed saturation with respect to the liquid phase, water vapour concentrations can still vary by more than 4 orders of magnitude between the ground and the tropical tropopause. In the upper troposphere where temperatures are persistently below -40°C, it is convenient to relate the water vapour concentration to relative humidity with respect to ice (RH<sub>i</sub>). Based on tropical *in situ* observations, it has been found that upper tropospheric RH<sub>i</sub> is close to 100% over convective regions and RH<sub>i</sub> is often less than 10% in regions with subsidence [Kley *et al.*, 1997]. However, formation of ice hydrometeors depends on the availability of ice condensation nuclei and on microphysics. Supersaturation (RH<sub>i</sub> > 100%) has been observed, probably caused by the virtual absence of aerosols that can act as nucleation centres. Jensen *et al.*, [1999] showed that supersaturation occurs below the tropical tropopause. Over mid-latitudes of the Northern Hemisphere large persistent supersaturations of up to 150% are a common occurrence [Gierens *et al.*, 1999]. Generally speaking, because of the upper limit on the water vapour partial pressure, set by the temperature dependent phase equilibrium between vapour and condensate, the maximum tropospheric water vapour mixing ratios are strongly coupled to atmospheric temperature. Hence, the water vapour mixing ratios tend to undulate with seasonally varying temperature, modified by meteorological processes which, together, can produce changes of relative humidity from a few to one hundred percent.

Relatively few papers appear in the literature describing the upper tropospheric water vapour large and small scale distribution and seasonal, annual and longer time scale changes. Moreover,

when we consider that the radiosonde network has not, and does not, provide accurate information on upper tropospheric water vapour, we are left with few data sets, especially those of a regional or global nature. *Kelly et al.*, [1991] found lower mixing ratios in the upper troposphere at middle to high latitudes of the southern hemisphere than those at the equivalent winter season of the northern hemisphere. *In situ* measurements from high quality research balloons or aircraft have provided sporadic data on upper tropospheric water vapour. They have shown that a strong seasonal cycle of upper tropospheric water vapour mixing ratio exists at mid-latitudes with a summer maximum and a winter minimum. This information comes from measurements over southern England, Washington and Boulder [*Oliver and Cluley*, 1978, *Mastenbrook and Daniels*, 1980, *Oltmans and Hofmann*, 1995]. *Dethof et al.*, [1999] showed that the surface topography has an impact on the dynamics of the UT/LS region and on the transport of water vapour into the stratosphere. *Duhnke* [1998], in the line of earlier work by *Briggs and Roach* [1963], investigated upper tropospheric water vapour mixing ratio and relative humidity in the coordinate system of the north Polar jet stream and found a downward transport of dry stratospheric air through the tropopause on the cyclonic side and an upward transport of high water vapour mixing ratio into the stratosphere on the anticyclonic side of the jet stream.

*Bates et al.*, [1996], used information from the Tiros Operational Vertical Sounder (TOVS) instruments to construct a quasi-global picture of upper tropospheric relative humidity. Unfortunately, the TOVS humidities are weighted over a fairly deep vertical altitude range and they are not well validated. The Microwave Limb Sounder (MLS) on the Upper Atmosphere Research Satellite (UARS) has produced results on the large scale distribution and time variability of upper tropospheric water vapour [*Stone et al.*, 2000] and can be used to determine the vertical distribution of upper tropospheric relative humidity with a resolution of approximately 3 km. *Sandor et al.*, [1998] presented the seasonal distribution of tropical to mid-latitude upper tropospheric relative humidity, derived from the MLS product. *Newell et al.*, [1996b, 1997] analysed MLS-derived upper tropospheric humidity fields and found moist plumes in tropical air over regions with rising motion and dryness in sinking regions. Based on their analysis, they concluded that a substantial fraction of upper tropospheric humidity to the west of South America originates over the South American continent. They also found a positive relationship between the zonal mean tropical moisture and Eastern Pacific sea surface temperature. *Zhu et al.* [2000] found from further MLS UT/LS analysis that the moisture in the tropical upper troposphere is mainly increased by intensified small-scale local convection.

## Chemical processes

The primary process for the increase of the water vapour mixing ratio with altitude in the stratosphere is photochemical CH<sub>4</sub> oxidation [*Brasseur and Solomon*, 1984; *LeTexier et al.*, 1988]. Oxidation of methane leads predominantly to production of H<sub>2</sub>O and to a small extent H<sub>2</sub>. The proportion of each molecule produced is a function of altitude and latitude and is dictated mainly by the age of air relative to the chemical lifetimes of the gases involved. Generally, one CH<sub>4</sub> molecule will lead to production of approximately two H<sub>2</sub>O molecules. Entry level air from the troposphere in the 1990's carried ~1.7 ppmv of CH<sub>4</sub> into the stratosphere [*Dlugokencky et al.*, 1998].

## Transport from the troposphere to the stratosphere

Progress in understanding the processes that control atmospheric water vapour and exchange between the troposphere and stratosphere has been slow. A major advance was provided by *Brewer* [1949] who used observations of low H<sub>2</sub>O mixing ratio in the stratosphere over Southern England to propose that influx to the stratosphere occurs by slow, large-scale

upwelling through the tropical tropopause where the water vapour partial pressure is in equilibrium with the ice phase. At a tropical tropopause temperature of  $-80^{\circ}\text{C}$  at 100 hPa the corresponding mixing ratio is 5.4 ppmv. Egress from the stratosphere occurs in conjunction with large-scale downward motion through the extratropical tropopause where the downward directed advective flow of air counteracts the effects of eddy diffusion which, in the absence of the advective component of the flow, would seed the stratosphere with much higher water vapour mixing ratios as they prevail in equilibrium at the higher extratropical tropopause temperatures. *Newell and Gould-Stewart* [1981] extended this picture by arguing that the tropical tropopause is generally too warm to explain the extremely dry stratosphere. Based on this, they further narrowed the region where air slowly ascends into the stratosphere to those regions and times in which the tropical tropopause is much colder than average. These include the western tropical Pacific, northern Australia, and Indonesia during the November to March period and over the Bay of Bengal and India during the monsoon. This space and time limited region has become known as the “stratospheric fountain”. *Atticks and Robinson* [1983] and *Frederick and Douglass* [1983] on the other hand showed results that were compatible with the idea that water enters the stratosphere year-round at all longitudes except  $0^{\circ}$  to  $30^{\circ}\text{W}$ . Later, results from satellite and *in situ* instrumentation (HALOE, MLS, SAGE II and Lyman- $\alpha$ ) [e.g. *Mote et al.*, 1996; *Weinstock et al.*, 1995] were published supporting the idea that air enters the stratosphere not just at limited times, but throughout the entire year. Satellite results showed that the tropical lower stratosphere is continually being modulated on an annual cycle with water vapour entering from below at values governed by the tropopause temperature. This phenomenon has been termed the “atmospheric tape recorder” [*Mote et al.*, 1996].

The observations of a minimum water vapour mixing ratio above the tropical tropopause over Panama [*Kley et al.*, 1979] and those that support a minimum in  $\text{H}_2\text{O}$  in the Western tropical Pacific very near the tropopause [*Kelly et al.*, 1993; *Rosenlof et al.*, 1997; and *Jackson et al.*, 1998] suggest that the process of exchange is more complicated than the “fountain” theory implies. While other plausible ideas have been put forward such as overshooting deep convection [*Danielsen*, 1982], no scientific consensus exists on what the dominant processes are that transport air across the tropical tropopause to the stratospheric “overworld”, the region consisting of isentropes (surfaces of constant potential temperature) that lie above the tropopause everywhere.

## Mechanisms of troposphere-stratosphere exchange in the tropics

The current view on transport of trace gases between the low stratosphere ( $\Theta < \sim 380\text{ K}$ ) and the “overworld”,  $\Theta > 380\text{ K}$ , is based on the top-down control principle of *Haynes et al.*, [1991] and expressed in a review article by *Holton et al.*, [1995]. According to *Holton et al.*, wave-induced forces in the extratropical overworld drive a global scale extratropical fluid-dynamical suction pump which draws air upward and poleward from the tropical lower stratosphere and pushes it poleward and downward into the extratropical troposphere. An important point in *Holton’s* review is the implication that the tropical troposphere-stratosphere exchange rate is not determined by details of near-tropopause phenomena, such as penetrating cumulus convection or small scale mixing. That is, non-local forces that drive the general circulation also control the global troposphere - to - stratosphere rate of transport.

## Goals and Purposes of this Report

The overall goal of this study is to provide a current assessment of the state of knowledge of the water vapour distribution, variability and long-term changes. While there is some review of the literature included in the report it is minimal and only used where needed to aid the assessment process. The same is true of historical records, references and limited measurement campaigns.

---

Results from short campaigns are applied where needed to assist in validating the data used for the assessment. The report is organised into three chapters. Chapter 1 describes the physical parameters measured, algorithms used, estimated errors, potential drifts, data record length, measurement frequency and spatial resolution for each instrument. This is an essential aid in assessment of data quality and interpretation of intercomparisons. Chapter 2 provides definitive statements regarding data quality for each measurement system used in the study, it shows how results intercompare with one another, discusses what the limitations are in vertical resolution, altitude and latitude and provides an overall description of what can and cannot be believed in the distributions and long-term changes. Chapter 3 provides a description of what is known about H<sub>2</sub>O in the context of the findings of chapters 1 and 2. It describes geographic distributions as a function of altitude, latitude and longitude in the Northern and Southern Hemispheres, seasonal cycles and the effects of the Quasi-Biennial Oscillation (QBO), El Nino and the Southern Oscillation (ENSO) and Tropical Intraseasonal Oscillation (TIO) on the water vapour distribution. It also discusses stratospheric entry level mixing ratios and long-term changes. Summaries, conclusions and recommendations are provided as needed in each chapter.

# Chapter 1

## Instrumentation

and

## Data Sets

### **Lead Authors**

E. Remsberg – C. Schiller

### **Co-authors**

J. J Bates - R. Bevilacqua - E. Browell - E.W. Chiou - W.P. Chu - G. Ehret  
D. Feist - D. Gaffen - L. Gordley, M.R. Gunson - P. Hartogh - M. Helten  
R. Herman - E. Hintsa - F. Irion - S. Ismail - D. Johnson - N. Kämpfer  
H. Kanzawa - K.Kelly - D. Kley - R. May - M. McHugh - H.A. Michelsen  
L. Miloshevish - G. Nedoluha - H. Oelhaf - S. Oltmans - J. Ovarlez  
H. Pumphrey - W. Read - G. Sachse - V. Sherlock - H. Smit - G. Toon - H. Vömel  
J. Waters - E. Weinstock - D. Whiteman

### **Contributors**

A. Chedin - D.H. Ehhalt - V. Yushkov,

## 1.1 Introduction

Measurements of water vapour in the upper troposphere and in the stratosphere require tremendous technical effort due to the large gradients around the tropopause and the low stratospheric mixing ratios of a few ppmv in contrast to the moist tropospheric air masses. Further, in the stratosphere, the spatial and temporal variability of the H<sub>2</sub>O abundance is relatively small, i.e. changes of a few tenths of 1 ppmv need to be detected with a similar accuracy of the measurement.

No single existing instrument is capable of H<sub>2</sub>O measurements at all altitudes, with adequate global and temporal coverage. A combination of different instruments and techniques is necessary in order to meet the objectives of this Assessment. Owing to the importance of water vapour in the atmosphere, a large number of techniques for its measurement from different platforms have been developed and are used both for mechanistic case studies and the determination of its climatological distribution. Figure 1.1 shows a diagram of the altitude range and platforms for the most important techniques.

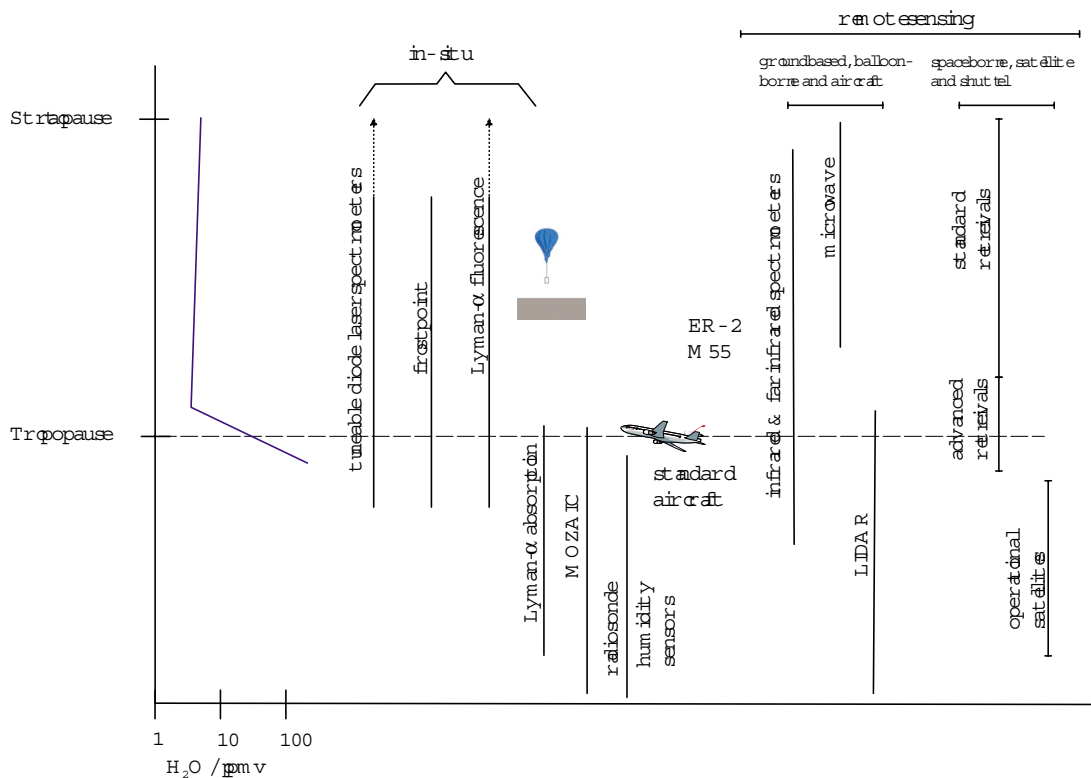


Figure 1.1 Typical vertical profile of water vapour in the upper troposphere and the stratosphere, the altitude range where the techniques described in this Assessment can be applied, and the carriers available for integration of the different instruments.

The purpose of this Chapter is to describe individual well characterised hygrometers for the upper troposphere and the stratosphere that produced data used in the following Chapters of this Assessment. Emphasis is put on the description of instrument quality parameters such as accuracy and precision as determined from laboratory and field studies, the description of the calibration procedures, and technical differences between the instruments. For a detailed description of the applied techniques of each instrument the reader is referred to the literature. It is not intended and not possible to give a complete review of all hygrometers used up to now,

---

and no instruments that are still under development or which are not described in the peer reviewed literature are included. However, this summary of the most advanced instruments may provide an update and complement to previous reviews and summaries such as those of *Wexler and Ruskin* [1965] and *Deepak et al.* [1980].

Absolute calibration of hygrometers is crucial but very difficult, in particular at low mixing ratios of a few ppmv or frost points of  $-60^{\circ}$  to  $-80^{\circ}\text{C}$  as occur in the UT/LS. In this Chapter it is described to which reference the absolute calibration of each instrument is traceable. Primary standards for humidity measurements are gravimetric hygrometers and precision humidity generators, the latter based on saturating air with respect to water or ice at a given temperature. Reviews of these methods, which have been developed in the middle of this century and continuously improved, are given by *Wexler and Wildhack* [1965] and more recently by *Sonntag* [1994] and *Wiederhold* [1997]. Often, chilled mirror hygrometers are used as calibration standards since they are based on a fundamental hygrometric technique. Absorption cross sections of  $\text{H}_2\text{O}$  and interfering trace gases in the vacuum ultraviolet (VUV) and infrared (IR) spectral region have been calculated or determined based on such techniques and are used for calibration of a large number of instruments. For some instruments, a combination of different calibration methods is applied. Further possible error sources such as contamination and sampling problems which affect the *in situ* hygrometers and retrieval algorithms for the remote sensing instruments are discussed.

Another focus of this Chapter is to list available data sets obtained with the described instruments. An overview of the data sets from aircraft, balloons and the ground since 1970 is given in Figures 1.2a and b for the tropopause region and for the stratosphere, respectively. Data obtained before 1980 have to be regarded as ‘historic’ since they are available from published reports only; however, some of these data sets have been re-evaluated and digitised recently. A corresponding Table for satellite data sets is given in Section 1.4.1 (Table 1.22). The following Chapters are based on the data sets listed in these Tables. Most of them are archived at the SPARC Data Center (<http://www.sparc.sunysb.edu>) and can be made available by SPARC and/or by the respective principal investigator upon request.

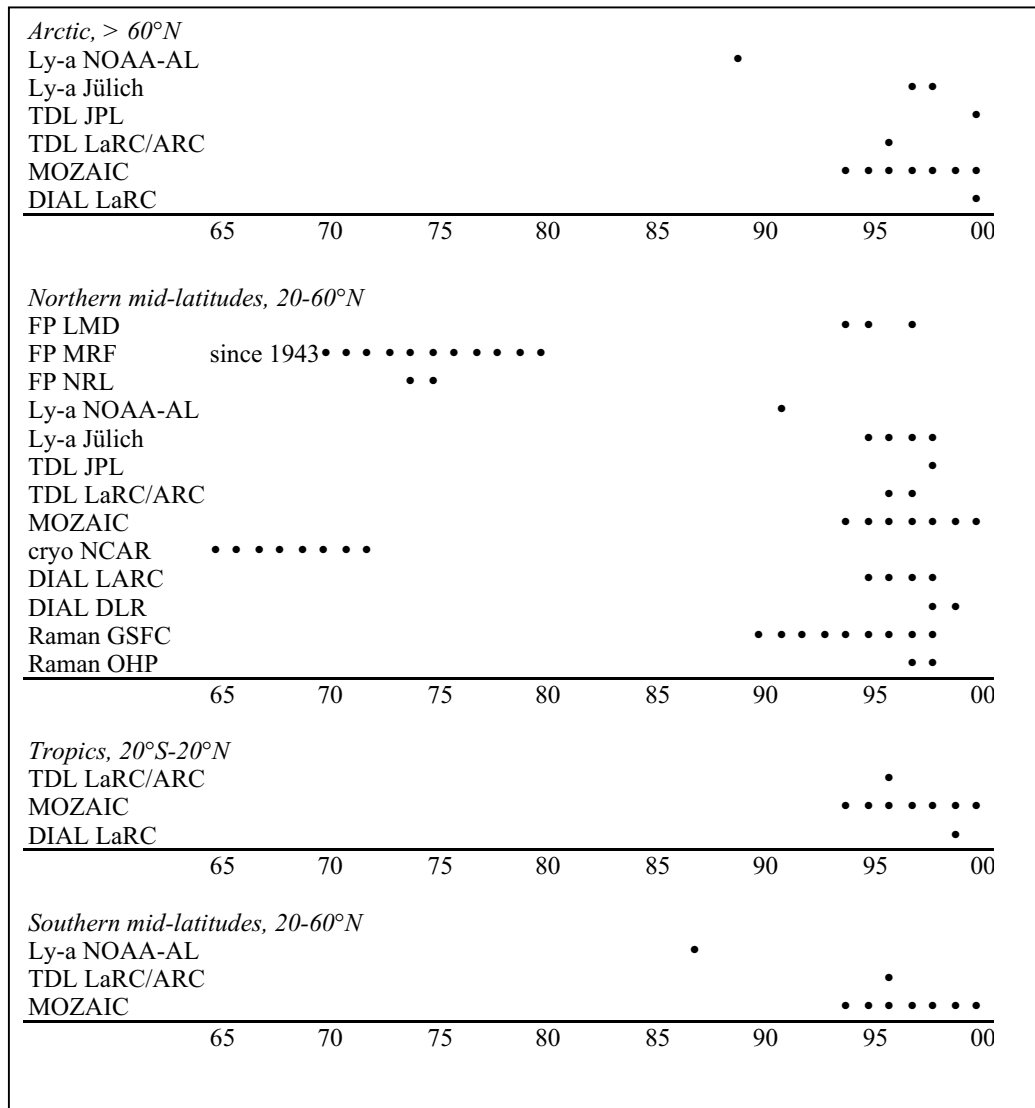


**Figure 1.2a** Timetable of water vapour measurements in the upper troposphere and in the lower stratosphere (<420 K) using different airborne and ground-based hygrometers. Measurements at these altitudes from profiling observations listed in Figure 1.2b are not included.

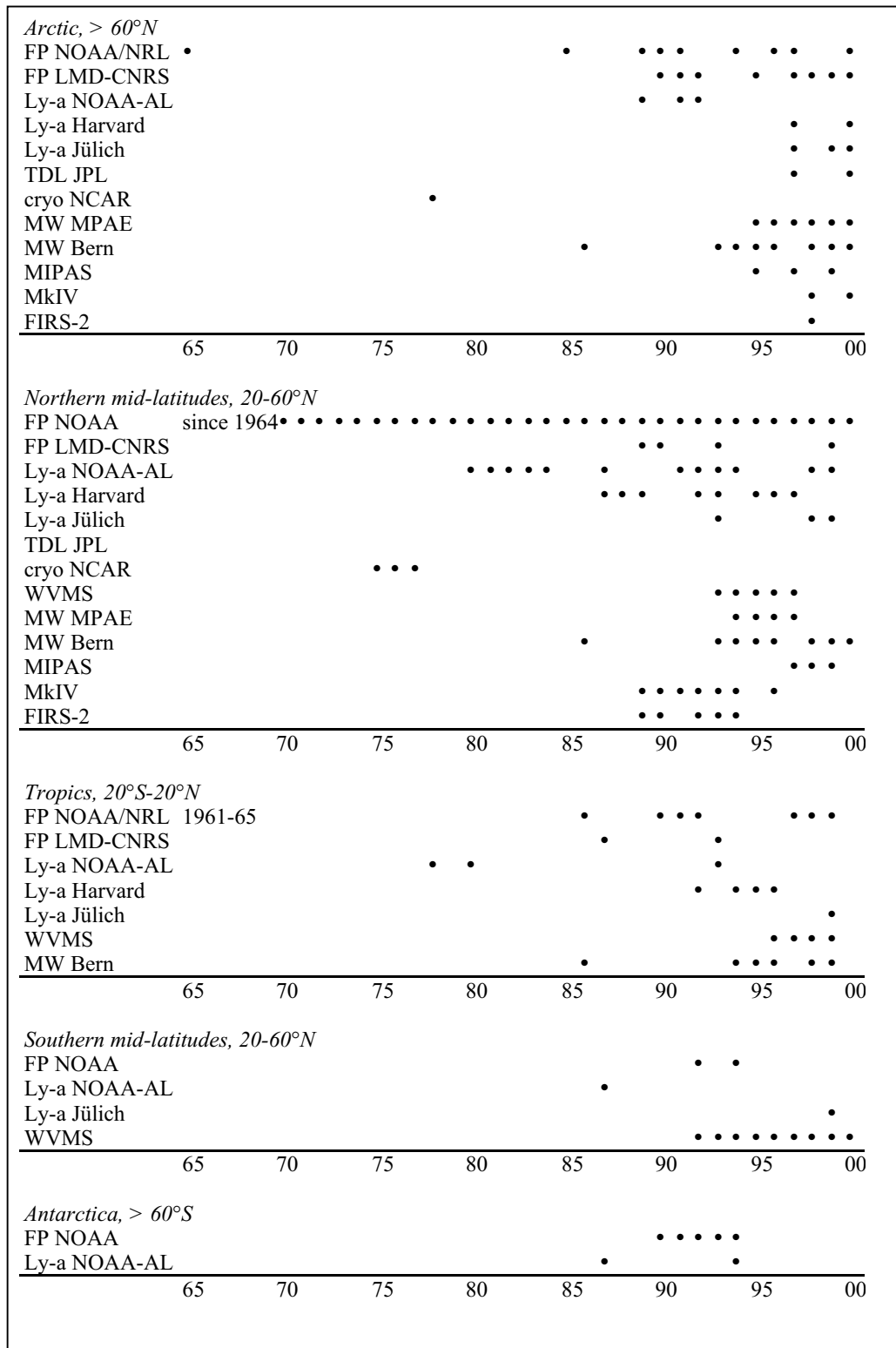


Figure 1.2b Timetable of water vapour measurements in the stratosphere above 420 K using different airborne, balloon-borne and ground-based hygrometers.

---

## 1.2 *In situ* hygrometers

*In situ* measurements of H<sub>2</sub>O in the UT/LS have been reported for over five decades beginning with those of Brewer [1944] and Brewer *et al.* [1946]. Since then, a variety of experimental techniques have been developed and used. The most important of these are frost point detection, absorption and fluorescence techniques in the vacuum ultraviolet (VUV) spectral region (typically using Lyman- $\alpha$  radiation), and more recently, absorption measurements in the infrared using tuneable diode laser spectrometers. In the UT, techniques with lower sensitivity developed for meteorological soundings can also be applied and are briefly described below, but special maintenance and calibrations are required to make such measurements reliable up to tropopause altitudes. Due to the range of H<sub>2</sub>O mixing ratios and the required calibration procedures, the development and operation of precise and accurate hygrometers for the UT/LS as well as their accurate calibration is still at the research level and is far from being routine.

One of the most crucial problems in making *in situ* measurements of H<sub>2</sub>O is to ensure contamination-free probing. Proper selection of wall materials, optimisation of probe location, heating of the instrument and its inlet, large flow rates or open-cell designs have to be used in order to avoid or minimise measurement artefacts. The different approaches are discussed below for the individual hygrometers. The instruments presented here have proven that such contamination-free measurements are possible, while a number of other instruments described in the literature, though based on the same basic techniques, reported obvious contamination problems. The design of the inlet probe and its non-isokinetic sampling properties have been the subject of several studies, in particular when measurements in clouds were made.

The advantage of most *in situ* techniques is their higher precision and spatial resolution compared to remote sensing instruments; thus *in situ* instruments are well suited particularly for case studies on smaller scales. Their absolute calibration either in the laboratory or in flight, tracing to calibration standards can be repeated at regular intervals and possible instrument drifts are easier to detect. There is no need for additional algorithms for the measurement geometry. *In situ* instruments are therefore often used for the validation of space-borne remote sensing experiments. Since the operation of *in situ* instruments in the UT/LS requires the use of platforms such as balloons or aircraft, which are either expensive to operate, have limited availability, or both, the data sets cover only limited regions and time periods. This disadvantage is partly compensated by the large number of measurements made to date.

### 1.2.1 Frost point hygrometers

Most conventional frost point hygrometers are based on the chilled-mirror technique. In this technique, a layer of condensate (frost or dew) is formed on the surface of a small mirror. This layer of condensate is detected by an optical system and maintained at a constant extent by heating and cooling the mirror. Under these conditions, the amount of water vapour can be determined by measuring the temperature of the mirror, which represents the frost point or dew point temperature of the air passing over the mirror. The mirror temperature is controlled either by heating a resistor, which works against a cryogenic bath, or by a thermoelectric heat pump (Peltier device). The temperature of the mirror is measured using a thermistor or a platinum temperature sensor. The water vapour mixing ratio and relative humidity are derived from the frost-point temperature using ambient pressure and temperature.

On balloons, the measurements are made predominantly during descent to prevent contamination by the balloon wake. The altitude resolution depends on the time response and on the balloon descent rate. On aircraft, the spatial resolution is related to the speed of the aircraft.

---

### The NOAA-CMDL and NRL frost point hygrometers

In the cryogenic frost point hygrometers used at the Climate Monitoring and Diagnostics Laboratory of the National Oceanic and Atmospheric Administration (NOAA/CMDL), the mirror is thermally connected to a cryogenic bath. The temperature of the mirror is controlled with a heating element, which heats the mirror against this cold sink. Solid state elements are used for frost-detection, and a simple controller is used to maintain a constant frost-layer.

The temperature of the mirror is measured using individually calibrated thermistors. The overall accuracy of the instruments is about  $0.5^{\circ}\text{C}$  in temperature, which translates to roughly 10% in water vapour mixing ratio.

The hygrometers used at NOAA/CMDL were originally developed at the Naval Research Laboratory (NRL) in Washington D.C., U.S.A., [*Mastenbrook and Dinger*, 1961]. These instruments used a mirror, across which a temperature gradient of around  $3^{\circ}\text{C}$  was maintained to concentrate the ice layer in the centre of the mirror. The extent of the ice layer was adjusted such that the ice edge would lie over the thermistor embedded in the mirror. It was assumed that the temperature at the ice edge is equal to the frost-point temperature. However, the accuracy to which the ice edge was maintained over the thermistor depended on the skill of the individual operator setting the instrument as well as on the accuracy of the controller to maintain an ice layer of constant size and shape. This mode of operation caused some variation in the data and was changed when the instruments were taken over by NOAA/CMDL.

The current version of the balloon-borne frost-point hygrometer, which has been used with only minor modifications since 1980, uses a mirror with a uniform temperature distribution allowing a more precise measurement of the frost-point temperature [*Oltmans*, 1985]. The instrument samples air in a 50 cm long and 2.5 cm diameter stainless steel tube. The flow through this tube is ram flow of about 5 m/s depending on the ascent/descent velocity of the balloon. Tests have shown that solar scatter within this tube does not affect frost detection. The largest uncertainties in the frost-point temperature measurement are the stability of the controller ( $<0.3^{\circ}\text{C}$ ), uniformity of the mirror temperature ( $<0.1^{\circ}\text{C}$ ), thermistor calibration ( $0.05^{\circ}\text{C}$ ), and self-heating of the thermistor ( $<0.05^{\circ}\text{C}$ ). The overall accuracy of this instrument is about  $0.5^{\circ}\text{C}$  in frost point temperature, or about 10% in mixing ratio. The vertical resolution is mostly determined by the response time of the instrument, which is typically between 10 and 30 seconds for most of the region of interest.

The co-condensation of water and other trace gases (for example  $\text{HNO}_3$ ) is not considered to be important, since water vapour is several orders of magnitude more abundant. Furthermore, at roughly 500 hPa the mirror is heated to about  $+80^{\circ}\text{C}$  to remove any contaminants collected in the boundary layer. The time of measurement after this is not considered to be long enough to build up large amounts of contaminant tracers. Laboratory tests have been run using large amounts of  $\text{CO}_2$  and  $\text{CH}_4$  and have not shown any influences on the frost-point measurements.

A modified version of this instrument has been used in extensive laboratory intercomparisons. This version uses the same thermal, optical and electronic components, but has a special flow system, which allows its use in the laboratory. Intercomparisons with the Lyman- $\alpha$  instruments of the NOAA Aeronomy Laboratory (NOAA/AL) and Harvard University under controlled laboratory conditions are discussed in Chapter 2. Its measurement accuracy and response time is similar to the balloon instrument.

Roughly 200 instruments have been flown from Boulder, Colorado, U.S.A., and about 120 at other locations. On a few occasions multiple sondes have been flown at the same time and have always shown a good consistency amongst each other. The Mastenbrook data set until 1980

---

contains about 130 soundings from Washington D.C. and about 35 soundings from other locations. Table 1.1 summarises the NOAA-CMDL data sets obtained since 1964. All of the profiles before 1990 were obtained with an analog data recording system and data were extracted from a recorder strip chart at 30 s intervals. The instrument used the VIZ radiosonde for pressure and temperature information and data transmission to the ground station. Beginning in 1990, a digital interface (Tmax) to a Vaisala radiosonde was used, which provides 8 s resolution. All data are mapped onto a 250 m vertical resolution. Data from Washington D.C. are summarised in *Mastenbrook and Oltmans* [1983]. Those from 1964-1976 were obtained with an earlier version of the frost point hygrometer. Beginning in 1977 through the end of the program at Washington D.C. in 1980 the data were obtained using a redesigned instrument using solid state circuitry. These soundings were instrument development flights and may have incomplete data and, in some cases, somewhat suspect values. The data from 1964-76 were extracted from published data reports and not subjected to additional screening. Data for 1977-80 were also taken from previously processed data.

Data with the early version of the hygrometer were obtained since 1961 by NRL from balloon flights at different locations (Table 1.2). The hygrometers were also used onboard a NASA C141 aircraft for measurements up to 12.5 km altitude in 1974-1975 at mid-latitudes over the western United States and the eastern Pacific [*Mastenbrook, 1976*]. These historic data are available only from the published data reports.

### **The LMD-CNRS frost point hygrometers**

Three kinds of instruments have been developed at the Laboratoire de Météorologie Dynamique (LMD), Centre National De Recherche Scientifique (CNRS), in France. In the first version of the hygrometer for balloons, the cooling and heating of the mirror was controlled by a thermoelectric module. Then a cryogen was used to cool the mirror for an instrument used on both aircraft and balloons. For all types of instruments, the temperature sensor of the mirror, which measures the frost-point temperature, is calibrated with respect to a platinum sensor which is traceable to the National Temperature Reference Standards. In addition, calibration and tests of the instruments are made with the LMD water vapour calibration system which allows the generation of frost-point temperatures down to  $-90^{\circ}\text{C}$  in a large air pressure range, from 1000 hPa to 20 hPa [*Ovarlez, 1985*]. Thus the hygrometers are tested in the same environmental conditions as those encountered during the balloon flights as well as during the aircraft flights. In order to verify the accuracy and proper operation of the hygrometers, comparisons between the frost point produced by the calibration device and the corresponding frost-point measured by the hygrometer (using the calibration of the mirror sensor) are performed and checked to fit within the precision of the hygrometer.

#### *The thermoelectric hygrometer*

This instrument was first developed for long-duration balloons (MIR = InfraRed Montgolfiere). In this version, the mirror temperature is controlled by a Peltier device, so that the hygrometer has the necessary autonomy for measurements for several days [*Ovarlez, 1991, Ovarlez et al., 1996*]. The uncertainty ( $2\sigma$ ) on the frost-point determination is  $0.5^{\circ}\text{C}$ , the resolution is  $0.1^{\circ}\text{C}$ , and the time response is about 100 seconds in the middle stratosphere. The frost-point temperature range is  $-50$  to  $-95^{\circ}\text{C}$ . This instrument has also been used on open stratospheric balloons, for single profiles, before 1994 [*Ovarlez and Ovarlez, 1994*]. Since then, the performance of this instrument has been improved to be almost equivalent, in the stratosphere, to the cryogenic device described below.

**Table 1.1** Listing of the NOAA/CMDL data set

Location	Station code	Lat.	Long.	Dates	No. of profiles	Remarks
<b>Mid-latitudes</b>						
Boulder, Colorado	bl	40N	105W	1980-1998	194	
Crows Landing, California	cl	37N	121W	7-11 May 1993	3	w/ NOAA & Harvard Ly- $\alpha$ on ER-2
Daggett, California	da	35N	121W	02 Feb 1992	2	
Edwards, AFB, California	ew	32N	123W	25,26 Feb 1991	4	w/ NOAA Ly- $\alpha$ on ER-2, SAGE II
Ft. Sumner, New Mexico	fs	34N	104W	21 Sep 1996 18 May 1998	4	OMS
Laramie, Wyoming	lw	45N	105W	12 Feb 1983 30 Nov 1984, 29 Aug 1989	5	w/ SAGE II
Lauder, New Zealand	nz	45S	169E	14 Jan 1992 25,26 Nov 1992	2	
Palestine, Texas	pl	32N	96W	07 May 1981 16,17 Apr 1983 11,13 Oct 1983 05 Jul 1985	8	BIC
Washington, D.C.	dw	39N	78W	1964-1980	129	NRL instrument
<b>Tropics</b>						
American Samoa	sm	14S	171W	17/18 Jul 1986 19/20/21 Jan 1988	5	w/ SAGE II
CEPEX	cx	9S-2N	160E-157W	7-25 Mar 1993	13	
Hilo, Hawaii	hi	20N	155W	17 Jul 1991 22, 24 Mar 1992	3	
Juazeiro do Norte, Brazil	jn	7S	64W	14 Feb 1997 11 Nov 1997	2	OMS
San Cristobal	sc	1S	90W	Mar, Sep 1998 Mar 1999	10	SOWER
<b>Antarctica</b>						
McMurdo	mm	79S	167E	Sep, Oct 1990-92, Feb-Oct 1994	30	ASHOE/ MAESA
South Pole	as	90S		May 1990-Jan 1994	22	
<b>Arctic</b>						
Alert, NWT	al	82N	62W	Jan 1989,1990,1991	5	
Fairbanks, Alaska	fb	65N	148W	7,10,11 Aug 1985	3	w/ SAGE II
Keflavik, Iceland	ic	64N	21W	24, 25 Mar 1994	2	
Kiruna, Sweden	kr	68N	21E	Feb 1991,1992,1997 Jan-Mar 2000	6 5	SOLVE
Sodankyla, Finland	so	67N	27E	23 Jan, 17 Feb 1996	2	

**Table 1.2** Listing of the NRL balloon data set

Time	Location	Lat.	Long.	No. of profiles	Reference
April 1961	Hyderabad, India	17N	78E	3	<i>Mastenbrook</i> , 1962
Nov 1963	Kwajalein Atoll	9N	167E	5	<i>Mastenbrook</i> , 1965
Jan 1964-Dec 1965	Trinidad, West Indies	10N	61W	23	<i>Mastenbrook</i> , 1966
July-Aug 1965	Thule, Greenland	77N	69W	3	<i>Mastenbrook</i> , 1966

*The cryogenic hygrometers for open stratospheric balloons (BSO)*

In this instrument the mirror temperature is controlled cryogenically: the mirror is cooled through a copper rod immersed in liquid nitrogen enclosed in a Dewar container, and the heating is produced by a resistance wire wrapped around the copper rod [Ovarlez and Ovarlez, 1995]. The uncertainty on the frost point temperature determination is 0.3°C, and the resolution is 0.05°C. The response time depends on the frost point: the lower the frost point, the higher the response time, from about 20 seconds in the upper stratosphere to about 10 seconds in the upper troposphere. The frost point temperature range is -10 to -95°C. The range is quite large for stratospheric measurements, the extension to -10°C has been made for use on aircraft.

**Table 1.3** LMD frost point hygrometer balloon flights

Project	Carrier	Date	Altitude range (km)
<b>Mid-latitudes (44N, 0W)</b>			
French national program	BSO	12 Oct 1989	16 – 22.5
French national program	BSO	06 Oct 1990	14 – 25.5
TRAVERSE	BSO	07 Mar 1993	14 – 24
THESEO	BSO	05 May 1999	10 – 29.5
<b>Arctic (68N, 21E)</b>			
CHEOPS	BSO	19 Jan 1990	14.5 – 24
	BSO	26 Jan 1990	11.5 – 22
	BSO	20 Nov 1991	11 – 24
	BSO	04 Dec 1991	12 – 25
	BSO	11 Dec 1991	13.5 – 24.5
EASOE	BSO	31 Jan 1992	13 – 23.5
	BSO	09 Feb 1992	13 – 28
	BSO	10 Mar 1992	13 – 23
	BSO	20 Mar 1992	11 – 27
SESAME	BSO	13 Feb 1995	11 – 26.5
	BSO	20 Mar 1995	11 – 27.5
ILAS validation campaign	BSO	14 Feb 1997	21.5 – 27.5
SABINE	BSO	10 Aug 1998	11 – 30
THESEO	BSO	18 Jan 1999	10.5 – 23.5
	BSO	30 Jan 1999	10 – 23
	BSO	19 Jan 2000	10 – 27
THESEO2000	BSO	25 Jan 2000	10 – 27
<b>Tropics (0 to 15S)</b>			
AMETHYSTE	MIR	Jan - Feb 1994	17/22 - 26

*The cryogenic hygrometer for aircraft*

This instrument is the same as the open stratospheric balloon version; however, it has been adapted to aircraft installation and certification requirements [Ovarlez and van Velthoven, 1997]. During aircraft flights on the DLR Falcon (maximum altitude: 13 km), the ambient air flows into the instrument through an air inlet from the aircraft fuselage (a modified Rosemount temperature housing). Thus gas-phase measurements are accomplished without sampling ice particles. The airflow is generated by the difference between the dynamic pressure at the air inlet and the static pressure at the outlet. To prevent contamination from dense low-level clouds, the air inlet is opened after the first kilometres of the aircraft ascent. The air pressure is measured immediately at the sensor head of the hygrometer, so that the water vapour volume mixing ratio is given by the ratio between the water vapour saturation pressure at the measured frost-point and the measured air pressure.

**Table 1.4** LMD aircraft missions

Project	Period	No. of flights	Latitudes	Longitudes	Comparisons
POLINAT*	Nov 1994	8	30-60N	0-30W	
POLINAT*	May-Jun 1995	8	30-60N	0-30W	
POLINAT2**	Sep-Oct 1997	8	30-60N	0-30W	<i>Vay et al.</i> , 2000 <i>Helten et al.</i> , 1999

\* *Ovarlez and van Velthoven* [1997] and *Ovarlez et al.* [1999]; \*\* *Ovarlez et al.* [2000].

### Other airborne frost point hygrometers

The Meteorological Research Flight (Farnborough, UK) has carried out humidity measurements since 1943 using frost point hygrometers. The first measurements were obtained from a B17 Flying Fortress up to 37700 ft [*Brewer*, 1944]. From 1944 to 1952, the hygrometers were employed onboard several Mosquito aircraft for measurements up to 44000 ft or 160 hPa [*Bannon et al.*, 1952]. The instrument characteristics of this first hygrometer used in the UT/LS are described by *Brewer et al.* [1946]. Since 1954, a Canberra aircraft was used for regular measurements from the upper troposphere up to approximately 150 hPa. Data obtained from this aircraft are reported in several reports and publications, such as *Helliwell* [1960], *Roach* [1962], *Cluley and Oliver* [1978] and *Foot* [1984]. Measurements in the 1970s were made on a regular basis every 3-4 months between 45°N and 65°N. *Cluley and Oliver* [1978] estimate that the standard deviation of the frost point arising from random effects is 0.5°C; in the range 2 to 10 ppm this is equivalent to a standard deviation of about 7% in mass mixing ratio.

The *Spyers-Duran* [1991] NCAR instrument, a cryogenic frost point hygrometer, has been used on aircraft.

The hygrometers made by Buck Research, e.g. used on the German Falcon research aircraft by DLR [*Busen and Buck*, 1995] and on the NASA DC-8 aircraft, are cryogenic frost-point hygrometers, working in the range +30 to -95°C, with an uncertainty of 0.3°C, and a response time of 6 to 30 seconds depending on the environmental parameters.

Other commercial instruments are used on research aircraft, in the mid troposphere, such as the General Eastern instrument. They use a Peltier device to cool the mirror.

### Chilled mirror hygrometers used for calibration standards

Advanced commercial chilled mirror hygrometers are used as calibration standards for some of the hygrometers discussed in this Assessment as well as by National Standard Institutes such as in the U.S., in Germany and in Spain.

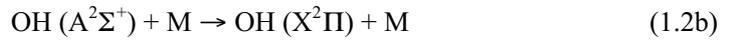
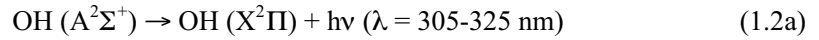
The General Eastern Instruments thermoelectric sensor series 1311 DR (DRX) is designed for frost point measurements down to -70°C (-75°C). The accuracy of the instrument is quoted to  $\pm 0.2^\circ\text{C}$  ( $\pm 0.15^\circ\text{C}$ ). Lower frost points, i.e. -90°C (-95°C), can be determined with a hygrometer of MBW Elektronik AG (Switzerland), the K-1806/DP30-SHS (SHSX) system. This hygrometer system is accurate to  $\pm 0.1^\circ\text{C}$ . More technical details and other commercial chilled mirror hygrometers are reviewed by *Wiederhold* [1997].

## 1.2.2 Lyman- $\alpha$ hygrometers

The method used to measure H<sub>2</sub>O by a fluorescence technique was developed by *Kley and Stone* [1978] and *Bertaux and Delannoy* [1978]. The photodissociation of H<sub>2</sub>O molecules by radiation at wavelengths  $\lambda < 137$  nm produces electronically excited OH:



The electronically excited OH relaxes to the ground state by fluorescence or by collisions with other molecules M:



By measuring the intensity of the emitted fluorescence, the H<sub>2</sub>O abundance can be determined. The number of fluorescence photons  $N_f$  is given by

$$N_f = \frac{[\text{H}_2\text{O}] \cdot J \cdot \Phi}{[\text{air}] \cdot k_q/A_0 + 1} \quad (1.3)$$

[H<sub>2</sub>O] and [air] denote respectively the concentration of H<sub>2</sub>O and air molecules, J the photodissociation rate of reaction (1.1),  $\Phi$  the quantum efficiency for excited state OH production via (1.1),  $A_0$  the Einstein coefficient of reaction 1.2a, and  $k_q$  the quenching coefficient of the OH radical in air (reaction 1.2b). In the UT/LS, that is, for altitudes below 20 km,  $[\text{air}] \cdot k_q/A_0 \gg 1$ , and equation 1.3 can be approximated by

$$N_f = C \cdot \frac{[\text{H}_2\text{O}]}{[\text{air}]} \quad (1.3')$$

The factor C includes molecular coefficients from the literature as well as instrument specific quantities. If C is a constant, the number of detected fluorescence photons is proportional to the H<sub>2</sub>O mixing ratio [H<sub>2</sub>O]/[air] for measurements in the UT/LS. For measurements at higher altitudes, equation 1.3 has to be used to obtain correct water vapour mixing ratios.

In reality, C is a function of J and thus depends on the photon flux in the fluorescence volume, which in turn depends on variations of the lamp intensity and absorption by atmospheric gases. In the vacuum UV (VUV) spectral region, absorption by oxygen and water vapour has to be taken into account. The attenuation and variation of the VUV radiation have to be monitored when determining H<sub>2</sub>O mixing ratios by measuring the fluorescence signal. The Lyman- $\alpha$  line at  $\lambda = 121.6$  nm coincides with a narrow deep minimum in the oxygen absorption cross section and thus enables measurements with the fluorescence technique down to the middle troposphere. Measurement of the absorption of Lyman- $\alpha$  radiation at higher concentrations can be used for quantification of H<sub>2</sub>O abundances in the troposphere as well [e.g. *Tillman*, 1965]. Such instruments [e.g. *Buck*, 1976] are used on several research aircraft as part of the basic instrumentation.

The most advanced Lyman- $\alpha$  fluorescence hygrometers have been developed in the laboratories at NOAA in Boulder, at Harvard and in Jülich (Germany). Though they are based on the same technique, they differ in several experimental details, and also in their calibration procedure. The instruments are employed on different aircraft and balloons from the UT up to 35 km

altitude. Rocket borne measurements in the mesosphere using this technique have been reported by *Khaplanov et al.* [1996].

One of the advantages of this technique is the large dynamic range for measurements from the UT at several hundred ppmv to dry stratospheric air masses where changes of the order of 0.1 ppmv can still be detected. Large flow rates through the hygrometers can be achieved for contamination-free measurement together with integration times on the order of 1 s for detection of small-scale features in the atmosphere.

### The NOAA Lyman- $\alpha$ hygrometers

The NOAA balloon-borne Lyman- $\alpha$  fluorescence hygrometer was developed by *Kley and Stone* [1978]. The actual flight instrument for use in the stratosphere has been described and characterised by *Kley et al.* [1979]. This was an open-cell design with a radio-frequency discharge Lyman- $\alpha$  light source. The stray light intensity across the cell and the intensity in the fluorescence region were monitored by nitric oxide ionisation cells. The instrument was flown at night to eliminate solar scatter.

A characteristic of this and successive NOAA Lyman- $\alpha$  fluorescence hygrometers is their method of *in situ* calibration through the simultaneous measurement of water vapour concentration by absorption and OH fluorescence. The *in situ* calibration uses Beer's law at the wavelength of Lyman- $\alpha$  radiation and has two constants, namely the water vapour absorption cross section at Lyman- $\alpha$  [*Kley*, 1984] and the distance between light source and nitric oxide intensity monitor. The balloon instrument makes use of the fact that, during ascent or descent, the absorption by water vapour across the cell changes from >90% in the middle troposphere to <10% in the upper troposphere, allowing the determination of absolute water vapour concentrations and, from the simultaneously-recorded OH fluorescence intensity, the determination of the fluorescence sensitivity constant C over a considerable range of water vapour absorption. Absorption by oxygen at Lyman- $\alpha$  varies between 35 and 20% between 500 and 250 hPa and is numerically considered using the measured cross section of O<sub>2</sub> [*Kley*, 1984]. Table 1 of *Kley et al.* [1979] gives an example for the determination of C for a typical balloon flight. The precision of C obtained from 48 *in situ* calibrations, over the altitude range of 6-10 km with water vapour absorption ranging from 90% to 5%, was 18%, and constituted the single largest error in the overall accuracy of the balloon-borne instrument. The  $2\sigma$  uncertainty of the water vapour absorption cross section at Lyman- $\alpha$  is 6%. Other error sources are negligible.

The first aircraft instrument was a closed cell design with a microwave discharge lamp. This instrument was operated in a pressurised container for thermal stability. Lyman- $\alpha$  intensity was monitored across the cell with a NO ionisation cell. This instrument was built for the Panama STEP U-2 campaign. The instrument design and calibration procedure are documented by *Kley et al.* [1983]. In short, the *in situ* calibration of the Panama instrument was achieved during level flight in the tropopause region whenever short duration events of large water vapour mixing ratios occurred, superimposed on much smaller background mixing ratios. Thus, the calibration is equivalent to the one described above for the balloon instrument except that the total pressure and, therefore, the oxygen absorption does not change during an absorption event. A disadvantage of the Panama instrument was the irregular and relatively infrequent occurrence of natural absorption events.

The U2 aircraft instrument was modified in 1981 for regular (every 15 minutes) calibration procedures. A small (200 cm<sup>3</sup>) cylinder is filled with 100-200 atm of air. The high pressure air is allowed to flow over a frit with a saturated cotton swab, then over a capillary into a second small cylinder, filling it with humidified air over a period of 15 minutes to a pressure of

---

approximately 1000 hPa. A magnetically operated valve then opens and allows the second cylinder to empty its contents through a second capillary into the main air stream, upstream of the fluorescence chamber. The small pressure increase in the fluorescence chamber is negligible, but the mixing ratio of water is increased, initially to mixing ratios of approximately 500 ppmv. Set by the conductance of the second capillary, the mixing ratio decays exponentially to ambient levels with a time constant of approximately 1 min. From the measurement of transmitted Lyman- $\alpha$  light intensity it is possible to derive absolute water vapour mixing ratios (above ambient background). The calibration was performed every 15 minutes over a wide range of mixing ratios. Water vapour mixing ratios of approximately 500 ppmv at the high end, down to values around 20 ppmv at the low end were used to derive the calibration constant. Accounting for preabsorption of Lyman- $\alpha$  light before entering the field of view of the OH fluorescence detector, the response of the fluorescence signal was extremely linear. The slope of fluorescence intensity versus absolute water vapour mixing ratio yields the sensitivity constant. The precision of the in-flight calibrations (every 15 minutes during a 5 hour flight) was typically 1-2%.

Error sources for the U2 instrument include a negligible error from photon counting statistics from fluorescence and background signal and a contribution from water vapour outgassing. However, the latter contribution would decay to very small amounts after approximately 1.5 hours into the flight and played no role during the final descent profiles. Since the Lyman- $\alpha$  absorption cross section is accurately known with a  $2\sigma$  standard deviation of 6% [Kley, 1984] and the only other parameter (distance between the Lyman- $\alpha$  light source and the nitric oxide ionisation chamber) is measured, it follows that the calibration of the fluorescence instrument must be accurate to the uncertainty of the Lyman- $\alpha$  water vapour absorption cross section.

Since the calibration is always done at ambient conditions of pressure, flow rate, oxygen partial pressure and trace gas composition, errors in the calibration constant that might arise from systematic errors possibly connected to the above parameters are avoided.

The present NOAA Lyman- $\alpha$  instrument is also a closed cell design, optimised for a high flow rate to minimise the effect of trapped water. Heated inlet lines vaporise the ice before reaching the hygrometer. The Lyman- $\alpha$  source is a DC discharge lamp. The Lyman- $\alpha$  intensity is monitored with an iodine ionisation cell that is sensitive from 115 nm to 135 nm. A magnesium fluoride beam splitter samples the source with the ionisation cell placed equidistant from the source and the detected fluorescence region. This arrangement accounts for the preabsorption in the cell from oxygen and water. Water vapour is injected into the air stream and the absorption and fluorescence are measured as above to provide an in-flight calibration. A calcium fluoride filter is inserted during the calibration sequence to measure background radiation from the lamp at 309 nm (about 200 counts per second) and any radiation between 125 and 135 nm. Two hygrometers were built in an attempt to independently measure total water and water vapour. They were flown in the partially pressurised Q bay of the ER-2 [Kelly *et al.*, 1989]. The instrument has since been modified to fly unpressurised on the WB-57.

The main sources of error of the present aircraft instrument are the accuracy of the water Lyman- $\alpha$  absorption cross section and the Poisson counting statistics of the signal and background. The  $2\sigma$  uncertainty of the water vapour absorption cross section uncertainty is 6%. The counting period for both instruments is 1 s. Count rates are in the range of 500-1000 counts per second per ppmv of water. For 4 ppmv the  $1\sigma$  counting error is about 4%. The total  $2\sigma$  error is 10% at 4 ppmv for 1 second data and 6.6% at 4 ppmv and 10 second data.

Areas of concern in the present NOAA instrument are spectral impurities in the DC lamp and trapped water. Other wavelengths are not as effective as Lyman- $\alpha$  in producing fluorescence. The spectral purity of the lamp is checked during the descents by using the oxygen and the

water Lyman- $\alpha$  absorption cross-sections and the measured pressure and water to remove their absorption effects. If the lamp intensity is constant then the result should be independent of pressure unless there are spectral lines with different cross sections. The calcium fluoride cut-off filter gives a second measure of any Lyman- $\beta$  and contamination, usually less than 0.1%.

**Table 1.5** Missions of the NOAA-AL Lyman- $\alpha$  hygrometer

Mission	Location	Lat.	Long.	Dates	No. of flights	Carrier
-	Brazil	5S	39W	27 Sep 78	1	balloon
-	Wyoming	41N	105W	19 Sep 79 - 12 Feb 83	5	balloon
STEP	Panama	6-11N	77-82W	30 Aug 80 - 16 Sep 80	8	U-2
-	Texas	32N	96W	07 May 81, 10 Oct 83	2	balloon
ACE	California	38N	122W	02 Dec 80 - 21 Jan 83	23	U-2
-	Kansas	38N	97W	29 Apr 81 - 09 May 81	4	U-2
-	Texas	32N	96W	05 May 81 - 12 Oct 83	7	U-2
-	Wyoming	41N	105W	14 Jul 81	1	U-2
STEP	California			20 Apr 84 - 06 May 84	4	U-2
STEP	California			04 Apr 86 - 24 Apr 86		ER-2
STEP	Darwin	12S	131E	08 Jan 87 - 19 Feb 87	11	ER-2
	+ transits				6	
AAOE	Chile	53S	71W	12 Aug 87 - 03 Oct 87	12	ER-2
	+ transits				6	
	Chile	44-90S	71W	22 Aug 87 - 29 Sep 87	13	DC-8
	+ transits				1	
AASE	California	38N	122W	06 Oct 88 - 05 Dec 88	5	ER-2
	Norway	59N	6E	29 Dec 88 - 21 Feb 89	13	
	+ transits				4	
	Norway	59-90N	6E	02 Jan 89 - 15 Feb 89	14	DC-8
	+ transits				2	
-				25 Feb 91, 26 Feb 91	2	ER-2
PEM west				01 Sep 91 - 21 Oct 91		DC-8
AASE II	Alaska,	65N	147W	04 Oct 91 - 14 Oct 91	4	ER-2
	Maine,	45N	69W	02 Nov 91 - 26 Mar 92	15	
	+ transits				4	
SPADE				09 Nov 92 - 22 Oct 93	14	ER-2
ASHOE	California	38N	122W	02 Feb 94 - 04 Nov 94	6	ER-2
MAESA	Hawaii	20N	160W		5	
	New Zealand				24	
	+ transits				6	
WAM	Texas	25N	95W	09 Apr 98-07 May 98	6	WB-57
				99		WB-57

### The Harvard Lyman- $\alpha$ hygrometers

The Harvard balloon-borne Lyman- $\alpha$  has been described by *Weinstock et al.* [1990]. Briefly, Lyman- $\alpha$  radiation from a RF discharge lamp photodissociates water vapour in a 6 inch duct. The OH fluorescence is collected at right angles to the lamp and airflow through an interference filter centred at 315 nm with a 10 nm bandwidth and detected with a photomultiplier tube. A photodiode sensitive to vacuum ultraviolet radiation was used to both monitor lamp intensity and, with the aid of an actuator to change absorption path length, to measure water vapour by absorption. The walls are maintained at about  $-100^{\circ}\text{C}$  to prevent outgassing while data is taken during a valve-down descent at velocities of 3-6 m/sec. A large fan is used to aid in the airflow through the duct.

This instrument performed successfully in 4 flights launched from Palestine, Texas, during the summers of 1987-1989, as described in *Schwab et al.* [1990]. The data were taken during balloon valve-down descent as tabulated below. The quoted accuracy of these 2- $\sigma$  data is 40% in 1987 for a 2-minute average and 30% in 1988 and 1989 for a 30-second average.

**Table 1.6** The Harvard balloon data set

Date	Altitude range (km)	Latitude	Longitude
15 Jul 87	15-32	32 N	98 W
06 Jul 88	16-34	32 N	98 W
28 Jul 89	17-37	32 N	98 W
25 Aug 89	18-37	32 N	98 W

The Harvard Lyman- $\alpha$  instrument for the NASA ER-2 aircraft was described in detail by *Weinstock et al.* [1994], with an update in *Hints et al.* [1999]. Briefly, Lyman- $\alpha$  (121.6 nm) radiation from a RF discharge lamp photodissociates water vapour in a 3 inch square duct. The OH fluorescence is collected at right angles to the Lyman- $\alpha$  beam through a filter and detected with a photomultiplier tube. At ER-2 altitudes (5-21 km) the observed detector signal is proportional to the water vapour volume mixing ratio. Solar and lamp scatter near 315 nm is measured by using a quartz window to periodically block the Lyman- $\alpha$  beam. The fluorescence signal is normalised to lamp intensity measured by a vacuum photodiode opposite the lamp. A rear-surface MgF<sub>2</sub> mirror surrounding the diode reflects some of the radiation back across the duct to a second diode, allowing water measurements by direct (Beer's Law) absorption in the mid-to-upper troposphere. Flow velocities in the duct are typically 30-70 m/sec for fast time response and to avoid (and directly test for) contamination from walls. Data are typically reported every 4 seconds, corresponding to 1 km horizontal resolution on the ER-2, but 8 Hz data are available for high resolution work (aircraft wake crossings, etc.). The precision is typically  $\pm 0.1$  ppmv for a 4 second measurement in the stratosphere.

The instrument is calibrated in the laboratory by flowing known amounts of water vapour in air through the detection axis. Saturated air-water mixtures are prepared by passing air from 50 to 500 ccm at standard temperature and pressure through a two-stage bubbler apparatus, then diluted with dry air at approximately 5000 to 40000 ccm at standard temperature and pressure before being sent to the detection axis. Brooks flow controllers, individually calibrated to an accuracy of 1%, are used to control the respective flows. The bubbler apparatus is held in a well-insulated water bath with temperature measured to  $\pm 0.1$  degree, providing a partial pressure of water accurate to better than 1% at the bubbler. The instrument response is linear up to concentrations of  $\sim 10^{16}$  H<sub>2</sub>O/cm<sup>3</sup> (typical of the mid-troposphere). The accuracy of the calibration system is 5% based on uncertainties in temperature, pressure, and gas flow, and has been verified by direct absorption both along and across the detection axis.

The calibration is checked in-flight by comparing Lyman- $\alpha$  photofragment fluorescence with direct absorption measurements of water vapour, similar to the method of *Kley et al.* [1979], using the atmosphere to provide a wide range of H<sub>2</sub>O concentrations. Data at ER-2 cruise altitudes (where concentrations are  $\sim 10^{13}$ /cm<sup>3</sup>) are used to provide a reference signal ( $I_0$ ) for absorption on ascent and descent. At lower altitudes, concentrations are high enough ( $10^{14}$ - $10^{16}$ /cm<sup>3</sup>) for measurements of  $I$ , and hence the water vapour concentration by direct absorption:  $\ln(I/I_0) = \sigma \cdot [\text{H}_2\text{O}] \cdot l$ , where  $\sigma$  is the absorption cross-section of H<sub>2</sub>O at 121.6 nm and  $l$  (9.2 cm) is the path length. The first diode measures the lamp intensity at the mirror surface (to account for changes in lamp flux), and the second diode detects the intensity of the reflected beam after it has passed through the absorption path, so the ratio (diode 1 signal/diode 2 signal) is used for  $I$  and  $I_0$ . Absorption by O<sub>2</sub> is also accounted for. During nearly 100 flights from 1992 to 1997, the

abundance of water vapour determined by absorption typically agreed to within  $\pm 10\%$  of fluorescence measurements.

Level flight tracks of the ER-2 in the mid-to-upper troposphere provide near-ideal conditions to compare water vapour measured by fluorescence and absorption. Water vapour can vary by 10-100 ppmv at one altitude with other atmospheric conditions (temperature, pressure, etc.) nearly constant. This approach has very high stability, and in addition,  $O_2$  number density changes very little on level flight tracks, so even large errors in the  $O_2$  cross-section have only a minor effect on these measurements. Since 1995, these in-flight comparisons have been made on seven flights, with agreement between absorption and fluorescence averaging 1%. Figure 1.3 shows an example of the agreement between delta water vapour measured by absorption and fluorescence taken from a level segment of the July 25, 1996 flight. The slope is very close to unity, better than can be expected from estimated measurement uncertainties. The slight offset is related to the choice of initial and final segments and can be positive or negative on different flights. Forcing the best fit to go through the origin has at most a  $\sim 2\%$  effect.

Based on laboratory calibrations and in-flight calibration checks, the instrument is accurate to  $\pm 5\%$ , with an additional systematic uncertainty of 0.1 ppmv. A number of possible sources of error in the measurements have been examined. Contamination (desorption of water) from walls is checked for by periodically varying the duct velocity during each flight, and is found to be absent. To investigate the temperature dependence of quenching, the Lyman- $\alpha$  hygrometer was calibrated from room temperature to  $-30^\circ\text{C}$ , and no change in sensitivity was found. Radiation from the Lyman- $\alpha$  lamp other than at 121.6 nm is another potential source of error. Lamp spectra from 115 to 150 nm usually show less than 1% intensity at wavelengths other than Lyman- $\alpha$ , and these are blocked by a flowing cell containing  $O_2$  and  $N_2$  in front of the lamp. The lamps do produce some radiation near 315 nm, but the use of an anti-reflection coated quartz window to block the Lyman- $\alpha$  beam (for measurements of background) reduces the required correction to the data to  $< 2\%$ .

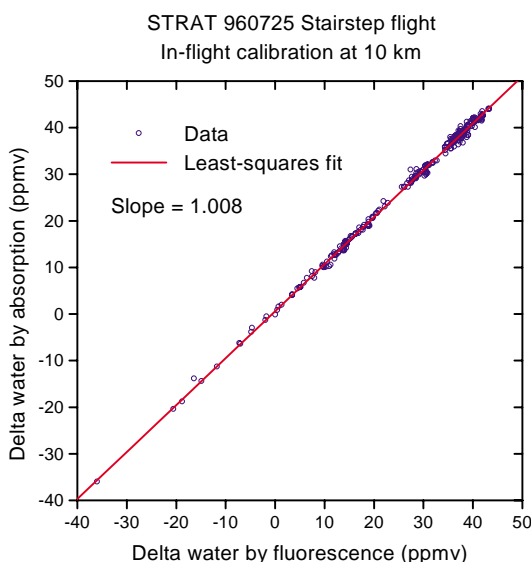


Figure 1.3 Regression of delta water vapour by absorption and fluorescence on a level flight track on July 25, 1996. An average water vapour mixing ratio of 124 ppmv, corresponding to the start and end of the flight track, has been subtracted from the fluorescence measurement to give the changes over the flight segment. Because there is no way to get a true  $I_0$  for absorption, only changes in water vapour can be compared. The slope is very close to unity, indicating excellent agreement between the two methods for this flight.

**Table 1.7** The Harvard ER-2 data set

Campaign	Location	Latitude	Longitude	Altitude (km)	No. of flights	Dates	
SPADE	Ames	21N - 41N	117-125W	8-20	3	09 - 20 Nov 92	
	Ames	15N - 60N	117-125W	8-20	11	23 Apr - 18 May 93	
CEPEX	Fij	17S - 2N	176W-178E	8-20	3	18 Mar - 06 Apr 93	
STRAT	Ames	15N - 41N	117-123W	8-20	4	08 - 17 May 95	
	Ames	20N - 60N	117-123W	8-20	6	20 Oct - 02 Nov 95	
	Hawaii	2N - 35N	120-160W	8-20	3	05 - 09 Nov 95	
	Ames	15N - 41N	117-123W	8-20	5	26 Jan - 02 Feb 96	
	Hawaii	2N - 35N	120-160W	8-20	4	05 - 15 Feb 96	
	Ames	15N - 41N	117-123W	8-20	4	18 - 30 Jul 96	
	Hawaii	2N - 35N	120-160W	8-20	7	01 - 10 Aug 96	
	Ames	15N - 41N	117-123W	8-20	4	13 - 21 Sep 96	
	Hawaii	2N - 35N	120-160W	8-20	4	06 - 11 Dec 96	
	Ames	15N - 41N	117-123W	8-20	5	04 - 13 Dec 96	
	POLARIS	Ames	15N - 60N	117-147W	8-20	4	16 - 24 Apr 97
		Alaska	64N - 90N	110-148W	8-20	7	26 Apr - 13 May 97
Alaska		64N - 90N	110-148W	8-20	6	26 Jun - 10 Jul 97	
Alaska		20N - 90N	110-160W	8-20	8	08 - 21 Sep 97	
Hawaii		2N - 41N	117-160W	8-20	2	23 - 25 Sep 97	
SOLVE	Sweden	68N	21E	8-20	6	20 Jan - 03 Feb 00	
	Sweden	68N	21E	8-20	5	03 - 15 Mar 00	

### The Jülich Lyman- $\alpha$ hygrometers (FISH)

The Fast *In situ* Stratospheric Hygrometer (FISH) developed at the Forschungszentrum Jülich (Germany) is described in detail by Zöger *et al.* [1999a]. Today, three different hygrometers exist, one for employment on large stratospheric balloons, and two for use on different aircraft (German Falcon of DLR, Dutch Cessna Citation of TU Delft, German Lear Jet of GFD, Russian M55 Geophysika of MDB).

FISH consists of a closed, vacuum-tight fluorescence cell, a Lyman- $\alpha$  radiation source, a PMT in photon-counting mode, detectors to monitor the VUV radiation output of the Lyman- $\alpha$  lamp, and a mirror drive that controls the measuring cycle: determination of the fluorescence and background count rate ( $N_1$  and  $N_3$ ) and of the lamp intensity  $U_B$ . Thus the relative count rate

$$N_f^* = \frac{N_1 - f_u N_3}{U_B} \quad (1.4)$$

with an instrumental parameter  $f_u$ , is used in equation 1.3, and  $C$  and  $f_u$  are determined by calibration in the laboratory.

The FISH measurement frequency is 1 Hz. At this frequency the noise equivalent mixing ratio at 3 ppmv is 0.2-0.15 ppmv, and the detection limit is 0.18-0.13 ppmv, depending on the quality of the lamp. Applying an autocovariance analysis on field data obtained with FISH confirms this precision.

On aircraft, FISH is usually connected to a forward-directed heated inlet that allows for measurement of total water. The enhanced sampling efficiency of larger particles has been quantified in Schiller *et al.* [1999]. The ram pressure maintains flow rates that allow an exchange of the air in the whole system within approximately 1 s. For balloon measurements,

also using a heated inlet line, measurements are carried out only during descent, with a pump used to enhance the flow.

FISH is calibrated between flights in the laboratory using a calibration bench [Zöger *et al.*, 1999a] under realistic conditions, that is varying the H<sub>2</sub>O mixing ratio of the test air from a few ppmv to several hundred ppmv and the pressure from 1000 to 10 hPa. A frost point hygrometer (General Eastern 1311 DRX, recently also MBW K-1806/DP30-SHSX) is used as a reference instrument. The quoted accuracy of the frost point measurement is  $\pm 0.15$  K ( $\pm 0.1$  K for the MBW instrument), corresponding to an uncertainty of 4% (3%) in the H<sub>2</sub>O partial pressure at 210 K. Including an error of the pressure measurement in the calibration bench, the H<sub>2</sub>O mixing ratio can be determined with an accuracy better than 5%. As a result of several field campaigns, the factors  $C$  and  $f_u$  determined in this calibration do not change significantly from flight to flight except when a detector has to be exchanged [Eicke, 1999].

FISH can also be calibrated during in-flight operation by measuring the absorption of Lyman- $\alpha$  radiation whenever the optical depth of H<sub>2</sub>O is sufficient [Zöger *et al.*, 1999a]. This method is occasionally applied as a cross check of the aforementioned laboratory calibration. Figure 1.4 shows an example using cross sections determined by Kley *et al.* [1984]. Both methods yield a discrepancy of the H<sub>2</sub>O mixing ratios of 15%, which however is not significant within the combined errors (including that of O<sub>2</sub> absorption to be considered in the UT). As discussed in Zöger *et al.* [1999a], the discrepancy might be caused by differences of the effective cross sections used, which depend on the line shape of the individual Lyman- $\alpha$  radiation sources.

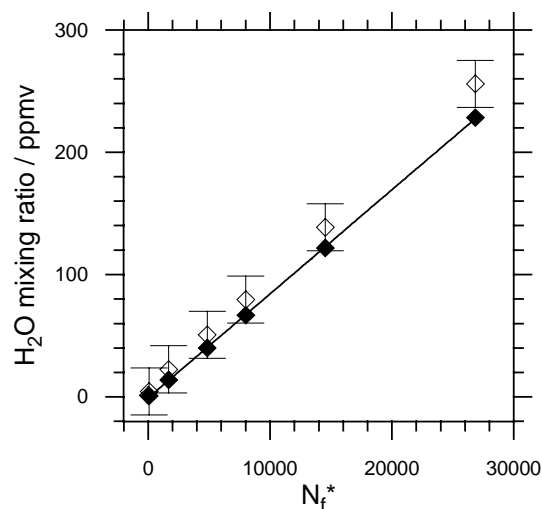


Figure 1.4 Relative count rate  $N_f^*$  as a function of the H<sub>2</sub>O mixing ratio for the FISH calibration for the aircraft mission on the 10th March 1997. Solid symbols and the corresponding regression line show the laboratory calibration before the flight using the frost point hygrometer as reference. Open symbols denote calibration points obtained in the same calibration cycle, but the H<sub>2</sub>O mixing ratio is calculated from the simultaneous absorption measurements of FISH.

FISH measurements focus on the tropopause region at mid and high northern latitudes in different seasons. A couple of balloon flights, again at mid and high latitudes, extend the data set into the middle stratosphere. Recently, measurements from the Russian M55 Geophysika aircraft up to 20 km altitudes have been made at mid-latitude and in the tropics.

**Table 1.8** Aircraft and balloon experiments with FISH

Project	Platform	Period	No. of flights	Location	Lat.	Long.	Altitudes
- <sup>1</sup>	balloon	20 Sep 93	1	France	44N	0E	8-33 km
- <sup>2</sup>	Falcon	Mar 95	2	Germany	47-54N	9-12E	5-13 km
STREAM IIa <sup>3</sup>	Citation	May-Jun 96	8	Ireland	52-57N	14W-5E	5-13 km
POLSTAR I <sup>3,4</sup>	Falcon	Jan-Feb 97	6	Sweden	66-82N	10W-23E	5-13 km
			1	transit	68-48N	10-21E	
ILAS	balloon	11 Feb 97	1	Sweden	68N	21E	8-26 km
STREAM IIb <sup>3</sup>	Citation	Mar 97	4	Sweden	63-73N	10-22W	5-13 km
			2	transit	52-68N	5-21E	
-	Falcon	Aug 97		Germany	46-53N	2-18E	5-13 km
POLSTAR II <sup>3</sup>	Falcon +	Jan-Feb 98	6	Sweden	62-82N	10W-21E	5-13 km
	Lear Jet		2	transit	48-68N	10-21E	
STREAM III	Citation	Jun-Jul 98	8	Canada	46-56N	90-74W	5-13 km
			2	transits	48-64N	80W-5E	
			2	Netherlands	52N	5E	
APE ETC	M55	Dec 98	5	Italy	44N	12E	8-20 km
THESEO	balloon	06 Feb 99	1	Sweden	68N	21E	7-28 km
		03 May 99	1	France	44N	0E	7-31 km
APE THESEO	M55	Feb-Mar 99	7	Seychelles	3N-10S	48-62E	8-20 km
			2	transit	44N-5S	12-55E	8-20 km
APE-GAIA	M55	Oct 99	3	transit	54S-37N	68-6W	8-20 km
THESEO 2000	balloon	27 Jan 2000	1	Sweden	68N	21E	7-26 km
		01 Mar 2000	1	Sweden	68N	21E	7-27 km

<sup>1</sup> Zöger *et al.* [1999b], <sup>2</sup> Zöger *et al.* [1997], <sup>3</sup> Eicke [1999] and Schiller *et al.* [1998],

<sup>4</sup> Schiller *et al.* [1999]

## Others

A Lyman- $\alpha$  fluorescence hygrometer has been developed and operated by the Central Aerological Observatory (CAO) in Moscow, Russia [Yushkov *et al.*, 1995]. The instrument is designed with an open layout for contamination-free measurements, therefore its use is restricted to nighttime observations (solar zenith angle  $<94^\circ$ ). Since 1991, a series of balloon flights up to 35 km using these hygrometers has been made at high northern latitudes [Khattatov *et al.*, 1994, Yushkov *et al.*, 1998].

### 1.2.3 Tuneable Diode Laser (TDL) spectrometers

#### JPL open-path tuneable diode laser spectrometers

Measurement of water vapour from aircraft platforms using external, open-path, optical absorption spectrometers provides a simple and direct *in situ* approach to the problem of obtaining water vapour abundances in the troposphere and lower stratosphere. With no containing walls or sample inlets, measurements can be made free of concerns related to wall reactions, flow rate restrictions, or "sticking", and with a high sampling rate limited only by the capability of the signal processing electronics and software. In addition, high-resolution detection of individual rotation-vibration lines in the near- and mid-infrared regions allows complete discrimination against liquid or solid H<sub>2</sub>O (i.e. rain or ice particles) allowing accurate measurements of water vapour in clouds.

Two near-infrared aircraft instruments have been developed recently at the Jet Propulsion Laboratory (JPL) [May, 1998] and have been flown on the NASA ER-2 and DC-8 research aircraft since 1997. Both operate with similar electronics and software, but differ in their external optical arrangements.

The JPL laser hygrometers utilise second harmonic absorption spectroscopy [Webster *et al.*, 1988]. While this technique alters the observed spectroscopic line shape and requires a quantitative transfer function for the signal processing electronics, gas concentration is ultimately derived from the Beer-Lambert law which relates observed line centre absorption to absorber number density,

$$\rho = \frac{-\ln[\tau(\nu)]}{k(\nu)L} \quad (1.5)$$

$\rho$  is the absorber number density,  $\tau(\nu)$  is the observed transmission at wave number  $\nu$ , and  $L$  is the optical absorption path length.  $k(\nu)$  is the absorption coefficient and requires knowledge of the line strength and molecular line shape for the transition of interest.

In the second harmonic detection technique a small-amplitude sinusoidal modulation is added to the base sawtooth laser current scan ramp. The detector signal is demodulated at twice the sine wave frequency to produce second harmonic line shapes. To quantify an observed  $2f$  spectral line the amplitude of the sine wave modulation must also be known precisely. Techniques for determining the modulation amplitude are described by *May and Webster* [1993].

The ER-2 instrument contains a multipass Herriott cell [Herriott *et al.*, 1964; Altmann *et al.*, 1981] and was designed primarily for measurements in the stratosphere where water vapour concentrations typically fluctuate around a mean value near 5 ppmv. The optical path length is 11.13 m enabling measurements in the range from 400 to 0.1 ppmv. For the DC-8, which could not reach the stratosphere during CAMEX-3, measurements were desired from the ground to the aircraft ceiling of 42000 feet and an optical path length of 50 cm was chosen. In this case a multipass system is not required and the laser beam travels a simple "there and back" path between the laser/detector head, and a small return mirror. With this system, measurements from 30000 to 8 ppmv can be made.

The optical absorption paths are located outside the aircraft boundary layer on both aircraft. On the ER-2 this required locating the optical path  $>5$  cm from the superpod skin. For the DC-8 the location required a much larger distance from the aircraft skin, and the optical path was positioned 15.3 cm away. The total optical path within the evacuated optical housings is  $<1$  cm, which eliminates any residual  $H_2O$  absorption which could add uncertainty to the measurement.

The base spectrum scan rate for the ER-2 instrument is 10 Hz, meaning that measurements can, in principle, be made at this sampling rate. However, spectrum processing times dictate slower sampling rates and multiple spectra were averaged for the POLARIS and WAM missions to produce a net sampling period of 1-2 seconds. Recently, a new laser controller was designed which increased the signal detection frequency by more than an order of magnitude (from 20 kHz to 256 kHz). The base scan rate dropped to 8 Hz and the number of averaged scans adjusted accordingly to maintain an approximate 2 s sampling period. The higher frequency controller was used for the DC-8 instrument (where beam jitter was not a problem due to the double-pass arrangement) and is expected to result in significantly improved SNR for future ER-2 and WB57F flights. Figure 1.5 shows ER-2 data from a POLARIS flight (May 2, 1997) of the ER-2 where a measurement precision of  $+0.05$  ppmv for a two second integration time is demonstrated.

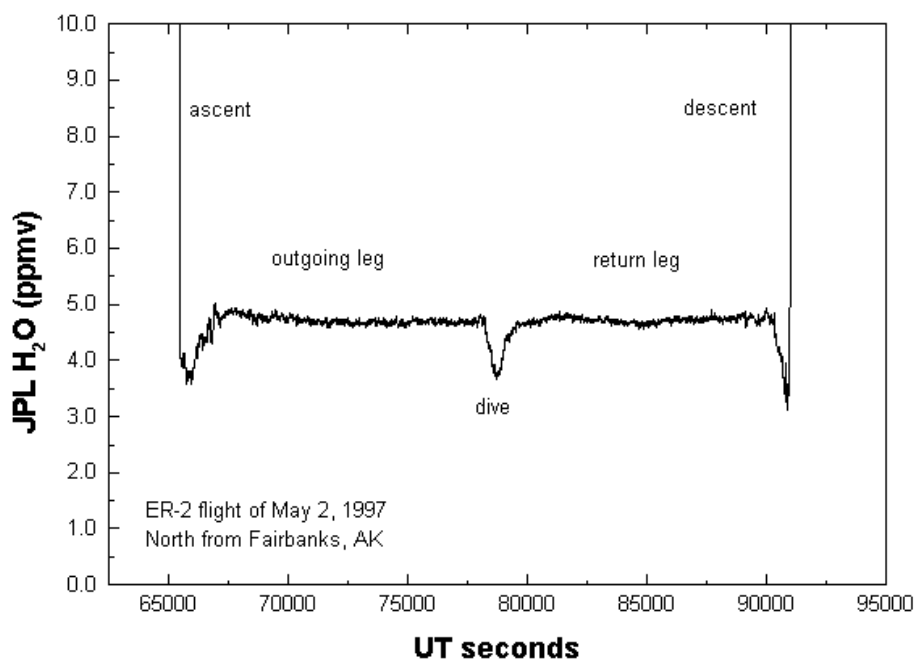


Figure 1.5 ER-2 data from a POLARIS flight on 02 May 1997. The noise level in the data is  $\pm 0.05$  ppmv for a 2 s spectrum integration time (i.e. 20 spectra averaged to produce each data point).

If all spectral line parameters and the electronics response are known with high precision, the data processing matrix (with appropriate Beer's law corrections) would be sufficient to produce accurate water vapour volume mixing ratios at all pressures and temperatures. However, uncertainties in several independent parameters can cause pressure- and temperature-dependent errors that are difficult to quantify at the few percent level in a second-harmonic spectrometer. The most important of these parameters are the air-broadening coefficient and its dependence on temperature, the exact value for the laser modulation amplitude, and the detailed behaviour of the electronic signal demodulator with respect to residual amplitude (RAM) noise generated by the laser. Analytical laboratory calibrations are therefore used to derive correction curves to the data after initial processing.

The laboratory calibration procedure is to flow a standard gas mixture through the optical cell and then immediately through a NIST-traceable chilled mirror hygrometer (General Eastern model 1311DR, see Section 1.1.1). Two methods have been used to make a leak-tight chamber: either the entire H<sub>2</sub>O instrument is installed in a thermal-vacuum chamber, or a telescoping tube is installed between the two mirrors of the optical cell. Calibration measurements are made over wide ranges in mixing ratio, temperature and pressure (50-200 ppmv, 50-500 hPa, 250-300 K) to map out differences between the actual instrument response, and the predicted response [May, 1998].

Number density is the fundamental quantity measured by the laser hygrometers, as defined by Equation 1.5. This can be converted to volume mixing ratio, dew point, etc. using measurements of pressure and temperature. For the POLARIS ER-2 flights the final accuracy in the measurements was a function of pressure and has been estimated at 5% for pressures <100 hPa,

8% for pressures 100-200 hPa, and 10% for pressures >200 hPa [May, 1998]. Using analytical correction curves derived from laboratory calibrations the accuracy for the CAMEX-3 DC-8 measurements is expected to be reduced to approximately 5% at all pressures.

A summary of the missions of the JPL laser hygrometers is given in Table 1.9 (flight count does not include engineering and test flights). For the ER-2 and WB57F, measurements were made from approximately 5 km altitude up to the aircraft ceilings in the 18-20 km range. The DC-8 measurements were made from the surface to the aircraft ceiling of 13 km.

**Table 1.9** JPL laser hygrometer missions.

Mission	Platform	Dates	No. of flights	Deployment site	Latitude	Longitude
POLARIS	ER-2	Apr-Sep 1997	24	Fairbanks, Alaska	3S-90N	73-171W
WAM	WB57F	Apr 1998	3	Houston, Texas	9-46N	73-108W
CAMEX-3	DC-8	Jul-Sep 1998	20	Cocoa Beach, Florida	14-40N	63-86W
SOLVE	DC-8	Dec 1999 - Mar 2000	24	Kiruna, Sweden	68N	21E
	ER-2		11			

### The LaRC/ARC diode laser hygrometer (DLH)

The Diode Laser Hygrometer (DLH), developed by NASA's Langley and Ames Research Centers (LaRC and ARC), has flown on the NASA DC-8 aircraft in several field missions including those given in Table 1.10 [Vay *et al.*, 1998; Vay *et al.*, 2000; Cho *et al.*, 2000]. The sensor consists of a compact laser transceiver mounted to a DC-8 window port and the sheet of retro-reflecting "road sign" material applied to the DC-8 engine enclosure that completes the optical path. The retro-reflecting sheet returns the beam to the laser transceiver thereby completing a 28.5 meter round trip in the free airstream. This sensor approach has a number of advantages including compactness, simple installation, fast response time, no wall or inlet effects, and wide dynamic measurement range (several orders of magnitude).

Using differential absorption detection techniques similar to those described in Sachse *et al.* [1987 and 1991], gas-phase water ( $\text{H}_2\text{O}(\text{v})$ ) is sensed along the external path. For dry conditions (generally altitudes > 6 km), the diode laser wavelength is swept across a strong, isolated line at  $7139.1 \text{ cm}^{-1}$  while for altitudes typically < 6 km the laser wavelength sweep is locked onto a weaker line at  $7133.9 \text{ cm}^{-1}$ . By normalising the laser differential absorption signal with the laser power signal, the  $\text{H}_2\text{O}(\text{v})$  measurement is unaffected by clouds, haze, plumes, etc. thereby enabling high spatial resolution measurements in and around clouds. The  $\text{H}_2\text{O}(\text{v})$  mixing ratio is computed by an algorithm from the differential absorption magnitude, ambient pressure and temperature, and coefficients derived from laboratory calibration of the sensor. The calibration is conducted prior to each field mission and involves measuring the sensor response to humidified air flowing through each of two chambers (of lengths 1 and 3 meters). A matrix of optical depth and pressure values is generated in these chambers by varying: (1) moisture content in the flow (ultra dry air and humidified air typically ranging from  $0^\circ$  to  $10^\circ\text{C}$  dew point), (2) path length (1 or 3 m), and (3) chamber pressure from 100 to 1000 hPa. The moisture content in the calibration flow is monitored by an Edgetech model 2001 dew point hygrometer with accuracy of  $\pm 0.2^\circ\text{C}$  traceable to NIST. Sensor response to varying magnitudes of laser wavelength sweep is also recorded. From this collection of calibration data and temperature-dependent line parameter information taken from HITRAN 96 [Rothman *et al.*, 1998], separate sets of calibration coefficients for the strong and weak  $\text{H}_2\text{O}(\text{v})$  lines are calculated and provided to the algorithm which reduces raw sensor data to  $\text{H}_2\text{O}(\text{v})$  mixing ratio.

**Table 1.10** Missions using the LARC/ARC Diode Laser Hygrometer.

Mission	Dates	No. of flights	Deployment site	Latitude	Longitude
SUCCESS	Apr - May 1996	6	Salina, Kansas		
PEM-Tropics A	Aug - Oct 1996	22	Honolulu, Hawai Tahiti Fiji New Zealand Easter Island	72S - 45N	150E-110W
SONEX	Oct - Nov 1997	12	Bangor, Maine Ireland Azores	10N - 70N	130W - 15E
PEM-Tropics B	Mar - Apr 1999	17	Hilo, Hawai Tahiti Fiji Easter Island Costa Rica	36S - 36N	87W - 163E
SOLVE	Nov 1999 - Mar 2000	24	Kiruna, Sweden	68N	21E

### 1.2.4 Radiosondes

Radiosondes have for several decades been the primary means of obtaining atmospheric vertical profile data from the surface to the lower stratosphere, for use in operational meteorological forecasts and, more recently, for assessment of climate trends from the archived data. The instrument packages are carried aloft by balloons (or dropped from aircraft or rockets, in the case of dropsondes) and are generally equipped with temperature, humidity, and pressure sensors. An overview of radiosonde instruments is given in *WMO* [1996], and *Pratt* [1985] reviews the quality of temperature and humidity data.

Currently, the global radiosonde network includes about 900 upper-air stations, and about two-thirds make observations twice daily (at 0000 and 1200 UTC). The network is predominantly land-based and favours the Northern Hemisphere. Radiosondes can achieve heights of about 35 km, although many soundings terminate below 20 km.

Measurements are made and transmitted during ascent, however the data archives may not contain the complete sounding. Radiosonde data are commonly acquired either every 2 s or every 10 s during flights. Given balloon ascent rates of about 5 m/s, the sounding data offer vertical resolution of 10-50 m. Operational data transmissions are required by the WMO at about 20 mandatory reporting levels up to 1 hPa (although soundings rarely attain that pressure level), and significant level data are required when the profiles deviate substantially from linearity between mandatory levels, thus detailed structure may not be fully captured in the archived operational reports. However, since 1995, the U.S. National Weather Service has archived data every 6 s for greatly enhanced vertical resolution.

Of the three basic radiosonde measurements, humidity observations are the most difficult to make because of the wide dynamic range needed for an instrument to measure water vapour concentrations varying by four or five orders of magnitude throughout the sounding. Humidity sensor performance depends on rapid exchange of water molecules with the air, and at cold temperatures, low water vapour mixing ratios make the measurement difficult. For this reason, the quality of humidity data from radiosondes is generally thought to decrease with decreasing water vapour content, temperature, and pressure [*Elliott and Gaffen, 1991*]. Stratospheric

humidity data from radiosondes are essentially useless [WMO, 1996, Schmidlin and Ivanov, 1998], and much of the archived upper-tropospheric humidity data for the past several decades is unsuitable for the purposes of this Assessment.

The data come from radiosondes by various manufacturers, some producing multiple models, based on a variety of humidity sensor types. In each case, the fundamental quantity measured is relative humidity. The most commonly used are: goldbeater's skin sensors (used mainly in China, Russia, and the FSU); lithium chloride sensors (used in U.S. radiosondes before 1965, currently only in India); carbon hygristors; and thin-film capacitors. Goldbeater's skin (beef peritoneum) sensors, more commonly used in the early decades of upper-air observations, give reliable humidity observations only at temperatures above 0°C [Schmidlin and Ivanov, 1998], making the upper-tropospheric and stratospheric observations of no value. Lithium chloride sensors, perform poorly at very high or very low humidity; have long time constants of response; are severely affected by wetting by rain [Mathews, 1965, Showalter, 1965]; and are deemed unreliable at pressures lower than 600 hPa [WMO, 1996].

Because of the widespread use of radiosondes carrying carbon hygristors and thin-film capacitors, much of the existing data archive is based on these sensors. Here, the recent findings on the performance of these two sensors in the upper-troposphere and the possibility of correcting some upper-tropospheric humidity data from thin-film capacitors are summarised.

Carbon hygristors are polystyrene strips, coated with a hygroscopic film containing carbon particles, whose electrical resistance increases with relative humidity. Carbon hygristors respond very slowly at temperatures below -40°C (typical of the upper troposphere and lower stratosphere) and do not function at all at -60°C. These data are considered so unreliable that many countries have special data reporting practices for low temperatures [Gaffen, 1993]. For example, humidity measurements below -40°C were not reported by the U.S. National Weather Service until 1993 (when they were introduced in response to requests from data users), and significant caveats are warranted with the post-1993 data [Wade, 1994, 1995]. Recent tests suggest that carbon hygristors have a moist bias at relative humidities above about 60% [Schmidlin and Ivanov, 1998]. They can also experience hysteresis after exiting clouds, resulting in significant humidity errors.

Thin-film capacitors (marketed as Humicap) are used on Vaisala and Meisei radiosondes. The capacitors have one electrode treated with a polymer film whose dielectric constant varies with ambient water vapour pressure. Though thin-film capacitors also respond more slowly at low temperatures, they are faster than carbon hygristors. Therefore, the upper-tropospheric humidity data from thin-film capacitors are potentially more valuable. There are three types of Vaisala humidity sensors:

a) Humicap A (RS80-A). This is the original RS80 humidity sensor and the only one in use until the mid-90s. It has a time constant of 100 s at -50°C and 400 s at -70°C, thus it will respond to 63% of a step change in humidity over a vertical distance of 0.5 and 2 km respectively. Experience has shown that there is a dry bias in the A type sensor at cold temperatures (see below).

b) Humicap H type (RS80-H). This sensor is smaller than the A type and responds more quickly. It appears not to suffer the same biases as the A type [Kley *et al.*, 1997] and is capable of measurement up to the tropopause. The sensor's reproducibility in the lower troposphere is quoted as  $\pm 3\%$  in relative humidity [http://www.vaisala.com]. Unfortunately, there is at present no reliable estimate of the accuracy of this sensor at the higher levels.

c) RS90 sensor. The new Vaisala radiosonde has an improved humidity sensor, which is designed to counter the problem of icing in clouds (see below). Other than this change the sensor is similar to the Humicap-H, with a modest improvement in accuracy in the upper troposphere. To date few countries have adopted the RS90 operationally, and its performance in the upper troposphere has not been determined.

The sensors are subject to several well-understood sources of measurement error. Corrections for some of these are now becoming available. However, before applying corrections to archived data, it is recommended to consult the operating weather services because the information on which type of sensor was used for a particular sounding is not archived with the data. The known error sources are:

1. An approximation for the temperature dependence of the calibration causes an error that increases with decreasing temperature, and is significant at temperatures below  $-30^{\circ}\text{C}$  for RS80-A measurements and below  $-50^{\circ}\text{C}$  for RS80-H measurements. Observations by *Heymsfield and Miloshevich* [1995] and *Kley et al.* [1997] showed significant low biases of up to 30% relative humidity at  $-65^{\circ}\text{C}$  in measurements from the RS80-A sensor within ice clouds (where the relative humidity should be at least saturated with respect to ice, about 55%). This error is merely a data processing error, not an inherent limitation of the sensor, and a temperature-dependent correction is available (see Chapter 2.2.4, figure 2.12).
2. A time-lag error is caused by an increase in the sensor's time constant (63% response time) with decreasing temperature. The time constant for both sensors exceeds one minute at temperatures below about  $-50^{\circ}\text{C}$  and two minutes below about  $-60^{\circ}\text{C}$ . Given typical balloon rise rates, the sensors will respond to 63% of a step change in humidity over vertical distances of about 0.6 or 1.2 km at these temperatures [*Paukkunen*, 1995]. The time constant for the sensors has been measured as a function of temperature, so it may be possible to correct these errors if the sounding data possess sufficient time resolution.
3. The sensors are susceptible to dry-bias errors that result from chemical contamination of the sensor polymer and from long-term sensor instability (sensor ageing). Corrections for these errors are being developed; however, the contamination issue is being addressed by Vaisala with changes in the radiosonde packaging, thus the applicability of the corrections will often be questionable for archived data.
4. Icing of the sensors when passing through clouds renders the remainder of the humidity profile invalid. The new Vaisala radiosonde, model RS90, addresses this problem by alternating observations between two sensors, heated to remove ice.

Although radiosonde sensors respond to relative humidity, sounding data can be reported in terms of either relative humidity or dew point depression, depending on the data archive. Differences in data reduction methods lead to small differences in reported dew point depression that are largest in cold dry conditions [*Elliott and Gaffen*, 1993]. In addition, errors in temperature and pressure observations will influence humidity variables computed using those data. Temperature and pressure errors tend to be larger in the upper-troposphere and stratosphere than in the lower troposphere. Many, but not all, radiosonde stations adjust the temperature data for solar and infrared radiation errors, and lag errors. However, these adjustments are empirical and not tailored to detailed atmospheric conditions (e.g. cloudiness) that influence the actual errors.

The simultaneous use of different radiosonde types within the global network can lead to differences in upper-tropospheric humidity across geopolitical boundaries, as seen by *Soden and Lanzante* [1996]. For long-term climate studies, changes in radiosonde instrumentation and

methods of observation can introduce artificial signals into the data record [Gaffen, 1993,1994, Ross and Gaffen, 1998]. Therefore, care must be taken to verify both the spatial and temporal homogeneity of radiosonde data used to determine climatological features as well as interannual and longer changes in atmospheric water vapour.

In conclusion, of the many different radiosonde humidity sensors, only the thin film capacitor sensors are capable of measuring in the upper troposphere. The Humicap sensors are and have been widely used all over the world, and so offer, potentially, a valuable climatological archive. However, the existence of several uncorrected and poorly documented sources of measurement error at cold temperatures, as well as changes in radiosonde instrumentation and reporting practices, render most archived humidity data unsuitable for upper-tropospheric climate studies without extreme care in assessing the accuracy of individual radiosonde types and reporting practices and their changes with time. The availability of corrections to known errors and newer humidity sensor technologies may offer improved data in the upper troposphere. Global deployment of more reliable radiosondes on a routine basis would provide a very valuable source of *in situ* water vapour profiles.

### 1.2.5 MOZAIC sensors

MOZAIC (Measurement of Ozone by Airbus In-Service Aircraft), operated since August 1994, is a project for the automated measurement of ozone and water vapour onboard five Airbus A340 aircraft on scheduled flights of commercial European airlines [Marenco *et al.*, 1998]. The flights cover a large extent of both hemispheres and will go on for several years on a regular time schedule. The percentage of different flight routes is shown in Figure 1.6. For the period between August 1994 and December 1998, data from more than 10,000 flights with an average of more than 8 hours length are available in the MOZAIC database at Centre National de Recherche Météorologique, (CNRM, Toulouse, France). Also, for nearly each flight altitude profiles of ascent and descent at the respective airports are available, giving a total of more than 19,000 profiles.

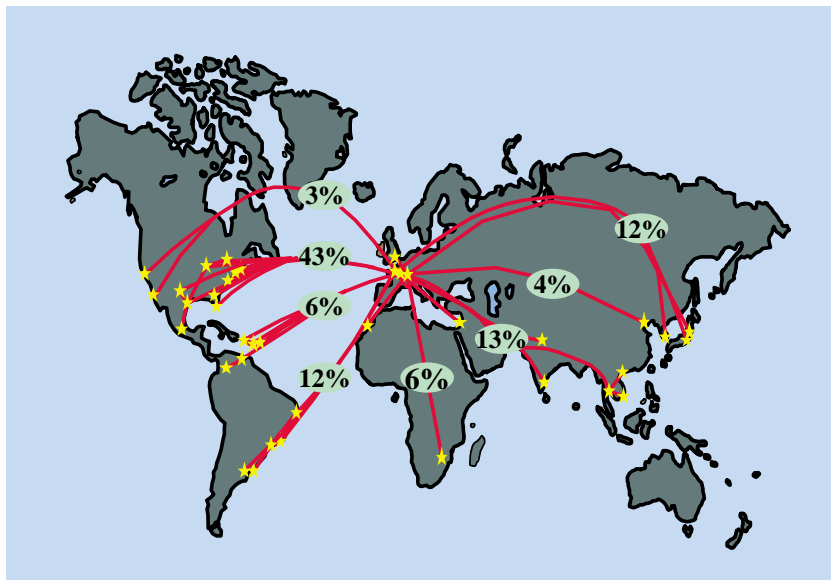


Figure 1.6 Overview of flight routes with MOZAIC water vapour measurements for the period August 1994 to December 1998. The numbers give the percentage of flight routes.

Relative humidity and temperature are measured *in situ* with an airborne sensing device AD-PS2 (Aerodata, Braunschweig, Germany) mounted in an appropriate housing (Model 102 BX, Rosemount Inc., Aerospace Division, United States) [Helten *et al.*, 1998]. The humidity sensor (Humicap-H, similar to the Vaisala RS80) is a capacitive sensor with a hydroactive polymer film as dielectric whose capacitance depends on the relative humidity (see section 1.2.4). The temperature sensor, a platinum resistance sensor (PT100), is mounted parallel to the humidity sensor near its sensing surface for the direct measurement of the temperature.

The housing with both sensors is positioned outside the fuselage, 7 m backward from the aircraft nose on the left side just below the cockpit. The air is sampled at 7 cm distance from the aircraft skin, well outside the aircraft boundary layer. Inside the housing the air is divided into two parts. The main flow traverses straight through the housing. The minor flow makes a right angle turn to a smaller channel, perpendicular to the main channel, passing over the sensor elements before leaving the housing through a small outlet, located at the lower back side of the housing. The right angle turn of the secondary airflow protects the sensors against dust, water droplets, and particles. The internal boundary layer air is sucked off through small holes in the sidewalls of the housing, minimising internal boundary layer effects.

The air entering the housing is subject to adiabatic compression by the strong speed reduction in the inlet part of the housing. The conversion of the kinetic energy of the sampled air into heat leads to a significant temperature increase of the air sampled by the sensor. The temperature of the ambient air, called static air temperature (SAT), can be computed from the air temperature measured inside the housing, called total recovery temperature (TRT), if the air speed of the aircraft is known. TRT deviates by less than 1°C from the total air temperature (TAT) which is to be expected by an exact 100% conversion of the kinetic energy of the sampled air into heat inside the housing. The correction of the TRT is performed with an empirical correction factor provided by the housing manufacturer, determined from a series of wind channel experiments. The relationship between SAT and TAT is a function of the Mach number.

Due to adiabatic heating, the relative humidity measured inside the sensor housing, called dynamic relative humidity ( $RH_D$ ), is much lower than the ambient relative humidity, called static relative humidity ( $RH_S$ ), which has to be determined. Their ratio is given by

$$\frac{RH_S}{RH_D} = \left( \frac{SAT}{TAT} \right)^{c_p - c_v} \frac{E_w(TAT)}{E_w(SAT)} \quad (1.6)$$

where  $E_w(SAT)$  and  $E_w(TAT)$  are the water vapour saturation pressures of pure liquid water at static air and total air temperature respectively.  $C_p$  ( $= 1005 \text{ J kg}^{-1} \text{ K}^{-1}$ ) and  $C_v$  ( $= 717 \text{ J kg}^{-1} \text{ K}^{-1}$ ) are the specific heats of dry air at constant pressure and volume respectively.

The ratio  $RH_S/RH_D$  is the product of two factors. The first compensates for adiabatic compression, while the second accounts for the different water vapour saturation pressures at SAT and TAT, respectively. The dynamic relative humidity,  $RH_D$ , measured by the sensing element is appreciably lower than the static relative humidity,  $RH_S$ , due to the adiabatic temperature increase in the housing. Therefore, at cruise altitude, typically above 8 km, the sensor is working in the lowest 10% of its full dynamic range. In this region the ratio  $RH_S/RH_D$  increases to values of 13, and it is obvious that individual calibrations of each sensor are necessary.

The temperature in the housing is typically 27°C higher than the ambient air temperature, so that the sensor temperature is always operated above -40°C. This increases the accuracy of the sensor, and makes its response faster in comparison with Humicap-H sensors operated on radiosondes.

Each MOZAIC humidity sensor is normally changed each month and calibrated in the laboratory before installation and again after 500 hours of flight operation. The calibrations are executed in an environmental simulation chamber in the laboratory [Smit *et al.*, 1994]. Pressure, temperature, and frost point temperature are computer-controlled to simulate typical tropospheric conditions, including tropopause and lower stratosphere up to 15 km altitude. Frost point temperatures down to -70°C can be reached. The water vapour mixing ratio is determined with a Lyman- $\alpha$  fluorescence hygrometer [Kley and Stone, 1978; Kley *et al.*, 1979; Helten *et al.*, 1998], installed in the simulation chamber as a reference instrument for the measurement of the water vapour mixing ratio. The accuracy of the H<sub>2</sub>O mixing ratio measurements in the fluorescence mode of the instrument is  $\pm 6\%$ , including random and systematic errors with inclusion of the accuracy of the absorption cross sections of H<sub>2</sub>O and O<sub>2</sub> at 121.6 nm wavelength [Kley, 1984], which determines the calibration of the fluorescence measurement.

These calibrations revealed that the relative humidity of a calibrated sensor ( $RH_C$ ) for a constant temperature can be expressed by a linear relation

$$RH_C = a + b \cdot RH_{UC}, \quad (1.7)$$

where  $RH_{UC}$  is the uncalibrated output from an individual sensor, and  $a$  and  $b$  are coefficients that result from the calibration procedure. Each calibration is executed at three temperatures: -20°C, -30°C, and -40°C, resulting in three pairs of calibration coefficients  $a$  and  $b$ .

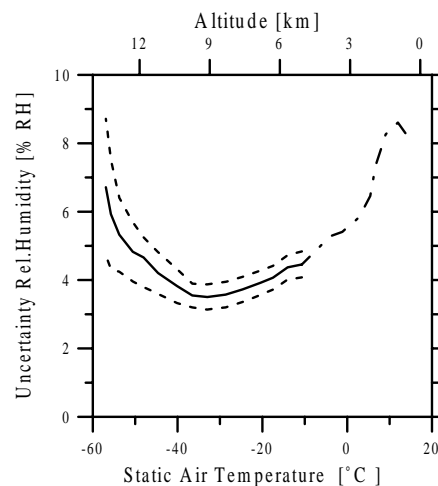


Figure 1.7 Mean uncertainty in percent RH of all 1995 MOZAIC relative humidity measurements (solid curve) as a function of static air temperature (bottom x axis). The corresponding altitude is indicated on the top x axis. The standard deviation of the mean is marked by the dashed curves. The region not covered by pre-flight and post-flight calibrations (lower troposphere, see text) is indicated with an estimated mean uncertainty (dashed/dotted line).

The mean of the pre- and post-flight calibration coefficients of each flight period are used to evaluate the measurements. The differences between both sets of these calibration coefficients give the main contribution to the uncertainty of the measurement [Helten *et al.*, 1998]. The variations of the uncertainties of the RH measurements were determined as the mean of all

individual total uncertainties over all MOZAIC data from 1995 as a function of SAT (Figure 1.7). The standard deviation is also shown. The uncertainty ranges from  $\pm 7\%$  RH at  $-55^\circ\text{C}$  ( $\approx 13$  km) down to  $\pm 4\%$  RH at  $-40^\circ\text{C}$  ( $\approx 10$  km). At a lower altitude, for SAT ranging between  $-40^\circ\text{C}$  ( $\approx 9$  km) and  $-20^\circ\text{C}$  ( $\approx 6$  km) the uncertainty is within  $\pm (4-6)\%$  RH, increasing above  $0^\circ\text{C}$  (near ground level) to  $\pm 8\%$  RH. For the region below 5 km altitude, only an interpolation between our sensor calibrations below  $-20^\circ\text{C}$  and the nominal calibration of the sensor manufacturer is used, indicated as a dashed dotted line in Figure 1.7. A standard deviation is also not quoted for this altitude range. For the data in 1999, the sensor calibration procedure in the environmental calibration chamber will also include this temperature (=altitude) range.

### 1.2.6 Cryogenic collection

Compared to other *in situ* techniques, cryogenic collection of water vapour is a somewhat cumbersome technique and it also offers a lower spatial resolution. Its use is restricted to some studies in the 60s and 70s. However, it allows one to measure also the concentration of the isotopic water molecules HDO and HTO. Historically, the first simultaneous *in situ* measurements of the vertical distribution of the major hydrogen compounds  $\text{H}_2\text{O}$ ,  $\text{CH}_4$ , and  $\text{H}_2$  in the stratosphere have been made using this technique [Pollock *et al.*, 1980].

The NCAR cryogenic whole air sampler [Lueb *et al.*, 1975] and its operation have been modified for a number of balloon flights for measurement of the water content of the air samples collected [Pollock *et al.*, 1980]. The various sampling systems consist of up to 16 stainless steel cylinders designed as a cryopump and which are filled during balloon descent. In the laboratory, aliquots of the sample are drawn into separate containers for gas chromatographic analysis of  $\text{CH}_4$ ,  $\text{H}_2$ , and other long-lived tracers. The amount of water vapour is measured by separating the water from air in a cold trap. This is followed by reduction of  $\text{H}_2\text{O}$  to  $\text{H}_2$  whose amount is measured volumetrically.

Although the principle of this technique is very simple, it is complicated by contamination. There are several steps during sample collection and transfer at which the original amount of water in the samples can be disturbed. Pollock *et al.* [1980] determined correction factors in separate experiments to compensate these artefacts. For the measurement of the  $\text{H}_2\text{O}$  amount, the factors are generally below 20%. The accuracy of stratospheric  $\text{H}_2\text{O}$  measurement is 0.3-1.0 ppmv for most of the samples analysed.

Between 1975 and 1978, the NCAR whole air sampler was used on eight balloon flights at different latitudes and analysed for water (Table 1.11). Data of  $\text{H}_2\text{O}$ , the water isotopes,  $\text{CH}_4$  and  $\text{H}_2$  obtained during these flights including the individual uncertainties are listed in Pollock *et al.* [1980].

**Table 1.11** Balloon-borne measurements using the NCAR cryogenic whole air sampler.

Date	Latitude	Longitude	Altitude [km]	No. of samples
02 Jun 1975	32N	96W	17-34	14
14 Aug 1975	52N	102W	20-43	8
24 Sep 1975	32N	106W	33-39	4
27 Jan 1976	32N	96W	16-34	13
27 Feb 1976	32N	96W	36-41	4
10 Aug 1976	52N	102W	32-40	12
14 Aug 1977	52N	102W	21-40	7
23 Apr 1978	65N	148W	21-40	7

Measurements of tropospheric H<sub>2</sub>O and HTO vertical profiles were made aboard two aircraft between 1965 and 1973 [Ehhalt, 1971; Ehhalt, 1974]. Here, the water was separated from the air aboard the aircraft by passing the air through liquid N<sub>2</sub> or dry ice cooled traps and freezing out water. Sampling time varied from 15 to 60 min, depending on altitude. In the laboratory, the water amount was measured by weighing.

On the NCAR Queen Air flights, samples were collected at eight altitudes from 1.5 to 9 km. These flights were carried out in regular intervals in different periods given in Table 1.12. The flights on the Sabreliner extended the measurements to the upper troposphere, i.e. samples were taken at seven flight levels from 6 to 13 km. All the aircraft data are listed in Ehhalt [1974].

**Table 1.12** NCAR aircraft measurements of H<sub>2</sub>O and HTO in the 60s and 70s.

Period	Latitude	Longitude	Frequency / No. of flights
Queen Air			
Nov 1965	41N	102W	1
Feb-Jun 1966	41N	102W	3 per month
Jul 1966 – Jan 1967	41N	102W	monthly
Jul 1966 – Aug 1967	34N	125W	monthly
Jul 1966 – Aug 1967	36N	117W	monthly
Mar 1971 – Jan 1972	41N	102W	nearly monthly
Nov 1972	41N	102W	1
Sabreliner			
Mar 1971 – Sep 1973	32N	96W	irregular
Feb 1972	Florida		1
Sep 1972	37N	122W	1

### 1.3 Ground based, balloon-borne and airborne remote sensing instruments

A number of remote sensing instruments are used to measure water vapour on balloons, aircraft, or from the ground. They are discussed in this Chapter separately from space-borne sensors because the spatial and temporal coverage of such measurements is more comparable to that of in-situ hygrometers.

Several instruments are presented based on techniques exploiting absorption or emission features in the IR and far-IR spectral region in order to measure vertical profiles of water vapour and many other species from balloons and aircraft. Generally, they use similar measurement geometry, and thus retrieval algorithms, as satellite experiments and are therefore a useful tool for their validation. LIDARs are based on a profiling technique. They have been applied to H<sub>2</sub>O measurements mainly at higher concentrations in the troposphere, but have recently also been extended to the lowest layers of the stratosphere. Microwave techniques are used for altitudes of the upper stratosphere and higher altitudes. As an independent technique, they provide useful information on the absolute H<sub>2</sub>O abundance in the stratosphere.

Remote sensing measurements can also be influenced by contamination problems when the payload is outgassing in the stratosphere. If the measurement is carried out from the troposphere, the large ‘background’ signal from the moist lower levels reduces the data quality or resolution for stratospheric measurements.

#### 1.3.1 Microwave instruments

The retrieval of water vapour profiles as a function of altitude with ground-based and aircraft-based microwave instruments relies upon the sensitivity of the observed spectrum to pressure broadening. The line width of the spectrum decreases monotonically with altitude, and the resultant signal can be deconvoluted to retrieve a vertical profile. A retrieval of the mesospheric portion of the water vapour profile therefore relies primarily on the emission measurements very near to the centre of the emission line, while the stratospheric portion is determined primarily from emission measurements further from line centre (Figure 1.8a). While tropospheric water vapour emission dominates the total signal received at the ground, the large line width of this tropospheric signal makes it possible to separate this contribution from the middle atmospheric component of the emission.

While ground-based instruments necessarily must simultaneously observe all of the layers of the atmosphere, limb sounders can make use of a narrow beam, and thereby measure emission that contains a large contribution from a narrow layer of the atmosphere near the tangent height. In making comparisons between instruments with large differences in resolution, the effect of the resolution difference can be quantitatively assessed by creating a lower resolution profile ( $x$ ) from the original high-resolution profile ( $x_h$ ). This is done by convoluting the higher resolution profile with the averaging kernels ( $A$ ) of the lower resolution measurement, so that

$$x = Ax_h + (I-A)x_a \quad (1.8)$$

where  $I$  is the identity matrix [Rodgers, 1990].  $x_a$  is the a priori used in the lower resolution measurement, and the averaging kernels are determined by calculating the sensitivity of the lower resolution retrieval to changes in mixing ratio at different altitudes. A typical set of averaging kernels is shown in Figure 1.8b.

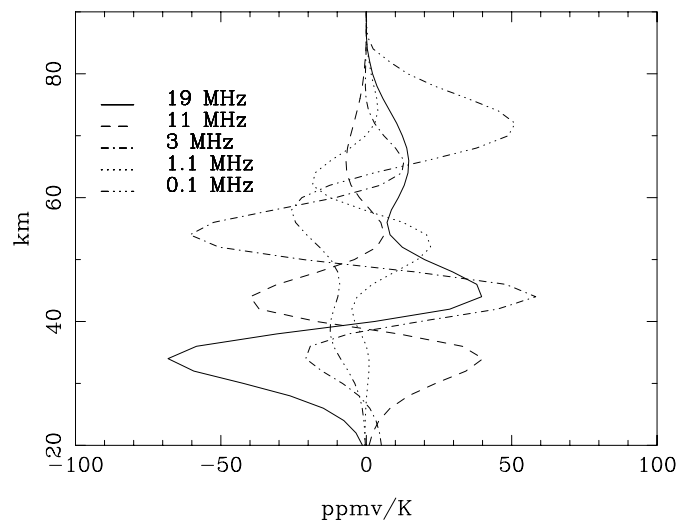


Figure 1.8a Each curve represents the change in the retrieved mixing ratio for a 1 K change in brightness temperature in a filter at the indicated frequency.

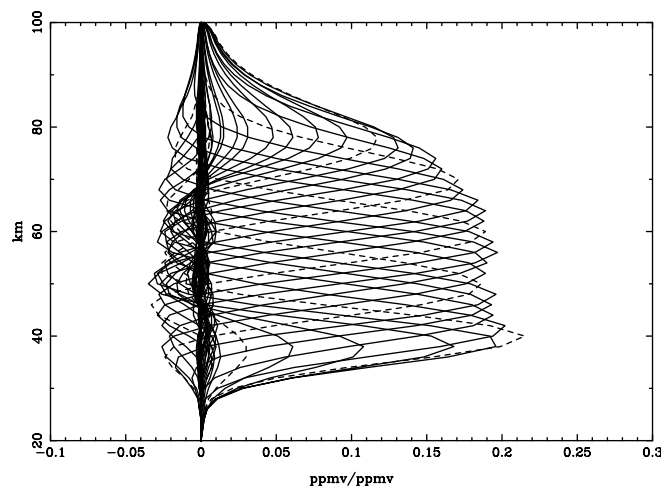


Figure 1.8b Each curve represents the change in the retrieved mixing ratio for a 1 ppmv perturbation at a given altitude. Dashed lines indicate kernels at 10 km increments.

Ground-based measurements of water vapour are generally made at 22.2 GHz, since this line is optically thin in the troposphere and thus allows continuous measurements of the middle atmosphere. At 22.2 GHz retrievals are possible up to ~80-90 km, at which point the Doppler broadening becomes greater than the pressure broadening. The 183 GHz line is usually optically thick in the troposphere, and can therefore be used for ground-based observations only at very high altitudes or when the troposphere is very dry. For aircraft-based measurements made from the stratosphere the strength of the 183 GHz transition makes it a better choice for water vapour observations. The line strengths of the 22.2 and 183 GHz transitions are taken from the calculated values given in the JPL spectral line catalogue [Pickett *et al.*, 1998], and the line widths are taken from Liebe *et al.* [1993].

The microwave instruments described below are heterodyne spectrometers, i.e. they consist of a heterodyne receiver front end and a real-time spectrometer back end. In the heterodyne receiver the high frequency microwave radiation from the atmosphere is converted to a much lower

frequency band. In this low frequency band electronic methods can be applied in order to perform spectral analysis with a resolution  $f/\Delta f$  of  $10^7$  or even higher. Down-conversion creates two bands, the Lower Side Band (LSB) and the unwanted Upper Side Band (USB). The latter has to be suppressed, either by a wave guide filter (as for the MPAE instrument) or by an interferometer (as for the Bern instrument).

Because the intensity of the atmospheric microwave emission is very low, the receiver sensitivity is an important quantity. It is defined in terms of noise temperature  $T_N$ , i.e. related to the emitted radiation (“noise”) of a blackbody of a certain temperature. The atmospheric emission is defined in terms of brightness temperature,  $T_B$ , of a blackbody. In general,  $T_B$  is 1-3 orders of magnitude smaller than  $T_N$ . For instance,  $T_B$  of the water line at 22 GHz is about 1 K, while a state-of-the-art receiver’s sensitivity is about 100 K. The only way to resolve such an atmospheric line like water vapour is to average millions of water vapour spectra. This requires a real-time spectrometer. In a real-time spectrometer a time sequence  $\tau$  of the atmospheric radiation has to be processed within this time interval  $\tau$ . Three types of real-time spectrometers are used for the instruments described below: Filterbank (WVMS), Chirp Transform Spectrometer (MPAE) and Acousto-Optical Spectrometer (Bern).

The combination of a very sensitive receiver with a real-time spectrometer, i.e. a device, which measures channel-to-channel variations that are much smaller than the overall signal, is very sensitive to all kinds of systematic errors created by unwanted emissions and reflections in and around the system. One way to eliminate these is to calibrate the system using blackbodies at one or two well known temperatures (calibration loads), assuming that the systematic errors are the same when looking either on the blackbody or the atmosphere. The difference of the atmospheric spectrum and the flat blackbody spectrum then removes most of the systematic errors (see Equation 1.10 below).

For more details of microwave radiometry of the atmosphere the reader is referred to *Janssen [1993]*.

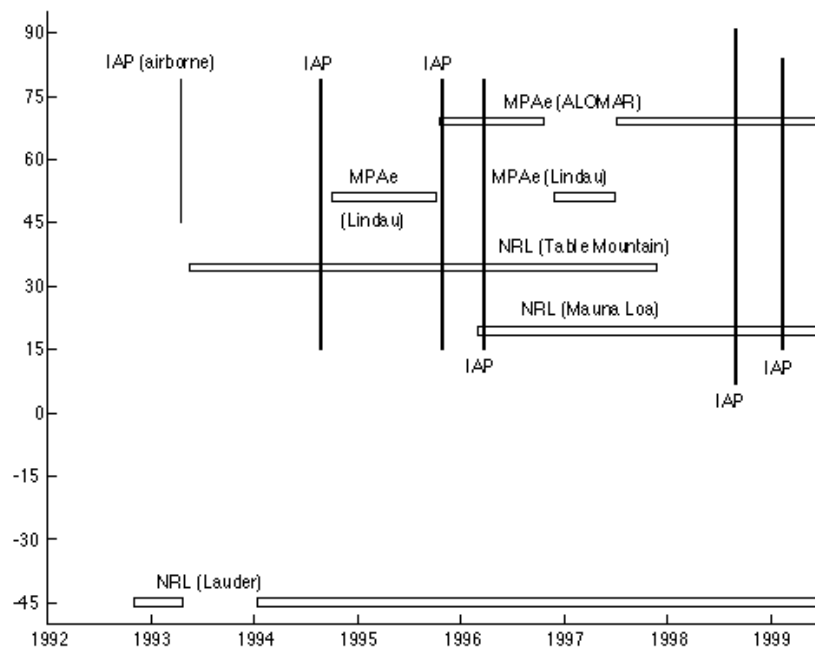


Figure 1.9 Microwave data sets of  $H_2O$  obtained during the 1990s.

### The Naval Research Laboratory (NRL) ground-based water vapour millimeter-wave spectrometer (WVMS)

The Water Vapor Millimeter-wave Spectrometer (WVMS) instruments make high spectral resolution measurements at 22.2 GHz, the emission frequency of the  $6_{16}-5_{23}$  rotational line of  $H_2O$ . The radiometer is based on a High Electron Mobility Transistors amplifier which is refrigerated to 20K and provides 30 dB gained over a 500-MHz bandwidth. Radiation enters the radiometer through a scalar feedhorn that has a FWHM beam size of  $\approx 8^\circ$ , after being reflected from an elliptical aluminium plate. A stepper motor rotates the aluminium plate that is inclined at a  $45^\circ$  angle to the axis of the motor and the horn, thus allowing variation of the measurement elevation angle. The WVMS2 and WVMS3 instrument spectrometers consist of a filter bank with thirty 14 MHz wide filters, thirty 2 MHz filters, twenty 200 kHz filters, and ten 50 kHz filters.

An estimate of the optical depth of the troposphere ( $\tau_{\text{trop}}$ ) is obtained by tipping the instrument through 11 angles from  $45^\circ$  to  $75^\circ$  from zenith, using a high density of angles near  $75^\circ$  where the rate of change of air mass ( $\mu$ ) as a function of angle is highest. To solve for the tropospheric optical depth NRL uses the measured system temperature from the widest filters ( $T_{\text{sys}}$ ), estimate the receiver temperature and the atmospheric temperature ( $T_{\text{rx}}$  and  $T_{\text{atm}}$ ), and then solve for the tropospheric optical depth using a best fit to the equation

$$T_{\text{sys}} = T_{\text{rx}} + T_{\text{atm}} (1 - \exp(-\mu\tau_{\text{trop}})) \quad (1.9)$$

Following the determination of the tropospheric optical depth, the instrument observes for two  $\approx 20$  minute scans with the mirror switching between a near zenith (reference) and low elevation angle (signal) position. In the reference position a blackbody target at ambient temperature is placed in the field of view in order to noise balance the measurements in the signal and reference position. The difference between the signal and reference measurements is the fundamental quantity used in the retrievals. The measurements are calibrated with a noise diode, which is itself calibrated weekly by alternately placing an ambient temperature and a liquid nitrogen load in front of the feedhorn. An optimal estimation technique [Rodgers, 1976] is used for the retrievals. Details of the measurement and retrieval technique are discussed in Nedoluha *et al.* [1995] and Nedoluha *et al.* [1996].

Three WVMS instruments have been in operation, providing nearly continuous measurements of water vapour from  $\approx 40$ -80 km. An integration time of  $\approx 1$  week is required in order to achieve adequate signal-to-noise for retrievals at 80 km, while in the stratosphere daily retrievals are possible. For weekly retrievals the random error is estimated to be 4-7%, with the largest error at the highest altitudes. The altitude resolution is  $\approx 10$  km, and systematic uncertainties are  $\approx 5$ -10%. The systematic uncertainties arise primarily from errors in the calibration and pointing. Uncertainties in the derived linear trends can be estimated from the accuracy to which the calibration and pointing can be re-established whenever repairs or improvements are made to the system. It is estimated that over a 4-5 year period the uncertainty in the derived linear trend is  $\sim 1\%$  of the mixing ratio. Data is available from three sites, listed in Table 1.13.

**Table 1.13** Measurement history of WVMS

Measurement Site	Measurement Period
Table Mountain, CA (34.4°N, 242.3°E)	17 May 1993 - 18 Nov 1997
Lauder, New Zealand (45.0°S, 169.7°E)	03 Nov 1992 - 21 Apr 1993
	14 Jan 1994 to present
Mauna Loa, Hawaii (19.5°N, 204.4°E)	4. Mar. 1996 to present

### The MPAE ground-based microwave spectrometer (WASPAM)

The ground-based microwave spectrometer of the Max Planck Institut für Aeronomie (MPAE), the WASPAM (Wasserdampf und Spurengasmessungen mit Mikrowellen) experiment [Hartogh and Jarchow, 1995], observes the same water vapour transition as the WVMS, i.e. 22.235 GHz and the water vapour continuum at 31.5 GHz. A rotating mirror reflects the microwave radiation of the atmosphere, a cold load and a hot load alternately to a polarisation grid. While one polarisation passes the grid into the horn antenna of the 31.5 GHz receiver, the other polarisation is reflected via an elliptic mirror to the horn antenna of the 22 GHz receiver. The signal level is amplified by about 30 dB using three High Electron Mobility Transistors. The amplifier covers the frequency range of 20 to 24 GHz and is cooled to 20 K by a closed Helium loop. A steep low-pass filter at the output of the amplifier cuts off all frequencies above 22.5 GHz. The single sideband (SSB) receiver temperature is about 100 K. The filtered signal is down-converted to 300 MHz using a local oscillator frequency of 22.535 GHz and then applied to a 1.5 GHz wide amplifier. A Chirp Transform Spectrometer (CTS) with 2048 channels of 21 kHz resolution (i.e. 43 MHz bandwidth) performs the spectral analysis. The input centre frequency of the CTS is 300 MHz. The USB rejection is better than 15 dB. The CTS provides spectra every 47  $\mu$ s. 128000 of these spectra are averaged, i.e. data are stored in 6-second intervals. The hot load consists of a microwave absorber temperature-stabilised to 300 K. The cold load consists of a microwave absorber cooled by a second closed helium loop and provides a brightness temperature of 77 K. The microwave window of the cold load consists of HDPE 1000 and is matched to 22.235 GHz. The brightness temperature of the atmosphere is calculated using

$$T_{\text{atm}} = [(P_{\text{atm}} - P_{\text{cold}}) / (P_{\text{hot}} - P_{\text{cold}})] * (T_{\text{hot}} - T_{\text{cold}}) + T_{\text{cold}}. \quad (1.11)$$

$P$  denotes the relative power output of the spectrometer in the three mirror positions,  $T_{\text{hot}}$  and  $T_{\text{cold}}$  are the temperatures of the calibration loads. This approach works well for this system due to the excellent linearity of the CTS.

The atmospheric radiation is received with a fixed elevation angle of 18 degrees and a beam width of 7 degrees FWHM. The tropospheric transmission is derived from the measured brightness temperature in the line wings of the water vapour line, assuming that the troposphere is a single layer with a constant temperature. It can be shown that the error of this approach is negligible for low brightness temperatures of the atmosphere and small line amplitudes [Jarchow, 1998]. This is also the case for the water vapour measurement at 22 GHz.

Two retrieval techniques have been applied to determine altitude profiles of water vapour from the measured spectra: the approach by *Backus and Gilbert* [1970] and the optimal estimation technique [Rodgers, 1976]. While the latter gives the best results when retrieving single spectra, for instance for a weekly or monthly mean, the former has advantages for retrieving continuous data sets, especially when there are large variabilities in the tropospheric transmission [Jarchow and Hartogh, 1995]. The altitude coverage of the data is 35 to 85 km. For weekly retrievals in the altitude range of 40-80 km the random error is estimated to be 0.15 ppmv. The altitude resolution is about 10 km. The systematic errors range between 0.1 ppmv at 80 km and 0.5 ppmv at 40 km. The main source of systematic errors, the so-called baseline, occurs due to reflections in the receiver. The contribution of pointing errors to the total systematic error is negligible for our system. A detailed error analysis is described in Jarchow [1998].

The 22 GHz system provided the first useful data in 1993. It has been in almost permanent operation since 1994 at mid-latitudes [Hartogh and Jarchow, 1995] and since 1995 in the Arctic [Seele and Hartogh, 1999] (Table 1.14).

A 183 GHz system has been developed and used from 1991 until 1994 [Hartogh *et al.*, 1991]. The system consists of a Schottky receiver cooled to 20 K with a single sideband (SSB) noise temperature of 500 K and a combined filterbank (28 channels, 1.2 GHz bandwidth)/CTS (1024 channels, 40 MHz bandwidth) back-end. Most of the time the system has been operated from MPAE, a site with only moderate microwave observation conditions (140 m altitude). Therefore, only a few useful profiles of middle atmospheric water vapour during mid-February 1993 have been obtained. The advantage of the 183 GHz measurement is that once the line can be observed it is likely to be much stronger than the 22 GHz line and therefore much less sensitive to baselines. As a result water vapour can be retrieved down to altitudes of 20 or even 15 km. Hartogh *et al.* [1994] showed that ground-based water vapour data at 183 GHz can be obtained from central European measurement sites above 3000 m altitude for more than 100-150 days per year.

**Table 1.14** Measurement history of MPAE instruments

Measurement Site	System	Measurement Period
Lindau, Germany (51°N, 10°E)	183 GHz	14 - 16 Feb 1993
Lindau, Germany (51°N, 10°E)	22 GHz	01 Oct 1994 - 5 Oct 1995 27 Nov 1996 - 27 Jun 1997
ALOMAR (69°N, 16°E)	22 GHz	15 Oct 1995 - 21 Oct 1996 6 Jul 1997 to present

### Microwave radiometry of water vapour from aircraft

If microwave observations of H<sub>2</sub>O are performed above the troposphere, from aircraft or balloons, the transition at 183.310 GHz is much better suited as its line strength is stronger by two orders of magnitude than the 22.235 transition. The brightness temperature for the 183 GHz line observed from aircraft is approximately 100 K in contrast to that measured from the ground at 23 GHz that is only a few tenths of a degree. Therefore the integration time of a microwave receiver will be much shorter for the stronger line. This offers the opportunity to deduce latitudinal variations of water vapour if observed from a moving platform. For this reason a microwave radiometer for operation from aircraft was built at the University of Bern several years ago and used in a first test flight in 1984 followed by an aircraft campaign in 1988 [Peter *et al.*, 1988]. The instrument has been modified and optimised since then and used in new campaigns in the nineties [Peter and Kämpfer, 1994; Peter, 1998a; Peter, 1998b, see also Kämpfer, 1995, for a review of the techniques used at the University of Bern in Switzerland]. These campaigns, which took place in different seasons, offered the opportunity to investigate the seasonal and latitudinal variability of water vapour from the subtropics to the Arctic. An overview of the campaigns performed so far with an indication of the latitudinal coverage is given in Table 1.15. The instrument also has been modified for use together with a submillimeter receiver for the detection of ClO, HCl and O<sub>3</sub>. Today the instrument with its millimetre receiver for water vapour offers a very reliable and easy to use instrument which can be incorporated in a Learjet for campaigns within a few hours.

**Table 1.15** Summary of the aircraft campaigns of the Bern microwave radiometer

Date of campaign	Latitudinal range	References
02 - 04 Dec 1986	Northern Europe, 45N to 75N	Peter <i>et al.</i> , 1988
13 - 15 Apr 1993	Northern Europe, 46N to 78N	Peter and Kämpfer, 1994
22 - 25 Aug 1994	16N / 23W to 78N / 18E	Peter, 1998a; Peter, 1998b
23 - 26 Oct 1995	16N / 23W to 78N / 18E	Peter, 1998a; Peter, 1998b
18 - 21 Mar 1996	16N / 23W to 78N / 18E	Peter, 1998a; Peter, 1998b
24 - 28 Aug 1998	8N / 14W to north pole	
05 - 12 Feb 1999	17N / 23W to 81N / 16E	
08 - 14 Mar 2000	29N / 40W-28E to north pole	

The University of Bern system consists of a heterodyne receiver with an uncooled Schottky diode mixer that converts the high frequency signals to an intermediate frequency of 3.7 GHz. The radiometer has a single sideband system temperature of 4000 K. A Martin-Puplett interferometer acts as a filter to suppress the unwanted sideband. This sideband filter can be tuned to measure alternately in either of the two sidebands around 183.3 and 175.9 GHz that enables measurement of radiation in the very far wing of the water vapour line. Side band switching is controlled by the onboard computer. A rotating mirror switches the instrument's field of view approximately every 1.5 seconds between the atmosphere at an elevation angle of 15° and two microwave absorbers at temperatures of 77 K and 312 K, that serve as calibration loads. The intermediate frequency signal is analysed simultaneously with two acousto-optical spectrometers (AOS). One AOS has a large bandwidth of 1 GHz and a resolution of 1.2 MHz. It is well suited for the observation of spectral lines from the stratosphere. The second AOS has a total bandwidth of 50 MHz at a high resolution of 50 kHz. It is used for the analysis of narrow spectral lines emitted from the mesosphere. Furthermore, the instrument has its own independent GPS receiver to record position and altitude for each measurement.

Water vapour profiles are retrieved between 15 km and 75 km with an altitude resolution of approximately 8 km in the lower stratosphere and approximately 15 km in the upper mesosphere. The root sum square of all error contributions is below 0.6 ppmv.

### 1.3.2 Water vapour LIDAR

Water vapour can be measured by using either the Differential Absorption LIDAR (DIAL) or the Raman LIDAR techniques. The advantage of LIDAR (LIght Detection And Ranging) methods is that range-resolved water vapour measurements can be made at a high resolution during day or night. LIDAR systems can be operated in spectral regions that avoid interference from absorption by other species and LIDAR retrievals require fewer assumptions than those for passive techniques and do not require complex inversion algorithms.

#### Differential Absorption LIDAR (DIAL)

In the DIAL technique, two laser pulses are transmitted into the atmosphere, one at the peak of the absorption line called the "on-line" and another in the wing of the absorption line called the "off-line". Using the DIAL method, the average molecular number density between ranges  $R_1$  and  $R_2$  is calculated using the relation:

$$n = \frac{1}{2\Delta\sigma(R_2 - R_1)} \ln \frac{S_{\text{on}}(R_1)S_{\text{off}}(R_2)}{S_{\text{on}}(R_2)S_{\text{off}}(R_1)} \quad (1.11)$$

where  $n$  is the average water vapour number density between the ranges  $R_1$  and  $R_2$ ,  $S$  is the LIDAR signal, and  $\Delta\sigma$  is the differential absorption cross-section between the on- and off-lines. The  $\Delta\sigma$  values are computed from the line parameters for water vapour lines in the near visible region measured using high resolution spectroscopic techniques [Grossmann and Browell, 1989, and Ponsardin and Browell, 1997]. The DIAL method provides a self-calibrated absolute water vapour measurement capability. The DIAL technique can be used to directly obtain the concentration profile of water vapour using the LIDAR signals and  $\Delta\sigma$ . This method for water vapour uses single absorption lines that are typically 10 pm wide. DIAL measurement simulations involving these narrow absorption lines show that the quality of laser spectral radiation has to be controlled very well in order to avoid undesirable systematic influences [Ismail and Browell, 1989]. In addition, the signals and  $\Delta\sigma$  are influenced by a number of atmospheric and instrumental effects that need to be taken into consideration during the operation of DIAL and during data analysis [Ismail and Browell, 1989]. For example, gradients

---

in the atmospheric aerosol scattering, Doppler broadening and the near range LIDAR overlap region present challenges in DIAL data reduction [Bosenberg, 1998].

The advantage of the DIAL method is that in addition to measuring gas concentration profiles, high spatial resolution aerosol back-scattering distributions are simultaneously obtained as part of the DIAL measurement using the off-line LIDAR signals. The vertical and/or horizontal resolution can be adjusted in the DIAL analysis by changing how the high-resolution LIDAR data are averaged. With the DIAL method, LIDAR measurements can be made during day or night and in between and up to cloudy regions in the atmosphere.

The first detection of water vapour using the DIAL technique was made in 1966 [Schotland, 1966] with a laser system that had a fortuitous coincidence with a water vapour absorption line. The DIAL technique for water vapour measurements using tuneable lasers was demonstrated from the ground by Browell *et al.* [1979], and subsequently by Cahen *et al.* [1982] and Bosenberg [1987]. The first airborne measurements of water vapour came in 1981 [Browell *et al.*, 1984], and this was followed by subsequent airborne measurements [Ehret *et al.*, 1993, Higdon *et al.*, 1994]. A ground-based water vapour DIAL for the lower troposphere has been developed and operated in Germany [Wulfmeyer and Bosenberg, 1998]. The DIAL method can be used for long-range measurement of water vapour. However, because of the high absorption of the on-line in the lower troposphere, airborne DIAL systems are more suitable for water vapour measurements in the nadir-viewing mode and from space.

### **The LaRC airborne DIAL system, LASE**

Following a long history of ground-based and airborne water vapour DIAL developments (discussed in the previous section), the NASA Langley Research Center developed the first autonomously operating DIAL system for the measurement of water vapour and aerosol profiles across the entire troposphere. This system, called LASE (LIDAR Atmospheric Sensing Experiment), is a compact DIAL system that was initially developed for operation from a high-altitude ER-2 aircraft, and in 1995, LASE completed its development and validation phases [Browell *et al.*, 1997]. LASE operates in the 815-nm absorption band of water vapour and it uses a Ti:sapphire laser that is locked onto a strong and temperature insensitive water vapour line. The spectral characteristics of the water vapour lines are documented [Ponsardin and Browell, 1997] and the lines are chosen to have a residual temperature sensitivity of less than a few percent [Ismail and Browell, 1989]. Water vapour over the entire troposphere is measured by electronically tuning the on-line to operate at any spectral location of the water vapour absorption line profile. This is done by first locking to the line centre and then adjusting the diode current a known amount from the line centre before the Ti:sapphire laser is fired. Since the actual water vapour line is used to lock the diode and the known spectral properties of the absorption line, the LASE water vapour measurement is self-calibrated.

LASE was operated autonomously from the NASA ER-2 aircraft during flight experiments from 1994 to 1996. It has also been configured to fly on the NASA P-3 and DC-8 aircraft. LASE has demonstrated the capability to measure water vapour over the entire troposphere [Browell *et al.*, 1997] with an accuracy of 6% or 0.01 g/kg. The horizontal resolution of LASE water vapour measurements is about 24 km (or two minutes of data averaging) and vertical resolutions of 300 m and 500 m in the lower and upper troposphere, respectively. LASE has participated in five major field experiments during 1995-1999; a list of these field experiments is given in Table 1.16. Archived data from these experiments are available from NASA Langley Distributed Data Archive Centre (DAAC) at <http://eosweb.larc.nasa.gov/HPDOCS/index.html>.

**Table 1.16** LASE field experiments from 1995-2000

Date	Experiment	Base of operations	Latitude	Longitude	Altitude
Sep 1995	LASE Validation Experiment	Wallops Island, VA	29-42N	63-86W	0-15 km
Jul 1996	TARFOX	Wallops Island, VA	32-39N	72-77W	0-15 km
Jul 1997	SGP97	Oklahoma City	34-38N	97-99W	0-7 km
Aug/Sep 1998	CAMEX-3	Cocoa Beach, FL	16-41N	63E-86W	0-14 km
Mar/Apr 1999	PEM B	Hawaii, Fiji, Tahiti	36S-34N	87-197W	0-14 km
Dec1999- Mar2000	SOLVE	Kiruna, Sweden	57-90N	100W-100E	0-14 km

### The DLR airborne water vapour DIAL

At DLR (Deutsches Zentrum für Luft- und Raumfahrt) in Oberpfaffenhofen, Germany, airborne water vapour DIAL systems have been operated since 1989 [Ehret *et al.*, 1993]. The first H<sub>2</sub>O DIAL was operated in the near infrared spectral region at 724 nm and was routinely installed nadir viewing onboard the DLR's meteorological research aircraft Falcon 20 and later modified for operation onboard the NCAR Electra research aircraft. This system took part in several field experiments to investigate processes in the boundary layer.

In order to increase both accuracy and spatial resolution, and to be sensitive for water vapour measurements in the stratosphere, a new water vapour DIAL system has been developed at DLR. Based on a high peak and average power optical parametric oscillator, its transmitter fulfils the spectral requirements for water vapour measurements in the troposphere as well as in the stratosphere [Ehret *et al.*, 1998]. The residual systematic error caused by the spectral properties of the new radiation source amounts to only 2%. The transmitter is designed to be operated at either the weak 4v vibrational absorption band of water vapour near 830 nm, suitable for tropospheric measurements, or at the 3v vibrational absorption band lying in the 940 nm spectral region which is one order-of-magnitude stronger. The latter has the advantage of much higher measurement sensitivity in regions of low water vapour content at upper tropospheric and lower stratospheric heights. The spectroscopic parameters of the relevant water vapour absorption lines at 940 nm were measured in the lab [Poerberaj and Weiss, private communication, 1999].

The new DLR H<sub>2</sub>O DIAL can be used for measurements of water vapour in the range from 5-100 ppmv [Ehret *et al.*, 1999]. In the downward looking mode it can scan vertical cross sections of up to 6 km in range, with a resolution of about 20 km in the horizontal and 250-500 m in the vertical. In 1999, this system participated in the Mesoscale Alpine Programme (MAP'99) field campaign (Table 1.17) in order to investigate strong horizontal and vertical gradients of the water vapour profile at tropopause level.

**Table 1.17** DLR's water vapour DIAL field experiments

Time	Experiment	Latitude	Longitude	Altitude	Remarks
Nov 1998	Validation experiment	44-48N	0-12E	6-12 km	10 Hz transmitter
Oct/Nov 1999	MAP 99	44-52N	2W-14E	5-12 km	100 Hz transmitter PV-streamers over Central Europe

### Raman back-scatter LIDAR

The Raman LIDAR technique uses the relative intensity of vibrational Raman scattering from water vapour and nitrogen to make a direct measurement of mixing ratio [Melfi *et al.*, 1969, Cooney, 1970]. The technique is relatively free of systematic errors (e.g. aerosol effects) and

can be operated from the ground because the radiation is not absorbed by water vapour in the lower troposphere. It is versatile, allowing studies of cloud liquid water and droplet radius, direct measurement of cirrus cloud optical depth, and direct measurement of aerosol extinction [Whiteman and Melfi, 1999]. Its disadvantage is the very weak Raman scattering cross-section, which has traditionally meant a long averaging time (several hours) for a precise measurement near the tropopause [e.g. Vaughan *et al.*, 1988]. However recent systems based on excimer lasers have extended the Raman technique to the tropopause [Ansmann *et al.*, 1992].

The ratio of the Raman back-scatter signals from water vapour  $S_W$  and molecular nitrogen  $S_N$  collected simultaneously on the same receiving telescope is proportional to the water vapour mixing ratio  $W$  (specific humidity) [Whiteman *et al.*, 1992]

$$W = K \cdot S_W / S_N \quad (1.12)$$

The LIDAR calibration coefficient  $K$  is the product of two terms - a system independent term describing the ratio of the molecular masses of  $H_2O$  and  $N_2$  and the mixing ratio of  $N_2$  in dry air (0.78), and a system-dependent term describing the product of the Raman back-scatter cross sections with the instrument function.

The Raman back-scatter signals  $S_W$  and  $S_N$  are corrected for differential atmospheric attenuation, photomultiplier nonlinearity and background noise. The atmospheric differential attenuation correction is calculated using standard atmosphere models, complemented with boundary layer aerosol extinction measurements where necessary. The LIDAR calibration coefficient can (and should) be determined independently. In practice it is typically deduced from a least squares regression of a simultaneous co-located radiosounding. The LIDAR water vapour measurement is temperature-independent for all practical purposes.

Most Raman LIDARs have been calibrated by fitting the ratio profiles to radiosonde humidity profiles. Ferrare *et al.* [1995] and Wang *et al.* [1995] compared water vapour measurements made by the NASA Goddard Space Flight Centre (GSFC) Raman LIDAR (see below) and radiosondes (both AIR and Vaisala). Agreement between LIDAR and radiosondes was generally good up to 8 km, but the calibration constant (determined by the average LIDAR/sonde ratio) varied from sonde to sonde. There is a clear need for further work in this area to characterise the performance of both LIDARs and sondes.

An absolute calibration is possible [Vaughan *et al.*, 1988, Sherlock *et al.*, 1999a]. This calibration is ultimately limited to  $\pm 6\%$  by spectroscopic uncertainties. However, changes of the calibration coefficient over time can in principle be monitored with a precision of 4 to 6% [Goldsmith *et al.*, 1998; Sherlock *et al.*, 1999a; Turner *et al.*, 1999]. In the upper troposphere the precision error dominates for an individual profile, unless the signals are averaged over many hours when variability in the humidity itself becomes a major concern.

Several Raman LIDAR systems have been operated from the ground over 30 years. In this report, the NASA/GSFC and OHP systems are described as examples, data will only be shown for the NASA/GSFC Raman LIDAR. Further, the US Department of Energy (DOE) has set up an operational Raman LIDAR system at the DOE Atmospheric Radiation Monitoring site in Lamont, Oklahoma [http://dev.ec.arm.gov/~turner/raman\_lidar\_quicklooks.html for data images; Goldsmith *et al.*, 1998]. Turner *et al.* [1999] have discussed the systematic influences in Raman LIDAR systems, and they have also described procedures for correcting them to retrieve water vapour profiles. Several European institutions have also developed Raman LIDAR systems for tropospheric water vapour measurements [Renaut *et al.*, 1980; Weitkamp *et al.*, 1986; Vaughan *et al.*, 1988; Mattis *et al.*, 1998].

### The GSFC Raman LIDAR

At the NASA Goddard Space Flight Center, Raman LIDAR have been developed and operated since the 80s [*Melfi and Whiteman, 1985; Whiteman et al., 1992*]. The present NASA/GSFC Scanning Raman LIDAR is housed in a single mobile trailer and has participated in numerous field campaigns since its first deployment in 1991. The system has received several modifications since that time and now contains two lasers for optimised performance during either nighttime or daytime [*Whiteman and Melfi, 1999*]. For nighttime operation, an excimer laser with an output wavelength of 351 nm is used. The return wavelengths for water, nitrogen and oxygen are 403, 382 and 371 nm, respectively. They are collected by a telescope and detected by eight photomultipliers (two for each wavelength, for different altitude ranges) tubes using dichroitic beamsplitters and interference filters. To facilitate daytime measurements, SRL uses a Nd:YAG laser in combination with frequency-tripling optics transmitting pulses at 355 nm.

The precision for ground-based measurements is typically quoted as <10% up to 8 km with 1 minute averaging and 75 m vertical resolution (night-time). The daytime precision is 10% random error at 4 km using 10 minute average.

**Table 18** Field deployment of Scanning Raman Lidar

Campaign	Dates	Longitude	Latitude
SPECTRE	13 Nov - 07 Dec 1991	37.1N	95.6W
ATMIS-II	15 Jul - 06 Aug 1992	37.8N	75.5W
CAMEX-1	13 Sep - 06 Oct 1993	37.8N	75.5W
ARM	15 Apr - 01 May 1994	36.6N	97.5W
LITE	10 - 21 Sep 1994	38.8N	76.7W
CAMEX-2	25 Aug - 21 Sep 1995	37.8N	75.5W
TARFOX	10 - 31 Jul 1996	37.8N	75.5W
ARM	10 - 30 Sep 1996	36.6N	97.5W
ARM	15 Sep - 04 Oct 1997	36.6N	97.5W
CAMEX-3	06 Aug - 23 Sep 1998	24.7N	77.8W

### The OHP Raman LIDAR

The Raman backscatter water vapour measurement at the Network for Detection of Stratospheric Change (NDSC) station at the Observatoire de Haute Provence (OHP, 44°N, 6°E) operates on a routine basis at night except in the presence of low cloud [*Sherlock et al., 1999b*]. From July 1997 - March 1998, 300 profiles were obtained. The instrument provides vertical profiles of water vapour from 2 km to the tropopause and/or specific humidity less than or equal to  $1 \times 10^{-5}$  g/g dry air. With a temporal integration of 1 to 2 hours and a vertical resolution ranging from 75 meters at and below 7 km to 375 meters at 11 km the random measurement error is of the order of 10% in the mid troposphere increasing to 20 to 30% in the upper troposphere. The systematic error in measurement is less than or equal to  $2 \times 10^{-6}$  g/g dry air, and the instrumental response varies by -0.02%/K. The OHP LIDAR system uses a 532.1 nm exciting wavelength, OH-rich fibre optic cables for signal transfer and Q-branch signal selection. These instrumental characteristics minimise the atmospheric transmission correction, the background noise, and the systematic measurement errors, and improve short-term instrumental stability.

The OHP LIDAR system is calibrated both independently and with co-located radiosoundings [*Sherlock et al., 1999a*]. Current calibrations have an associated error of the order of 10%. The implementation of means to improve the accuracy of the independent calibration is envisaged in the near future.

---

### 1.3.3 Infrared and far infrared measurements of H<sub>2</sub>O

Water vapour in the middle atmosphere can be well measured by passive remote sensing in the infrared. Appropriate absorption lines of H<sub>2</sub>O are available from the near to the far infrared. Corresponding spectrometers detect either the attenuated solar radiation or the emitted radiation of the atmosphere. By inverting the radiative transfer equation, atmospheric parameters such as the temperature and trace gas mixing ratios can be determined from the radiance measurements.

Profile measurements above the location of the instrument are possible in principle with spectrally highly resolving instruments, but the upper level of the altitude range depends on the wave number (for 1000 cm<sup>-1</sup> at about 30 km and for 100 cm<sup>-1</sup> at about 48 km). This is caused by the fact that the shape of the absorption lines is dominated by the Doppler effect above this height level. In the case of H<sub>2</sub>O it is even more difficult to sound the stratosphere from the ground because there is only a small amount of the H<sub>2</sub>O column above the tropopause. In order to achieve profiles with good vertical resolution in the middle atmosphere the limb sounding technique, i.e. viewing the atmosphere along tangential slant paths, has to be applied from balloon gondolas or high flying aircraft. Vertical profiles can in addition be derived from up-looking measurements during ascent or descent of the balloon or the aircraft.

In the case of limb sounding, the profiles of trace gases are determined from several measurements with different elevation angles, thus sensing the various atmospheric layers with different weighting. Inversion methods used are e.g. the onion peeling or the global fit technique [e.g. *Goldmann and Saunders, 1979*]. In the first case the atmosphere is peeled like an onion starting with the highest layer and working through the atmosphere to the lowest layer. Performing a global fit involves using all the measured spectra in one non-linear least-square fit in order to generate the vertical profile of the trace gas under investigation. If, in addition, a priori knowledge of the atmosphere is taken into account, the retrieval procedure is called optimal estimation technique.

A number of infrared spectrometers from different laboratories have been used from balloons and aircraft so far. Since the technique allows the determination of vertical distribution of many atmospheric trace constituents, these experiments were not usually designed primarily for the H<sub>2</sub>O retrieval. Below, three instruments are described; information on other IR spectrometers from which H<sub>2</sub>O profiles have been derived is found in *Murcray et al. [1990]* and references therein.

#### **The MIPAS balloon and aircraft experiments**

Several Fourier Transform Infrared (FTIR) spectrometers, known as MIPAS (Michelson Interferometer for Passive Atmospheric Sounding), using a special configuration to provide the optical path difference, have been developed for operation on ground, aircraft, and stratospheric balloon gondolas by the Institut für Meteorologie und Klimaforschung in Karlsruhe, Germany (for a review see *Fischer, 1993*).

A cryogenic balloon-borne version of MIPAS (called MIPAS-B) was developed to measure vertical profiles of a comprehensive set of stratospheric chemical compounds that are relevant for ozone chemistry and climate research. The instrument is specially tailored for operation on a stratospheric balloon gondola and equipped with suitable subsystems to precisely allow limb emission sounding of the stratosphere independent of external radiation sources. As such it can be operated day and night, not being restricted to any solar zenith angle. MIPAS-B is the only cryogenic limb emission FTIR sensor in routine operation worldwide. A first version was flown between 1989 and 1992 twice during spring turn-around and twice near the northern polar circle inside the vortex in winter (*Fischer and Oelhaf, 1996*, and references cited therein).

A second version (MIPAS-B2) was built in 1993/94 that incorporated many improvements such as increased spectral coverage (*Friedl-Vallon et al.*, 1995, *Oelhaf et al.*, 1996). The interferometer provides two-sided interferograms with a maximum optical path difference of 15 cm, resulting in an unapodized spectral resolution of  $0.033 \text{ cm}^{-1}$ . The four-channel detector system with Si:As detectors allows the simultaneous coverage of the most important absorption bands of ozone- and climate-relevant trace gases between 5 and 14  $\mu\text{m}$ . Typical signal-to-noise ratios of single  $\text{H}_2\text{O}$  lines are between 50 and 200. A novel solution has been realised for the line-of-sight stabilisation and reference system that provides tangent heights to better than 200 m ( $3\sigma$ ). Radiometric calibration is performed on the basis of blackbody and deep-space spectra that are recorded several times during flight. The calibrated spectra are analysed using multi-parameter non-linear least-square curve fitting in combination with the onion-peeling technique (see e.g. *von Clarmann et al.*, 1995, *Wetzel et al.*, 1997 and references therein). The estimation of the error budget is carried out using an elaborate scheme that takes into account random noise, mutual influence of fitted parameters, temperature and pointing uncertainties, onion-peeling error propagation, and errors in spectroscopic data. MIPAS-B is suitable to simultaneously obtain vertical profiles of ozone and a considerable number of species such as  $\text{O}_3$ ,  $\text{NO}$ ,  $\text{NO}_2$ ,  $\text{HNO}_3$ ,  $\text{HO}_2\text{NO}_2$ ,  $\text{N}_2\text{O}_5$ ,  $\text{ClONO}_2$ ,  $\text{COF}_2$ ,  $\text{CH}_4$ ,  $\text{N}_2\text{O}$ ,  $\text{H}_2\text{O}$ ,  $\text{HDO}$ ,  $\text{CF}_2\text{Cl}_2$ ,  $\text{CCl}_3\text{F}$ ,  $\text{CHF}_2\text{Cl}$ ,  $\text{CCl}_4$ ,  $\text{CF}_4$ ,  $\text{C}_2\text{H}_6$ , and  $\text{SF}_6$  with an altitude resolution of 2-3 km. The precision of the retrieved  $\text{H}_2\text{O}$  mixing ratio is typically near 5% with temperature errors being the dominant source of errors, and the absolute accuracy of  $\text{H}_2\text{O}$  profiles derived from MIPAS-B2 spectra is between 6 and 11% assuming a 5% uncertainty of the spectroscopic data.

Since 1995, MIPAS-B2 was flown 5 times in polar regions in winter and spring and 3 times at mid-latitudes during spring and summer (Table 1.19). Water vapour profiles were retrieved along with profiles of methane and deuterated water from MIPAS-B2 [*Stowasser et al.*, 1999]. From these MIPAS-B2 data the hydrogen budget ( $[\text{H}_2\text{O}] + 2[\text{CH}_4]$ ) was also derived.

**Table 1.19** Balloon flights with the MIPAS-B2 instrument

Date	Site	Ceiling altitude	Altitude coverage	Project	Remarks
11 Feb 95	Kiruna/Sweden - 68°N	29.1 km	10 – 28 km	SESAME	inside vortex
21 Mar 95	Kiruna/Sweden - 68°N	28.9 km	10 – 28 km	SESAME	inside vortex
10 Feb 97	Kiruna/Sweden - 68°N	29.3 km	11 – 29 km	CHORUS	inside vortex
24 Mar 97	Kiruna/Sweden - 68°N	30.0 km	11 - 29 km	CHORUS/ ILAS	inside vortex ILAS validation
02 Jul 97	Gap/France - 45°N	39.4 km	7 - 39 km	CHELOSBA	vortex remnants
08 May 98	Aire sur l'Adour/F - 44°N	38.4 km	8 - 38 km	CHELOSBA	
27 Jan 99	Kiruna/Sweden - 68°N	32.5 km	3 – 32 km	THESEO	inside vortex
30 Apr 99	Aire sur l'Adour/F - 44°N	38.2 km	0 – 38 km	THESEO	

An instrument similar to MIPAS-B was flown on a Transall aircraft (MIPAS-FT) during the first half of the 1990s [*Gulde et al.*, 1994]. Observations were made from the low flying aircraft through a window by upward sounding at an elevation angle of  $7^\circ$ . As a consequence, only column amounts of different trace species have been determined. More recently a MIPAS instrument has been completed for use aboard the stratospheric aircraft M55 Geophysika. This MIPAS-STR is also a limb sounder like MIPAS-B and therefore delivers vertical profiles of various trace gases, among others  $\text{H}_2\text{O}$ , in the lower stratosphere. After a series of test flights in spring 1999 an Antarctic field measurement campaign followed in autumn 1999.

### The JPL MkIV interferometer

The Jet Propulsion Laboratory MkIV interferometer is a high resolution Fourier Transform InfraRed spectrometer, designed to remotely sense atmospheric composition [Toon, 1991]. This instrument is very similar to the ATMOS instrument (Section 1.4.4) which flew during four missions on the Space Shuttle. The MkIV instrument made ground-based observations from McMurdo, Antarctica, in September and October 1986, and flew on board the NASA DC-8 aircraft for the 1987 Antarctic polar campaign (AAOE) and the Arctic polar campaigns (AASE) of 1987 and 1992. Additionally, it has made 17 flights from high altitude research balloons since 1989 (Table 1.20).

**Table 1.20** Summary of MkIV balloon flights

Date	Tangent latitude	Tangent longitude	Minimum altitude	Balloon altitude	Launch site	Observation mode
05 Oct 89	34.6N	105.7W	13 km	37 km	New Mexico	sunset
27 Sep 90	34.2N	106.0W	10 km	36 km	New Mexico	sunset
05 May 91	37.5N	111.8W	16 km	37 km	New Mexico	sunset
06 May 91	36.5N	103.0W	15 km	32 km	New Mexico	sunrise
14 Sep 92	35.2N	110.2W	23 km	38 km	New Mexico	sunset
15 Sep 92	35.3N	103.9W	22 km	40 km	New Mexico	sunrise
3 Apr 93	34.8N	115.5W	17 km	37 km	California	sunset
25 Sep 93	34.0N	109.4W	04 km	37 km	New Mexico	sunset
26 Sep 93	33.2N	100.4W	14 km	38 km	New Mexico	sunrise
22 May 94	36.6N	109.7W	15 km	36 km	New Mexico	sunset
23 May 94	36.3N	100.8W	11 km	37 km	New Mexico	sunrise
24 Jul 96	56.8N	101.0W	11 km	24 km	Manitoba	ascent
08 May 97	68.0N	147.0W	08 km	38 km	Alaska	sunrise
08 Jul 97	67.0N	148.0W	08 km	32 km	Alaska	ascent
09 Jul 97	65.0N	150.0W	10 km	32 km	Alaska	descent
03 Dec 99	64.0N	19.0E	04 km	33 km	Sweden	sunset
15 Mar 00	64.0N	19.0E			Sweden	

The interferometer operates in solar absorption mode, meaning that direct sunlight is spectrally analysed and the amounts of various gases at different heights in the Earth's atmosphere are derived from the depths of their absorption lines. In the mid-infrared spectral region, the sun is so bright that emission from the atmosphere or the instrument is negligible. This provides spectra of high accuracy without the need for in-flight radiometric calibration.

The entire 700-5700  $\text{cm}^{-1}$  spectral region is observed simultaneously at 0.01  $\text{cm}^{-1}$  resolution. Over this wide interval more than 30 different gases have spectral signatures that can be identified, including  $\text{H}_2\text{O}$ ,  $\text{CO}_2$ ,  $\text{O}_3$ ,  $\text{N}_2\text{O}$ ,  $\text{CO}$ ,  $\text{CH}_4$ ,  $\text{N}_2$ ,  $\text{O}_2$ ,  $\text{NO}$ ,  $\text{NO}_2$ ,  $\text{HNO}_3$ ,  $\text{HNO}_4$ ,  $\text{N}_2\text{O}_5$ ,  $\text{ClNO}_3$ ,  $\text{HOCl}$ ,  $\text{HCl}$ ,  $\text{HF}$ ,  $\text{SF}_6$ ,  $\text{COF}_2$ ,  $\text{CF}_4$ ,  $\text{CH}_3\text{Cl}$ ,  $\text{CHFCl}_2$ ,  $\text{CFCl}_3$ ,  $\text{CF}_2\text{Cl}_2$ ,  $\text{CCl}_4$ ,  $\text{OCS}$ ,  $\text{HCN}$ ,  $\text{C}_2\text{H}_2$ ,  $\text{C}_2\text{H}_6$  and many isotopic variants. Profiles of these gases can be retrieved from cloud-top to balloon altitude. The vertical resolution of 2-3 km is limited mainly by the 1-3 km separation of the tangent altitudes, and by the 3.6 mrad diameter circular field-of-view of the instrument, which subtends 1.8 km at a tangent point 500 km distant.

The MkIV  $\text{H}_2\text{O}$  retrievals are performed by fitting 14 different spectral intervals between 1400 and 5500  $\text{cm}^{-1}$ . Since there are a large range of strengths encompassed by these lines,  $\text{H}_2\text{O}$  abundance from  $<1$  ppmv to  $>20000$  ppmv is easily measured.

For  $\text{H}_2\text{O}$ , a retrieval precision of 5% is estimated limited mainly by uncertainty in the pointing and by the presence of horizontal gradients. The overall accuracy is estimated to be 7% in the upper stratosphere, limited mainly by uncertainties in the spectral line intensities. In the lower-most stratosphere and troposphere, the accuracy progressively worsens to 12% due to

inadequacies in the pressure-dependent molecular spectroscopic parameters (e.g. half-width, shifts) and due to the presence in the spectrum of poorly fitted interfering absorption).

### The SAO Far Infrared Spectrometer (FIRS-2)

The Smithsonian Astrophysical Observatory Far-infrared Spectrometer (FIRS-2) is a high-resolution Fourier transform spectrometer that measures the thermal emission of the atmosphere from balloon and aircraft platforms, and from the ground [Johnson *et al.*, 1995]. From balloon platforms, vertical mixing ratio profiles are retrieved extending from the balloon altitude to near the tropopause [Jucks *et al.*, 1998], while from aircraft and from the ground overhead column densities are retrieved [Traub *et al.*, 1994]. The following discussion is limited to the balloon configuration.

The spectrometer produces mostly one-sided interferograms with an unapodized resolution of  $0.004\text{ cm}^{-1}$ . The number of detectors and wavelength range has changed several times since the FIRS-2 was first flown in 1987; in its present configuration gallium-doped and copper-doped germanium photoconductors for the far- ( $80\text{--}330\text{ cm}^{-1}$ ) and mid- ( $330\text{--}1250\text{ cm}^{-1}$ ) infrared bands, respectively, are used. With this wide spectral coverage it is possible to make simultaneous measurements of many radical and reservoir species, including  $\text{CO}_2$ ,  $\text{O}_2$ ,  $\text{O}_3$ ,  $\text{OH}$ ,  $\text{HO}_2$ ,  $\text{H}_2\text{O}_2$ ,  $\text{HCl}$ ,  $\text{HOCl}$ ,  $\text{ClNO}_3$ ,  $\text{HBr}$ ,  $\text{NO}_2$ ,  $\text{HNO}_3$ ,  $\text{HNO}_4$ ,  $\text{N}_2\text{O}_5$ ,  $\text{N}_2\text{O}$ ,  $\text{CO}$ ,  $\text{OCS}$ ,  $\text{HCN}$ ,  $\text{C}_2\text{H}_6$ ,  $\text{C}_3\text{H}_6\text{O}$  (acetone),  $\text{HF}$ ,  $\text{SF}_6$ ,  $\text{CFC-11}$ ,  $\text{CFC-12}$ ,  $\text{HCFC-22}$ ,  $\text{CCl}_4$ ,  $\text{CH}_3\text{Cl}$ ,  $\text{CH}_4$ , and  $\text{H}_2\text{O}$ , as well as temperature and pressure (derived from  $\text{CO}_2$ ).

The instrument field-of-view is 0.22 and 0.16 degrees in the far- and mid-infrared, respectively, corresponding to 1.3 and 0.65 km at the limb, respectively. Typically the limb is scanned at intervals of 3-4 km in tangent height, retrieving slant columns in onion-peeling fashion. Then, a set of linear equations is solved for the smoothest mixing ratio profile which reproduces the observed slant columns [Johnson *et al.*, 1996], producing profiles with a 1 km step size and a vertical resolution equal to the scan interval in tangent height.

The measurements of  $\text{H}_2\text{O}$  include profiles for  $\text{H}_2^{16}\text{O}$ ,  $\text{H}_2^{17}\text{O}$ ,  $\text{H}_2^{18}\text{O}$ , and HDO. The precision (accuracy) of a typical profile is 4% (5%), 60‰ (110‰), 40‰ (100‰), and 20‰ (45‰) for  $\text{H}_2^{16}\text{O}$ ,  $\delta^{17}\text{O}$ ,  $\delta^{18}\text{O}$ , and  $\delta\text{D}$ , respectively.

The FIRS-2 has had 10 balloon flights starting in 1987. In 1989, a mid-infrared channel for temperature and pressure retrievals was added, resulting in reduced systematic errors for the 7 flights listed in Table 1.21. Profiles for each flight are retrieved from the minimum altitude up to the balloon altitude. The profile above the balloon has an assumed shape (derived from a climatology in the case of  $\text{H}_2\text{O}$ ) which is scaled to match the observed overhead column density.

**Table 1.21** Summary of the SAO FIRS-2 balloon flights

Launch date (GMT)	Tangent latitude	Tangent longitude	Minimum altitude	Balloon altitude	Launch site	Duration of flight
26 Sep 1989	31.0°N	105.4°W	16 km	36 km	New Mexico	23.1 h
04 Jun 1990	36.9°N	112.0°W	18 km	38 km	New Mexico	28.1 h
29 May 1992	37.2°N	103.4°W	17 km	38 km	New Mexico	8.7 h
29 Sep 1992	34.2°N	98.6°W	16 km	36 km	New Mexico	7.8 h
23 Mar 1993	38.3°N	107.3°W	18 km	39 km	California	6.7 h
22 May 1994	36.5°N	105.3°W	15 km	37 km	New Mexico	21.6 h
30 Apr 1997	69.1°N	151.9°W	10 km	37 km	Alaska	5.0 h

---

## 1.4 Satellite sensors

Measurements of UT/LS water vapour radiances by satellite sensors are obtained within specific spectral absorption and/or emission bands or lines of this molecule. An early review of the various measurement approaches is given in *Harries* [1980]. The various instruments use spectral channels or frequencies in the UV/visible/near infrared (SAGE II, POAM), the middle infrared (HIRS, LIMS, ATMOS, HALOE, and ILAS), and microwave (MLS, MAS, SSMT2, AMSU-B) regions [*Goody and Yung*, 1989; *Harries*, 1996; *Pickett et al.*, 1998; *Rothman et al.*, 1998]. Retrievals of water vapour or relative humidity then rely on a detailed knowledge of its absorption cross section. So far, there are no satellite measurements using the far infrared region, which has an abundance of rotational water vapour lines and would be suitable for sounding the upper troposphere. Some instruments measure the absorption of solar energy by water vapour from direct sunlight passing through the limb of the atmosphere during a sunrise or sunset event (ATMOS, SAGE II, HALOE, POAM, ILAS), while others use the limb emission (LIMS, MLS, MAS) or nadir emission (TOVS) techniques.

The spatial and temporal resolutions afforded by the satellite sensors dictate the scientific utility of a given satellite data set. In general, these attributes are discussed in the following subsections or references therein. The Earth limb-view techniques provide good vertical resolution for the retrieved profiles. Their measurements are obtained in the manner of vertically-scanning a pencil beam across the horizon of the atmosphere. Information for a single profile represents a tangent layer integration over several hundred kilometres along the line of sight, while being much narrower in width and depth (a few kilometres). The effective length of the tangent path is shortened as the vertical resolution improves. More complete daily coverage must be obtained by a suitable interpolation of those scans across nearly a thousand kilometres in the zonal direction. Limb, solar-occultation measurements provide about thirty profiles of water vapour per day. The orbital inclination of the spacecraft determines whether these occultation measurements progress over (or sweep across) most of Earth's latitude zones within a few weeks (SAGE II, HALOE) or are restricted to a narrower high latitude region (ILAS, POAM). A consequence of this measurement method is that it is difficult to find a meaningful coincidence between a satellite profile measurement and a correlative measurement unless it was carefully planned. The cross-track scanning, nadir-viewing TOVS measurements are based on radiances integrated over deeper layers of the atmosphere, providing much better coverage each day and with a horizontal resolution of tens of kilometres. The TOVS measurements of the upper troposphere are of particular value because they provide for both good horizontal resolution and daily coverage, revealing the effects of the synoptic-scale circulation on the water vapour field. Table 1.22 contains the information on coverage for each data set.

Chapter 2 contains intercomparisons of data sets having disparate spatial scales. For example, an *in situ* correlative measurement will be sensitive to the small spatial scales that the satellite measurement can only be integrating over. If coincidence in time is not so critical, one way to intercompare water vapour fields from two satellites is to Fourier analyse the profile data at a pressure, altitude, or potential temperature surface and then construct field values that are co-located with the correlative measurement. Alternatively, one can use another quantity, such as potential vorticity, to transform the satellite and correlative measurement spatially.

The parameter that defines the quality of relative variations within a satellite water vapour field is the data precision, which is defined as the random error for the retrieved profile. Accuracy is defined by the combination of the random and systematic errors. It is noted at this point that the term systematic error should often be thought of as an uncertainty because if a bias were truly

known, one could correct for it in the data set. Nevertheless, we refer to biases or systematic effects as errors in this report. When assessing trends from a satellite data set, one is usually analysing its daily zonally-averaged field. This averaging reduces its random errors. The long-term changes in its systematic error components must be known in order to quantify any trend in water vapour. Therefore, the error assessments for the satellite data are given in terms of their random and systematic terms.

Sources of systematic error for each of the data sets depend on their specific measurement technique, but are generally dominated by uncertainties in spectral parameters and/or on the stability and knowledge of the instrument pointing. While these potential biases should not be affecting trends, any changes of the smaller biases are harder to characterise. For example, the long-term stability of the measured radiances or transmittances must be traced back to the instrument calibration. In addition, all satellite techniques must either account for the effects of clouds and heavy aerosol or at least mitigate their presence spectrally, especially as one begins to view the upper troposphere. Nevertheless, for those altitude regions where the measurement signal-to-noise (S/N) is high, all of the satellite data sets in this report have good precision (small random measurement error) and should provide for large-scale water vapour distributions that are qualitatively believable.

Although each instrument was carefully characterised and calibrated prior to flight, all experiments employ some onboard calibration or at least provide some information on long-term changes in instrument health as part of their operational mission parameters. Nevertheless there can be long-term instrument degradation or atmospheric effects (for example, decay of interfering volcanic aerosols) that may not be known very well - potentially affecting the accuracy of a time series of the retrieved water vapour. The interpretation of data time series obtained from several successive instruments (e.g., TOVS on operational satellites) must also consider instrument-to-instrument calibration uncertainties. The following subsections contain estimates of measurement and retrieval errors for individual water vapour profiles, as well as some discussion of effects that could impart a false trend to a time series of those profiles. The TOVS, SAGE II, and HALOE data sets of Table 1.22 are potentially useful for trend study, and their descriptions are more extensive and focused on those sources of systematic error that could affect a trend analysis.

**Table 1.22** Coverage and time spans for satellite data sets

Instrument	Latitude	Period of assessment	Vertical range
TOVS	global	1979 -1999 (daily)	200 hPa to 500 hPa
LIMS	64S-84N	Oct 1978 -May 1979 (daily)	1 h Pa to 100 hPa
SAGE II (solar occultation)	60S-60N	Jan 1986-Jun 1991	3 hPa to cloud tops
ATMOS (solar occultation)	specific latitudes each Shuttle mission	Apr/May 1985, Mar/Apr 1992 Apr 1993, Nov 1994	0.01 hPa to 100 hPa
HALOE (solar occultation)	70S-70N	Oct 1991 -Sep 1999	0.01 hPa to 200 hPa
MLS stratospheric	34N-80S or 34S-80N per yaw cycle	Sep 1991 -Apr 1993	0.01 hPa to 100 hPa
MLS UTH	see MLS stratospheric	Sep 1991 - Sep 1994; intermittent thereafter	147, 215, 316, 464 hPa
MAS	near-global range of latitudes per Shuttle mission	Mar/Apr 1992, Apr 1993 Nov 1994	0.01 hPa to 50 hPa
ILAS (solar occultation)	57N-73N, 64S-88S	Nov 1996 -Jun 1997	0.1 hPa to cloud tops
POAM III (solar occultation)	54N-71N, 63S-88S	Mar 1998 -Sep 1999	3 hPa to cloud tops

---

The experiments and data sets in this section are ordered according to when each instrument began operations. At the time of this report the TOVS, SAGE II, HALOE, and POAM instruments were still taking data. In some cases, major satellite instruments have provided water vapour data with good coverage each day (SAMS on Nimbus 7 and ISAMS and CLAES on the UARS spacecraft), but they are not part of this assessment because their measured distributions are not of value to the UT/LS region. Another reason for not including those results is because their data uncertainties are either large or not well characterised. Still, much has been learned from those particular approaches for measuring and retrieving water vapour, and that understanding is being applied to the design of next-generation satellite instruments and retrieval algorithms.

### 1.4.1 Operational satellite upper tropospheric humidity (UTH)

#### **Infrared and microwave observations by polar-orbiting satellites**

The TIROS Operational Vertical Sounder (TOVS) is a suite of instruments that has flown on the NOAA series of operational polar-orbiting satellites since late 1978. Each NOAA satellite provides nearly contiguous, global coverage of the Earth twice per day and there are normally two satellites operational observing the Earth every 6 hours. The TOVS consists of three instruments; the High Resolution Infrared Sounder (HIRS) for sounding temperature and moisture profiles, the Microwave Sounding Unit (MSU) for sounding temperature profiles, and the Stratospheric Sounding Unit (SSU) for sounding temperature profiles. Although the TOVS instruments were designed for quantitative use to provide temperature and moisture sounding input into numerical weather prediction models, the long-term, global coverage provided by TOVS has become an important source of observational data for climate monitoring [NRC, 2000].

The HIRS is a twenty channel infrared filtered radiometer that includes three channels for measuring water vapour in the lower, middle, and upper troposphere. Since the HIRS is a filter radiometer, the upper tropospheric water vapour channel that measures upwelling radiation in the 6.5 micrometer region is sensitive to a broad atmospheric layer from about 200-500 hPa [Wu *et al.*, 1993]. The spatial resolution of the HIRS is about 25 km at nadir and decreases to about 40 km at the end of the scan. Calibration through the entire optics of the HIRS instrument is performed every 40 scan lines by viewing Space and an internal calibration target [Smith *et al.*, 1979]. There are usually two NOAA polar-orbiting satellites operational at any time, thus providing data four times per day globally in cloud-free and up to approximately 70% in partially cloudy regions. There are three upper tropospheric water vapour products, each with relative advantages and disadvantages, that are discussed here: (1) use of upper tropospheric water vapour channel radiances (brightness temperatures), (2) a simple retrieval of upper tropospheric humidity (UTH), and (3) a complete inversion of all HIRS/MSU channels to obtain temperature and moisture profiles.

Infrared upper tropospheric water vapour channels are also used on the geostationary satellites and these channels are very similar to the HIRS. The METEOSAT spacecraft was the first to carry such a channel. The sounder on the GOES satellites also carried an upper tropospheric water vapour channel. These early channels on the geostationary satellites were intended for semi-quantitative work and on-board calibration was not always possible. Efforts are now underway to intercalibrate the upper tropospheric water vapour channels, in order to compile a climatology from the geostationary satellites.

More recently, microwave water vapour sounders have begun to fly on the operational polar-orbiting satellites of both the Defense Meteorological Satellite Program (DMSP, the SSMT2

instrument) and NOAA (the AMSU-B instrument). These microwave instruments produce measurements of layer-mean upper tropospheric water vapour similar to HIRS, but have the advantage of extending into cloudy, non-precipitating atmospheres. The first SSMT2 instrument began flying in April 1993, and there has been nearly continuous coverage from a single DMSP satellite since then. There is as yet, however, no climatology compiled from these data. The first AMSU-B instrument on the NOAA series satellites began operating in June 1998, and all future NOAA satellites will carry the AMSU-B in addition to the HIRS. Unfortunately, this first AMSU-B instrument on the NOAA-15 spacecraft has been plagued by instrument noise problems.

The data set of HIRS infrared radiance and upper tropospheric humidity (UTH) available for this assessment is derived from the clear column radiance (CCR) data set produced by NOAA NESDIS. (Future updates of the data will be produced from lower level data from the TOVS radiance pathfinder project.) The CCR brightness temperature data are subject to extensive quality control and binned into grids of 2.5 degrees latitude-longitude and time averages of 5 day and monthly means [Bates and Jackson, 1997; Bates et al., 1996]. Table 1.23 describes the characteristics of this data set. There are numerous possible sources of both random and systematic error involved in the production of this data set and these are discussed in detail in the references. The accuracy figure in Table 1.23 refers to the random errors associated with instrumental noise, an angular correction to nadir, the cloud clearing, and the averaging of at least 5 observations per grid box per month. In practice, each grid box contains substantially more than 5 observations per month (typically 50-100 per month), so the random error asymptotes to a lower threshold that depends upon the systematic error. The largest source of systematic error is due to the slightly different filter response function from the ten different instruments used over the twenty-year time period. Forward radiative transfer simulations are used to estimate these errors and have used an empirical method to adjust all instruments to a baseline instrument. The residual systematic error is estimated at less than 0.1K. The accuracy of these observations relative to other observations will be discussed in more detail in later chapters.

**Table 1.23** Characteristics of the HIRS channel 12 upper tropospheric water vapour data set.

Parameter	Character
technique	clear infrared emission near 6.5 micrometers
accuracy (random)	1.11K (5 obs/month), 0.11K (100 obs/month)
accuracy (systematic)	0.1K global/interannual
precision	0.01K
time/space resolution	monthly, 2.5 degrees latitude-longitude
altitude range	200-500 hPa. (varies with water vapour amount)
measured quantity	upwelling radiance
calibration procedure	on-board blackbody and cold space views

A main advantage in the use of radiance data versus retrievals of UTH or temperature and moisture profiles is that the error characteristics for the radiances are much simpler than for the retrievals. This is a critical issue for the use of these data in both numerical weather prediction and in climate. In numerical weather prediction, the use of radiances, and particularly the use of upper tropospheric water vapour radiances in the tropics, has led to a large positive impact in forecasts [McNally and Vesperini, 1996]. The use of radiances, however, requires highly accurate and very fast radiative transfer models for these regions of the spectrum. A recent intercomparison of radiative transfer models has demonstrated that this requirement has been met [Soden et al., 2000].

### Sensitivity analysis

One way to visualise the sensitivity of water vapour sounding channels to the emission of radiation from typical temperature and moisture profiles is through the use of the weighting function. Figure 1.10 shows a comparison of the weighting functions for infrared water vapour channels for the HIRS channel 12 and a microwave water vapour channel of the SSMT2.

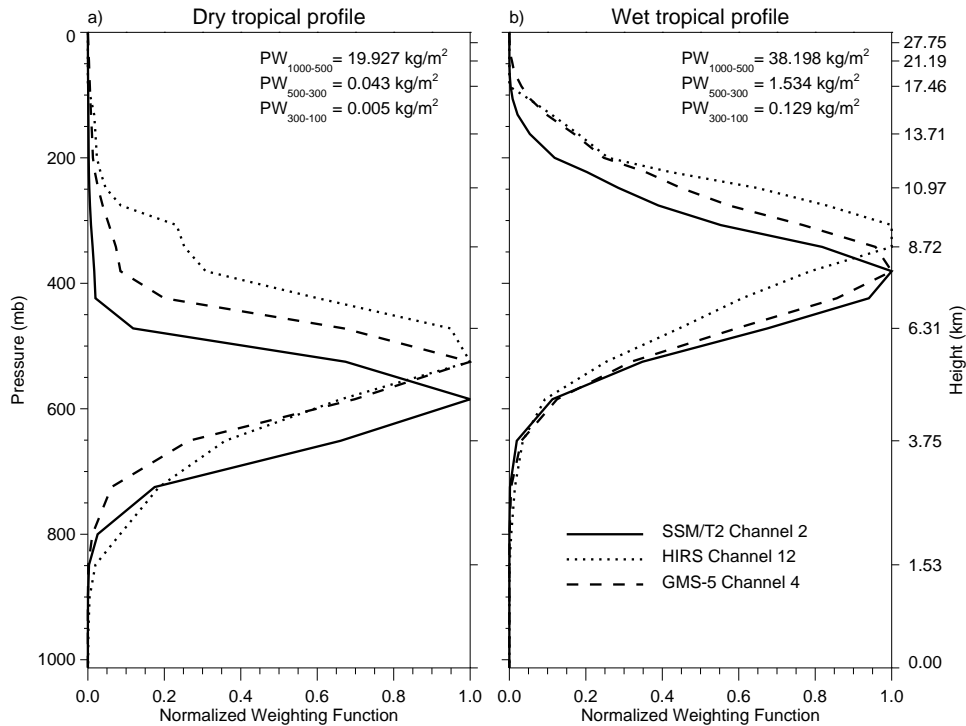


Figure 1.10 Comparison of normalised weighting functions for SSMT2 and HIRS for a dry (left) and a wet (right) tropical atmosphere.

A sensitivity analysis of the modelled HIRS and microwave (SSMT2 and AMSU-B) radiance or brightness temperature,  $T_B$ , to changes in temperature and moisture profiles was carried out for the tropical profiles using a carefully sampled radiosonde data base, the Thermodynamic Initial Guess Retrieval [Chevallier *et al.*, 1998]. This involved two sets of analyses: (1) comparing simulated  $T_B$  as a function of three vertical layer mean relative humidity (RH) values over oceans for 100-300 hPa, 300-500 hPa, and 500-1000 hPa, and (2) perturbing the temperature and moisture profiles in these three layers by a small amount in order to identify the differences in the sensitivity of HIRS and microwave instruments. Because the SSMT2 and HIRS water vapour channels are sensitive to both water vapour and temperature, the  $T_B$  is more highly correlated to relative humidity than water vapour mixing ratio or overburden. All relative humidity perturbations were constrained between 0 and 100%. It should be noted that the relative humidity values were computed with respect to liquid water, as is the convention with radiosonde data. As a result, cold upper tropospheric temperatures can reduce the relative humidity maximum from 100% to as little as 70% due to saturation with respect to ice. The first two layers were chosen to quantify the sensitivity each instrument has at different levels of the upper troposphere.

The sensitivity of the SSMT2 and the HIRS  $T_B$  to moisture and temperature perturbations is described here as the difference in  $T_B$  from the perturbed case and the non-perturbed case  $\{\Delta T_B = T_B(\text{perturbed}) - T_B(\text{non-perturbed})\}$ . Sensitivity analyses were performed by modifying the

relative humidity field by 10% (holding temperature constant) and then by modifying the temperature field by 2K (holding specific humidity constant). These increments were chosen arbitrarily in order to illustrate the sensitivity differences between SSMT2 and HIRS and are not intended to explain observed differences in the SSMT2 and HIRS  $T_B$ . Because the interest for climate studies is on systematic differences, random errors due to instrument noise were considered to be negligible when averaged over a large number of individual samples and are therefore ignored. Tables 1.24 and 1.25 summarise the results of the perturbation analysis for the two upper layers. As shown in these tables, the results are essentially symmetric for positive and negative perturbations in temperature, but not for changes in relative humidity. The SSMT2 has the strongest sensitivity to moisture perturbations and both instruments have a similar sensitivity to temperature perturbations. For a 10% increase in relative humidity in the highest levels (100 to 300 hPa) the SSMT2  $T_B$  drops by 4.90 K while the HIRS  $T_B$  only drops by 3.71 K. The change for a 10% decrease in relative humidity, however, is even larger with a  $T_B$  increase of 6.69 K for the SSMT2 and 6.41 K for HIRS.

The sensitivity of HIRS  $T_B$  to the water vapour continuum effects was examined using the MODTRAN-3 spectral model. It was found that the continuum contribution to the  $T_B$  was slightly dependent on latitude with a 1.61 K increase in temperature for the tropical profiles and a 1.15 K increase in temperature for the polar profiles.

**Table 1.24** Modelled  $T_B$  perturbations using tropical Thermodynamic Initial Guess Retrieval (TIGR)-2 profiles and perturbing the relative humidity profile by  $\pm 10\%$ . The scatter plot summary statistics between SSMT2 and HIRS channel 12 (H12)  $T_B$  are given in the columns slope, mean diff., and rms. diff.  $\Delta T_B$  columns show the  $T_B$  changes due to perturbing relative humidity in the given layers.

	SSMT2/H12 slope	SSMT2/H12 mean diff	SSMT2/H12 rms diff	H12 $\Delta T_B$	SSMT2 $\Delta T_B$
TIGR +10% RH(100-300 hPa)	1.30	6.23	1.41	-1.57	-2.52
TIGR +10% RH(300-500 hPa)	1.23	6.05	1.29	-1.98	-3.12
TIGR NO CHANGE	1.28	7.18	1.42	0.00	0.00
TIGR -10% RH(100-300 hPa)	1.23	7.79	1.56	1.54	2.14
TIGR -10% RH(300-500 hPa)	1.24	8.20	1.65	2.66	3.68

**Table 1.25** As in Table 1.24, except temperature perturbations of  $\pm 2K$  were performed.

	SSMT2/H12 slope	SSMT2/H12 mean diff	SSMT2/H12 rms diff	H12 $\Delta T_B$	SSMT2 $\Delta T_B$
TIGR +2K (100 to 300 hPa)	1.27	7.27	1.41	0.45	0.53
TIGR +2K (300 to 500 hPa)	1.27	7.41	1.39	1.08	1.30
TIGR NO CHANGE	1.28	7.18	1.42	0.00	0.00
TIGR -2K (100 to 300 hPa)	1.30	7.08	1.44	-0.43	-0.53
TIGR -2K (300 to 500 hPa)	1.30	6.93	1.46	-1.06	-1.31

### Retrieval of upper tropospheric humidity

Some investigators [Soden and Bretherton, 1993; Stephens *et al.*, 1996] have developed regression relationships between the upper tropospheric water vapour radiance and upper tropospheric humidity (UTH). The advantages of retrieving UTH are that it uses a subset of all the sounding channels, which allows for rapid processing of large volume data sets and it retrieves a parameter that can be more easily compared to other satellite observations and more traditional *in situ* observations. The disadvantages are that the UTH retrieval does not use the

complete set of sounding channels (it does not use all available information), it is biased to the dependent data sample used to derive the regression, and it will tend to underestimate the extremes.

A regression was developed for UTH using a combination of the methods above and using the TIGR data set as the dependent data set. The UTH regression equation is of the form,

$$\text{UTH} = \text{BETA} * \text{EXP}(A1 + A2 * T12) \quad (1.13)$$

where  $\text{BETA} = B1 + B2(T6 - T4)$ , and where the T values are the HIRS brightness temperatures in channel 12 (the upper troposphere water vapour channel) and channels 4 and 6, which are temperature sounding channels in the lower and upper troposphere (a measure of the tropospheric lapse rate). In this method the use of the temperature channels does not allow a retrieval of the specific humidity; it only provides a slight correction to the UTH for the gross character of the lapse rate. Figure 1.11 shows the regression fits for these two parameters using the TIGR data set for UTH with respect to ice.

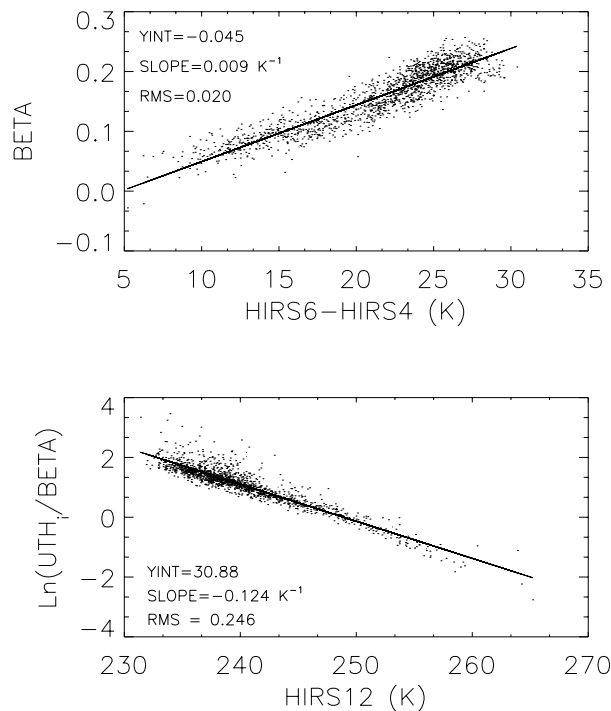


Figure 1.11 Plots of regression parameters for upper tropospheric humidity (UTH) in terms of (top) the lapse rate of HIRS brightness temperature, and (bottom) the absolute brightness temperature from HIRS in the upper troposphere.

### Retrieval of temperature and moisture profiles from HIRS/MSU data

Numerous retrieval methods using HIRS/MSU data have been developed in the past 20 years for a variety of applications. It is beyond the scope of this discussion to survey all the strengths and weaknesses of the various techniques. The Improved Initialisation Inversion (3I) method [Chedin *et al.*, 1985; Chedin, 1994; and Scott *et al.*, 1999] also referred to as Pathfinder Path B, is the consensus retrieval algorithm for climate applications. The advantages of a complete retrieval method are that it makes use of all the available radiance information, is a true solution

to the radiative transfer equation, and complete profiles of temperature and moisture are obtained for the troposphere. The disadvantages of a complete retrieval are that it is very time consuming and the inversion process is ill conditioned so that ancillary data are required to stabilise the inversion. Great care must be taken in the choice and use of ancillary information, since this information can create complex and systematic errors in retrievals.

The 3I/Path B inversion algorithm is a direct, non-iterative, physico-statistical method that uses information from all channels of the HIRS/MSU instruments. The algorithm includes many steps: calibration and HIRS/MSU spot collocation, initial air mass classification, cloud detection and correction, first guess selection using the TIGR data set, temperature profile retrieval using Bayesian estimation, cloud parameter determination, cloud clearing of moisture sensitive channels, surface temperature retrieval, and water vapour retrieval using a neural network approach. Data from January 1989 to August of 1994 are currently available and processing is continuing for the entire TOVS period of record, 1979-present. This approach will allow for an estimate of long-term trends of layer-mean specific humidity in the future from HIRS data.

The water vapour retrieval uses a non-linear neural network estimate [Charboureau *et al.*, 1998]. The vertical distribution of specific humidity is obtained by using the 4 HIRS channels most sensitive to water vapour absorption (HIRS channels 8, 10, 11, and 12) combined with 6 HIRS channels sensitive to tropospheric temperature (HIRS channels 2-7). The outputs from the neural network are the layer precipitable water for 5 standard layers (100-300, 300-500, 500-700, 700-850, and 850-surface). These outputs are then transformed into water vapour contents above the surface, 850 hPa, 700 hPa, 500 hPa, and 300 hPa. No retrieval is performed for any pressure level if the surface pressure is lower than 850 hPa. Training of the neural network is performed using the TIGR data set. Validation of this technique against *in situ* observations has been presented in Scott *et al.* [1999] and is discussed in chapter 2.

#### 1.4.2 Limb Infrared Monitor of the Stratosphere (LIMS)

The Nimbus 7 Limb Infrared Monitor of the Stratosphere (LIMS) experiment yielded near-global distributions of stratospheric water vapour from October 25, 1978 through May 28, 1979 [Gille and Russell, 1984; Remsberg *et al.*, 1984]. LIMS was a cryogenically cooled, broadband filter radiometer with a water vapour channel centred at 6.9 micrometers. A complete profile was obtained every 12 seconds both day and night and with a vertical resolution for retrieved water vapour of about 5 km. Calibrations against an internal blackbody and views to cold Space were performed for each pair of scans. Line parameters for H<sub>2</sub>O were obtained from the 1980 AFGL tape [Rothman, 1981] and the interfering effects from the O<sub>2</sub> continuum were adapted from Timofeyev and Tonkov [1978].

The LIMS data provided the first comprehensive picture of stratospheric H<sub>2</sub>O. Its distributions have also been used in studies of the stratospheric budget of water vapour by Jones *et al.* [1986] and Hansen and Robinson [1989], and, in particular, to estimate the H<sub>2</sub>O mixing ratio as it ascends into the tropical stratospheric "overworld" from below. Those estimated entry-level values ranged from 2.7 ppmv to 3.3 ppmv, respectively.

##### **Quality of the archived (Version 5) LIMS data**

The precision of the Level 2 data is estimated to be 10% for pressures greater than 10 hPa, 15% from 5 to 10 hPa, and 20% for pressures less than 5 hPa [Russell *et al.*, 1984]. The accuracy of individual water vapour profiles retrieved from the LIMS radiances is also evaluated in Russell *et al.* [1984] and Remsberg *et al.* [1984] by simulating the effects of known sources of LIMS water vapour error and by comparisons with correlative measurements. Uncertainties for daily

---

zonal averages of those profiles are reported in *Remsberg and Russell* [1987] and are repeated here: 27% at 1 hPa, 17% from 30 hPa to 3 hPa, and 20% at 50 hPa. Profile quality degrades below the 50 hPa level.

Water vapour data quality is affected at the stratopause (1 hPa) because of its poor precision (low signal-to-noise ratio for the LIMS water vapour radiances) and because of significant uncertainties in the radiances from the field-of-view spatial side lobes [*Russell et al.*, 1984]. *Kerridge and Remsberg* [1989] considered the effects of an additional complication for the retrieval of upper stratospheric LIMS water vapour during daylight. The values at those levels are significantly larger for day versus night - a possible consequence of non-local thermodynamic equilibrium emission at 6.9 micrometers from water vapour and perhaps NO<sub>2</sub>. As a result, they recommended that scientific studies of LIMS water vapour should be based on the vertical distribution of its nighttime values. Uncertainties in the line parameters for water vapour and from the effects of profile registration and temperature bias tend to limit the quality of LIMS water vapour in the middle stratosphere.

The Version 5 water vapour is less accurate in the lower stratosphere. In particular, there are systematic errors just above the tropical tropopause due to LIMS temperatures that are too warm, to uncertainties in the interfering effects of the pressure-induced O<sub>2</sub> continuum, and possibly to contaminating emission from aerosols and clouds that was not accounted for. Furthermore, in the tropics there is a sharp increase of water vapour and temperature just below the tropopause. The instantaneous finite vertical field-of-view width of 3.6 km for the LIMS water vapour channel smoothes across that region, and its effects must be carefully removed in the radiance deconvolution procedure. Uncertainties due to all of these effects cause the position of the retrieved tropical water vapour minimum to occur at an altitude that is 1 to 2 km too high and to be too dry.

### **Improvements for a Version 6 of the LIMS data**

A major effort has been underway to improve the LIMS algorithm and incorporate the latest line parameter data for the retrievals of both temperature and species. One finding that has altered the character of the distributions of all the species is a better estimate of spacecraft attitude along an orbit, based on a match of the calculated and observed LIMS radiances in the lower mesosphere for its narrow-band CO<sub>2</sub> channel. This refinement altered both the pressure registrations of the water vapour radiances and its associated temperature profile. The Version 6 Level 2 water vapour distributions have better overall symmetry across both hemispheres, especially for the low altitude increases that are due to tropospheric water vapour and to interfering emissions from clouds. Spectral line parameters are from HITRAN 92 [*Rothman et al.*, 1992] and the O<sub>2</sub> continuum model is from *Orlando et al.* [1991]. Version 6 temperatures are colder at the tropical tropopause. Because of all these changes the isolines of minimum water vapour in the lower stratosphere slope downward toward the Poles in the manner of the isentropic surfaces. Minimum zonal-mean water vapour values are of order 3.5 ppmv in the tropics. Preliminary estimates indicate that the Version 6 single profile random errors are similar to those of Version 5 but the systematic uncertainties are smaller.

There is confidence that the daily zonal mean distributions are improved over those from Version 5. It is expected that the reprocessing of the profile data will be finished and available in 2000. Version 6 is not being considered for this assessment, however.

### 1.4.3 Stratospheric Aerosol and Gas Experiment (SAGE) II

The Stratospheric Aerosol and Gas Experiment II (SAGE II) is a third generation satellite-borne sensor that utilises the solar occultation technique in the visible to near infrared spectral region to measure the concentration of different species in the atmosphere. SAGE II is flying on the Earth Radiation Budget Experiment (ERBE) spacecraft launched by the Space Shuttle in October of 1984. As of this time, the spacecraft and instrument are functioning normally even though half of the batteries on the spacecraft are dead. Continuous measurements from the SAGE II instrument have been obtained for the last fifteen years. Water vapour measurements are obtained from a spectral channel centred at the 940 nm water vapour band.

#### Measurement and retrieval technique

SAGE II is a seven channel sun-pointing radiometer consisting of a grating and spectral filters together with photodiode detectors. *Mauldin et al.* [1985] gives a detailed description of the SAGE II instrument. Because of the solar occultation geometry, SAGE II provides 30 measurement events per day, consisting of fifteen sunrises and fifteen sunsets. With a 57 degree inclination orbit for the ERBE spacecraft, the locations of the SAGE II measurements are generally restricted to latitudes within about 60°S and 60°N. Figure 1.12 illustrates the coverage of the SAGE II measurements from 1985 to 1986. The coverage pattern nearly repeats from year to year.

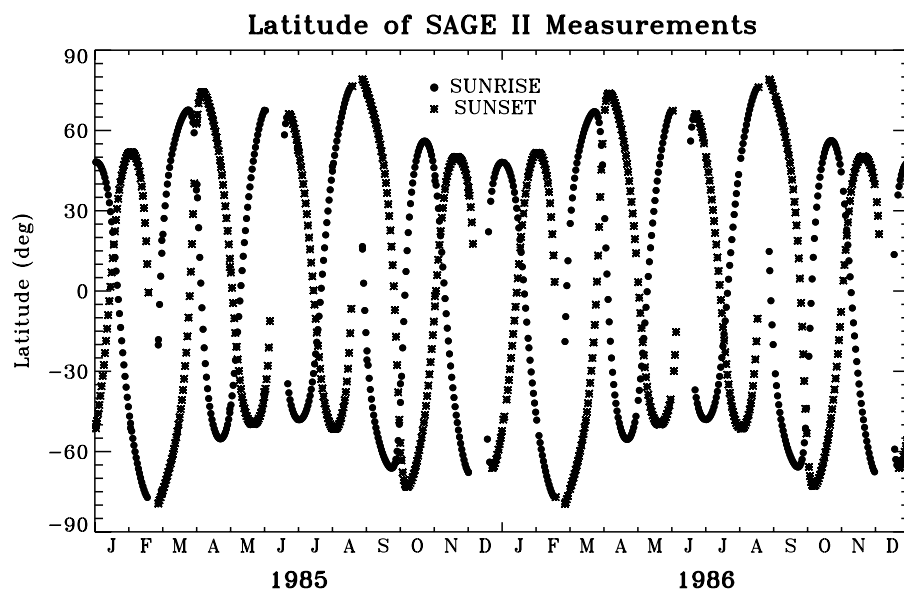


Figure 1.12 Latitude locations for the daily-averaged SAGE II sunrise and sunset measurements during 1985-86.

The SAGE II instrument records the Sun's radiance when its scan mirror views both above and through the Earth's atmospheric limb. Because the retrieval algorithm considers the profile of the ratio of the atmospheric to the exo-atmospheric radiances, its transmittance as a function of altitude, the SAGE results are essentially self-calibrated. In other words the effects of any degradation of the optical throughput within the instrument is avoided by performing the ratios of those radiance measurements except at altitudes where the signal approaches the noise level. The description of the Version 5.90 inversion algorithm for the SAGE II water vapour is given in *Chu et al.* [1993] and in *Pruvost et al.* [1993]. Spectral line parameters were taken from the

1982 compilation of AFGL. Validation and data use for the SAGE II water vapour have been reported [McCormick *et al.*, 1993; Chiou *et al.*, 1993; Rind *et al.*, 1993; Chiou *et al.*, 1997]. The overall SAGE II inversion methodology for the species that affect water vapour (aerosol, ozone, and nitrogen dioxide) can also be found in Chu *et al.* [1989].

### Uncertainty and potential systematic error for the SAGE II water vapour

For the occultation measurements in the 940 nm spectral region, water vapour absorption typically accounts for about 25 % of the total measured extinction, while aerosols, ozone absorption, and Rayleigh scattering account for the other 75 % under normal conditions. However, after a major volcanic eruption the aerosols dominate the extinction at 940 nm. Chu *et al.* [1993] and Larsen [1998] have performed extensive studies of the sensitivity of the SAGE II water vapour data to its error sources. Systematic errors have been considered from the water vapour line parameters, the emissivity growth approximation computation scheme, temperature bias, and the interference from Rayleigh and aerosol scattering and ozone absorption. It is found that in a low aerosol environment, systematic errors of 20 to 30 percent are typical between the tropopause and 30 km, and the total error is still dominated by the ability to completely remove the aerosol contribution. For altitudes above 30 km and below the tropopause the systematic error is about 10 %, primarily due to line parameter uncertainties. Random errors arise from uncertainties in the measured signal, altitude registration, and the effects of ozone, temperature, and aerosol. The combined random error for single profiles is between 10 and 20 % up to 40 km. Table 1.26 summarises the error analysis for the SAGE II water vapour profiles.

**Table 1.26** Summary of SAGE II Water Vapour Data Errors

Error source	Altitude (km)	Systematic error (%)	Random error (%)
forward model	0-25	10	
(line parameters, emissivity growth approximation tables)	5-40	6	
aerosol correction (1990 level at midlatitude)	trop-25	25	5
ozone correction	15-35	12	1
Rayleigh correction	10-30	2	1
measurement error	0-30		5-10
altitude error	0-40		5-10

### Potential short-term and long-term errors

As discussed above, the water vapour retrieval accuracy is extremely sensitive to the correct removal of aerosol interference. Even with relatively low aerosol levels, such as the condition in 1990 at mid-latitudes, the estimate of potential systematic error in the water vapour profile due to aerosol is about 25%. Sensitivity analyses by Chu *et al.* [1993] for the higher levels of aerosol in 1985 show that the systematic error in water could be as high as 100% at mid-latitudes and much higher at tropical latitudes.

Besides the time dependent errors due to aerosol interference, there are still two other potential time dependent errors caused by changes in the SAGE II instrument. The first problem is the scan mirror reflectivity with scan angle, which was very stable from 1984 through 1990. However, after 1990 the functional behaviour of the reflectivity with angle started to change. A correction has been attained, but it must be implemented a year to two years after data acquisition because of the large number of calibration data that are required for its

characterisation. This process has been complicated with the recent failure of the spacecraft batteries. As a result, there is a potential for systematic error in the water vapour retrieval, especially for values at higher altitudes. The second potential problem is a drift in the 453 nm filter. While such a drift primarily affects retrieved  $\text{NO}_2$ , it can also produce a drift in the retrieved aerosols for the 450 nm region. Any drift in the 450 nm aerosol, even at low aerosol amounts, can potentially affect the water vapour retrieval because of its high sensitivity to aerosol interference.

After considering all the short term and long term errors it is questionable whether the SAGE II data can be used to assess changes in water vapour after 1990 with an accuracy of less than 50%. Prior to that time, trends are uncertain from the top of the volcanic aerosol layer to near tropopause altitudes. A better estimate of the quality of SAGE II water vapour should be possible from the Version 6 algorithm, which will incorporate better corrections for the drifts in scan mirror reflectivity and in the 453 nm filter.

#### **Currently available SAGE II water vapour data**

SAGE II water vapour data from January 1986 to May 30, 1991 are available at the NASA Langley Distributed Active Archive Center (DAAC). This 5-year data set was obtained with the Version 5.90 algorithm. The El Chichon aerosols severely affected the water vapour data through 1985. Similarly, the Pinatubo aerosols affected the water vapour data after May 1991; aerosol extinction levels did not become equivalent to those of 1986 until 1996.

### **1.4.4 Atmospheric Trace Molecule Spectroscopy (ATMOS)**

#### **General description**

The Atmospheric Trace Molecule Spectroscopy instrument (ATMOS) is a Space Shuttle-borne Fourier transform infrared spectrometer that simultaneously measures vertical profiles of a variety of atmospheric species from the upper troposphere to well above the stratosphere [Farmer *et al.*, 1987; Gunson *et al.*, 1990 and 1996]. ATMOS is a fast-response Michelson interferometer, which obtains high resolution ( $\sim 0.01 \text{ cm}^{-1}$ ), broadband spectra through orbital sunrises and sunsets during solar occultation by the Earth. This observational technique provides immediate calibration data with each occultation, making the instrument self-calibrating and thereby eliminating long-term drift. The accuracy of such measurements is generally insensitive to changes in background transmission, e.g., resulting from heavy volcanic aerosol loading, although precision will be degraded with a significant reduction in the signal.

ATMOS is currently packaged to fly on the Space Shuttle. From a low-Earth orbit of  $\sim 300 \text{ km}$  altitude typical for the Space Shuttle, an occultation observation requires  $\sim 4 \text{ min}$ . With an instrument scan time of 2.2 s, approximately 100 spectra are recorded, resulting in a vertical spacing of  $\sim 2 \text{ km}$  in the lower stratosphere to  $\sim 4 \text{ km}$  in the upper stratosphere. At tangent heights in the middle stratosphere, the vertical spacing is 2-3 km. The vertical spacing coupled with the instantaneous instrument field-of-view of 1.0-2.8 mrad leads to an effective vertical resolution of 3-6 km [Gunson *et al.*, 1996].

ATMOS has been deployed four times as part of the Spacelab 3 and ATLAS-1, ATLAS-2, and ATLAS-3 missions [Kaye and Miller, 1996]. Observations from these missions cover the following periods of time and ranges of latitude:

**Table 1.27** Listing of ATMOS missions

Mission	Period	Latitudes	Measurement mode
Spacelab 3	30 Apr - 1 May 1985	47 - 51S	sunrise
		26 - 35N	sunset
ATLAS-1	25 Mar - 2 Apr 1992	0 - 55S	sunrise/sunset
		0 - 31N	sunrise
ATLAS-2	8 - 16 Apr 1993	10 - 50S	sunset
		63 - 68N	sunrise
ATLAS-3	3 - 12 Nov 1994	65 - 72S	sunrise
		3 - 49N	sunset

In order to enhance the signal-to-noise ratio and minimise zero-level offsets, measurements are made in selected spectral regions defined by optical bandpass filters given in the following Table.

**Table 1.28** Spectral regions of ATMOS

Filter 1	600 - 1180 $\text{cm}^{-1}$
Filter 2	1100 - 2000 $\text{cm}^{-1}$
Filter 3	1580 - 3450 $\text{cm}^{-1}$
Filter 4	3100 - 4800 $\text{cm}^{-1}$
Filter 9	625 - 2450 $\text{cm}^{-1}$
Filter 12	625 - 1450 $\text{cm}^{-1}$

For each sunrise or sunset occultation, spectra are recorded in one of these six transmission regions; the filter selection determines which species can be retrieved for that occultation [Gunson *et al.*, 1996; Abrams *et al.*, 1996a]. The accuracy of the ATMOS measurements is generally dominated by experimental uncertainty in the line strengths and the isolation of spectral features (e.g., the degree of blending or overlap with spectral features of other species), particularly at the lower tangent heights. The precision is a statistical measure of the scatter in the retrievals and is largely determined by random spectral noise and by uncertainties in the tangent altitudes and the assumed temperature-pressure profiles.

### Retrieval description

After the interferograms have been transformed to spectra, the spectra are referenced to an average exo-atmospheric spectrum (from measurements above 165 km), eliminating solar and instrumental spectral features [Norton and Rinsland, 1991]. An initial “first-guess” tangent height is assigned based on the spacecraft ephemeris data. The tangent pressure is retrieved by fitting temperature-insensitive  $\text{CO}_2$  absorption bands [Abrams *et al.*, 1996b], and refined temperature-pressure profiles are retrieved from absorption features that provide the populations of  $\text{CO}_2$  rotational states [Stiller *et al.*, 1995]. These retrievals provide pressures with an estimated accuracy of 4-10% and precision of 1-3% and temperatures with an accuracy of 2-3 K.

Smaller spectral intervals (micro-windows) containing predominantly the absorption features of a selected trace gas are used for the retrieval of the volume mixing ratio profiles. These micro-windows differ with species and altitude and depend on the location, shape, and strength of the target gas absorption, spectral congestion, and temperature dependence of the spectral features [Gunson *et al.*, 1990, Brown *et al.*, 1996]. Line strengths used to retrieve water vapour are given by Brown *et al.* [1996].

The Version 3 algorithm was adapted from an algorithm developed for the analysis of MkIV balloon spectra (see Section 1.3.3) and differs from that of Version 2 in several ways. In particular, the Version 3 algorithm employs a simultaneous global fit for multiple species and tangent pressures rather than the sequential onion-peeling approach for individual species used for Version 2. This new version of the ATMOS data extends to lower altitudes and includes additional species. Version 3 retrievals provide  $[H_2O]$  for all filters ( $[X]$  denotes volume mixing ratio of species  $X$ ). Both versions of water vapour are retrieved in the altitude range of  $\sim 10$ -80 km for Filters 2, 3, and 9 with an average estimated ( $1\sigma$ ) accuracy of 6% [Abrams *et al.*, 1996a, Gunson *et al.*, 1996]. Water vapour is retrieved for Filter 4 with a much larger uncertainty and a significant systematic bias for both versions. In addition, Version 3 water vapour retrievals are available for Filter 12, and comparisons among  $[H_2O]$  profiles from Filters 3, 9, and 12 show excellent agreement [Michelsen *et al.*, 2000a]. Version 3 retrievals of water vapour are available for Filter 1, but these retrievals currently appear to be unreliable, perhaps because of the lack of temperature-insensitive  $H_2O$  lines in Filter 1. A preliminary estimate of the random error for Version 3 yields an average value of 11% in the stratosphere with uncertainties as high as 30% in the troposphere.

### 1.4.5 Halogen Occultation Experiment (HALOE)

The HALOE experiment uses solar occultation measurements to infer high resolution mixing ratio profiles of  $H_2O$  at 6.61 micrometers and over an altitude range of 10-85 km. HALOE also provides for the effects of aerosol extinction at four infrared wavelengths, plus absorption profiles of other gases including  $CH_4$  and  $CO_2$ . The nearly conserved chemical quantity,  $2*CH_4 + H_2O$ , has also been obtained with the HALOE profiles. The instrument measures the atmospheric transmission of sunlight as the sun rises and sets relative to the spacecraft. A description of the experiment and its retrieved quantities is found in Russell *et al.* [1993]. Here its measurements, retrieval algorithm, and error sources are briefly described, focusing on issues relating to the accuracy of stratospheric water vapour.

#### Measurement and retrieval description

The angular resolution of the HALOE instantaneous field-of-view is 2 arcmin in elevation by 6 arcmin in azimuth. Projected to the limb tangent point, this is about  $1.6 \times 4.8$  km, respectively. The combined effect of optical resolution and electronic signal smoothing yields an effective vertical resolution of about 2.3 km. Figure 1.13 depicts the projection of the instantaneous field-of-view onto the solar disk image. As the Sun sets, its refracted image shrinks in apparent elevation and the instantaneous field-of-view, which is positioned at a fixed angle from the top edge, covers more area of the Sun and moves closer to the centre of the limb darkening curve. This changing effective source function is explicitly modelled using exoatmospheric solar scans and detailed limb path refraction calculations.

The UARS orbit ( $57^\circ$  inclination, 600 km altitude circular) provides HALOE with 15 sunrises and 15 sunsets each day and near-global coverage over the 36-day yaw cycle. Figure 1.14 shows the global sunrise and sunset locations for 1995. HALOE samples at 8 Hz, equating to a tangent altitude grid of 0.18 to 0.4 km depending on Sun sink rate (a function of orbital beta angle). This over-samples the effective 2.3 km resolution by a factor of 5 or greater. The measurements are interpolated onto a 0.3 km grid for processing by the retrieval algorithm.

HALOE uses two distinct measurement techniques: broadband radiometry and gas correlation radiometry. In broadband radiometry the transmission in a channel is estimated by  $\tau(t) = V(t) / V_{\text{exo}}$ , where  $V(t)$  is the detector voltage signal in time and  $V_{\text{exo}}$  is the exoatmospheric value. The retrieval algorithm compares  $\tau$  to a modelled transmission to determine the target-

gas mixing ratio. Note that this ratio measurement does not require absolute radiance calibration, a feature that greatly benefits the ability to infer long-term trends. Broadband radiometry measurements are used to retrieve  $\text{H}_2\text{O}$  and temperature/pressure (using  $\text{CO}_2$  absorption measurements).

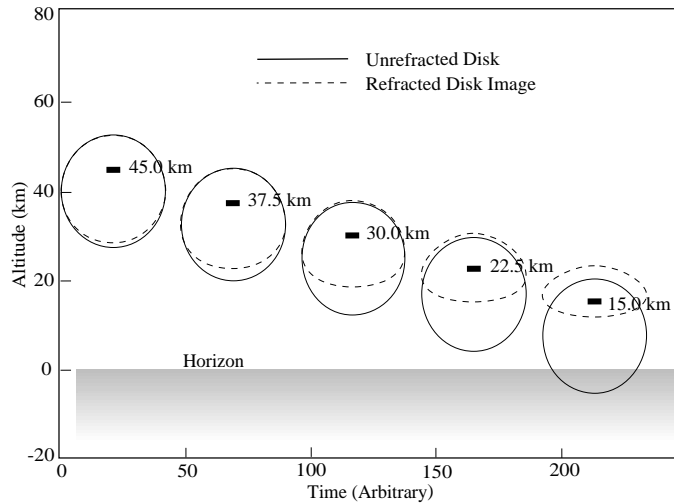


Figure 1.13 HALOE instantaneous field-of-view location on the solar disk during a sunset occultation event. Note that the instantaneous field-of-view is locked (fixed) relative to the top apparent edge of the Sun. Event duration (from 150 km to bottom of profile) ranges from about 40 to 110 sec, depending on beta angle.

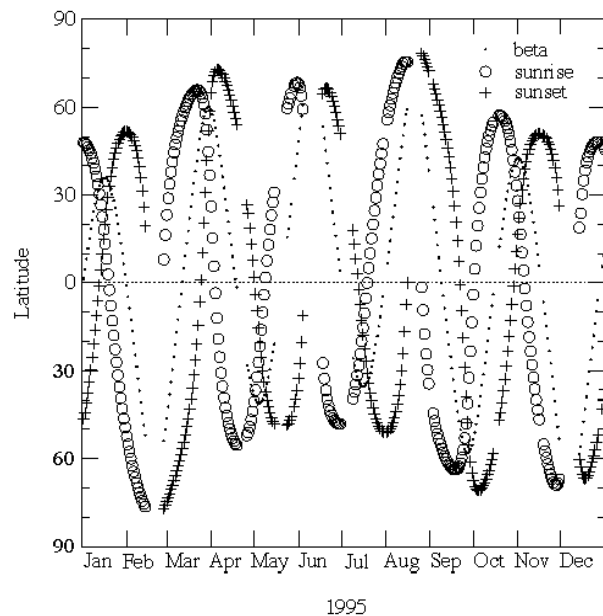


Figure 1.14 HALOE global sampling pattern for 1995. There are 15 sunrise and 15 sunset occultations each day. Plotted are the daily mean sunrise and sunset locations and beta angles. Successive individual sunrise (or set) events are separated by  $24^\circ$  in longitude and within  $\pm 0.6^\circ$  in latitude.

---

In gas correlation radiometry the incoming beam is split between two paths: one through a cell filled with the target gas and one through a vacuum path. Voltage signals resulting from these,  $V_G(t)$  and  $V(t)$ , respectively, are electronically balanced exoatmospherically. The retrieval models the modulation signal,  $M = [V_G(t) - V(t)] / V(t)$ , to infer  $\text{CH}_4$ . The value of  $M$  is nearly independent of absorption from aerosol. Gas correlation radiometry is used to retrieve gaseous species in four separate infrared channels, and aerosol extinctions are then retrieved from the  $V(t)$  signal as in broadband radiometry.

The first task in the processing is the pressure registration of the transmission profiles. In the 30–40 km region, the algorithm matches a band averaged  $\text{CO}_2$  channel transmission with a modelled transmission derived from National Center for Environmental Prediction (NCEP) temperature and pressure data. Next, temperature/pressure is retrieved from 35 to 85 km, and the pressure registration is repeated using these data.  $\text{H}_2\text{O}$ , T/P, and aerosol extinction are then obtained by broadband radiometry and  $\text{CH}_4$  by gas-cell correlation radiometry using a modified onion-peel algorithm.

Retrievals are done sequentially in an iterative fashion for computational simplicity and stability. Studies determined there is no significant compromise in accuracy from this approach. Altitudes above ~80 km are treated as one extended layer in the water retrieval. This boundary condition has less than a 5% effect at 75 km and negligible effect below 70 km. Although each transmission profile is sampled at 0.3 km spacing, it is separated into 7 profiles having 2.1 km spacing. Each of these 7 is used to retrieve the target gas, and the results are re-interlaced into a final 0.3 km spaced profile and then smoothed. Aerosol extinction retrieved from the 5.26  $\mu\text{m}$  channel is extrapolated to the radiometer channels with a sulphate aerosol model [Hervig *et al.*, 1995].

### **Error sources and their impact on trends**

The 3<sup>rd</sup> public release of the HALOE water vapour profiles (from the Version 19 algorithm) is used in this report. They are accompanied by a quality profile of mixing ratio uncertainties due to random instrument and tracker noise plus aerosol effects. Systematic error effects have been tabulated in Harries *et al.* [1996] and Hervig *et al.* [1996] for an earlier version of the HALOE algorithm, but those estimates are nearly the same as those for Version 19. There are systematic errors from the forward model and the altitude registration of profiles. There are also uncertainties in the line parameters for  $\text{H}_2\text{O}$  and in the knowledge of the interfering effects from  $\text{CH}_4$  and from aerosols. Line parameters for the Version 19 retrievals were taken from the HITRAN 1992 compilation. In the lower stratosphere there are biases in the corrections based on the  $\text{O}_2$  continuum model of Orlando *et al.* [1991], and the minor effects of  $\text{H}_2\text{O}$  continuum absorption are not accounted for. The combined, single-profile HALOE errors are discussed in Harries *et al.* [1996] and summarised later in Table 1.30.

Error sources dominating trend determination are different than those for individual profiles. Random errors become insignificant when huge amounts of data are used to infer trends. Systematic errors such as calibration errors, if stable, also have small effects on trends. The complicated observation pattern can alias seasonal and latitudinal changes, confusing trend determinations. In the following paragraphs the main sources of error affecting water vapour and their potential impact on trends are summarised.

#### *Pointing/Tracking*

Pointing uncertainty is often the dominant source of measurement error in the lower stratosphere and below. Pointing geometry can be determined from spacecraft location and solar ephemeris data, if the Sun is accurately tracked. HALOE tracks the top edge of the Sun

and relies on ephemeris data and an atmospheric refraction model to compute tangent point locations. The tracking system centres the instantaneous field-of-view on the Sun image in azimuth and locks it a fixed angle below the top edge with a 16.2 arcsec precision and a knowledge of half that value. The pointing is known to about 100 m at the limb. The system has proven extremely reliable throughout the stratosphere and mesosphere, inducing random retrieval mixing ratio errors of less than 3% in clear air. Pointing errors become most pronounced below the 100 hPa level, where water vapour mixing ratio errors from tracking biases can exceed 10%. In heavy aerosol or cirrus clouds, the tracker cannot always accurately distinguish the top edge of the Sun and the retrievals terminate when the track is lost.

The tracking system has shown stable performance. Since the solar source function is non-uniform, it is essential that the tracking system provide exact instantaneous field-of-view location on the solar image. Periodically, HALOE performs diagnostic solar scans to calibrate the tracking system. Although there has been a response decrease of about 22% (through 1997, six years from launch) for the vertical tracking diodes, there has been no observable change in vertical tracking performance, precision, or knowledge. This is because the tracking logic uses only relative responses of diodes to detect the solar edge. This stability is expected to continue until response is down by 90% or more (after year 2015).

A possible concern is the azimuth tracking stability. As the azimuth-sensor optics degrade with time (13% through 1997), a slight change in stability could change results at low altitudes. Fortunately, the solar intensity is relatively flat at 6.61  $\mu\text{m}$  ( $\text{H}_2\text{O}$ ) and the 2.80  $\mu\text{m}$  ( $\text{CO}_2$ ) channel is used only above 35 km (NCEP temperatures are used below 35 km). Thus, HALOE water vapour trends should not be susceptible to small changes in azimuth tracking performance.

#### *Source Function*

High-resolution exoatmospheric scans are measured for each event and provide well-calibrated source functions. Sunspots are detected in the source functions on rare (<5%) occasions, mostly during solar maximum. When a sunspot is near the instantaneous field-of-view, errors can be induced in the source function due to tracking jitter, relative image rotation of the solar disk image, and refraction. The effects are minor in the 6.61  $\mu\text{m}$   $\text{H}_2\text{O}$  channel source compared to shorter wavelengths and again the 2.80- $\mu\text{m}$  ( $\text{CO}_2$ ) channel is used only above 35 km. The few events that do contain significant error due to sunspots are noted in the quality comments in the data files.

#### *Relative Spectral Response*

Spectral response functions of all the HALOE radiometers are believed to be extremely stable. Witness filters have been found stable for over 15 years. Trends in peak voltages during exoatmospheric scans show that through 1997 (over six years) the peak output of the  $\text{H}_2\text{O}$  channel changed only 0.5%, and only 2.5% in the  $\text{CO}_2$  channel. Spectral changes of this order would have a negligible effect on results because the mean atmospheric spectral characteristics for these channels would not change appreciably. There are also indications that these changes are non-spectral, imparting no effects on trends. Finally, analysis of signals from an internal 1000 K blackbody also indicates spectral stability of the radiometer channels.

The only other possible source of spectral change is from the contents of the gas cells. This indirect effect arises from using the nitric oxide (NO) gas correlation channel to infer aerosol extinction in the radiometer channels. That procedure is nearly insensitive to gas cell content. Also, the cell content for all correlation channels has proven stable over the mission according to an in-depth analysis of retrievals at various orbital beta angles. The overall conclusion is that

---

HALOE has been spectrally stable throughout the mission. Changes in the relative spectral response of the H<sub>2</sub>O and CO<sub>2</sub> signals, if they exist, must be well below the 1% level.

#### *Noise*

The instrument noise equivalent absorption for the H<sub>2</sub>O channel is insignificant below 10 hPa, and less than 4% at 1 hPa. Noise is a primary error source only above the middle mesosphere.

#### *Forward Model*

The forward models used in the HALOE processing utilise the BANDPAK [Marshall *et al.*, 1994] and LINEPAK [Gordley *et al.*, 1994] codes. The broadband calculations use either the Curtis-Godson or pseudo-mass approximation, along with a spectral overlap correction for secondary species [Marshall *et al.*, 1994]. The choice of approximation method was determined by accuracy analyses using line-by-line methods. The gas correlation measurements are simulated by rigorous line-by-line calculations. The forward model for H<sub>2</sub>O is accurate to within 1% in the stratosphere. The broadband transmissions of fundamental vibration bands have only slight temperature dependence, making the temperature uncertainty a small contribution to the total H<sub>2</sub>O retrieval error. The forward model for the T/P (CO<sub>2</sub>) channel is accurate to within 1% at altitudes where it is used-above 35 km. Below that, NCEP data are used. Since the forward model does not vary, it should have no effect on trends, except in conditions of significant and changing aerosol interference.

#### *Aerosol and Cloud Extinction*

During the period of large volcanic aerosol loading after the eruption of Pinatubo, the water channel transmission at tangent altitudes below 25 km was strongly affected by aerosol extinction. It was determined through correlative comparisons that the HALOE algorithm removes the effects of aerosol with a residual uncertainty equivalent to 7% of the aerosol extinction [Steele and Turco, 1997]. Aerosol error profiles are included in the HALOE quality data. A changing aerosol or cloud-related error would induce changes in inferred trends. Therefore, researchers should consider those changing aerosol-related error profiles when estimating upper limits of those effects on trends. Because this module of the HALOE algorithm assumes that the extinction is due to sulphate aerosol, corrections to the data in cloudy conditions are suspect. However, a new cloud identification process has been developed [Hervig and McHugh, 1999]. That procedure is described on the HALOE web site and can be used to screen out cloud contaminated data.

#### *Contaminant absorption*

Contaminant absorption from other species in the H<sub>2</sub>O channel is small because of the relatively high absorption by water vapour in its spectral band. The two primary interferences are O<sub>2</sub> (continuum) and CH<sub>4</sub>. The O<sub>2</sub> absorption is calculated with an assumed constant mixing ratio at all altitudes and with a band strength uncertainty of less than 5%, leading to systematic errors in water vapour of up to 10% below 100 hPa but less than 4% above 10 hPa. Methane absorption has a smaller effect, and causes errors of less than 4% at all altitudes. However, none of these effects should be a source of trend error.

#### *Time Response*

The time response of the measurement system can change the effective resolution due to the Sun sink rate. Time response changes can be observed by analysing scans on and off of the Sun. No change in response time constant has been observed. A 1% change in resolution can cause up to a 0.05% change in retrieved water vapour. The resolution is believed to have changed less than 2%.

---

### *Optical Degradation*

Signal characteristics when scanning on and off the Sun can also be used to infer off-axis scatter and resolution changes. No detectable change has been observed. In addition, the gas correlation difference signals give an extremely sensitive response to field-of-view differences (~1 ppmv) between effective vacuum path and gas cell path signals. There has been no significant change in these signals. Although these findings do not directly relate to the water channel, they provide further confidence that the instrument has been optically stable.

### *Orbital Geometry and Sampling*

Because the UARS orbit precesses with a period of about 70 days, the occultations occur at various beta angles (angles relative to the orbital plane) and induce changes in Sun sink rate. The eccentricity of the orbit and the Earth's oblateness also combine to cause a time-dependent change in the zenith angle vs. height relationship at large beta angles. These effects are important—they can cause up to 25% error in mixing ratio if not included—and are most pronounced at specific latitudes (such as the mid and high latitudes in the southern hemisphere) and seasons. The natural variation in pressure-altitude also contributes more error at large beta angles. The beta angle shifts phase by five days per year; one 70-day orbital precession cycle will take 14 years. Although great care has been taken to explicitly incorporate all of these effects in the data analysis, the results for very high beta angle (>55°) can often differ by up to 3%. The effect on trends is expected to be negligible.

On the other hand, trends obtained with small subsets of data at specific latitude bands can give degraded results because the five-day shift each year has the potential of aliasing the results with season and latitude (see Figure 1.14). Correlative comparisons at a particular site also have the potential to incur a systematic change in space and time coincidence, leading to false trends from a series of comparisons. Of course, there were periods when HALOE was not taking data, and one should recognise that prolonged gaps in the observations can affect a determination of trends. However, that possibility is not evaluated in this chapter because it would not arise from an instrument or algorithm error. In summary, changes in the sampling for occultation measurements can lead to trend biases in H<sub>2</sub>O.

### *Algorithm*

The processing algorithm can be a source of faulty trends if time dependent errors occur. For example, the HALOE algorithm assumes a 1.5 ppmv (0.45%) yearly growth in CO<sub>2</sub> mixing ratio. An error in this increase can lead to a nearly equal percentage error in inferred water mixing ratios. Another time dependent error that may be quite significant comes from the aerosol correction. In fact, if the data from the first year of the mission were used, the Pinatubo aerosol would likely be the largest contributor to trend error in the lower stratosphere. However, by filtering out data through 1992 the errors related to corrections for aerosol extinction are insignificant. HALOE temperatures are retrieved upward from 35 km and therefore are not susceptible to errors from auxiliary data in that region. Below 35 km, the NCEP temperatures are used. The HALOE registration with density at all altitudes is insensitive to NCEP errors. The algorithm does not use any *a priori* information other than the upper boundary profile shape, as discussed above. However, retrieval constraints limit the ability of the algorithm to accurately follow extremely sharp vertical gradients, in particular the large changes in water vapour in the troposphere. Such constraints contribute up to a 40% low bias to HALOE water vapour below the hygropause, an error that will be more severe at particular latitudes and seasons but otherwise independent of time. Consequently, a systematic elevation or lowering of the tropopause could induce false trends at altitudes just above the tropopause. Researchers should take great care in inferring trends near the tropopause.

---

### Summary comments and algorithm improvements

Generally, HALOE water vapour in the stratosphere is believed to be accurate and stable. Some small sunrise/sunset discrepancy remains at the very highest beta angles ( $>60^\circ$ ) but those instances occur for only a small fraction of the data. Researchers using Version 19 data for extracting trends in the lower stratosphere and troposphere should screen for cloud contamination and heavy aerosol conditions, as mentioned above. For comparisons with other measurements one should pay attention to the random errors that are provided in the archive for each Level 2 profile. Combined systematic errors are given in Table 1.30 at the end of this chapter.

Improvements are being made to the algorithm that will affect distributions of HALOE water vapour in the lower stratosphere. For example, a better model for the temperature-dependent effects of the interfering  $O_2$  continuum is now available. The effect of that change is considered along with the HALOE Version 19 comparisons with correlative measurements of Chapter 2. Constraints in the interleave procedure for combining individual profiles into a final retrieved profile can be relaxed for the lower stratosphere. This modification yields a more accurate transition when going from the dry values of the hygropause to the much higher mixing ratios of the upper troposphere. Both of these improvements are envisioned for a Version 20 and will lead to larger values of water vapour (and  $2*CH_4 + H_2O$ ) below about the 50 hPa level. However, neither of these improvements should have a significant impact on a determination of  $H_2O$  trends after 1992. Sampling bias is the only remaining concern for a determination of trends.

#### 1.4.6 Microwave Limb Sounder (MLS) - lower stratosphere

##### Measurement description

The UARS Microwave Limb Sounder (MLS) measurements are observations of millimetre-wavelength thermal emission at 183 GHz as the instrument field-of-view is vertically scanned through the atmospheric limb [Barath *et al.*, 1993; Waters, 1993]. The antenna is scanned mechanically across the limb and completes one full scan every 65 seconds. The signal entering the radiometer contains radiances emitted by the limb of the Earth averaged over the antenna field-of-view and a small extraneous radiance or baseline comprised mostly of radiation scattered and thermally emitted by the antenna. The baseline is spectrally flat but weakly dependent on scan-angle. Calibration is accomplished by interspersing several space views (at 2.7 K) and calibration target views (at about 300 K) with the 26 limb views during each limb scan. The switching is done using a mirror located between the antenna and the radiometers; this means that the baseline cannot be accounted for by the calibration process [Jarnot *et al.*, 1996].

MLS uses double-sideband heterodyne radiometers. Signals from two sidebands, equally spaced about the local oscillator frequency, are combined (with slightly unequal weights) into a single measurement. The weights, or sideband ratios, are measured for the six broadest channels in each band as part of pre-launch instrument calibration. There are 15 channels across each of the six 510 MHz wide filter banks. Channel widths vary from 2 MHz at the line centre to 128 MHz at the band edges. Signal-to-noise is roughly proportional to the square root of the channel width. The fifteen channels dedicated to the 183.3 GHz  $H_2O$  line (wavelength 1.64 mm) are referred to as “Band 5”.

This write-up describes two versions of the MLS water vapour data. Version 4 was the latest public release of the MLS data at the time of this study. The MLS validation papers refer to

Version 3 data; in this report is described briefly how the data changed between Version 3 and Version 4. Prototype Version 0104 was generated during the development of Version 5. This prototype has been shown to be an improvement on Version 4 in a number of ways [Pumphrey, 1999], and it is used for the inter-instrument comparisons in Chapter 2.

The horizontal resolution is approximately 400 km, limited by radiative transfer in the view direction and by the motion of the satellite. The vertical resolution is limited to about 3 km by the antenna field-of-view. The MLS data (for Version 4 and earlier) are produced on a vertical grid with points spaced each factor of  $10^{1/3}$  change in atmospheric pressure, giving a vertical grid of  $\sim 5.4$  km. The prototype version 0104 data set is produced with points spaced each factor of  $10^{1/6}$ , giving a vertical grid of  $\sim 2.7$  km. The resolution actually achieved is close to this value in the mid and upper stratosphere, but broaden in the mesosphere and the extreme lower stratosphere.

The limb scan used in normal operations consists of discrete steps between about 90 and 0 km tangent heights with the step spacing for the scan varying between 1 km in the lower stratosphere to 5 km in the mesosphere; individual spectra are measured during 1.8 s dwells between steps. The poor vertical resolution achieved in the mesosphere is a result of the large scan step used in this region.

MLS performs routine measurements continuously every day. The latitudinal coverage is from  $34^\circ$  on one side of the equator to  $80^\circ$  on the other. UARS performs a yaw manoeuvre at 36-day intervals, and at these times MLS high-latitude coverage switches between north and south. The typical profile spacing is 3 to  $4^\circ$  in latitude, with significantly denser coverage in small bands close to the turn-around points (near  $34^\circ$  or  $80^\circ$  latitude). The spacing between orbits in longitude is typically about 25 degrees, but since there is overlap arising from ascending and descending orbits the average daily sampling in longitude is about  $12^\circ$ . The stratospheric water vapour product is available between 19 September 1991 and 15 April 1993 at which time the 183 GHz Radiometer failed. The data coverage is shown in Figure 1.15.

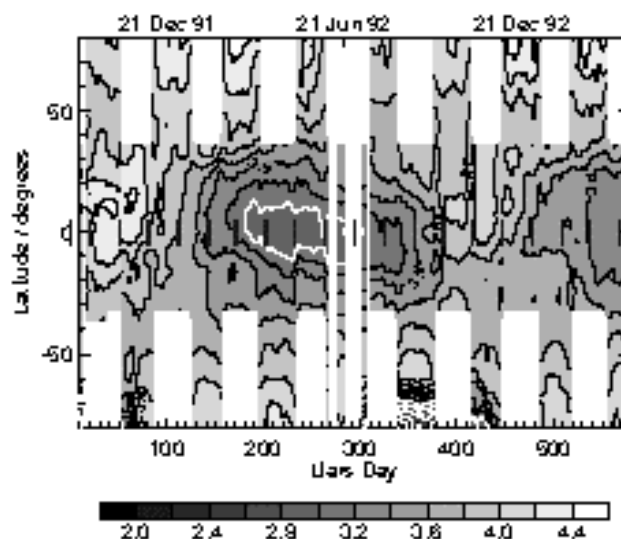


Figure 1.15 The coverage of MLS H<sub>2</sub>O data. The gaps poleward of  $34^\circ$  are a result of the UARS yaw cycle. The gaps in June 1992 are due to problems with the solar panels on the UARS spacecraft. The quantity contoured is mixing ratio at 68 hPa.

---

## Algorithm descriptions

In this subsection the standard Version 4 and the prototype Version 0104 data sets are described. In both cases the retrieval is done using a Maximum Likelihood (Optimal Estimation) formula [Rodgers, 1976]. This approach gives an estimated profile which is a correctly weighted mean of an a priori estimate of the profile and a weighted least squares fit to the radiances. A forward model  $F$  is required - this calculates the radiances  $y = F(\mathbf{x})$  that the instrument would measure if the atmosphere were in a given state  $\mathbf{x}$ . The forward model also calculates the influence function matrix  $\mathbf{K} = dy / dx$ . The optimal estimation formula gives an estimate of the error of the solution based on the errors in the radiances and in the a priori profile.

### *The Version 4 Algorithm*

The main forward model is a line-by-line radiative transfer calculation. Line parameters are taken from the Jet Propulsion Laboratory catalogue [Pickett *et al.*, 1992]. A continuum due to water vapour and dry air is included. Effects of refraction are included but line-of-sight gradients are not. This forward model is used to calculate radiance  $y_L$  and influence functions  $\mathbf{K}$  for a linearisation profile  $\mathbf{x}_L$ .

The Version 4 retrieval calculation uses a linear approximation to the forward model: the radiances  $y$  are calculated using the formula  $y = F(\mathbf{x}_L) + \mathbf{K}(\mathbf{x} - \mathbf{x}_L)$ . If this approximation is valid, the optimal estimation formula gives a solution when applied once - no iteration is needed. The optimal estimation formula is used in its sequential form. The retrieval is carried out in stages: the temperature and pointing are retrieved in the first stage and the mixing ratios in subsequent stages. The extraneous baseline radiance is handled by retrieving it along with the mixing ratio profile. The calculated radiances  $F(\mathbf{x}_L)$  and their derivatives,  $\mathbf{K}$ , are obtained by look-up table from climatological conditions and then interpolated in the vertical to the tangent pressure.

To ensure that the errors returned by the optimal estimation formula are a reasonable estimate of the accuracy, the errors assumed for the radiances include not only the measurement noise but also terms to account for errors in the retrieved temperature, retrieved tangent pressure and interfering species. These terms are included in an ad-hoc way. A limitation of the sequential formula is that it assumes that the measurement error covariance matrix is diagonal, preventing these terms from being included in the theoretically correct manner. A further term is added to account for the lack of accuracy of the linear approximation to the forward model. Nonlinearity errors are worst for measurements with large optical depths. An "opacity criterion" is used to reject such measurements. Radiances with tangent pressure greater than 100 hPa are also not used.

The a priori values used for water vapour are based on the climatology from Pumphrey *et al.* [1998]. The a priori uncertainty is set to 2 ppmv throughout the middle atmosphere. Averaging kernels [Rodgers, 1990] for MLS water vapour are well-peaked functions with some degradation in measurement sensitivity occurring in the lower mesosphere and at 46 and 22 hPa. Examples for Version 3 are presented in Lahoz *et al.* [1996]; functions for Version 4 are similar. Most of the smoothing arising from the MLS measurements is caused by the use of the fairly coarse Level 2 retrieval grid.

### *Prototype Version 0104 Algorithm*

This version of the data was produced using an independently developed forward model. Given identical input data, the model produces output that agrees very well with the JPL Forward Model. For the purposes of producing Version 0104 the forward model is run with two parameters per channel adjusted to values chosen in order to improve the 'closure' of the

retrieval. These parameters are (1) the sideband ratio of the channel and (2) the frequency offset of the channel from the line centre. Further details are in *Pumphrey* [1999] and *Pumphrey and Buehler* [2000].

The prototype retrieval is for water vapour only; Version 4 temperatures and pressures are used and are assumed to lie within the errors in the Version 4 files. The OE formula is used in its matrix multiplication form. The covariance matrix for the error in  $\mathbf{y}$  is not assumed to be diagonal, so the errors in temperature and pressure can be included correctly. An extra term is added to account for modelling errors. The Inverse Hessian or Newtonian iteration algorithm is used, as the problem is mildly non-linear. A linearised forward model is not used; the full radiative transfer calculation is done as part of the retrieval process. As with Version 4, an opacity criterion is employed to ensure that those radiances, which depend in a very non-linear way on mixing ratio, are not used. The criterion is less strict for Version 0104, so that more of the radiance measurements are used than is the case for Version 4.

The state vector has an element for every UARS pressure surface in the stratosphere, giving a grid resolution that is twice as fine as the Version 4 grid. The resolution achieved is almost as good as the grid resolution. The averaging kernels in Figure 1.16 suggest that the data are usable through 68 hPa. At mid-latitudes the data are useful even at 100 hPa.

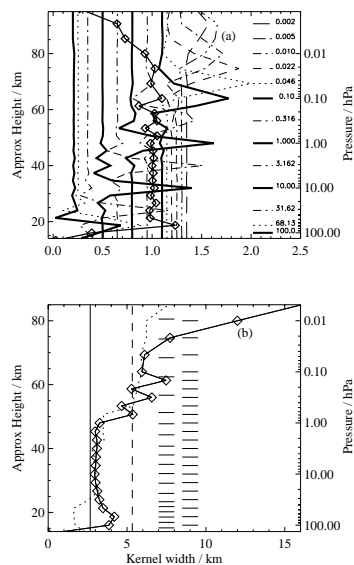


Figure 1.16 The upper panel, (a), shows the averaging kernels for some of the pressure levels on which water vapour is retrieved. The kernels are displaced to the right by an amount proportional to the altitude to which they refer in order to make the figure clearer. Kernels are not shown for all retrieval levels in order to reduce clutter. The line with diamonds is the sum of all the averaging kernels at each altitude. The lower panel, (b), shows the width of the averaging kernels as a function of altitude. The width is presented in the same 'approximate height' units as the altitude. The two sets of horizontal lines indicate the tangent altitudes for this scan (left) and the retrieval grid (right). The faint dotted line is the distance between the closest two scan altitudes. All data are for an equatorial scan.

The a priori error is 3 ppmv throughout the stratosphere. The a priori covariance matrix  $\mathbf{S}$  has off-diagonal elements given by  $S_{ij} = (S_{ii} S_{jj}) \exp(-(z_i - z_j)^2 / h_z^2)$ , where  $z_i$  and  $z_j$  are the pressure heights of the  $i$ th and  $j$ th surface and  $h_z$  is a smoothing length (which is approximately 3 km in the stratosphere).

The baseline signal was determined for an array of 26 numbers, one for each scan position. Above 3 hPa the baseline can be estimated accurately because there is no signal from the atmosphere in the wing channels. It becomes difficult to separate baseline from atmospheric signal at lower altitudes, so the baseline is assumed the same as its 3 hPa value. However, its error becomes larger for those lower altitudes.

### Estimates of error

#### *Version 4*

A few changes were made over the Version 3 H<sub>2</sub>O data described by *Lahoz et al.* [1996]. A post-launch estimate of the pointing offset between the 63 and 183 GHz radiometers is now used, as obtained from MLS antenna scans across the moon [*Jarnot et al.*, 1996]. The pointing offset change from Version 3 corresponds to a tangent height change of about +180 m. Sideband ratios estimated from the in-flight radiances were used instead of ones based on pre-launch calibrations. The manner in which temperature and pressure errors were accounted for was updated also. The Version 4 profiles are drier in the upper stratosphere, the retrieved error bars are smaller in the middle stratosphere, and the a priori contribution is much reduced in the polar winter lower stratosphere.

The error sources that affect MLS water vapour are: (1) radiance noise; (2) radiance scaling error (includes radiometric, sideband ratio, and line strength errors); (3) error in filter shapes; (4) error in FOV direction (relative to the 63 GHz radiometer FOV used for tangent-point pressure retrievals); (5) error in FOV shape (includes spectral dependence); (6) error in H<sub>2</sub>O line width; (7) errors from retrieval numerics; (8) error contribution from a priori; (9) error in tangent pressure; (10) error in atmospheric temperature; (11) error in dry air continuum; and (12) error in knowledge of O<sub>3</sub>.

The radiance noise, temperature, and tangent pressure are sources of random error. All except radiance noise may be causes of systematic errors, too. The main sources of systematic error (especially in the lower stratosphere) are errors in tangent pressure, temperature, and the modelled dry air continuum. Precision and accuracy values are plotted and tabulated in *Lahoz et al.* [1996]. Estimates of the pressure-dependent (total) accuracy and single-profile precision are plotted in Figure 1.17. The precision estimate is just the standard deviation of the water vapour over a period of three days at the equator, where there is little variability. This must be regarded as an upper bound on the precision. Accuracy estimates include the square roots of the diagonal elements of the covariance matrix returned by the retrieval plus the effects of errors in the forward model.

#### *Prototype Version 0104*

Version 0104 water vapour is drier than Version 4 in the middle and upper stratosphere, but they agree well in the lower stratosphere. Version 0104 precision and accuracy in Figure 1.17 were obtained in the same way as for Version 4.

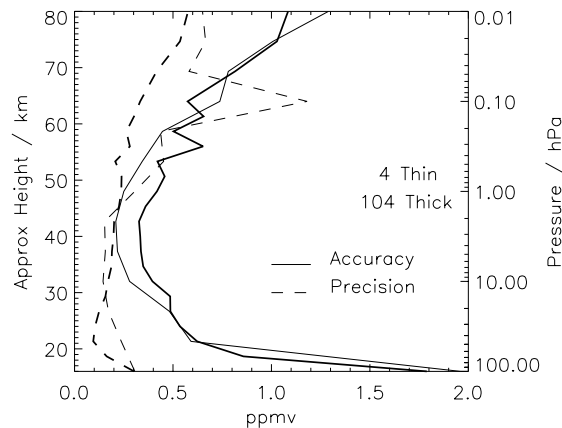


Figure 1.17 Estimates of accuracy (solid line) and precision (dashed line). The thin lines are for Version 4 and the thick ones are for Prototype Version 0104.

### Version 5 and further improvements

MLS Version 5 has been archived recently, and it provides much improved temperature and pointing retrievals using the same vertical grid as prototype V0104. The OE formula is used in its matrix form, allowing errors in quantities retrieved from the other bands to be included correctly. The baseline radiance is included by retrieving it as in Version 4. While the Version 5 water vapour retrieval includes many of the improvements found in Version 0104, the initial results suggest that it has more problems between 46 and 100 hPa than V0104.

There is still a gap at 100 hPa in the MLS measurements of water vapour between the stratospheric data set described here and the upper tropospheric data set described in Section 1.4.7. It is hoped that it will be possible to extend the stratospheric retrieval to give better data at 100 hPa and perhaps extending to the 147 hPa level. It may eventually be possible to combine the data from the 183 and 205 GHz bands in a single retrieval.

### 1.4.7 Microwave Limb Sounder (MLS) - Upper Troposphere

The Microwave Limb Sounder (MLS) experiment [*Waters et al.*, 1999] on the NASA Upper Atmosphere Research Satellite (UARS) has provided a new data set for upper tropospheric humidity (UTH). Although not designed for this measurement, the UARS MLS instrument is sensitive to upper tropospheric water vapour when the field-of-view of its 205 GHz radiometer is scanned through the troposphere, which happens every 65 seconds on each limb scan. The measurements are from limb thermal emission at 1.5 millimetre wavelength (near 205 GHz), and are much less degraded by contamination from cirrus than are shorter-wavelength visible and infrared measurements. Measurements are obtained at all times of day and night; under normal operation there are 1318 or 1319 vertical profiles obtained each day. Latitude coverage on each orbit is from 82 degrees in one hemisphere to 34 degrees in the other, with high-latitude coverage switching between the northern and southern hemispheres every 36 days. There are nearly continuous measurements from late September 1991 through late September 1994, with intermittent measurements thereafter. Specific days for which measurements exist can be obtained from the MLS web site (<http://www.met.ed.ac.uk/~hcp/watvap.shtml>).

The UARS MLS measurement of upper tropospheric water vapour is obtained from ‘continuum’ emission (in contrast to well-defined spectral line emission for other MLS measurements), and it currently relies upon empirical expressions for absorption coefficients

describing the continuum emission from water vapour and dry air near 205 GHz [Read *et al.*, 1995]. These expressions are thought to be accurate to ~20% and their uncertainty is thought to be the dominant contributor to errors in the MLS UTH measurement. Effects of cirrus ice on the water vapour measurement are generally expected to be less than ~20% at 215 hPa [Read *et al.*, 1995]. Initial results, primarily at 215 hPa, showed that scientifically useful measurements could be produced [Read *et al.*, 1995], and the data were found reasonably consistent with coincident aircraft measurements [Newell *et al.*, 1996a] and with the expected tropical Walker circulation [Newell *et al.*, 1996b]. Stone *et al.* [1996] found features in these MLS data to be consistent with paradigms for the structure and evolution of baroclinic disturbances. Good qualitative agreement was also obtained between synoptic-scale features observed by MLS over the east coast of the U.S. in March 1993 and independent results obtained from the Goddard Space Flight Center data assimilation model [Read *et al.*, 1995; Rood *et al.*, 1997; Chen *et al.*, 1998]. Sandor *et al.* [1998] analysed the improved MLS V490 UTH data (see below) and found values at the peak of the frequency distribution at ~300 hPa to be drier in the tropical wet season than in the dry season, in agreement with analyses of other data sets by Spencer and Braswell [1997] and Chiou *et al.* [1997]. However, the MLS data at ~150 hPa (where publications using the other data sets do not report results) show values of this peak that are wetter in the tropical wet season than in the dry season.

The MLS upper tropospheric water vapour data set is a distinct and separate product from the MLS stratospheric water vapour data described in section 1.4.6, and it is obtained from a different MLS radiometer (at 205 GHz) than used for stratospheric water vapour (at 183 GHz). The two data sets are not yet at the stage of maturity where they can be used together reliably for examining connections between tropospheric and stratospheric water vapour near the tropopause region.

Calibration of the UARS MLS instrument is described by Jarnot *et al.* [1996], and the estimated calibration uncertainty of the 205 GHz radiometer used for the UTH measurements is 2.6% ( $3\sigma$ ). Comparisons of stratospheric ozone, measured by this radiometer with the same calibration used for UTH, show agreement to typically better than 5% with other well-calibrated near-coincident measurements of ozone (see Figure 4 of Waters *et al.*, 1999). Radiometric calibration of UARS MLS is performed on each limb scan by observations of an onboard, ambient-temperature blackbody target and of 'cold' space. Analyses of the space radiance variation over a period of 6 years indicated less than 0.02% ( $2 \times 10^{-4}$ ) change in the reflectivity of the antenna surfaces (and its concomitant effect on calibration), which is thought to be the dominant contributor to overall calibration degradation.

MLS "Version 4.90" (V490) upper tropospheric H<sub>2</sub>O data are used in this assessment and are available for the entire UARS mission on the UARS Central Data Handling Facility. These data are an improvement over the initial data set described in Read *et al.* [1995]. Parameters in the empirical expressions were determined by fitting them to MLS radiances under the driest and wettest conditions observed (after screening for obvious cloud effects). The dry continuum parameters were estimated by fitting an appropriate pressure-squared function to the driest radiances and assuming no water vapour contribution. The wet continuum parameters were then determined by fitting to the wettest conditions, assuming 100% relative humidity with respect to ice (RHi) and an insensitivity to ice emissions. Retrievals use an optimum estimation technique, similar to that used for retrievals of other MLS parameters (see Froidevaux *et al.*, 1996). The V490 data set consists of retrieved vertical profiles of relative humidity with respect to ice (using NCEP temperatures). Vertical resolution is approximately 3 km, and horizontal resolution is ~100 km × 100 km. The retrieved vertical profile is represented as a piecewise linear function of log pressure, with breakpoints at 147, 215, 316 and 464 hPa (UARS standard pressure surfaces). Results for the lower surfaces (316 and 464 hPa) are less reliable under relatively moist conditions. Data for retrieved relative humidity and its estimated uncertainty

---

are available as standard UARS Level 3AT files for each day of measurement. Additional information including the temperature used in the retrievals, the corresponding water vapour mixing ratios, and useful diagnostics are contained in ASCII 'Level 2' files for each day (and at the UARS Central Data Handling Facility). The ASCII Level 2 file contains a header that describes the file contents and format. The estimated accuracy of the retrieved relative humidity data depends upon temperature and, at the lower levels, on the amount of water vapour present. At low and middle latitudes the accuracy is estimated to be between 10% RHi and 35% RHi at 147 hPa and 20% RHi to 50% RHi at the lower altitudes. Precision is expected to be better than 25% RHi under most circumstances. Retrieved relative humidity values greater than 120% RHi indicate the presence of cloud, and these values should be truncated to 100% to obtain the best-estimated value of water in vapour phase.

MLS "Version 5" (V5) upper tropospheric H<sub>2</sub>O data have recently been processed for the entire UARS mission and are now on the UARS Central Data Handling Facility, but were not available in time for use in this assessment. Humidity measurements from near-coincident Vaisala sonde data were used to establish empirical terms in the continuum absorption for the V5 algorithms. The V5 relative humidity values are slightly drier on average than V490: by ~3% RHi at 464 hPa, ~5% RHi at 316 hPa, ~4% RHi at 215 hPa, and ~9% RHi at 147 hPa.

A manuscript describing the quantitative validation of the MLS upper tropospheric H<sub>2</sub>O data is nearing completion. The next-generation MLS experiment [*Waters et al.*, 1999], scheduled for launch in late 2002 on the NASA EOS CHEMISTRY (CHEM) mission, will have upper tropospheric H<sub>2</sub>O measurement capability significantly improved over that of UARS MLS described here.

#### 1.4.8 Millimeter-wave Atmospheric Sounder (MAS)

The Millimeter-wave Atmospheric Sounder, MAS, is a Shuttle-based, limb-scanning millimeter-wave spectrometer for making measurements of constituents of the middle atmosphere. The measurement complement includes ozone, water vapour, chlorine monoxide, and temperature. The MAS instrument is similar in concept and scientific capabilities to the UARS MLS instrument, and it is described in detail in *Croskey et al.* [1992]. MAS was part of the NASA Atmospheric Laboratory for Applications and Science (ATLAS) series of Spacelab Shuttle missions, and it has flown on ATLAS 1 (24 March-2 April 1992), ATLAS 2 (8-17 April 1993), and ATLAS 3 (3-14 November 1994). In all 3 ATLAS missions the orbit had a 57-degree inclination and an altitude of 300 km. MAS measurements were made perpendicular to the orbital velocity vector, looking toward the south when the orbiter was in the nose-forward attitude and toward the north in the tail-forward orientation. Most of the measurements on ATLAS 1 were obtained in the north-looking orientation, giving a measurement latitude range of 70°N to 40°S. Roughly equal nose and tail forward observations were obtained from ATLAS 2, giving a measurement latitude range of 70°N-70°S. Only 10 hours of observations were obtained from ATLAS 3 (70°N to 40°S).

The water vapour retrievals for the MAS/ATLAS data sets were obtained using the MAS high spectral resolution measurements of the 183.310 GHz rotational spectral line. In the MAS data acquisition mode a limb-scan measurement (including a cold space and temperature-controlled load calibration) was obtained in 12.8 seconds. In the MAS data analysis ten of these scans were integrated (using along-track averaging in 3 km bins from 20 to 80 km) to obtain the spectral measurements used in the operational retrievals, giving an individual profile integration time of 128 seconds. From the Shuttle altitude the spatial smearing during each 128-second measurement is 7 degrees in latitude and 4 degrees in longitude for observations near the Equator, and approximately 1 degree in latitude and 28 degrees in longitude for observations at

high latitudes. In addition to this basic operational data set, a so-called "LatBin" data set was produced for each mission. The LatBin data sets were constructed using extensive radiance averaging to integrate the spectral data obtained in an entire mission into 5-degree latitude bins.

For both the individual scan profiles and the radiance-averaged zonal data sets, the water vapour mixing ratio profile was retrieved, along with ozone, in a 2-step process using an optimal estimation approach. The details of the MAS retrieval methodology are given in *Hartmann et al.* [1996] and *Daehler et al.* [1998]. The retrieval altitude range is 20 to 80 km for the individual retrievals and 20 to 85 km for the zonal-average spectra. The field-of-view of the antenna is about 3 km at 183 GHz, and retrieval vertical resolution is about 5 km. The estimated retrieval precision is 5-10%, and the estimated accuracy is about 10%.

The MAS instrument was configured identically for each ATLAS mission. Therefore, both the random and systematic errors should be the same for each flight. However, there appears to be a retrieval artefact in the ATLAS 1 data from  $-15$  to  $-20\%$  over a range of 7 km, centred at about 12 hPa. This bias does not appear in the other two data sets. This retrieval artefact is most likely the result of a measurement error for the spectral baseline. However, it is unclear why this problem was not present for the other two missions.

The MAS water vapour measurements obtained during the ATLAS 1 and 2 periods are compared to coincident measurements obtained by MLS (MLS Version 3 retrievals). The measurements generally agreed to within 10% [*Hartmann et al.*, 1996]. However, there was a tendency for MAS to be biased somewhat low with respect to the MLS retrievals. Comparisons with WVMS, MLS, HALOE, and ATMOS for all three ATLAS missions are given in *Nedoluha et al.* [1997]. The data sets generally agreed to within 20%. Besides the retrieval artefact at 12 hPa for the ATLAS 1 data, there were no consistent biases in the MAS water vapour retrievals from those comparisons.

The zonal average water vapour distribution during the ATLAS 1 mission (24 March-2 April 1992) is given in *Hartmann et al.* [1996]. In addition, *Aellig et al.* [1996] used the MAS water vapour measurements to examine a Northern Hemisphere vortex remnant in the mesosphere during the ATLAS 1 mission. They found vortex containment up to the 2100 K potential temperature level (the lower mesosphere), and they saw the clear signature of descent of air within the vortex. In other words, water vapour within the remnant was smaller than its surroundings above the water vapour peak but larger below the peak. Finally, *Bevilacqua et al.* [1996] used radiance-averaged retrievals to examine the latitudinal distribution of water vapour in the upper mesosphere during the ATLAS 2 mission (8-15 April 1993).

#### 1.4.9 Improved Limb Atmospheric Spectrometer (ILAS)

The Improved Limb Atmospheric Spectrometer (ILAS) instrument was developed by the Environment Agency of Japan, and it operated on board the Advanced Earth Observing Satellite (ADEOS) spacecraft of the National Space Development Agency (NASDA) of Japan. In its sun-synchronous polar orbit, ILAS routinely measured atmospheric trace species in the stratospheric ozone layer for November 1996-June 1997. ILAS-II, a successor to ILAS, will be on board ADEOS-II, which is scheduled to be launched in 2001. ILAS is a suite of solar occultation infrared and visible spectrometers, and it obtained vertical profiles of ozone ( $O_3$ ), nitric acid ( $HNO_3$ ), nitrogen dioxide ( $NO_2$ ), nitrous oxide ( $N_2O$ ), methane ( $CH_4$ ), water vapour ( $H_2O$ ), and aerosol (including polar stratospheric cloud) extinction coefficients at several wavelengths in the altitude range of about 10-70 km (depending on species) with an altitude resolution of 1-2 km. Its measurement frequency was about 14 occultation events per day both for Arctic and Antarctic latitudes with a latitude coverage varying from 57 to 73 degrees North

and from 64 to 88 degrees South, depending on the season (see Figure 1.18 taken from *Sasano et al.* [1999a]). The horizontal extent of measurements along the line of sight is about 200 to 230 km.

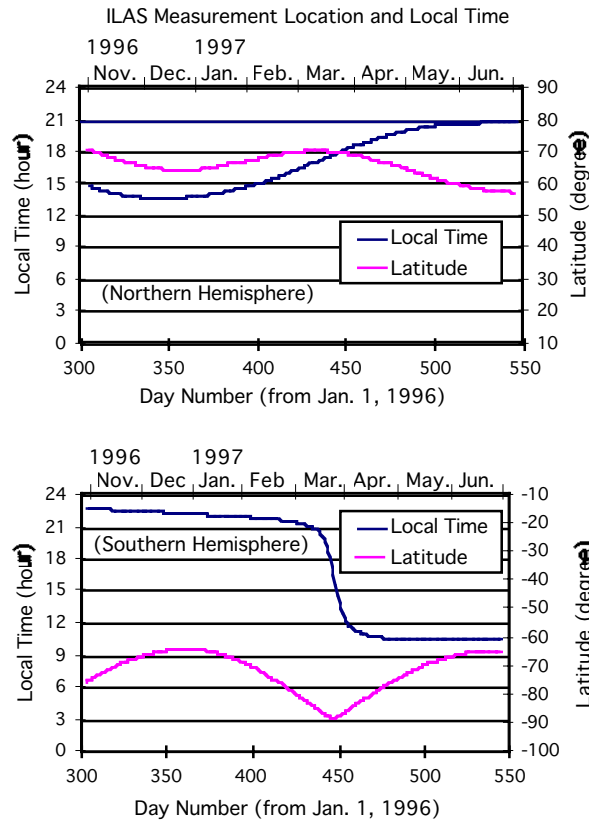


Figure 1.18 Temporal changes of ILAS latitude coverage and measurement location time for Northern (top) and Southern (bottom) Hemispheres [*Sasano et al.*, 1999a]. The Northern and Southern Hemisphere measurements are provided by sunrise and sunset occultation events, respectively.

The major characteristics of the ILAS instruments are as follows: (1) grating spectrometers with linear array detectors: 1024-pixel MOS photodiode array for the visible channel and 44-pixel pyroelectric detector for the infrared channel; (2) in the visible the spectral coverage is 753 ~ 784 nm and resolution (full width at half maximum (FWHM)) 0.15 nm, in the infrared the spectral coverage is 850 ~ 1610  $\text{cm}^{-1}$  (6.21 ~ 11.77  $\mu\text{m}$ ) with 0.12  $\mu\text{m}$  FWHM; (3) instantaneous field-of-view at a tangent point: 1.6 km vertical \* 2 km horizontal for the visible channel and 1.6 km vertical \* 13 km horizontal for the infrared channel; (4) positioning: tracking radiometric centre of the sun from the tops of clouds up to 200 km; onboard instantaneous field-of-view position measurement relative to the sun edge with a resolution of 8 arc seconds provided by 1024-pixel linear array detector [*Suzuki et al.*, 1995; *Sasano et al.*, 1999a].

ILAS transmittance spectra (Level 1 data) for the infrared channels were simulated by considering the instrument characteristics, such as the instrument function, spectral resolution, signal digitisation, and cross talk among IR detector elements. The ILAS water vapour measurement is not expected to have strong interference from other gases; there are slight effects from  $\text{CH}_4$ . Vertical profiles (Level 2 data) of gas mixing ratios are retrieved from the Level 1 data. A table look-up and interpolation method was adopted for calculating cross

---

section values over a set of pressures and temperatures for the radiative transfer calculations. At the table look-up calculation stage, the spectral line parameters and cross sections were taken from the HITRAN 96 compilation. Calculations for the water vapour continuum were performed with the code CKD 2.1 supplied by Dr. Shepard A. Clough. The retrieval fits a theoretically synthesised spectrum to the observed spectra with a non-linear, least squares method and uses an onion peeling method for the vertical profiling of its gas components [Yokota *et al.*, 1998; Sasano *et al.*, 1999a].

An on-board calibration was performed for each occultation event as part of the Level 1 processing. A pseudo-transmittance spectrum was calculated from the measured signal, where the 0% level signal (bias) was estimated from a linear interpolation of deep space signals before and after the atmospheric scan. The 100% signal level was estimated from a linear extrapolation of the exoatmospheric Sun signals. The interpolation and extrapolation of the 0% and 100% signal levels for the atmospheric measurement period was done to reduce the uncertainties resulting from e.g., effects of changes in the instrument temperature.

The ILAS Project organised a number of validation experiments [Kanzawa *et al.*, 1995; Kanzawa, 1997], including a balloon campaign at Esrange, near Kiruna, Sweden during the period from February to March 1997 - the main field experiment [Kanzawa *et al.*, 1997]. A number of vertical profiles of water vapour as well as other gaseous species were obtained during that campaign.

The validation analyses of O<sub>3</sub>, HNO<sub>3</sub>, and aerosol extinction coefficient at 780 nm gave good results for Version 3.10 of the data processing algorithm [Sasano *et al.*, 1999b; Lee *et al.*, 1999; Koike *et al.*, 2000; Burton *et al.*, 1999]. ILAS Version 3.10 H<sub>2</sub>O compared well with data from the FISH hygrometer in the balloon campaign [Sasano *et al.*, 1999c], but shows some shortages for H<sub>2</sub>O. Moreover, the Version 3.10 algorithm provided values larger than anticipated for N<sub>2</sub>O and CH<sub>4</sub> in the lower stratosphere.

Version 4.20 data were released recently and are used in this report. Its data are of better quality. The major difference between Version 3.10 and 4.20 is due to how the sun-edge sensor measurements have been used to determine the tangent height. Version 3.10 relied on comparisons of measurements of the O<sub>2</sub> A-band (P-branch) transmittance and its theoretical values based on UKMO assimilated temperature and pressure data, while Version 4.20 uses the sun-edge sensor data.

Error bars at each altitude for the retrieved parameters in Version 4.20 are presented in two classes: internal error and total error. Total error is the root sum of squares of the internal and external errors. "Internal" error for H<sub>2</sub>O is calculated from the final residuals from convergence in the non-linear least squares spectral fitting. External errors are the uncertainties of the model atmosphere used to correct for aerosol plus uncertainties in the temperatures used in the theoretical transmittance calculation. The total error is considered as the precision of the ILAS infrared gas products. There may be additional systematic errors that vary with altitude due to the ILAS tracking uncertainties, the exact location of the tangent altitude, and corrections for aerosols. Since the ILAS instrument function also varies depending on the changes in instrument temperature, which are correlated with the distance between the Sun and the Earth, the systematic error might have a small seasonal variation. Thus, the true accuracy could be worse than has been indicated by the estimates of total error given below. Comparisons with correlative or other satellite measurements provide a check on that possibility.

The Version 4.20 H<sub>2</sub>O data and its errors are given from about 10 km up to 70 km with an altitude resolution of 1 km. Average precision for all the H<sub>2</sub>O profile measurements from November 1996 through June 1997 is less than 10 % from 10-35 km, 10-30 % from 35-45 km,

---

and over 30 % from 45-70 km. The vertical profile of the total error nearly agrees with estimates based on our simulations of precision. H<sub>2</sub>O data above about 35 km exhibit vertical oscillations that are larger than anticipated, most likely because of problems with our onion-peeling routine. Researchers should apply some averaging to the data with altitude to reduce those oscillations.

#### 1.4.10 Polar Ozone and Aerosol Measurement (POAM III)

The Polar Ozone and Aerosol Measurement (POAM III) instrument is a satellite-based, nine-channel visible/near-infrared photometer for making measurements of aerosol extinction, ozone, water vapour, and nitrogen dioxide in the polar stratosphere using the solar occultation technique. The instrument is a follow-on to the successful POAM II experiment which obtained measurements from October, 1993, through November, 1996 [*Glaccum et al.*, 1996 and *Bevilacqua*, 1997], and is similar in measurement technique and scientific capabilities to the Stratospheric Aerosol and Gas Experiment (SAGE) II instrument. The POAM III instrument is described in *Lucke et al.* [1999]. POAM III was launched on the French SPOT 4 spacecraft on 21 March 1998 into a polar, sun-synchronous orbit. The SPOT 4 orbit is identical to the POAM II orbit on SPOT 3 and provides 14 solar occultation profile measurements per day around a circle of latitude in each hemisphere, having successive observations separated by about 25 degrees longitude. The latitude of the observations varies slowly over the course of a year with an approximate semi-annual period. The latitudinal variation of the POAM III measurement coverage over a 1-year period (the coverage has nearly an exact annual periodicity) is shown in the top panel of Figure 1.19. The bottom panel gives the local time of the measurements. All POAM III Northern Hemisphere measurements are made during satellite sunrise, but at local sunset. All Southern Hemisphere observations are obtained during satellite sunset but at local sunrise from April through September and at local sunset from October through March. Transitions occur at the equinoxes.

The POAM water vapour measurement is made using the 940 nm water vapour absorption band. Specifically, the difference between the measured slant optical depth at 935.9 nm (on a water vapour feature) and 922.4 nm (off a water vapour feature) is used to retrieve the water vapour concentration as a function of altitude. The retrieved concentrations are converted to mixing ratio using United Kingdom Meteorological Office (UKMO) T/P profiles. The retrievals shown in this report were obtained using the POAM III Version 2 algorithm. This algorithm is very similar to the POAM II Version 5 algorithm described in detail by *Lumpe et al.* [1997], and to the POAM III Version 1.4 algorithm described in *Lucke et al.* [1999]. Briefly, the retrieval is performed in a 2-step process. In Step 1 the total slant optical depths for all POAM measurement channels are separated into their various species components. In Step 2 the species slant optical depths as a function of altitude are inverted to yield species concentration profiles. Both retrieval steps employ an optimal estimation approach. The retrieval is global in that all species (ozone, water vapour, nitrogen dioxide, and aerosol extinction) are retrieved simultaneously. The water vapour line strengths used in the retrieval algorithm to compute the absorption cross sections are taken from the HITRAN-96 data base and include the 14.4% correction (line strength increase) in the 940 nm absorption band that was reported by *Giver et al.* [2000]. The dependence of the cross sections on temperature, pressure, and absorber amount is treated using a mass-weighted Curtis-Godson approach.

The approximate water vapour retrieval altitude range is 10-40 km. The vertical resolution is about 1 km in the lower stratosphere. It broadens with increasing altitude above 30 km, becoming about 3 km at 40 km altitude. The water vapour precision is about 5% ( $1\sigma$ ) from 16 to 40 km and better than 10% down to 14 km. The total systematic error is estimated to be better than 15% from 16 to 40 km. The dominant sources of error include random altitude

registration uncertainties, incomplete sun spot removal, and aerosol extinction uncertainties. Residual contamination from the largest sunspots leads to errors as large as 20% at 20 km in individual profiles, increasing to 40% at 40 km. Aerosol extinction is mainly an issue in the presence of polar stratospheric clouds. Errors greater than 40% can occur at the altitude of the polar stratospheric cloud in individual profiles for the most optically thick clouds. The POAM measurements are made by solar occultation and are inherently self-calibrating (the fundamental measurements are optical depths). Thus, no further instrument calibration monitoring is required.

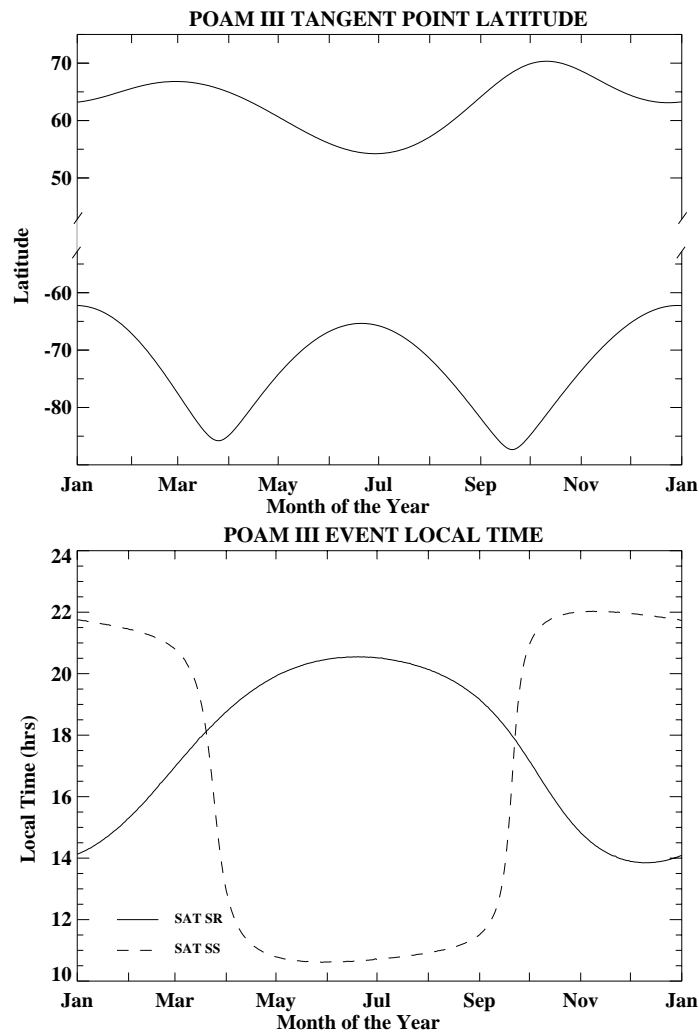


Figure 1.19 (top) POAM III measurement coverage at high latitudes of each hemisphere for a one-year period; (bottom) local time of measurement for Northern Hemisphere (solid) and Southern Hemisphere (dashed).

---

## 1.5 Summary and conclusions

In this Chapter, a variety of different techniques to measure water vapour have been presented with the description of the most important instruments providing data for this Assessment. The instruments are designed and optimised for specific measurement tasks and therefore their characteristics differ as well.

Table 1.29 summarises the most important technical parameters of *in situ* and balloon-borne, airborne and ground-based remote sensing instruments for the following discussion, i.e. precision and accuracy, along with information on the approximate range (mixing ratio or altitude) and the time and/or vertical resolution. Radiosonde characteristics are not listed here due to their limited capabilities for UT/LS altitudes.

Table 1.29 echoes the known advantage of *in situ* techniques for measurements whenever small-scale structures have to be investigated. The fastest instruments certainly are open-cell tuneable diode laser spectrometers and Lyman- $\alpha$  fluorescence hygrometers, the latter depending on purge rates. However, in order to achieve precision on the order of 0.1 ppmv in the stratosphere, integration times of at least 1 s are typically required for all instruments. Modern frost point hygrometers especially designed for measurements in the UT/LS can be as fast as 10-30 s, also permitting good spatial resolution both from balloons and aircraft. Remote sensing instruments operated from balloons, aircraft or from the ground provide vertical profile measurements with a resolution of several 100 m in the case of LIDARs, a few kilometres for the infrared and far infrared spectrometers and approximately 10 km for the microwave instruments.

The accuracies given in Table 1.29 are based on known or estimated systematic uncertainties and errors in the calibration procedures and/or the retrieval algorithms including parameters such as absorption cross sections and line strengths. They do not consider intercalibration between different instruments that can result in either smaller or larger discrepancies (see discussion in the Chapter 2). The accuracies given in Table 1.29 range from approximately 5 to 10%. In fact, the quoted accuracy for the different instruments is remarkably similar. As with the precision, it depends strongly on the method used to determine this quantity by each group and by the number of individual errors that have been added. We recommend that the Table be interpreted as saying that almost all the techniques, if properly applied and calibrated, can claim an accuracy of approximately 5-8%.

Reversing this statement, none of known techniques can currently provide a measurement of water vapour that is more accurate than 5%. The reason for this is, that producing standards for low H<sub>2</sub>O mixing ratios with high accuracy and subsequently the determination of more accurate cross sections and line parameters is limited by available techniques.

The time spans and altitude ranges for the satellite data were given in Table 1.22. Precision and accuracy may be judged from the summary estimates of the random and systematic errors in Table 1.30 for single representative profiles of each of the stratospheric satellite data sets. Precision is based on the random error, while accuracy is normally a combination of both the random and systematic error components of Table 1.30. Those estimates are based on the information in Section 1.4 or its references. Although some error estimates have been cited at an altitude (e.g., SAGE II), an approximate conversion to pressure-altitude has been performed here. For some data sets the errors were cited at specific altitudes or pressures, while for others they have been given for a range of pressure-altitudes. The errors in Table 1.30 have been estimated for ranges of vertical levels to achieve better consistency across altitude or pressure-layer boundaries. It is important to note that some systematic error components are often quasi-

random from profile to profile (e.g., profile registration errors due to pointing uncertainties for limb measurements). Those error components become much less significant for daily or seasonal zonal means. Therefore, a zonal-average stratospheric error profile is dominated by the truly systematic error components, whose signs are often unknown. Some data sets extend well into the mesosphere; the reader must refer to the individual sections and the cited references for those error estimates.

**Table 1.29** Summary of calibrations and uncertainties of the non-satellite borne instruments discussed in this Assessment: (1) systematic uncertainties; (2) reproducibility of calibration or flight-to-flight variability of uncertainties, or additional random calibration uncertainties; (3) precision or random uncertainty (given for typical integration interval); (4) total accuracy (i.e. sum of all systematic and random errors), given in percentage of mixing ratio for typical measurement range of instrument. Unless otherwise stated, the uncertainties do not contain potential sampling artefacts. The numbers of uncertainties are for typical measurement conditions and for the most advanced versions of the instruments; for details the reader is referred to the individual instrument descriptions and references therein. Secondary calibration procedures, applied irregularly for a number of instruments for crosscheck, are given in brackets.

laboratory	technique or acronym	range	resolution time or vertical	calibration procedure (secondary calibration procedure)	range for calibration	standard, reference instrument or spectroscopic parameters used	uncertainties	
							source	magnitude
NOAA-CMDL	FPH	-15 to -95°C	10-30 s	thermistor calibration		thermistor, NIST traceable	(1) thermistor calibration (2) instrumental (3) (4)	0.05° 0.4°  0.5° / 10%
LMD-CNRS	FPH	-10 to -95°C	10-20 s	temperature sensor calibration (humidity generation in a calibration bench)		platinum sensor, traceable to national T reference standard	(1) sensor calibration (2) (3) at 10 s (4)	0.1° (2σ) 0.1° 0.05° 0.3° / 3-6%
NOAA-AL	Lyman-α PFF	600 - 0.15 ppmv	1s	in-flight absorption measurement by injection of H <sub>2</sub> O generation of humidified air (absorption measurement in the laboratory and in-flight)	500-20 ppmv ambient p	σ <sub>H<sub>2</sub>O</sub> (121.6 nm) [Kley, 1984]	(1) σ <sub>H<sub>2</sub>O</sub> (2) (3) at 1 s (4) at 10 s	6% (2σ)  0.15 ppmv 6.6% (2σ)
Harvard	Lyman-α PFF	0.2 - 500 ppmv	0.125 s	generation of humidified air (absorption measurement in the laboratory and in-flight)	10-300 ppmv 15-400 hPa	T, p measurement at saturation	(1) (2) (3) at 4 s (4)	5% 3% 2%/0.1ppmv 6%
Jülich	FISH	500 - 0.2 ppmv	1 s	generation of humidified air via a laboratory bench (in-flight absorption measurement)	2-500 ppmv 50-200 hPa	Frost Point Hygrometer GE 1311 DRX, calibration traceable to NIST and national H <sub>2</sub> O standard	(1) calibration of FPH (2) (3) at 1 s (4)	0.15° / 4% 3% 0.15 ppmv 6%
JPL	TDL	ER-2: 400 - 0.1 ppmv. DC-8: 30000 - 8 ppmv	0.1 s	generation of humidified air in a calibration chamber	50-200 ppmv 50-500 hPa 250-300 K	Frost Point Hygrometer GE 1311 DR, calibration NIST traceable	(1) calibration of FPH (2) FPH reproducibility (3) at 2s (4)	0.2° / 5% 3% 1% 5-10%
LaRC/ ARC	DLH	1 - 20000 ppmv	0.05 s	generation of flowing humidified air in 1 or 3 m long chamber	equivalent of 0-1000 ppmv 100-1000 hPa	DPH Edgetech 2001, NIST traceable calibration spectral parameters [Rothman et al., 1996]	(1) Calibration (2) electronics, thermal (3) at 50 msec (4)	3% 8%or1ppmv 2% 10%or1ppm
Jülich	MOZAIC	> 20 ppmv	0.5-180s	generation of humidified air (calibration chamber)		Lyman-α absorption: σ <sub>H<sub>2</sub>O</sub> (121.6 nm) [Kley, 1984]	(1) σ <sub>H<sub>2</sub>O</sub> (2) flight-to-flight (3) (4)	6% (2σ) 30% 8% (2σ) 4-7% RH

NRL	WVMS (ground-based)	40-80 km	1-7 d 10 km	blackbody calibration		line parameters [Pickett et al., 1998; Liebe et al. 1993]	(1) baseline, instrumental + profile retrieval errors (3) 7d (4) 40-80 km	0.5-0.1 ppmv 0.15 ppmv 0.6-0.2 ppmv
MPAE	ground-based microwave	40-80 km	1-7 d 10 km	blackbody calibration		line parameters [Pickett et al., 1998; Liebe et al. 1993]	(1) baseline, instrumental + profile retrieval errors (3) 7d (4) 40-80 km	0.5-0.1 ppmv 0.15 ppmv 0.6-0.2 ppmv
Bern	airborne microwave	15-75 km	30 min 8-15 km	blackbody calibration		line parameters [Pickett et al., 1998; Liebe et al. 1993]	(1) (2) (3) (4)	0.6 ppmv
LaRC	LASE	troposphere	2 min 300-500 m	self-calibrating (DIAL technique)	0.01-20 g/kg	$\sigma_{\text{H}_2\text{O}}$ (813 nm) [Ponsardin and Browell, 1997]	(1) $\sigma_{\text{H}_2\text{O}}$ (2) (3) (4)	6%
DLR	DIAL	UT/LS 5-100 ppmv	1-2 min 300-500 m	self-calibrating (DIAL technique)		$\sigma_{\text{H}_2\text{O}}$ (935.43, 935.35, 942.82 nm) [Poerberaj and Weiss, priv. comm.]; [Rothman et al., 1996]	(1) $\sigma_{\text{H}_2\text{O}}$ (2) laser transmitter (3) profile retrieval (4)	3% 2% 1-5% 5-7%
Karlsruhe	MIPAS	5-40 km	2-3 km	calibration based on "deep space" (+20° elevation angle) and internal blackbody spectra recorded during flight		HITRAN data base [Rothman et al., 1998], spectral intervals within 808-825 $\text{cm}^{-1}$ , 1210-1245 $\text{cm}^{-1}$ , 1589-1610 $\text{cm}^{-1}$	(1) line parameters (2) profile retrieval (3) (4)	5% 1-5% 4-8% 6-11%
JPL	MkIV	20000-1 ppmv	2 km	self-calibrating (solar occultation)	-	HITRAN data base [Rothman et al., 1998], 12 intervals at 1500-4630 $\text{cm}^{-1}$	(1) line parameters (2) profile retrieval (3) (4)	5% 5-12% 7-13%
SAO	FIRS-2	10-40 km	2-4 km; 60 min per profile at 4 km vertical resolution	ambient-temperature blackbody + cold space view (intensity calibration)		HITRAN data base [Rothman et al., 1998], with strengths and positions from Couderc [1999] and Toth [1991]; 18 intervals at 80-480 $\text{cm}^{-1}$	(1) line parameters (2) profile retrieval (3) (4)	3% 4% 5%

**Table 1.30** Estimates of random and systematic error of satellite stratospheric H<sub>2</sub>O profiles

Instrument and data set	Random error	Systematic error
LIMS (version 5)	20-15% from 1 to 5 hPa 15-10% from 5 to 10 hPa 10% from 10 to 50 hPa	31-24% from 1 to 5 hPa 24-20% from 5 to 10 hPa 20-37% from 10 to 50 hPa
SAGE II (version 5.9)	10-5% from 3 to 10 hPa 5-14% from 10 to 25 hPa 14% from 25 to 300 hPa	6-13% from 3 to 7 hPa 13% from 7 to 25 hPa 13-27% from 25 to 100 hPa 27% from 100 to 300 hPa
ATMOS (version 3)	9-11% from 1 to 300 hPa	6% from 1 to 300 hPa
HALOE (version 19)	9-7% from 1 to 10 hPa 7-13% from 10 to 40 hPa 13% from 40 to 100 hPa	10-14% from 1 to 10 hPa 14-19% from 10 to 40 hPa 19-24% from 40 to 100 hPa
MLS (version 0104)	4% from 1 to 10 hPa 3% from 10 to 50 hPa 3-8% from 50 to 100 hPa	6-9% from 1 to 10 hPa 9-16% from 10 to 50 hPa 16-50% from 50 to 100 hPa
MAS	5-10% from 1 to 50 hPa	10-15% from 1 to 50 hPa
ILAS (version 4.20)	More than 10% above 2 hPa 10-5% from 2 to 300 hPa	30% from 1 to 2 hPa 30-10% from 2 to 7 hPa 10% from 7 to 300 hPa
POAM III (version 2)	5% from 3 to 100 hPa	15% from 3 to 100 hPa

---

It should be appreciated that there are instances when comparisons between data sets consistently indicate very good agreement, such that one might conclude that the total error for the least accurate data set is too conservative. In other words, some of its systematic error components may be overestimated or have unknown but opposing signs. Conversely, it should also be apparent that only known error mechanisms have been characterised for each data set, and it is often the intercomparison with other data sets that reveals any remaining problems.

Similar estimates of random and, especially, systematic errors for the MLS and TOVS upper tropospheric humidity data sets can not be characterised as easily. These products are derived as layer-averaged results for a region of the atmosphere where the vertical gradient of water vapour (and temperature for TOVS) is changing significantly. Estimates of systematic error are dependent on the atmospheric state for the measurement, and it has been more appropriate to report the sensitivity of the retrieved upper tropospheric humidity to those atmospheric state variables. Those sensitivities are provided in the MLS and TOVS subsections and their cited references. The reader should consult them for the details. Even so, the precision of the MLS and TOVS upper tropospheric humidity data sets is generally good, which is why the spatial water vapour patterns that they report are useful. SAGE II data are reasonably accurate in the upper troposphere, but they do have a “clear-air” bias.

The TOVS upper tropospheric humidity measurements and two of the stratospheric data sets (SAGE II and HALOE) have relatively long records, and they are being used to look for changes that may be related to increases in greenhouse gases and/or surface warmings. The reader is referred back to their individual sections for the more complete estimates of measurement and/or retrieval errors that could affect such trend analyses. The primary concern for the long record of TOVS data is the intercalibration of the series of instruments that have been flown on the operational satellites. The Version 5.9 SAGE II H<sub>2</sub>O time series is affected by uncertainties in its correction for aerosol extinction between the tropopause and about 27 km (for volcanically perturbed periods). SAGE II H<sub>2</sub>O data may also be affected by changes in the reflectivity of the scan mirror and in the characteristics of the filter for the NO<sub>2</sub> (453 nm) channel that is part of the aerosol correction algorithm. The HALOE time series seems to be free of long-term instrument and/or retrieval effects. However, its near-global trends may be affected by changes in HALOE sampling frequency and pattern, particularly for the late 1990s.

In summary, all of the satellite data sets are well characterised and can be used to define zonal-mean distributions of water vapour and its large-scale, zonal variations. Because their precision is generally good, they can provide the seasonal and even interannual cycles of water vapour. Longer-term changes can also be addressed with HALOE data at those latitude zones where the sampling has been consistent over the life of the experiment. It is now the purpose of Chapters 2 and 3 of this report to evaluate whether the distributions and long-term changes from each of these data sets are consistent with each other and meaningful.

The data sets of the individual instruments presented in this Chapter provide a wide coverage in space (different altitude range and regions) and in time. First measurements in the UT/LS date back to the 1940s. The longest continuous and well-documented record of measurements in the UT/LS is that of the balloon-borne NOAA-CMDL frost point hygrometers beginning in 1964 up to present days. Since the late 1970s, the Lyman- $\alpha$  technique provides complementary measurements both from balloon and aircraft. In the 1980s and 1990s, the number of *in situ* and remote sensing instruments for balloon-borne and airborne measurements has increased rapidly (see Figure 1.2) involving established and new techniques. The only ground-based technique ranging into the stratosphere is microwave spectroscopy, which has been used for continuous measurements at different places since 1993 (Figure 1.9).

---

Satellite instruments of stratospheric water vapour are available since the late 1970s (Table 1.22). Today, they are the most important data source for most applications due to their nearly global coverage and the continuity of the measurements.

A large number of techniques is available for probing the upper troposphere and tropopause region, i.e. radiosonde and MOZAIC sensors, LIDARs, satellites (operational upper tropospheric humidity and more recently, also extended retrievals of other satellite experiments) for regular measurements, as well as airborne *in situ* hygrometers on campaign-basis. However, the large variability and strong gradients in the H<sub>2</sub>O distribution at these altitudes plus the sometimes limited accuracy and precision, the characterisation of the instruments or their low sampling frequency, are still limiting the factors for determining the global distribution of H<sub>2</sub>O and its possible long-term changes.

# Chapter 2

## Data Quality

### **Lead Authors**

S. Oltmans - K. Rosenlof

### **Co-authors**

H. A. Michelsen - C. Schiller - W. G. Read,  
G. E. Nedoluha - L. Pan - E. E. Remsberg

J. J. Bates - R. M. Bevilacqua - M-L. Chanin

E-W. Chiou - W. P. Chu - H. Fischer

D. G. Johnson - L. L. Gordley - P. Hartogh

M. Helten - R. L. Herman - E. J. Hintsa

S. Ismail - H. Kanzawa - K. K. Kelly

D. Kley - R. D. May - L. M. Miloshevich

H. Oelhaf - J. Ovarlez - H. C. Pumphrey

P. N. Purcell - J. M. Russell III - G. W. Sachse

V. Sherlock - H. G.J.Smit - G. C. Toon

S. A Vay - H. Vömel - E. M. Weinstock

## 2.1 Introduction

The need for improvements in the comparability of water measurements in both the stratosphere [Harries, 1976] and troposphere [Elliott and Gaffen, 1991] has long been recognised. Water vapour is measured in the atmosphere from multiple platforms with a large variety of sensors. Instruments developed in more recent years, particularly satellite-based sensors, have included correlative measurement campaigns as part of their validation procedure. For those that measure tropospheric water vapour, the conventional radiosonde has often been used for validation. The measurement of upper tropospheric water vapour by radiosondes is, however, fraught with numerous problems. In the stratosphere, the most commonly used *in situ* water vapour measurement instruments have shown significant biases between each other [Albritton and Zander, 1985]. As a result of correlative measurement programs, special intercomparison activities, and continuing measurement and algorithm improvements, discrepancies between measurement systems have been better quantified. In some instances, revised data sets have been prepared. Extensive use is made of these revised data sets for this report. In several of the cases, the results presented here are updates of validation studies carried out at the inauguration of the instrument measurement program. Revisions have also been made in some cases to the correlative data as well as the data to be validated.

Data quality questions are addressed from two perspectives. The first is the comparability of data obtained using a wide variety of techniques and from a large number of platforms. The other is the suitability of the data for use in various scientific studies investigating processes controlling the distribution of water vapour or the role of water vapour in responding to or initiating climate change. Important data quality questions addressed in this chapter include:

- What is the relationship among various measurement systems in the water vapour concentration that is derived?
- Is there a standard to which all measurements can be compared?
- Where there are significant differences in the measured water vapour concentration among the sensors and platforms, do we have an understanding of the reason for these differences?
- Can upper tropospheric water vapour data obtained by satellites be adequately validated by existing *in situ* measurements using balloon-borne (radiosondes, frostpoint hygrometers), airborne (campaigns, MOZAIC), and LIDAR techniques?
- Are the primary global data sets in the troposphere (TOVS) and stratosphere (HALOE) sufficiently well validated to form the basis for the analysis of water vapour in these regions?
- From the longer-term (~8 years or longer) observations made in the stratosphere, is there consistency among the changes deduced from these measurements?

An extensive list of instruments is described and characterised in Chapter 1 of this report. Several data sets have been included despite relatively short measurement histories because of their usefulness in validating longer-term or more geographically extensive data sets. The approach taken here is to compare the measurements from a variety of techniques on a number of platforms and try to quantify the differences and where they exist; inconsistencies will be pointed out as well as areas of substantial agreement. Comparisons are carried out using several approaches. Extensive use is made of direct comparison of individual profiles. Where a sufficient number of direct comparisons between two instruments exist, differences are typically presented as average biases with  $1\sigma$  standard deviations. In a few cases, only individual profile comparisons are presented. Because of a limited number of profiles, particularly from *in situ* techniques, several different profile-matching criteria are used. In some cases, matches are improved by using dynamical tracers such as potential vorticity (PV) to better characterise the

air mass in which the profiles were measured. Additionally,  $N_2O$  is used to group measurements with similar histories when applicable. Average profiles from a location or period of time are also compared in order to check that features such as the lower tropical stratosphere seasonal cycle are consistently represented in different data sets. Average profile comparisons are also useful when the period of observation for various platforms is not coincident. Especially in the troposphere where spatial and temporal variability is large, it is often necessary to combine *in situ* measurements so that they can be compared with satellite observations. Finally, an analysis of the spatial and temporal averages and the derived products  $2 \times CH_4 + H_2O$  and tropical stratospheric entry value for water vapour are compared among different data sets to see how consistent these quantities are. Possible causes of long-term changes in water vapour are discussed in Chapter 3. However, estimates of changes in the stratosphere derived from a variety of moderately long data sets from as early as the 1950's are given here, and their consistency is assessed. For the longer-term data sets, the potential for changes with time is pointed out, for example, design changes of the frostpoint hygrometer or the use of multiple satellites for the TOVS series of upper troposphere water vapour measurements. These are discussed more completely in Chapter 1.

## Plan of comparisons

Using the approaches described above, comparisons are made among aircraft-borne, balloon-borne, and ground-based sensors that obtain data in both the stratosphere and troposphere. Data from these sensors are also compared to data obtained with satellite instruments. An outstanding issue for the comparability of observations in the lower stratosphere has been the disagreement among various *in situ* measurements obtained by several balloon and aircraft platforms that are operated by United States agencies and universities. Unfortunately the discrepancies are not resolved in this report but several aspects of this disagreement are investigated and summarised in this chapter. Comparisons among European instruments using similar principles to the United States instruments are also reported with somewhat different results. Results of a laboratory comparison of the NOAA-CMDL frostpoint, NOAA-AL Lyman- $\alpha$ , and the Harvard Lyman- $\alpha$  techniques are reported but do not resolve the differences between these instruments. Three instruments flown on balloons (MIPAS, FIRS-2, and MkIV) make stratospheric measurements using infrared techniques. These are compared with *in situ* instruments as well as among themselves.

Most of the airborne and balloon-borne techniques have also been compared with various satellite-borne instruments. Comparisons are presented between these techniques and the HALOE, MLS, SAGE II, ATMOS and ILAS instruments. The ground-based microwave water vapour measurements (WVMS and WASPAM) provide another opportunity for comparison with the satellite systems, particularly in the middle and upper stratosphere and mesosphere.

In the upper troposphere, the most extensive data set in both time and space is the TOVS data (since 1979) obtained from the HIRS sensor on a number of operational meteorological satellites. More recently (1992-1998) the Microwave Limb Sounder (MLS) on the Upper Atmosphere Research Satellite (UARS) has also obtained data at several levels in the upper troposphere. These two data sets are compared with one another and with a newly available set of *in situ* measurements in the upper troposphere from observations on commercial passenger aircraft (MOZAIC). The MOZAIC data are also compared with data from several sensors flown on upper tropospheric aircraft. Although radiosondes have a number of limitations in their measurement capability of water vapour in the upper troposphere (see Chapter 1), they are widely used and will likely still play a role in the future in validation of remotely sensed tropospheric water vapour. A useful correction to the data for a particular type of sensor (*Humicap A*) on the widely used Vaisala RS80 radiosonde is presented. LIDAR for measuring

---

tropospheric water vapour profiles is an emerging technique that is compared to several *in situ* measurements.

Comparisons are also made among different satellite systems. In the stratosphere, the water vapour measurements from the HALOE and SAGE II instruments are the longest near global data sets. Because of problems due to interference from aerosol and ozone at the wavelength from which water vapour is retrieved, the version of the SAGE II data available for this assessment has several drawbacks that are discussed more fully later in this chapter. For this reason, only limited attention is paid to assessing the data quality of the current data set. ATMOS is compared with the MAS, HALOE and MLS measurements in the stratosphere and the mesosphere. The MLS and HALOE instruments, both flying on UARS, provide a number of comparison opportunities during the approximately 1.5 year life of the MLS 183 GHz stratospheric water vapour channel. Although the ILAS sensor on the ADEOS satellite only obtained data for 9 months before the satellite failed, several comparisons were carried out with balloon-borne packages and HALOE. The ILAS sensor is used as a transfer for comparisons between several instruments when direct comparisons were not possible. The currently operating HALOE and POAM III instruments provide stratospheric comparisons during the periods when HALOE coverage extends to high latitudes. In the troposphere, the TOVS and MLS provide overlapping measurements. In the upper troposphere, the stronger water vapour signal allows SAGE II to make measurements of good enough quality that they provide some opportunity for comparison. Finally, the tropospheric MLS and TOVS data are compared. A summary of differences found between all the instruments compared is presented in section 2.6. Conclusions and recommendations are also given in the final sub-section of this chapter.

## 2.2 Comparisons between aircraft-borne, balloon-borne, and ground-based sensors

### 2.2.1 Stratospheric measurements

#### NOAA-AL Lyman- $\alpha$ and NOAA-CMDL frostpoint hygrometer

There have been eight coincident flights between the NOAA Aeronomy Laboratory (AL) Lyman- $\alpha$  instrument and the NOAA Climate Monitoring and Diagnostics Laboratory (CMDL) frostpoint balloon instrument. In the early 1980's, these used both a Lyman- $\alpha$  balloon instrument and an aircraft instrument. Coincident comparison flights occurred in Texas, Wyoming and California. The percent difference as a function of altitude between 15 and 30 km is shown in Figure 2.1. Differences are on the order of 20%, with the Lyman- $\alpha$  instrument measuring larger values.

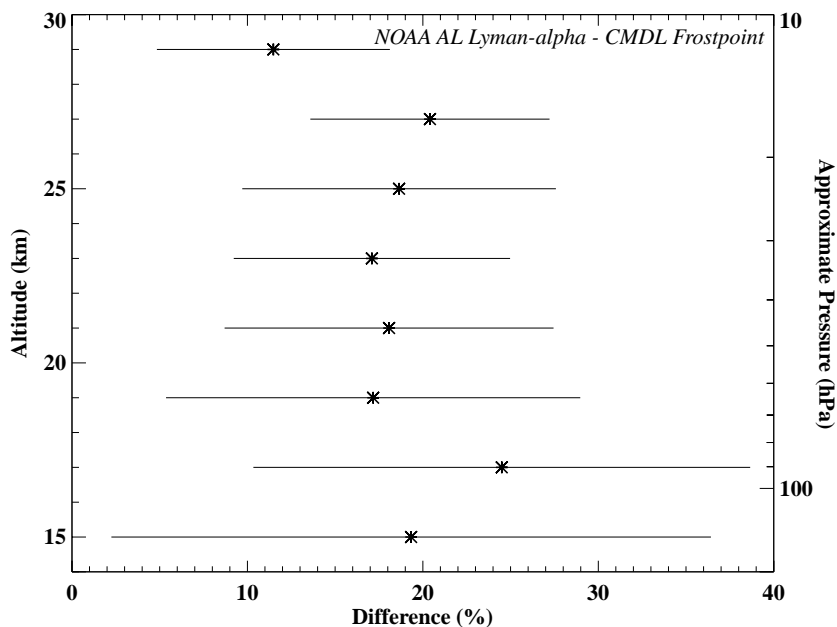


Figure 2.1. Percent difference between the NOAA-AL Lyman- $\alpha$  and NOAA-CMDL frostpoint balloon instruments. 8 comparison flights were included in this calculation. Data from all flights were put into 2-km bins, the mean is shown by the symbol, and the standard deviation ( $1\sigma$ ) denoted by the horizontal lines. Percentage differences were calculated by taking  $(AL-CMDL)/average$ .

#### Harvard Lyman- $\alpha$ and NOAA-CMDL frostpoint hygrometer

There are only a few comparisons between the Harvard Lyman- $\alpha$  ER-2 and NOAA-CMDL frostpoint instruments. The only direct comparison consists of three flights in May 1993 at Crows Landing, California, as part of the SPADE aircraft mission. The same 3 days are also included in the NOAA-AL:NOAA-CMDL comparison. Percent differences between the Harvard and NOAA-CMDL instruments are shown in Figure 2.2. There is a wide range of percentage differences as a function of altitude, the average being 27%, with Harvard values larger.

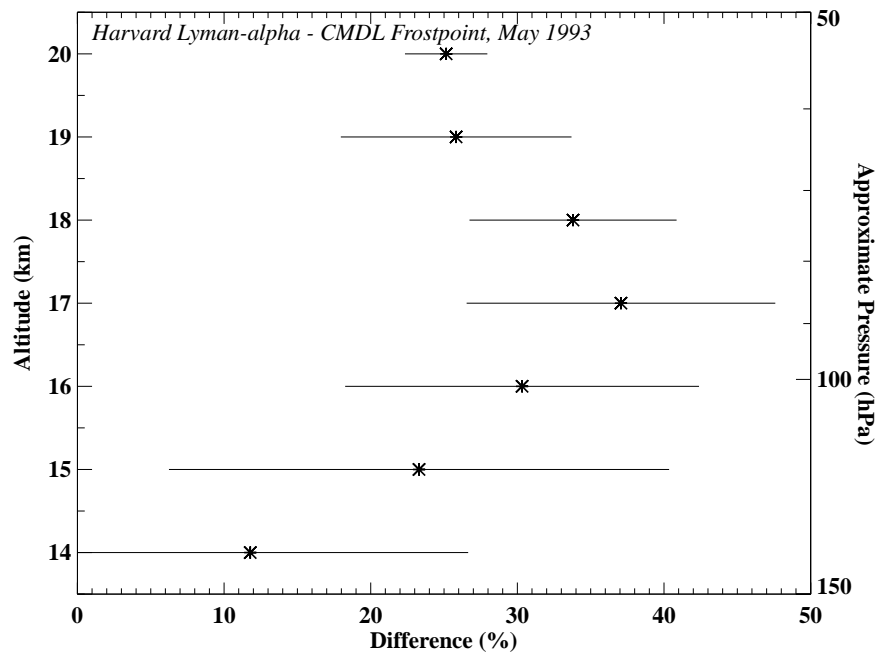


Figure 2.2. Percent difference between the Harvard Lyman- $\alpha$  and NOAA-CMDL frostpoint balloon instruments. 3 comparison flights were included in this calculation. Data from all flights were put into 1-km bins, the mean is shown by the symbol, and the standard deviation ( $1\sigma$ ) denoted by the horizontal lines. Percentage differences were calculated by taking  $(\text{Harvard}-\text{CMDL})/\text{average}$ .

The only other near coincidences between the Harvard and NOAA-CMDL instruments were during the Central Equatorial Pacific Experiment (CEPEX) campaign in the equatorial Pacific during March 1993. In this case, there were no geographic coincidences, but the two instruments were both measuring in the same general area. For this comparison, all the NOAA-CMDL measurements were averaged into one profile, as were all the Harvard measurements. The offset between the two instruments is  $\sim 1.4$  ppmv, with the Harvard measurements greater. This amounts to approximately a 30% difference at ER-2 cruise altitudes (near 20 km) and over 40% differences at lower altitudes near the hygropause. Gradients in satellite measurements taken during the same month across the Central Pacific near 20 km are less than 0.1 ppmv across the width of the basin. It is therefore unlikely that the differences noted between the two *in situ* measurements at ER-2 cruise altitudes are a result of geographic biases, but instead indicative of an actual measurement difference.

### Jülich Lyman- $\alpha$ (FISH) and LMD frostpoint

Balloon-borne profiles of the Jülich Lyman- $\alpha$  fluorescence hygrometer FISH and the LMD frostpoint hygrometer can be compared using  $2\times\text{CH}_4+\text{H}_2\text{O}$  even when data are not sampled in spatial and temporal coincidence. For a number of flights of both hygrometers,  $\text{CH}_4$  was measured by the same whole air sampler instrument with gas chromatographic analysis traceable to a single standard [Schmidt *et al.*, 1987]. Given a precision of better than 3% for the  $\text{CH}_4$  measurement and assuming variations of  $2\times\text{CH}_4+\text{H}_2\text{O}$  in the middle stratosphere (420-700 K) at mid- to high latitudes covering the period of a few years are of the same magnitude, discrepancies of more than 5% between the  $\text{H}_2\text{O}$  measurement techniques should be detectable.

A series of balloon flights of the LMD frostpoint and the whole air samplers during the European Arctic Stratospheric Ozone Experiment (EASOE) in winter 1991/92 at 68°N has been

used to determine  $2\times\text{CH}_4+\text{H}_2\text{O}$  [Engel *et al.*, 1996]. This quantity was found to be  $6.91\pm 0.41$  ppmv at potential temperatures from 430 K to 750 K. There were no significant differences between data obtained inside or outside of the polar vortex. From a mid-latitude balloon profile on 20 September 1993 using FISH and the whole air sampler,  $2\times\text{CH}_4+\text{H}_2\text{O}$  was determined to be  $7.17\pm 0.62$  ppmv for potential temperatures ranging from 420 K to 900 K [Zöger *et al.*, 1999b]. Two more flights of this payload at  $68^\circ\text{N}$  yielded a value of  $7.02\pm 0.11$  ppmv (11 February 1997, 400-600 K) and  $7.05\pm 0.12$  ppmv (6 February 1999, 420-580 K). LMD frostpoint measurements are slightly smaller than FISH data by 0.1-0.2 ppmv.

In May 1999, both hygrometers were launched on balloons from Southern France within 60 hours of one another. Despite a few filamentary structures which differ in both profiles due to atmospheric variability, Figure 2.3 shows that both measurements agree to within 0.2 ppmv at 90-50 hPa with a maximum deviation of 8%.

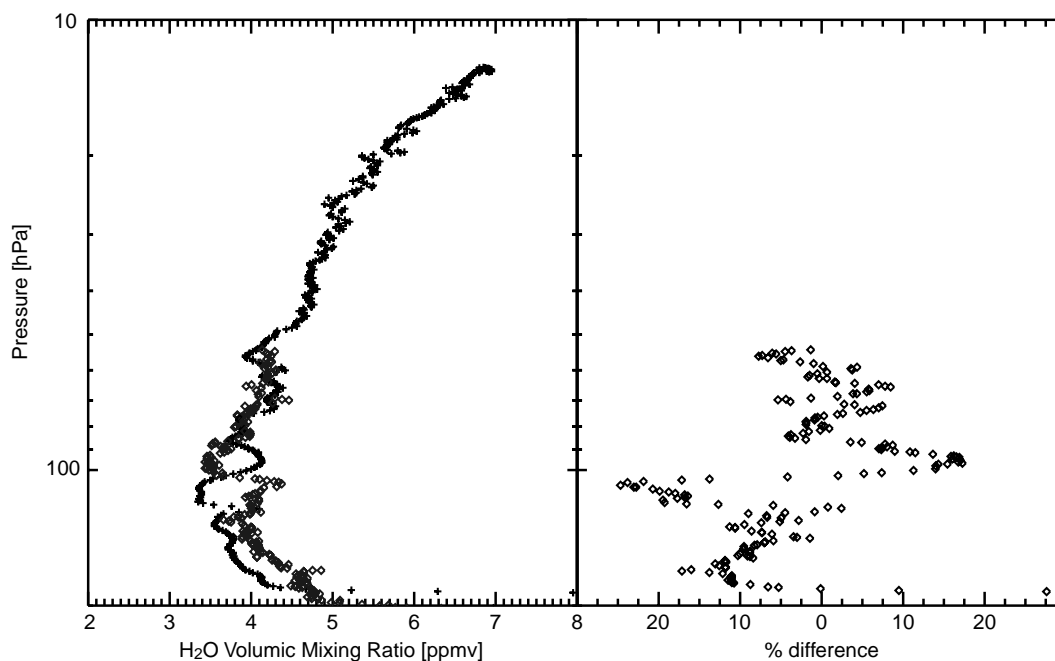


Figure 2.3 Intercomparison of  $\text{H}_2\text{O}$  balloon profile measurements of the LMD frostpoint hygrometer (crosses, 5<sup>th</sup> May 1999) and of the Jülich Lyman- $\alpha$  hygrometer (open diamonds, 3 May 1999) at  $44^\circ\text{N}$ .

### NOAA-AL and Harvard Lyman- $\alpha$ on the ER-2

During the NASA SPADE mission (April-May 1993), both Harvard and NOAA-AL Lyman- $\alpha$  instruments flew on the ER-2 high altitude aircraft. The average difference over the nine flights used in this comparison is  $\sim 15\%$ , with the Harvard measurements larger. The offset in mixing ratio is  $\sim 0.7$  ppmv. The vertical distribution of the percent differences is shown in Figure 2.4. Percent differences are fairly constant with altitude above 15 km. Comparisons of measurements below 15 km taken during aircraft ascent and descent show more vertical structure and greater variability in the differences. As discussed later in the laboratory intercomparison (2.2.2), the reasons for the disagreement are not understood, nor reproducible under controlled laboratory conditions.

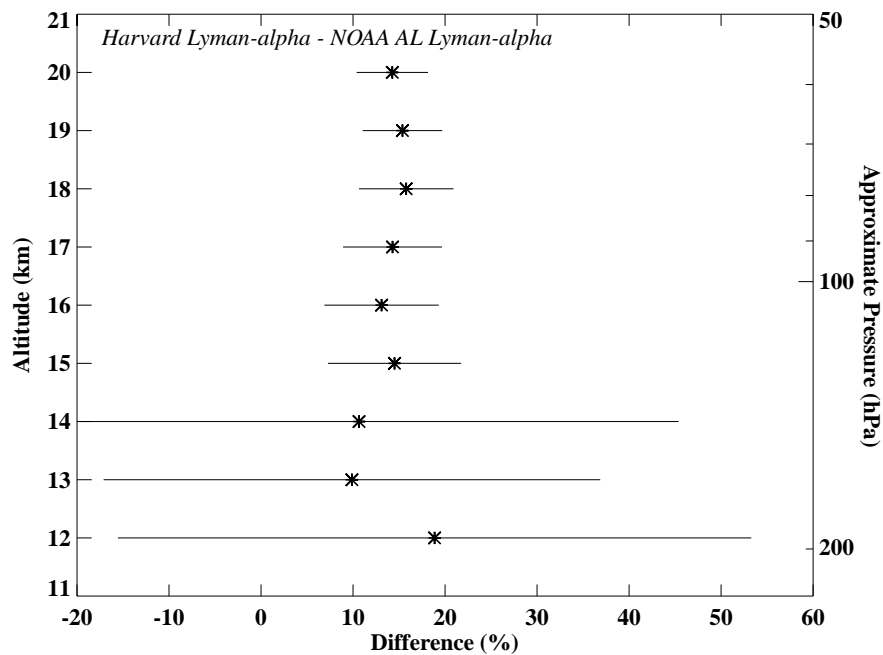


Figure 2.4 Percent difference between the Harvard and NOAA-AL Lyman- $\alpha$  instruments flying on the ER-2 during SPADE. 9 comparison flights were included in this calculation. Data from all flights were put into 1-km bins, the mean is shown by the symbol, and the standard deviation ( $1\sigma$ ) denoted by the horizontal lines. Percentage difference is calculated by taking  $(\text{Harvard}-\text{AL})/\text{average}$ .

### Lyman- $\alpha$ and JPL TDL

During the NASA POLARIS mission (April-September 1997), the Harvard Lyman- $\alpha$  instrument was compared with the TDL hygrometer from JPL [May, 1998; Hintsa, 1999]. Average agreement for the entire June-July deployment was 1% from 0-200 ppmv  $\text{H}_2\text{O}$  with an offset of less than 0.2 ppmv; most measurements agreed to within 5%. Nonetheless, there were significant pressure-dependent differences at pressures between 100 and 300 hPa as shown in Figure 2.5, where the Harvard instrument measured less than the JPL instrument. These are thought to arise from uncertainties in the modulation amplitude placed on the diode laser for second harmonic detection. Using a fixed modulation amplitude produces a pressure-dependent uncertainty because of undermodulation at higher pressures. Some variation is seen between deployments during POLARIS, especially at pressures greater than 100 hPa. At cruise altitudes (19-21 km), where water is low and the JPL TDL calibration was most reliable, the agreement is within 1% with an offset of  $< 0.1$  ppmv.

During the NASA/NOAA WBS7F Aerosol Mission (WAM) mission (April 1998), the NOAA-AL Lyman- $\alpha$  and JPL TDL hygrometers had two coincident flights on the WB57F high altitude aircraft. Considering data just above 15 km, the average difference is 16%, with the JPL TDL measurements larger. If the entire altitude range is considered, the average difference is  $\sim 10\%$ . This reflects the vertical structure in the percent differences, plotted in Figure 2.6. The shape is similar to that in the percent differences between the Harvard Lyman- $\alpha$  and JPL TDL instruments shown in Figure 2.5, except offset by 10-15%. Reasons for the pressure-dependent differences are discussed above. In spite of these differences, the JPL TDL instrument can be used as a transfer agent between the Harvard and NOAA-AL Lyman- $\alpha$  instruments. This comparison would also indicate that the differences between the Harvard and NOAA-AL Lyman- $\alpha$  instruments would be  $\sim 15\%$ , with the Harvard instrument larger.

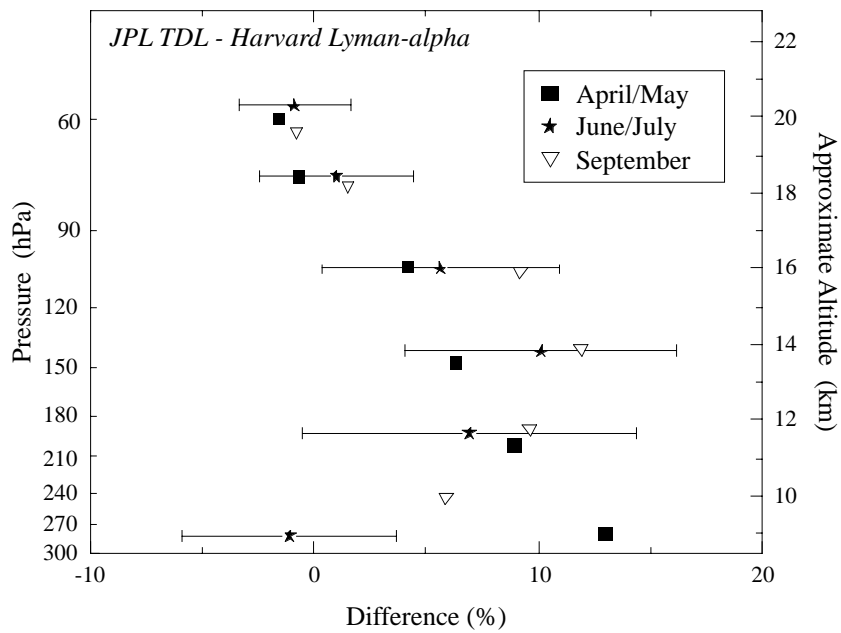


Figure 2.5 Percent difference between the JPL TDL and Harvard Lyman- $\alpha$  instruments flying on the ER-2 during POLARIS in 1997. Data from 0 to 200 ppmv H<sub>2</sub>O from all flights are included in this calculation, with the mean shown for each deployment: April/May (squares), June/July (stars), and September (triangles). The standard deviation ( $1\sigma$ ) is denoted by the horizontal lines. Percentage difference is calculated by taking (JPL-Harvard)/average.

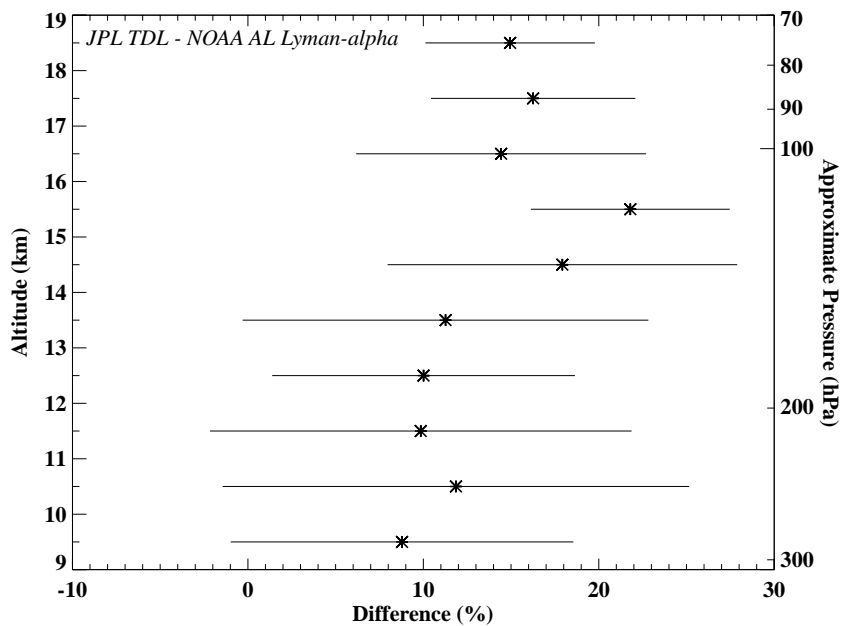


Figure 2.6 Percent difference between the JPL TDL and NOAA-AL Lyman- $\alpha$  hygrometers. Two comparison flights were included in this calculation. Data from both flights were put into 1-km bins, the mean is shown by the symbol, and the standard deviation ( $1\sigma$ ) denoted by the horizontal lines. Percentage difference is calculated by taking (JPL-AL)/average. Data was binned in altitude space, but plotted in pressure space for easier comparison with Figure 2.5.

### 2.2.2 Laboratory intercomparison of the NOAA-CMDL, NOAA-AL, and Harvard *in situ* instruments

Because atmospheric comparisons between the NOAA-CMDL frostpoint hygrometer and the NOAA-AL and Harvard Lyman- $\alpha$  instruments (discussed in section 2.2.1) showed systematic differences with the frostpoint smaller, several laboratory intercomparisons were conducted to study this problem under controlled conditions. The goal of the laboratory intercomparisons was to investigate potential systematic differences between instruments in a controlled environment that attempted to duplicate atmospheric conditions. These laboratory measurements covered a wide range of parameters, with the hope of identifying the source of the disagreement. The set-up relied on simultaneous measurements of the same air source, rather than an independent mixing ratio standard, which may itself not be reliable. This allowed a limited systematic investigation of the behaviour of each instrument under varying conditions. These experiments tested whether the disagreement between the instruments depends on water vapour mixing ratio, pressure, and temperature, on CO<sub>2</sub> and methane concentrations, on flow rate, and on several instrument parameters.

The three instruments are described in detail in Chapter 1. All three instruments operate under different temperature conditions during flight and use different calibration procedures. The NOAA-AL Lyman- $\alpha$  hygrometer is a temperature-controlled instrument, including heated intake lines. The instrument performs calibration cycles at regular intervals during flight. A modified version of the NOAA-CMDL frostpoint hygrometer balloon instrument was built to operate in a laboratory configuration. It was calibrated and operated at ambient temperatures as described in Chapter 1, however, for practical reasons, a different cryogen (liquid nitrogen) was used. The Harvard Lyman- $\alpha$  hygrometer operates at slightly above ambient temperature in flight with calibrations performed in the laboratory before and after atmospheric measurements. Attempts were made in the laboratory, but with varying degrees of success, to bring air into the instruments in a way similar to flight operation. Accordingly, this provides a potential source of uncertainty when comparing flight and laboratory operation for all three instruments.

While the two Lyman- $\alpha$  hygrometers measure mixing ratio directly, the frostpoint hygrometer measures the frostpoint temperature, which has to be converted to mixing ratio using a form of the Clausius-Clapeyron equation as well as an independent pressure measurement. The Goff-Gratch formula [List, 1949], which agrees to within 2% with the most recent direct measurements by Marti and Mauersberger [1993], was used to convert frostpoint temperature to water vapour partial pressure. The pressure measurements were accurate to within 1%, and thus the error introduced by the conversion of frostpoint temperature to mixing ratio is less than 3%.

On several occasions, test runs were influenced by contamination from the outgassing of lines in the flow system. However, this was always due to extremely low flow rates or insufficient settling times after closing the flow system or after sudden changes in mixing ratio. These runs did not give any indication that contamination could be a source of the disagreement in atmospheric measurements. No experimental run reproduced the disagreement between any of the three instruments and all measurements agreed to well within the instrumental uncertainties. A summary of these runs is shown in Figure 2.7.

The laboratory comparisons did not reveal the cause of the systematic difference between the three instruments in atmospheric comparisons. Under the controlled conditions of the laboratory, all instruments agreed to within the instrumental uncertainty. The average difference between the NOAA-CMDL frostpoint hygrometer and the NOAA-AL Lyman- $\alpha$  hygrometer was  $3.3 \pm 5\%$  ( $1\sigma$ ), while the difference between the frostpoint hygrometer and the Harvard Lyman- $\alpha$  was  $4.4 \pm 5.0\%$  (frostpoint smaller). This is based on mixing ratios greater than

5 ppmv. At lower mixing ratios, the laboratory configuration and difficulty in controlling the dry air source led to much greater scatter in the differences as can be seen in Fig 2.7. The 15% difference between the NOAA-CMDL frostpoint and the NOAA-AL Lyman- $\alpha$  hygrometer, as well as the 15% difference between the NOAA-AL and the Harvard Lyman- $\alpha$  hygrometer in atmospheric measurements could not be reproduced in laboratory measurements. Tests between the NOAA-CMDL frostpoint and the NOAA-AL Lyman- $\alpha$  hygrometer were run to determine whether differences depend on temperature, pressure, mixing ratio, or other trace gases. No such dependence was found. Tests were run to determine whether the agreement found in the laboratory could have been caused by the differences in the set-up compared to atmospheric measurements. None of the instruments appeared to have inherent biases and seemed to be capable of measuring low water vapour concentrations accurately under controlled laboratory conditions. The differences in atmospheric measurements remain unexplained, but are most likely connected to the installation on the respective platform. Outgassing is of concern, but no indication of such a problem connected to the installation on the respective platforms was found. This disagreement still needs to be resolved to allow accurate and reliable measurements of water vapour in the stratosphere.

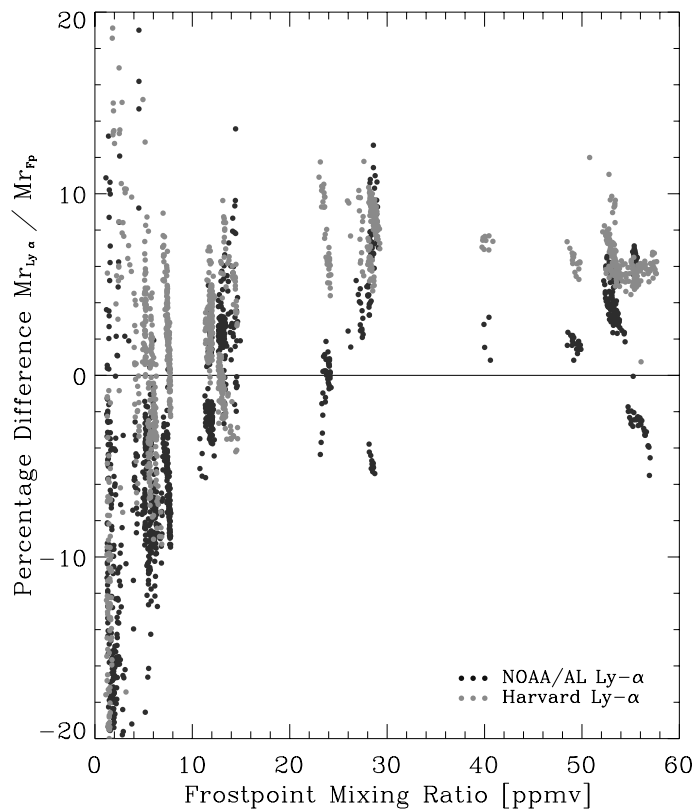


Figure 2.7 The percentage difference in water vapour mixing ratio measured by the NOAA-AL Lyman- $\alpha$  hygrometer and the Harvard Lyman- $\alpha$  hygrometer as a function of the water vapour mixing ratio measured by the NOAA-CMDL frostpoint hygrometer.

### 2.2.3 Balloon infrared instrument comparisons

#### MIPAS intercomparisons

Balloon-borne profile measurements of water vapour using the MIPAS payload and the LMD frostpoint hygrometer have been made within 48 hours of each other (11 February 1995 and 13 February 1995) at 68°N [Stowasser *et al.*, 1999]. Figure 2.8 shows the retrieved profile measurements of both instruments. At nearly all stratospheric altitudes, the difference is less than 0.2 ppmv, except at 80 hPa where the LMD frostpoint instrument encountered a laminae of dry air that was probably not present during the MIPAS balloon flight two days before.

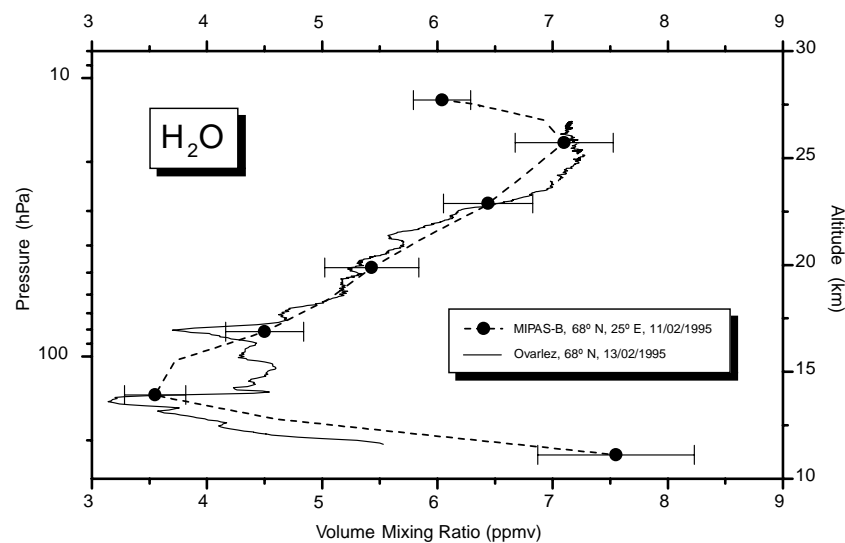


Figure 2.8 H<sub>2</sub>O profiles retrieved from two MIPAS-B flights inside the Arctic vortex in 1995 and 1997. The 1995 profile is compared to an *in situ* measurement obtained two days later at the same location [Ovarlez and Ovarlez, 1996]. Errors bars denote the 1 $\sigma$  confidence limit and include random noise, mutual influence of fitted parameters, temperature and pointing uncertainties, and onion-peeling error propagation, but not errors in spectroscopic data. Figure adopted from Stowasser *et al.* [1999].

In 1997, several balloon-borne measurements using different techniques were made for validation of the ADEOS-ILAS satellite programme. Even though further improvements of the retrieval of ILAS water vapour are under development, the currently available data can be used as an independent reference measurement (see section 2.3.5). A MIPAS balloon instrument measurement was taken on 24 March 1997 at 68°N, approximately 560 km from an ILAS overpass. Between 16-20 km, both water vapour profiles agree within 0.2 ppmv. At higher altitudes, ILAS data are larger than MIPAS. For example, the difference at 25 km is approximately 0.5 ppmv. Similar qualitative and quantitative results were observed on 11 February 1997 using the Jülich Lyman- $\alpha$  hygrometer (FISH) measuring at a distance approximately 140 km from an ILAS overpass. Using ILAS as a transfer standard, indirect evidence is provided that MIPAS and FISH measurements do not differ by more than 0.3 ppmv in the lower and middle stratosphere.

From the MIPAS measurements, a mean mixing ratio of  $2\times\text{CH}_4+\text{H}_2\text{O}$  was determined to be  $7.25\pm 0.2$  ppmv (11 February 1995) and  $7.28\pm 0.1$  ppmv (24 March 1997) [Stowasser *et al.*, 1999]. These values are within 0.3 ppmv of those determined for FISH and the LMD frostpoint (see section 2.2.1). Since no obvious discrepancies for the CH<sub>4</sub> techniques greater than

0.1 ppmv have been observed [Stowasser *et al.*, 1999], differences in the sum  $2\times\text{CH}_4+\text{H}_2\text{O}$  largely reveal differences in the water vapour measurements. Therefore, it appears that the LMD frostpoint, FISH, and MIPAS, all based on independent techniques, give results within 0.2-0.3 ppmv.

### MkIV and aircraft comparisons

The JPL MkIV interferometer flew from Fairbanks, Alaska in May 1997 during the Photochemistry of Ozone Loss in the Arctic Region in Summer (POLARIS) campaign. MkIV is a balloon-borne FTIR spectrometer operated in solar occultation mode. The instrument is described more fully in Chapter 1. Several ER-2 flights took place within a few days of the MkIV balloon flight. Two instruments on the ER-2 measured water vapour during POLARIS, the JPL TDL hygrometer and the Harvard Lyman- $\alpha$  hygrometer. Only those data acquired within approximately 500 km of the balloon observations, which were well outside the polar vortex in a region of uniform potential vorticity were considered for the comparison presented in Figure 2.9. Data is compared as a function of  $\text{CH}_4$  (from both the MkIV and ALIAS instruments) to minimise variations due to differences in airmass origin. Additionally, the MkIV  $\text{CH}_4$  was scaled by 0.975 to eliminate a bias reported by Toon *et al.* [1999]. Data points having a potential temperature less than 375 K were excluded from this comparison, to avoid any tropospheric airmasses, where spatial gradients are known to be greater. Although these results show significant variability from flight to flight (which may well be real), in general the aircraft *in situ*  $\text{H}_2\text{O}$  measurements are 0 to 20% larger than those measured remotely by MkIV, with the bias largest near the tropopause.

### FIRS-2 and aircraft comparisons

The FIRS-2 spectrometer flew from Fairbanks, Alaska, on 30 April 1997 as part of the Alaska Balloon Campaign in support of the ADEOS satellite. The balloon campaign overlapped in time with the POLARIS campaign, and the NASA ER-2 was flying near Fairbanks when FIRS-2 was launched. FIRS-2 measurements were obtained  $6^\circ\text{N}$  of the aircraft flight track, but within the longitude range covered by the ER-2, providing an opportunity for intercomparison. The balloon profiles were obtained well outside the vortex, and back trajectory calculations show that the flow was out of the south at all altitudes sampled by the ER-2, so that mixing ratio gradients were small between the ER-2 flight track and FIRS-2 measurement locations. In addition, ILAS measurements made at the same latitude as the ER-2 measurements are consistent with FIRS-2 measurements (section 2.3.5.), again suggesting that local gradients were small.

The ER-2 flight on 30 April consisted of the climb out of Fairbanks, 5.5 hours of level flight between the 490 K and 510 K potential temperature surfaces, and the descent back into Fairbanks. Roughly half the flight took place before sunrise. The aircraft payload included both the JPL TDL and Harvard Lyman- $\alpha$  water vapour instruments, as well as the ALIAS instrument from JPL. ALIAS provided measurements of  $\text{N}_2\text{O}$ , among other species.

Because a remote sensing balloon instrument provides measurements at a limited spatial resolution, it will underestimate the amplitude of small-scale variability in a heterogeneous airmass at a given altitude, unlike the aircraft *in situ* measurements. It is possible to compensate for some of the variability mismatch by comparing correlations with a long-lived tracer like  $\text{N}_2\text{O}$ , but only if the relationship is independent of airmass origin. This is not the case for the correlation between  $\text{H}_2\text{O}$  and  $\text{N}_2\text{O}$ . In the tropics, the annual cycle causes the correlation to depend on altitude and season at all altitudes accessible to the ER-2. Outside the tropics, the difference between vortex and middle latitude correlations relating  $\text{CH}_4$  and  $\text{N}_2\text{O}$  [Michelsen *et al.*, 1998] causes a complementary dependence in the relationship between  $\text{H}_2\text{O}$  and  $\text{N}_2\text{O}$ .

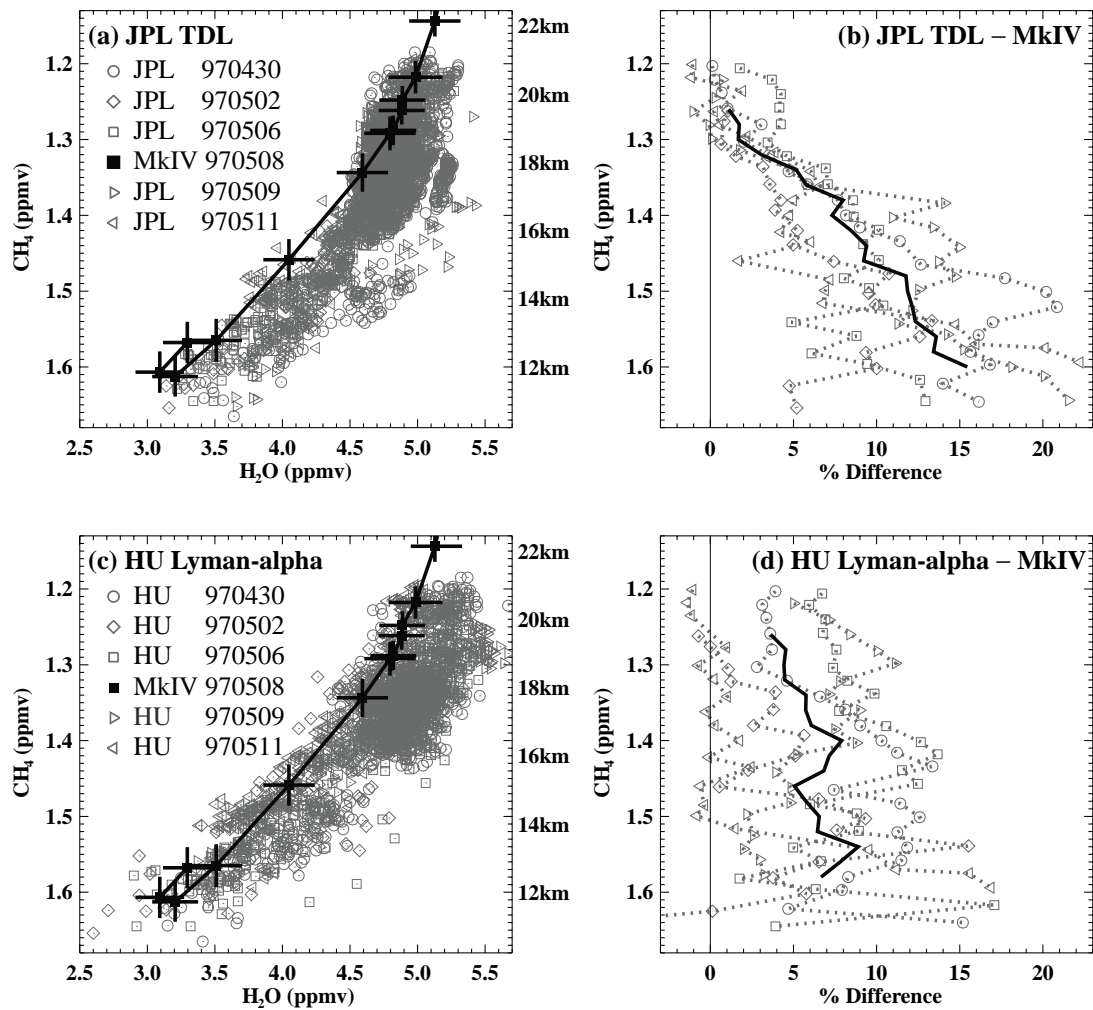


Figure 2.9 Comparison of  $\text{H}_2\text{O}$  profiles measured by MkIV with those measured by two *in situ* instruments on board the NASA ER2 above Fairbanks, Alaska in May 1997. The profiles are plotted as a function of  $\text{CH}_4$ . Approximate altitude is also given. The top panels are comparisons with the JPL TDL hygrometer, the bottom panels with the Harvard Lyman- $\alpha$  hygrometer. The left-hand panels show the measurement, black squares in the left hand panels are from the JPL MkIV interferometer, the other points are the *in situ* aircraft measurements. The right panels show percent average biases between the MkIV measurements and 5 aircraft flights, the grand average bias is given by the black solid line.

However, similar airmasses have been identified by binning the data by both potential temperature and  $\text{N}_2\text{O}$  mixing ratio. The ascent and descent data are binned separately by potential temperature and compared with FIRS-2 profiles for  $\text{H}_2\text{O}$  in the top panels of Figure 2.10. The nighttime and daytime cruise data are binned separately by  $\text{N}_2\text{O}$  and compared in the middle panels of Figure 2.10 with the  $\text{H}_2\text{O}$ - $\text{N}_2\text{O}$  relationship observed by FIRS-2. As shown in the bottom panel of Figure 2.10, cruise data obtained at  $\text{N}_2\text{O}$  mixing ratios between 200 and 215 ppbv are most similar (on the basis of potential temperature and  $\text{N}_2\text{O}$  mixing ratio) to the airmasses observed by FIRS-2.

The  $\text{H}_2\text{O}$  mixing ratio retrieved by both *in situ* instruments is systematically smaller after sunrise, with the JPL TDL measurements showing a larger change. Above 450 K the average water vapour mixing ratio measured by FIRS-2 is less than the Harvard and JPL descent measurements by 6.5% and 2.4%, respectively (top panels of Figure 2.10), while the FIRS-2

measurements at an  $\text{N}_2\text{O}$  mixing ratio of 205 ppbv are less than the Harvard and JPL daylight cruise measurements by 6.5% and 4.0%, respectively (middle panels of Figure 2.10). Air masses at cruise altitude having  $\text{N}_2\text{O}$  mixing ratios substantially different from 205 ppbv have a different origin than the air observed by FIRS-2 and will have a different water vapour mixing ratio for the reasons listed above.

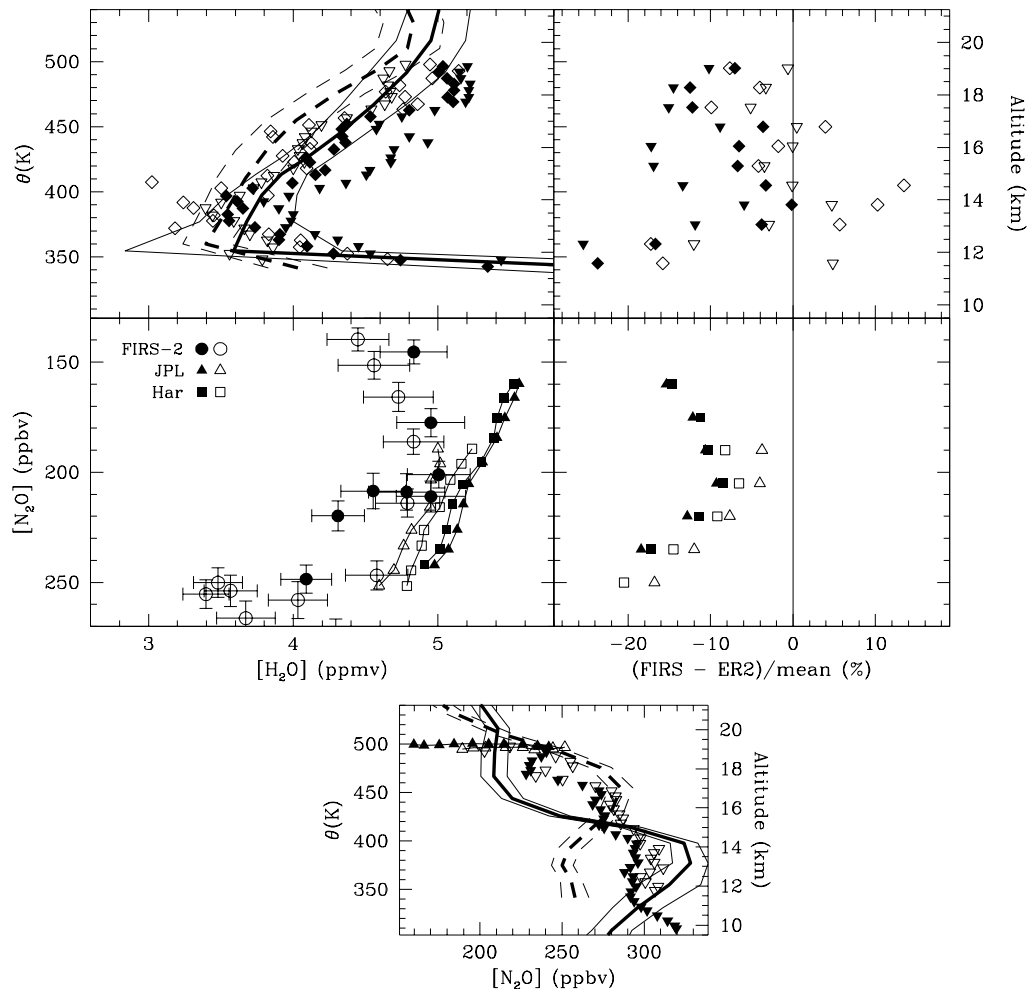


Figure 2.10 Comparison of vertical profiles obtained by the balloon-borne FIRS-2 and *in situ* instruments on board the NASA ER-2 during flights on 30 April 1997 near Fairbanks, Alaska. Shown in the top left panel are FIRS-2 profiles obtained 250 km North (dashed curve) and Northwest (solid curve) of the ER-2 flight track, as well as *in situ* measurements of  $\text{H}_2\text{O}$  made during ascent (solid symbols) and descent (open symbols). Harvard data are shown as diamonds and JPL as inverted triangles. Average differences between FIRS-2 and *in situ* measurements of  $\text{H}_2\text{O}$  during ascent and descent are shown in the top right panel. Also shown in the middle left panel is a comparison of  $\text{H}_2\text{O}/\text{N}_2\text{O}$  correlations for FIRS-2 measurements obtained 250 km North (open circles) and Northwest (solid circles) of the ER-2 flight track with JPL TDL (triangles) and Harvard Lyman- $\alpha$  (squares) measurements made during cruise before (solid symbols) and after sunrise (open symbols). Differences between average FIRS-2 and *in situ* cruise measurements of  $\text{H}_2\text{O}$  are shown in the middle right panel. Also shown is a comparison of FIRS-2 profiles and ALIAS measurements of  $\text{N}_2\text{O}$  obtained during cruise (triangles), ascent, and descent (inverted triangles, bottom panel).

Comparison of profiles below 450 K is complicated by the large gradients in  $\text{H}_2\text{O}$  caused by propagation of the annual cycle out of the tropics and the difference in horizontal and vertical resolution of the remote sensing and *in situ* instruments, particularly near the tropopause. Under conditions near 17 km where the comparison is likely to be best, the Harvard and JPL instruments give mixing ratios about 8% larger than FIRS-2.

### FIRS-2 and MkIV comparisons

The FIRS-2 and MkIV spectrometers made simultaneous measurements during a balloon flight launched from Ft. Sumner, New Mexico, on 22 May 1994. The gondola was configured to allow FIRS-2 and MkIV to observe  $90^\circ$  apart in azimuth so that FIRS-2 could observe atmospheric thermal emission while MkIV observed the solar absorption spectrum. Early in the flight the gondola was oriented so that FIRS-2 would observe in the same azimuth heading in which MkIV would observe the sunset 7.5 hours later. The stratospheric winds were light during the flight (the balloon drifted less than 50 km between launch and sunset) and so that FIRS-2 and MkIV observed nearly the same airmass. Vertical mixing ratio profiles from this flight are compared in Figure 2.11. Differences between the profiles are generally less than the combined uncertainty of 7%.

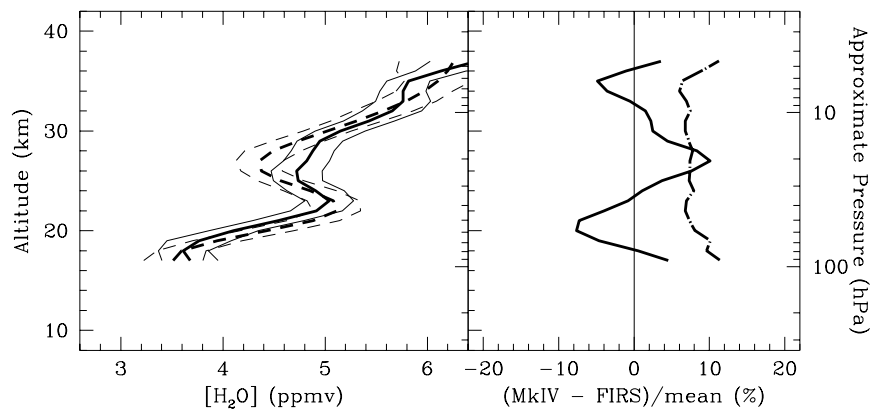


Figure 2.11 Comparison between FIRS-2 (dashed curve) and MkIV (solid curve) profiles obtained during a simultaneous balloon flight on 22-23 May 1994. Individual profiles were derived from observations made 7.5 hours apart in the same azimuth heading (left panel). The difference between the two profiles (solid curve) and combined precision (dot-dash curve) is also shown in the right panel.

## 2.2.4 Tropospheric measurements

### Comparison of Vaisala RS80-A radiosondes and the NOAA-CMDL frostpoint hygrometer

Radiosonde relative humidity (RH) measurements are widely known to be unreliable at cold temperatures. A recent study by *Miloshevich et al.* [2000] characterised RH measurements from Vaisala RS80-A radiosondes, the most frequently used radiosonde in the world, and developed a correction for the measurements in the temperature range  $0^\circ\text{C}$  to  $-70^\circ\text{C}$ . A data set of simultaneous RH measurements from RS80-A radiosondes and the NOAA-CMDL frostpoint hygrometer (described by *Vömel et al.* [1995]) was used to derive a statistical correction factor for RS80-A measurements based on the hygrometer measurements. These were operational measurements rather than a controlled intercomparison. The frostpoint hygrometer provides an

*in situ* measurement standard using a technique independent of the operational radiosonde methodology. The calibration uncertainty of the hygrometer is not temperature dependent, and its response time at cold temperatures is relatively fast. The ratio of each RS80-A and corresponding hygrometer measurement is shown in Figure 2.12 with curves that indicate the mean and standard deviation of the ratio in each 1°C temperature bin. Relative to the hygrometer, the mean RS80-A measurements decrease with decreasing temperature to about 40% of the value of the corresponding hygrometer measurements at  $-70^{\circ}\text{C}$ . The RS80-A data are clearly unsuitable for upper tropospheric research studies unless the measurement errors are corrected.

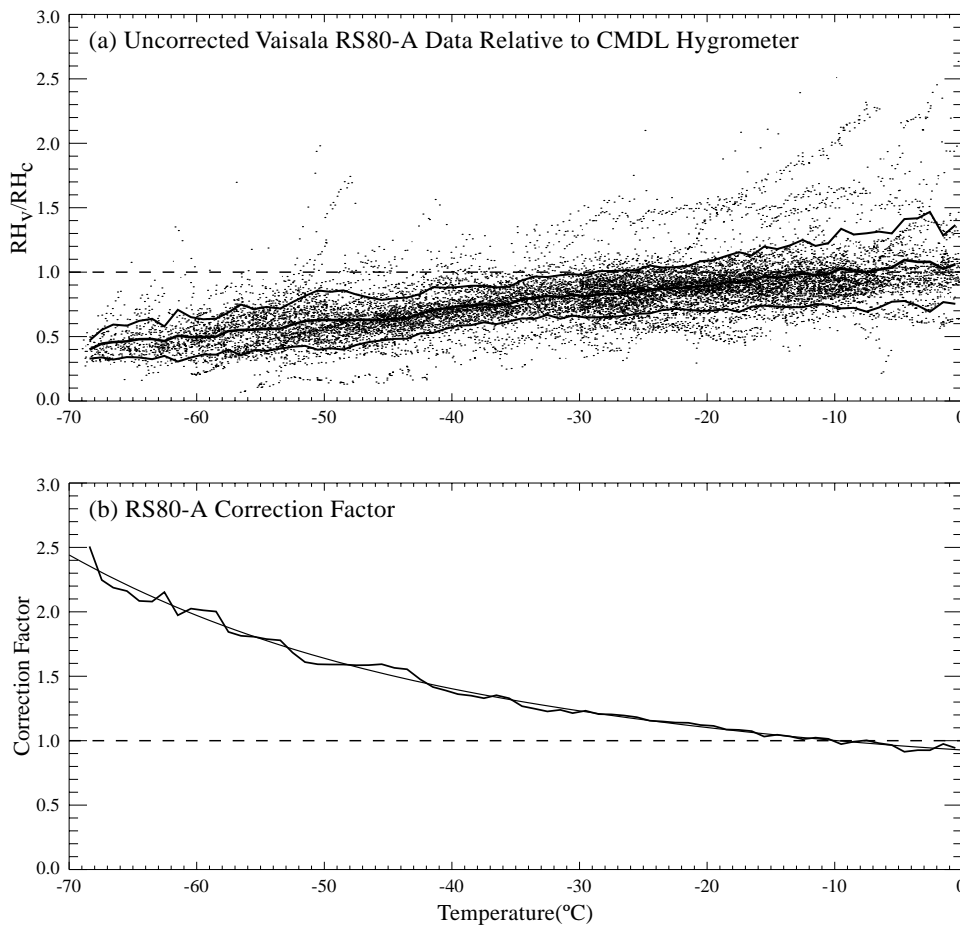


Figure 2.12. (a) Ratio of simultaneous relative humidity measurements from Vaisala RS80-A radiosondes ( $\text{RH}_V$ ) and the NOAA-CMDL frostpoint hygrometer ( $\text{RH}_C$ ), from eight years of monthly launches at Boulder, Colorado. Curves are the mean and standard deviation ( $1\sigma$ ) of the ratio in  $1^{\circ}\text{C}$  temperature bins. (b) A statistical correction factor for RS80-A measurements is given by the reciprocal of the mean ratio shown in Panel (a), approximated by the polynomial curve fit shown.

The reciprocal of the mean ratio in Figure 2.12 is the normalisation factor that, when multiplied by RS80-A data, gives corrected RH values that are on average equal to the hygrometer data. This statistical correction factor (curve fit shown in Figure 2.12) accounts for the mean of all sources of RS80-A measurement error combined, as a function of temperature. The magnitude of the correction factor is about 1.1 at  $-20^{\circ}\text{C}$ , 1.3 at  $-35^{\circ}\text{C}$ , 1.6 at  $-50^{\circ}\text{C}$ , 2.0 at  $-60^{\circ}\text{C}$ , and 2.4 at  $-70^{\circ}\text{C}$ . (The curve fit is not valid outside the temperature range  $0^{\circ}\text{C}$  to  $-70^{\circ}\text{C}$ ). The fractional

---

uncertainty in the mean of the corrected RS80-A data, when the correction factor is applied statistically to a large data set (such as when constructing a climatology), is estimated to be 0.06 at 0°C and 0.11 at -70°C, which is about 6% RH at ice-saturation at all temperatures. However, the uncertainty when the correction factor is applied to any individual profile is considerably larger, as indicated by the dispersion of the data around the mean in Figure 2.12. This dispersion results from RS80-A measurement errors that are not simply temperature-dependent, but are also sensor-specific or profile-specific. Only the mean value of these errors at a given temperature is considered by this statistical approach.

The RS80-A is subject to several sources of measurement error, and correction of the individual measurement errors is an alternative approach for correcting RS80-A data that is under development. A "temperature-dependence error" is caused by using a linear approximation in the data processing algorithm to represent the actual non-linear temperature dependence of the sensor calibration, and is in general the largest RS80-A measurement error at cold temperatures. The temperature-dependence error depends only on temperature, so it is completely accounted for in the statistical correction. A correction factor for temperature-dependence error has been derived from laboratory measurements conducted at Vaisala. The magnitude of the correction factor is about 1.1 at -35°C, 1.4 at -50°C, 1.8 at -60°C, and 2.5 at -70°C. A "time-lag error" is caused by the exponential increase in the sensor time-constant with decreasing temperature. The time-lag error depends strongly on the rate of change of the ambient RH, so only its average effect at a given temperature is represented in the statistical correction. Simulations show that maximum time-lag errors for conditions when the ambient RH is changing rapidly with altitude are about 5% RH (positive or negative) at -20°C, 15% RH at -40°C, and 30% RH at -60°C; typical time lag errors are considerably less. A correction algorithm for time-lag error is in progress. Chemical contamination of the sensor polymer by non-water molecules, and long-term sensor instability, both lead to dry-bias errors that depend in part on the age of the radiosonde. The magnitude of the combined dry-bias errors is typically 2-6% RH. A moist-bias error of a few percent RH may result from sensor drift under sustained conditions of high ambient RH. Random uncertainty caused by the combination of production variability and uncertainty in the calibration model and the calibration chamber is 4% RH at the 95% confidence level. The RS80-A, like any (unheated) solid-state sensor, is incapable of measuring ice-supersaturation.

It is critical that these corrections be applied only to Vaisala RS80-A data, not to radiosonde RH data in general, and specifically not to Vaisala RS80-H data. The RS80-A and RS80-H both use the *Humicap* thin-film capacitive sensors, and they differ primarily in the chemical composition and properties of the sensor dielectric material, and in the accuracy of the algorithm for sensor temperature dependence used in the data processing. Although both sensor types are subject to the same general sources of measurement error, the magnitude of each error is highly dependent on the sensor type. This difference is illustrated by the simultaneous RS80-A and RS80-H measurements shown in Figure 2.13. At temperatures colder than -40°C the radiosonde was in a thick orographic cloud where the RH is expected to be near ice-saturation based on independent cloud particle measurements. Most of the difference between the two profiles is due to the difference in their temperature-dependence errors, since the time-lag errors would be minimal after the sensors had been in the cloud at nearly constant RH for 1-2 minutes. It is apparent that the temperature-dependence algorithm for the RS80-H is considerably more accurate than the algorithm for the RS80-A.

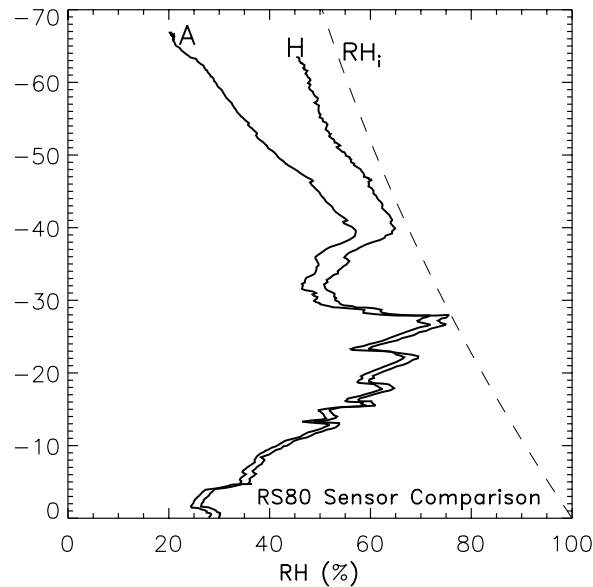


Figure 2.13 Profiles of relative humidity measured simultaneously by Vaisala RS80-A and RS80-H radiosondes. Dashed curve is ice-saturation ( $RH_i$ ).

In conclusion, comparison of relative humidity measurements from Vaisala RS80-A radiosondes using the NOAA-CMDL frostpoint hygrometer as an *in situ* measurement standard demonstrates that uncorrected RS80-A data are not suitable for upper tropospheric research applications. Correction for well-understood measurement errors substantially improves the accuracy of RS80-A measurements at cold temperatures, probably into the realm of usefulness in the upper troposphere. Further improvement is possible and in progress.

#### LMD cryogenic frostpoint and LaRC/ARC DLH comparison

An in-flight intercomparison between the aircraft borne LMD cryogenic frostpoint hygrometer and the NASA-LaRC/ARC Diode Laser Hygrometer (DLH) was conducted during the coordinated phases of the Pollution from Aircraft Emissions in the North Atlantic Flight Corridor 2 (POLINAT2) European campaign and the Subsonic Assessment Ozone and NO<sub>x</sub> Experiment (SONEX) U.S. campaign in October 1998. The LMD frostpoint and DLH were flown aboard the DLR Falcon and NASA DC-8 research aircraft, respectively. Good spatial and temporal overlap between both aircraft during two co-ordinated flights provided an excellent opportunity for the intercomparison, which occurred in the upper troposphere between approximately 7 and 10 kilometres.

From the data obtained it has been shown [Vay *et al.*, 2000] that both instruments agreed within 10% over the range of mixing ratios 82 to 900 ppmv. In general, the DLH reported greater water vapour mixing ratios than the frostpoint hygrometer except at the smaller mixing ratios where the best agreement was noted. This may be explained in part by an offset caused by the presence of residual water vapour within the laser head of the DLH discovered during post-mission calibrations. Figure 2.14 is a comparison of the LMD frostpoint and the DLH data for one of the flights. Here the data from both instruments are averaged to 15 seconds to take into account the difference in time response of the DLH (50 ms) and the LMD frostpoint (10 s).

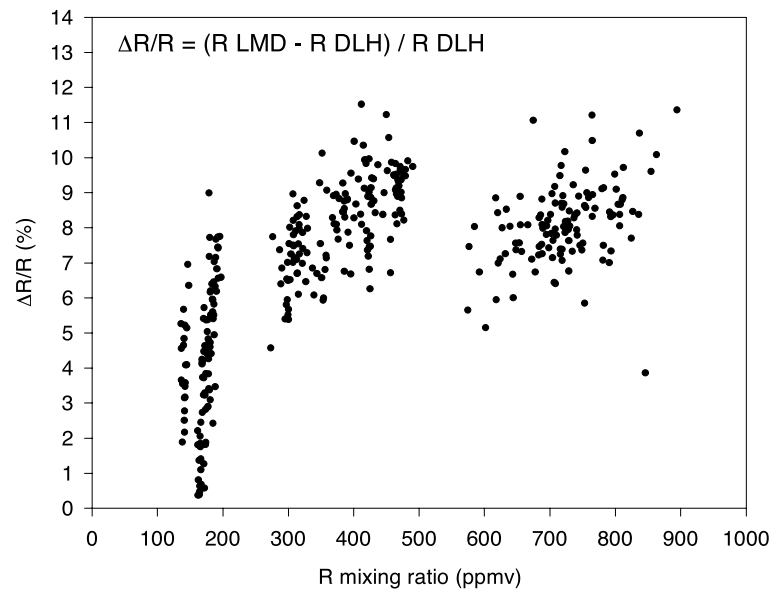


Figure 2.14 Intercomparison between the LMD cryogenic frostpoint hygrometer and the LaRC Diode Laser Hygrometer for the wing tip to wing tip flight on 23 October 1997. Three different altitude legs were sampled at 7.6, 8.9, and 10 km respectively.

### In-flight comparison of the MOZAIC humidity device with Lyman- $\alpha$ and LMD frostpoint hygrometer

In Chapter 1 the in-flight uncertainty of the MOZAIC humidity sensing devices (AD-FS2) employed on board five A340 in-service aircraft has been evaluated. From the regular pre- and post flight calibration of each flown sensor, typical  $2\sigma$  uncertainties of  $\pm 5$ -10% in relative humidity between 10 and 12 km altitude were derived [Helten *et al.*, 1998]. During two dedicated missions with a Fanjet Falcon E research aircraft of the Deutsches Zentrum für Luft- und Raumfahrt (DLR), the in-flight performance of the MOZAIC humidity device was assessed by intercomparison with reference instrumentation.

#### *In-flight comparison, March 1995: Time response and spatial resolution*

The first in-flight comparison of the MOZAIC humidity-sensing device against reference instrumentation was conducted in March 1995 with the MOZAIC device mounted aboard the Falcon aircraft [Helten *et al.*, 1998]. As reference instruments for the water vapour concentration measurement, two different types of airborne hygrometers were used: the Jülich Lyman- $\alpha$  fluorescence hygrometer, FISH, with a relative humidity accuracy of  $\pm 5\%$  [Zöger *et al.*, 1999a], and a DLR cryogenic frostpoint hygrometer, with a relative humidity accuracy of  $\pm 10\%$  [Busen and Buck, 1995]. During two comparison flights which took place over Germany, the FISH Lyman- $\alpha$  and the frostpoint hygrometers agreed within their combined uncertainties [Zöger *et al.*, 1999a]. In the middle and upper troposphere, the MOZAIC humidity device agreed to within  $\pm 10\%$  RH ( $2\sigma$ -uncertainty level) with the two reference instruments, if averaged over more than one minute. A dry bias of about 10% is indicated for the MOZAIC device. The MOZAIC sensor smoothes the structure in the water vapour that is measured with the reference instruments. This is caused by the response time of the MOZAIC device that increases with decreasing sensor temperature due to the adsorption and diffusion of water molecules into the sensor material [Antikainen and Paukkunen, 1994]. At sensor temperatures of about  $-30^\circ\text{C}$  (the ambient air temperature is below  $-30^\circ\text{C}$ ) the response time is several minutes. At higher temperatures the MOZAIC instrument tracks fine structures in the humidity field within  $\pm 5$ -10% RH ( $2\sigma$ -uncertainty level).

Based on these comparisons, it was found that the response time of the MOZAIC sensor during ascent and descent is less than 10 seconds near the ground and less than one minute around 9-km altitude. This means that at an ascent/descent rate of the MOZAIC-aircraft of about 8 m/s, the vertical resolution of measured vertical humidity profiles is better than 100 m in the lower troposphere, and approximately 500m in the upper troposphere. At cruise altitude, the response time is about 1-3 minutes. At a horizontal aircraft speed of 250 m/s, the horizontal resolution is about 15-50 km, which is sufficient to record large-scale features in upper tropospheric water vapour.

*In-flight comparison, September 1997: MOZAIC versus POLINAT-2*

In September 1997, during the European POLINAT-2 (Pollution from Aircraft Emissions in the North Atlantic Flight Corridor) aircraft mission [Schumann *et al.*, 1998], an intercomparison of airborne *in situ* water vapour measurements was performed between water vapour sensors aboard the Airbus A340 (MOZAIC) and Falcon (POLINAT) aircraft [Helten *et al.*, 1999]. The POLINAT aircraft used the LMD frostpoint hygrometer developed for airborne water vapour mixing ratio measurements [Ovarlez and van Velthoven, 1997]. The intercomparison took place southwest of Ireland on 24 September 1997 at the 239 hPa flight level. The ambient air temperature ranged from  $-53$  to  $-55^{\circ}\text{C}$ . The Falcon approached the flight path of the Airbus at  $13^{\circ}\text{W}$  longitude and followed until  $7^{\circ}\text{W}$  longitude. The Falcon followed the Airbus at a distance of 7-35 km. This corresponds to a time lag increasing from 30s to 160s. The relative humidity measured on the POLINAT aircraft (thin curve) was shifted with respect to the MOZAIC measured relative humidity (thick curve) such that the POLINAT data are for the same longitude as the MOZAIC data (Figure 2.15). The shift was computed using the measured horizontal wind and assuming isobaric transport.

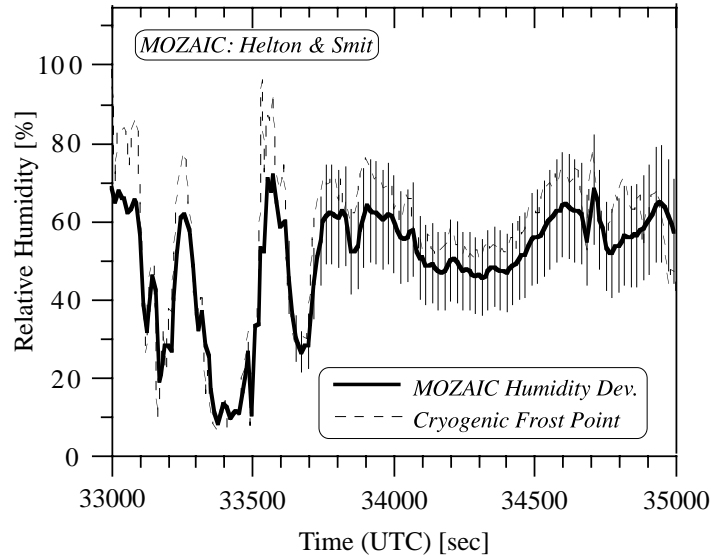


Figure 2.15 Relative humidity measured by the MOZAIC humidity device and the LMD frostpoint hygrometer as a function of flight time during the tropospheric segment of a comparison flight on board the DLR Falcon aircraft in March 1997. The thin vertical lines represent the  $\pm 2\sigma$  uncertainty levels derived from pre- and post flight calibration of the flown MOZAIC sensor.

The accuracy of the POLINAT water vapour measurements was better than  $\pm 3\%$  [Ovarlez and van Velthoven, 1997]. Figure 2.16 reveals agreement within  $\pm 5\%$  for segment C of the intercomparison where the trajectories of both aircraft were closest. Even mesoscale structures of the water vapour mixing ratio are reproduced. One exception is the strong decrease in water vapour concentration at  $8^\circ\text{W}$  longitude, where the values measured by MOZAIC decreased much faster. This occurred in a region with a strong relative humidity gradient, where the time delay between both measurements is a maximum ( $\sim 160\text{s}$ ). Additionally, the POLINAT measurement on its flight back at this position showed a strong change of the water vapour mixing ratio within a short period of time. Therefore, a change in the water vapour distribution could have contributed to the larger deviation. In segment B, where the Falcon flew into a contrail of the Airbus, frostpoint mixing ratios are significantly larger than the MOZAIC measurements. Local increases in mixing ratio of about 3 ppmv are to be expected in aircraft plumes of 100s age [Schumann et al., 1998]. The structures of both measurements in segment A are similar, but the POLINAT values are up to 14% greater than the MOZAIC measurement. This could be partly due to the horizontal water vapour gradient present, since the flight trajectories differ up to 5 km in latitude. The water vapour volume mixing ratio measurements in the range of 80 to 120 ppmv of both instruments differ by less than  $\pm 5\%$ , where the trajectories of both aircraft are very close. The corresponding relative humidity was changing between 50 and 75%. Relative humidity and mixing ratio from MOZAIC and LMD during POLINAT agreed to within 5% for mixing ratios above 80 ppmv. This indicates that the MOZAIC instrument measures upper tropospheric relative humidity and water vapour mixing ratio with an absolute overall accuracy similar to that of the LMD frostpoint hygrometer aircraft sensor.

The results of the two in-flight comparisons of the MOZAIC humidity device with reference instrumentation agree within the  $2\sigma$ -uncertainties of  $\pm 5\text{-}10\%$  derived from the individual pre- and post-flight calibration of each flown sensor. It appears that in the upper troposphere at a cruise altitude between 10 and 12 km the MOZAIC humidity device measures relative humidity with an in-flight  $2\sigma$ -uncertainty of  $\pm 5\text{-}10\%$ .

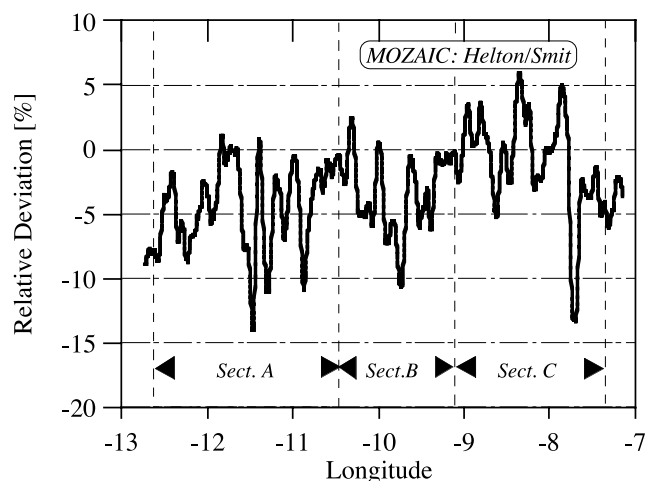


Figure 2.16 Relative differences (MOZAIC–LMD Hygrometer)/LMD Hygrometer in percent obtained during comparison flights between the MOZAIC device on the Airbus aircraft and the LMD frostpoint hygrometer on the DLR Falcon aircraft. Different segments of the flight as described in the text are noted with arrows. The MOZAIC measurement is shifted by 15 seconds opposite to the flight direction to correct for the slower response compared to the LMD frostpoint sensor on the Falcon aircraft.

---

### Comparison of airborne DIAL LIDAR (LASE) with other instruments

The Lidar Atmospheric Sensing Experiment, LASE, uses the DIAL method that provides direct detection of absorption due to water vapour and makes absolute measurements of water vapour profiles without the need for inversion methods. In principle, no field calibration is needed for the LASE measurements, which use the known spectroscopic characteristics of the water vapour absorption lines. Prior to the LASE measurements, very high-resolution laser spectroscopy was conducted for accurate characterisation of water vapour line parameters. The estimated combined error in the water vapour absorption cross-section is ~2-3% in the 720 and 820 nm regions [Grossmann and Browell, 1989a; Grossmann and Browell, 1989b; Ponsardin and Browell, 1997].

Because LASE operates locked to a water vapour line and no wavelength drifts are possible [Browell *et al.*, 1997], no in-flight calibrations of wavelength or linewidth are performed. However, regular checks are done on the ground to ensure proper operation of the LASE system. In addition, to assess the water vapour measurement capability of LASE, a comprehensive LASE Validation Field Experiment was conducted in September 1995 at the NASA Wallops Flight Facility. LASE measurements were intercompared with a number of *in situ* and remote sensors from the ground and other aircraft [Browell *et al.*, 1997]. These sensors included radiosondes, airborne dew point and frostpoint hygrometers, and remote LIDAR water vapour measurements from the ground and aircraft. An example of an intercomparison of water vapour profile measurements is given in Figure 2.17, illustrating the sensitivity and accuracy of the LASE measurements as shown in the agreement with other sensors. The Vaisala sondes appear to underestimate water vapour measurements compared to LASE in the upper-troposphere. This feature is consistent with the known dry bias of Vaisala sondes [Clough *et al.*, 1996]. For the entire field experiment, 39 profile comparisons were made when the time difference was less than 30 minutes. The mean of the average profile differences was less than 2% with standard deviations less than 10% [Browell *et al.*, 1997]. When small altitude shifts ( $\leq 120$  m, well within the uncertainty in the height determination from the radiosondes) are used to align prominent atmospheric features in the comparison profiles, then standard deviations decrease to 7%. In order to account for horizontal variability, comparisons were also performed with the *in situ* aircraft flying at several different constant altitudes. An average of the 65 comparisons showed a mean difference of 1.6% with a standard deviation of 6%. When compared with all the water vapour measurements acquired during this experiment, LASE water vapour measurements were found to have an accuracy of better than 6% or 0.01 g/kg whichever is larger, across the entire troposphere [Browell *et al.*, 1997].

LASE has been operated from the NASA ER-2, DC-8, and P-3 aircraft, and has participated in five major field experiments during 1995-1999 as discussed in Chapter 1. During each of these field experiments the LASE water vapour measurement accuracy has been verified by comparison with other remote and *in situ* water vapour sensors.

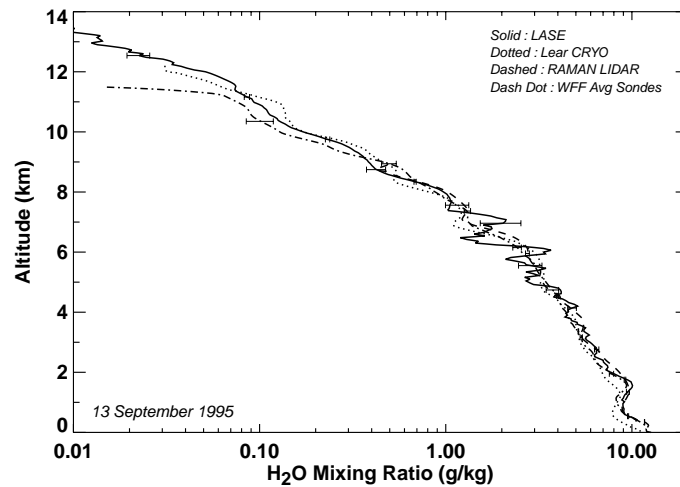


Figure 2.17 Comparison of LASE measurements with the Lear Jet cryogenic hygrometer, NASA Goddard Raman LIDAR, and Vaisala radiosonde measurements made near the Wallops Flight Facility on 12 September 1995.

### Raman LIDAR and H-Humicap sensor comparisons

The comparison of water vapour mixing ratio measured by the OHP LIDAR and radiosondes (H-Humicap, RS80) launched simultaneously at the same site reveals a dispersion of 2% and no significant bias (<1%) up to 9 km for 20 coincident measurements. Above 9 km, the water vapour density measured with the LIDAR exceeds radiosonde measurements by 2-5%. This is probably due to temperature dependence and hysteresis effects of the H-Humicap sensor. When the comparison is performed as a function of mixing ratio values, H-Humicap underestimates water vapour (2%) for densities larger than 0.001 g/g of dry air and overestimates water vapour (2-5%) for densities smaller than 0.0001 g/g of dry air. This effect leads to a discrepancy in the water vapour distribution observed with the two instruments mainly at the extremes of the distribution. It also appears that the H-Humicap sensor has a bias (5%) for temperatures lower than 220-230 K, corresponding to typical upper tropospheric conditions.

## 2.3 Comparisons made for the validation of satellite measurements

### 2.3.1. HALOE comparisons

#### ***In situ* measurements**

##### *Aircraft measurements*

In this subsection, intercomparisons are shown between HALOE profiles and *in situ* aircraft measurements of water vapour. Coincidences were required to occur within 2.5 days, 3 degrees of latitude, and 45 degrees of longitude. It can be argued that even these separations do not constitute coincidence, but choosing tighter criteria leads to fewer comparisons. Even though our comparisons with the aircraft data consist of only 5 profile pairs per set, the root-mean-square (RMS) differences for each set are not much larger than their mean differences. Thus, one can be confident that the individual profile pairs in each set are showing consistent differences. In Figures 2.18 to 2.24, the standard HALOE profiles are from its Version 19 (V19 or 3<sup>rd</sup> public release data set) and denoted with a solid curve, the correlative data are dotted, and recent updates to the HALOE retrieval are dashed. The right panels of each of these figures show the mean of the differences for the paired profiles (as opposed to the difference of the mean correlative and mean HALOE profiles of the left panels). RMS differences for the pairs are also shown in the right panels.

Sunrise (SR) and sunset (SS) HALOE comparisons were made with Harvard Lyman- $\alpha$  measurements [Weinstock *et al.*, 1994] from multiple ER-2 missions occurring from October 1995 through May 1997 and from 20°N to 66°N. Comparisons do not extend above the 50 hPa level, which is about the upper flight level of the ER-2 aircraft measurements. The *in situ* measurements have a reported accuracy of ~5%. Comparisons were made against both climb and descent measurements from the ER-2, but the results were not significantly different. Figure 2.18 shows results for a set of five SR pairs whose average longitude separation was 14 degrees. A systematic, nearly constant mean offset of 15% to 20% was found for the HALOE V19 SR (solid) versus descent profiles from the ER-2 (dotted) for the entire interval from 50 hPa to 150 hPa (HALOE smaller). Very similar results were found for the SS comparisons (not shown), although the percentage differences are larger below the 150 hPa level. The overall shapes of the average HALOE and average *in situ* profiles are also very similar. Although the profile comparisons were obtained at latitudes near 20°N, 30°N to 40°N, and near 65°N, there is no clear variation with latitude for the comparison differences. Figure 2.18 includes the averages for modified HALOE V19 retrievals (dashed) that use no constraint in the procedure for vertically interleaving each of the 7 separate retrievals of a given scan and also use an improved model [Thibault *et al.*, 1997] for the effects of the interfering pressure-induced O<sub>2</sub> continuum for the cold temperatures of the lower stratosphere. Biases are reduced and those updates indicate the nature of the uncertainties that affect the V19 profiles in the lower stratosphere. Such algorithm improvements will be included in the upcoming Version 20 processing.

Similar comparisons were performed against the NOAA Lyman- $\alpha$  measurements on the ER-2. Figure 2.19 shows an average of five comparisons for descending flight legs at northern middle latitudes from November 1992 through November 1994. Average longitude separation is 8 degrees. Differences in water vapour range from 5% at 60 hPa to 20% at 130 hPa with HALOE being smaller. While the unconstrained results are somewhat noisy, the average profile is essentially the same as the V19 profile above the 120 hPa level without the modification to

the  $O_2$  continuum. Below that level, the unconstrained results follow the aircraft data more closely than V19.

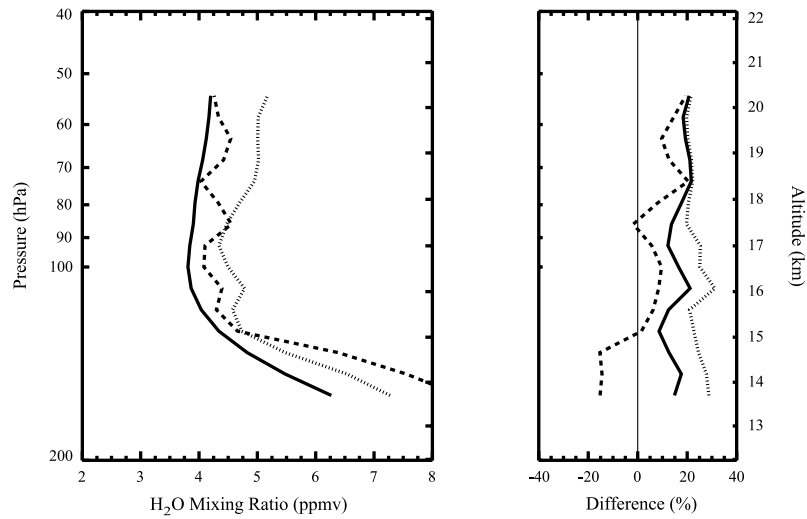


Figure 2.18 Average of 5 comparisons of HALOE SR/ER-2 Harvard Lyman- $\alpha$  profiles during aircraft descent, latitudes range from 20° to 64°N. (left) Solid curve is HALOE average, dotted curve is Lyman- $\alpha$ . (right) Solid curve is mean difference (Lyman- $\alpha$  minus HALOE); dotted curve is RMS difference. The dashed curves show the effect of eliminating constraints plus a better correction for the  $O_2$  continuum in the V19 retrieval in the mean difference (left) and its percentage difference (right).

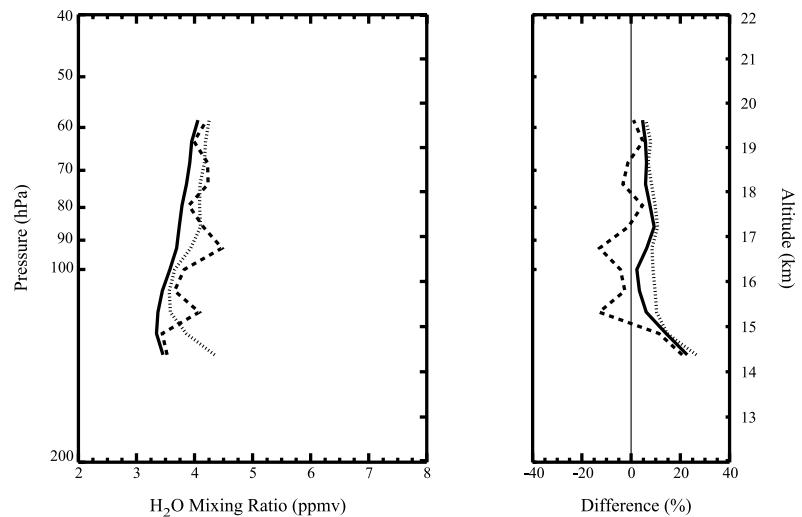


Figure 2.19 Average of 5 Northern Hemisphere comparisons of HALOE/ER-2 NOAA-AL Lyman- $\alpha$  profiles during aircraft descent, latitudes range from 34° to 39°N. (left) Solid curve is HALOE, dotted curve is Lyman- $\alpha$ . (right) Solid curve is mean difference (Lyman- $\alpha$  minus HALOE); dotted curve is the RMS difference. Dashed curves show the effects of removing the constraints plus a better correction for the  $O_2$  continuum in the HALOE retrieval.

Figure 2.20 shows five comparisons with NOAA-AL Lyman- $\alpha$  measurements at southern middle latitudes for April through October 1994. Average longitude separation is 12 degrees. Although the shapes of the differences with the NOAA-AL data are similar in both Figures 19

and 20, their percentage differences are larger in the Southern Hemisphere. These comparisons for the Southern Hemisphere occurred in 1994, when the aerosol extinction tended to be less than that for most of the northern middle latitude pairings. It is likely that when the interference from aerosol absorption is large, as it was in 1992/1993, the uncertainties in the correction are more important than the effects of the positive bias in the earlier O<sub>2</sub> continuum model being used for V19.

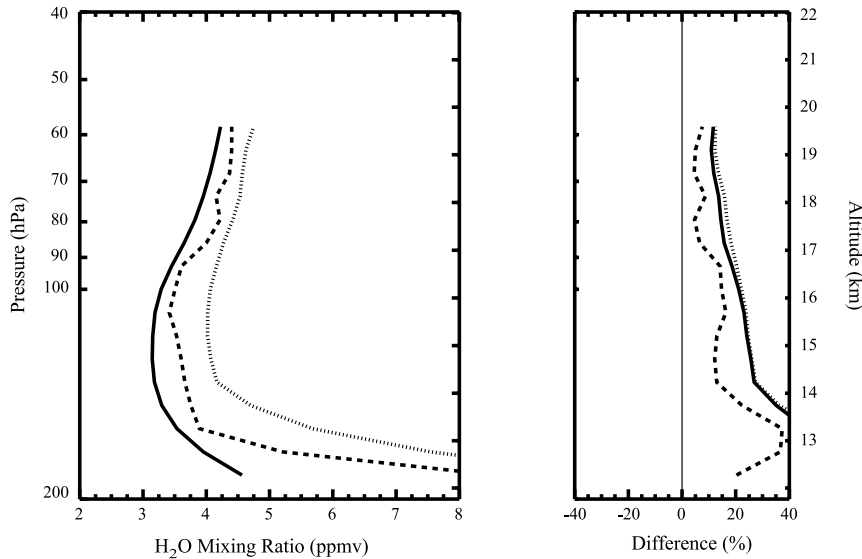


Figure 2.20 As in Figure 2.19, but for an average of 5 Southern Hemisphere comparisons, latitudes range from 41° to 47°S.

#### *Balloon frostpoint hygrometers*

A set of 14 SR profile-pair comparisons with NOAA-CMDL frostpoint hygrometer measurements near 40°N makes up the statistical average shown in Figure 2.21. All pairs are coincident to within 1 day, 3 degrees of latitude, and 17 degrees of longitude. Average longitude separation for the set is 8 degrees. Cloud signatures have been screened out of the HALOE profiles, but their effects do not have an impact above the 150 hPa level. The mean difference profile shows agreement between the frostpoint and HALOE SR measurements to within 5% from 15 hPa to 70 hPa. Systematic differences between the two measurements reach 15% (HALOE smaller) at 100 hPa and 20% at 125 hPa. Because of profile imprecision, lack of better coincidence, atmospheric variability, and different spatial averaging for the two measurement techniques, the RMS differences in Figure 2.21 are larger than the mean differences. Those differences reach 10% from 15 hPa to 60 hPa, increasing to 20% at 100 hPa. Both the mean and RMS differences are well within the combined HALOE V19 and frostpoint estimates of accuracy. The HALOE V19 error estimates are the same as those for V17 reported in *Harries et al.* [1996]. The balloon measurement has an accuracy of about 10%, based mainly on the uncertainty in the frostpoint temperature (see Chapter 1.1). When the retrieval constraint is removed, the dashed HALOE profile “turns the corner” more sharply at about 150 hPa, resulting in smaller differences with the balloon profile.

Eleven HALOE SS comparisons with NOAA-CMDL frostpoint soundings were obtained, and the average result in Figure 2.22 is similar to that for SR. Average longitude separation is 14 degrees and time difference is less than 1 day. Several HALOE profiles stopped abruptly near 150 hPa, but no cloud was indicated by our screening criteria. Although the HALOE cloud-screening algorithm [*Hervig and McHugh, 1999*] indicated a cloud in several other cases, each

comparison was still good at and below the cloud altitude indicated by the screening. This suggests that not all flagged cloud events are having a significant effect on the retrieved water vapour. Most of the SS profile pairs extend downward to the tropopause and agree to within the error bars for the two data sets. The small differences for both the SS and SR correlative comparison plots represent the primary improvement in the V19 retrievals of water vapour over earlier data versions.

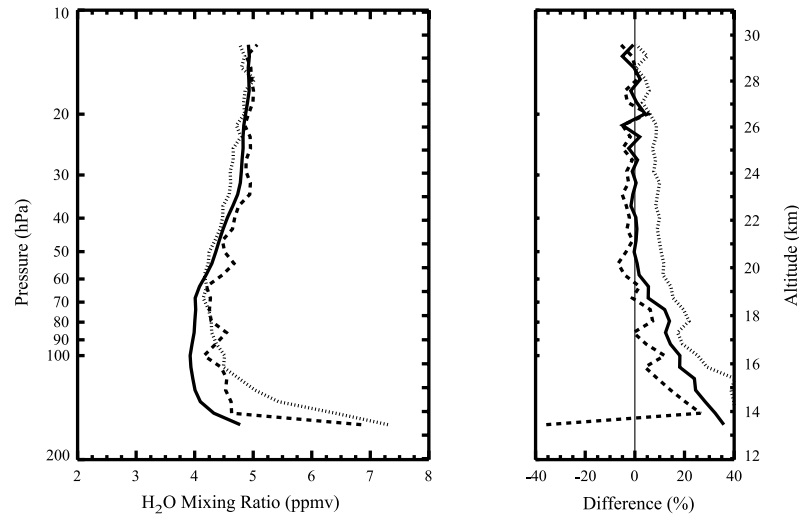


Figure 2.21 (Left) Averages of 14 HALOE V19 SR profiles (solid) and frostpoint balloon profiles (dotted) near  $40^{\circ}\text{N}$ . Dashed curve represents the average HALOE profile obtained by removing an interlevel retrieval constraint plus using a better correction for the  $\text{O}_2$  continuum. (Right) Average differences (frostpoint minus HALOE V19) for the paired profiles in the set (solid); RMS differences for that set (dotted). Dashed curve is the mean difference for the modified HALOE algorithm.

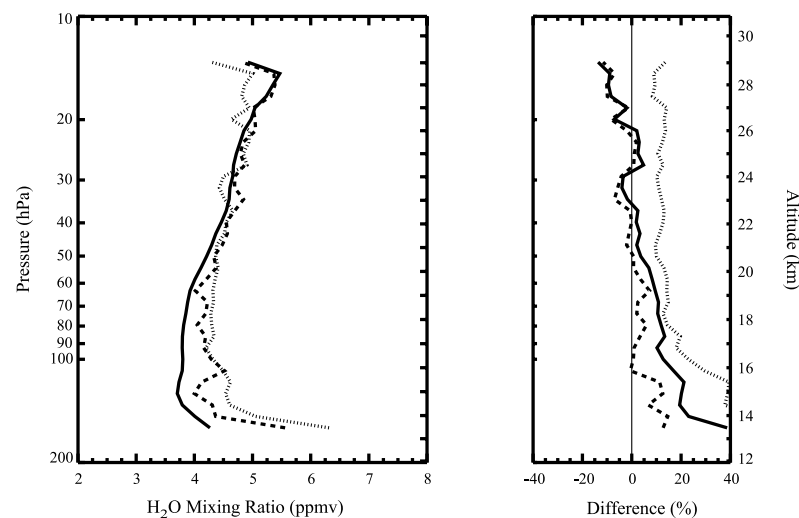


Figure 2.22 As in Figure 2.21, but for a set of 11 HALOE V19 SS comparisons.

Three comparisons have been made between HALOE SR profiles and LMD frostpoint hygrometer profiles [Ovarlez and Ovarlez, 1996; Ovarlez *et al.*, 1996] in the region of Indonesia to Diego Garcia. Average longitude separation is 7 degrees. Figure 2.23 shows

averages for these tropical comparisons of January 1994. HALOE values are smaller than the frostpoint by 15 to 20% between 25 hPa and 75 hPa. It should be noted that only one frostpoint profile extends below 60 hPa (note that the RMS difference in the right panel goes to zero at that point). Results for this small sample show larger differences than indicated for the sets of HALOE comparisons with the NOAA-CMDL frostpoint measurements over the same altitude range. For the comparison shown in Figure 2.24 at Kiruna, Sweden, on 20 March 1995, the profile shapes are similar. In this instance, HALOE is up to 15% larger between 25 hPa and 60 hPa but the differences are smaller above and below that altitude range. This comparison occurs near the early springtime polar vortex, where differences between a local and a path-averaged measurement may be an important factor. No modified V19 profile was generated for Figure 2.24.

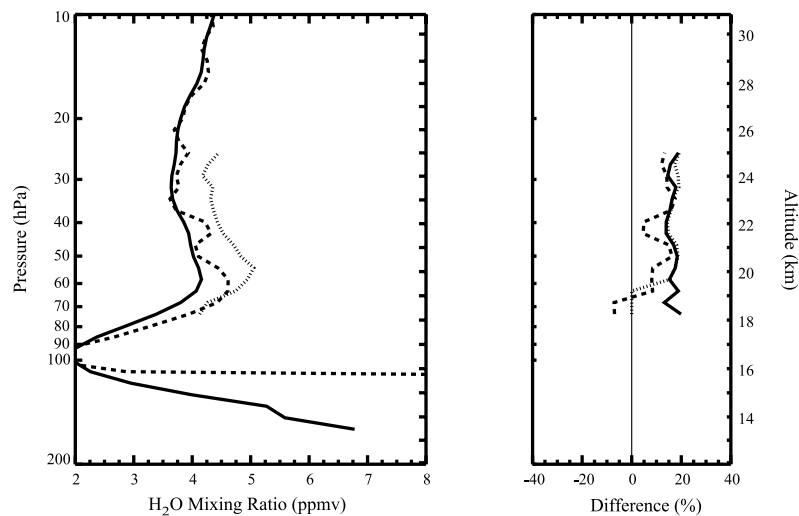


Figure 2.23 (left) Average of three HALOE (solid)/LMD frostpoint balloon (dotted) comparisons at tropical latitudes in January 1994. Dashed is HALOE result using its modified algorithm. (right) Average (solid or dashed) and RMS (dotted) differences.

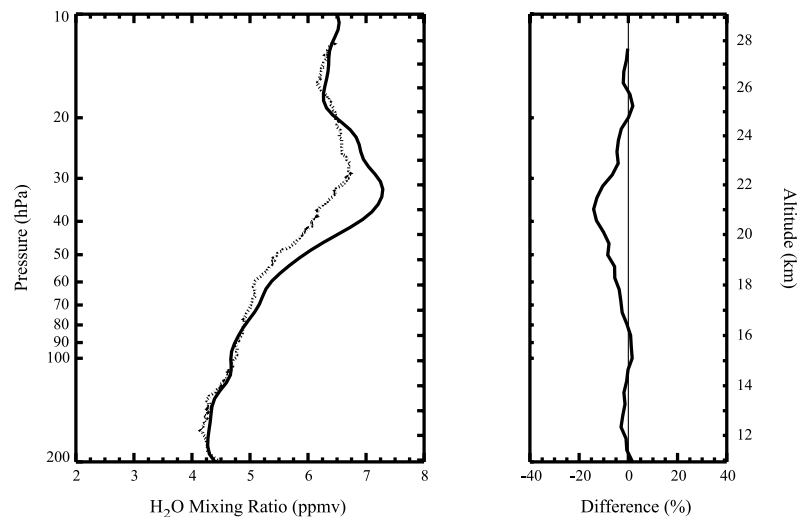


Figure 2.24 As in Figure 2.23, but for a single comparison at Kiruna, Sweden, in March 1995.

### *Jülich Lyman- $\alpha$ hygrometer (FISH)*

One HALOE comparison opportunity was obtained with the Jülich Lyman- $\alpha$  hygrometer (FISH) on 20 September 1993, at 44°N, 0°W [Zöger *et al.*, 1999b]. Comparisons are shown in Figure 2.25 with two nearby HALOE SS profiles from 21 and 22 September. Note that FISH data have been measured using the prototype instrument, resulting in less precise and noisier measurements than with the current instrument. In this comparison, the FISH profile was smoothed with a cosine bell function of width  $\pm 1.05$  km, but this did not reduce its fine structure oscillations much. The difference is within the combined error bars for both instruments. When the FISH profile is convolved with the HALOE field of view (in order to reduce the noise and approximate the vertical resolution of the HALOE measurement), the *in situ* profile is altered where water vapour turns sharply and is biased toward larger values. At about the 150 hPa level the HALOE profiles in Figure 2.25 diverge somewhat; the interlevel retrieval constraint has not been eliminated for these comparisons. Nevertheless, the Jülich profile tends to split the differences for the nearby HALOE profiles at 100 hPa to 150 hPa. There is no clear HALOE bias with the FISH Lyman- $\alpha$  measurement below the 30 hPa level, even at the water vapour profile minimum. Minor differences only occur at low altitudes close to the tropopause, below 150 hPa, where both the precision and accuracy of the HALOE retrieval degrades. These differences are at variance with the preponderance of other HALOE comparisons with the Harvard and NOAA-AL Lyman- $\alpha$  profiles from the ER-2. More comparisons with the Jülich sonde would be helpful to see whether the agreement in Figure 2.25 is found repeatedly.

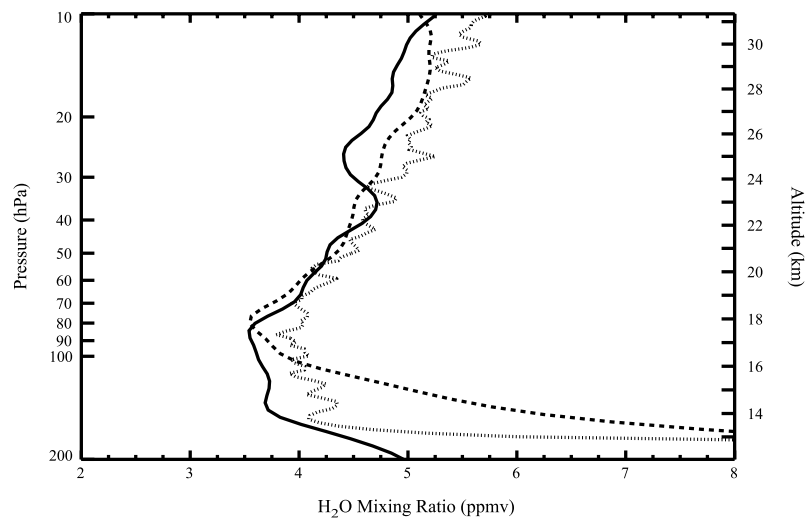


Figure 2.25 HALOE V19 SS comparisons with a vertically smoothed Jülich Lyman- $\alpha$  profile (dotted) on 20 September 1993, at 44°N, 0°E. The two nearby HALOE V19 profiles are from 22 September (solid) at 46°N, 351°E and 22 September (dashed) at 43°N, 14°E.

## Remote sensing measurements

### *FIRS-2*

Thus far, FIRS-2 has had three balloon flights coinciding with one or more HALOE occultation events, where observations made within 24 hours inside a radius of 850 km are considered coincident. A comparison of multiple FIRS-2 and HALOE profiles showed that local gradients are small enough for useful intercomparison for two of the flights. The selected flights were launched from Ft. Sumner, New Mexico on 29 September 1992 and 22 May 1994. Average FIRS-2 and HALOE (version 19) profiles are compared in Figure 2.26. Differences are generally less than 5%, with HALOE indicating larger water vapour mixing ratios than FIRS-2

above 30 km and smaller mixing ratios near the hygropause. The feature seen in the HALOE profile near 23 km results from a vortex fragment seen by HALOE in 1994 which was not observed in the FIRS-2 observations some 800 km to the south.

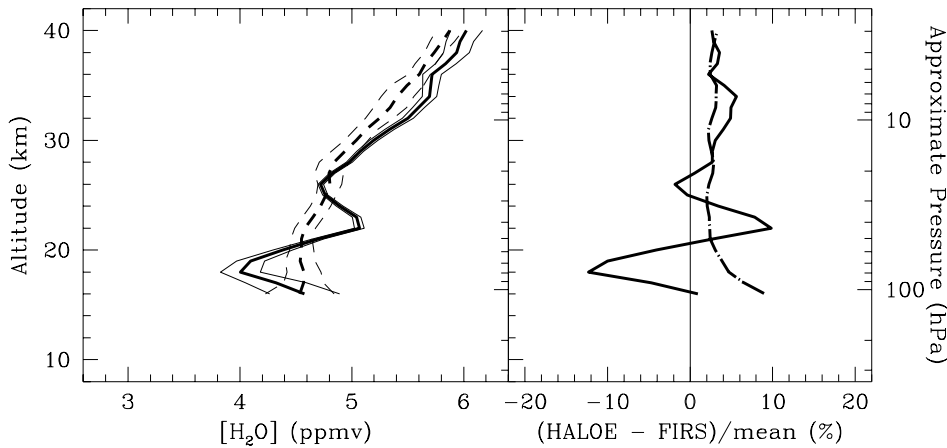


Figure 2.26 The left panel shows the comparison between average FIRS-2 (dashed curve) and HALOE version 19 (solid curve) profiles discussed in the text. The right panel shows the mean difference (solid curve) between FIRS-2 and HALOE, and estimated combined precision (dot-dash curve).

#### *MkIV*

MkIV balloon profiles meeting the criterion of being within 5° in latitude, 10° in longitude, and 3 days of a HALOE overpass, were selected for comparison. This latter criterion (3 days) may seem rather lenient, but one must remember that these MkIV balloon flights were all made at turn-around, when the winds in the middle and lower stratosphere are light and variable. Under turn-around conditions air masses do not move very far, even in three days. Only three of eight balloon flights made since 1992 met this criterion.

The first three panels of Figure 2.27 show all possible comparisons, with the H<sub>2</sub>O profiles observed at each location plotted. The 1993 September comparison is the closest in terms of the time separation. Here it is apparent that the HALOE profiles (open triangles) are systematically 10-20% less than those measured by MkIV (solid symbols). Two MkIV profiles were measured on this particular flight, a sunset (filled diamonds) and a sunrise (solid squares) 12 hours later. All of these MkIV and HALOE profiles were measured within a 35-hour period, and some within 1 hour of each other.

For the 1994 May profiles, little bias is apparent. However, this may be fortuitous given the MkIV profile was measured 3 days after most of the HALOE observations. Later HALOE profiles measured on the same date in 1994 May as the MkIV profile but 10° further north show much worse agreement with the MkIV profile than those presented here. The 1996 September intercomparison again shows the MkIV profile is systematically larger than the near coincident HALOE profiles, which were measured 35 hours after the MkIV profile.

The fourth panel of Figure 2.27 summarises the average biases obtained from each near coincident MkIV-HALOE pair. Above 20 km altitude the MkIV profiles are in general 5-10% (0.3-0.6 ppmv) larger than those measured by HALOE. Below the hygropause (typically 18 km), it becomes very difficult to determine a meaningful bias because the H<sub>2</sub>O volume mixing ratio is decreasing so rapidly with increasing altitude that even a small altitude difference can cause a large apparent discrepancy.

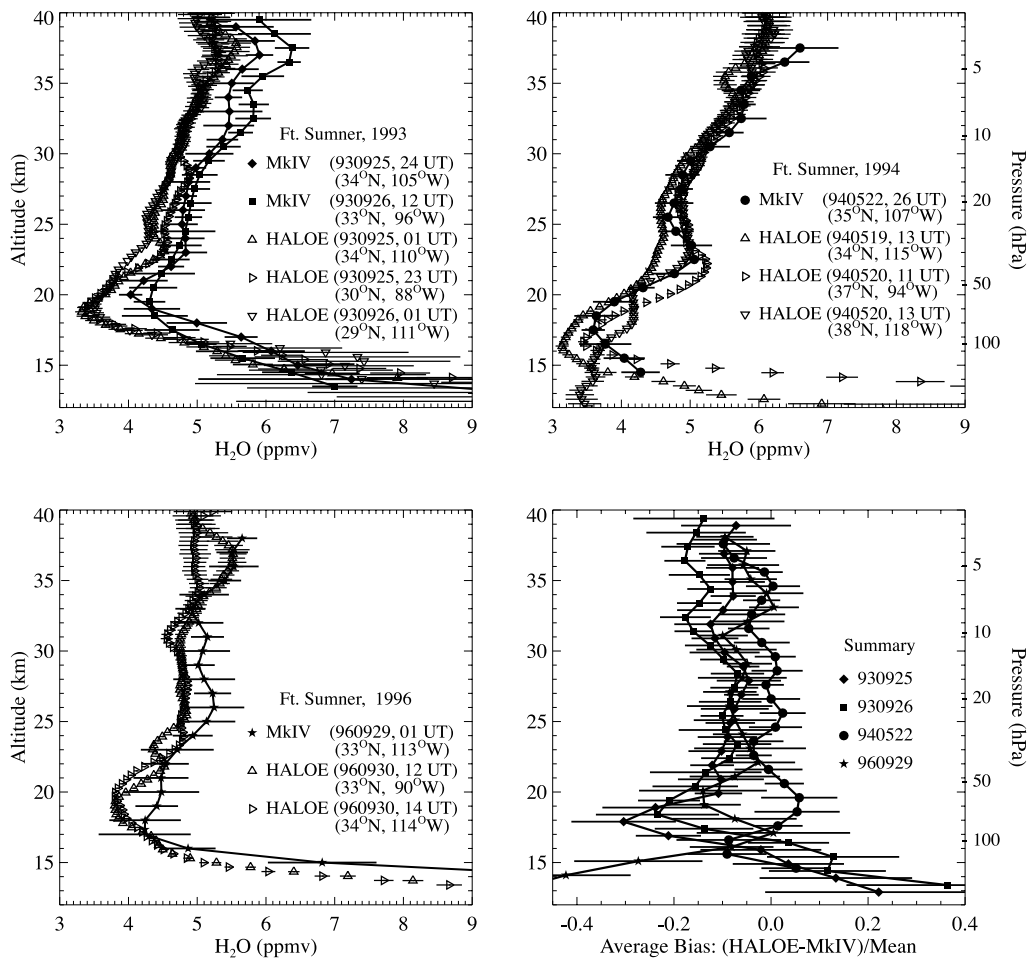


Figure 2.27 MkIV–HALOE comparisons for 3 balloon flights at Ft. Sumner, New Mexico. The first 3 panels show individual water vapour profiles, the final panel shows the average biases for each balloon flight.

### Effects of the modified O<sub>2</sub> continuum on the HALOE retrieval

In general, the HALOE comparisons with the *in situ* and remote sounding balloon measurements are within the uncertainties for HALOE water vapour in the lower stratosphere. With the inclusion of a modified O<sub>2</sub> continuum and a less constrained retrieval, the differences become smaller in most cases. The effects of interference from the H<sub>2</sub>O continuum are not considered in the V19 algorithm. Inclusion of a model for the H<sub>2</sub>O continuum will decrease retrieved water vapour at low altitudes of the stratosphere and offset some of the changes brought about by the better O<sub>2</sub> model. However, at this time it is not clear that an adequate model exists for characterising the effects of the H<sub>2</sub>O continuum at the low water vapour mixing ratios and cold temperatures of the lower stratosphere.

### 2.3.2 MLS comparisons

In this section, the MLS data are compared to various balloon-borne, airborne and ground-based data sets. The MLS data used are the prototype Version 0104 data described in Chapter 1.4.6 and [Pumphrey, 1999]. For each of the comparisons, the difference was taken between the non-MLS profile and the closest MLS profile for the same day. Less than  $15^\circ$  in longitude and  $2^\circ$  in latitude typically separate the two profiles. A mean difference is obtained by averaging over a number of pairs of profiles. This difference gives an indication of the systematic bias between the two instruments and is shown in the comparison figure as a solid line. The square of the difference is averaged and the square root taken to give a root-mean-square (RMS) difference shown in each comparison figure as a dotted line. The RMS difference will be equal to the absolute value of the mean difference if all of the difference is systematic and greater if some of the difference is random. To aid this comparison where the mean difference is negative, the absolute mean difference is shown in the figures as a dashed line. The RMS difference should be of a similar size to the root-sum-square combined uncertainties of the two measurements, which is shown in the figures as a dot-dash line.

#### Comparison with balloon frostpoint hygrometer

Comparisons are shown with both the NOAA-CMDL frostpoint and LMD frostpoint balloon instruments. There are 16 profiles from the NOAA-CMDL instrument for which reasonably close MLS measurements exist. Most of these profiles are equatorial or middle latitude profiles, with one profile taken in the Antarctic spring. Figure 2.28 shows the average of the MLS-CMDL differences. The short horizontal lines on the left show the levels at which the MLS data are retrieved. Between these levels, MLS mixing ratio is assumed to vary linearly with logarithmic pressure.

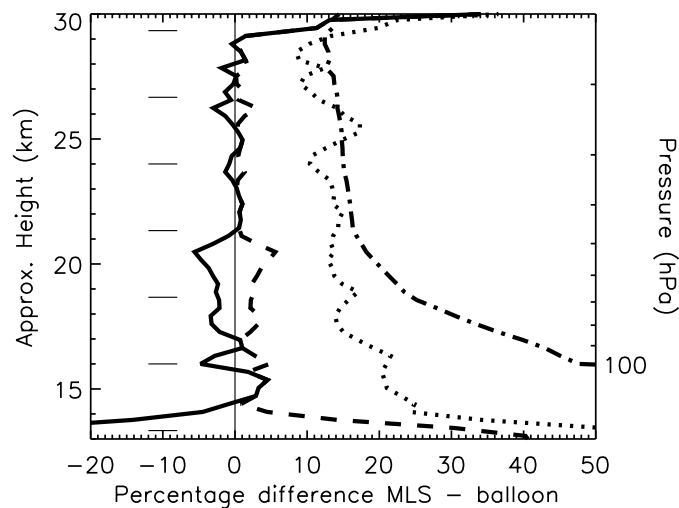


Figure 2.28 Comparison between the NOAA-CMDL frostpoint hygrometer and MLS. The solid line is the mean difference between the two instruments and the dotted line is the RMS difference. The dashed line is the absolute value of the mean difference. The dot-dash line represents the quoted errors for MLS. The line segments on the left side indicate the MLS retrieval levels.

Below 29 km, the bias between the NOAA-CMDL frostpoint and MLS is small compared to the random differences, and the RMS differences are similar to the errors supplied with the MLS data. Above 29 km, there are only a small number of comparisons. Figure 2.29 shows a similar comparison with the LMD frostpoint hygrometer. Seven profiles are available for which there are coincident MLS measurements. Of the seven profiles, six were taken at Kiruna in northern Sweden, the remaining one at Aire sur l'Adour, France. There are clear differences between the two comparisons. The LMD data show larger biases with MLS than do the NOAA-CMDL data, particularly at higher altitudes. Overall, MLS tends to show small differences with the NOAA-CMDL frostpoint balloon instrument, and is biased 8-20% low relative to the LMD frostpoint balloon instrument. Part of this discrepancy with the LMD may be due to the difficulty of obtaining matches within similar air masses at high latitudes during the winter.

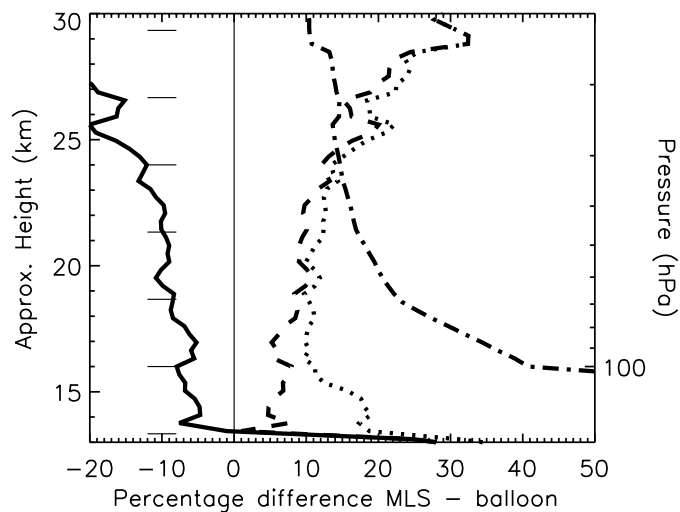


Figure 2.29 As Figure 2.28 but for the LMD balloon frostpoint hygrometer.

### Comparisons with the Harvard Lyman- $\alpha$ instrument

Although a detailed comparison was not carried out between these two instruments, when the Harvard Lyman- $\alpha$  instrument flew on the ER-2 during the CEPEX campaign in March and April 1993, the Harvard instrument measured mixing ratios approximately 0.75 ppmv (~20%) larger than those seen by MLS. Most of the data is at a pressure of about 70 hPa and the flights were all made within 20° of the equator in latitude and between 170° and 180° E. longitude.

### Comparison with ground-based microwave (WVMS)

A detailed comparison of the ground-based water vapour millimetre-wave spectrometer (WVMS) with other instruments is given by *Nedoluha et al.* [1997]. This paper and that of *Lahoz et al.* [1996] both show comparisons between WVMS and MLS version 3 data. Both MLS version 4 and prototype version 0104 discussed in this report show smaller differences with WVMS than does MLS version 3. Figure 2.30 shows the mean profiles from MLS and WVMS for the period 9 January to 9 February 1993, for the Lauder, New Zealand (45°S) WVMS site. The results from Table Mountain Observatory, California are similar. Figure 2.30b shows the mean and RMS differences between MLS and WVMS. WVMS and the MLS agree to within their quoted uncertainties at most levels. The systematic component of the difference is a substantial proportion of the total difference, but the difference is smaller than for earlier MLS versions. The most significant disagreement between the prototype and WVMS occurs at 0.2-

0.3 hPa, where the MLS profiles show a notch. This feature probably has too small a vertical extent for WVMS to detect it.

### Comparison with FIRS-2

The FIRS-2 has had three balloon flights coinciding with MLS overpasses, where observations made within 24 hours inside a circle with a 400 km radius are considered coincident. By comparing multiple FIRS-2, MLS, and HALOE profiles, it was determined that local gradients were small enough for useful intercomparison for two of the flights. The selected flights were launched from Ft. Sumner, New Mexico, on 29 September 1992 and from Barstow, California, on 23 March 1993. The average FIRS-2 and MLS (prototype version 0104) profiles are compared in Figure 2.31. Water vapour mixing ratios retrieved by MLS are generally smaller than those retrieved by FIRS-2, with the difference increasing from 5% near 3 hPa to 20% at 70 hPa.

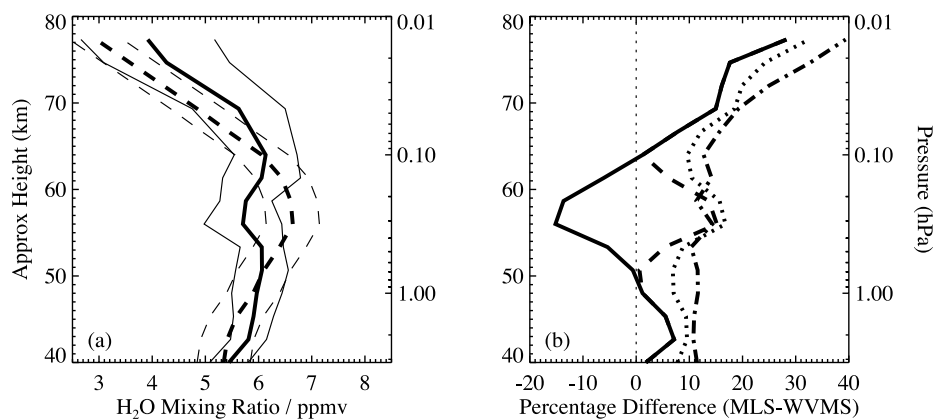


Figure 2.30 Panel (a) shows the mean WVMS (dashed) and mean coincident MLS (solid) profiles for the period 9 January to 9 February 1993 for the WVMS Lauder, New Zealand instrument. Panel (b) shows the percentage difference.

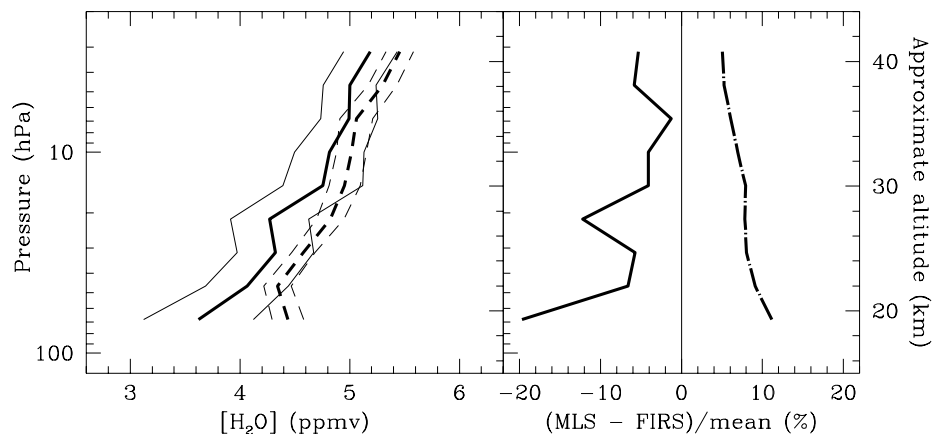


Figure 2.31 The left panel shows the comparison between average FIRS-2 (dashed curve) and MLS prototype 0104 (solid curve) profiles discussed in the text. The right panel shows the mean percentage difference (solid curve) between FIRS-2 and MLS, and estimated combined precision (dot-dash curve).

### 2.3.3 SAGE II comparisons

Five years of version 5.9 SAGE II water vapour data are presently available for validation purposes. Aerosol contamination from the El Chichón and Mount Pinatubo volcanic eruptions make the retrievals prior to 1986 and after mid-1991 unsuitable for comparisons with other data sets. Several individual profiles comparisons are shown in *Rind et al.* [1993] and are not repeated. Comparisons from one aircraft experiment in 1987 and from several frostpoint balloon measurements are presented here.

#### Comparison with NOAA Lyman- $\alpha$ AAOE measurements

The Airborne Antarctic Ozone Experiment (AAOE) conducted in the austral spring of 1987 included measurements of water vapour from the NOAA-AL Lyman- $\alpha$  hygrometer onboard the NASA ER-2 high altitude aircraft [*Kelly et al.*, 1990]. All the ER-2 measured profiles during AAOE are compared with all available SAGE II observed water vapour profiles in the southern high latitude region during austral spring of 1987. Results of these comparisons over two latitude ranges are shown in Figure 2.32. At the high latitudes near the vortex edge, the averages include profiles from different air masses, contributing to the ranges denoted in Figure 2.32. In the 50°-60°S band, SAGE II average values are less than 3 ppmv in the range 350 K <  $\theta$  < 395 K while ER-2 averages show mixing ratios less than 3 ppmv for a wider range (350 K <  $\theta$  < 410 K). In the 60°-70°S band, both instruments indicate average water vapour mixing ratios less than 2.3 ppmv in the 345-385 K potential temperature range. Below the 350 K potential temperature surface, the comparisons show small differences with respect to the absolute values and the slope. In the range 420 K <  $\theta$  < 500 K, SAGE II exhibits a much steeper vertical gradient. This results in a 20% difference between the two instruments above the 450 K potential temperature surface, with SAGE II larger.

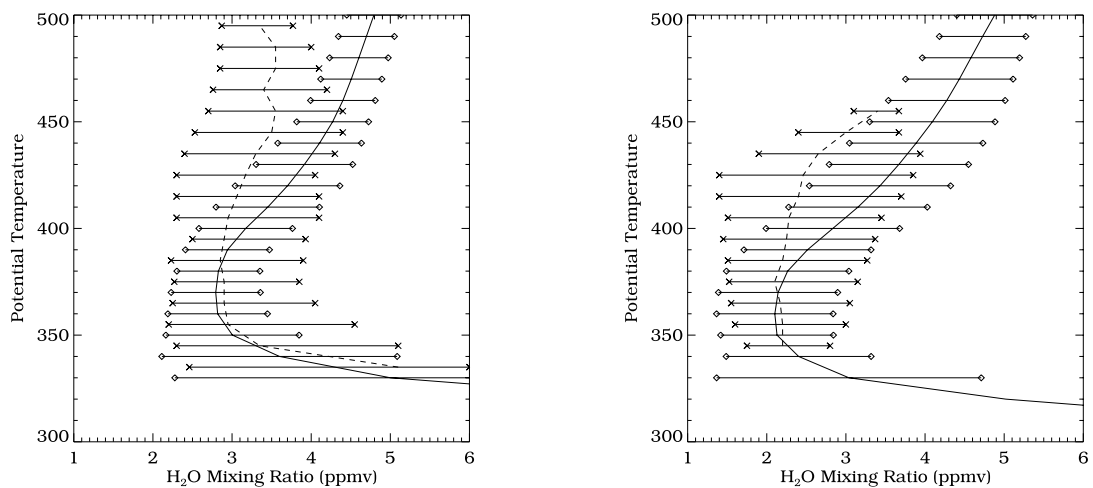


Figure 2.32 SAGE II versus NOAA-AL Lyman- $\alpha$  H<sub>2</sub>O measurements on board the ER-2. (a) Dotted curve: Lyman- $\alpha$  average profile over Punta Arenas (53°S, 71°W): Solid curve: SAGE II monthly zonal mean for 50°S-60°S, September 1987. The horizontal bars represent data range (*in situ* measurements) and standard deviations ( $1\sigma$ ) (SAGE II). (b) Dotted curve: Lyman- $\alpha$  average profile inside the vortex (near 72°S, 70°W). Solid curve: SAGE II monthly zonal mean for 60°S-70°S, September, 1987. The horizontal bars represent data range (*in situ* measurements) and standard deviations ( $1\sigma$ ) (SAGE II).

## Comparison with balloon-borne frostpoint measurements

As discussed in *Rind et al.* [1993], *in situ* water vapour measurements using frostpoint hygrometer measurements have made significant contributions to the validation of SAGE II observed water vapour profiles. A more extensive investigation has recently been carried out to re-examine the intercomparison based on the complete set of the SAGE II archived water vapour data set (January 1986 through May 1991) and the whole catalogue of the NOAA-CMDL balloon-borne frostpoint data set released for this assessment activity.

Pairs of comparisons were selected using 1-day and 1000-km coincidence criteria. Coincident pairs include comparisons where one balloon profile is compared with several different SAGE II profiles. For the two middle latitude locations (Boulder, Colorado and Edwards AFB, California), there exist 36 and 15 coincident pairs respectively. The intercomparison at low latitudes (American Samoa) consists of 13 pairs while the comparison for southern high latitudes (McMurdo) consists of a much smaller size of samples (8 coincident pairs). The coincident pairs for Boulder include samples for various seasons and cover observations in four different years (1986, 1988, 1989 and 1990).

A summary of all the comparisons with NOAA-CMDL frostpoint measurements is shown in Figure 2.33. Average percentage differences (SAGE II–frostpoint) are given for all coincident pairs for Boulder, Edwards AFB, Samoa, and McMurdo. Systematic differences are seen (with SAGE II larger) above 21 km for middle latitude measurements (left panels). Differences increase upwards in the altitude range 21 to 27 km. There seem to be less significant differences in the opposite sense (SAGE II smaller) below 18 km. The large variability in the differences below 13 km (shown by the solid curves) reflects the steep vertical gradient and significant spatial inhomogeneities that exist in these altitude regions near the tropopause. Differences for measurements over Samoa (upper right panel) decrease upward in the altitude range 18 to 26 km. However, one should note that the points below 18 km and above 25 km in this figure represent comparisons in July only (8 pairs), while the remaining data points are the average differences for all 13 cases (both July and January). For comparison over McMurdo (lower right panel), SAGE II and NOAA-CMDL frostpoint measurements overlap only in a smaller altitude range (12 to 22 km). Since all 8 cases that contribute to this figure are measurements in October, the increasing differences with decreasing altitude below 16 km could be attributed to spatial inhomogeneities due to vortex activity during austral spring in the southern high latitude region. In general, above 20 km differences are less than 20%, with SAGE II larger. Below 20 km, the sign changes for the middle and high latitude comparisons, and the magnitude increases.

Comparisons were also made with the LMD frostpoint hygrometer. These intercomparisons are described by *Pruvost et al.* [1993]. Comparisons were made for balloon flights from Aire sur l'Adour, France, in October 1987, 1989, and 1990. In terms of percentage differences, the discrepancies are 12% or less, with SAGE II larger.

It should be noted that a new version (6.0) of the SAGE II water vapour retrieval was released during the summer of 2000, too late to be used in this assessment. A validation paper has not yet been published, but major changes are expected. Changes incorporated into the SAGE II v6.0 inversion algorithm that affect the water vapour retrieval are:

- 1) An improved position registration algorithm that will change the transmission profile computation.
- 2) Correction of the 453 nm channel drifts, which affected the NO<sub>2</sub> retrieved values.
- 3) Update of the 600 nm aerosol estimation algorithm, which will affect the 525 nm aerosol values used in the 940 nm aerosol estimate.
- 4) Use of the 1992 compilation of line parameters for water vapour at the 940 nm region.

- 5) Update of the ozone absorption cross section at the 940 nm region.
- 6) Update on the EGA computational scheme.

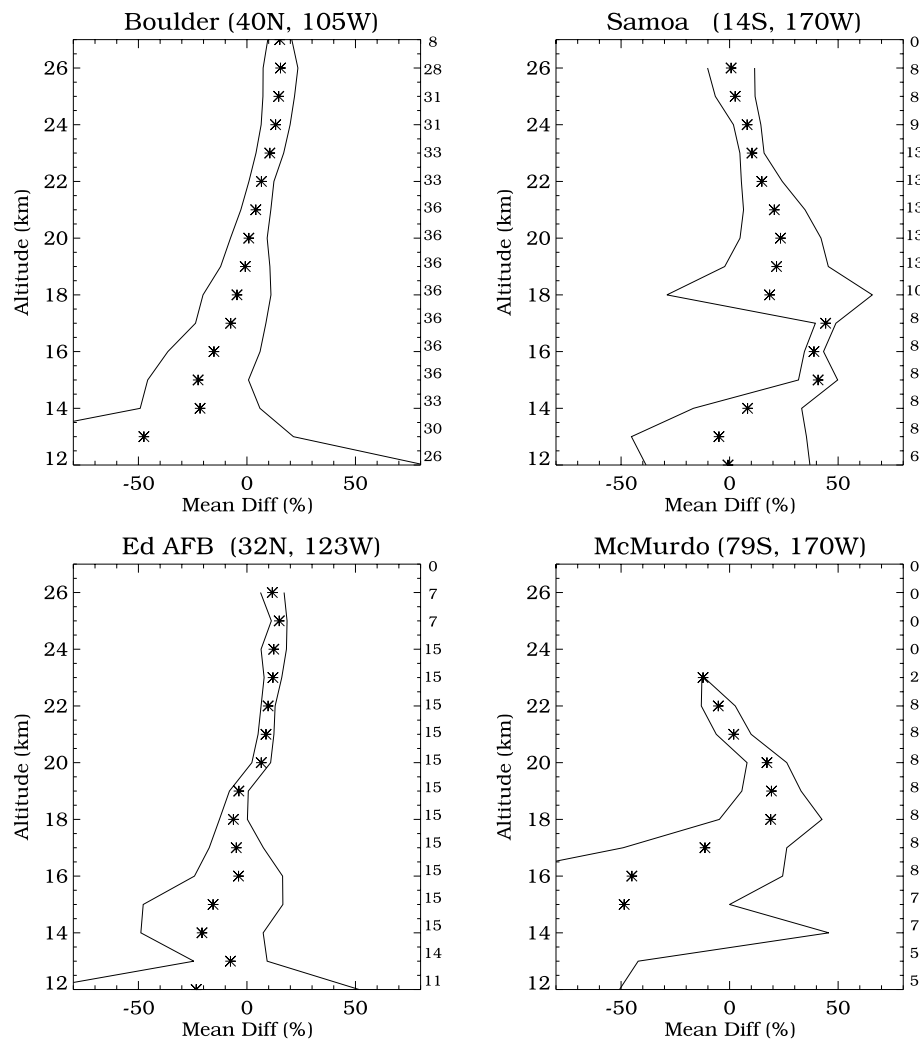


Figure 2.33 Overall percentage differences [SAGE II minus *in situ*] for comparisons with the NOAA-CMDL frostpoint over Boulder, Edwards AFB, Samoa, and McMurdo. The solid curves represent the standard deviation ( $1\sigma$ ) at each altitude and the numbers on the right indicate the number of valid pairs of comparison at each altitude.

### 2.3.4 ATMOS comparisons

#### Lyman- $\alpha$ hygrometers

Measurements made at the beginning of the Atmospheric Laboratory for Applications and Science-3 (ATLAS-3) mission nearly overlapped in time and location with observations made from the ER-2 during the Airborne Southern Hemisphere Ozone Experiment/Measurements for Assessing the Effects of Stratospheric Aircraft (ASHOE/MAESA) aircraft mission. A previous comparison of observations made with the NOAA-AL Lyman- $\alpha$  hygrometer during ASHOE/MAESA with Version 2 retrievals of  $\text{H}_2\text{O}$  from ATMOS/ATLAS-3 demonstrated differences smaller than 8% [Chang *et al.*, 1996].

The ATLAS-2 mission also provided an opportunity to compare ATMOS observations with those from the NOAA-AL Lyman- $\alpha$  hygrometer. Between 8 and 16 April 1993, ATMOS made observations at northern high latitudes inside and outside the Arctic vortex. In the few weeks following this mission, between 23 April and 18 May, the NOAA-AL instrument flew at northern middle latitudes aboard the ER-2 as part of the SPADE aircraft campaign. Between the ATLAS-2 and SPADE missions (20 April), the Arctic vortex broke into large fragments, which were encountered by the ER-2 during Stratospheric Photochemistry Aerosols and Dynamics Expedition (SPADE). A comparison of SPADE and ATMOS data revealed small differences between ATMOS (Version 2) retrievals of H<sub>2</sub>O inside and outside the vortex and NOAA-AL H<sub>2</sub>O measurements inside and outside vortex fragments, as long as the distinction between these air masses was taken into account [Michelsen *et al.*, 1999a].

The left panels of Figure 2.34 show a similar analysis to that of [Michelsen *et al.*, 1999a] using ATMOS Version 3 observations. The *in situ* data were sorted into several categories based on the relative abundance of long-lived tracers: measurements in vortex fragments, those in air influenced by the vortex and/or tropics, and those in middle latitude (apparently unperturbed by vortex or tropical) air (see Michelsen *et al.* [1999a] for more details about the sorting procedure). The *in situ* observations made in vortex fragments by the NOAA-AL instrument are compared with ATMOS observations from inside the vortex in the top panel. The NOAA-AL measurements in air masses influenced by the tropics and/or vortex are compared with ATMOS data from outside the vortex. Since ATMOS only measured at high latitudes and did not appear to sample air with tracer characteristics completely unperturbed by the vortex, a comparison is not shown for the middle latitude case. The data are plotted relative to N<sub>2</sub>O. For the *in situ* observations, N<sub>2</sub>O was provided by ALIAS [Webster *et al.*, 1994]. The error bars in all panels represent the weighted standard deviation of the weighted mean. The percent differences are plotted in the lowest left panel of Figure 2.34, which shows that the ATMOS measurements are 0-4% greater than those provided by the NOAA-AL Lyman- $\alpha$  hygrometer for this case. An indirect comparison where both the NOAA-AL Lyman- $\alpha$  and ATMOS are compared to HALOE suggests that the NOAA-AL Lyman- $\alpha$  is ~5% greater than ATMOS, which is somewhat different than shown by the direct comparison.

The Harvard Lyman- $\alpha$  hygrometer also flew during SPADE, and the right panels of Figure 2.34 show the corresponding comparison of ATMOS data with measurements from the Harvard instrument made simultaneously with those from the NOAA-AL instrument. This analysis demonstrates that the ATMOS measurements are systematically smaller than the Harvard observations by 11-16% for comparisons with the SPADE data set.

Figure 2.35 presents comparisons of potential water ( $2\times\text{CH}_4+\text{H}_2\text{O}$ ) derived from simultaneous measurements of H<sub>2</sub>O and CH<sub>4</sub> for the same ATMOS occultations and ER-2 flights as those shown in Figure 2.34. For the ER-2 observations, CH<sub>4</sub> was provided by ALIAS [Webster *et al.*, 1994]. Observations of CH<sub>4</sub> from this instrument have an estimated ( $1\sigma$ ) accuracy of  $\pm 5\%$  and have been shown to be consistent with ATMOS Version 3 observations to within 5% [Michelsen *et al.*, 1999b]. ATMOS observations of CH<sub>4</sub> have an estimated ( $1\sigma$ ) accuracy of  $\pm 5\%$  and precision of  $\pm 5\%$  [Abrams *et al.*, 1996a].

Measurements from each of the instruments demonstrate that potential water is constant within experimental uncertainty outside the vortex (Figures 2.35b and 2.35e). Comparison of Figures 2.35a and 2.35b demonstrates that potential water based on the ATMOS observations is approximately 0.4 ppmv less inside the vortex than outside.

This difference in potential water between vortex and extra-vortex air is smaller than the 0.7 ppmv difference noted in a previous analysis based on ATMOS Version 2 data [Michelsen *et al.*, 1999a]. The NOAA-AL Lyman- $\alpha$  hygrometer yields a mean difference of 0.1 ppmv,

whereas the Harvard Lyman- $\alpha$  hygrometer suggests that potential water is 0.1 ppmv larger inside than outside vortex fragments. Given an average upward trend in potential water of  $\sim 0.07$  ppmv/yr (see section 2.5.3), potential water inside the vortex is expected to be smaller than extra-vortex values by at least 0.1 ppmv in the absence of dehydration by PSC sedimentation. As summarised in Figures 2.35c and 2.35f, values of potential water based on ATMOS data are 0-5% larger than those derived from NOAA-AL Lyman- $\alpha$  hygrometer data and 6-12% smaller than values derived from Harvard Lyman- $\alpha$  hygrometer data.

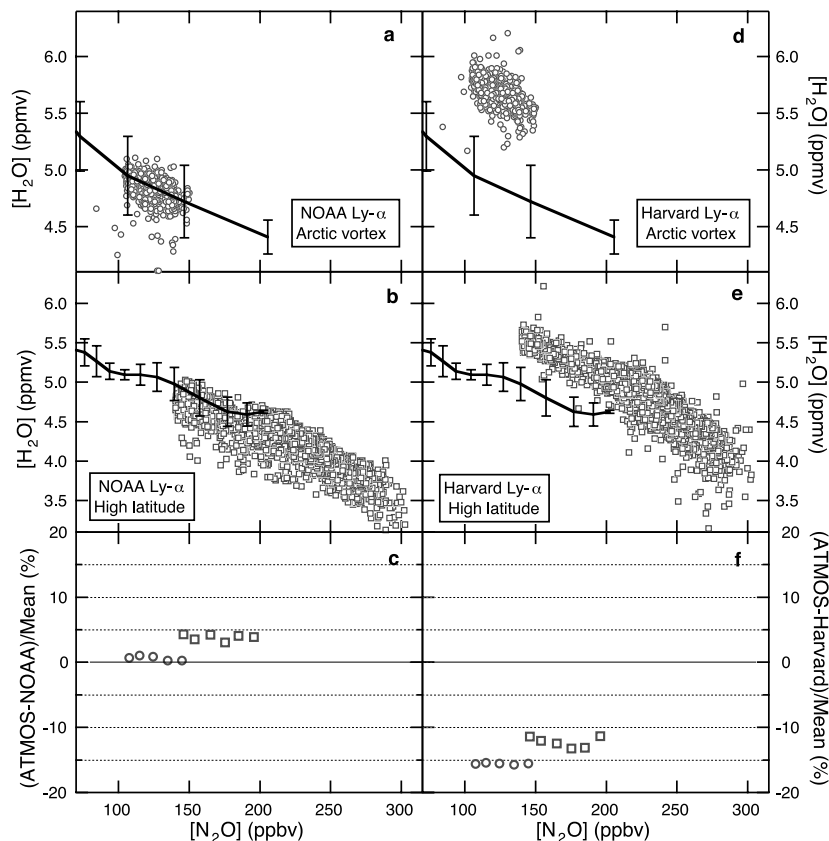


Figure 2.34 Comparison of ATMOS Version 3 retrievals of  $\text{H}_2\text{O}$  with Lyman- $\alpha$  hygrometer observations from the SPADE ER-2 aircraft campaign. The volume mixing ratio of  $\text{H}_2\text{O}$  is plotted relative to the mixing ratio of the long-lived tracer  $\text{N}_2\text{O}$ . ATMOS observations are compared with measurements from the NOAA-AL instrument in the left panels and with measurements from the Harvard instrument in the right panels. Symbols represent the *in situ* observations, and lines represent weighted averages of ATMOS profiles with error bars showing the weighted standard deviation ( $1\sigma$ ) of the weighted mean. The SPADE observations are sorted into 3 categories, as described by *Michelsen et al.* [1999a]. (a) and (d) SPADE data associated with vortex fragments are compared with ATMOS observations made during ATLAS-2 inside the Arctic vortex before it broke up. (b) and (e) SPADE data characterised as being influenced by vortex and/or tropical air are compared with ATMOS/ATLAS-2 data recorded outside the Arctic vortex. (c) and (f) The percent differences between the ATMOS observations and those from the NOAA-AL instrument (c) and the Harvard instrument (f) are plotted as a function of  $\text{N}_2\text{O}$  for the vortex case (circles) and the vortex (or tropics) influenced case (squares). For the *in situ* data, simultaneous observations of  $\text{N}_2\text{O}$  were provided by ALIAS.

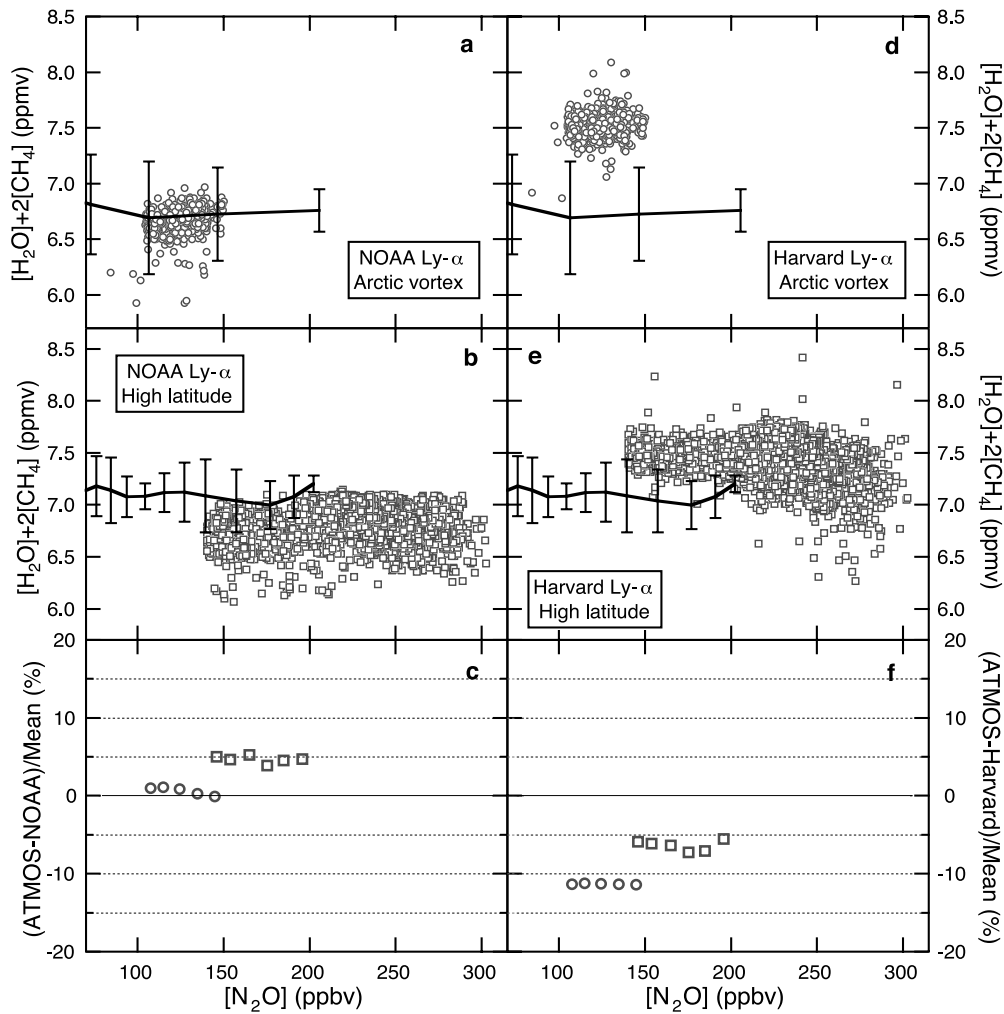


Figure 2.35 Comparison of ATMOS Version 3 values for  $2 \times CH_4 + H_2O$  with observations from the SPADE ER-2 aircraft campaign. Potential water  $2 \times CH_4 + H_2O$  is plotted relative to the volume mixing ratio of the long-lived tracer  $N_2O$ . ATMOS observations are compared with potential water derived from ALIAS  $CH_4$  with NOAA-AL  $H_2O$  in the left panels and with Harvard  $H_2O$  in the right panels plotted against ALIAS  $N_2O$ . Symbols represent the *in situ* observations, and lines represent weighted averages of ATMOS profiles with error bars showing the weighted standard deviation ( $1\sigma$ ) of the weighted mean. The SPADE observations are from the same flights shown in Figure 2.34. (a) and (d) SPADE data associated with vortex fragments are compared with ATMOS observations made during ATLAS-2 inside the Arctic vortex before it broke up. (b) and (e) SPADE data characterised as being influenced by vortex and/or tropical air are compared with ATMOS/ATLAS-2 data recorded outside the Arctic vortex. (c) and (f) The percent differences between the ATMOS observations and those from the NOAA-AL instrument (c) and the Harvard instrument (f) are plotted as a function of  $N_2O$  for the vortex case (circles) and the vortex (or tropics) influenced case (squares).

## MkIV

Although ATMOS and the MkIV instrument have never made coincident observations, they have collected data in similar air masses. Comparisons between these data sets are shown in Figure 2.36. Figure 2.36a shows the mean of ATMOS data collected at southern middle latitudes during ATLAS-1 (25 March-2 April 1992) compared with MkIV observations from northern middle latitudes on 14 and 15 September 1992. Figure 2.36b shows data from a MkIV flight on 3 April 1993 at northern middle latitudes compared with the extra-vortex observations made by ATMOS during ATLAS-2 (8-16 April 1993) at high northern latitudes. The ATMOS data shown in this panel are the same as those shown in the second set of panels in Figure 2.34. Figure 2.36c shows a comparison of data from the MkIV at northern middle latitudes during fall 1993 (23 and 24 September) with observations from ATMOS at northern middle latitudes during ATLAS-3 in fall 1994 (3-14 November). Figure 2.36d shows the percent differences between the ATMOS and MkIV observations for the cases shown in the first three panels. These comparisons indicate that the ATMOS and MkIV measurements of  $\text{H}_2\text{O}$  differ by less than 5% under similar atmospheric conditions when plotted relative to  $\text{N}_2\text{O}$ .

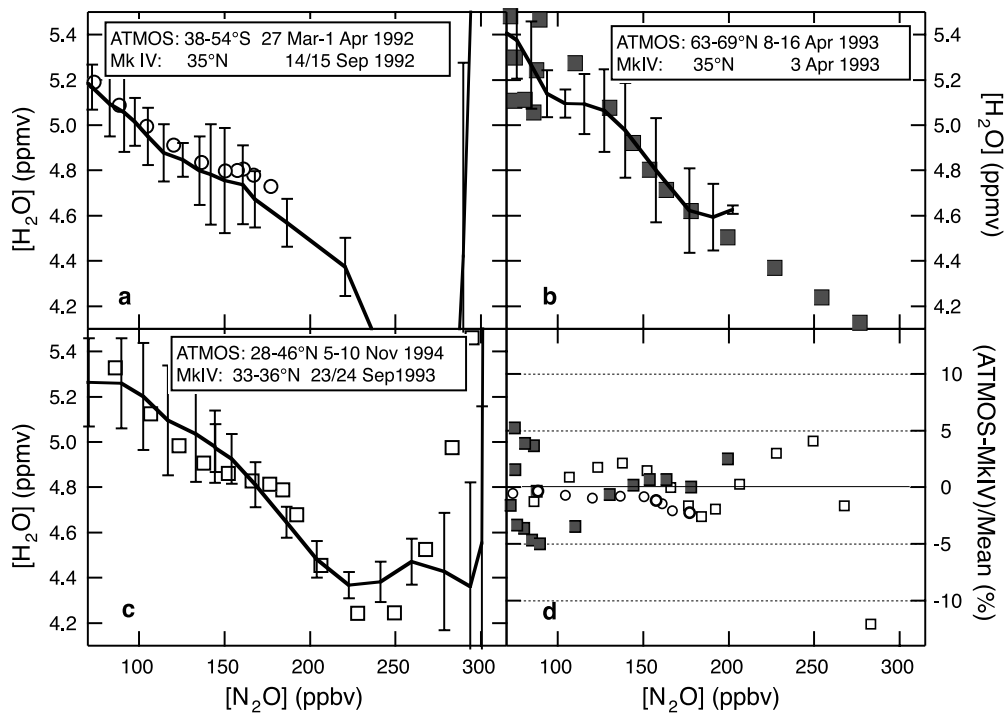


Figure 2.36 Comparison of ATMOS Version 3 retrievals of  $\text{H}_2\text{O}$  with MkIV observations. The volume mixing ratio of  $\text{H}_2\text{O}$  is plotted as a function of  $\text{N}_2\text{O}$ . Symbols represent the MkIV observations, and lines represent weighted averages of ATMOS profiles with error bars showing the weighted standard deviation ( $1\sigma$ ) of the weighted mean. (a) ATMOS observations made during ATLAS-1 at southern midlatitudes are compared with MkIV measurements from northern midlatitudes on 14 and 15 September 1992. (b) ATMOS observations made during ATLAS-2 outside the Arctic vortex are compared with MkIV measurements from northern midlatitudes on 3 April 1993. (c) ATMOS observations made during ATLAS-3 at northern midlatitudes are compared with MkIV measurements from northern midlatitudes on 23 and 24 September 1993. (d) The percent differences between the ATMOS observations and those from the MkIV are shown for the 3 cases; symbols correspond to those used in (a)-(c).

MkIV also measures  $\text{CH}_4$  with an accuracy ( $1\sigma$ ) of  $\pm 5\%$  [Toon *et al.*, 1999]. A comparison between MkIV and ATMOS values of potential water for the cases shown in Figure 2.36 is presented in Figure 2.37. The difference is within 5% (3% in the middle stratosphere) and is similar to that shown for the  $\text{H}_2\text{O}$  comparisons. The small differences are expected given the similarity of the MkIV and ATMOS instruments and their data reduction methods. This demonstrates that the selection criteria employed for these comparisons is valid, particularly given that the data shown in Figures 2.36 and 2.37 were separated by a much greater time period than any of the data sets used in the other comparisons presented.

For the cases presented here, ATMOS Version 3 water vapour observations are within 0-4% of measurements from the NOAA-AL Lyman- $\alpha$  hygrometer and MkIV instruments. The ATMOS observations are 11-16% dryer than those from the Harvard Lyman- $\alpha$  hygrometer for comparisons with measurements made in April and May 1993. These results are consistent with comparisons of potential water ( $2\times\text{CH}_4+\text{H}_2\text{O}$ ) derived from NOAA-AL, Harvard, MkIV, and ATMOS water vapour measurements, and show that in general the direct comparisons of water vapour mixing ratios between sensors do a reasonable job of representing the differences.

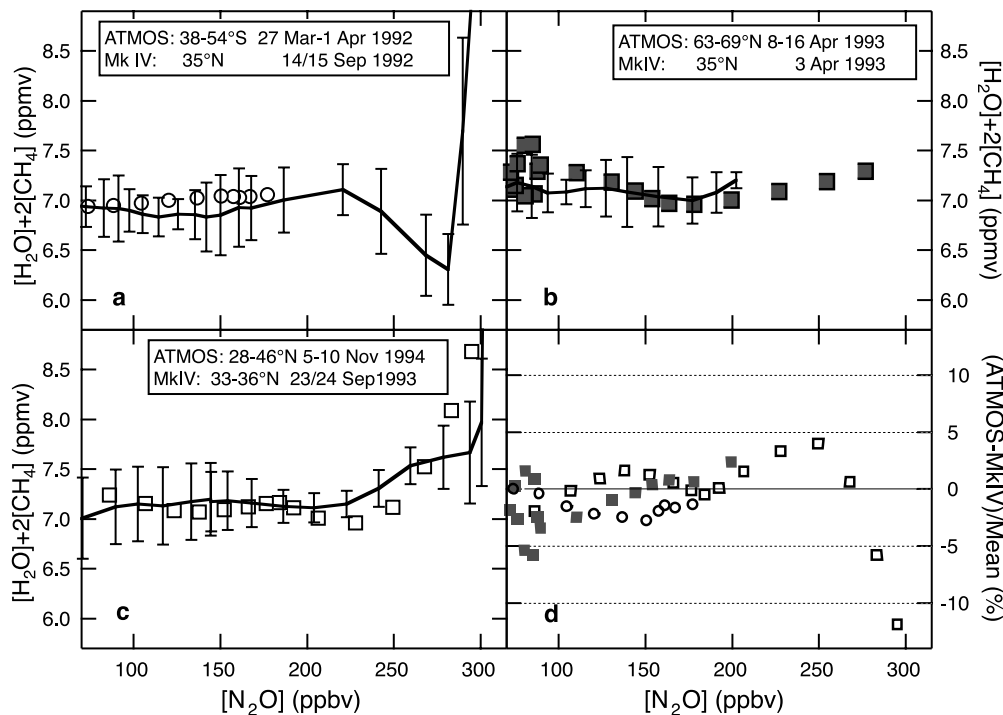


Figure 2.37 Comparison of ATMOS Version 3 values for  $2\times\text{CH}_4+\text{H}_2\text{O}$  with MkIV observations. Potential water  $2\times\text{CH}_4+\text{H}_2\text{O}$  is plotted as a function of  $\text{N}_2\text{O}$ . Symbols represent the MkIV observations, and lines represent weighted averages of ATMOS profiles with error bars showing the weighted standard deviation ( $1\sigma$ ) of the weighted mean. (a) ATMOS observations made during ATLAS-1 at southern mid-latitudes are compared with MkIV measurements from northern mid-latitudes on 14 and 15 September 1992. (b) ATMOS observations made during ATLAS-2 outside the Arctic vortex are compared with MkIV measurements from northern mid-latitudes on 3 April 1993. (c) ATMOS observations made during ATLAS-3 at northern mid-latitudes are compared with MkIV measurements from northern mid-latitudes on 23 and 24 September 1993. (d) The percent differences between the ATMOS observations and those from the MkIV are shown for the 3 cases; symbols correspond to those used in (a)-(c).

### 2.3.5 ILAS comparisons

During the eight-month period of operation of the ADEOS satellite, balloon validation experiments were conducted at two high latitude sites. For the validation of ILAS water vapour measurements, five instruments using different techniques and described in this report, made balloon-borne correlative measurements from February until May 1997. These comparisons are listed in Table 2.1.

**Table 2.1.** Balloon flights for validation of the ILAS experiment. The LMD frostpoint, FISH, and MIPAS instruments were launched from Kiruna, Sweden (68°N, 21°E); the MkIV and FIRS-2 instruments were launched from Fairbanks, Alaska (65°N, 148°W).

Balloon experiment	Date	ILAS tangent point at 20 km	Distance between launch site and 20 km tangent point	Comparison altitude range
LMD FP	14 Feb 1997	68.7°N, 41.0°E	818 km	22-27.5 km
FISH	11 Feb 1997	68.4°N, 17.9°E	142 km	15-24 km
MIPAS	24 Mar 1997	68.9°N, 34.5°E	<sup>1</sup> 557 km	13-29 km
MkIV	08 May 1997	62.2°N, 142.1°W	940 km	13-38 km
FIRS-2	30 Apr 1997	63.6°N, 149.3°W	629 km	14-40 km

<sup>1</sup>Distance between balloon measurement and 20 km tangent point: 150 km

The operational data processing software was developed at NIES in Japan [e.g. *Yokota et al.*, 1998]. In this assessment, the most recent complete release of data products (Version 4.20) is used. Comparisons using earlier retrievals are found in *Sasano et al.* [1999]. The relatively recent release of these data products limits the validation for this report to a relatively straightforward comparison of near-coincident profiles without detailed examination of possible dynamical effects.

Figure 2.38 shows the percentage difference of water vapour measurements for the five ILAS validation flights given at satellite data altitudes. Positive values denote ILAS values greater than those of the correlative measurement. On 14 February, LMD frostpoint measurements were available from 22 to 27 km. At the highest altitude, the difference is less than 10%, but for the lower altitudes, ILAS data are up to 28% larger than the LMD frostpoint data. These measurements were obtained near the edge of the polar vortex. A few days earlier from the same site, the Jülich Lyman- $\alpha$  hygrometer (FISH) obtained data very close to an ILAS measurement. Both profiles were obtained inside the polar vortex near its edge. At 15-19 km the difference was -2 to +12%, increasing with altitude. A similar result was found for the intercomparison of ILAS with the remote-sensing measurements by MIPAS on 24 March. In general, these high latitude winter measurements may be affected by atmospheric variability or different viewing geometries. The tangent altitudes of an ILAS profile correspond to different latitudes, while the *in situ* measurements were made more or less at a single latitude. The viewing geometry of MIPAS is such that it looks in the opposite direction to ILAS. The variability of water vapour abundance near the vortex edge is a plausible explanation for the observed altitude dependent differences between the measurements and limits the conclusions that can be drawn from this set of comparisons.

The validation flight on 8 May of the MkIV IR spectrometer yields differences between -5 and +5% in the 18-31 km altitude range increasing up to +10% at lower altitudes. The FIRS-2 spectrometer was flown on 30 April up to an altitude of 40 km. The difference from 15-33 km was found to be -4% to +10%. Differences of ILAS data with both MkIV and FIRS-2 measurements do not indicate a clear altitude dependence. Both balloon observations as well as the corresponding ILAS measurements were made in air masses that were not influenced by the

vortex, which was still lingering over Northern Europe and Russia in early May 1997 [Toon *et al.*, 1999]. Further, the viewing geometry of both instruments is similar to that of ILAS. Thus, the conditions were more favourable for an intercomparison than those at Kiruna. This may be the reason for smaller differences than those seen for the validation measurements by the LMD frostpoint, FISH and MIPAS, despite the larger distance between the ILAS and correlative observations at Fairbanks.

At altitudes above about 30 km, the ILAS profile retrievals show artificial oscillations between two adjacent levels that are most likely caused by the onion peeling routine in V4.20 (see Figure 2.38, MkIV and FIRS-2 panels). Consequently, it is recommended that high altitude data from the current retrieval version not be used. Making some allowance for the variable conditions near the edge of the polar vortex, it can be concluded that the ILAS water vapour measurements in the 15-30 km altitude range fall within about 10% of the correlative measurements from a variety of techniques.

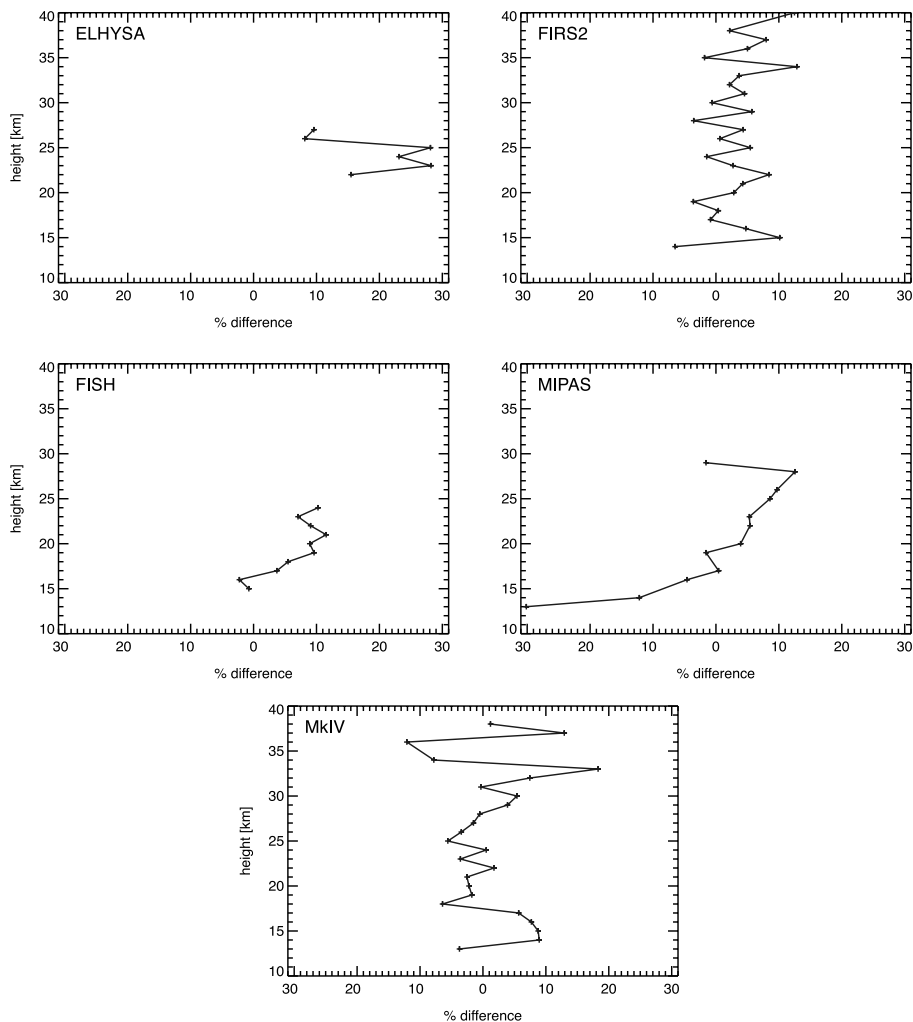


Figure 2.38 Percentage difference, (ILAS Version 4.20–validation measurement)/mean, for the five ILAS validation flights detailed in Table 2.1.

### 2.3.6 Upper stratosphere comparisons (WVMS and WASPAM)

An intensive period of stratospheric and mesospheric water vapour measurements occurred during the NASA ATLAS Spacelab shuttle missions in the early 1990's. During the March-April flights in 1992 and 1993, middle atmospheric water vapour data are available from the HALOE and MLS satellite instruments aboard UARS, and from the MAS and ATMOS instruments aboard ATLAS on the shuttle. In addition, there are ground-based retrievals available from the Water Vapour Millimeter-wave Spectrometer (WVMS) instrument, which made measurements from Table Mountain, California (34.4°N, 242.3°E) during 1992 and from Lauder, New Zealand (45.0°S, 169.7°E) during 1993. During the ATLAS-2 mission in 1993, measurements coincident with the Lauder site are available from three of the satellite instruments, while HALOE measurements are available several days later. Figure 2.39 shows nearly coincident water vapour profiles from all five instruments. No correction has been applied for the different sensitivity and altitude resolution of the five instruments, and the WVMS retrievals are limited to altitudes above ~3 hPa. All of the measurements show an increase up to ~1 hPa, a relatively flat region from 1 to 0.1 hPa with a peak mixing ratio of between 6 and 7 ppmv, and a sharp drop above 0.1 hPa. At altitudes below 0.1 hPa, the measurements all agree to within 1 ppmv. The range is slightly larger above this altitude, but the differences in resolution and sensitivity are largest in the upper mesosphere both because of the large gradient with altitude and because of decreasing signal to noise. Similar figures for all three ATLAS missions, albeit with older retrieval versions, are given by *Nedoluha et al.* [1997].

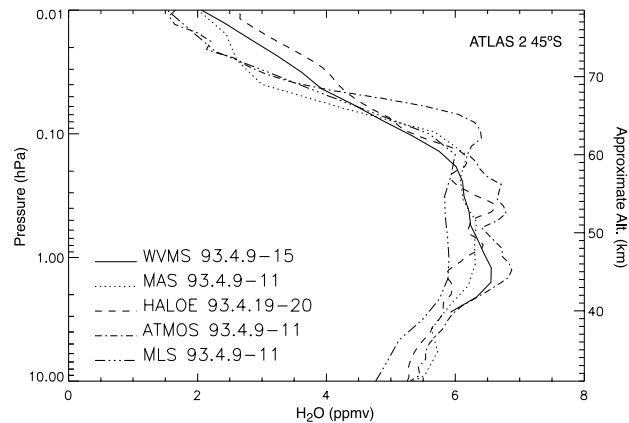


Figure 2.39 A comparison of zonal average water vapour mixing ratios retrieved during the ATLAS-2 mission in 1993 from MAS (V20, April 9-11), ATMOS (V3, April 9-11), MLS (V0104, April 9-11), HALOE (V19, April 19-20), and WVMS1 (V99, April 9-15).

In Figure 2.40, a comparison is shown of average coincident WVMS and HALOE retrievals for each of the NDSC sites where WVMS measurements are available. The coincidence criteria for the HALOE retrievals are  $\pm 7$  days,  $\pm 30^\circ$  longitude, and  $\pm 5^\circ$  latitude of the WVMS observation, which is generally obtained from a spectral integration covering ~1 week (see section 1.2 for more details).

In order to take into account differences in the resolution and sensitivity of the WVMS and HALOE instruments, we have convolved the HALOE data with the averaging kernels calculated for the WVMS instrument. The WVMS and HALOE instruments agree to within 1 ppmv at all altitudes, but there are biases apparent between the water vapour profiles retrieved by the ground-based and HALOE instruments. The difference between the WVMS and HALOE profiles generally peaks near 60 km, and then decreases in the upper mesosphere. The peak in

this difference coincides with the notch in the unconvolved HALOE profile near this altitude, as was noted in *Nedoluha et al.* [1999].

Additional profile comparison data are available from the WASPAM (Wasserdampf und Spurengasmessungen mit Mikrowellen) experiment, see *Hartogh and Jarchow* [1995], *Jarchow* [1998], and *Seele and Hartogh* [1999]. WASPAM and HALOE data have been compared for the periods from October 1994 until September 1995 (location; Max-Planck-Institute für Aeronomie, MPAe, Germany, 51.66°N, 10.13°E) and from January until December 1998 (location; ALOMAR observatory, Andoya, Norway, 69.29°N, 16.03°E). The coincidence criteria for the HALOE retrievals are  $\pm 10^\circ$  longitude and  $\pm 5^\circ$  latitude of the WASPAM observation. The WASPAM spectra have been integrated for 24 hours before retrieval; therefore, the time coincidence criterion is 1 day. In Figure 2.41 both the original HALOE data and the HALOE data convolved with the averaging kernels of WASPAM have been plotted. While the convolved 69°N data agree within 1 ppmv for all altitudes, the differences at 51°N show a distinct peak of about 1.5 ppmv at 60 km, qualitatively consistent with the peak shown in the Table Mountain middle latitude comparison shown in Figure 2.40.

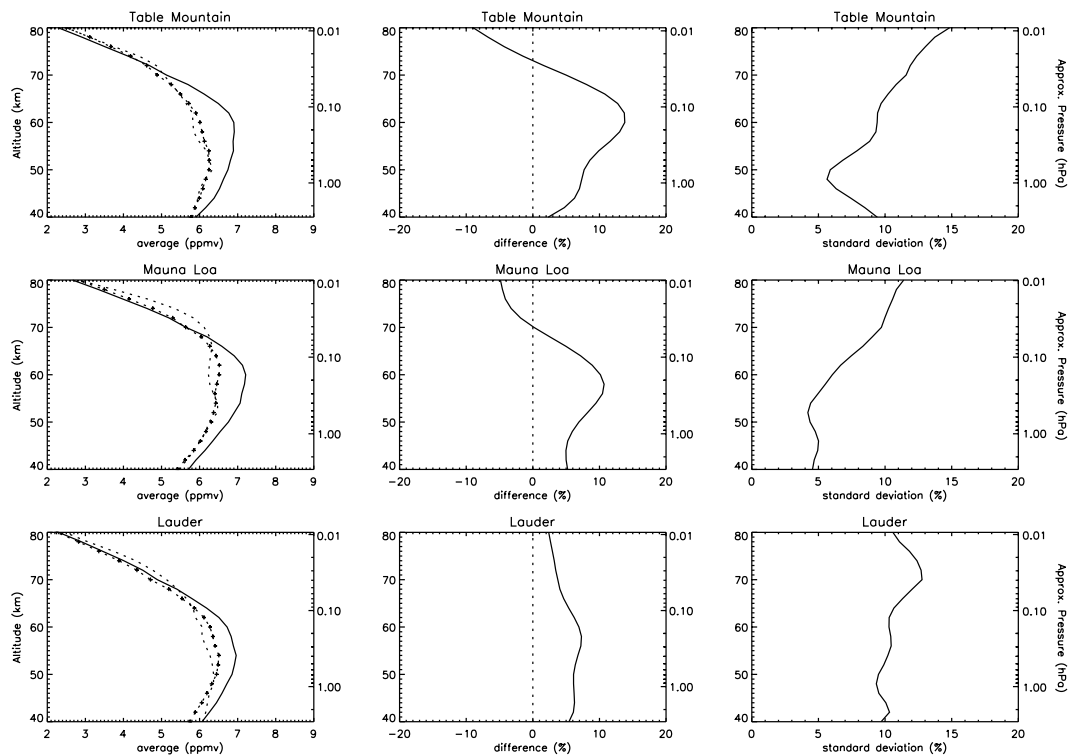


Figure 2.40 A comparison of average coincident water vapour retrievals from the WVMS instruments and HALOE. Column 1: Average of WVMS retrievals (solid), average of HALOE retrievals (dotted), average of convolved HALOE retrievals (dotted with crosses). Column 2: Difference of WVMS and HALOE retrievals (solid), and after convolution of the HALOE retrievals (dotted). Column 3: Standard deviation ( $1\sigma$ ) of the WVMS-HALOE difference (solid), and after convolution of the HALOE retrievals (dotted).

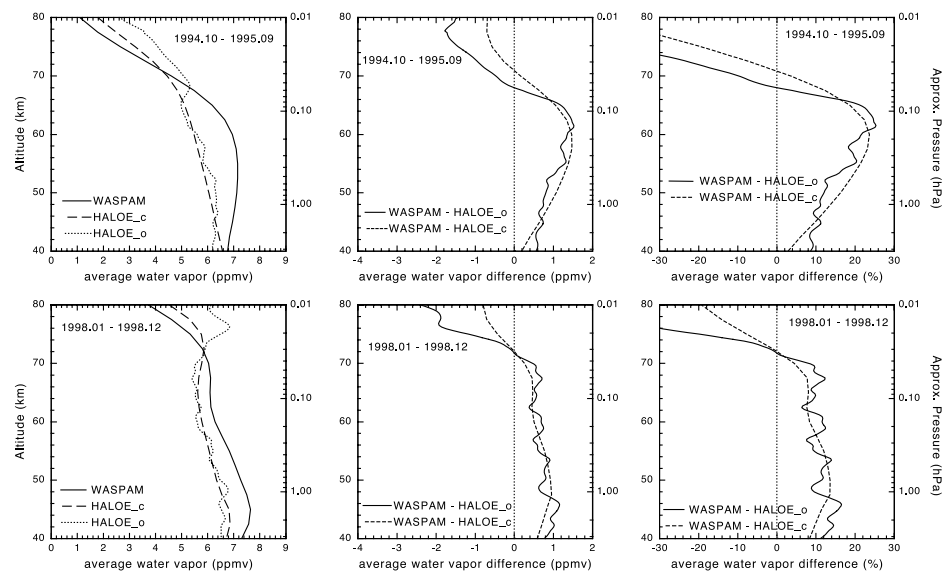


Figure 2.41 Comparison of average coincident water vapour retrievals from the WASPAM and HALOE instruments. Column 1: Average of WASPAM retrievals (solid), average of HALOE retrievals (dotted) and of convolved HALOE retrievals (dashed). Column 2: Difference of WASPAM and HALOE retrievals (solid) and after convolution of the HALOE retrievals (dashed). Column 3: Same as column 2 but difference in percent.

### 2.3.7 Comparisons with TOVS/HIRS

#### Radiosondes

The characteristics of radiosonde upper tropospheric water vapour observations are discussed in Chapter 1. The most comprehensive comparison between the upper tropospheric humidity (UTH) defined in Chapter 1 from the HIRS instrument on TOVS and radiosonde UTH was performed by *Soden and Lanzante* [1996]. They used the same HIRS clear column radiance data as described here but did not perform satellite-to-satellite intercalibration. For the period 1979-1991, they found the systematic differences in UTH between the HIRS and radiosondes showed a distinct geopolitical dependence that is a result of the different types of water vapour sensors used in different countries. For seasonal averages, they found RMS differences between satellite and radiosonde UTH of 10-12%, but this was reduced to about 6% when the radiosonde systematic bias was removed. A clear sky sampling bias exists in the HIRS UTH due to the requirement of clear or partly cloudy conditions. This clear sky sampling bias was estimated to be 4%. The radiosondes, however, have a spatial sampling bias because the radiosondes are concentrated over the Northern Hemisphere middle latitudes. *Soden and Lanzante* [1996] found that regionally, such as over the data sparse tropics, the radiosonde sampling bias could introduce systematic errors of 10-20%.

For individual matches with radiosondes and for layer-averaged specific humidity, the scatter between radiosondes and HIRS becomes much larger. For the layer 500-300 hPa, *Scott et al.* [1999] reported standard deviations ( $1\sigma$ ) of 35%, 46%, and 52% and biases of -1%, 15%, and 13% for HIRS-radiosonde matches in the tropics, middle latitudes, and polar regions. They found that the standard deviations between HIRS and radiosondes increased substantially with height, from about 22% in the layer 1000-850 hPa to 39% in the layer 500-300 hPa for all situations, reflecting the inaccuracy of the radiosonde observations at higher altitudes.

Operational numerical weather prediction centres, the National Centers for Environmental Prediction (NCEP) in the U.S, and the European Centre for Medium Range Weather Forecasting (ECMWF), have been directly assimilating HIRS radiance data for several years. Both centres report improved forecast skill using radiance data. In particular, ECMWF reports [McNally and Vesperini, 1996] that the HIRS upper tropospheric water vapour channel provides substantial positive impact to both water vapour and other aspects of the hydrological cycle prediction. Comparisons of HIRS UTH with these models are not presented since these models use the HIRS channel 12 radiance data and because the HIRS radiances are bias-adjusted at the numerical weather predictions centres to account for systematic differences between the models and the observations.

Improved radiosonde humidity detectors are being used and additional improvements are under development. These improvements are starting to have a positive impact on matches between satellite observations and radiosonde observations. Figure 2.42 shows a scatter plot of matches between the Vaisala RS80-H UTH and HIRS UTH for a research cruise in the eastern tropical Pacific Ocean for two months in 1997. Matches within 50 km and 3 hours show an RMS error of about 13% with a bias of 1.5%. Although the correlation is low (0.37), this error represents an improvement in the numbers quoted above for comparisons with archived radiosonde data sets. The relatively low correlation between the improved radiosonde moisture sensor UTH and HIRS UTH is partially a result of the limited range of humidity values that were compared, and highlights the difficulty in matching point measurements with the satellite data.

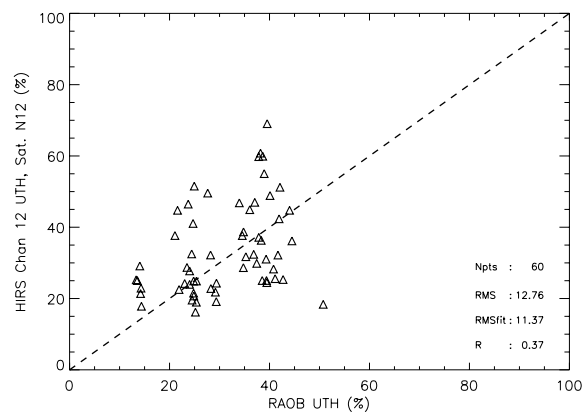


Figure 2.42 Scatter plot of UTH from the Vaisala RS80-H (*H-Humicap* sensor) radiosondes measured on a research cruise in the tropical Pacific and the HIRS UTH from the NOAA 12 satellite. Matches are taken to be within 50 km and 3 hours. The dashed line is a one-to-one line and not a fit to the data.

## MOZAIC

A number of methods for comparing the HIRS and MOZAIC data were examined. These range from comparing individual MOZAIC flights with coincident HIRS individual swath data to comparing monthly mean, spatially averaged products. In all cases, the results are similar; the flight level MOZAIC data results in a much more heterogeneous sampling of the water vapour distribution than the volume-averaged data from HIRS. This is illustrated in Figure 2.43, which shows a comparison of the MOZAIC data and HIRS data. The data have been averaged into monthly mean, 2° latitude-longitude bins, and the HIRS data have only been sampled along the MOZAIC flight tracks. Shown are the monthly mean MOZAIC data, the HIRS satellite data, the absolute difference between the two, and a scatter plot of the two data sets. In the monthly mean images, the HIRS data have much smoother gradients than the MOZAIC data. The flight tracks,

particularly across the equator to South America, Africa, and Southeast Asia, do have qualitatively similar gradients. The MOZAIC data, however, have much greater variability. These results are typical of all months analysed. For the months of June and July 1997, the correlations from the linear regression are 0.37 and 0.53 and the RMS differences are on the order of 20% of RH.

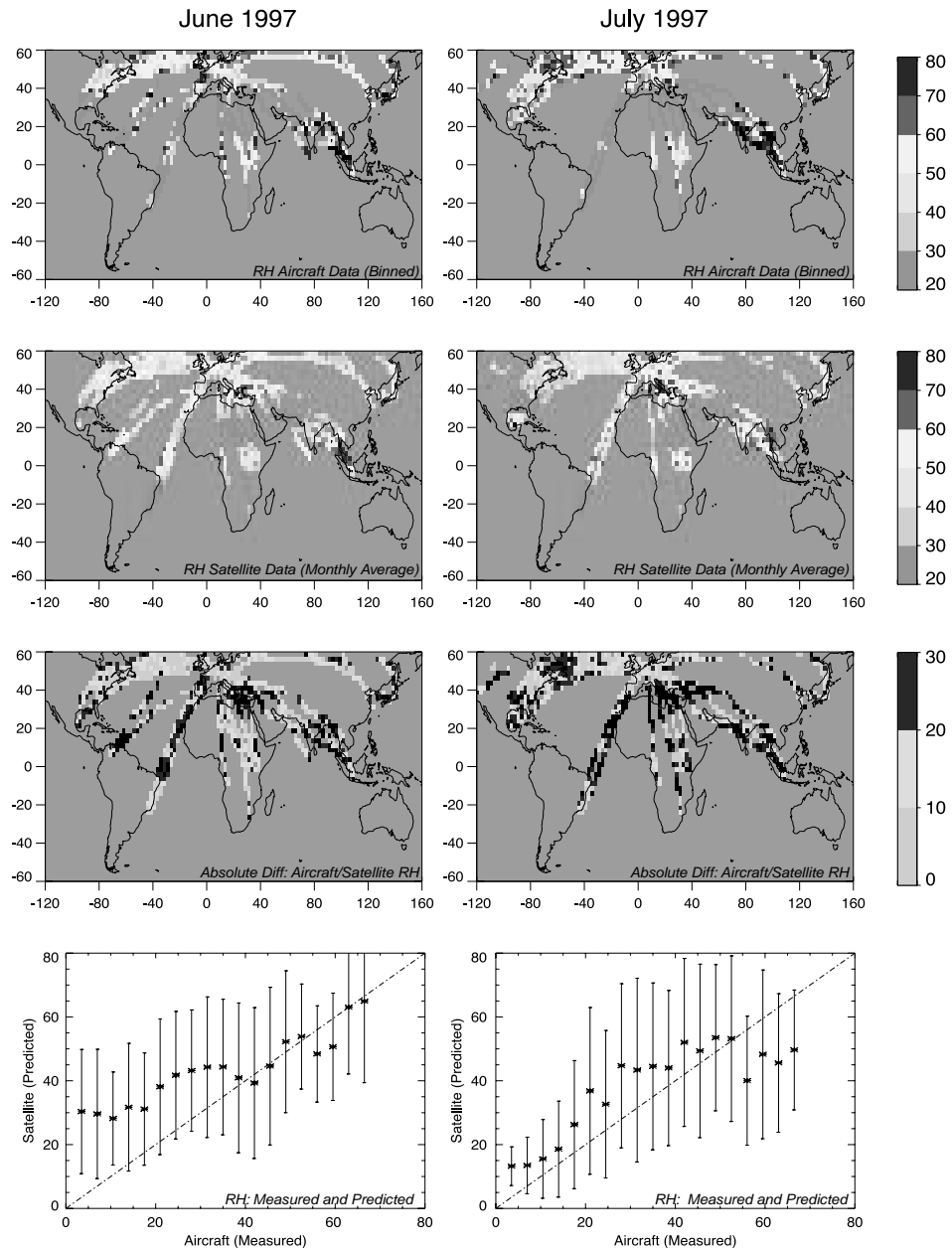


Figure 2.43 Comparison of the MOZAIC data and HIRS data that have been averaged into monthly mean, 2-degree latitude-longitude bins with the HIRS data only been sampled along the MOZAIC flight tracks. Shown are the monthly mean MOZAIC data, the HIRS satellite data, the absolute difference between the two, and a scatter plot of the two data sets.

### 2.3.8 MLS tropospheric comparisons

The MLS upper tropospheric humidity is compared with *in situ* measurements by frostpoint hygrometers, Vaisala radiosondes, and MOZAIC. The basis for assessing the quality of the MLS measurements is "coincident" comparisons. The *in situ* instrument suite considered here has incomplete global coverage and direct comparisons when both instruments sampled almost the same air provide the best results. Climatological or other average comparisons yielded larger differences, indicating differences in spatial and temporal sampling between these instruments are a dominant component of the measurement discrepancies noted between the instruments.

The MLS, a remote sensor, reports water vapour measurements that are an average over a volume  $100 \times 100 \times 3 \text{ km}^3$  (surface by height). The MLS forward model includes vertical but not horizontal gradients, hence there will be additional errors. The MLS measurement is not necessarily a simple volume average. The other techniques used here for validation measure water vapour *in situ* and give a one-dimensional string of data (vertically in the case of frostpoint and radiosondes and horizontally for MOZAIC). Nevertheless, with a sufficient number of coincidences it should be possible to determine the measurement biases between MLS and the other techniques.

Coincidences between MLS and the other techniques are found and their measurements are compared in a scatter plot. A simple linear fit with a correlation factor is computed for the fit. The correlation is a measure of how well the two measurement systems track each other. Random measurement noise tends to reduce the number toward zero, as will spatial and temporal atmospheric variability. Using the theoretical precision estimates for MLS (the random noise component), one would expect to get roughly 0.9, 0.9, 0.9, 0.6 correlation for 147, 215, 316, and 464 hPa levels. The MLS data can be used to estimate its de-correlation over distance, but this will include random noise as well. The MLS makes measurements approximately every 450 km. The correlation of the data with itself  $4^\circ$  later is 0.85, 0.62, 0.47, and 0.43 for 147, 215, 316 and 464 hPa respectively. Time coincidence is harder to measure for MLS because orbit repeats take five days. Twenty-four hours later, the orbit is shifted  $5^\circ$  in longitude and zero in latitude. At the four levels and 1 day later, the correlations are 0.67 at 147 hPa, 0.58 at 215 hPa, 0.44 at 316 hPa, and 0.38 at 464 hPa. These values, including a  $5^\circ$  spatial (longitude) difference, are only slightly worse than spatial de-correlation.

#### **NOAA-CMDL balloon frostpoint hygrometer comparisons**

The NOAA-CMDL frostpoint hygrometer measures the frostpoint temperature and is considered accurate to 10% (section 1.1.1). The data are available at 250 m intervals and are converted to relative humidity over ice for the comparisons. Data from Boulder, Colorado ( $40^\circ\text{N}$ ,  $105^\circ\text{W}$ ), Hilo, Hawaii ( $19^\circ\text{N}$ ,  $155^\circ\text{W}$ ), Lauder, New Zealand ( $45^\circ\text{S}$ ,  $169^\circ\text{E}$ ), McMurdo, Antarctica ( $77^\circ\text{S}$ ,  $166^\circ\text{E}$ ) and the Central Equatorial Pacific Experiment (CEPEX) were available for this assessment. There are limited NOAA-CMDL frostpoint hygrometer data available, and for the purposes of comparison, coincidence criteria of 5.0°, 3.0°, and 6.0 hours for longitude, latitude, and time are used. This produces 16 unique hygrometer profiles for comparison.

Figure 2.44 shows a summary scatter plot between MLS and the NOAA-CMDL hygrometer with a best-fit line through the points. The data at 316 and 464 hPa levels were screened for bad retrieved values. There are more than 16 points per level because sometimes MLS had two or more measurements coincident with the frostpoint measurement. The higher resolution frostpoint data was averaged vertically with an MLS averaging kernel function to give a better estimate of what MLS should measure. The linear correlation coefficients for each level are consistent with that expected for this degree of coincidence at all levels.

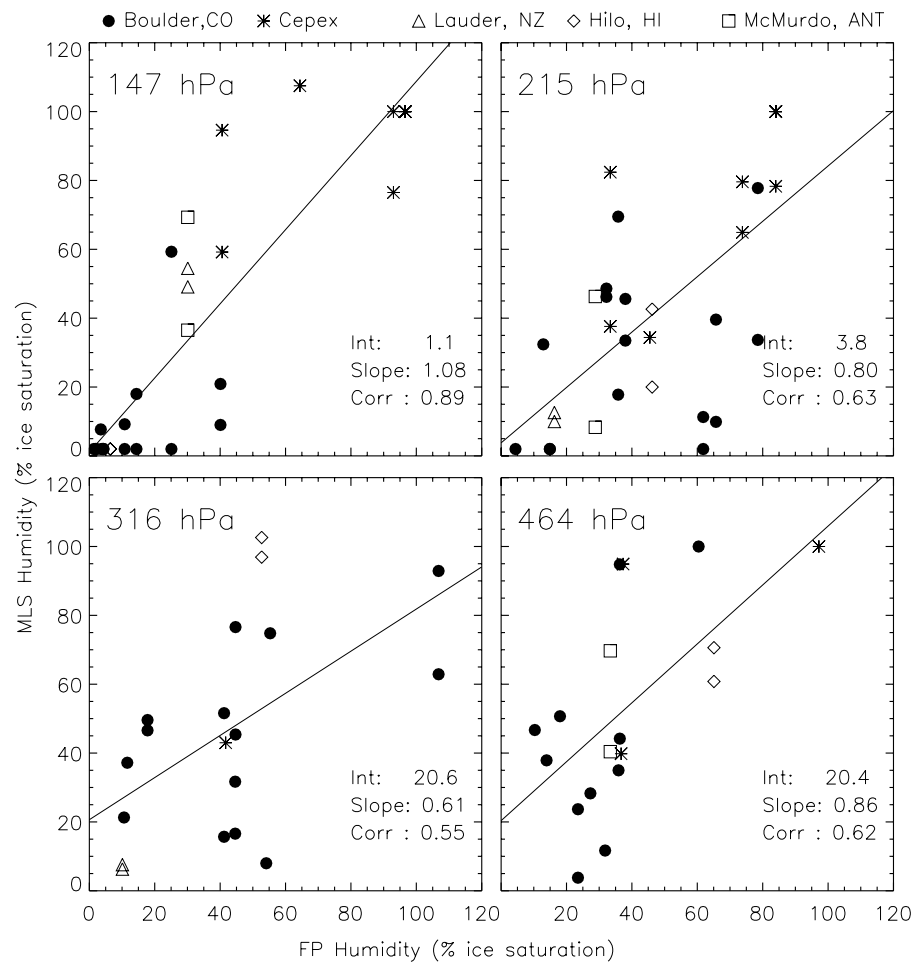


Figure 2.44 Scatter plot summary of all the MLS and NOAA-CMDL frostpoint hygrometer coincidences. The slope and correlation coefficient are supplied.

### Operational radiosondes

The global radiosonde network provides a rich supply of coincidence opportunities. The data are archived into files binned by Universal Time (UT) in six-hour increments (00, 06, 12, and 18 UT) for each day. Data for the entire UARS mission are available from the UARS Central Data and Handling Facility. Reporting stations are required to provide data (when available) on pre-defined mandatory levels (1000, 850, 700, 500, 400, 300, 250, 200, 150-hPa, and several levels above). The data on these levels are used in this analysis. Data on intermediate significant levels are also supplied, but for data processing simplicity, the intermediate data are not used. Relative humidity is archived as dew point depression. The dewpoint data are converted to water vapour pressure using the Wexler expression in [Elliott and Gaffen, 1991]. Water vapour pressure is converted to ice relative humidity ( $RH_i$ ) or mixing ratio based on the Goff-Gratch expression for ice saturation vapour pressure [List, 1949] using the radiosonde temperature measurement.

Several radiosonde types are used around the world. Based on the characteristics of the humidity sensors as discussed in Chapter 1, for MLS validation purposes only the Vaisala radiosonde is used. The Vaisala *Humicap* detector comes in three versions, RS-80 A, H, and RS-90. The A-sensor has been in use the longest, but at temperatures colder than about  $-30^\circ\text{C}$  has a significant dry bias [Miloshevich *et al.*, 2000; also see section 2.2.3]. The RS80-H and RS-

90 significantly correct this problem. The archived sonde files do not indicate which of these types are used; however, widespread use of the H and RS-90 types only started to be implemented in 1993 and 2000 respectively. For the 1991-1994 period considered here, only the A-sensor was in widespread use.

MLS made over 1300 measurements per day nearly daily from 1991 through 1994. Temporal coverage is intermittent thereafter. A coincidence is defined as  $1^\circ$  by  $1^\circ$  in latitude and longitude (or  $\sim 110 \text{ km}^2$ ) and 3 hours UT. Tighter coincidence criteria than these are not appropriate given the horizontal smearing present in the MLS data. This provides more than 3000 coincidences for comparisons. A four-panel scatter plot of the radiosonde versus MLS coincident measurements with best-fit lines using two different fitting procedures is shown in Figure 2.45. The thinner solid line shows the fit for a linear regression that assumes that the error is in the dependent variable (in this case MLS). The thicker solid line shows the fit using orthogonal distance regression, assuming that there is error in both variables. A retrieval screen for the MLS data at 316 and 464 hPa levels used to remove suspicious data. The correlation coefficients are in the neighbourhood of 0.5-0.7. Despite the relatively good coincidence, the correlation values are smaller than expected, indicating other factors are probably more important than coincidence issues. The results of the linear regression and orthogonal distance regression are quite different, and it is difficult to come to any conclusion about the relationship between radiosonde and MLS humidity from this analysis. The low correlations are a factor making the data sensitive to the type of regression used.

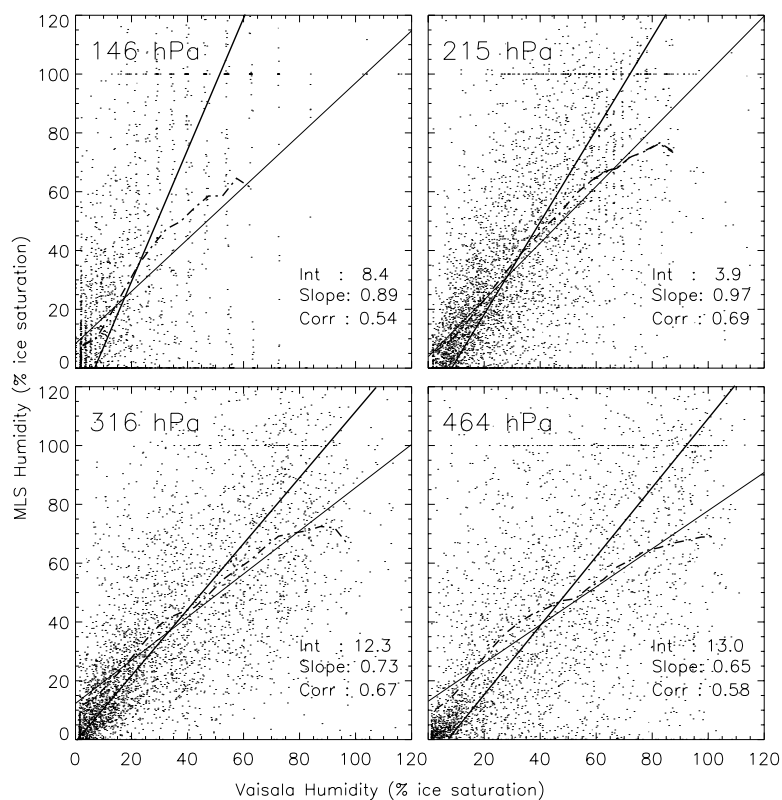


Figure 2.45 Scatter plot summary of all the MLS and Vaisala *Humicap* coincidences. The correlation coefficient and line fit parameters are annotated on the plot. The thin solid line is for the linear regression fit, the thick line for the orthogonal distance regression fit. The dashed dot line is a weighted smoothed average of the MLS values in 5 %RH<sub>i</sub> bins using the Vaisala measurements, indicating the linear regression fit is reasonable for these data.

## MOZAIC

The European programme MOZAIC began in 1993. MOZAIC consists of automatic measuring equipment installed on five Airbus A340 aircraft in normal airline service (see section 1.1.5). Data was made available from August 1994 to May 1998. The same coincidence criteria were used as that for comparing radiosondes: 1° longitude, 1° latitude, and 3 hours. Normally, several MOZAIC flight track measurements fall within a single MLS coincidence. Potential vorticity between -2.0 and 2.0 from the European Centre for Medium-Range Weather Forecasts (ECMWF) analyses that is supplied with the data, and level flight path were used to screen the coincident MOZAIC data. The coincident flight path data (temperature, pressure, and relative humidity) were averaged to yield a single value for comparing with the MLS measurement. The units were converted to ice relative humidity using the World Meteorological Organisation (WMO) relative humidity function supplied with the data and the MOZAIC temperature measurement. The MLS water vapour value was obtained from linearly interpolating its profile to the average MOZAIC pressure. The MLS 316 hPa upper tropospheric humidity was not quality screened because it has a very minor impact and reduces the number of coincidences. This produced 461 coincidences that are shown as a scatter plot in Figure 2.46. For clarity, bars indicating MLS error (typically 10-30%) and MOZAIC along track variability (typically 20-30%) are omitted.

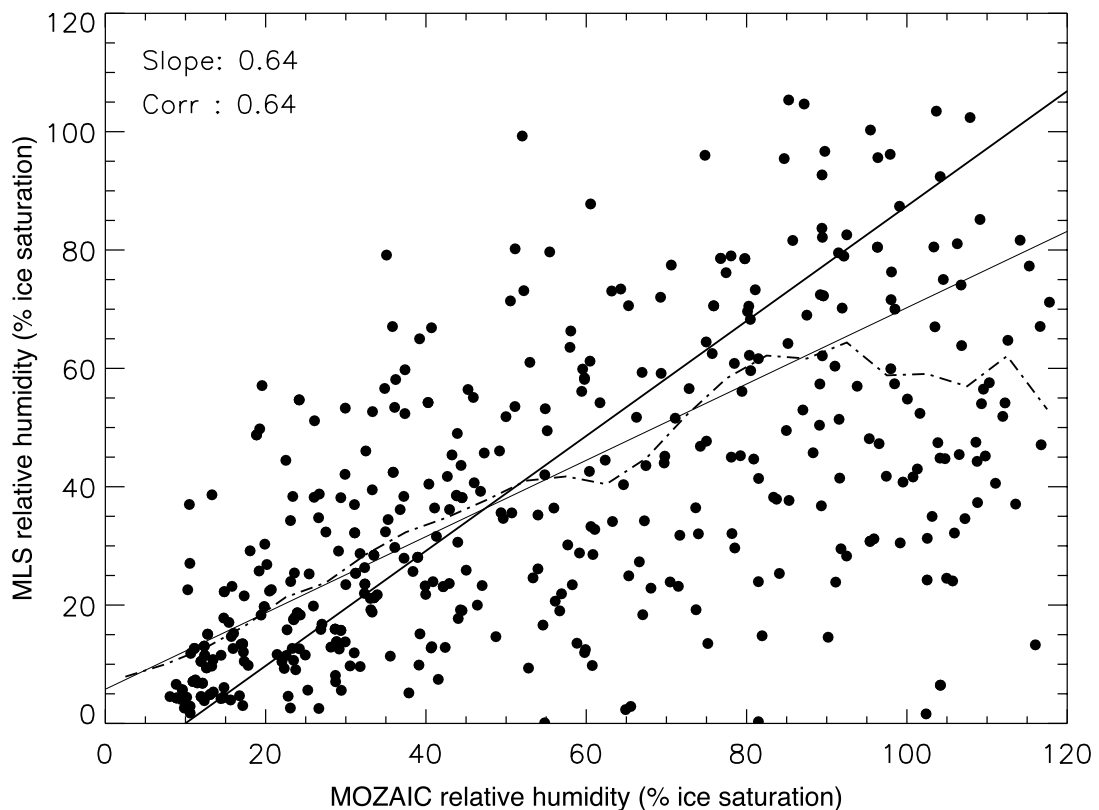


Figure 2.46 Scatter plot of coincident MOZAIC and MLS relative humidity measurements. The correlation coefficient and line fit parameters are annotated on the plot. The thin solid line is for the linear regression fit, the thick line for the orthogonal distance regression fit. The dashed dot line is a weighted smoothed average of the MLS values in 5% RHi bins using the MOZAIC measurements, indicating the linear regression fit is reasonable for these data.

---

The scatter between MLS and MOZAIC is considerable and comparable to the scatter seen when comparing radiosonde and frostpoint data to MLS. An important issue of course is that MOZAIC is a point vertical measurement whereas MLS has considerable vertical averaging. Also to be noted is that 77 out of 461 MOZAIC humidities are greater than 100%. As with the radiosonde data two fitting methods were applied to the data as shown in Figure 2.46. The fits were done to the 384 points where relative humidity is less than 100% is shown and gave a correlation of  $\sim 0.6$ . Again, the two different fitting methods give quite different results in the slope and intercept. The linear regression suggests that the MLS is drier than MOZAIC, but this is not clearly shown with the orthogonal distance regression fit. The typical MOZAIC measured atmospheric variability within the MLS footprint is consistent with the computed correlation factor. Including MOZAIC data greater than 100% RH<sub>i</sub> worsened the correlation significantly. For unknown reasons there is very poor correlation between MLS and MOZAIC RH<sub>i</sub> when the latter measures supersaturation.

The comparisons between MLS and the in-situ measurements do not provide strong constraints on the MLS data since they seem to be highly dependent on the fitting method that is used. Further work to understand these differences is needed.

---

## 2.4 Comparisons between satellite systems

### 2.4.1 ATMOS Comparisons

#### MAS

Figure 2.47 shows comparisons between ATMOS and MAS profiles from the ATLAS-3 mission. To account for atmospheric dynamical variability, the data (left panels) were sorted based on the scaled potential vorticity (sPV) derived from United Kingdom Meteorological Office (UKMO)-analysed winds (right panels) [Manney *et al.*, 1994]. Figures 2.47a and 2.47e show unweighted mean values of 10 middle latitude profiles for each instrument. Each ATMOS profile used in the average was paired with a MAS profile with comparable sPV. The data in Figures 2.47b and 2.47f are individual profiles obtained inside the developing vortex (proto-vortex). The data in Figures 2.47c and 2.48g are individual profiles more characteristic of middle latitude (extra-vortex/extra-tropical) air, and the data in Figures 2.47d and 2.47h are associated with tropical air. The comparisons of the individual profiles presented in Figures 2.47b-d suggest that the ATMOS data have a wet bias in the mesosphere relative to MAS, but the averaged profiles in Figure 2.47a indicate that this difference is not statistically significant. Figure 2.48a presents percent differences for the individual profiles shown in Figures 2.47b-d, and Figure 2.48b shows the average percent and RMS differences for the paired profiles used to produce Figure 2.47a. Figure 2.48 shows differences between ATMOS and MAS are generally within 5% in the middle and upper stratosphere. The variability is large, however, and differences between individual profiles are shown to be as high as 30% in the lower stratosphere and mesosphere, where ATMOS measurements tend to be larger.

#### HALOE

During the ATLAS-3 mission, ATMOS and HALOE were making observations in the same latitude region of the Northern Hemisphere. Figure 2.49a shows unweighted mean values of 10 middle latitude profiles for each instrument. Each ATMOS profile used in the average was paired with a HALOE profile with comparable sPV. Figures 2.49b-d show comparisons of individual ATMOS/ATLAS-3 sunset occultations with near coincident HALOE Version 19 sunset and sunrise occultations. Figures 2.49e-h show the sPV profiles corresponding to the ATMOS and HALOE profiles presented in Figures 2.49a-d. The ATMOS profiles are the same as those plotted in Figure 2.47 for comparison with MAS observations and represent observations from inside the proto-vortex (Figures 2.49b and 2.49f), at middle latitudes (Figures 2.49c and 2.49g), and in the tropics (Figures 2.49d and 2.49h). Shapes of the profiles in Figures 2.49a-d are very similar, even in the upper mesosphere. In particular, there is a match in the vertical registration of these profiles.

The percent differences between the individual ATMOS and HALOE observations shown in Figures 2.49b-d are presented in Figure 2.50a. Figure 2.50b shows the percent and RMS differences for the 10 paired profiles averaged for Figure 2.49a. Both panels show that the differences between these instruments are generally less than 10%, and are of order 5% (ATMOS larger) between 100 and 1 hPa; the RMS differences are slightly larger. Greater differences (as much as 30%) are observed in the mesosphere and lower stratosphere. Given the large random error, however, the systematic differences are not statistically significant. These differences are smaller than in a previous comparison of ATMOS Version 2 data with HALOE Version 17 observations, which showed that the ATMOS values were systematically larger than those from HALOE in the middle stratosphere by 10-15% [Harries *et al.*, 1996].

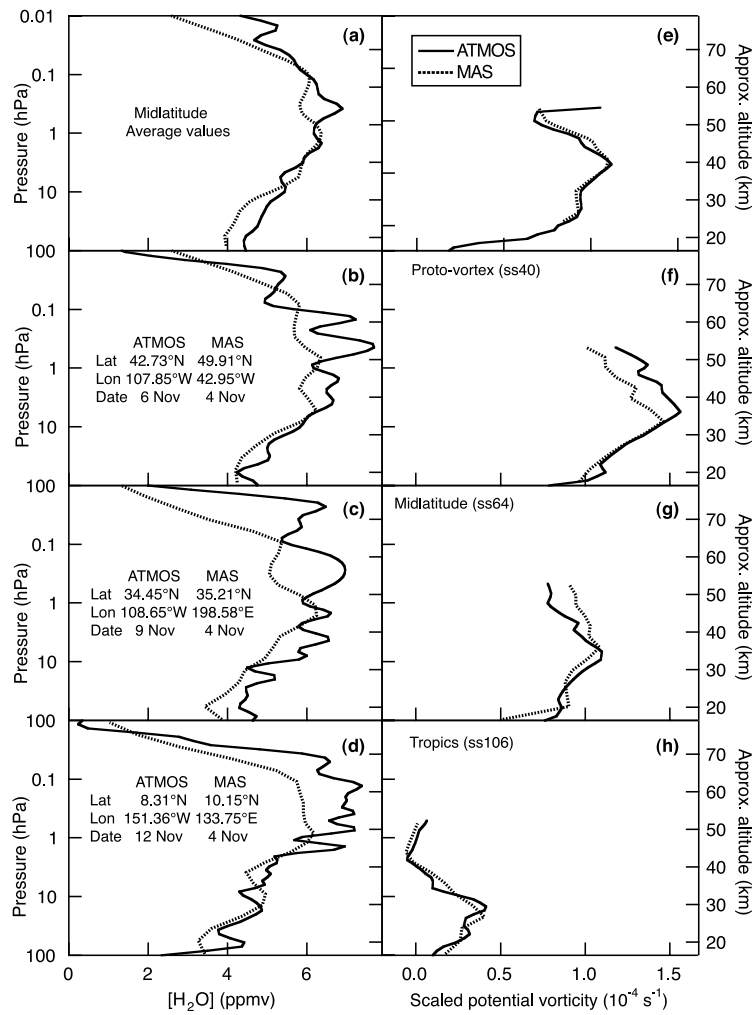


Figure 2.47. Comparison of ATMOS Version 3 with MAS observations of H<sub>2</sub>O. The volume mixing ratio of H<sub>2</sub>O is plotted as a function of pressure. The left panels (a-d) show ATMOS Version 3 (solid lines) and MAS (dotted lines) observations. The right panels (e-h) show the scaled potential vorticity corresponding to the measurements.

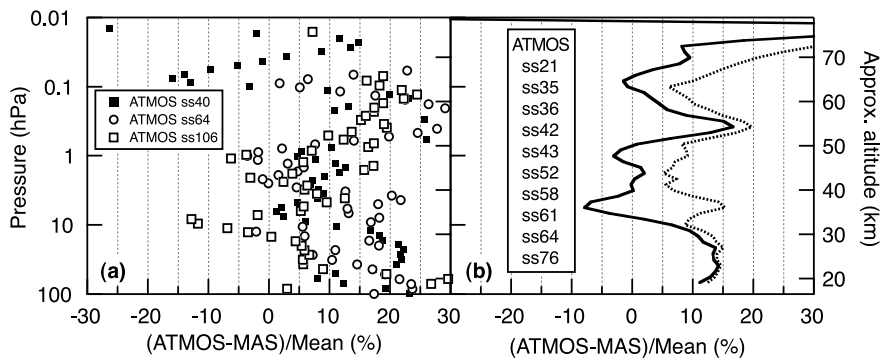


Figure 2.48 Percent differences between ATMOS Version 3 and MAS observations of H<sub>2</sub>O. (a) The percent differences for the observations compared in Figure 2.47 are shown as a function of pressure. (b) The (unweighted) average percent differences for the 10 profile pairs averaged for Figure 2.47a (solid line) are shown with the calculated RMS difference (dotted line).

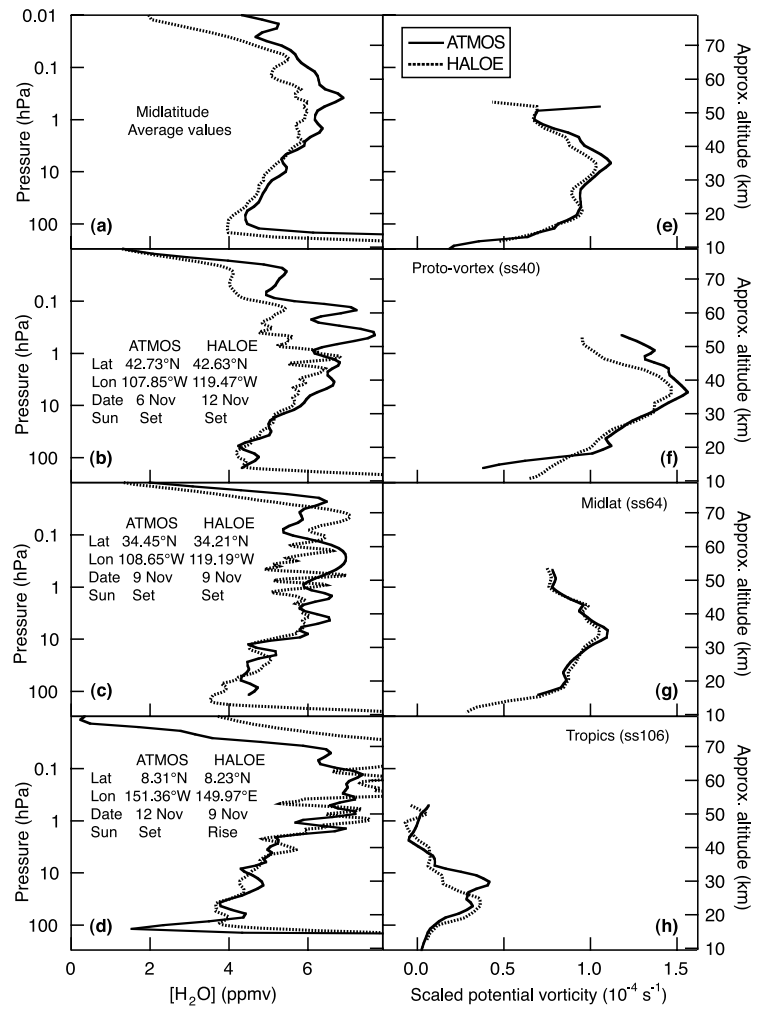


Figure 2.49 Comparison of ATMOS Version 3 with HALOE observations of H<sub>2</sub>O. The volume mixing ratio of H<sub>2</sub>O is plotted as a function of pressure. The left panels show ATMOS Version 3 (solid lines) and HALOE Version 19 (dotted lines) retrievals. The right panels show the scaled potential vorticity corresponding to the measurements.

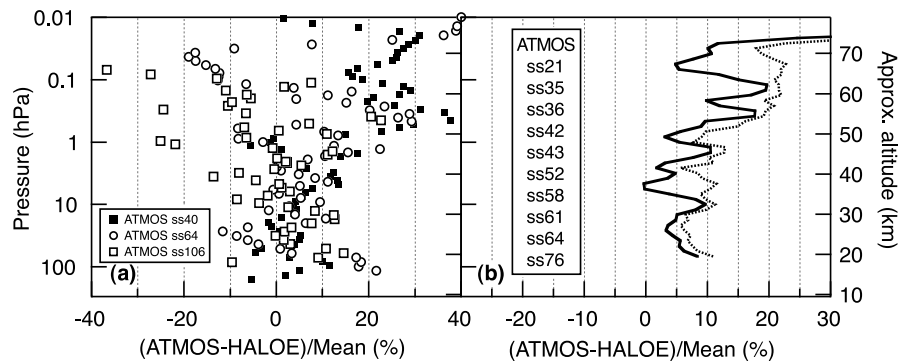


Figure 2.50 Percent differences between ATMOS Version 3 and HALOE Version 19 retrievals of H<sub>2</sub>O. (a) The percent differences for the observations compared in Figure 2.49 are shown as a function of pressure. (b) The (unweighted) average percent differences for the 10 profile pairs averaged for Figure 2.49a (solid line) are shown with the calculated RMS difference (dotted line).

## MLS

The left panels of Figure 2.51 show a comparison of ATMOS Version 3 data with MLS prototype Version 0104 observations [Pumphrey, 1999]. The ATMOS data shown represent mean values from sunset occultations at southern middle latitudes and were made during ATLAS-1 (25 March-2 April 1992) and ATLAS-2 (8-16 April 1993). The MLS data were similarly averaged and collected during the same time period and in the same latitude range. The data were sorted, as above, based on scaled potential vorticity, mean values of which are displayed in the right panels of Figure 2.51. The error bars represent one standard deviation of the mean. The data in the bottom set of panels is from 1993, and the other 2 sets of panels show data from 1992, inside and outside the developing vortex. In all 3 cases, the ATMOS data exceed the MLS measurements. The difference is consistently  $\sim 0.6$  ppmv in the middle and upper stratosphere, but decreases in the mesosphere, as shown by Figure 2.52a. This offset is consistent with a recent comparison of MLS Version 0104 with ATMOS Version 2 water vapour observations [Pumphrey, 1999] and corresponds to a percent difference of  $\leq 15\%$  throughout most of the stratosphere, as demonstrated in Figure 2.52b. Below 15 hPa for the 1993 middle latitude case, only a single profile was available from ATMOS; hence, the large fluctuation in the differences between the data sets at  $\sim 20$  hPa for this case should be viewed with caution. The large variability in the lower stratosphere and mesosphere, on the other hand, is apparent in all 3 cases.

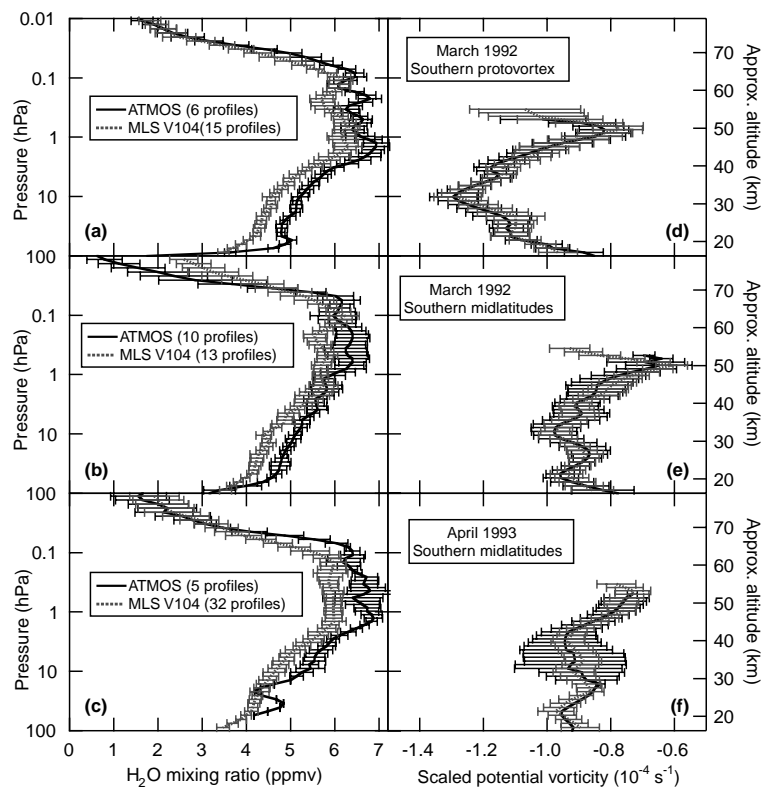


Figure 2.51 Comparison of ATMOS Version 3 with MLS Version 0104 retrievals of  $\text{H}_2\text{O}$  from southern middle latitudes during 1992 and 1993. Mean (unweighted) profiles are shown for MLS (dotted lines) and ATMOS (solid lines) occultations from (a) and (b) ATLAS-1 and (c) ATLAS-2. (a)-(c) The (unweighted) average volume mixing ratio of  $\text{H}_2\text{O}$  is plotted as a function of pressure. (d)-(f) The mean scaled potential vorticity corresponding to the measurements is also shown. The error bars represent one standard deviation ( $1\sigma$ ) of the unweighted mean.

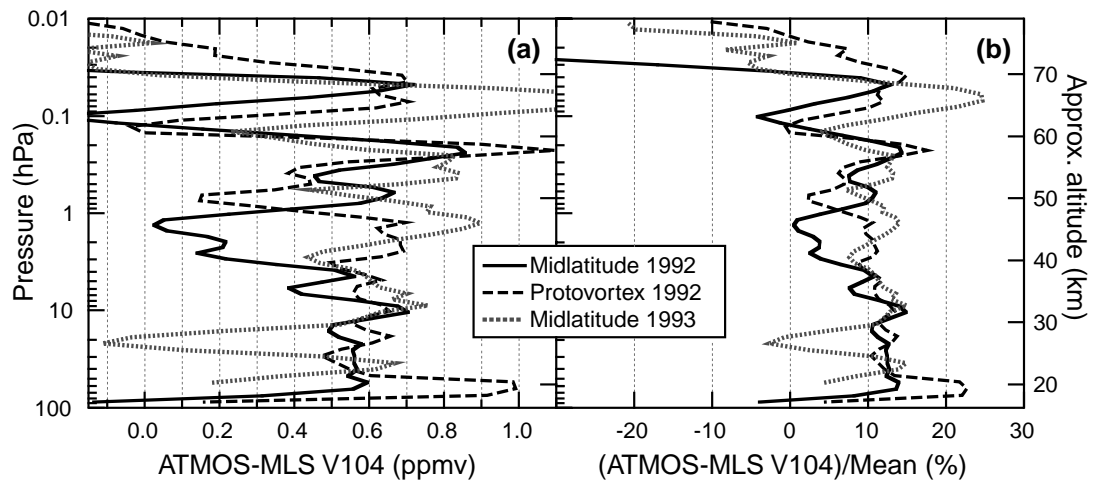


Figure 2.52 Differences between ATMOS Version 3 and MLS Version 0104 retrievals of  $\text{H}_2\text{O}$ . The absolute differences (a) and the percent differences (b) of the mean profiles compared in Figure 2.51 are shown as a function of pressure.

#### 2.4.2 MLS with HALOE

In this section, we show a comparison between MLS and HALOE. The comparison was done by taking every HALOE profile, finding the closest MLS profile, and taking the difference. These differences were then averaged, both for all latitudes and in  $10^\circ$  latitude bins. The comparison was carried out for the period between 12 October 1991 and 15 April 1993 covering the entire period for which both instruments were taking water vapour data. The global mean difference, indicating the bias between the two instruments, is shown in Figure 2.53 (right panel) as a solid line. Throughout the stratosphere and mesosphere this bias is small (0.1–0.3 ppmv) and negative (MLS drier than HALOE). In the upper mesosphere, MLS has a large dry bias compared to HALOE.

The systematic bias between the two instruments is not entirely independent of latitude. Figure 2.54 shows a contour plot of the difference as a function of latitude and height. In the mid-stratosphere and above, the bias depends only on altitude, but in the lower stratosphere, a strong latitude dependence is evident. In middle latitudes, MLS is 0.3–0.5 ppmv drier than HALOE, while over the equator, MLS is up to 0.3 ppmv wetter than HALOE.

Inspection of the differences as a function of time (not shown) suggests that the positive bias found in the equatorial lower stratosphere was largest at the beginning of the period, and had vanished or become slightly negative by the beginning of 1993. It is likely that it is caused by the effect of Mount Pinatubo aerosol on the HALOE data retrieval. In the absence of an unusual aerosol loading, the MLS-HALOE bias in the lower stratosphere would probably be about 0.4 ppmv, independent of latitude.

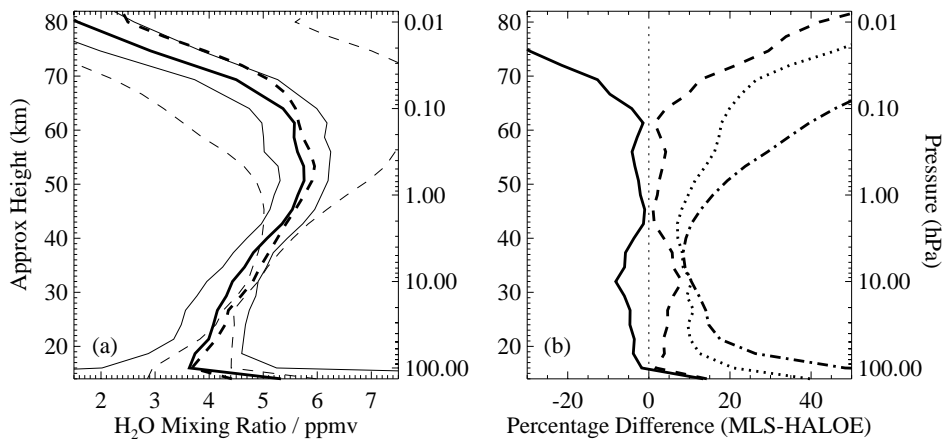


Figure 2.53 Panel (a): mean MLS (V0104) profile (solid lines) and mean HALOE (V19) profile (dashed lines) for the period 12 October 1991 to 15 April 1993. Thick lines are the profiles, thin lines indicate the mean single-profile uncertainty supplied with each data set. Panel (b): difference between MLS (V0104) and HALOE (V19) data. The solid line is the mean difference. The dotted line is the root-mean-square difference. This is generally much larger than the absolute value of the mean difference (shown dashed) indicating that random errors are a large part of the difference between the two instruments. In the stratosphere the RMS difference is similar to, or smaller than, the combined quoted uncertainties of the two instruments (shown as a dot-dash line) indicating that the quoted uncertainties are consistent with the differences between the instruments. In the mesosphere the quoted errors for the HALOE data are much larger than the MLS-HALOE difference.

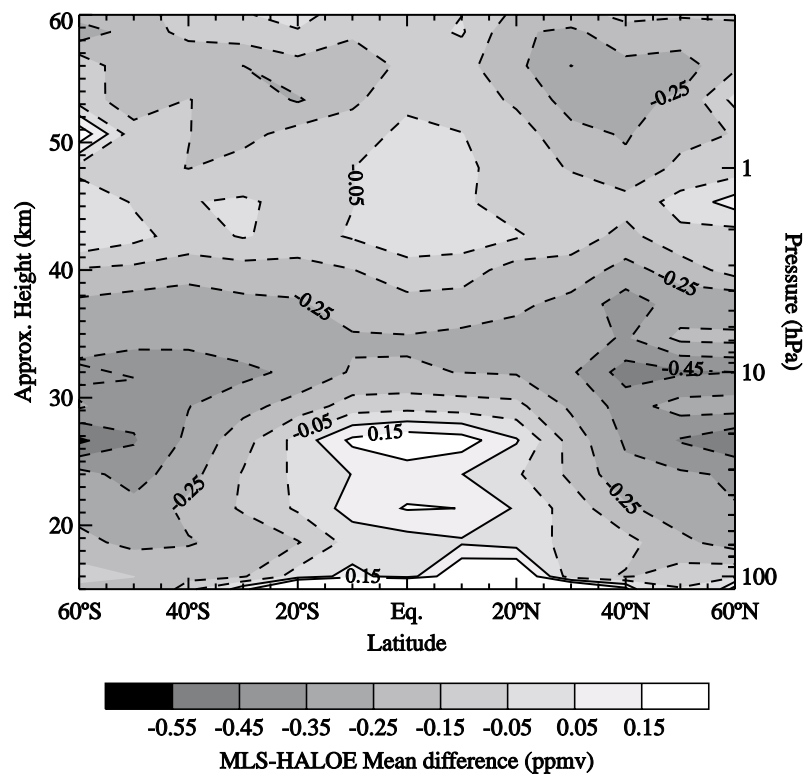


Figure 2.54 Contour plot of the mean difference between MLS and HALOE. Positive values (solid contour lines) imply that MLS is “wetter” than HALOE, negative values (dashed contour lines) imply that HALOE is “wetter” than MLS.

### 2.4.3 POAM III with HALOE

The POAM III satellite instrument was launched in March 1998 and is currently operational. During this time period the only other satellite-based stratospheric water vapour measurements available for comparisons are those obtained from HALOE. In this section, we compare POAM III Version 2 and HALOE Version 19 water vapour retrievals for 1998 and 1999. Lucke *et al.* [1999] shows the POAM III and HALOE measurement coverage in both hemispheres, indicating that POAM III-HALOE measurement coincidences occur in the spring and summer in each hemisphere. The times, location, and number of pairs of coincident profiles obtained since the launch of POAM III using coincidence criteria of 5° latitude, 12° longitude, and 12 hours are given in Table 2.2. As example comparisons, Figure 2.55 shows the results for the 11-12 June 1998 Northern Hemisphere orbit coincidence period. The left panel compares the average POAM III and HALOE water vapour mixing ratio profiles for the coincidence period. The middle panel gives the mean difference of the individual coincident pairs ( $(1/N)\sum(\text{POAM}-\text{HALOE})/[(\text{POAM}+\text{HALOE})/2]$ ) expressed in percent. The right panel shows the standard deviation ( $\sigma$ ) of the mean difference, which is a measure of the combined random error of both instruments and atmospheric variability. The error bars on the centre plot are given by  $\sigma/(N-1)^{-1/2}$ , where N is the number of coincident pairs.

**Table 2.2.** POAM III – HALOE Coincidence Periods

<b>Northern Hemisphere</b>		<b>Southern Hemisphere</b>			
<i>Period</i>	<i>Number of Coincidences</i>	<i>Period</i>	<i>Number of Coincidences</i>	<i>Avg. Lat.</i>	
				<i>POAM</i>	<i>HALOE</i>
8-10 May 1998	29			59.7°N	62.7°N
11-12 Jun 1998	27			55.3°N	58.4°N
18-20 Jul 1998	14			55.7°N	59.7°N
19-21 Aug 1998	24			61.7°N	64.8°N
		8-14 Nov 1998	82	70.8°S	70.4°S
		1-8 Dec 1998	116	65.2°S	65.5°S
		15-24 Jan 1999	103	64.6°S	65.7°S
		9-15 Feb 1999	72	71.1°S	72.3°S
16-24 Mar 1999	123			67.0°N	64.3°N
4 -6 May 1999	28			60.6°N	63.6°N
6 Jun 1999	7			55.9°N	60.3°N
14 Jul 1999	5			55.1°N	58.7°N
15-17 Aug 1999	16			60.6°N	62.5°N

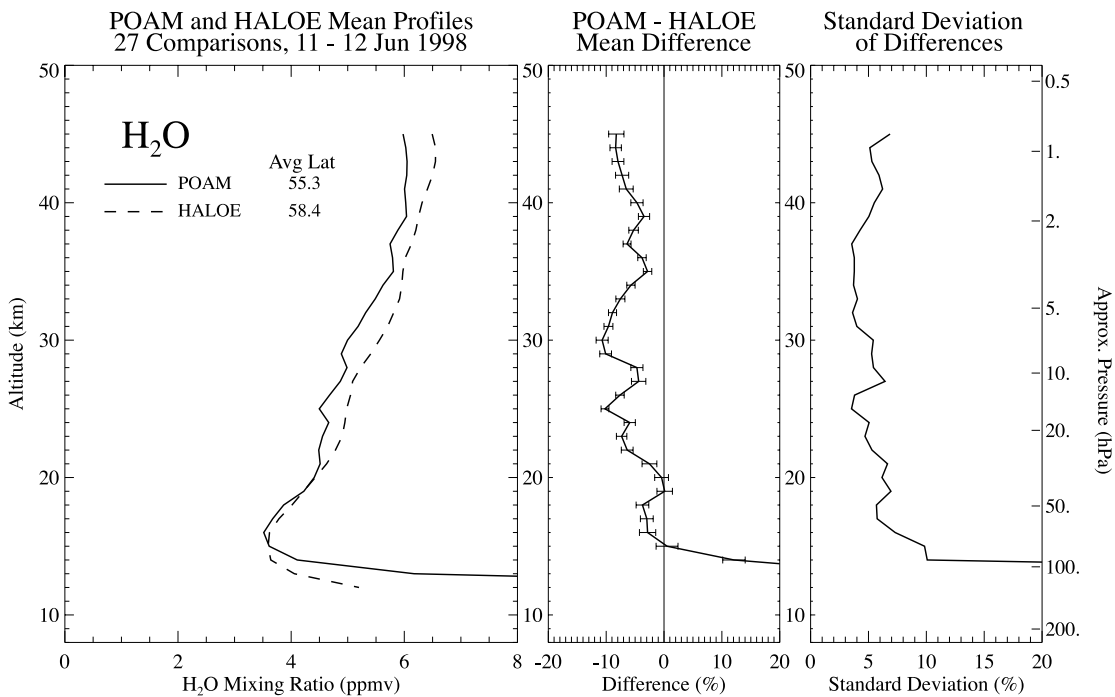


Figure 2.55 (left panel) Mean POAM III and HALOE water vapour mixing ratio profiles for the indicated coincidence period. (middle panel) Mean of the POAM III–HALOE individual profile differences expressed in percentage relative to the POAM III/HALOE average. Error bars are the  $\pm 1\sigma$  standard errors of the mean (see text). (right panel) Standard deviation ( $1\sigma$ ) of the mean differences is shown in the middle panel.

The overall mean differences for both hemispheres are given in Figure 2.56. The comparisons show that at nearly all altitudes above 15 km, POAM III and HALOE are within 10% of each other. The divergence below 15 km appears to be the result of instrument differences in resolving the hygropause. There is also evidence of a hemispheric bias, with POAM III mixing ratios tending to be biased low with respect to HALOE in the Northern Hemisphere, and high in the Southern Hemisphere. This could be indicative of a sunrise/sunset bias in the POAM III water vapour retrievals (all POAM III Northern Hemisphere measurements are obtained during satellite sunrise and all Southern Hemisphere measurements during sunset). However, as shown in Table 2.2, the HALOE measurements are systematically poleward of the POAM III measurements in the Northern Hemisphere comparisons. This occurs because of systematic gaps in the HALOE measurement coverage, near 50° latitude, which have occurred since April 1997 as a consequence of power sharing issues on board UARS. Climatologically, water vapour tends to increase with latitude in the Northern Hemisphere stratosphere [Randel *et al.*, 1998]. This latitudinal gradient will act to mitigate the apparent hemispheric bias in Figure 2.56. As a rough estimate of the magnitude of the effect, the UARS climatology developed by Randel *et al.* [1998] indicates that the water vapour latitudinal gradient may explain roughly half of the apparent hemispheric bias.

Finally, we note that the POAM III–HALOE differences exhibited in this report are considerably smaller than those shown in the HALOE Version 18 and POAM III Version 1.4 comparisons given in Lucke *et al.* [1999], which showed a 10–30% POAM high bias. This is the result of the fact that a recent analysis by Giver *et al.* [2000] indicates that there is a 14.4% error in the line strengths of the water vapour absorption lines in the 900 nm region in the HITRAN

database used in the POAM III retrieval algorithm. The inclusion of this correction in the POAM III version 2 retrievals shown here reduces water vapour mixing ratio by  $\sim 14.4\%$  in the upper stratosphere, and by  $\sim 20\text{-}25\%$  in the lower stratosphere.

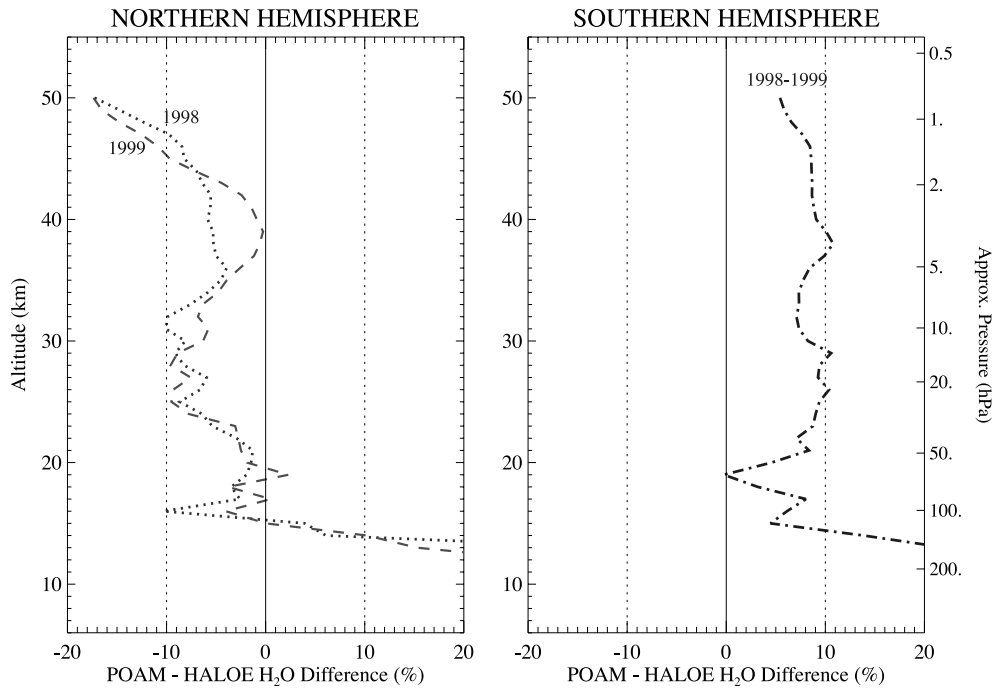


Figure 2.56 The overall mean POAM III–HALOE differences for all coincidences obtained each year (the coincidences included in these comparisons are given in Table 2.3) in the Northern Hemisphere (left panel) and Southern Hemisphere (right panel).

**Table 2.3.** ILAS-HALOE coincidence within 300 km in distance and 12 hours in time.

Period	Number of Coincidences	Average Latitude & Sunrise/Sunset <sup>1</sup>				Hemisphere <sup>2</sup>
		ILAS		HALOE		
19-24 November 1996	41	-68.7	SS	-68.9	SR	SH
10-16 December 1996	38	-64.9	SS	-65.6	SS	SH
28-31 January 1997	22	-68.6	SS	-69.6	SR	SH
18-20 February 1997	21	-75.6	SS	-74.8	SS	SH
25 March–1 April 1997	54	68.5	SR	68.1	SS	NH
13-14 May 1997	12	61.2	SR	61.1	SR	NH
16-18 June 1997	13	57.0	SR	57.2	SS	NH

Total number of coincidences: 201 (SH 122; NH: 79)

<sup>1</sup> SR: Sunrise from satellite; SS: Sunset from satellite

<sup>2</sup> SH: Southern Hemisphere; NH: Northern Hemisphere

## 2.4.4 ILAS with HALOE

In this section, ILAS Version 4.20 and HALOE Version 19 water vapour retrievals for the entire ILAS period between November 1996 and June 1997 are compared. Coincidence latitudes are restricted by the ILAS high latitude coverage ranging from 57 to 73 degrees in the Northern Hemisphere and from 64 to 88 degrees in the Southern Hemisphere, depending on the season (see section 1.4.9). The times, locations, and number of pairs of coincident profiles using a coincidence criterion of 300 km in distance and 12 hours in time are given in Table 2.3.

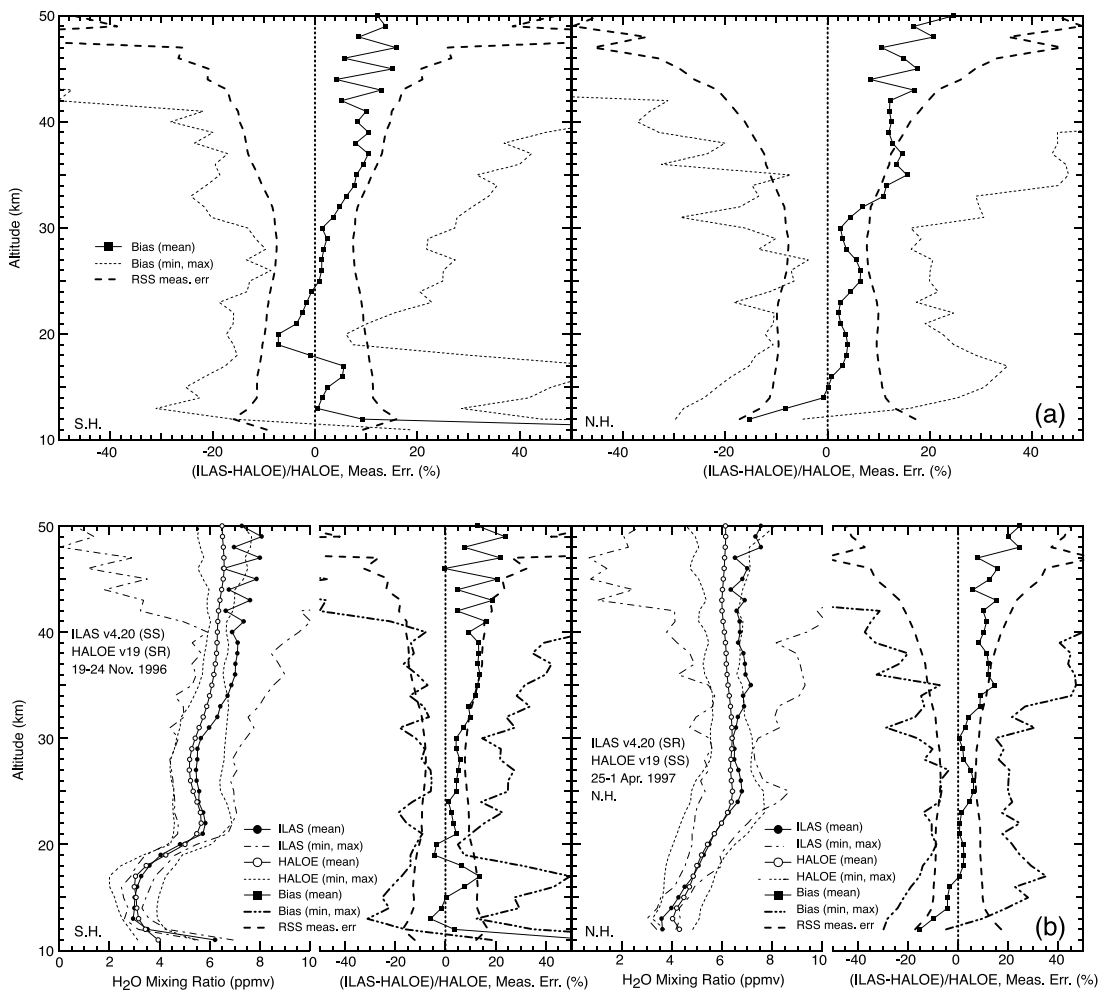


Figure 2.57 Mean, minimum, and maximum of  $(\text{ILAS}-\text{HALOE})/\text{HALOE}$  expressed in percentage for (a) left panel: 122 coincidences in the Southern Hemisphere, right panel: 79 coincidences in the Northern Hemisphere. “RSS meas. err.” shows average of root sum square of ILAS and HALOE measurement errors. (b) left panel: Mean, minimum, and maximum of ILAS and HALOE water vapour mixing ratio profiles for 41 comparisons of Southern Hemisphere measurements from 19–24 Nov. 1996, right panel: for 54 comparisons of Northern Hemisphere measurements from 25 Mar.–1 Apr. 1997.

Coincidences occur in the Southern Hemisphere during November 1996 - February 1997, and in the Northern Hemisphere during March - June 1997. All ILAS Northern Hemisphere measurements are obtained during satellite sunrise (SR), and all Southern Hemisphere measurements during sunset (SS). Figure 2.57a shows the results of all the ILAS-HALOE comparisons. Between 13 and 35 km, ILAS and HALOE are within 10% of each other. Above 35-km altitude, the range of the comparisons is large because the ILAS retrievals exhibit vertical oscillations that are larger than anticipated (see section 1.4.9). The larger range below 12 km is likely due to instrument differences in resolving the hygropause or other unknown factors. ILAS measurements are biased high relative to HALOE above 16 km in the Northern Hemisphere. For the Southern Hemisphere comparisons, ILAS measurements are biased high relative to HALOE at all levels except between 17 and 25 km.

Comparisons for the periods in each hemisphere with the maximum number of coincidences noted in Table 2.3 are shown in Figure 2.57b (19–24 November 1996, Southern Hemisphere; 25 March–1 April, Northern Hemisphere). The mean profiles of both ILAS and HALOE in Figure 2.57b show similar vertical structure, with minimum at ~15 km, maximum at ~22 km, and a secondary minimum at ~27 km. This is also seen in both instruments during the period of 10–16 December 1996 (not shown). The vertical structure for both instruments also agrees well during the Northern Hemisphere period shown in Figure 2.57b, with water vapour mixing ratio increasing with altitude up to about 25 km and then nearly constant above that level. Average differences throughout the bulk of the stratosphere are 10% or less.

#### 2.4.5 TOVS/HIRS upper tropospheric comparisons

##### MLS

At low latitudes, the sampling of upper tropospheric humidity with respect to ice (UTHi) by MLS and TOVS produces similar results on monthly mean grid boxes of 2.5° latitude by 2.5° longitude. Figure 2.58 shows a scatter diagram of these results for 4 months in 1991/1992. The figure also includes the mean and standard deviation estimate for averaging within 5% UTHi bins. The comparison was performed for the MLS layer at 316 hPa, corresponding to the peak of the HIRS channel 12 weighting function for moderate UTHi values. The correlations are 0.64 in October 1991, 0.51 in January 1992, 0.50 in April 1992, and 0.74 in July 1992. The overall range of HIRS UTHi is less in January and April, which partially explains the smaller correlations in these months. The standard deviations, however, remain very close to 18% for all months. The MLS only samples each grid box a few times per month while the HIRS samples each box 50-100 times. Thus, most of the scatter can be attributed to sampling as opposed to error between the observations. Averaging into 5% UTHi bins allows for the evaluation of the relative bias between MLS and TOVS as a function of the base UTHi. At low and high values of UTHi, the MLS shows a slightly low bias relative to TOVS, while in the middle range there is virtually no bias. The bias at the high and low ends is likely due to sampling, as there are only a very few coincident observations. HIRS and MLS therefore appear to produce highly comparable observations on monthly averaged time scales. At higher time and space scales, the comparisons show larger standard deviations and biases. This is both a reflection of sampling bias and differences in viewing geometry.

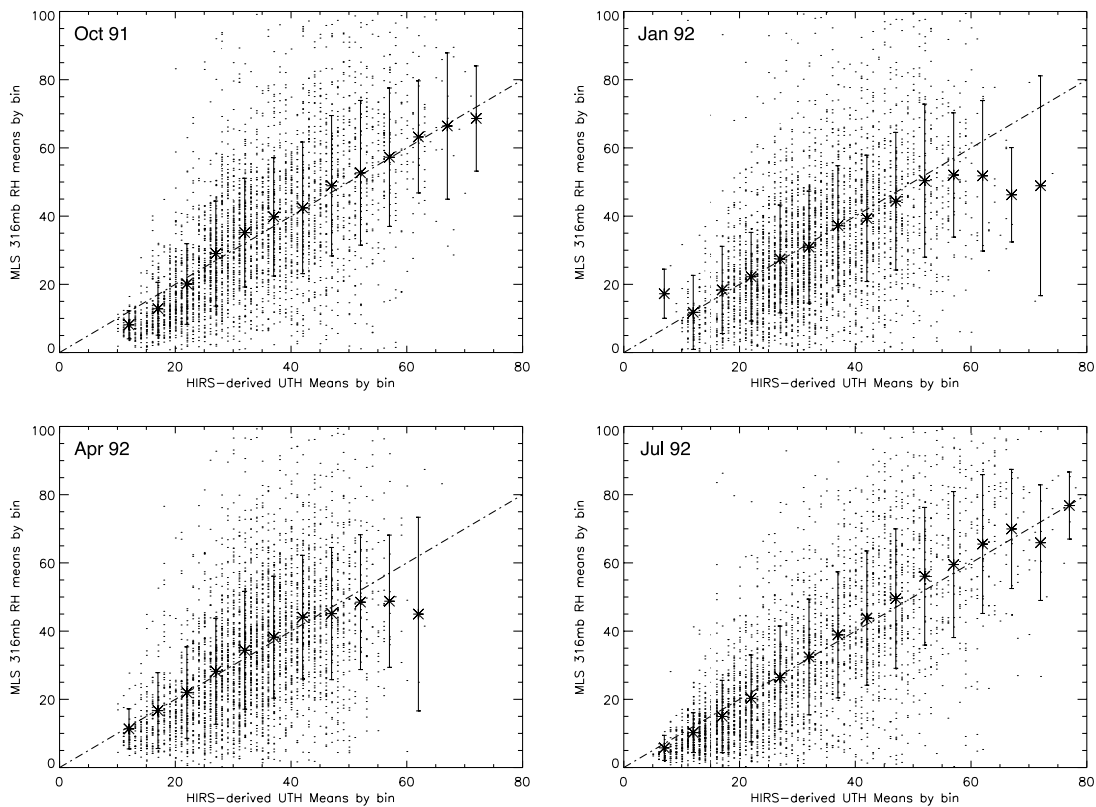


Figure 2.58 Scatter diagrams of TOVS-MLS comparisons. Grid boxes used were  $2.5^\circ$  latitude by  $2.5^\circ$  longitude. Comparisons were done between  $30^\circ\text{N}$  and  $30^\circ\text{S}$ .

## SAGE II

Since SAGE II uses solar occultation to retrieve water vapour, it is very sensitive to any cloud or high aerosol amount in its limb path. Monthly mean plots of SAGE II data on a  $2.5^\circ$  by  $2.5^\circ$  bin show that SAGE II does not retrieve water vapour in the centres of the seasonal monsoons or the Inter-tropical Convergence Zone. Simple zonal averaging of the SAGE II data is therefore not appropriate in the tropics.

SAGE II retrieves the water vapour mixing ratio at given pressure levels, therefore, integrated upper tropospheric water vapour between SAGE II levels ranging from 200 to 500 hPa was computed in order to perform comparisons between SAGE II and TOVS. These data were then binned on a  $2.5^\circ$  latitude by  $2.5^\circ$  longitude grid. Since the SAGE II is in units of integrated water vapour, these data must be compared with TOVS retrievals of integrated water vapour from the 3I method (described in Chapter 1). Figure 2.59 shows scatter plots between SAGE II and TOVS 3I at grid boxes common to both data sets for four months in 1988. The correlations vary by a large amount ranging from a low of 0.33 in January 1988, to a high of 0.64 in July 1988. The correlations were 0.49 in April 1988 and 0.52 in October 1988. The RMS deviations are moderate, ranging from 0.43 mm in January to 0.56 in July. In all months, the dynamic range of the SAGE II data is larger than that of TOVS 3I. This likely indicates a basic sampling mismatch between the two observational data sets. SAGE II sampling is apparently insufficient to properly characterise the variability of upper tropospheric water vapour captured by the TOVS sampling.

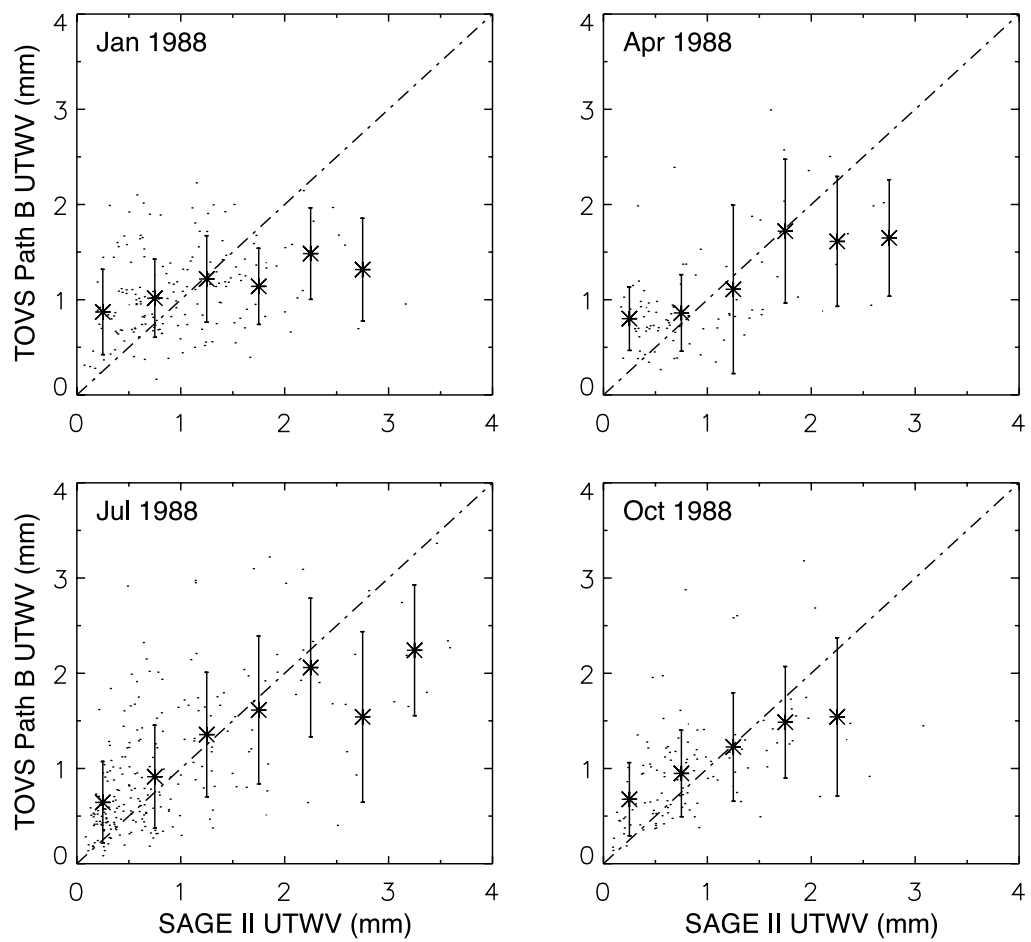


Figure 2.59 Scatter plots between SAGE II and TOVS 3I only at grid boxes common to both data sets for four months in 1988. SAGE II data are integrated between 200 and 500 hPa. Grid boxes used are 2.5° latitude by 2.5° longitude. TOVS 3I data processing is described in Chapter 1.

## 2.5 Comparisons of derived quantities

### 2.5.1 SAGE II and HALOE annual averages

Most of the comparisons shown in this chapter have considered measurement pairs nearly coincident in space and time. However, climatological comparisons are another means of assessing data quality and consistency between different data sets. Although the time period for which SAGE II water vapour data are available does not overlap with that for which HALOE is available, it is possible to compare annual averages. For one such comparison, SAGE II data were averaged from 1987 through 1990, and HALOE data were averaged from 1993 through 1999. The first year of each data set was left out of the averages to avoid periods with the heaviest aerosol. Heavy aerosol loading can negatively impact both retrievals. However, doing the same comparison including 1986 and 1992 in the SAGE II and HALOE averages respectively makes little difference. In constructing the SAGE II averages, the aerosol extinction filtering criteria given in *Rind et al.* [1993], where data is considered good if the  $1.02 \mu\text{m}$  extinction is less than  $5 \times 10^{-4}/\text{km}$ , was also used. Comparisons were done for both sunrise and sunset occultations. Differences were computed between  $50^\circ\text{N}$  and  $50^\circ\text{S}$ , where coverage for both instruments is most complete. The average percent difference, shown in Figure 2.60, is found to be a function of altitude, with SAGE II sunset measurements up to 15% smaller than HALOE below 25 km, and SAGE II sunset measurements larger than HALOE by up to 7% above 28 km. There is also a difference between SAGE II sunrise and sunset annual means, giving a profile of average of  $\sim 5\%$ , with sunrise occultation measurements larger. There is vertical structure to this difference too, with maximum values near 20 km.

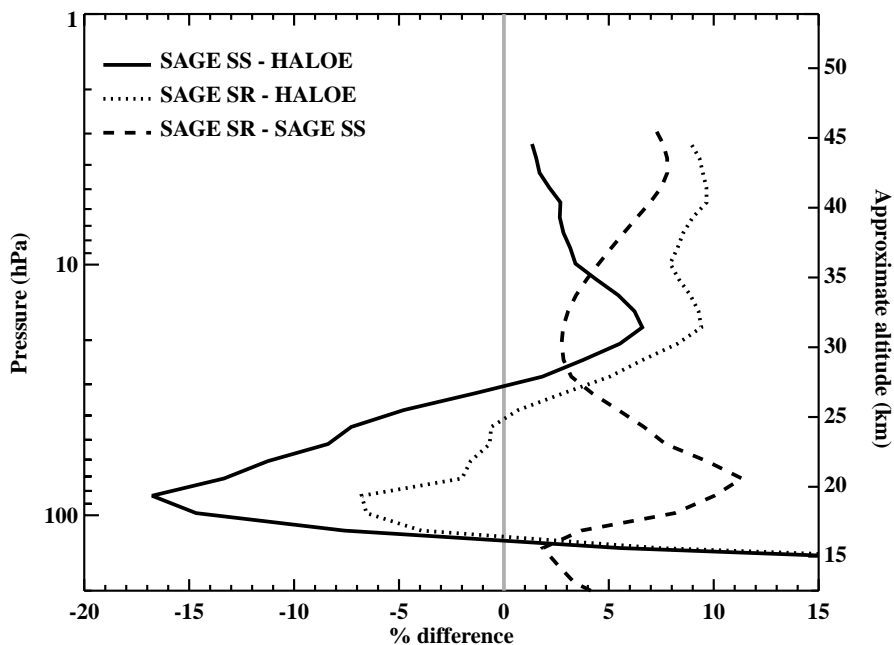


Figure 2.60 Percent differences between SAGE II and HALOE annual averages. The profile shown is the average difference between  $50^\circ\text{N}$  and  $50^\circ\text{S}$ . Differences presented are  $(\text{SAGE II} - \text{HALOE}) / \text{average}$  for the SAGE II sunset data (solid line), sunrise data (dotted line) and also for the SAGE II sunrise-sunset difference (dashed line).

For a second annual average comparison, eight years of HALOE data (1991-1999) and four years of SAGE II data (1987-1990) were binned according to equivalent latitude (based on potential vorticity) in  $4^\circ$  intervals, and on potential temperature ( $\theta$ ) levels (420-1300 K) nearest to the UARS standard pressures (six levels per decade of pressure). The HALOE analysis used UKMO-UARS potential vorticity (PV) and HALOE temperatures (based on NCEP analyses at these levels) for the binning calculation, while the SAGE II analysis used NCEP analyses for both PV and temperature. In this case, no aerosol-filtering criterion was used. Figure 2.61 shows the annual averaged HALOE and SAGE II water vapour as a function of equivalent latitude and potential temperature. The SAGE II results from sunset and sunrise occultations are presented separately. Overall features are similar between the three plots, with low mixing ratios near the tropical tropopause, and larger values at higher altitudes and latitudes, a consequence of water vapour production due to methane oxidation. The sunrise-sunset difference with the SAGE II data is apparent, with sunrise results  $\sim 0.2$ - $0.4$  ppmv larger than sunset. The SAGE II sunset annual mean is similar to that of HALOE at middle latitudes, but  $\sim 0.2$ - $0.4$  ppmv smaller than HALOE in the tropics. There are differences between HALOE and SAGE II in regards to vertical gradients in the tropics; this is likely the result of aerosol influence on the SAGE II water vapour retrieval discussed in Chapter 1 (Section 1.4.3).

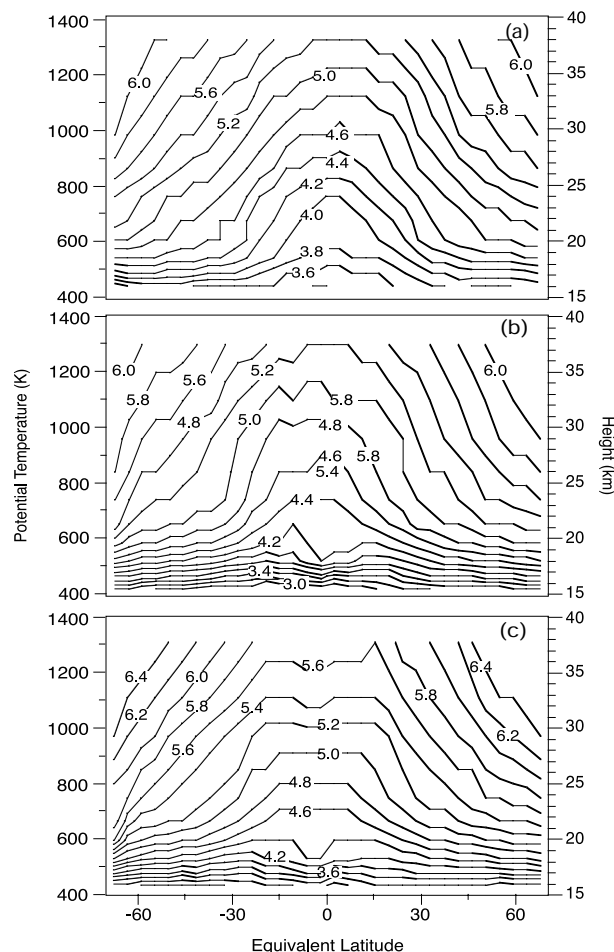


Figure 2.61 Water vapour annual zonal mean derived from the (a) HALOE, (b) SAGE II sunset and (c) SAGE II sunrise data. The zonal mean is derived from binned average on a  $4^\circ$  equivalent latitude grid and potential temperature levels nearest to the UARS standard pressure levels. The values are mixing ratios given in ppmv.

## 2.5.2 Satellite seasonal climatology comparisons

### SAGE II and HALOE

Seasonal climatology comparisons are another way to assess data quality. Here a comparison between HALOE and SAGE II monthly averages in the lower stratosphere is presented. Again eight years of HALOE data (1991-1999) and four years of SAGE II data were binned according to their equivalent latitude, in 4-degree intervals, and potential temperature levels nearest to the UARS standard pressure levels. The climatologies were derived from harmonic fits of the binned averages, following the method described in *Randel et al.* [1998]. The binning was done as described previously for the annual average HALOE-SAGE II comparison.

Figure 2.62 shows the time series of the monthly means of HALOE and SAGE II sunset data for two equivalent latitude bins (the equator and 40°N) on the 465 K isentropic surface (~19 km), together with the (repeating) seasonal cycle curves derived from the harmonic fits. Only four years of HALOE data are shown (1996-1999), for comparison to the four-year cycle of SAGE II data. The HALOE data exhibit a clear annual cycle in both tropics and middle latitudes. The SAGE II time series at 40°N shows a qualitatively similar seasonal cycle fit as HALOE. However, in the tropics, the seasonal cycle captures only a small component of the overall variance of the SAGE II data, and the fit is very different from that of HALOE. The large and irregular scatter in the tropical SAGE II data, and the negative trend, suggest the possible influence of aerosol artefacts in the SAGE II data, especially in the tropics. With the assumption that the better seasonal fit to the HALOE data gives a more precise representation of the seasonal pattern, it appears that the SAGE II data in the lower stratosphere and above the aerosol layer can provide reasonable seasonal variations at middle latitudes, but not in the tropics. Also shown in Figure 2.62 are time series of monthly mean SAGE II data for the equatorial and 40°N zone on the 375 K isentropic surface and the associated harmonic fit. At the level below the aerosol layer, both in the tropics and at middle latitudes, there is a clear seasonal cycle and reasonable agreement of monthly mean data with the harmonic fit.

The ability of SAGE II to describe the seasonal pattern at this lower level is further illustrated by comparison of the HALOE and SAGE II data on the 375 K potential temperature surface (approximately 120 hPa pressure level), shown in Figure 2.63. Although the time period of the measurements is different for the two data sets, HALOE and SAGE II data show similar seasonal variations with maximum values during Northern Hemisphere summer, and the latitude of the maximum near 30°N in both. Low values during Southern Hemisphere winter at high Southern latitudes are also apparent in both the HALOE and SAGE II distributions.

### ILAS and UARS Reference Atmosphere

The ILAS instrument made measurements at high latitudes and produced eight months (November 1996-June 1997) of stratospheric water vapour data near both the Arctic and Antarctic polar vortex. Although the measurements were only made at narrow latitude bands geographically (varying from 57°N to 73°N and from 64°S to 88°S), they covered a wide range of dynamic atmosphere due to the steep PV gradient near the vortex edge and the asymmetry of the vortex shape. When the measurements are sorted by the dynamic variable PV (expressed as the equivalent latitude), the ILAS measurements cover approximately from 30 degrees to the pole in equivalent latitude space in both hemispheres. Under these conditions, it is essential to use the equivalent latitude instead of the geographical latitude in the compilation of a climatology, and for comparison with other satellite climatologies. Shown in Figure 2.64 is the ILAS water vapour climatology (computed from Version 4.20 data) and the UARS reference atmosphere (based on 84 months of data, see *Randel et al.* [1998] for details) for the 72°S equivalent latitude band. Although the two data sets cover different years, in this cross-section

they show consistent climatological features in the stratospheric water vapour. The differences are potentially due to atmospheric interannual variability as well as the uncertainty of the measurements, as discussed in Chapter 1 (Section 1.4.9).

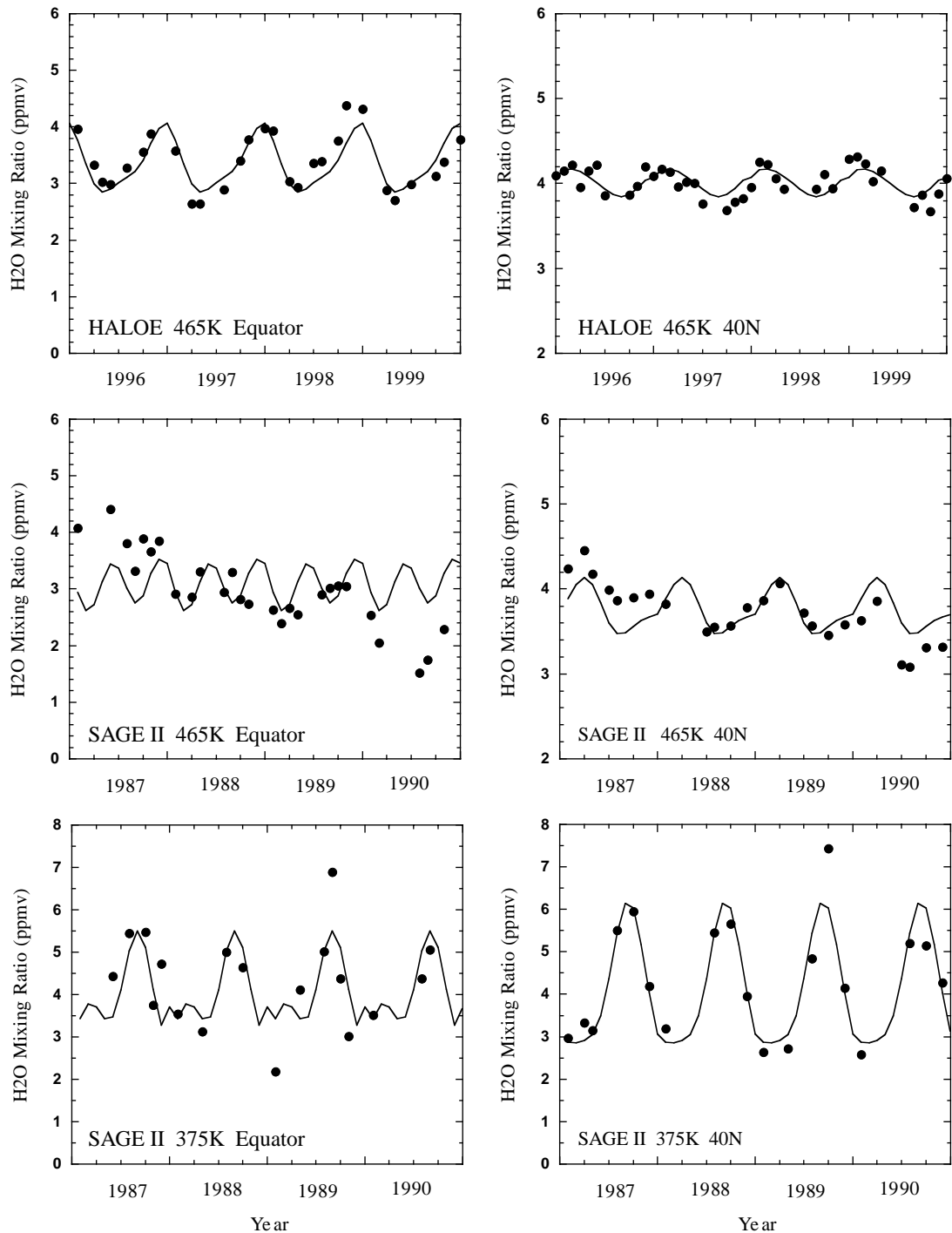


Figure 2.62 Time series of binned monthly average versus the fits for 465 K isentropes HALOE data (upper panels), 465 K isentropes SAGE II sunset data (middle panels) and 375 K SAGE II sunset data (bottom panels). Two latitudinal bins are shown in the figure, equatorial on the left and 40°N on the right.

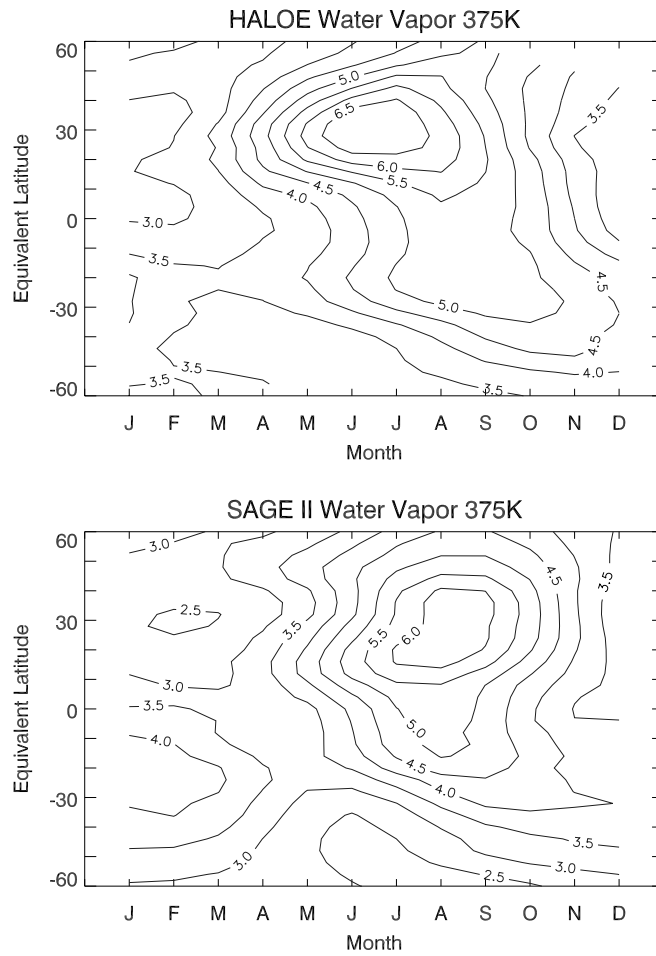


Figure 2.63 Seasonal cycles derived from HALOE and SAGE II (Sunset) data on the 375 K isentrope. Some smoothing has been applied to the SAGE II data. The values are mixing ratios given in ppmv.

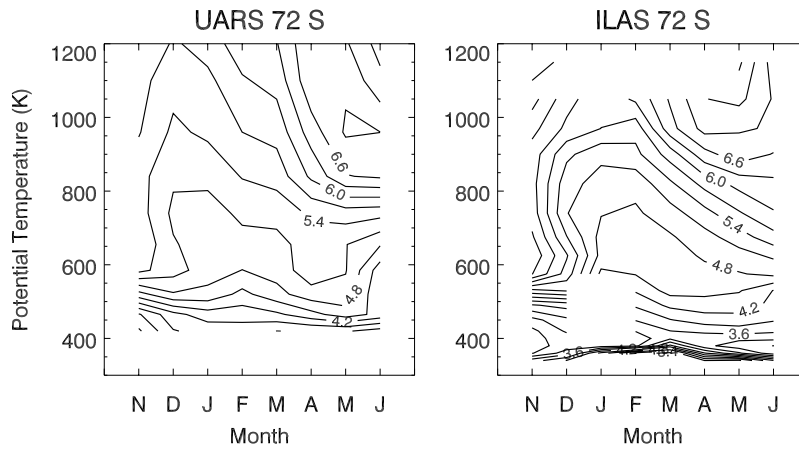


Figure 2.64 Comparison of ILAS water vapour climatology and UARS reference atmosphere. The contours are water vapour monthly zonal mean mixing ratio (in ppmv) calculated in 4 degree equivalent latitude band. Shown in the figure are time:height (month:θ) cross-sections for the ILAS measurement period of the year (November to June) for the 72°S latitude band.

### 2.5.3 Lowermost stratosphere *in situ* and satellite climatologies

Comparisons of the seasonal cycles derived from SAGE II, MLS upper tropospheric, and ER-2 data are made to assess the measured water vapour variability in this region. The ER-2 data used in this analysis are from the Harvard Lyman- $\alpha$  hygrometer during the Stratospheric Tracers of Atmospheric Transport (STRAT) and Photochemistry of Ozone Loss in the Arctic Region in Summer (POLARIS) missions (1995-1997).

Since the three data sets were taken in different years with different sampling strategies, it is advantageous to compare their climatologies in the dynamically based coordinates of PV and potential temperature [Hoskins, 1991]. PV values are also useful indications of how “deep” the air parcels are in the stratosphere. Using Ertel’s PV, values of 2-3 PVU or greater are associated with stratospheric air [Holton *et al.*, 1995]. PV and  $\theta$  information came from UKMO for the MLS data, from NCEP for the SAGE II data, and from the ER-2 mission data (consisting of measured temperatures and PV from the NASA-Goddard model assimilation) for the aircraft data.

Figure 2.65 gives examples of this comparison for measurements in the lowermost stratosphere and near the extratropical tropopause (PV = 3-4 PVU and 5-6 PVU,  $\theta=330$  and 350 K). The seasonal cycles in the figure are monthly means computed by binning the data according to their PV (in 1 PVU intervals) and  $\theta$  (in 10 K layers). Included in the calculation were 5 years of SAGE II data (1986-1990), 6 years of MLS data (1991-1997) and 3 years of Harvard Lyman- $\alpha$  data (1995-1997) (with at least 3 data points in each PV- $\theta$  bin). In cases of comparisons with the Harvard data, it is important to note there is a much smaller number of samples (total  $\sim 70$  flights) and that the measurements were taken over a narrow longitudinal range ( $\sim 120^\circ$ - $150^\circ$ W). The monthly average produced is more likely to be subject to longitudinal variations of the water vapour and the random effect of the sampling.

Typically, the mean values and the variances from MLS are larger than the SAGE II in the wetter seasons on the lower isentropes. This is consistent with the fact that MLS has a 3 km vertical resolution, as compared to the 1 km vertical resolution of SAGE II instrument. Note that water vapour has a steep vertical gradient in this region and MLS results represent the average of a 3 km layer. This needs to be considered in all intercomparisons presented in this section. Another possible factor contributing to the positive MLS-SAGE II difference in the wetter season is that SAGE II data are only for clear sky conditions, while MLS data include cloudy conditions. Harvard Lyman- $\alpha$  data, although agreeing with the satellite seasonal cycle in general, display more variability and tend to have larger water vapour values during the fall season relative to MLS and SAGE II on the lower isentropes. This is likely due to the small sample of the data and the longitudinal variability.

Average differences were computed between monthly means derived from SAGE II, MLS, and Harvard Lyman- $\alpha$  measurements over the annual cycles for the lowermost stratospheric region (2-7 PVU, 330-360 K for SAGE II and Harvard, 330-350 K for MLS). Detailed statistics are given in the caption for Figure 2.65. For the entire PV- $\theta$  range examined, the average Harvard-SAGE II differences are nearly always positive. The average MLS-SAGE II differences vary nearly monotonically from low to high PV bins, ranging from +26% for 2-3 PVU to -35% at 6-7 PVU. The overall pattern of the MLS-Harvard comparison is similar; varying nearly monotonically from +23.5% for 2-3 PVU to -19.2% for 5-6 PVU. This systematic variation is consistent with the fact that MLS has a 3 km vertical resolution, as compared to the 1 km vertical resolution of SAGE II and the fine resolution (0.1-0.2 km) of Harvard instrument. Since the water vapour mixing ratio has a steep vertical gradient in this region, MLS results, which represent the averages of 3 km thick layers, may show a wet or dry

bias in comparison with the SAGE II and Harvard data, depending on the shape and the peak position of the weighting function relative to the nominal pressure of the layer.

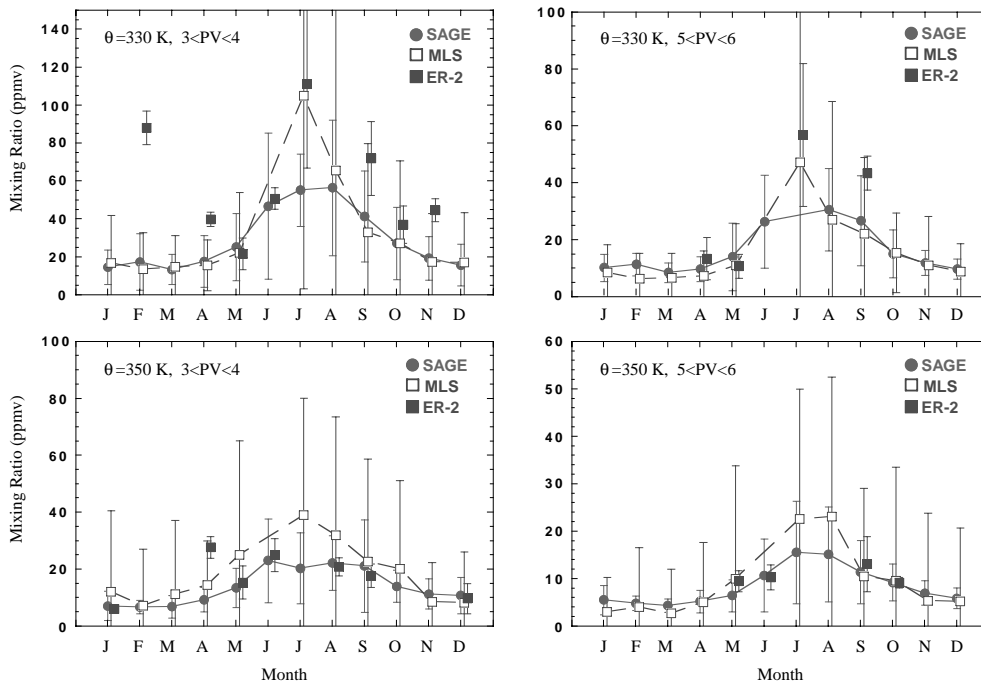


Figure 2.65 Examples of seasonal cycles derived from SAGE II, MLS and ER-2 measurements. Shown in the figure are monthly means in PV- $\theta$  bins using 1 PVU interval and 10 K  $\theta$  layers. The symbols represent the monthly mean from 5 years of SAGE II data, 6 years of MLS data and 3 years of ER-2 data. The error bars indicate the standard deviation. The four examples are for 330 K, PV=3-4, 5-6 PVU and 350 K, PV=3-4, 5-6 PVU. The average difference of the Harvard-SAGE II monthly means over the annual cycle for all the bins within the PV- $\theta$  range from 2-7 PVU and 330-360 K is 24%. The average MLS-SAGE II difference (for the 330-350 K range) in the lowest PV bin (2<PV<3 PVU) has the highest positive value (~26%). The difference then decreases with increasing PV value (22% for 3<PV<4, 10% for 4<PV<5, -8% for 5<PV<6 and -35% for 6<PV<7 bins, respectively). The average MLS-Harvard differences (in the 330-350 K range) are similar to the MLS-SAGE II comparison, with differences of ~23.5% for 2<PV<3 PVU, -2.0% for 3<PV<4 PVU, -6.4% for 4<PV<5 PVU, and -19.2% for 5<PV<6 PVU bins respectively.

#### 2.5.4 Entry level $[\text{H}_2\text{O}]_e$ and $2\times\text{CH}_4+\text{H}_2\text{O}$

Comparisons between different instruments can be complicated by the fact that air masses with different characteristics occur in close proximity to one another. In some cases discussed in this chapter, other species ( $\text{N}_2\text{O}$  and  $\text{CH}_4$ ) or dynamical quantities have been used to characterise the air mass prior to doing comparisons. In this section, comparisons of the quantities  $2\times\text{CH}_4+\text{H}_2\text{O}$  and  $[\text{H}_2\text{O}]_e$  are presented.  $[\text{H}_2\text{O}]_e$ , the entry level mixing ratio, is the mass weighted average of the mixing ratios at entry into the stratosphere of all the parcels that make up the sampled region [Hansen and Robinson, 1989].  $2\times\text{CH}_4+\text{H}_2\text{O}$ , sometimes referred to by the term "potential water", is considered to be a conservative quantity, assuming the effective yield of  $\text{H}_2\text{O}$  from  $\text{CH}_4$  destruction is 2 [Jones et al., 1986]. Modelling work by LeTexier et al. [1988] indicates a range in the effective yield, with an average near 2, as does a study with an older version of HALOE data than assessed in this document [Remsberg et al., 1996]. Given that the average effective yield is 2, and the common use of  $[\text{H}_2\text{O}]_e$  in the literature, a compilation of values found in the peer-reviewed literature and computed from data provided for this assessment is

presented in this report. If the methane values are assumed to be absent of uncertainties, and there are no long-term changes in either CH<sub>4</sub> or H<sub>2</sub>O, either entry level mixing ratio or potential water can be used to assess relationships between instruments even when no coincidences exist.

Care needs to be taken to ensure that the quantity is calculated away from effects of the seasonal cycle of lower stratospheric water vapour and polar dehydration. Restricting the estimates by using only data from pressure levels between 10 and 4 hPa and methane values greater than 0.5 ppmv filters seasonal and polar dehydration effects from the satellite data. This filtering also avoids regions where the mixing of mesospheric air with stratospheric air exerts significant leverage on the CH<sub>4</sub>/H<sub>2</sub>O relationship. However, for *in situ* aircraft data that does not extend even to 50 hPa, filtering using some measure of the length of time a given parcel has been resident in the stratosphere needs to be employed. N<sub>2</sub>O, SF<sub>6</sub> or CO<sub>2</sub> age, and CH<sub>4</sub> values have all been used to filter aircraft data [Hurst *et al.*, 1999; Dessler *et al.*, 1994]. Some checks are also required to avoid regions of polar dehydration in the aircraft data. Balloon measurements do not always extend above 10 hPa, so again a species filtering method needs to be used. For most calculations done specifically for this report, a CH<sub>4</sub> cut-off of 1.35 ppmv was used for the balloon measurements estimates, similar to that used in Hurst *et al.* [1999] and Dessler and Kim [1999].

Another point to consider in these comparisons is the time span valid for the entry of air parcels into the stratosphere. This is important, as long-term changes have been noted in both CH<sub>4</sub> [Dlugokencky *et al.*, 1994; Etheridge *et al.*, 1998] and water vapour (see Section 2.5.5 and Chapter 3 discussion). In cases where major changes have occurred in the retrievals, only the calculation done for the version of the retrieval discussed in this report is included. The publications cited in the table were chosen to cover the time span of the instruments discussed in this assessment. For some instruments, earlier publications do exist that present these quantities for subsets of the data available for this assessment. In other cases, multiple publications needed to be considered to cover the operating period of a given instrument.

A further item of note is that entry-level water (or residual water) has been estimated three different ways in the published literature. In one case [as in Jones *et al.*, 1986],

$$[\text{H}_2\text{O}]_e = \text{H}_2\text{O} - 2 \times ([\text{CH}_4]_e - \text{CH}_4)$$

In this expression, the effective yield of water vapour due to methane destruction is assumed to be 2. This technique will be referred to in Table 2.4 as the average residual water method. A second method [as in Remsberg *et al.*, 1996], uses a least squares regression analysis with simultaneous CH<sub>4</sub> and H<sub>2</sub>O measurements to compute the effective yield coefficient  $\beta$  (slope) and I (intercept). Then, using those estimated coefficients,

$$[\text{H}_2\text{O}]_e = \beta [\text{CH}_4]_e.$$

Hansen and Robinson [1989] were the first to use a variation of this method by calculating  $\beta$  for different time periods via a regression analysis and then averaging

$$[\text{H}_2\text{O}]_e = \text{H}_2\text{O} - \beta \times ([\text{CH}_4]_e - \text{CH}_4).$$

This will be referred to in Table 2.4 as the slope/intercept method. For both of these methods an assumption must be made about  $[\text{CH}_4]_e$ , which for the calculations presented here ranges from 1.6 ppmv (1980's) to 1.72 ppmv (recent observations). These two methods can give different results using exactly the same input data when  $\beta$  differs from  $-2$ . (Note: in Dessler and Kim [1999], the range over different years for  $\beta$  is  $-1.7$  to  $-1.96$ ). Using HALOE data during the period January 1993 until March 2000, and filtering by only considering measurements above

10 hPa with  $\text{CH}_4$  ranging from 0.5 ppmv to 1.35 ppmv, the regression method gives a value for  $[\text{H}_2\text{O}]_e$  of 3.5 ppmv and the residual water expression gives a value of 3.6 ppmv. If the exact same latitude/altitude/time filtering used in *Dessler and Kim* [1999] is employed, the results differ more, with the average residual water method giving  $[\text{H}_2\text{O}]_e=3.6$  ppmv, and the slope/intercept method giving  $[\text{H}_2\text{O}]_e=3.8$  ppmv. An additional consideration is what levels to average over. The way in which this plays a role is demonstrated by examination of the average vertical profile between  $50^\circ\text{N}$  and  $50^\circ\text{S}$  of HALOE  $2\times\text{CH}_4+\text{H}_2\text{O}$  plotted in Figure 2.66. Note that between 10 hPa and 1 hPa,  $2\times\text{CH}_4+\text{H}_2\text{O}$  decreases by  $\sim 0.2$  ppmv as will any estimate of  $[\text{H}_2\text{O}]_e$ . A third method to estimate  $[\text{H}_2\text{O}]_e$  is to average observations of water vapour just above the tropical tropopause. This is the only way to make such an estimate when coincident  $\text{CH}_4$  measurements are not available, and is used for making the SAGE II estimate given in Table 2.4. Again, HALOE measurements can be used for this calculation to demonstrate how it differs from other methods. Averaging the 100 hPa retrievals from 1993 through 1999 between  $20^\circ\text{S}$  and  $20^\circ\text{N}$  gives a low of  $2.7\pm 0.9$  ppmv for February, a high of  $4.7\pm 0.7$  ppmv for August, and a simple annual mean of  $3.6\pm 1.0$  ppmv. In terms of multi-year means of  $[\text{H}_2\text{O}]_e$ , the range presented here is 3.5 to 3.8 ppmv. This 0.3 ppmv range does not consider error estimates that come out of the individual methods. This demonstrates that, in addition to the uncertainties calculated due to data scatter, discrepancies with the method of computation introduce additional uncertainties of more than 5%.

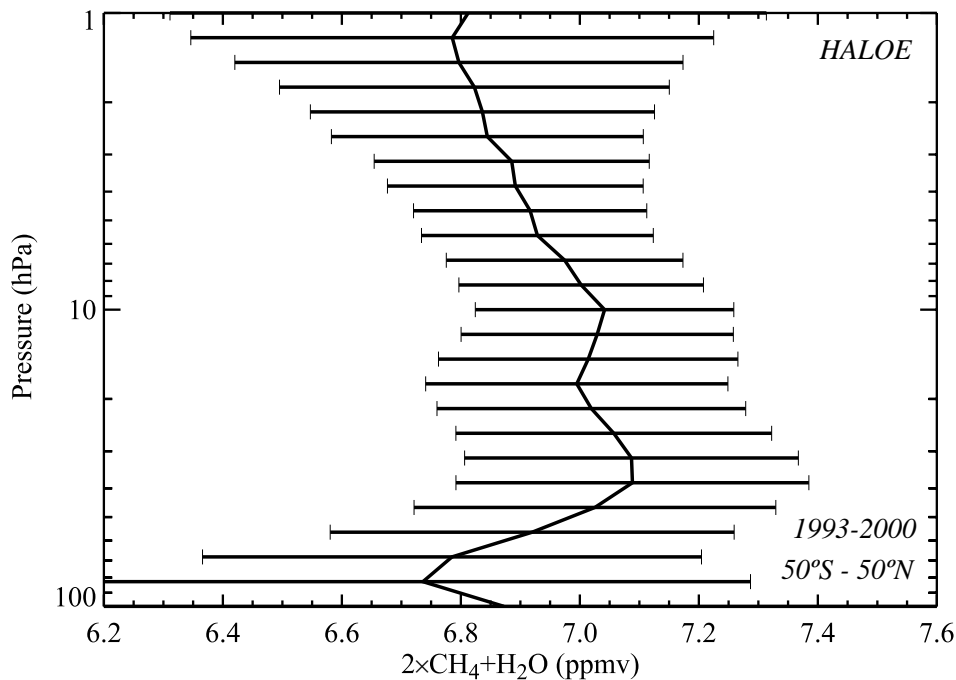


Figure 2.66 Average vertical profile of  $2\times\text{CH}_4+\text{H}_2\text{O}$  calculated with HALOE data from 1993 to 1999 and  $50^\circ\text{S}$  to  $50^\circ\text{N}$ .

A compilation of potential water and  $[\text{H}_2\text{O}]_e$  for the instruments discussed in this chapter is presented in Table 2.4. If a published value exists for the current data processing algorithm, it is included in the table; otherwise, an estimate was made with the data provided for this assessment. For the cases computed specifically for this assessment where a methane measurement or estimate was possible, the average residual water method [*Jones et al.*, 1986] was used. This was chosen because improperly filtered polar dehydration or seasonal cycle parcels affects the slope/intercept method more than it does the residual water method. Multiple entries exist for some instruments. These represent either different time periods or different

analyses with the same data. For POAM III, a significant difference was found between hemispheres (sunrise versus sunset occultations), so an entry is given for each hemisphere. The entries are roughly ordered by increasing  $2\times\text{CH}_4+\text{H}_2\text{O}$ . When multiple values exist for an instrument, the average was used to place it in the table. The methane measurement source and  $[\text{H}_2\text{O}]_e$  calculation technique are stated in the table. In a few cases, only potential water or entry level water was published. To fill in the table, the missing entries were inferred using the stated value of entry level methane.  $1\sigma$  standard deviations are given for calculations done specifically for this report, otherwise the published error estimate is given.

Potential water ranges from 6.0 to 7.5 ppmv, with the lowest value from LIMS (1979), and the highest value from the Harvard Lyman- $\alpha$  instrument (1990's). There is evidence from multiple data sets supporting an increase in stratospheric water vapour over this time period; this will be discussed in detail in section 2.5.5. For the period 1990-2000, the average of all entries are 7.1 ppmv for  $2\times\text{CH}_4+\text{H}_2\text{O}$ , and 3.7 ppmv for  $[\text{H}_2\text{O}]_e$  (with  $1\sigma$  standard deviation = 0.25). If one assumes saturation at 100 hPa, that corresponds to an average entry-level temperature of approximately  $-82.4^\circ\text{C}$ . The 1990's  $[\text{H}_2\text{O}]_e$  range of estimates is 3 to 4.1 ppmv, corresponding to a 100 hPa entry-level temperature range of  $-83.5^\circ\text{C}$  to  $-81.8^\circ\text{C}$ .

**Table 2.4.** Estimates of water vapour entering the stratosphere ( $[\text{H}_2\text{O}]_e$ ) and potential water ( $2\times\text{CH}_4+\text{H}_2\text{O}$ ). Instruments are ordered by increasing potential water.

Instrument	Source	$2\times\text{CH}_4+\text{H}_2\text{O}$ (ppmv)	$[\text{H}_2\text{O}]_e$ (ppmv)	Time period	Method for estimating $[\text{H}_2\text{O}]_e$	$\text{CH}_4$ measurement
LIMS	<i>Jones</i> [1986]	~6.0	$2.7 \pm 0.35$	1979	Average residual water $[\text{CH}_4]_e = 1.65$ ppmv Data up to 1 hPa	SAMS
	<i>Hansen and Robinson</i> [1989]	6.3	$3.3 \pm 0.2$	1979	Methane yield ( $\beta$ ) calculated for month and latitude bins. $[\text{H}_2\text{O}]_e$ calculated using $\beta$ and $[\text{CH}_4]_e = 1.6$ ppmv Data up to 3 hPa	
SAGE-II	<i>Chiou et al.</i> [1997]	(5.6 – 6.8 ave=6.2) Inferred using $2\times[\text{CH}_4]_e$ $+[\text{H}_2\text{O}]_e$	2.3 – 3.5 (DJF - SON) ave=2.9	1986-91	20°S-20°N seasonal hygropause average ( $[\text{CH}_4]_e = 1.65$ ppmv)	None
MLS	Calculation for this report	$6.4 \pm 0.26$	$3.0 \pm 0.27$	1992-93	Average residual water $[\text{CH}_4]_e = 1.7$ ppmv	HALOE coincidences
LMD	<i>Engel et al.</i> [1996]	$6.91 \pm 0.15$	$3.61 \pm 0.28$	1991-92	Slope/intercept $[\text{CH}_4]_e = 1.72$ ppmv	Cryogenic collection <sup>1</sup>
WVMS	Calculation for this report	$6.97 \pm 0.5$	$3.6 \pm 0.5$	1992-97	Average residual water $[\text{CH}_4]_e = 1.7$ ppmv	HALOE coincidences
ATMOS	Calculation for this report	$7.0 \pm 0.5$	$3.6 \pm 0.5$	1985-94	Average residual water $[\text{CH}_4]_e = 1.7$ ppmv	Simultaneous measurements
	<i>Michelsen et al.</i> [2000]	$6.9 \pm 0.3$	$3.5 \pm 0.3$	1985-94	slope/intercept, excluding tropics	
FIRS-2	Calculation for this report	$7.0 \pm 0.4$	$3.6 \pm 0.4$	1989-97	Average residual water, $[\text{CH}_4]_e = 1.7$ ppmv	$\text{N}_2\text{O}/\text{CH}_4$ relationship determined from MKIV data

**Table 2.4.** Continued from previous page

POAM-III	Calculation for this report	6.8 ± 0.4 (NH) 7.4 ± 0.5 (SH)	3.4 ± 0.4 (NH) 4.0 ± 0.5 (SH)	1998-99	Average residual water, [CH <sub>4</sub> ] <sub>e</sub> = 1.7 ppmv	HALOE coincidences
HALOE version 19	<i>Dessler and Kim</i> [1999]	(7.2 ± 0.5) Inferred using 2×[CH <sub>4</sub> ] <sub>e</sub> + [H <sub>2</sub> O] <sub>e</sub>	3.8 ± 0.49	1993-97	Slope/intercept [CH <sub>4</sub> ] <sub>e</sub> =1.7 ppmv	Simultaneous measurements
	Calculation for this report	7.0 ± 0.2	3.6 ± 0.2	1993-2000	Average residual water, [CH <sub>4</sub> ] <sub>e</sub> =1.7 ppmv	
FISH	<i>Zöger et al.</i> [1999]	7.17 ± 0.62	3.9 ± 1.0	Sept. 1993	Slope/intercept [CH <sub>4</sub> ] <sub>e</sub> =1.72 ppmv	Cryogenic collection <sup>1</sup>
	C. Schiller, personal Communication	7.02 ± 0.11	3.6 ± 0.3	Feb. 1997		
		7.05 ± 0.12	3.6 ± 0.4	Feb. 1999		
MkIV	Calculation for this report	7.2 ± 0.2	3.8 ± 0.2	1990-97	Average residual water [CH <sub>4</sub> ] <sub>e</sub> =1.7 ppmv	Simultaneous measurements
CMDL	Calculation for this report, using data from OMS balloon flight	7.2 ± 0.5	3.8 ± 0.6	1996-98	Average residual water [CH <sub>4</sub> ] <sub>e</sub> =1.7 ppmv	ALIAS coincident balloon measurements
MAS	Calculation for this report	7.2 ± 0.5	3.8 ± 0.5	1992-94	Average residual water [CH <sub>4</sub> ] <sub>e</sub> =1.7 ppmv	HALOE coincidences
MIPAS	<i>Stowasser et al.</i> [1999]	7.25 ± 0.2	(3.85 ± 0.2)	Feb. 1995	Inferred by taking Column 3 – 2× [CH <sub>4</sub> ] <sub>e</sub> with [CH <sub>4</sub> ] <sub>e</sub> = 1.7 ppmv	Simultaneous measurements
		7.28 ± 0.1	(3.88 ± 0.1)	Mar. 1997		
NOAA Ly-α	<i>Hurst et al.</i> [1999] <sup>2</sup>	7.1 ± 0.6	4.0 ± 0.4	1993-95	Slope/intercept [CH <sub>4</sub> ] <sub>e</sub> = 1.7 ppmv	ALIAS and ACATS coincident ER-2 measurements
	<i>Kelly et al.</i> [1990]	(6.9 – 7.4) Inferred using 2×[CH <sub>4</sub> ] <sub>e</sub> + [H <sub>2</sub> O] <sub>e</sub>	3.7 - 4.2	1987-89	Average residual water [CH <sub>4</sub> ] <sub>e</sub> = 1.6 ppmv	Whole air sampler coincident ER-2 measurements
	Calculation for this report	7.3 ± 0.1	3.9 ± 0.1	May 1998	Average residual water, [CH <sub>4</sub> ] <sub>e</sub> = 1.7 ppmv	NOAA TDL coincident WB57F measurements
JPL TDL	<i>Hurst et al.</i> [1999] <sup>2</sup>	7.4 ± 0.6	3.9 ± 0.3	1997	Slope/intercept [CH <sub>4</sub> ] <sub>e</sub> = 1.7 ppmv	ALIAS and ACATS coincident ER-2 measurements
Harvard Ly-α	<i>Hurst et al.</i> [1999] <sup>2</sup>	7.5 ± 0.5	4.1 ± 0.3	1993-99	Slope/intercept, [CH <sub>4</sub> ] <sub>e</sub> = 1.7 ppmv	ALIAS and ACATS coincident ER-2 measurements

<sup>1</sup>*Schmidt et al.* [1987]<sup>2</sup>Averages of entries in their Table 1

### 2.5.5 Comparison of water vapour long-term changes and seasonal oscillations

Multi-decadal changes in water vapour are of interest due to the radiative importance of water vapour in the upper troposphere and lower stratosphere [Forster and Shine, 1999]. The annual and semi-annual cycles are of interest as they can be used to elucidate mechanisms for transport and mixing. These topics will be discussed in detail in Chapter 3. In this section, comparisons of the harmonic amplitudes and long-term changes are presented for several of the instruments discussed in this chapter. In the upper troposphere, there are too few data sets available to this assessment effort to usefully compare long-term change and harmonic cycle determinations, so the discussion here will concentrate on stratospheric measurements.

Of the variety of data sets examined in this report, only a few are useful for assessing possible long-term changes or harmonic cycle amplitudes in stratospheric water vapour. The ideal data set would have extensive seasonal coverage, and come from a stable instrument that has been operating for an extended period of time. In the SPARC ozone trends study [SPARC, 1998], time series of 20 years or greater were used for trend determinations. For stratospheric measurements, the only continuous multi-decadal record assessed in this report is that of the NOAA-CMDL frostpoint hygrometer balloon instrument. Data starts in 1980 and extends to the present. Oltmans and Hofmann [1995] used the first 14 years of that data set to estimate long-term changes in the water vapour content of the stratosphere over Boulder, Colorado (~40°N). They found increasing long-term changes that were larger in magnitude than expected from observed increases in tropospheric methane. Long-term increases in lower stratospheric water vapour deduced from older measurements have been discussed by Mastenbrook [1968], Mastenbrook and Oltmans [1983], Harries [1976] and Cluley and Oliver [1978]. Michelsen *et al.* [2000] show evidence for water vapour increases over the ATMOS time frame, and Engel *et al.* [1996] combined measurements from a variety of instruments to show evidence for a long-term increase greater than that expected from known increases in tropospheric methane for the period 1975-1995. Since the launch of UARS in late 1991, HALOE water measurements have been available and studied extensively. Evans *et al.* [1998] and Randel *et al.* [1998] have studied the temporal behaviour of the HALOE measurements. Nedoluha *et al.* [1998a] showed long-term changes deduced from HALOE and WVMS are similar and increasing through the first part of the HALOE record. Details regarding changes deduced from HALOE and the NOAA-CMDL frostpoint record are given in Chapter 3.

Published estimates of long-term changes in water vapour are on the order of 1%/year. Agreement between the various instruments presented in this chapter ranges from 10% to 30%. Consequently, it is not possible to combine various data sets to obtain a suitable time series to do a long-term determination of UTLS water vapour changes as was done by combining SAGE I and SAGE II measurements in the SPARC ozone trends study. However, long-term changes can be estimated within individual instrument records. Although none is continuous throughout multiple decades, the aggregate of the data assessed in this report covers over 20 years in time. Two data sets not validated in this chapter are also used here for a long-term time series analysis of water vapour changes. The first of these additional data sets is the Naval Research Laboratory (NRL) frostpoint series over Washington DC from 1964 to 1976 [Mastenbrook, 1968; Mastenbrook and Oltmans, 1983]. The second is the measurement series from the airborne frostpoint instrument flown on Meteorological Research Flights (MRF) of the United Kingdom Meteorological Office (UKMO) from the early 1950's to the early 1980's, albeit with significant gaps in coverage in the 1960's. Both of these instruments are discussed in Chapter 1 of this report. Including these two data sets extends the time period of consideration to over 40 years. Coincident or climatological comparisons were not possible with these data sets, so they have not been discussed in the comparison sections of this chapter. However, some

quality control has been performed before including either set in the time series analysis. The NRL measurements, although available until 1979, were made with a redesigned instrument starting in 1977 and the sampling frequency decreased during the test phase of the new instrument design. Additionally, examination of the NRL time series showed a significant step-function decrease in measured mixing ratios occurred at the time of the instrument redesign. For this reason, only data taken prior to the 1977 redesign are used in the present long-term change analysis. The MRF data was extracted from tables in several published reports [Bannon *et al.*, 1952; Cluley and Oliver, 1978; Heliwell *et al.*, 1957; Murgatroyd *et al.*, 1955; Foot, 1984]. A correction for the older data [Oliver and Cluley, 1978] was applied to the data presented here. The MRF data is only available at levels below ~15 km and encompasses both tropospheric and stratospheric measurements. To ensure this analysis only considers stratospheric data, MRF measurements has been filtered by the published tropopause heights. This has also been done for the other UTLS data sets considered as well.

Although the satellite measurements have near global coverage, the bulk of the non-satellite data has been taken at Northern Hemisphere middle latitudes. For this reason, the long-term change and harmonic cycle comparisons are presented for the latitude band from 30° to 50°N. The raw data used in the analysis are shown in Figure 2.67a-f. Here all the satellite data available from 30°-50°N are shown, although for the time series regression analysis, a subset will be used as detailed later.

At the highest level shown (Figure 2.67a, 3 hPa), all the data are from remote sounding instruments. LIMS nighttime data (not validated in this report) are also included on the time series plots, although not used to determine long-term changes. LIMS measurements plotted are 1-month averages, and are included because they cover a period when little other data exists for stratospheric water vapour. The WVMS points are 1-week averages, while the rest are from individual profiles. Scatter in the data is fairly consistent between all the instruments with the exception of SAGE II, with apparently smaller precision at this level. However, this is at the very top of the SAGE II profile where the estimated errors are large. At lower levels, the SAGE II data scatter is similar to that of HALOE. With the exception of MLS (with only a 1.5 year record), all the instruments show a general indication of an increase with time, although it is not a simple linear change. In some of the longer data records, there are periods with large jumps (for HALOE, between 1993 and 1994, for WVMS between 1995 and 1996), and years with little or even negative changes. There are also changes in the data range for individual instruments from year to year. For example, with the HALOE data, there is a decrease in the maximum of the data envelope between 1996 and 2000, while the minimum of the data envelope shows little change between 1996 and 1999, then increases by 2000. Whether this type of interannual difference is the result of changes in spatial/temporal sampling or indicates a real geophysical change is not known, but is worthy of further investigation.

At the next level down (Figure 2.67b, 21 hPa), balloon-borne *in situ* data are also available. The NRL time series, starting in 1964, is considerably noisier than the redesigned version of the instrument flown by NOAA-CMDL starting in 1980, but still shows a distinct increase with time, as does the NOAA-CMDL frostpoint hygrometer record. ATMOS and the other balloon-borne instruments all indicate net increases over their time records, and HALOE and MLS show little change except from 1993-1996 where HALOE shows increases with time. As discussed in Chapter 1, the SAGE II retrievals are likely affected by the decrease in El Chichón aerosols in the lower stratosphere, and hence the long-term changes estimated are not reliable. For this reason, the SAGE II data has been neglected between the tropopause and 10 hPa.

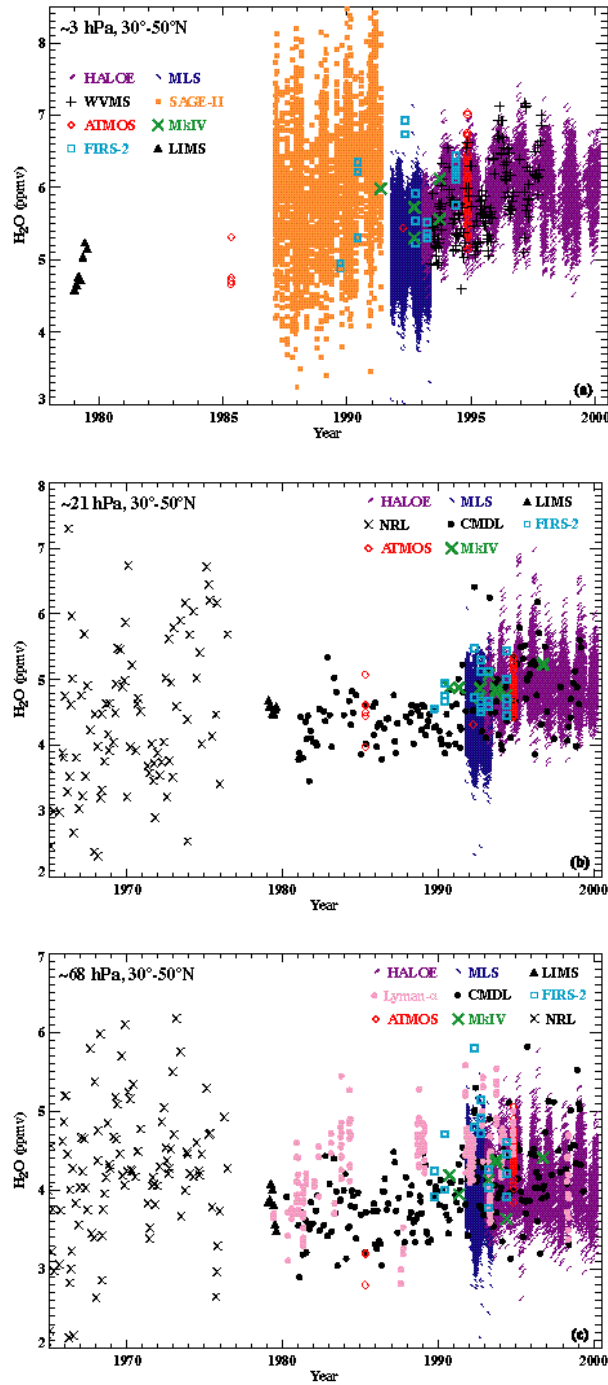
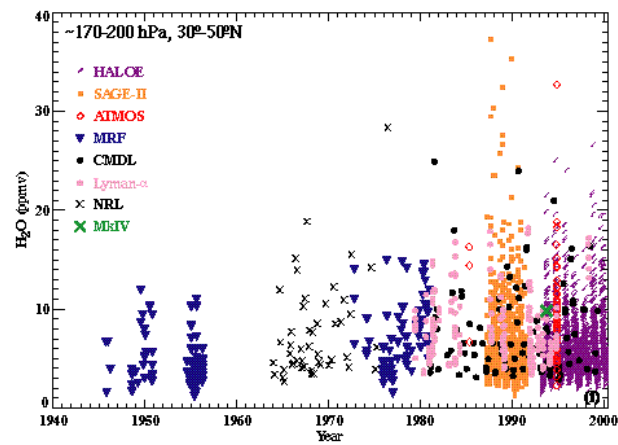
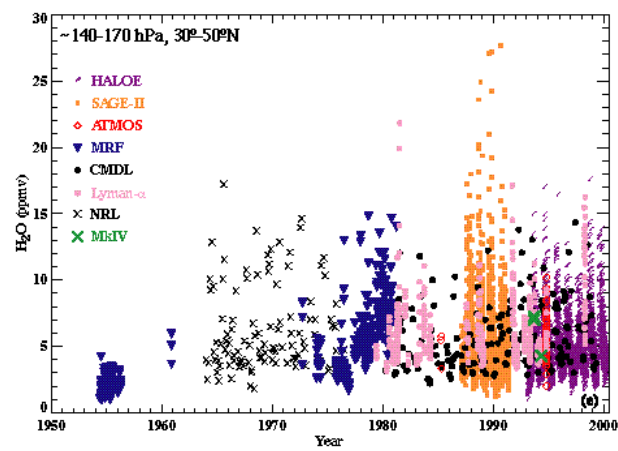
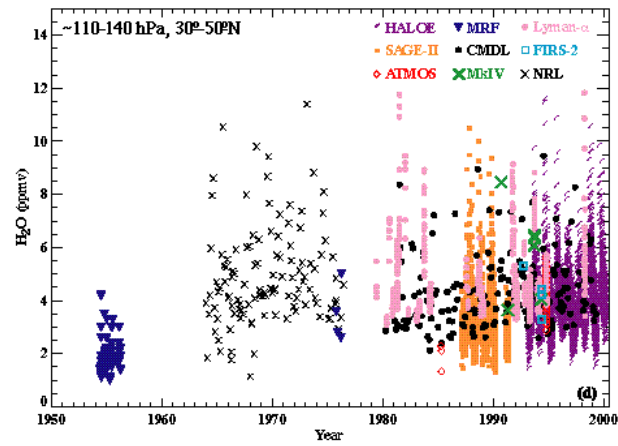


Figure 2.67 Water vapour time series for several instruments covering the depth of the stratosphere. Data plotted are individual measurements with the exception of LIMS (monthly averages), WVMS (weekly averages), and NOAA-AL Lyman-alpha (1 minute averages). Data below 100 hPa have been screened to omit tropospheric measurements. Six levels are plotted: a) ~3 hPa, b) ~21 hPa, c) ~68 hPa, d) 110-140 hPa, e) 140-170 hPa, and f) 170-210 hPa.



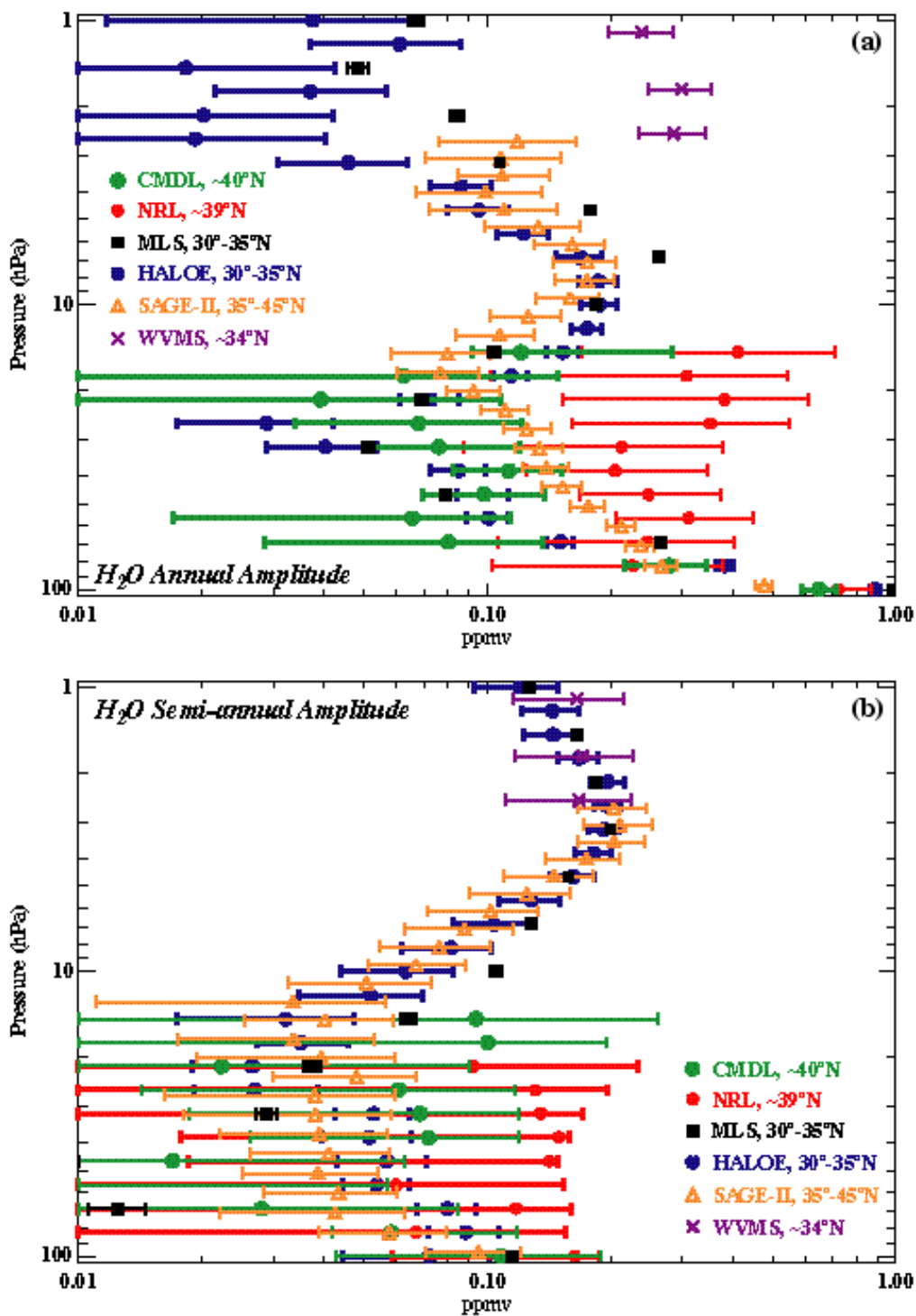


Figure 2.68. Water vapour mixing ratio annual (a) and semi-annual (b) amplitudes for the 30° to 50°N latitude range. Instruments and latitudes used are noted on the figure. Error bars indicate the 1  $\sigma$  uncertainties on the coefficients from the regression analysis.

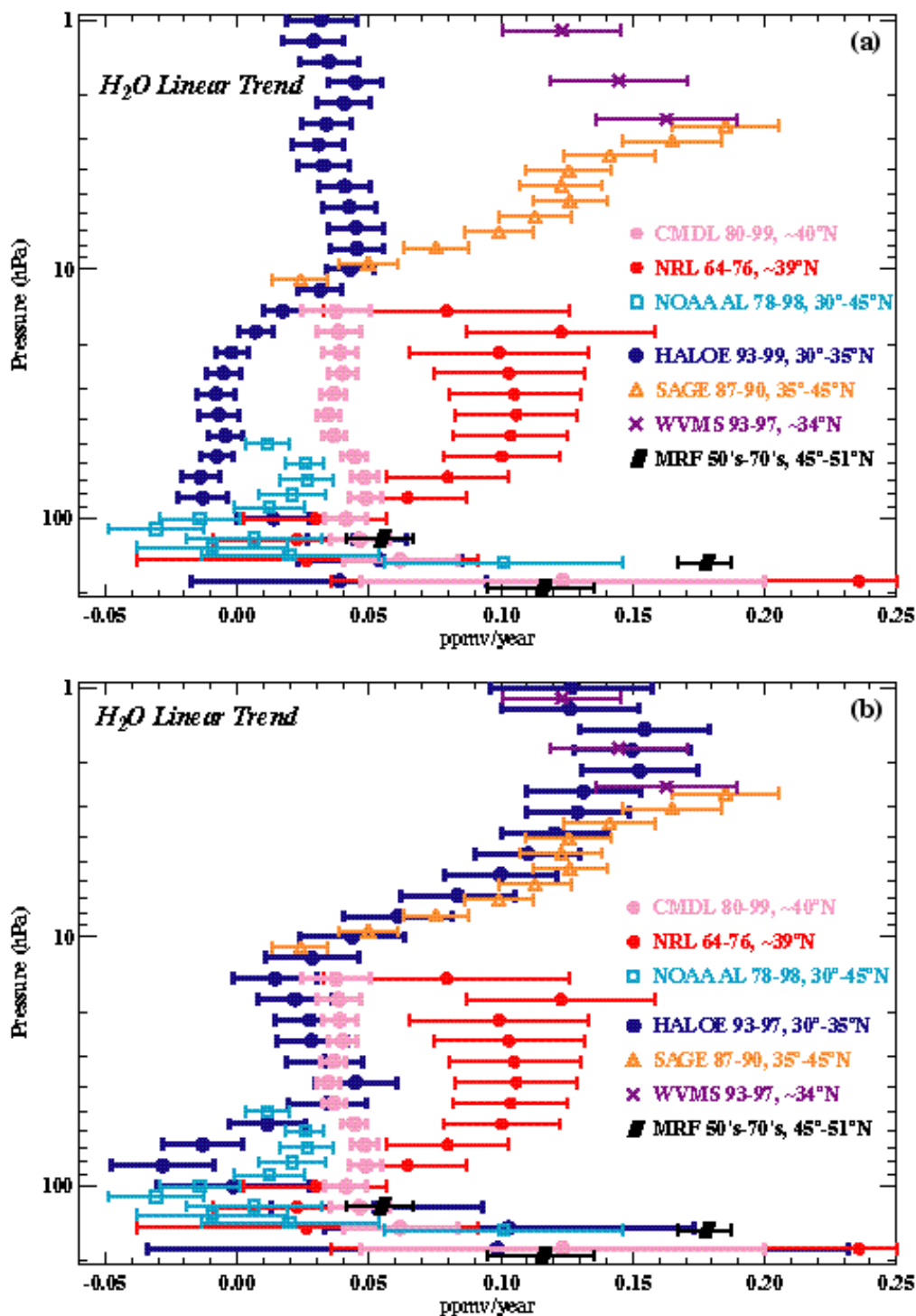


Figure 2.69. Water vapour mixing ratio linear change coefficient. Instruments, latitudes and valid time periods used are noted on the figure. Error bars indicate the 1  $\sigma$  uncertainties on the coefficients from the linear regression analysis. Panel (a) and Panel (b) are identical with the exception of the HALOE time period used. Panel (a) shows the HALOE linear change term computed for 1993–1999, while Panel (b) shows the HALOE linear change term computed for 1993–1997.

At 68 hPa (Figure 2.67c), one additional aircraft borne *in situ* measurement is included. The NOAA-AL Lyman- $\alpha$  measurements are more scattered than the NOAA-CMDL measurements over the same period, however they do span the entire 30°-50°N latitude range, while the NOAA-CMDL measurements are at just one location. Hence, some of the Lyman- $\alpha$  scatter is likely due to spatial gradients, as is also the case for the satellite measurements. Again, there appears to be an overall increase from the beginning to end of the data shown, although there are distinct decreases over some periods in most of the time series presented.

The bottom three levels (2.67d at ~130 hPa, 2.67e at ~155 hPa, and 2.67f at ~185 hPa) all extend back to the 1950's and include the early MRF aircraft data. The corrections detailed in *Oliver and Chuley* [1978] have been applied to the data. In Figure 2.67f, data from Brewer's earliest flights with the first versions of his frostpoint instrument are included. The data from the middle 1950's and the late 1970's were taken with an instrument of the same design, so changes between those two sets should be indicative of real atmospheric changes as opposed to instrument design changes. Observations were made between 1955 and the early 1960's, at which time the MRF high altitude aeroplane crashed. However, those data were not obtainable for this assessment. All data plotted has been filtered to include only stratospheric measurements. This was done using temperature profiles taken on the same platform where available, otherwise, the closest available NCEP temperature profile was used. The aircraft used for the MRF measurements in the 1970's did not have as high a ceiling as the earlier plane; consequently, there are few points at the 110-140 hPa level in the 1970s. At these lower levels, SAGE II measurements are again included on the plot. The scatter of the SAGE II measurements is slightly larger than that of the *in situ* data at the 140-170 hPa level. The minimum values from SAGE II appear to be biased dry relative to the *in situ* measurements. HALOE minima also appear to be slightly biased dry at these levels relative to the balloon and aircraft measurements. In all three plots there appears to be an overall increase with time, with the extremely low mixing ratios in the 1950's and mid 1960's not present in more recent data.

To quantify the temporal changes in the data shown above, a linear regression was done with all the time series of water vapour data available. In order to estimate harmonic amplitudes and long-term changes, a linear least squares regression was done for each time series using annual, semi-annual and linear change terms. The fits were done using data from individual measurements on constant pressure levels, with the exception of the WVMS time series which used one-week averages, and the Lyman- $\alpha$  aircraft data which used 10-second averages. In some cases, data was interpolated to constant pressure levels to do the regression. In an attempt to avoid periods of heaviest aerosol loading which can detrimentally impact retrieved water vapour amounts, the first year of the SAGE II and HALOE data sets were not included in the calculation. The remaining SAGE II data were filtered according to the aerosol cut-off given in *Rind et al.* [1993]. The algorithm used for the regression is detailed in *Bevington* [1969]. The regression was done with equal weighting on each point, and the 1- $\sigma$  uncertainties were estimated as detailed in Chapter 15 of *Press et al.* [1996].

Because latitudinal coverage for HALOE, SAGE II and MLS varies throughout the year, the 30°-35° N band was used for HALOE and MLS, and the 35°-45° N band was used for SAGE II to obtain the best possible seasonal cycle amplitude estimates. This does not affect the long-term change determination significantly, but does affect the annual cycle amplitude calculation. Because of the short time record for the MLS stratospheric water vapour measurements, MLS is only used in the seasonal cycle amplitude computations. POAM III and ILAS satellite measurements were not used for a seasonal cycle determination because neither instrument's latitudinal coverage overlaps the Northern Hemisphere mid latitude band considered. Some instruments do not have adequate seasonal coverage to make an annual cycle amplitude estimate, but have a long enough time record that they can be used for estimating long-term

changes. These include the remote sounding balloon- or shuttle-borne instruments, MkIV and FIRS-2, ATMOS, and the airborne MRF frostpoint and NOAA-AL Lyman- $\alpha$  instruments. The WVMS ground based remote sounding measurements were used for both annual cycle and long-term change determination in the upper stratosphere as were the *in situ* NOAA-CMDL frostpoint hygrometer measurements over Boulder, CO and the NRL frostpoint hygrometer measurements over Washington D.C.

The results for the annual cycle amplitude determination as a function of altitude in the Northern Hemisphere middle latitude band are shown in Figure 2.68a. Common to all data sets is a decrease in annual amplitude from 200 hPa to ~25 hPa. Between 20 and 3 hPa, only satellite data are available. There the shape of the satellite derived annual amplitude curves is similar for the three instruments, although with significant differences in magnitude. These differences between satellite derived amplitudes are quite large near 3 hPa, and also near 20 hPa. Above 3 hPa, the three available instruments (MLS, WVMS and HALOE) have different profile shapes, with annual amplitude differences of 200% or greater. Doing the regression analysis using an identical time period for the HALOE and WVMS data improves the agreement slightly, while using the identical time period for HALOE and MLS improves the annual amplitude agreement a great deal. Changes in the computed amplitude as a function of time period used in the regression are greatest above 8 hPa, although there are changes throughout the entire vertical profile.

Semi-annual amplitudes are plotted in Figure 2.68b. The uncertainties on the *in situ* measurements are large, indicating that data sampling is not sufficient to resolve the small amplitude semi-annual cycle. In the upper stratosphere, the semi-annual amplitude is larger, and the profile shapes and magnitudes are consistent between the satellite and WVMS measurements.

The results for the long-term change determination as a function of altitude for the Northern Hemisphere middle latitudes are shown in Figure 2.69a. The average long-term change of all the instruments plotted is 0.05 ppmv/year. It should be noted that even more so than for the annual amplitude, the time period chosen to do the regression analysis makes a large difference on the computed linear change. Doing the fit for the NOAA-CMDL data for just the first 5 years of the record (not shown) gives a linear change very similar to the NRL calculation, while using the last 5 years of the NOAA-CMDL record gives a linear change similar to the HALOE results. Matching the HALOE regression period to that of the WVMS record (Figure 2.69b) changes the estimated HALOE long-term changes by over 0.08 ppmv/year. This results in improved agreement between WVMS and HALOE determined long-term changes, and gives magnitude and profile shape quite similar to that computed for the SAGE II time period. The fact that the HALOE long-term changes are quite different when computed for different time periods demonstrates that the long-term water vapour change is not well modelled by a linear term. There are periods of rapid increase, and periods of little change or a decrease with time. This is also evident in the NOAA-CMDL and NRL records, and was noted by *Mastenbrook and Oltmans* [1983].

The MkIV, FIRS-2 and ATMOS instruments also have sufficiently long time records to consider a long-term change analysis. However, because of sampling issues, they cannot be calculated in the same manner as done for the data described previously. ATMOS flew on the space shuttle four times between 1985 and 1994; MkIV and FIRS-2 each had a small number of balloon launches at Northern Hemisphere sites. One method of determining a long-term change from the ATMOS data is described in *Michelsen et al.* [2000] and examines changes in the intercept calculated from CH<sub>4</sub>/H<sub>2</sub>O slope lines. For this study, a different approach was taken, and the water vapour data was first binned according to its measured N<sub>2</sub>O. N<sub>2</sub>O was chosen as opposed to CH<sub>4</sub> because FIRS-2 data set does not include CH<sub>4</sub>. The main assumption made is

that  $\text{N}_2\text{O}$  acts as a proxy for the length of time air has been in the stratosphere. This then allows a more extensive time series to be constructed from data collected at different altitudes and latitudes than would be possible considering a single latitude band. Implicit in this assumption is that there are not significant changes in  $\text{N}_2\text{O}$  chemistry during the time period considered. While the long-term changes plotted in Figure 2.69 will include a dynamical component possibly due to circulation changes, this method of binning should minimise that component. A positive trend in the  $\text{N}_2\text{O}$  binned water vapour should then indicate changes in the effective entry value of water into the stratosphere, or changes in chemical processes in the stratosphere affecting water vapour.

In Figure 2.70, the  $\text{N}_2\text{O}$  binned time series for ATMOS, MkIV and FIRS-2 are plotted. The ATMOS data only includes measurements north of  $50^\circ\text{S}$  to avoid an incident of polar dehydration encountered during the final ATMOS shuttle flight. For these calculations, a linear least squares fit was done using instrumental weighting [Bevington, 1969]. Results of the fit are shown in Figure 2.71. One concern in doing such an analysis is that tropospheric  $\text{N}_2\text{O}$  itself is also changing with time. However, the change over the period of consideration here is  $\sim 0.7$  ppbv/year [Butler *et al.*, 1998], yielding a net change of  $\sim 9$  ppbv over the time frame considered. The minimum bin size used in the trend analysis is 25 ppbv, so the  $\text{N}_2\text{O}$  trend should not greatly impact the analysis. At  $\text{N}_2\text{O}$  values below 200 ppbv, where the influence of the seasonal cycle in tropical lower stratospheric water should be a minimum, ATMOS and MkIV show significant increases at all levels. FIRS-2 shows significant increases at all levels except the 105 ppbv  $\text{N}_2\text{O}$  bin. Averaging the estimates for  $\text{N}_2\text{O}$  values less than 200 ppbv gives an increase of 0.05 ppmv/year between 1985 and 1997. This is consistent with that estimated from Figure 2.69a in the Northern Hemisphere  $30^\circ$ - $50^\circ\text{N}$  latitude bin. If each of the  $\text{N}_2\text{O}$  series used is corrected to 1985 values, the average is 0.047 ppmv/year, demonstrating that the  $\text{N}_2\text{O}$  trend does not significantly impact the calculated water vapour long-term change. Long-term changes for  $\text{CH}_4$  can also be computed for the ATMOS and MkIV data, and these are in general positive, with an average value of 0.006 ppmv/year. Methane long-term changes therefore do not negate the water vapour changes. This implies there has been a change in the actual average entry value of  $2\times\text{CH}_4+\text{H}_2\text{O}$  into the stratosphere, and not simply a redistribution of hydrogen between methane and water due to possible circulation changes affecting the length of time air parcels have been resident in the stratosphere.

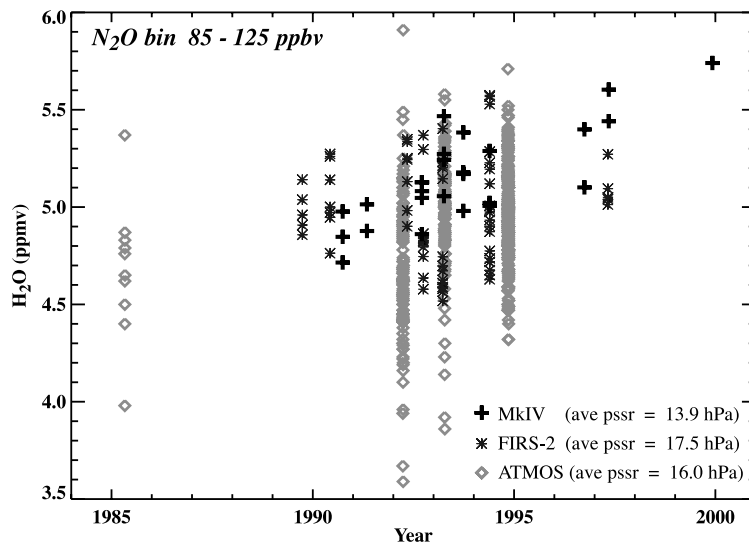


Figure 2.70 Water vapour time series for the MkIV, FIRS-2 and ATMOS instruments in the 85–125 ppbv  $N_2O$  bin, representative of the middle stratosphere.

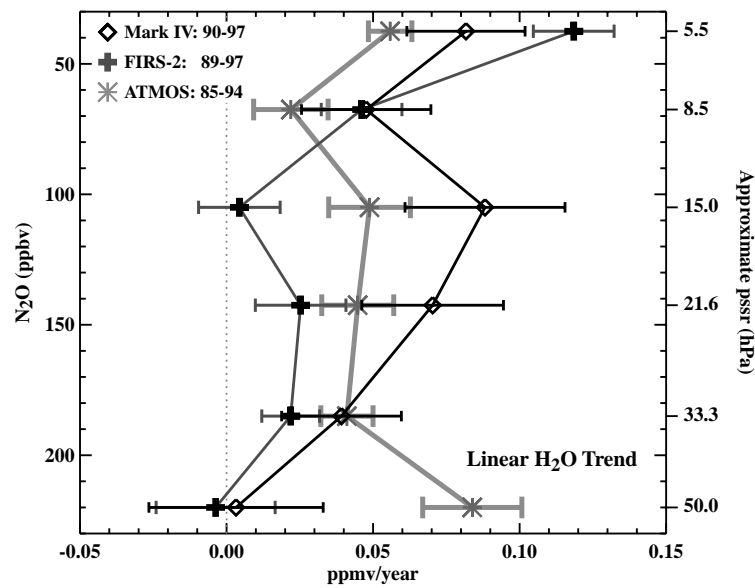


Figure 2.71 Water vapour linear change coefficient for the MkIV, FIRS-2 and ATMOS instruments. Data were binned by  $N_2O$  prior to doing the regression analysis. The approximate pressure valid for each  $N_2O$  bin is given on the right vertical axis. Error bars are the  $1\sigma$  uncertainties on the coefficients from the linear regression analysis. Years for each instrument are noted on the figure.

---

One problem with fitting the series with a linear term is that the long-term changes are not well described by a simple linear term. The lack of overlap of error bars in Figure 2.69 and 2.71 does not necessarily indicate errors in the measurements, but a failure of the imposed model to represent the actual time series. Different time periods are represented by each of the instruments considered, and the actual long-term change over those time periods may very well be different. It is probable that dynamical processes within the stratosphere are playing a role in the long-term water vapour changes computed in a single latitude band. They are undoubtedly playing a major role in producing the large range in the estimated water vapour trends seen in Figure 2.69. However, a similar analysis done with HALOE  $2\times\text{CH}_4+\text{H}_2\text{O}$  also shows large differences in the linear term computed for different time periods, with sign changes depending on whether the beginning or end of the HALOE record is examined (not shown). Using the quantity  $2\times\text{CH}_4+\text{H}_2\text{O}$  should filter out trends due to dynamical variability in a single latitude band. However, the fact that the linear term changes sign depending on the time period chosen implies there are multi-year changes in the average value of water into the stratosphere, with some periods of increase and some of decrease. Yet, when the entire multi-instrument time series is considered, there is evidence for a substantial increase of stratospheric water vapour over the past 40-50 years with an average magnitude of  $\sim 0.05$  ppmv/year (1%/year). This corresponds to an increase of  $\sim 2.0$  ppmv, or  $\sim 60\%$  increase of lower stratospheric water vapour since the middle 1950's.

---

## 2.6 Summary of comparisons

One goal of this assessment is to determine whether measurements from a variety of platforms and instrumental techniques are comparable. It can be seen from the discussion of specific instrument comparisons presented in this chapter, that there is significant variability among instruments even when sampling similar conditions. Some types of comparisons are difficult due to fundamental differences in types of measurements, as noted in the discussion of measurements of upper tropospheric humidity from satellite and *in situ* measurements. Sufficient numbers of coincidences may improve the statistics in comparing disparate instrumental techniques where spatial resolution is important. However, in the variety of comparisons presented, fairly small sample sizes are considered. Therefore, many of the differences presented are not statistically significant. This is demonstrated by comparing the absolute values of the mean difference and RMS difference as plotted on several other plots in this chapter. In Figure 2.28, the RMS difference is much larger than the absolute value of the mean difference. This indicates that random errors are a large part of the measured instrumental differences. Such random errors may be due to geophysical variability (none of measurements are exactly coincident in time or space) or to instrumental noise.

However, even though many of the differences noted are within stated instrumental errors, certain biases between specific instruments do appear. One difficulty in assessing the magnitude of those biases is that a complete set of comparisons does not exist. Thus, a question to consider is whether one instrument can be used as a transfer standard to assess the relationship between two different instruments. This may be possible to do with the lower stratospheric measurements. The geophysical and sampling issues overwhelm the tropospheric measurements, and therefore make it a much more difficult problem.

Of the sensors compared in this chapter, only the frostpoint instruments have been used extensively both in the troposphere and stratosphere. For this reason, the summary given below is divided into tropospheric and stratospheric sections.

### 2.6.1 Stratospheric comparisons

All the measurement comparisons discussed in this chapter are summarised in this section based on percentage differences. Any direct comparisons given in terms of mixing ratio differences have been converted to percent differences for the purposes of this section.

In many cases, differences are consistent when comparing across instruments. Since direct comparisons do not exist between all instruments, a third instrument was used as a transfer standard to determine the entire set of relationships between instruments. In some cases, this technique works well. One good example is demonstrated using the Harvard Lyman- $\alpha$ , NOAA-AL Lyman- $\alpha$  and JPL TDL airborne instruments discussed in section 2.2. The NOAA-AL-Harvard comparisons indicate a difference of  $\sim 15\%$  with the Harvard instrument reading larger values. The NOAA-AL-JPL comparisons indicate a difference of  $\sim 16\%$  with the JPL TDL instrument larger. From this, one would derive a JPL-Harvard difference of  $1\%$ , with the JPL TDL measurements larger. The POLARIS comparisons actually indicate a JPL-Harvard difference of  $1\%$  with the opposite sign. However, considering data scatter, the JPL-Harvard difference is essentially zero at cruise altitude, which would also be deduced using the NOAA-AL Lyman- $\alpha$  as a transfer standard. In other cases, using an third instrument as a transfer standard does not work as well. One such example uses the NOAA-CMDL frostpoint, the MLS, and the HALOE instrument. In the 60 to 100 hPa layer, MLS differs from HALOE by  $\sim 5\%$ , with HALOE larger. The NOAA-CMDL differs from MLS by  $\sim 3\%$ , with NOAA-CMDL larger,

leading one to conclude that the NOAA-CMDL instrument would read ~2% less than HALOE in this layer. However, the direct comparison between the HALOE and NOAA-CMDL instruments shows NOAA-CMDL 12% greater than HALOE. Because of these differences, both the direct comparisons and ranges deduced using a third instrument as a transfer standard will be presented.

One problem in consistency using an instrument as a transfer standard is that it is possible there are instrumental errors that change with time. This could be due to instrument degradation, or changes in atmospheric conditions that affect remote sensing retrievals, such as aerosol loading, temperature, or interfering gas corrections. These types of problems (aerosol in particular) likely affect the HALOE and SAGE II retrievals. Based on comparisons with MLS, it appears that HALOE problems related to aerosols are much lessened by 1993. This is fortunate, in that HALOE comparisons are possible with most of the stratospheric measurements. For this reason, it will be considered the baseline, and all other instruments compared with it. In some cases, there are gradients in the percentage differences throughout the altitude range (HALOE – NOAA-CMDL comparisons shown in Figure 2.21 are one such example). These gradients will be averaged over to give a single value for each table. Because the satellite measurements are reported to be less accurate below ~100 hPa, all comparisons will be presented above that level. The layer from 60-100 hPa contains the best overlap of satellite- and balloon-borne measurements. Layers from 10-50 hPa, and 1-10 hPa are also considered. By necessity, the *in situ* aircraft instruments will not be included in these comparisons.

Tables 2.5-2.7 show the direct HALOE and indirect comparisons deduced from the information presented in this chapter. The indirect comparisons are presented to show the range possible from the full set of measurements considered. These are constructed as described at the beginning of this section. Figure 2.72 summarises the range of measurements for three pressure layers. The mean values are plotted as symbols, and the range bars map out the extremes from the indirect comparisons. A small range does not necessarily translate into a small uncertainty for the estimate. It may mean that the comparisons are all consistent, or it may simply denote a dearth of indirect comparisons. In the cases of POAM III and SAGE II, no indirect comparisons were available, therefore, the range given is the internal sunrise/sunset difference deduced for each instrument.

In the 1-10 hPa layer (Table 2.5, top panel of Figure 2.72), 11 instruments are considered. Coincident comparisons with HALOE were possible with all the instruments except SAGE II. For SAGE II, climatological comparisons were included. All instruments are remote sounders, from satellite, high altitude balloon, space shuttle, and ground based platforms. At this level, aerosol contamination problems for the solar occultation instruments should be minimal, and geophysical variability should also be low, making this layer ideal for these sorts of comparisons. The absolute range of both direct and indirect comparisons with HALOE is -5% to +17%. The mean is +5% and the median is +6%. The mean comparisons (symbols in Figure 2.72) of 9 of the 11 instruments cluster between 0% and 10% greater than HALOE. All instruments considered for the 1-10 hPa layer agree within their stated levels of accuracy.

In the 10-50 hPa layer (Table 2.6, middle panel of Figure 2.72), 13 instruments are considered. Only climatological comparisons were possible between HALOE and SAGE II, and only indirect comparisons using other instruments transfer standards were possible for MIPAS. This layer allows comparisons between satellite and balloon-borne remote sounders and *in situ* balloon-borne instruments. The range of both direct and indirect comparisons with HALOE is -30 % to +27 %. However, this wide range is a consequence of a large range in the HALOE-LMD frostpoint comparison. If the LMD frostpoint comparisons are neglected, the range is reduced to -8 % to +16 %. The mean of the comparisons in this layer is +3%, and the median is +4%. The mean comparisons of 11 of the 13 instruments fall between -2% and +8%.

On average, the instruments considered for the 10-50 hPa layer also agree within their stated levels of accuracy.

The 60-100 hPa layer (Table 2.7, bottom panel of Figure 2.72) has the largest number (15) of instruments and measurement techniques of the 3 layers discussed here. The range of both direct and indirect comparisons with HALOE is large, from  $-15\%$  to  $+42\%$ , with the range of mean comparisons (symbols plotted) from  $-9\%$  to  $+20\%$ . The mean of the comparisons is  $+6.5\%$ , the median is  $+6\%$ , and 11 of the 15 instruments fall into the range  $-1\%$  to  $+14\%$ . The two lowest instruments are satellite sensors, and the two highest are aircraft borne *in situ* instruments. The balloon-borne *in situ* and remote sensor measurements cluster near the mean. In this layer, geophysical variability is larger, thereby making close coincidences for comparisons more important. A greater number of measurement techniques are used here, however accuracies quoted in Chapter 1 do not indicate that should be a problem. Although the bulk of the measurements at this level do agree to within stated accuracies, the low satellite and high *in situ* aircraft measurements do not. Similar differences are also present in the derived quantity  $[\text{H}_2\text{O}]_e$  (see Table 2.4), which should minimise sampling mismatch problems. Thus, it appears that the differences noted here are real. The differences between instruments occupying the extreme positions exceed what would be expected based on the uncertainties given in Chapter 1.

**Table 2.5.** Summary of the relationship for measurements of water vapour above 10 hPa and below 1 hPa. Percentages reflect differences from HALOE measurements. The first column shows direct comparisons with HALOE. The second column shows a deduced relationship with HALOE using the instrument in the previous column as a transfer standard..

Direct Comparisons with HALOE	Indirect Comparisons with HALOE using a transfer instrument
HALOE +0%	
MLS -5%	ATMOS +5% MAS -2% FIRS-2 0% WVMS -3%
SAGE II (SR) +9% (SS) +3% (climatological comparisons)	No indirect comparisons considered for climatological comparisons.
POAM III (NH,SR) -5% (SH,SS) +7%	No indirect comparisons available for this assessment.
ILAS (SH,SS) +8% (NH,SR) +12%	MkIV +16% FIRS-2 +17% (indirect ILAS comparisons valid for NH)
ATMOS +3%	MLS -2% MAS +6% MkIV +3%
MAS +5%	MLS -2% ATMOS +9% WVMS +8%
MkIV +10%	ILAS +14% ATMOS +10% FIRS-2 +12%
FIRS-2 +5%	MLS -5% ILAS +10% MkIV +3%
WVMS +6%	MLS +9% ATMOS +9% MAS +3%
WASPAM +12% 10% in 1994, 14% in 1998 absolute range from 9% to 17%	No indirect comparisons available for this assessment.

**Table 2.6.** Summary of the relationship for measurements of water vapour between 10 and 50 hPa. Percentages reflect differences from HALOE measurements. The first column shows direct comparisons with HALOE. The second column shows a deduced relationship with HALOE using the instrument in the previous column as a transfer standard. MIPAS had no direct comparison with HALOE available for this assessment, and is only included in the second column.

Direct Comparisons with HALOE	Indirect Comparisons with HALOE using a transfer instrument
HALOE +0%	
MLS -8%	ATMOS +5% MAS +1% FIRS-2 -1% CMDL -11% LMD balloon (frostpoint) +12%
SAGE II (SR) +6% (SS) +2% (climatological comparisons)	No indirect comparisons considered for climatological comparisons.
POAM III (NH,SR) -8% (SH,SS) +8%	No indirect comparisons available for this assessment.
ILAS (SH,SS) -1% (NH,SR) +5%	MkIV +3% FIRS-2 +7% MIPAS +11% FISH +15% LMD balloon (frostpoint) +17% (indirect ILAS comparisons valid for NH)
ATMOS +6%	MLS -7% MAS -4% MkIV +6%
MAS +4%	MLS -5% ATMOS +14%
MkIV +5%	ILAS +10% ATMOS +5% FIRS-2 +0%
FIRS-2 +4%	MLS -3% ILAS +9% MkIV +9%
FISH Lyman-alpha +6%	ILAS +16% LMD balloon (frostpoint) +1%
NOAA CMDL (frostpoint) -5%	MLS -2%
LMD balloon (frostpoint) (tropics) +15% (Sweden) -10%	MLS -30% to -5% ILAS +2% to +27% MIPAS -7% to +19% FISH -5% to +20%

**Table 2.7.** Summary of the relationship for measurements of water vapour between 60 and 100 hPa. Percentages reflect differences from HALOE measurements. The first column shows direct comparisons with HALOE. The second column shows a deduced relationship with HALOE using the instrument in the previous column as a transfer standard. Italicized instruments (JPL TDL and MIPAS) in the second column have no direct comparison with HALOE available for this assessment.

Direct Comparisons with HALOE	Indirect Comparisons with HALOE using a transfer instrument
HALOE +0%	
MLS -5%	ATMOS +8% FIRS-2 +10% HARV +15% CMDL -2% LMD balloon (frostpoint) +5%
SAGE II (SR) -4% (SS) -14% (climatological comparisons)	No indirect comparisons considered for climatological comparisons.
POAM III (NH,SR) -2% (SH,SS) +5%	No indirect comparisons available for this assessment.
ILAS (SH,SS) ~0% (NH,SR) +3%	MkIV +6% FIRS-2 +5% <i>MIPAS</i> -1% FISH -2% (indirect ILAS comparisons valid for NH)
ATMOS +5%	MLS -8% MkIV +3% AL +3% HARV +18%
MKIV +13%	ILAS +10% ATMOS +15% FIRS-2 +13% HARV +20% <i>JPL TDL</i> +15%
FIRS-2 +5%	MLS -10% ILAS +7% MkIV +5% HARV +21% <i>JPL TDL</i> +21%
NOAA AL Lyman-alpha (AL) +8%	ATMOS +10% HARV +23% CMDL -12% <i>JPL TDL</i> +23%
Harvard Lyman-alpha (HARV)+20%	MLS +0% ATMOS +7% MkIV +15% FIRS-2 +4% AL +5% CMDL -10% <i>JPL TDL</i> +21%
FISH Lyman-alpha +8%	ILAS +13% LMD Balloon (frostpoint) +3%
NOAA CMDL (frostpoint) +12%	MLS +15% AL +32% HARV +42%
LMD balloon (frostpoint) (tropics) +15% (Sweden) -5%	MLS -15% to +5% <i>MIPAS</i> -1% to +19% FISH +0% to +20%

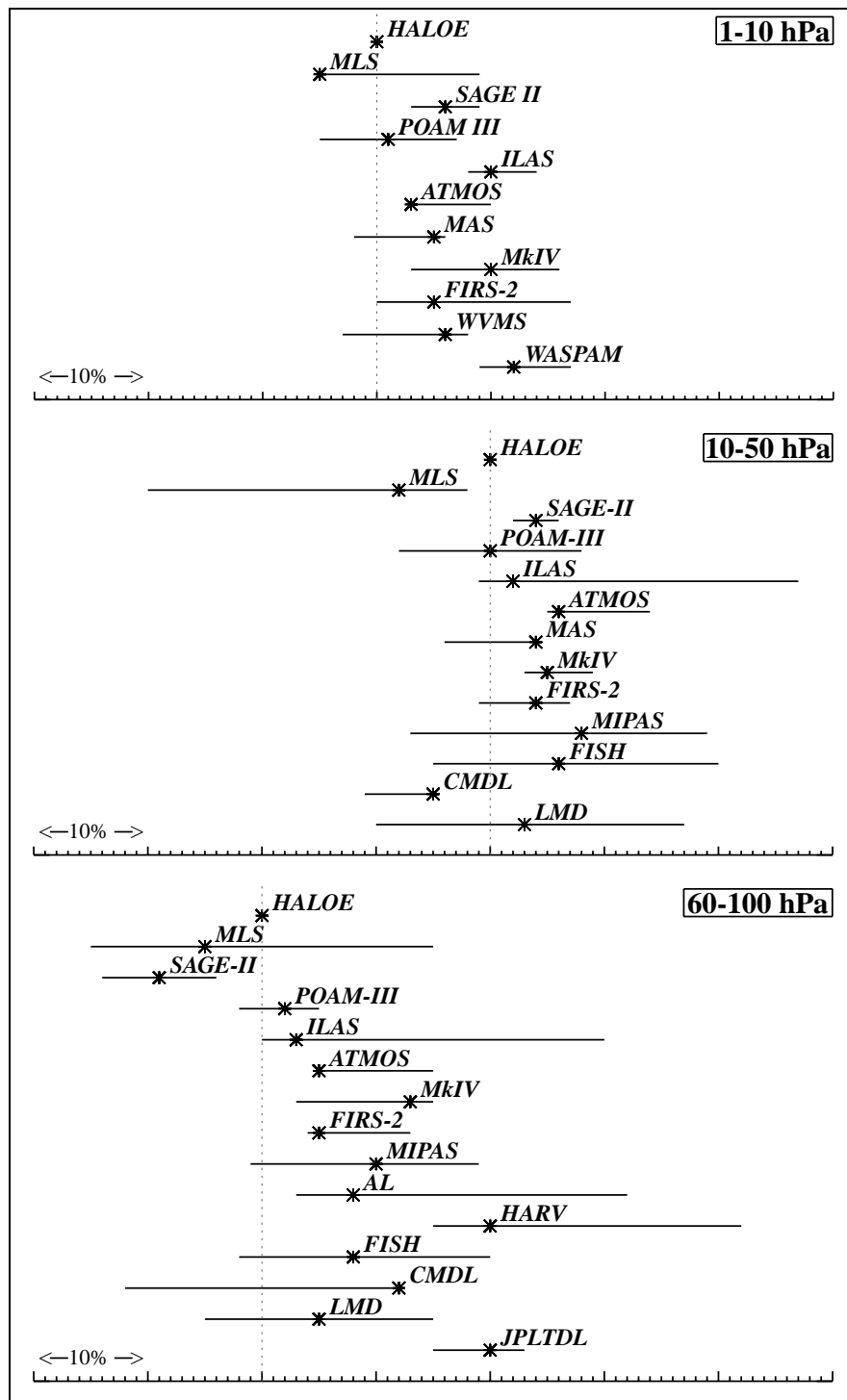


Figure 2.72. Summary of the relationship between stratospheric measurements assessed in this report for 3 altitude ranges. The symbols give the direct percentage difference from HALOE, and the horizontal lines show the range of the indirect comparisons presented in Tables 2.5–2.7. Each tick mark is 1%, and the placement for HALOE is indicated by the dotted line. Where no direct comparison was available, the symbols give the average of the indirect comparisons.

---

At levels above 50 hPa, overall agreement between the sensors compared is quite good. The range of the direct comparisons with HALOE is less than 20%, with a clustering of nearly all the instruments within a range of 10% and instruments agreeing to within their stated levels of uncertainty. In the lowest layer considered, the agreement is still good in general, although the direct comparison extremes cover a range of 30% and most of the instruments compared fall within a 15% range.

From this set of comparisons, it appears that the infrared instruments agree well with each other and with the balloon-borne *in situ* instruments. The MLS stratospheric water vapour is biased low relative to the other instruments at all levels. In the 10-50 hPa layer, the two frostpoint instruments considered tend to be biased slightly low relative to most of the other measurements. This is not true in the 60-100 hPa layer, where both frostpoint instruments fall in the middle of the cluster of comparisons. The one stratospheric aircraft TDL instrument was not only biased larger than the other instruments at its cruise flight level, but there was a pressure dependence to its difference with the coincident Lyman- $\alpha$  measurements. Three Lyman- $\alpha$  instruments were considered, and there was not a consistent bias associated with the three as a whole. However, one of the instruments was biased high relative to the others in flight, but agreed within stated uncertainties when compared with both a frostpoint and another Lyman- $\alpha$  instrument under controlled laboratory conditions. This indicates that the fundamental *in situ* techniques are well understood, but that implementations of those techniques on airborne platforms are not. The reason for the larger spread in flight conditions is not understood; the problem deserves further attention.

Three of the solar occultation satellite instruments (SAGE II, ILAS and POAM III) show significant sunrise-sunset differences that deserve further examination. SAGE II is biased low in the 60-100 hPa layer, but there are likely aerosol contamination problems with its lower stratosphere retrievals associated with the decay of aerosol from the eruption of El Chichón. Although useful for deducing certain aspects of atmospheric behaviour, one should ensure that the research application fits the capabilities of the SAGE II data set. Filtering to avoid regions of high aerosols is likely needed. A new retrieval has been recently released, but it remains to be seen what improvements result. It should be noted that such an aerosol contamination problem is not unique to the SAGE II data. As described in section 2.4.2, during its first year of operation, HALOE measurements in the tropics are also likely affected by Mt. Pinatubo aerosols.

In spite of the differences detailed above, it appears that the agreement between different instruments measuring stratospheric water vapour has improved significantly over the past 15 years. Results presented in Albritton and Zander [1985] (see their Figure C-7) show a range of 50-60% between different balloon-borne instruments in an organised comparison, with no clear apparent clustering of measurements. In the present set of comparisons, the majority of the instruments cluster within a 10% range at all levels, with the extremes of the indirect comparisons of clustered instruments separated by  $\sim 30\%$ . If the small number of instruments that fall at the high and low ends of the comparisons are considered, the extremes of the indirect comparisons are separated by  $\sim 50\%$ . Still, the bulk of the instruments agree well with their stated errors. This should be considered a vast improvement over the state of stratospheric water vapour measurements in the early 1980's.

Existing measurements should be adequate for describing the seasonality of lower stratospheric water vapour, and deducing certain aspects of stratospheric transport and stratosphere-troposphere exchange. Yet, even this seemingly good agreement is not sufficient to allow combining instrumental records to estimate long-term changes in stratospheric water vapour. Deduced changes presented in section 2.5.5 are on the order of 1%/year. 10% agreement is not sufficient to allow combination of time series from different instruments; the biases are still

---

larger than the signal of interest. A long data set from the same instrument is more valuable than a series of short data sets from different instruments for long-term change determinations. Continuing to fly instruments with extensive histories is important for monitoring the stratosphere for long-term changes in water vapour.

### 2.6.2 Upper tropospheric humidity comparisons

Because of the radiative importance of water vapour in the upper troposphere and the potential for long-term change, an assessment of the quality of the data in this region of the atmosphere is an essential part of this chapter. In terms of available data for describing the distribution and understanding the processes that control water vapour in the upper troposphere, the data set from the HIRS sensor on TOVS is the most comprehensive in geographic coverage and length of record. The world-wide radiosonde network has provided tropospheric humidity measurements since the 1940's. The length of record and global coverage suggest that radiosondes have the potential for providing data for addressing questions about water vapour behaviour, and could be an important tool for evaluating other measurement techniques. However, the radiosonde network humidity sensor performance tends to be of poor quality at cold temperatures and low pressures (see section 1.1.4), which are precisely the conditions experienced in the upper troposphere. Additionally, as noted in section 1.1.4, there have been numerous changes in instrumentation over the existing data record, this complicates analysis of such data for long-term changes. However, because of their relatively low cost, operational radiosondes have been, and likely will continue to be, used for validation purposes of upper tropospheric humidity. The recent improvement of radiosonde humidity sensors holds some promise for obtaining better data from these operational instruments. Comparisons presented in this chapter (section 2.2.3) between the widely used Vaisala *Humicap* A sensor and the NOAA-CMDL frostpoint instrument show, for example, that at temperatures of  $-60^{\circ}\text{C}$  the reported humidity from the radiosonde is only one half of the frostpoint instrument value. From this type of comparison, a correction algorithm to improve the quality of the upper tropospheric radiosonde data was developed. However, application of this correction to the archived Vaisala radiosonde data set for the period 1991-1994 for comparison with the MLS upper tropospheric water vapour product yielded inconsistent results that are not currently understood (see section 2.3.2). Appropriately calibrating the radiosonde humidity element for the temperature conditions of the troposphere can improve the accuracy of the measurements (section 2.2.3). Such calibrations are being implemented in newer radiosonde models.

In addition to radiosondes, several other non-satellite systems were compared primarily with a view toward their value in evaluating the TOVS and MLS upper tropospheric water vapour products, but also for their potential as new technologies for future measurements. Both DIAL and Raman LIDAR systems were compared with radiosondes as well as airborne systems using chilled mirror hygrometers. The LIDARs gave results in the troposphere within about 10% of the correlative measurements, suggesting that such systems can accurately measure water vapour, and that if deployed in sufficient numbers could provide profile data for satellite validation.

Commercial aircraft provide a platform from which upper tropospheric water vapour data can be obtained on a regular basis in heavily used flight corridors. The MOZAIC program currently provides such data using a specially calibrated sensor similar to the Vaisala radiosonde *Humicap*-H. This set also provides potential satellite correlative data. Comparisons of the MOZAIC sensor with airborne frostpoint and Lyman- $\alpha$  hygrometers as part of designed validation experiments show that the MOZAIC measurements are accurate to about 10% in mixing ratio for flight altitudes in the upper troposphere.

---

From the direct water vapour measurements summarised above, comparisons were carried out with the MLS and TOVS satellite observations. The high variability of water vapour in the upper troposphere leaves significant ambiguity in the conclusions from these comparisons. At present, it must be concluded that the direct measurements of UTH do not provide a strong constraint on the satellite measurements of UTH. At the two highest MLS retrieved levels (147 hPa and 215 hPa) the biases are smaller (about 10%) than those at the lower two altitudes where all of the comparisons suggest a dry bias of MLS. Published comparisons of radiosonde humidities with TOVS data show that the radiosondes indicate substantially smaller humidity values. A recent comparison of a fairly small number of properly calibrated radiosonde sensors with TOVS UTH showed only small biases. In the TOVS comparisons with MOZAIC, it was found that at higher latitudes, the satellite weighting function peaked at a different altitude than the aircraft observations. This results in biases between the derived humidities from the two techniques. For comparisons at low humidities, the MOZAIC measurements are smaller than are those from TOVS. However, the bias derived is not statistically significant. An important issue is that the variability of the means of the smaller MOZAIC data set differs significantly from that of the much larger TOVS data set. This indicates that the smaller MOZAIC data set is not adequately capturing the true atmospheric variability, and thus statistical comparisons between the disparate data may not be meaningful.

Comparisons of SAGE II integrated water vapour between 200-500 hPa with integrated TOVS data suggest that SAGE II sampling is insufficient to properly characterise the full variability of upper tropospheric water vapour. Although TOVS samples much more frequently than MLS, the two instruments have similar sampling volumes. These two instruments provided the best opportunity for comparison of satellite UTH. At the 316 hPa level (near the peak of the TOVS-HIRS channel 12 weighting function), the TOVS and MLS give similar results. At very low and at very high values of UTH, MLS averages are biased low relative to TOVS. This is likely due to the small number of coincidences. In the mid-range of UTH there is virtually no bias. Overall these two systems that use very different techniques appear to produce comparable results on monthly averaged time scales.

### 2.6.3 Conclusions and recommendations

Over 25 instruments representing several techniques were assessed for the quality of the data that they produce. More conclusive results about data quality could be drawn from the stratospheric comparisons than those in the upper troposphere. In some ways this reflects the fact that in the upper troposphere water is more dynamic and variable, making comparisons more difficult. It also appears, however, that greater emphasis has been placed on, and attention paid to, developing and validating stratospheric water vapour observations. For both the stratosphere and troposphere there is no single technique or instrument platform that is recognised as a standard to which other techniques should be compared, and thus comparisons were made relative to one another.

In the stratosphere, a reasonable degree of consistency was found among measurements made from near the tropopause up to 50 km (~1 hPa). The majority of the instruments considered clustered within a 10% range, although direct comparisons among other individual instruments showed larger differences, however, with some of these exceeding 30%, and indirect intercomparisons reached 50%. For differences smaller than about 10%, the quality of comparisons makes it difficult to determine the cause of the differences since they may be related to factors such as coincidence of measurements that are affected by atmospheric variability. However, even much larger differences, that indeed appear to be real, such as those between MLS and the Harvard Lyman- $\alpha$  instrument, do not seem to have causes that were revealed through this assessment process.

---

There is only one stratospheric water vapour data set of 20 years duration that has a nearly continuous time series available for determination of long-term changes. There are, however, a number of sets that have sampled periodically over a long period and several time series of intermediate length (8-15 years) that can be used for evaluating stratospheric changes. Although not definitive, these observations are consistent in suggesting that water vapour has increased at about 1%/year over the past 50 years. The record also suggests that this increase has not been uniform but has varied over this period.

In the upper troposphere the TOVS data set is the most extensive in length of record and geographic coverage, and is the only one capable of answering many of the scientific questions about water vapour in this region of the atmosphere. It was therefore the data set that was the focus of the UT data quality assessment. The tropospheric MLS sensor provided the best data set for comparison with TOVS and only small biases were found between them. Comparisons between TOVS and MLS and direct water vapour measurements from radiosondes and aircraft did not provide strong constraints on the performance of the satellite sensors. In part this was due to the shortcomings in the direct measurements, particularly the radiosondes. However, there are also difficulties with making comparisons in an inhomogeneous atmosphere when instruments have very different spatial coverage and altitude resolution. The assessment of the TOVS data did not reveal any major inconsistencies in this data set that would preclude its use in describing the behaviour of upper tropospheric humidity.

Several recommendations that can be made from this evaluation of data quality include:

- Further studies, including well designed intercomparison experiments and laboratory work, are required to quantify and understand the differences between stratospheric water vapour sensors, particularly *in situ* instruments that are required for providing high altitude resolution data for processes of water vapour transport between the troposphere and stratosphere.
- Strong validation programs including correlative measurements need to be a part of water vapour satellite measurement efforts. In the upper troposphere such validation has not been a part of the measurement program. Improvement of radiosonde observations of water vapour and wider use of LIDAR would aid in such validation.
- Greater attention needs to be paid to the continuity of measurements for determination of long-term changes in both the stratosphere and upper troposphere including overlap of satellite measurements. In particular, instruments with a history of high quality measurements should continue to operate in order to monitor long-term changes in stratospheric water vapour.

**Chapter 3**

**Distribution and Variability  
of Water Vapour in the  
Upper Troposphere and Lower Stratosphere**

**Lead Authors**

A. Gettelman - J. Harries - P.W. Mote

**Co-authors**

J. Anderson - J. Bates - R. Bevilacqua - A.E. Dessler - R. Fu  
D.J. Gaffen - E.J. Jensen - D. Kley - G.E. Nedoluha - S.J. Oltmans  
L. Pan - L. Pfister - H.C. Pumphrey - W.J. Randel - E.E. Remsberg  
E.P. Salathe - S.C. Sherwood - U. Schumann - H. Smit - C. Smith  
E.M. Stone - R. Toumi - H. Vömel - E.M. Weinstock - X. Zhou

## 3.1 Introduction

Knowledge of the distribution and temporal variability of water vapour in the UT/LS is important for a variety of current scientific problems. However, our knowledge shows some surprising gaps, given the wide range of observational and modelling power now available to us. Previous attempts have been made to summarise and understand this time-dependent distribution (e.g. see the book by *Ludlam*, [1980]; see also, *Harries*, [1976]; *Peixoto and Oort*, [1992]), with some success, though the fundamental questions of precisely what mechanisms control the distribution of water vapour in the UT/LS have in many cases remained unsolved. This chapter brings together a summary of our understanding of the mechanisms that control the distribution and variability of water vapour in the UT/LS, based on the findings of Chapters 1 and 2. The remainder of this Introduction illustrates some of the scientific issues of radiation, dynamics and chemistry that depend on this understanding.

### 3.1.1 Radiation

The principal impact of water vapour on the radiative balance of the Earth is through the long-wave, infrared part of the spectrum. Water vapour has an intense pure rotation band stretching from about 50 to 400  $\text{cm}^{-1}$  (200-25  $\mu\text{m}$  wavelength), and a strong  $\nu_2$  vibration-rotation band centred at about 1590  $\text{cm}^{-1}$  ( $\approx 6.3 \mu\text{m}$ ), extending for over 100  $\text{cm}^{-1}$  in both directions [*Goody*, 1964]. In addition, water vapour exhibits the curious ‘continuum’ absorption across wide reaches of the infrared spectrum, being most noticeable in the ‘window’ region between about 800 and 1250  $\text{cm}^{-1}$  (12.5-8.0  $\mu\text{m}$ ; see *Bignell*, [1970]; *Burch*, [1981]). Because of the strong absorption and emission by these bands, water vapour is the dominant greenhouse gas in the atmosphere. Figure 3.1 shows a calculation of the spectrally resolved greenhouse parameter for a tropical and a sub-Arctic winter model atmosphere [*Brindley and Harries*, 1998]. The greenhouse parameter shows the difference between the flux of radiation leaving the Earth’s surface (at an assumed temperature), and the flux leaving the top of the atmosphere. This is a measure of the energy trapped in the earth system by the atmosphere, as a function of wave number. The importance of the pure rotation band of water vapour (50 to 400  $\text{cm}^{-1}$ ), highlighted in work by *Doherty and Newell* [1984] and *Clough et al.*, [1992], is clear from this diagram. Figure 3.2, also taken from work by *Brindley* [1998] shows the cooling rate for the same two model atmospheres, showing the importance of the far infrared emission to space, between about 100 and 500  $\text{cm}^{-1}$  (100-20  $\mu\text{m}$ ). This cooling is largest in the mid to upper troposphere. Clearly, this mechanism of planetary cooling is important in maintaining the energy balance of the Earth, and so is of great importance in climate models. However, due to the considerable uncertainty over the concentration and variability of water vapour in the upper troposphere, it is unclear at present whether or not these models correctly represent these cooling rates. More work is required to establish upper tropospheric concentrations and variability, and to measure radiative flux divergences *in situ* in the atmosphere.

Current radiative problems that require an accurate knowledge of water vapour distributions include:

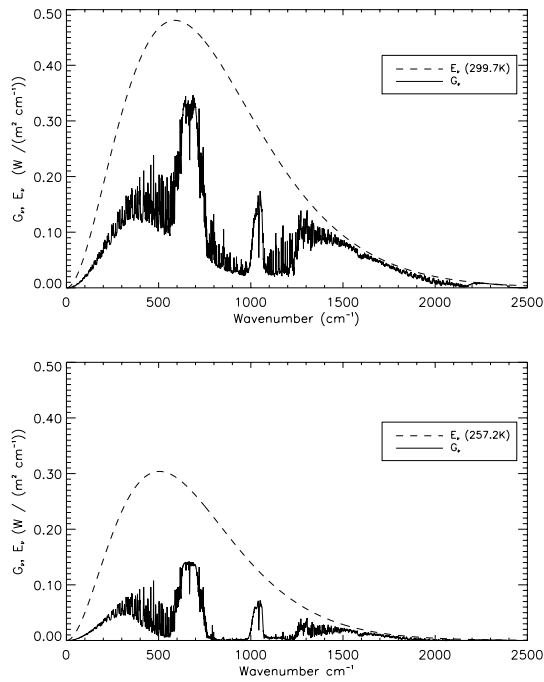


Figure 3.1. Water vapour greenhouse effect as a function of wave number for an atmospheric profile typical of (top) the tropics and (bottom) sub-Arctic winter. The dashed curve in each panel shows the Planck blackbody radiation for the indicated temperature, and the solid curve shows downward long-wave emission from the atmosphere.

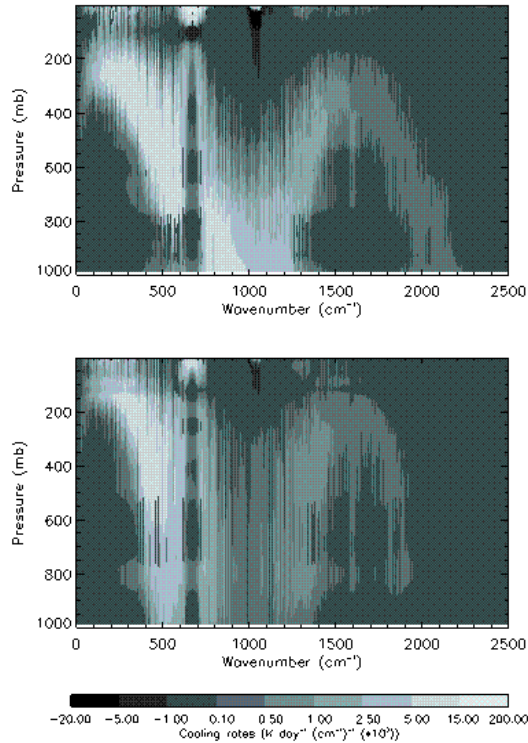


Figure 3.2. Variation of long-wave cooling rates with pressure and wave number for the Tropical (top) and sub-Arctic winter (bottom) model atmospheres depicted in Figure 3.1. Adapted from Brindley and Harries [1998]. Units of K per day per wave number.

- The stability of UT cooling to space in the presence of water vapour concentration variations. An interesting compensation exists between density and temperature in the UT, because if optical density increases (decreases), emission takes place from a higher, colder (lower, warmer) layer, because of the negative lapse rate with height (see, for example, *Sinha*, [1995]; *Slingo and Webb*, [1997]). The radiative response of the UT to a changing climate depends on the balance between these two effects.
- Some controversy still surrounds the related question of whether the water vapour climate feedback effect is positive or negative in the UT [*Lindzen*, 1990; *Rind et al.*, 1991]: a question remains as to whether dynamical motions might respond to global warming by producing a drier UT.
- Recent studies by *Allan et al.*, [1999] have demonstrated that in the tropics, where high humidity effectively decouples surface radiation from the energy that emerges from the top of the atmosphere, the outgoing long-wave radiation depends strongly on atmospheric humidity, but only weakly on surface temperature. Conversely, at higher latitudes, where humidity is lower, the outgoing long-wave radiation is strongly coupled to the surface conditions, but less so atmospheric humidity. It is not clear how such dependence might change with time.
- Work on the spectral distribution of the impact of climate change on the outgoing long-wave radiation spectrum [*Slingo and Webb*, 1997, *Brindley and Harries*, 1998, *Allan et al.*, 1999], has increased our understanding in recent years of how water vapour and its variability affects the spectrum of outgoing long-wave radiation, and therefore the climate system. Some recent work has suggested that observations of spectrally resolved outgoing long-wave radiation may contain signatures of climate change, but more work is required in order to establish this possibility.
- In the stratosphere, the humidity is extremely low: mixing ratios of a few parts per million are typical, as has been well known for many years. Even so, the radiative effects of stratospheric water vapour are significant [*Goody*, 1964; *Forster and Shine*, 1999; *Shindell*, 2000]. Evidence has been accumulating over many years [e.g. *Oltmans and Hofmann*, 1995] that mixing ratios in the lower stratosphere may change with time: the question therefore arises as to what is the radiative impact of such changes.

In all these areas, key uncertainties include an accurate knowledge of the distribution, variability and trends of water vapour, and how these effects interact with the radiation field and the climate.

### 3.1.2 Dynamics

Water vapour distributions are strongly influenced by atmospheric dynamics, but also influence them in turn. Thus, observed water vapour distributions can serve as useful diagnostics of the atmospheric circulation. Water vapour condensation also provides a substantial reservoir of heat in the atmosphere, so that accurate knowledge of water vapour is also mandatory for accurate predictions of the future development of the circulation.

The diagnostic applications of water vapour observations are clear. First, imagery of upper tropospheric water vapour now available from geostationary satellites demonstrate structures which have been used to improve our understanding of the general circulation of the middle and upper troposphere [e.g. *Woodberry et al.*, 1991]. Nimbus 7 provided quantitative near-global measurements of lower stratospheric humidity for the first time [*Gille and Russell*, 1984; *Russell et al.*, 1984; *Remsberg et al.*, 1984]. The nearly one decade of measurements of water vapour in the lower stratosphere from the HALOE instrument on UARS have been particularly valuable [*Russell et al.*, 1993; *Harries et al.*,

1996], as have the long time series of balloon frost point measurements by Oltmans, and before him, Mastenbrook [Oltmans and Hofmann, 1995].

Conversely, the influence of water vapour on dynamics is also well recognised by forecasters and climatologists. The atmospheric temperature structure would be dramatically different if not for water vapour condensation. Storm initiation and development have also been shown to depend on water vapour abundance, not only in the boundary layer [Normand, 1938] but also in the middle and perhaps upper troposphere [e.g. Stommel, 1947, Pepler and Lamb, 1989]. The ability of vapour to influence cloud populations also gives it a strong indirect influence on large-scale dynamics, including those in the UT/LS.

Despite this progress, the dynamical processes that control the dryness of the stratosphere have remained enigmatic for more than three decades, despite a huge volume of work, much too voluminous to list in this report with any adequacy. The original Brewer-Dobson hypothesis [Brewer, 1949, Dobson *et al.*, 1946], and other early pioneering work [e.g. Mastenbrook, 1968] remains the foundation of thinking, but many other subtle effects have been identified. These include:

- The prospect of a stratospheric ‘fountain’ identified by *Newell and Gould-Stewart* [1981], that is the possible existence of particularly important regions for stratospheric injection, caused by variation of the power of the convective ascent of air in tropical regions, at different longitudes;
- The discovery of the ‘hygropause’, a minimum in tropical mixing ratios at a height above the local tropopause, by Kley and colleagues [Kley *et al.*, 1979];
- Evidence for steep latitudinal gradients of water vapour (and other constituent) mixing ratios at the edge of the tropics [Murphy *et al.*, 1993; Holton *et al.*, 1995];
- Work on the exchange between the lower stratosphere and the upper troposphere associated with the sub-tropical jet stream [Vaughan and Timmis, 1998];
- Ideas about the role of tropopause-penetrating thunderclouds as sources of dry air from Johnston and Solomon [1979] and Danielsen [1982, 1993];
- Observations of the distribution of water vapour by many workers, notably by Kley *et al.* [1979], Kelly *et al.* [1993], Rosenlof *et al.* [1997], and others using the Lyman- $\alpha$  hygrometer;
- Observations and analysis of hemispheric and polar vortex distributions of water vapour [e.g. Tuck *et al.*, 1997];
- Polar orbiting satellite observations, pioneered by the Nimbus 7 LIMS experiment [Russell *et al.*, 1984], and followed by others: SAGE II [McCormick *et al.*, 1993], the UARS instruments, HALOE (see earlier references), ISAMS [GossCustard *et al.*, 1996] and MLS [Waters *et al.*, 1999]. HALOE and MLS data have led to the identification of the ‘tape recorder’ idea – see Mote *et al.*, [1996]. Work to combine the observations from different instruments has proved valuable, for example by Jones *et al.*, [1986] to merge the water vapour from the LIMS experiment on Nimbus 7 with the methane measurements provided by the SAMS experiment on the same satellite;
- Recent work [Rosenlof *et al.*, 1997, Dethof *et al.*, 1999] has illustrated the impact of the surface topography (e.g. the Tibetan plateau) on the dynamics of the UT/LS region, and the transport of humidity into the stratosphere.

Despite the huge progress achieved, substantial uncertainties exist. Most prominent, of course, is the remaining uncertainty over the specific processes that keep the stratosphere so dry! Behind this and many related questions lies the difficulty that the *large scale* phenomenon that we observe – the dry stratosphere - is probably due to the collective effect of one or more *small scale* processes occurring over a large regime of the tropopause region (see section 3.3.3). The processes that control the dryness of the stratosphere are almost certainly smaller than the scales represented in our models, and also difficult to parameterise. They are also extremely difficult to observe, maybe because of this small scale, or simply because of the difficulty of their detection (e.g. detecting the drying effect of penetrating thunderclouds).

### 3.1.3 Chemistry

Water vapour is important for atmospheric chemistry in several ways. It is the source of OH, the hydroxyl radical, in both the troposphere and the stratosphere. OH is of direct importance in many chemical cycles in both regions [Brasseur and Solomon, 1984, Wayne, 1985]. OH and more generally hydrogen oxides ( $\text{HO}_x = \text{OH} + \text{HO}_2$ ) take part in an important catalytic cycle for regulating the production and destruction of ozone in both the troposphere and stratosphere [Wennberg *et al.*, 1994]. OH also controls the oxidising capacity (cleansing) of the atmosphere for short lived gases and regulates the lifetimes of the longer lived species such as CO and CH<sub>4</sub>. Thus, it is important to understand the dynamics driving the concentration and distribution of water vapour, as well as the chemical and photochemical reactions transforming water vapour into OH.

The budget of hydrogen in the stratosphere has been studied by a number of workers, including Le Texier *et al.* [1988], the satellite work already mentioned by Jones *et al.* [1986], and by Pyle *et al.* [1983]. These papers, and many others, have discussed the oxidation of methane to produce water vapour, as an *in situ* stratospheric source of humidity.

In this chapter we discuss the variability of water vapour in the upper troposphere and lower stratosphere using the observations discussed in Chapters 1 and 2. We start with the annual mean distribution in section 3.2. The seasonal cycle, which is the dominant time scale of variability in both the UT and LS is discussed in section 3.3. In section 3.4 we discuss longer (interannual) and shorter (intraseasonal) variations in water vapour, along with small scale or ‘transient’ variations. Finally, in section 3.5 we discuss long-term variations in the distribution of water vapour in the upper troposphere and lower stratosphere. These various time and space scales require using a full suite of *in situ*, ground-based and satellite observations of water vapour. This analysis focuses on those data sets with significant time and space resolution to cover the various modes of variability. As a result, extensive use is made of satellite data where possible. *In situ* data are also shown where appropriate. Having available the analysis in chapter 2, we show only those data that best illustrate the variability discussed.

## 3.2 Mean Distribution of LS/UT Water Vapour

The mean distribution of water vapour is best described using global satellite data sets, which offer a large number of measurements in space and time. In the stratosphere, we focus on data from HALOE and to a lesser extent MLS and POAM. In the troposphere, we focus on data from HIRS and MLS.

Trace constituents in the stratosphere, water vapour included, tend to have relatively small variations along a latitude circle except in the lower-most stratosphere. These variations are even smaller along a streamline and smaller still along a curve with constant potential vorticity (PV) and constant potential temperature ( $\theta$ ). The zonal dimension adds little information about water vapour, at least once the zonal variations of the flow have been noted. Therefore, most of the results we show in the stratosphere either have been zonally averaged or have been averaged along a PV- $\theta$  contour.

In the troposphere, by contrast, the water vapour distribution is more fully three-dimensional, with very large variations (up to four orders of magnitude) in the vertical. Even so, in the tropics and subtropics, the horizontal patterns are qualitatively similar over a considerable range of altitudes, so that the vertical variations can to some extent be ignored. Therefore, for the troposphere, we focus on horizontal variations.

### 3.2.1 Lower Stratosphere

The annual mean water vapour distribution in the lower stratosphere is shown in Figure 3.3. The key features are a sharp vertical gradient at the tropical tropopause and in the extratropical lower stratosphere, a minimum in the tropics at or just above the tropopause, and gradual increases upward and poleward. Following *Kley et al.* [1979], we refer to the minimum in water vapour as the “hygropause,” and we note that in the annual zonal mean it occurs near the 400 K potential temperature surface. As noted in Chapter 2, HALOE has a slight dry bias at these altitudes, so it is possible that the sharpness of the dry feature in Figure 3.3 is an exaggeration.

Before discussing the mechanisms responsible for producing these features, we first describe how the figure was constructed. HALOE water vapour measurements for the years 1991-1999 were averaged following the method of *Randel et al.* [1998], making use of MLS data in polar regions only to fill in gaps in the HALOE coverage. The data are averaged following a PV- $\theta$  contour (see above) and then mapped to the “equivalent latitude” [*Buchart and Remsberg, 1986*] of the PV contour, i.e., the latitude at which the area enclosed by a latitude circle equals the area enclosed by the PV contour. Equivalent latitude better preserves geophysical gradients around the polar vortex by classifying air dynamically [see *Randel et al., 1998*]. Outside of polar regions the values are nearly identical to zonal means. The vertical sampling of these HALOE data is  $\sim 0.3$  km and it has a vertical resolution of  $\sim 2$  km, with observations available in cloud-free regions above the tropopause.

The key features in the mean distribution can be understood primarily as a balance among the following processes: (1) a mean meridional circulation, (2) stratospheric photochemistry, (3) dehydration at the tropical tropopause, (4) seasonal dehydration in the polar regions and (5) a variety of processes through which tropospheric moist air leaks into the extratropical lower stratosphere (below about 100 hPa). We now discuss each of these processes in more detail.

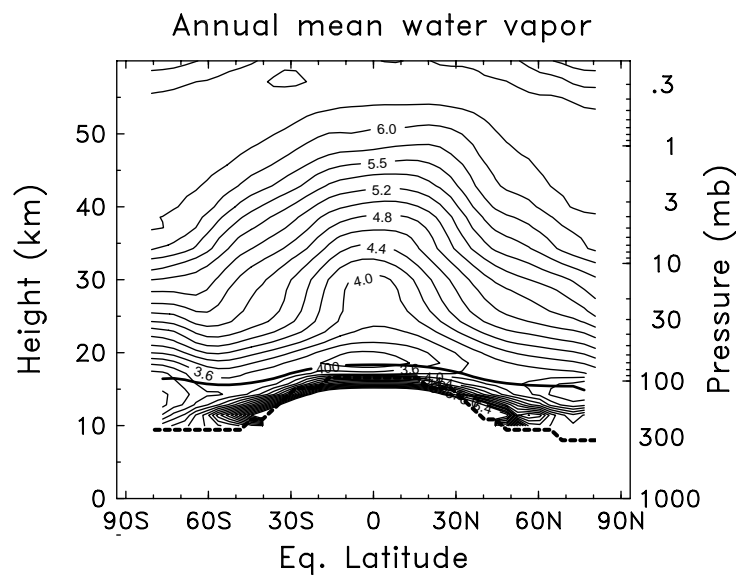


Figure 3.3 Annual zonal mean water vapour from HALOE and MLS data by height and equivalent latitude. Contour interval of 0.2 ppmv. The thick dashed line is the tropopause, and the thick solid line is the 400 K potential temperature surface.

### (1) Mean meridional circulation

Measurements of water vapour in the mid-latitude lower stratosphere in the 1940's led *Brewer* [1949] to the deduction that air entered the stratosphere at the tropical tropopause and spread poleward. From Figure 3.3 it can be seen that the layer of driest air extends fairly far poleward, but is fairly shallow. *Murgatroyd and Singleton* [1961] deduced, on the basis of radiative calculations, that in the lower stratosphere, air must rise in the tropics and sink at the poles (Figure 3.4). This circulation, combined with the vertical gradient produced by methane oxidation (see below), explains the upward bulge in the tropics of isopleths in Figure 3.3 [see, for example, *Remsberg et al.*, 1984].

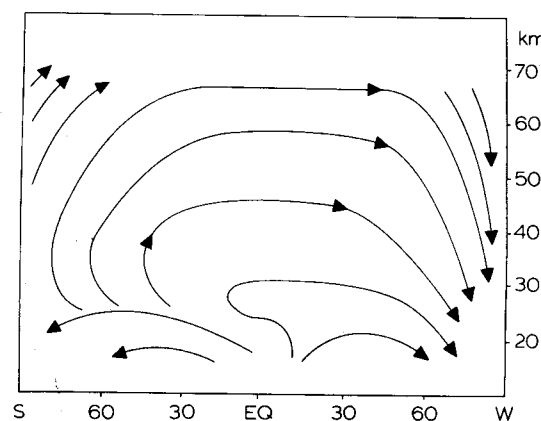


Figure 3.4 Schematic streamlines of the Lagrangian-mean circulation during solstice season (summer on the left, winter on the right). From *Dunkerton* [1978].

At all levels in the extratropics, but especially in the lowest few kilometres of the stratosphere, nearly isentropic outward transport and mixing of dry tropical air combines with subsidence of moister air. Nearly isentropic transport and mixing are also suggested by

radioactive isotopes [Newell, 1963], laminae of high- and low-ozone air [Dobson, 1973], stratospheric aerosol observations [Trepte *et al.*, 1993, Hitchman *et al.*, 1994] and temperature anomalies associated with aerosol plumes [Newell, 1970]. These data suggest that it is rapid isentropic mixing that produces the layer of dry air in the lower stratosphere that covers much of the globe. This near-global minimum in the lower part of the stratosphere (below 20 km or so) is also observed in SAGE II water vapour data [Chiou *et al.*, 1997]. Tuck *et al.* [1997] have also noted that the meridional mixing process above the tropical tropopause “recirculates” mid-latitude air with higher water vapour concentrations back into the tropical lower stratosphere in this layer.

A useful concept in describing distributions of trace constituents in the stratosphere is the “age of air” [Hall and Plumb, 1994]. In this view, each air parcel is composed of fluid elements that followed different paths to that point, each path with different photochemical exposure histories. The water vapour mixing ratio of the air parcel is determined by the combination of those fluid elements. Thus, the moist air in the upper stratosphere has a high mean age [Hall and Plumb, 1994]. The dry layer of the extratropical lower stratosphere (near 400 K; see Figure 3.3) is composed primarily of fluid elements with low mixing ratio that have travelled rapidly out from the tropical tropopause, but also of some fluid elements of high mixing ratio that have travelled all the way to the stratopause and then down at middle and high latitudes.

In addition to the mean meridional circulation, mixing of air by planetary-scale waves is also important in determining some of the details shown in Figure 3.3. Wave mixing varies strongly in latitude, height, and season, with weak mixing in the subtropics in all seasons (hence the tilting of isopleths there), seasonally varying strong mixing in middle latitudes of the winter hemisphere, and weak mixing at the edge region of the polar vortex in winter [Nakamura and Ma, 1997].

## (2) Stratospheric photochemistry

Another important mechanism in determining the distribution of stratospheric water vapour is the oxidation of one molecule of methane into roughly two molecules of water [LeTexier *et al.*, 1988; Brasseur and Solomon, 1986]. In addition to H<sub>2</sub>O, air entering the stratosphere from the troposphere carries ~1.7 ppmv (1990s value) of CH<sub>4</sub> [Dlugokencky *et al.*, 1998] and ~0.5 ppmv of H<sub>2</sub>. In the stratosphere, CH<sub>4</sub> and H<sub>2</sub> are destroyed by photolysis [e.g., Scholz *et al.*, 1970]. On time scales relevant to the mean distribution of water vapour (months to years), the oxidation of H<sub>2</sub> produces one H<sub>2</sub>O molecule. Oxidation of CH<sub>4</sub> is more complicated, and leads to the production of both H<sub>2</sub>O and H<sub>2</sub>. The exact amount of these produced is a function of altitude and latitude, but generally results in ~2 water molecules for each methane molecule oxidised [Jones *et al.*, 1986; LeTexier *et al.*, 1988, Dessler *et al.*, 1994; Hurst *et al.*, 1999; Zöger *et al.*, 1999]. The sum 2×CH<sub>4</sub>+H<sub>2</sub>O is, as a consequence, nearly constant except where air is significantly influenced by dehydration, like the polar regions (see below) and where air retains the seasonal cycle of tropopause temperatures (see section 3.2.2).

The lifetimes of CH<sub>4</sub> and H<sub>2</sub> are similar, more than 100 years in the lower stratosphere, decreasing to a few years at 30 km and a few months at 40 km. Because air in the stratosphere has a mean age of a few years, all of the stratospheric oxidation of CH<sub>4</sub> and H<sub>2</sub> is occurring in the middle and upper stratosphere. Therefore, air with low values of CH<sub>4</sub> or high values of H<sub>2</sub>O in the lower stratosphere has been transported down from higher altitudes.

### (3) Dehydration at the tropical tropopause

There is widespread agreement that nearly all of the air that reaches the stratosphere above the global hygropause originally travelled through the tropical tropopause [Holton *et al.*, 1995] and that the tropopause region acts like a “cold trap”, in which air is dehydrated to very low values. Indeed, only in the tropics are tropopause temperatures low enough to dehydrate air to the mixing ratios observed in the stratosphere [Brewer, 1949]. It is also generally agreed that convection, along with the mean meridional circulation mentioned above, plays a role in dehydration, but many important details are unclear. What is known about the effect of these processes on the water vapour distribution is discussed in detail in section 3.3.3. The combination of convection and the mean circulation creates a mean “entry mixing ratio”  $[\text{H}_2\text{O}]_e$  of air into the tropical lower stratosphere, as discussed in detail in Section 2.5.4.

### (4) Polar dehydration

In the polar vortices, temperatures are sometimes low enough in winter for the air to reach saturation, and the water vapour mixing ratio is lowered by dehydration [Kelly *et al.*, 1989, Kelly *et al.*, 1990]. Such dehydration is strong enough in the southern polar vortex, even though it is only seasonal (between late May and mid-October), to affect the annual mean there (Figure 3.3). Below about 400 K in spring and early summer, dehydration can affect mid-latitudes (see Section 3.3.1), but has little influence on the rest of the stratosphere [Mote, 1995, Rosenlof *et al.*, 1997]. While dehydration has been observed in the Arctic [e.g., Kelly *et al.*, 1990], it occurs much less frequently owing to the Arctic’s warmer temperatures. Consequently, significant decreases of vortex-averaged water vapour have not yet occurred in the Arctic. The poleward decrease seen in Figure 3.3 may result from high values over the northern mid-latitude monsoon rather than from polar dehydration.

### (5) Tropospheric leakage to the extratropics

Air in the mid-latitude lower stratosphere below the altitude of the tropical tropopause has considerably higher water vapour mixing ratios than air in the tropical stratosphere (Figure 3.3), and must have leaked from the troposphere without passing the tropical tropopause cold trap [Brewer, 1949; Dessler *et al.*, 1995]. This leakage occurs through two primary pathways, as we discuss in the next paragraph. However, because of the subsidence at these latitudes (Figure 3.4), very little of this air influences the stratosphere above about 380 K. The Southern Hemisphere lower stratosphere between the tropopause and the 380 K potential temperature surface is slightly drier than the northern hemisphere, partly because of moistening by the vigorous northern monsoon [e.g., Stone *et al.*, 2000].

The moist air observed must have reached the lowermost stratosphere along one of two paths: (A) vertically from the extratropical troposphere, or (B) quasi-isentropically from the tropical troposphere through the subtropical gap. Many observational studies [Murgatroyd, 1965; Dobson, 1973; Ray *et al.*, 1999] showed that entry through path B is probably occurring. Evidence for the convective injection path has also been found (e.g., Roach [1966], Johnston and Solomon [1979], Poulida *et al.* [1996]), but convection rarely reaches 2 km above the local tropopause.

Quasi-isentropic exchange (path B) occurs when synoptic events create “tropopause folds” in the subtropics [Reed and Danielsen, 1959] that significantly deform the tropopause structure and eventually deposit stratospheric air into the troposphere, and vice versa. One possible mechanism is advection by low-latitude troughs [e.g., Mote *et al.*, 1994; Mecikalski and Tripoli, 1998; Kiladis, 1998]. Chen [1995] noted that this exchange is restricted above

340 K in the winter hemisphere, and that the permeable summer subtropical barrier is due to the monsoon circulation in each hemisphere: the Asian and Mexican monsoons in northern summer [e.g., *Dunkerton*, 1995], and the Australian and South American monsoons in southern summer. Aircraft directly inject water vapour into the lowermost stratosphere [*Hoinka et al.*, 1993, *Gettelman and Baughcum*, 1999], but model simulations [*Danilin et al.*, 1998] suggest that this will have a negligible impact on the abundance of water vapour in this region.

### Concluding remarks about the annual mean

In summary, the annual mean distribution of water vapour illustrated in Figure 3.3 can be understood broadly as a balance of the above processes. However, a fuller understanding of water vapour, even in the annual mean sense, requires considering the seasonal variations in the mechanisms that influence it. We return to this subject in section 3.3.1.

A useful quantity in the total hydrogen budget of the stratosphere is the mean entry mixing ratio,  $[\text{H}_2\text{O}]_e$ , (see section 2.5.4).  $[\text{H}_2\text{O}]_e$  is, in principle, an aggregate result of the various conditions under which air enters the stratosphere (see point 3 above, and section 3.3.3), but because these conditions are not uniform in space or time,  $[\text{H}_2\text{O}]_e$  cannot be calculated directly from observed saturation mixing ratios at the tropical tropopause. Instead, it is generally estimated by sampling the methane and water vapour content of air some distance from the tropopause. Table 2.5 presented estimates of  $[\text{H}_2\text{O}]_e$ , with annual mean values for the 1990's ranging from 3.0 to 4.1, and a mean value of 3.7 ppmv. For this range of saturation mixing ratios, the range of temperatures is approximately 2°C. The differences between estimates of  $[\text{H}_2\text{O}]_e$  shown in Table 2.5 are consistent with the instrumental biases discussed in section 2.6.1.

### 3.2.2 Upper Troposphere

In the troposphere, water vapour amounts are strongly modulated by thermodynamic constraints, and mixing ratios decrease by several orders of magnitude from the surface to the tropopause. Thus, relative humidity is preferable to absolute humidity. Examining and understanding upper tropospheric moisture. However, since tropospheric humidity exhibits strong seasonal and interannual variations, the long-term mean distribution is discussed only briefly. Section 3.3.2 will follow with a more thorough examination of tropospheric vapour in the context of the seasonal cycle.

For an overview of the long-term mean, we utilise data from HIRS (Figure 3.5). A broad band of high relative humidity is clearly visible extending across the tropics, even in the long-term mean. This band possesses three prominent maxima: over the maritime continent near 90°E, over South America around 60°W and over tropical west and central Africa near the Greenwich meridian. Similar patterns are observed with column water vapour measurements from SAGE II [*Chiou et al.*, 1997]. The tropical maxima are associated with the ascending branches of the three tropical monsoon systems: the African Monsoon over central Africa, the Austral-Asian monsoon over the maritime continent, and the South American monsoon over the Amazon. These patterns are consistent with the Walker cell [*Bjerknes*, 1969] patterns of convective uplift of air with high moisture from below, and downwelling regions of low moisture from above. The maxima also coincide with areas of more frequent sub-visible cirrus clouds, as observed by *Wang et al.* [1996].

Minima in upper tropospheric humidity are found in the subtropics, also clearly illustrated in Figure 3.5. These minima are not symmetrical, and vary significantly with season. The

most persistent, and therefore most prominent in the annual mean, are those straddling the equator over the east Pacific. Dynamically, these can be accounted for as descending branches of a steady circulation forced by a tropical atmospheric heat source located in the deep tropics of the Indo-Pacific region where abundant latent heat release is known to occur [Gill, 1980]. Poleward of the subtropics, the upper tropospheric humidity increases with latitude. This gradient reflects decreasing temperatures at higher latitudes, rather than higher mixing ratios, and results mainly from the properties of meridional mixing as discussed in Section 3.3.2. The modest zonal asymmetries that occur are best understood seasonally and will also be discussed in Section 3.3.2.

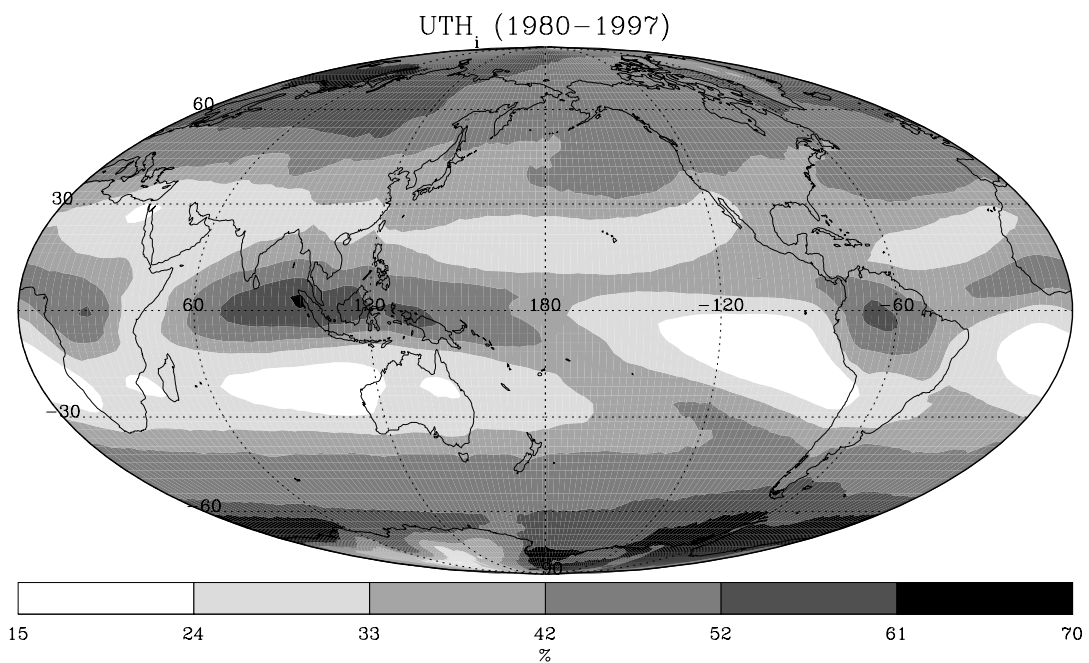


Figure 3.5 Annual mean Upper Tropospheric Humidity over ice (UTH<sub>i</sub>) averaged for 1980–1987 from HIRS instruments, in percent.

### 3.3 Seasonal Cycle

The seasonal cycle is the largest source of variability for water vapour in the lower stratosphere and upper troposphere. The seasonal cycle in water vapour is well characterised by numerous *in situ* and remote observational data sets collected during the last decade, as discussed in Chapter 2, and here we use a number of these data sets to characterise the observed seasonal variability. Because of the physical differences between regions, we separate the observations and processes in the lower stratosphere (3.3.1), upper troposphere (3.3.2) and the region around the tropical tropopause (3.3.3).

Throughout these three regions, the processes mentioned in section 3.2 contribute to varying degrees to produce the seasonal cycle in water vapour, with different factors dominating in different locations. In most of the stratosphere above about 20 km, the circulation dominates the seasonal cycle. In the southern polar lower stratosphere, a very low minimum occurs during winter because of dehydration. In the mid-latitude lower stratosphere below about 20 km, the maximum occurs in summer largely because of exchange with the moist upper troposphere. In the upper troposphere, the seasonal variation in the distribution of water vapour is dominated by the seasonal migration of the Hadley-Walker circulation cells. Relative humidity in the upper troposphere in middle latitudes is generally lower in summer than in winter, owing to the strong annual cycle of temperature there. In the tropical tropopause region, a complex mix of large-scale circulation, local dehydration, and radiative and convective processes combine to produce a seasonal cycle (with a minimum in roughly February) whose signature remains detectable for a year and a half as air rises slowly through the tropical stratosphere.

#### 3.3.1 Lower Stratosphere

##### Overview

The seasonal cycle of water vapour between the tropopause and ~28 km altitude is shown in Figure 3.6, derived from HALOE data during 1991-99. The seasonal cycle is derived from a harmonic fit of the data set formed by combining HALOE and MLS data as described in section 3.2. It is important to note that the effective vertical resolution of HALOE is ~2 km, and this vertical smearing results in an underestimate of seasonal extremes in the lower stratosphere [Mote *et al.*, 1996, Andrews *et al.*, 1999]. HALOE observations near the tropopause are at the lower limit of the instrument's useful range, and individual profiles may have large errors as discussed in section 1.4.5. The monthly means in Figure 3.6 present a qualitative picture near the tropopause.

Perhaps the most striking features of the seasonal cycle shown in Figure 3.6 are the variations in the tropical minimum and the seasonal dehydration in the southern polar vortex, both highlighted by the shading of low values. The low mixing ratios that form near the tropical tropopause in January spread poleward to cover much of the lower stratosphere between 60°N and 60°S by April, approximately following the sloping isentropes near the ~380-400 K levels, and is evidence for relatively fast isentropic mixing between tropics and mid-latitudes.

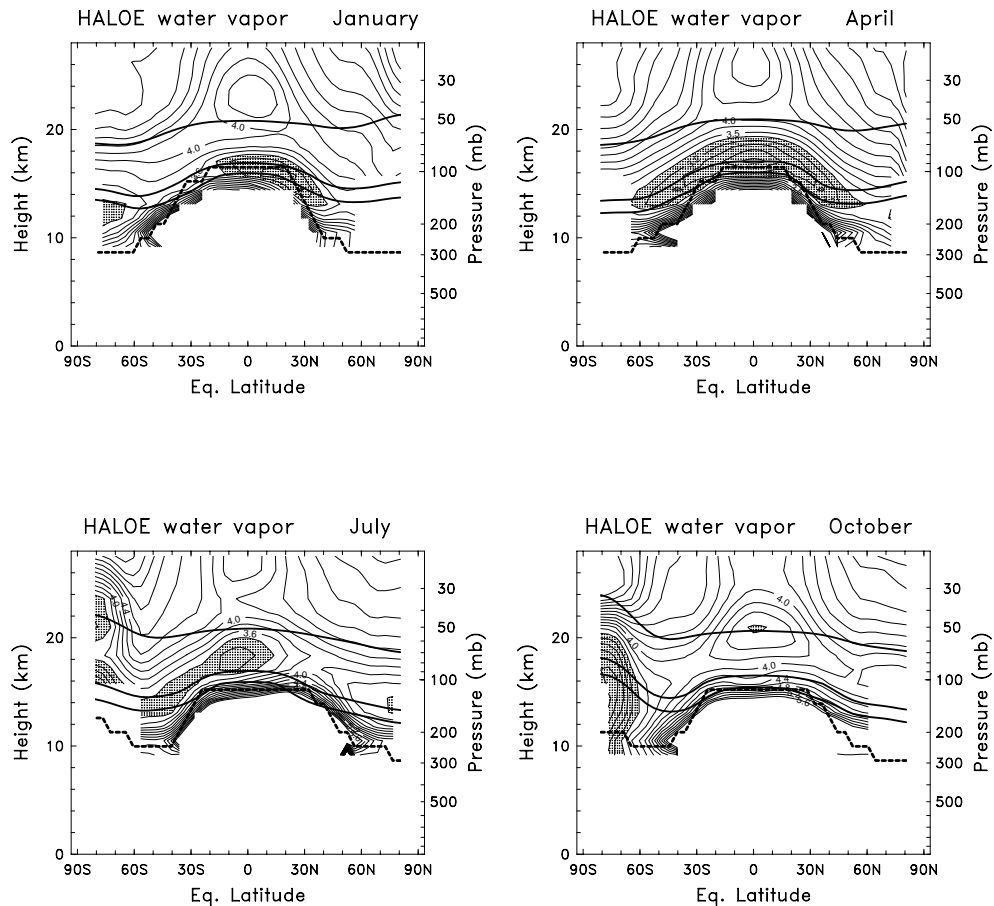


Figure 3.6. Meridional cross-sections of water vapour mixing ratio between the tropopause and  $\sim 28$  km derived from HALOE measurements. Plots are shown for January, April, July and October, illustrating the seasonal cycle. For each month the dashed lines represent the tropopause, and the solid lines show the 380 K, 400 K, and 500 K isentropes.

The seasonal variation of water vapour in the lowermost stratosphere is further illustrated in Figure 3.7, showing the latitude-time evolution of HALOE data on the 380 K isentropes ( $\sim 15$  km); similar details in meridional structure are shown by *Rosenlof et al.* [1997] and *Jackson et al.* [1998]. These HALOE data suggest an absolute minimum centred slightly north of the equator during January–March, with the driest air then propagating both poleward and into the Southern Hemisphere. Relatively high water vapour values are observed during Northern Hemisphere summer centred near  $30^\circ\text{N}$ , coincident with the convective phases of the Asian and North American summer monsoons. The high water vapour air also appears to propagate poleward and into the Southern Hemisphere, in a similar manner to that of the low values 6 months earlier. The result of the asymmetric maxima in Figure 3.7 is that the annual cycle is substantially larger in the Northern Hemisphere than in the Southern Hemisphere, and also that the Northern Hemisphere is wetter than the Southern Hemisphere on a time mean basis [see *Rosenlof et al.*, 1997]. As discussed in chapters 1 and 2 measurements at low altitudes are difficult to make, especially in the presence of cirrus clouds, which may bias the results towards dry values.

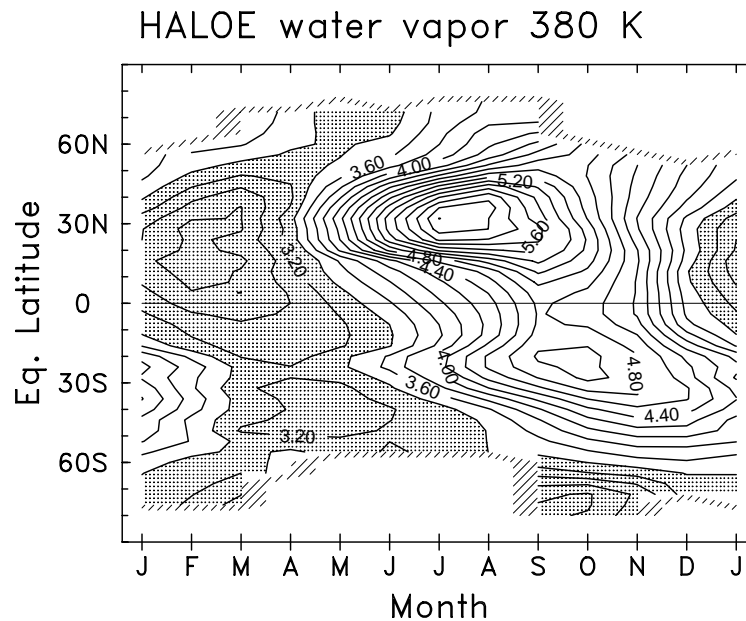


Figure 3.7. Latitude-time evolution of water vapour mixing ratio near 380 K derived from seasonal cycle fits of the HALOE data.

### Polar lower stratosphere

Low values of water vapour in Southern Hemisphere polar regions during winter-spring, associated with dehydration in the Antarctic polar vortex, have been observed from aircraft [Kelly, 1989; Kelly *et al.*, 1990; Watterson and Tuck, 1989] and satellites [Russell *et al.*, 1993; Pierce *et al.*, 1994; Rosenlof *et al.*, 1997; Randel *et al.*, 1998; Morrey and Harwood, 1998]. Because of the intermittent sampling of HALOE, SAGE and MLS data, the temporal development of Antarctic dehydration is best observed by instruments on polar satellites, such as POAM or ILAS. Figure 3.8 shows POAM observations of water vapour over the south polar region (64°–88°S) during 1998, illustrating strong dehydration in the lower stratosphere over 12–22 km, beginning in midwinter (July) and persisting until vortex breakdown in December. The dehydration is consistent with polar stratospheric cloud observations by Watterson and Tuck [1989]. Vömel *et al.* [1995a] note that dehydration in the Antarctic sometimes begins in mid-June and is mixed out in September, finally disappearing in early December, broadly consistent with Figure 3.8. HALOE observations in Figure 3.6 indicate that the effects of dehydration may continue until January at 11–13 km poleward of ~60°S, though the data at these low altitudes should be treated with some caution.

The latitudinal extent of dehydration covers the interior of the Antarctic polar vortex in the lower stratosphere (out to equivalent latitudes of ~60°S, see Figure 3.6), with a sharp radial gradient in dehydration near the vortex edge [Pierce *et al.*, 1994, Morrey and Harwood, 1998]. Rosenlof *et al.*, [1997] estimate that 40% of vortex air per month mixes out below 450 K at the end of the austral winter, consistent with estimates from aircraft by Kelly *et al.*, [1989], Tuck [1989] and Tuck and Proffitt [1997]. Satellite data, such as the HALOE data in Rosenlof *et al.*, [1997] and the data in Figures 3.6 and 3.7 indicate that the dehydration influences latitudes 10°–20° outside the vortex. For example, the October frame of Figure 3.6 shows dry air extending to 45°S at 16 km (420 K). Mote [1995] shows that the influence from polar dehydration in the Southern Hemisphere extends equatorward

to 50°S after vortex break-up. Polar dehydration thus significantly affects the bulk (zonal mean) concentration of water vapour in the lowest regions of the stratosphere poleward of 40°-50°S. It is not clear that there is significant effect equatorward of these latitudes.

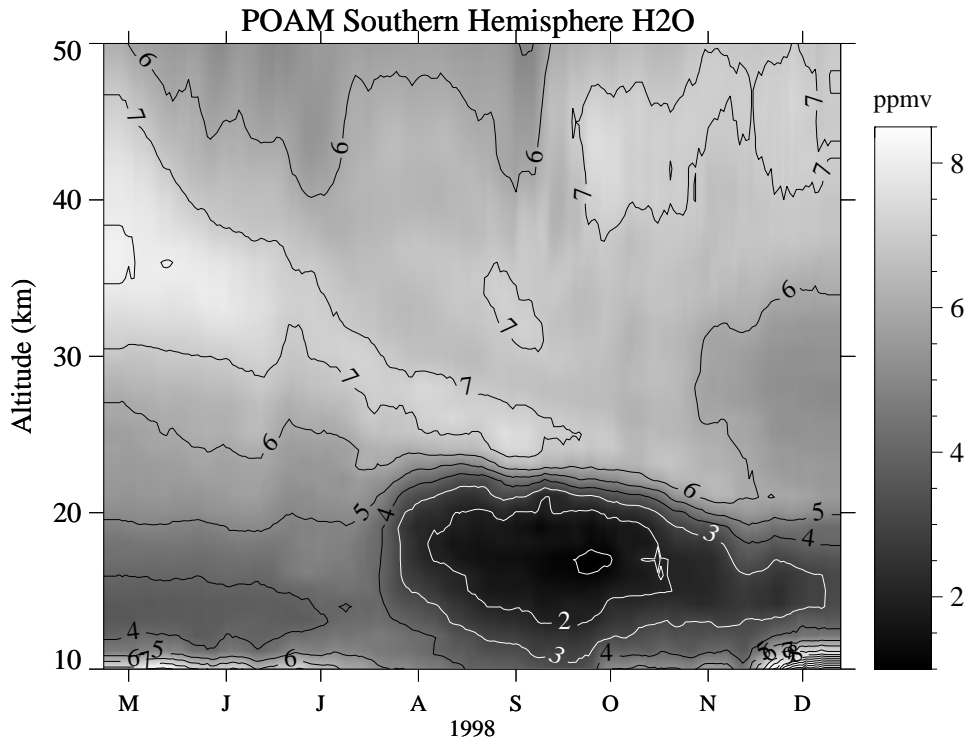


Figure 3.8. Water vapour mixing ratio as measured by POAM in the Southern Hemisphere from April to December 1998. The profiles are obtained as daily averages of the POAM measurements, which are taken at latitudes from 64°-88°S. There is strong descent within the vortex during the first half of the period. In July, cold temperatures in the lower stratosphere result in dehydration, which persists for several months. In October, lower latitude air begins to mix in above the vortex, resulting in a double peaked structure in the profile.

Time series of polar water vapour measurements furthermore show evidence of downward mass flux in the middle stratosphere throughout winter in both hemispheres. This is seen for the Southern Hemisphere in the POAM data in Figure 3.8 and in both polar regions in the seasonal cycle derived from combined HALOE and MLS data (Figure 3.9). Downward motion is most evident in the movement of high water vapour values, which originate in the summer upper stratosphere (the result of methane oxidation). Eulerian estimates of isopleth movement give a rough estimate of the descent rate. In Figure 3.9 isopleths suggest downward movement with magnitude of ~1.5 km/month, similar to values inferred from CH<sub>4</sub> observations [Randel *et al.*, 1998] and from radiative heating estimates [Schoeberl *et al.*, 1995, Rosenfield *et al.*, 1994] above 25 km. Lagrangian estimates of descent rates [Pierce *et al.* 1994, Manney *et al.* 1994] are a maximum of 1.5-4 km/month at 470 K [Manney *et al.* 1994]. A comparison of patterns in the Northern Hemisphere and Southern Hemisphere in Figure 3.9 suggests the high water vapour mixing ratios propagate more continuously throughout the winter in the Southern Hemisphere. This may be a result of the stronger isolation of the Antarctic vortex and with enhanced cross-vortex mixing in the Arctic [e.g., Bowman, 1993; Manney *et al.*, 1994].

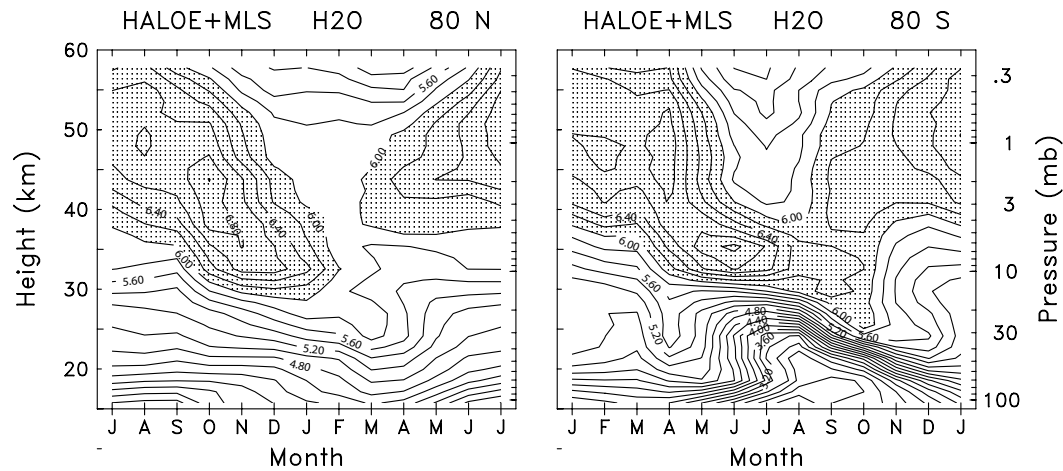


Figure 3.9. Altitude-time seasonal cycle of water vapour at 80°N (left) and 80°S (right) derived from seasonal cycle fits of HALOE+MLS data. Note the time axes are shifted by six months between the two panels to facilitate inter-hemispheric comparison.

### Mid-latitude lower stratosphere

Evidence for a seasonal cycle of water vapour in the mid-latitude lower stratosphere was observed by *Bannon et al.* [1952]. The cycle was also described by *Mastenbrook* [1968, 1974] from balloon-borne frost point measurements taken from Washington DC between 1964 and 1973. The amplitude of the seasonal cycle was found to decrease from 1.2 ppmv at 90 hPa to about 0.6 ppmv at 60 hPa, with a relative maximum during summer. *Mastenbrook and Oltmans* [1983] presented the data updated to 1982. A similar data set with extended sampling has been obtained from frost point measurements made at Boulder, Colorado (40°N) since 1979 [*Oltmans and Hofmann*, 1995]. Seasonal variability in the mid-latitude lower stratospheric water vapour has also been observed from *in situ* aircraft measurements [*Hintsa et al.* 1994, *Dessler et al.* 1995]. Figure 3.10 shows the average seasonal cycle over 1981-98 derived from balloon data over Boulder, Colorado, showing a pronounced annual cycle with a maximum during summer. These data show a relative minimum in the vertical profile of water vapour in the lower stratosphere, centred near 15 km in winter and near 18 km in summer. This minimum in the lower stratosphere is consistent with the zonal mean seasonal cycle seen in Figure 3.6. Such a minimum is impossible to achieve by local processes because water vapour is not locally close to saturation. Rather, this minimum is further evidence of rapid isentropic transport between the tropics and mid-latitudes in the lower stratosphere.

In mid-latitudes, care must be taken to separate seasonal variability from large amplitude meteorological variations, which can be substantial for infrequent and spatially localised measurements. One method to minimise such meteorological variations is to use the observed compact relationship between water vapour and long-lived tracers [e.g., *Schoeberl et al.*, 1989, *Boering et al.*, 1995]. Using simultaneous water vapour and N<sub>2</sub>O measurements taken on board the NASA ER-2 research aircraft during 1992-1993, *Hintsa et al.* [1994] showed how water vapour at mid-latitude in the Northern Hemisphere exhibited a close relationship with N<sub>2</sub>O, and exhibited a seasonal cycle with higher values in fall than in spring.

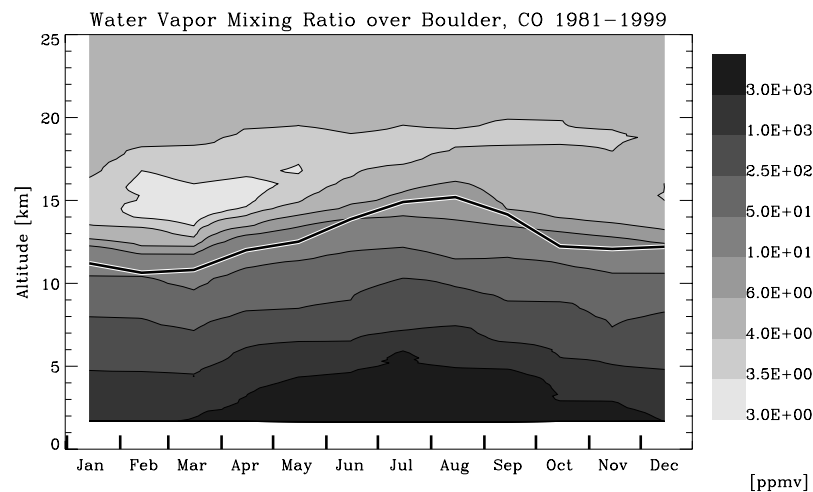


Figure 3.10. Altitude-time section of the seasonal cycle of water vapour at Boulder (40°N, 105°W), derived from frost point hygrometer measurements over 1981-1999. The solid line denotes the local tropopause.

### Tropical lower stratosphere

There is a strong annual cycle in water vapour in the tropical lower stratosphere (Figures 3.6 and 3.7), with minimum values in January-April and maximum values during August-November. Hints of these seasonal variations were noted by Mastenbrook [1968] from balloon observations over Trinidad, and by *Kelly et al.* [1993] from high altitude aircraft data taken over Panama in 1980 and Darwin, Australia in 1987. On the basis of such limited observations, *Kley et al.* [1979] and others offered a number of hypotheses to explain the “elevated hygropause” – that is, the existence of a minimum in water vapour at altitudes higher than the local tropopause.

With the benefit of satellite observations like those shown in Figure 3.11, we now know [*Mote et al.*, 1995, 1996] that the variably elevated hygropause moves vertically throughout the annual cycle and is produced by seasonal variations in saturation mixing ratios at the tropical tropopause. The water vapour minimum is transported slowly upward, with typical vertical velocities of  $\sim 0.3 \text{ mm s}^{-1}$  [*Rosenlof*, 1995, *Mote et al.*, 1998b], by the mean circulation, under conditions of very weak diffusion. The anomalies imprinted at the tropopause are identifiable for up to 18 months during which time they rise to altitudes of nearly 32 km. This phenomenon was termed the ‘atmospheric tape recorder’ by *Mote et al.* [1996].

Two aspects of the seasonal variations in tropical lower stratospheric water vapour offer clues about the dynamics of the lower stratosphere. First, the relationship in phase between the seasonal cycle measured in the tropics and mid-latitudes provides a measure of the transport time from the tropics to mid-latitudes. *Angell and Korshover* [1974] calculated a lag between tropical tropopause temperatures and stratospheric mid-latitude water vapour of a few months. From water vapour measurements presented by *Mastenbrook and Oltmans* [1983] (see also Figure 3.10) and *McCormick et al.* [1993], it appears that the seasonal cycle in mid-latitude lower stratospheric water vapour lagged that in the tropics by perhaps 2 months. *Boering et al.* [1995] inferred a transit time of 4-6 months in both November and May from the tropical tropopause (16.5 km) to 18-19 km in mid-latitudes. *Volk et al.* [1996] found a transport time scale from the tropics of less than 6 months below 19 km.

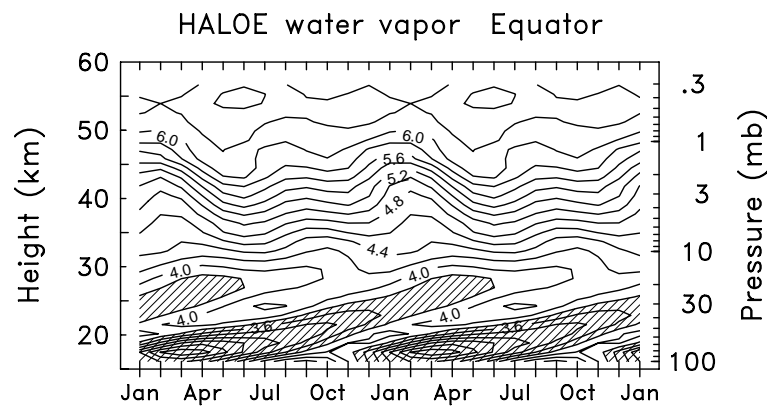


Figure 3.11. Altitude-time evolution of water vapour mixing ratio over the equator, derived from seasonal cycle fits of HALOE measurements. Two consecutive seasonal cycles are shown here.

The second aspect is the attenuation of the tape recorder signal itself, which can be used to deduce the rate at which mid-latitude air dilutes tropical air and simultaneously (provided other information is available as well) the vertical diffusion rate. Estimates of the dilution or in-mixing time scales between the tropics and mid-latitudes have been made using the tape recorder signal [Mote *et al.*, 1996; Hall and Waugh, 1998; Mote *et al.*, 1998b; Andrews *et al.*, 1999] and also using other trace constituents [Avallone and Prather, 1996; Volk *et al.*, 1996; Minschwaner *et al.*, 1996; Herman *et al.* 1998]. The in-mixing time scales are generally in the range of 12-18 months, but Herman *et al.* [1998] found a value of 30 months, and the most detailed calculation (using HALOE data at high vertical resolution) included the effects of vertical diffusion, and found much longer mixing time scales, as long as 80 months at about 22 km [Mote *et al.*, 1998b]. Collectively these studies suggest a region of strong mixing in the lower tropical stratosphere below about 20 km, and a region that is much more isolated from mid-latitudes between 20 km and about 28 km. This isolation has important implications for ozone chemistry and the ozone distribution in the tropical lower stratosphere [Avallone and Prather, 1996].

### Extratropical lowermost stratosphere

The “extratropical lowermost stratosphere” is the region in middle and high latitudes above the tropopause but below isentropes of  $\sim 380$ -400 K. It is a dynamically distinctive region because it exhibits properties similar to the stratosphere (including low water vapour), but is closely connected to the low latitude troposphere by isentropes that cross the subtropical tropopause [Holton *et al.*, 1995].

The main terms influencing the budget of water vapour in this region (also noted in Section 3.2.1) are (A) downward transport (of very dry air) from the stratosphere, (B) isentropic transport of (moist) tropospheric air from lower latitudes and (C) direct upward transport of air from the mid-latitude troposphere. The seasonal cycle of water vapour in this region is a powerful measure of the relative importance of these processes. Both *in situ* and satellite data show that water vapour in this region of the lower stratosphere has a pronounced seasonal cycle with a maximum in summer [Bannon *et al.* 1952, Mastenbrook, 1968, Dessler *et al.*, 1995; Pan *et al.*, 1997]. Figure 3.12 (identical to one of the panels in Figure 2.66) shows a comparison of the SAGE II and the MLS satellite with ER-2 aircraft measurements of the water vapour seasonal cycle in the Northern Hemisphere lowermost stratosphere. Winter mixing ratios are near 6-10 ppmv, characteristic of air with a large

stratospheric component (A), whereas summer measurements show values of  $\sim 20$ -40 ppmv; a similar seasonal cycle is observed in the Southern Hemisphere [Pan *et al.*, 1997]. These relatively wet summer measurements demonstrate that a significant component of the air either must originate in the low-latitude troposphere (B) or must be transported directly from the mid-latitude troposphere (C). This moist air can be seen in MLS data at 215 and 147 hPa, particularly over the Indian subcontinent in July-August [Newell *et al.*, 1997]. Ray *et al.* [1999] have used long-lived halocarbons with corroborative water vapour data to estimate that a significant fraction of air in the northern hemisphere lower stratosphere below 360 K must have originated in the low latitude upper troposphere without having passed above the 380 K surface, as discussed by Dessler *et al.* [1995]. In September, most of the air is from the tropics (B), while in March most of the air comes from higher altitudes in the extratropical stratosphere (A) [Ray *et al.*, 1999].

The Northern Hemisphere lowermost stratosphere below 380 K is in general wetter than the Southern Hemisphere lowermost stratosphere [Pan *et al.*, 1997, Rosenlof *et al.*, 1997]. The largest hemispheric asymmetry is in Northern Hemisphere summer and fall. Differences in summer and fall seasons between the two hemispheres are probably related primarily to differences in the summer monsoon circulation, which is stronger in the Northern Hemisphere. Exchange of water vapour from the troposphere into the stratosphere during the season of the Asian monsoon significantly moistens the northern hemisphere lower stratosphere, as illustrated by Rosenlof *et al.* [1997] with HALOE observations, and Gettelman *et al.* [2000] using a transport model. Dethof *et al.* [1999], using contour advection, suggest that mid-latitude disturbances pull filaments of water vapour rich air from the northward flank of the Asian monsoon anticyclone. Other asymmetries between hemispheres include annual variations in the strength of upward (tropical) and downward (extratropical) motion associated with the Brewer-Dobson circulation [Rosenlof 1995] and the influence of polar dehydration at higher latitudes of the Southern Hemisphere.

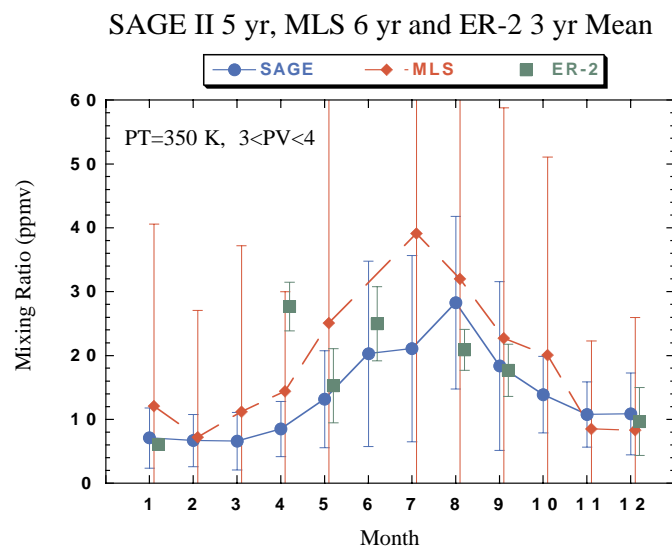


Figure 3.12. Seasonal cycle variation of water vapour from SAGE II, MLS and ER-2 aircraft measurements for the  $\pm 5$  K layer centred on the 350 K isentropes and  $3 < PV < 4$  (typically  $40^{\circ}$ - $50^{\circ}$ N). The SAGE II data represent five-year means (1986-1990), MLS are six-year means (1992-1997), and the aircraft data cover the STRAT/POLARIS missions (1995-1997). Error bars indicate the RMS deviation from the mean.

### 3.3.2 Upper Troposphere

Several satellite data sets provide information on moisture in the upper troposphere, with near-global coverage and multi-year records that provide accurate characterisation of the annual cycle. Two data sets discussed here include relative humidity estimates derived from HIRS and MLS (MLS data are also converted to mixing ratio using NCEP global temperature analyses). The HIRS retrieval is sensitive to relative humidity in a layer from approximately 5-11 km in the tropics, and 4-8 km in the extratropics. MLS data give vertical profile estimates for ~3 km thick layers centred on pressure levels 316, 215, and 147 hPa (~8, 11 and 13.5 km, respectively). *In situ* data will also be shown for corroboration of the satellite-observed behaviour.

#### Observations: tropical and subtropical upper troposphere

The seasonal cycle of HIRS-derived upper tropospheric humidity (UTH) is shown in Figure 3.13, in the form of latitude-longitude maps for each season. Within the deep tropics, the maxima in UTH in the annual mean (Figure 3.5) over the African monsoon, the Austral-Asian monsoon, and the American monsoon, appear throughout the year but with a large seasonal excursion of each monsoon centre. In December-January-February (DJF) the monsoon centres and maxima in UTH are found over Southern Africa, Indonesia, and the Amazon. In June-July-August (JJA), strong maxima in UTH appear north of the equator over the Indian monsoon, and other maxima are found over North Africa and Central America. Over the Pacific Ocean, moist signatures of the Intertropical Convergence Zone are present in northern-hemisphere summer and fall, and the South Pacific Convergence Zone is most pronounced in the Southern Hemisphere summer.

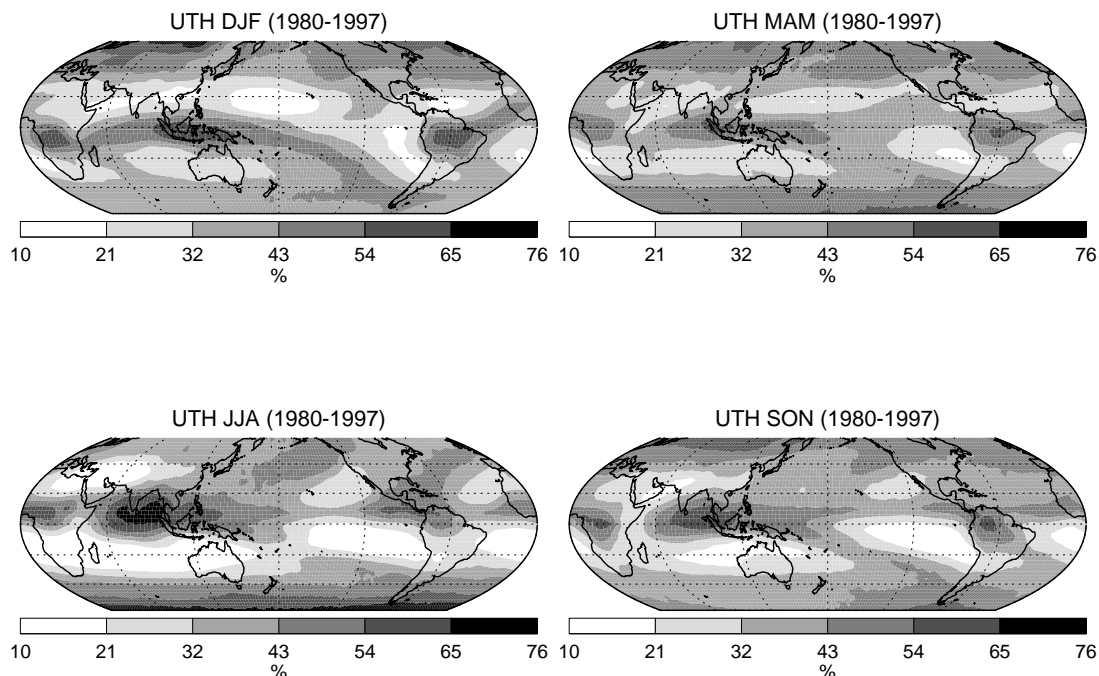


Figure 3.13. Long-term seasonal means (1979-1998) of upper tropospheric humidity over ice derived from HIRS data.

The very dry regions of the subtropics also undergo strong seasonal shifts, occurring particularly in the winter hemisphere. Especially notable are dry regions occurring over the Atlantic and Pacific oceans ( $\sim 15^{\circ}$ - $40^{\circ}$ N) in December-January-February, and over  $15^{\circ}$ - $40^{\circ}$ S during June-July-August. Large areas off the west coasts of South America and Australia are relatively dry year-round, but still with significant seasonal modulation. A dry region also appears during JJA northwest of the Asian monsoon. The exceeding dryness of these regions is illustrated further in Figure 3.14, where daily MLS data show that relative humidity  $< 10\%$  is observed for up to 70% of the observations in these regions [Stone *et al.*, 2000]. Similar dryness statistics have been found in SSMT2 data [Spencer and Braswell, 1997].

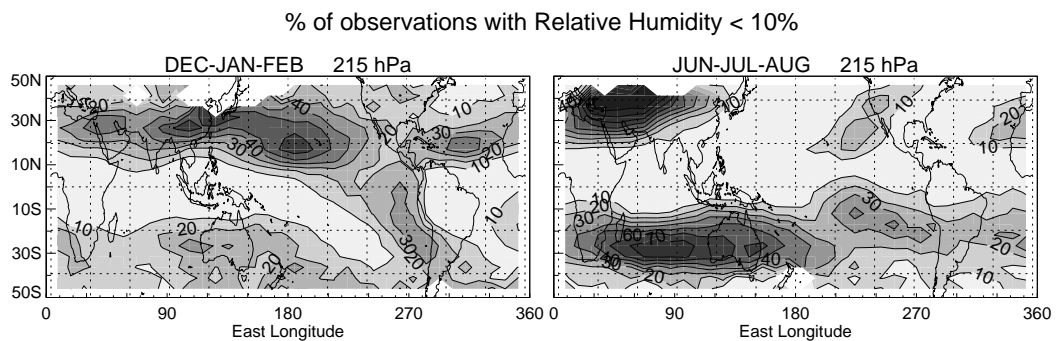


Figure 3.14. Percentages of MLS upper tropospheric humidity observations (at 215 hPa) during 1991-97 in which relative humidity values are less than 10%. Contour interval is 10%. From Stone *et al.* [2000].

Seasonal water vapour variability in the upper troposphere is closely tied to the vertical circulation cells associated with the seasonal Hadley and Walker circulation. Following Newell *et al.* [1996] and Stone *et al.* [2000], this is demonstrated in Figure 3.15, which shows the 215 hPa water vapour mixing ratio derived from MLS data superimposed on the divergent circulation velocity potential (statistics derived from NCEP data) for December-January-February and June-July-August. These show that upper tropospheric water vapour maxima are associated with upward motion and minima with downward circulation, and show that water vapour seasonality is closely tied to the meridional movement of tropical convective upwelling. This meridional movement is further highlighted in Figure 3.16, which shows the seasonal variation of zonal mean MLS mixing ratio at 215 hPa during 1991-93. This meridional motion mimics that of the Intertropical Convergence Zone throughout the year (see, for example, Hartmann, [1994]). Similar seasonality is observed for MLS retrievals at 316 and 147 hPa, with the average mixing ratio dropping by at least a factor of two between adjacent vertical layers [Read *et al.*, 1995].

### Observations: Mid-latitude upper troposphere

Mid-latitudes also experience significant seasonal changes in upper-tropospheric moisture, but with a few features that persist throughout the year, as can be seen in Figure 3.13 from HIRS. At middle latitudes, the HIRS retrievals represent altitudes of  $\sim 4$ - $8$  km (which is below the extratropical tropopause). Figure 3.13 illustrates relatively little longitudinal structure compared with the tropics and subtropics, but moist areas are evident throughout the year off the West coast of Southern South America and in the Northeast Pacific and Atlantic areas. Enhanced descent and equatorward flow to the east of the semi-permanent surface oceanic anticyclones is associated with upper tropospheric dryness, while enhanced

ascent and poleward flow to the west of these anticyclones is associated with moist anomalies. Overall, the relative humidity is greater in winter than summer.

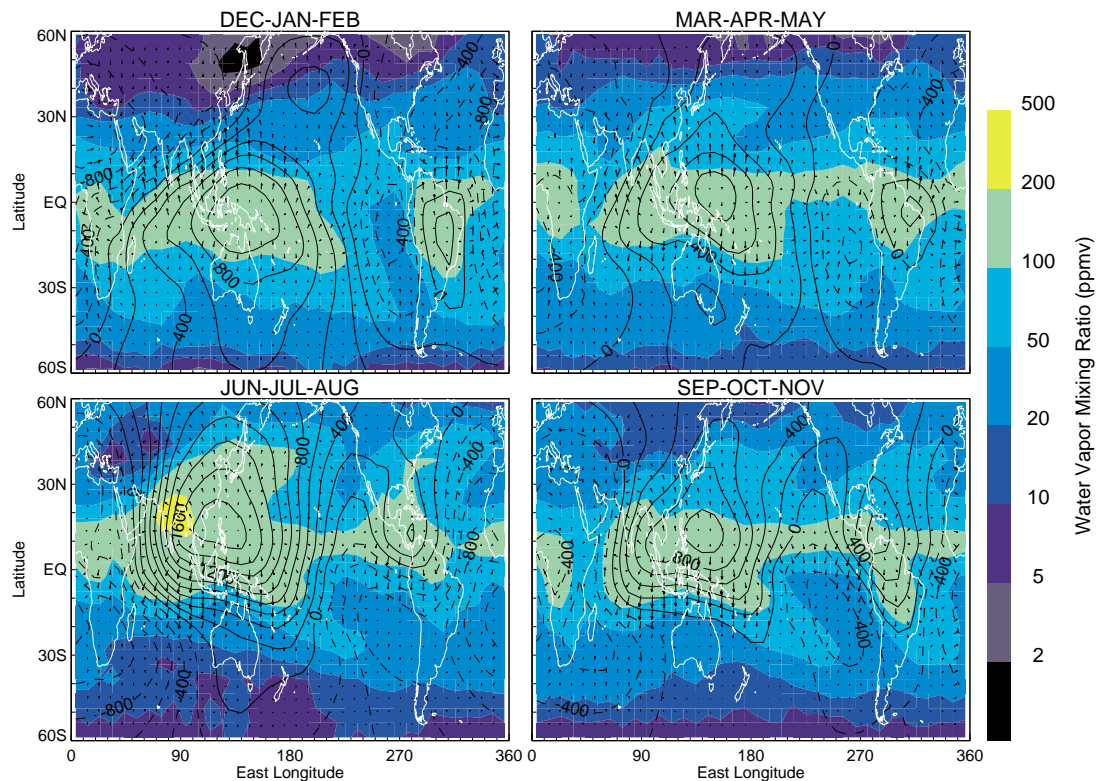


Figure 3.15. Seasonal averages of MLS upper tropospheric water vapour mixing ratio on the 215 hPa surface, overlaid with contours of velocity potential (in increments of  $200 \times 10^4 \text{ m}^2 \text{ s}^{-1}$ ) and divergent wind vectors (with maximum amplitude of  $7.6 \text{ ms}^{-1}$ ). From Stone *et al.* [2000].

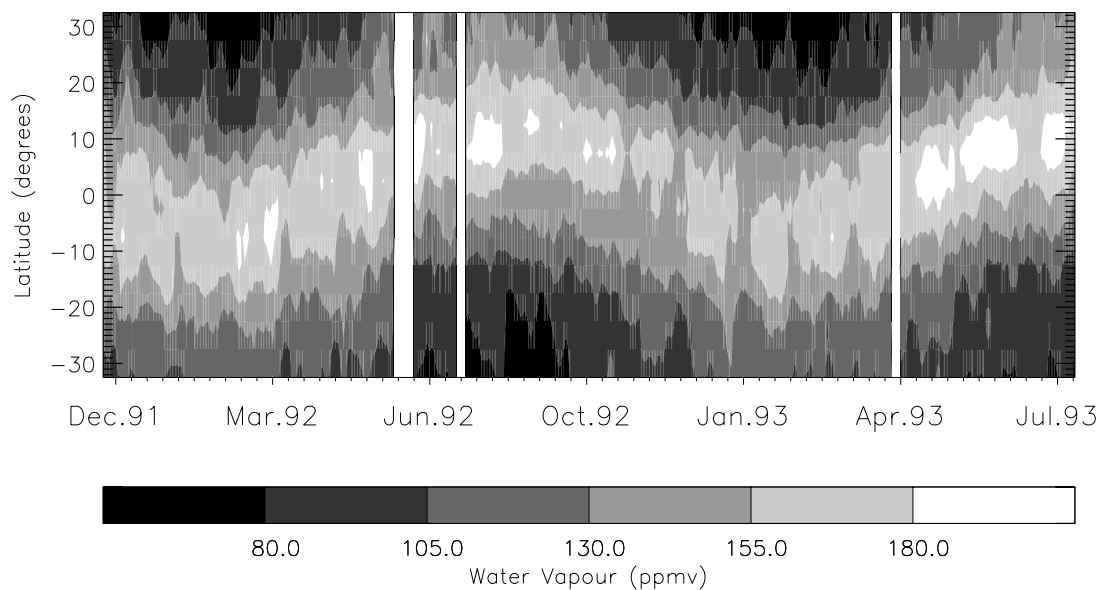


Figure 3.16. Variation in zonally-averaged upper tropospheric water vapour (at 215 hPa) in the tropics during 1991-1993, derived from MLS data.

Observations over Boulder, Colorado ( $40^{\circ}\text{N}$ ,  $105^{\circ}\text{W}$ ) using the NOAA frost point balloons indicate a strong annual cycle in water vapour mixing ratio, with summer values at 10 km higher than those in winter by a factor of  $\sim 6$  (Figure 3.10). This is far greater than the changes in relative humidity indicated by HIRS, indicating that seasonal changes in specific humidity here are predominantly related to the seasonal variations in temperature. Note also that the tropopause height has a large annual cycle, such that the water vapour mixing ratio (as well as the relative humidity) at the tropopause is actually lower in summer than in winter. A more extensive climatology of water vapour in the mid-latitude upper troposphere is available from data on commercial aircraft, taken as part of the MOZAIC project (Section 1.1.5). Data from the North Atlantic in two different latitude bands is presented in Figure 3.17a (mid-latitudes,  $40\text{--}60^{\circ}\text{N}$ ) and Figure 3.17b (subtropics,  $20\text{--}40^{\circ}\text{N}$ ). In the mid-latitude belt the specific humidity has a strong seasonal cycle similar to that shown in the frost point balloon data, with a pronounced winter minimum of  $0.03\text{ gkg}^{-1}$  ( $\sim 50\text{ ppmv}$ ) and late summer a maximum of  $0.09\text{ gkg}^{-1}$  ( $\sim 140\text{ ppmv}$ ). The specific humidity cycle follows the seasonal changes of temperature. The most pronounced changes of the specific humidity are coincident with the sudden temperature increase of  $5\text{--}7\text{ K}$  in May-June and the rather steep temperature drop of  $5\text{--}7\text{ K}$  in November-December. In summer and fall in mid-latitudes, the specific humidity is a factor of 2 larger than in Winter-Spring, while the temperature in Summer-Fall is about  $7\text{ K}$  higher. However, the corresponding relative humidity of about  $85\%$  with respect to ice in Summer-Fall is about  $10\%$  lower than in Winter-Spring, a change consistent with that shown by HIRS. Similar seasonal behaviour of moisture was found at the  $500\text{ hPa}$  level by Gaffen *et al.* [1992].

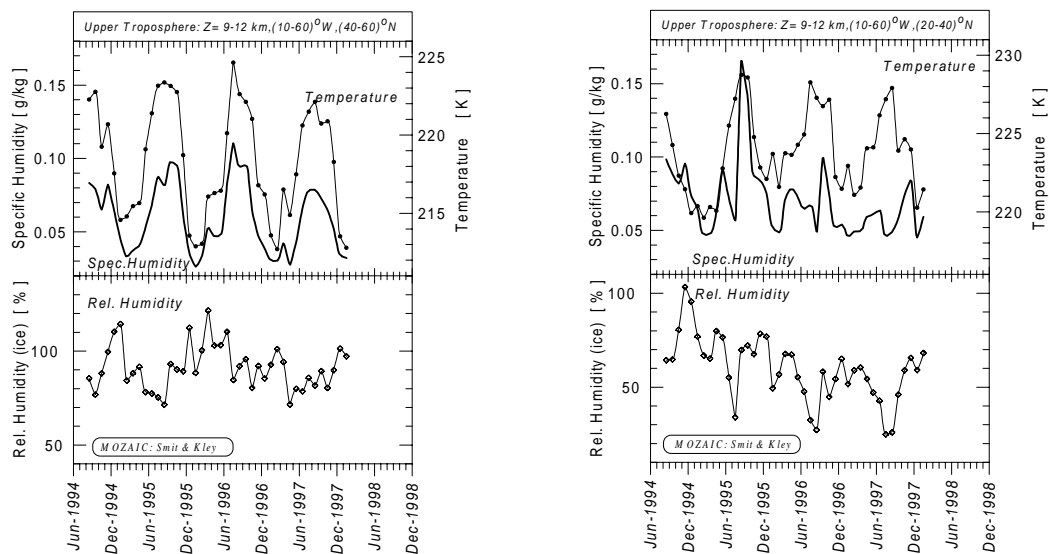


Figure 3.17. Seasonal variation of specific humidity, temperature, and relative humidity over ice in the upper troposphere ( $\text{PV} < 2\text{ PVU}$ ) over the North Atlantic, sampled during MOZAIC flights at  $9\text{--}12\text{ km}$  between August 1994 and January 1998. Results are shown for the mid-latitudes ( $40^{\circ}\text{--}60^{\circ}\text{N}$ , left) and the subtropics ( $20^{\circ}\text{--}40^{\circ}\text{N}$ , right). Data coverage is about 60 flights/month at mid-latitudes and 20 flights/month in the subtropics.

In contrast to mid-latitudes, in the sub-tropical belt (Figure 3.17b) the seasonal cycle in specific humidity is not as pronounced as the large interannual variability. The specific humidity is about  $0.08\text{ gkg}^{-1}$  ( $\sim 130\text{ ppmv}$ ) in Summer-Fall and  $0.06\text{ gkg}^{-1}$  ( $100\text{ ppmv}$ ) in Winter-Spring, and is positively correlated with temperature whose corresponding seasonal means are roughly  $225.0^{\circ}\text{K}$  ( $-48^{\circ}\text{C}$ ) and  $221.8^{\circ}\text{K}$  ( $-51.2^{\circ}\text{C}$ ) respectively. For comparison,

the relative humidity in Summer-Fall of about 57% is about 10% lower than in Winter-Spring. Thus, mean relative humidity from 20°-40°N is about 30% lower than from 40°-60°N. The same conclusion can be drawn from the HIRS UTH data in Figure 3.13.

The observed sudden changes of temperature and specific humidity, particularly within the mid-latitudinal belt, are probably due to changes of the large-scale circulation over the North Atlantic. These changes can be related to the seasonal northward migration of the subtropical jet stream from 30°N to 40°N in April-May and southwards from 40°N to 30°N in October-November. In the summertime, continental convection plays an important role in the water vapour distribution, as the storm tracks are weaker and move farther poleward.

### **Mechanisms influencing the global upper troposphere**

The data presented in this report and many previous studies clearly indicate that upper tropospheric water vapour is influenced by dynamics and by seasonal changes in temperature. The ability of dynamics to influence relative humidity and mixing ratio follows from the steep slope of the Clausius-Clapeyron equation, i.e. the rapid increase in water vapour holding capacity of the atmosphere with increasing temperature. The environmental lapse rate then leads to a rapid decrease of water vapour mixing ratio with altitude, characterised by a scale height of ~2 km. Because of this vertical gradient, vertical motions can quickly lead to large changes in mixing ratio at a given altitude. By the same token, adiabatic lifting of an unsaturated air mass lowers its temperature without changing its mixing ratio, thus increasing its relative humidity. Such lifting can quickly lead to saturation. Dynamical influences are also, however, associated with sources and sinks of water vapour, complicating matters as will be discussed below. In the tropical upper troposphere, horizontal temperature variations are small, so horizontal structure in moisture is similar whether viewed in terms of relative humidity or mixing ratio. Outside the tropics this is not generally true.

Global horizontal transport of total water occurs most readily on isentropic surfaces, making these a useful vertical coordinate. These surfaces are approximately level (hence isothermal) in the tropics and slope downward in the sub-tropics, but slope upward at higher latitudes, reaching colder temperatures. In the tropics, moist air is injected into the middle and upper troposphere in convective systems. Tropical air parcels that move isentropically to the extratropical upper troposphere encounter significantly lower temperatures and thus attain (on average) higher relative humidity. This is especially true in the winter (colder) hemisphere, leading to the higher relative humidity observed in this season. The high relative humidity in the extratropics overall leads to significant loss of water vapour through precipitation, leaving large, seasonal excursions in temperature to be the dominant regulator of the annual cycle in specific humidity. Air that returns to the tropics from high latitudes will have been dehydrated by the colder temperatures; also, moist tropical air that remains in the tropics, after precipitating (removing water), gradually cools and sinks to lower isentropes and higher temperatures. The air thus experiences a gradual decrease in relative humidity. The combination of isentropic and convective transport accounts for the coexistence of dry and moist air in the tropics and subtropics (though they do not apply close to the tropopause). This "big picture" ignores many important meteorological details, some of them as yet poorly understood, and relies upon a number of supporting arguments. Furthermore, much work remains to be done before water vapour can be reliably simulated in climate models. Many of these matters are discussed in the following sections.

### Tropical mechanisms

Upper tropospheric water vapour is maintained through balance between moistening by detrainment from updrafts and/or large-scale ascent, drying by condensation or freezing of water vapour in updrafts, and moistening by re-evaporation of detrained hydrometeors and precipitation. These mechanisms may be broadly divided into dynamics (or advection), and sources/sinks due to hydrometeor transport. Dynamics in the tropical troposphere is dominated by diabatic motion, ranging from the global-scale Hadley and Walker circulation all the way down to transient cumulus cells. Unfortunately, since hydrometeor sources and sinks are themselves almost completely controlled by the dynamics, it is not easy to discuss these two mechanisms separately. Instead, this discussion will begin with the rising, moist branches of the general circulation (including embedded convective motions and mesoscale organisation of these motions), and end with the sinking, dry branches of this circulation.

The planetary-scale tropical circulation is quasi-steady. Ascending branches tend to prefer certain regions, typically over warm surfaces like the tropical west Pacific, and coincide with convection. The circulation may be understood as a response either to the deep convective heating that occurs over warmer surfaces [Gill, 1980] or to forces generated by horizontal gradients in boundary-layer air temperature [Lindzen and Nigam, 1987]. Their ascending regions are generally much moister than elsewhere, accounting for the tropical patterns shown above by HIRS. Further, it is clear from recent satellite observations that high tropical UTH tracks the large-scale ascent and convection as it moves seasonally, intraseasonally, and interannually [Soden and Fu, 1995; Clark *et al.*, 1998; Sandor *et al.*, 1998; Chen *et al.*, 1999]. However, it must be remembered that due to variability on shorter time scales, even favourable areas sometimes experience dry, stable periods [Graham and Barnett, 1987; Lin and Johnson, 1996]. Such dry periods are associated with a break in the usual large-scale ascent pattern.

In principle, the tight association observed between ascent and high moisture could easily be explained on the basis of the dynamical arguments given earlier, but the effects of smaller-scale motions complicate matters. The large-scale view is indeed bolstered by the fact that the moisture supply to balance precipitation comes not from surface evaporation, which shows no systematic relationship with convection on large space and time scales, but from large-scale atmospheric transport and low-level convergence of moist air [Cornejo-Garrido and Stone, 1977]. On the other hand, the upward motion in areas of large-scale ascent is actually concentrated exclusively within relatively narrow, saturated, convective-scale and mesoscale updrafts, which generate evaporative sources of water vapour for nearby air in the mid- and upper levels [Riehl and Malkus, 1958; Houze, 1977]. This too is a way of explaining the high relative humidity in regions of large-scale ascent. These differing viewpoints on the scale of the processes controlling the water vapour distribution have fuelled debate within the scientific community as to how best to approach tropospheric water vapour.

The convective-scale motions, with velocities of up to  $50 \text{ ms}^{-1}$  or more and horizontal scales of  $\sim 10 \text{ km}$ , serve both to transport material and energy vertically and to condense great amounts of water vapour. The condensation liberates the heat required to balance the general circulation [Gill, 1980], while the convective transport creates an additional upward flux of moisture, or flux convergence in the upper troposphere. Furthermore, these convective motions generate liquid and ice clouds that exit the updrafts and spread horizontally.

Such behaviour is observed to be highly organised on the mesoscale ( $\sim 100 \text{ km}$ ). In the classical squall line [e.g., Houze, 1993, p. 348ff], a large mesoscale region of stratiform

anvil cloud and slow ( $\sim 1 \text{ ms}^{-1}$ ) upward motion above the freezing level is fed by the strong convective updrafts at the leading edge of the line. Ice particles continue to grow and fall slowly through the anvil, removing water substance. The top of this mesoscale updraft is at or just below the tropopause, where the air motions are downward; this is probably a mesoscale gravity wave response of the stable upper troposphere to the strong upward motion at the leading edge of the squall line [Johnson *et al.*, 1990]. A third to a half of the total precipitation from major convective systems comes from this stratiform region. This precipitation moistens the unsaturated layer below the anvil through evaporation, which sinks in a “mesoscale downdraft.”

Away from the ascending branches of the general circulation, small-scale vertical transports, sources, and sinks appear to be less important, and the picture is dominated by advection by large-scale horizontal motions in a slowly subsiding environment. While cloud evaporation may account for the observed decrease in UTH at increasing distance from convective systems [Udelhofen and Hartmann, 1995], typical water contents of non-precipitating clouds are small compared to the water vapour content in a relevant portion of the atmospheric column [e.g., Strom and Heintzenberg, 1994]. Sherwood [1999a] found that the water vapour field is so sensitive to dynamics that the radiative effects of typical cirrus clouds should drive sufficient vertical motions to produce greater moist anomalies than are produced by actual sublimation of the cloud ice. Accordingly, there is growing evidence that throughout the middle and upper troposphere away from convective systems, moisture levels are determined to good approximation simply by the character of the motion field at large scales with no attention paid to additional sources. This has been tested by performing calculations using analysed wind fields where the humidity in cloudy or ascending regions is somehow brought (or assigned) to a near-saturated value, then comparing globally-predicted humidity to that observed by a variety of observational platforms [Sherwood, 1996b; Salathé and Hartmann, 1997; Pierrehumbert and Roca, 1998; Dessler and Sherwood, 2000].

These results imply that in principle, general circulation models should be able to simulate the water vapour fields well in a coarse-grained sense if they have good energetics, dynamics, and numerics. Though models and assimilation products generally produce reasonable moisture patterns, most are unfortunately not dry enough in the most arid regions. Studies of this problem [Soden and Bretherton, 1994; Salathé *et al.*, 1995; Sherwood, 1996a] lead to the conclusion that in the models studied, parameterised convection typically mixed too much moisture out of the boundary layer under conditions where little or no transport really occurs. Numerical problems in model advection may also limit the ability of general circulation models to reproduce the steep curvature of the vertical water vapour profiles in areas of (presumably) little real mixing. Conversely, some assimilation products are not moist enough in convective or high-relative-humidity regions [Lin and Johnson, 1996, Ovarlez *et al.*, 2000]. This is probably due to forecast model problems though data problems may also be responsible. Model representation of convection and its interaction with moisture continues to be an active area of research.

### **Extratropical mechanisms**

Almost all of the discussion of the tropics also applies to the extratropics, but a few unique aspects are discussed here. These include the importance of coherent synoptic circulation patterns, the seasonality of convection, and interaction with the stratosphere.

During most of the year (fall through mid-spring), cyclonic, baroclinic disturbances dominate the regulation of extratropical upper tropospheric water vapour [Stone *et al.*, 1996]. These large-scale disturbances advect moisture poleward and upward from the

tropics and subtropics. The correlation of upward and poleward flow in the disturbances is characteristic of the unstable baroclinic waves that initiate the disturbances [cf. *Pedlosky*, 1979, p. 452]. The adiabatic cooling of the poleward-moving air produces widespread cloudiness extending to the top of the troposphere, especially during the winter season along the mid-latitude storm tracks. This can be seen in the enhanced cloudiness in cloud climatologies of high clouds along the mid-latitude storm tracks (e.g., HIRS climatologies, *Wylie and Menzel*, [1989]), and, to a lesser extent, in upper tropospheric MLS water vapour climatologies [e.g., *Sandor et al.*, 1998; *Haas and Pfister*, 1998]. The flow that returns to the tropics and subtropics sinks quasi-isentropically and is quite dry, having lost its water vapour to precipitation in the mid-latitudes. This process has been described by *Yang and Pierrehumbert* [1994] as “quasi-isentropic advection-condensation.” At lower latitudes, poleward-propagating Rossby waves may enhance this process. *Iskenderian* [1995] has shown that in certain preferred regions, such as the eastern tropical Pacific, mid-latitude Rossby waves can propagate deep into the tropics and excite convection there. The result can be a so-called “moisture burst” [*McGuirk et al.*, 1988] that has a strong southwest-northeast tilt. The quasi-isentropic process also appears to extend to high latitudes, producing lower upper-tropospheric mixing ratios at middle and high latitudes in the Southern Hemisphere (where polar regions get colder) than in the Northern Hemisphere, during their respective winters [*Kelly et al.*, 1991].

Local transport across isentropes is also important at mid-latitudes. Buoyancy-driven convection, not directly associated with baroclinic instability, is quite extensive in the summer mid-latitudes and often extends all the way to the tropopause [*Poulida et al.*, 1996]. This summertime convection resembles that described previously for the tropics, including convective and mesoscale features that transport moisture vertically in solid, liquid, and ice phases. Its contribution to upper tropospheric water vapour is clear, for example, in the comparisons between MLS upper tropospheric water measurements and HIRS high altitude cloudiness shown by *Haas and Pfister* [1998]. Water vapour and convection are enhanced over the major convective zones in the North American and Asia/Western Pacific regions. Quantitative evidence of the importance of local convection is given by *Yang and Pierrehumbert* [1994], who noted that their quasi-isentropic advection-condensation model predicted an excessively dry upper troposphere if only tropical sources of water vapour were considered.

As in the tropics, upper tropospheric moisture at middle and high latitudes is ultimately limited by condensation of moisture in excess of saturation, resulting in rapidly decreasing water vapour mixing ratio with height. However, recent *in situ* water vapour measurements have shown that large supersaturation with respect to ice (relative humidity with respect to ice up to 160%) is common in the mid-latitude upper troposphere, both in clear and cloudy regions [e.g., *Heymsfield et al.*, 1998; *Jensen et al.*, 1998a, 1999; *Gierens et al.*, 1999; *Vay et al.*, 2000]. This high supersaturation is consistent with recent laboratory experiments that indicate large supercooling is required to initiate ice cloud formation by freezing of sulphate aerosols [*Bertram et al.*, 1996; *Koop et al.*, 1998]. In fact, the common occurrence of clear-sky, upper tropospheric supersaturation is necessary to explain the frequent observations of persistent contrails [*Brewer*, 1946].

Another influence on upper tropospheric humidity is irreversible, turbulent mixing with stratospheric air in the tropopause region. Long, narrow streamers of dry upper tropospheric air are often apparent in satellite water vapour imagery [e.g., *Appenzeller and Davies*, 1992]. These streamers are caused by intrusions of stratospheric air into the upper troposphere from tropopause folding events [*Reed*, 1955]. These eventually dry the upper troposphere [*Langford and Reid*, 1998], though quantitative analysis of their overall

impact on the upper tropospheric water vapour budget is challenging because of the complexity and small spatial scales of the events [Cox *et al.* 1995].

### **Models of the tropospheric water vapour distribution and climate**

Mechanistic theories of the water vapour abundance in the middle and upper troposphere and its sensitivity to climate change appearing in the literature have mostly focused on convective transport with a tropical emphasis. Here, the relevant issues are those determining the detrainment profile of water vapour from convective elements [Lindzen, 1990], the “precipitation efficiency” or fraction of plume moisture that is removed as precipitation [Rennó *et al.*, 1994], and the microphysical properties of ice after it has detrained from the plumes [Sun and Lindzen, 1993]. Climate change studies using such models often predict that relative humidity in the middle and upper troposphere would decrease in warmer climates, i.e., that there would be a weaker or negative water vapour feedback [Lindzen, 1990; Sinha and Allen, 1994].

The above approaches neglect the role of horizontal mixing and large-scale processes, whose possible role in influencing climate variations has been discussed by Betts [1990], Yang and Pierrehumbert [1994], Salathé and Hartmann [1997], and Pierrehumbert and Roca [1998]. The cumulus-based approaches also do not consider mesoscale convective features and organisation. A recent simple model incorporating explicit control of moisture by the large-scale circulation rather than by draft physics [Sherwood, 1999b] found a positive water-vapour feedback, in agreement with those found by general circulation models.

The importance of large-scale dynamics to the present moisture distribution and its radiative impact, which is becoming increasingly apparent, suggests that models (such as general circulation models) that represent both global and cumulus-scale processes will be required to simulate water vapour sensitivity dependably. General circulation models are also beginning to include aerosols and their interaction with cloud processes [e.g., Lohmann *et al.* 1999]. These interactions may produce climatic variations in relative humidity in addition to those resulting from dynamics. Though such models carry water vapour as a prognostic variable and explicitly simulate the large-scale circulation, they include convection only through relatively crude physical parameterisations. Also, they may lack the proper vertical resolution to simulate the convective influence on water vapour correctly [Tompkins and Emanuel, 2000]. Further, many models in use today exhibit significant moisture biases [Gaffen *et al.*, 1997, Bates *et al.*, 1997]. Thus, there is much room for development and validation of these models before their water vapour feedback predictions can be fully trusted.

### **3.3.3 The Tropical Tropopause Region**

Because the tropical tropopause region (between 15-20 km altitude or about 150 and 70 hPa) plays a critical role in governing the distribution of water vapour in the lower stratosphere, the seasonal variability at the tropical tropopause and the processes responsible for it are treated here in a separate section.

#### **Observations**

Observations of water vapour in the tropical tropopause region are extremely limited. Some isolated frost point measurements using aircraft were performed over tropical Africa in June 1958 [Kerley, 1961] up to 15km, indicating frost points as low as  $-80^{\circ}\text{C}$  ( $\sim 4$  ppmv). The

seasonal cycle of water vapour in the tropics was illustrated by *Mastenbrook* [1968] over Trinidad (17°N) using a frost point hygrometer. *Kley et al.* [1979] measured water vapour up to 20 km in September 1978 from a balloon over Brazil. Measurements were also taken from two campaigns aboard the NASA ER-2 research aircraft in different seasons in 1980 and 1987 as part of the STEP project [*Kley et al.* 1982, *Kelly et al.* 1993]. The CEPEX campaign measured water vapour in the tropical tropopause region using aircraft [*Weinstock et al.* 1995] and balloons [*Vömel et al.* 1995b] and several mid-latitude aircraft campaigns also have flown into the tropics. More recently, the MLS instrument and the HALOE instrument on UARS measure water vapour in the upper troposphere and lower stratosphere respectively. All these observations are consistent with the annual cycle illustrated in Figure 3.11 (derived from HALOE data). Air in the tropical tropopause region is driest in Northern Hemisphere winter, and wettest in Northern Hemisphere summer. While the basic picture of ascent in the tropics driven by the mean meridional circulation presented in section 3.3.2 can explain many of these observations, it cannot explain some of the details, such as the extremely dry July hygropause of 2 ppmv noted by *Kelly et al.* [1993]. To explain these observations, the source and sink terms for water vapour in the tropical tropopause region are important.

Observations of clouds provide the key source or sink terms for water vapour in the tropopause region. It has long been known that deep convective clouds may penetrate the tropopause in mid-latitudes (see for example *Roach* [1966]). *In situ* evidence from aircraft [*Kelly et al.* 1993, *Danielsen*, 1993] and evidence from satellites [*Ebert and Holland*, 1992] clearly show that some convective clouds also penetrate the tropopause in the tropics. These clouds are extremely cold with ice recorded at up to 18 km or 75 hPa [*Danielsen* 1993] and saturation mixing ratios measured below 2 ppmv by *Kelly et al.* [1993] and as low as 1 ppmv by *Vömel et al.* [1995b]. The extent of this deep penetrating convection is currently uncertain. *Robinson and Atticks-Shoen* [1987] have estimated that observations of very cold clouds are of sufficient frequency to supply mass to the stratosphere. *Zhang* [1993] has noted that there is a seasonal cycle in the coldest clouds in the tropics, with maximum frequency of the coldest cloud tops ( $T < 200^{\circ}\text{K}$ ) peaking in boreal winter (January) throughout the tropics.

In the tropical upper troposphere, horizontal patterns of water vapour near the tropopause are like photographic negatives of those at lower levels. That is, convective areas tend to be drier than non-convective areas near the tropopause and wetter than non-convective areas farther down. The level at which the transition occurs lies somewhere between 100 and 150 hPa; unfortunately the vertical resolutions of the various upper tropospheric water vapour data sets are inadequate to locate this reversal level more precisely. These patterns appear both in long-term means [*Rind et al.*, 1993] and connected with the tropical intraseasonal oscillation [*Mote et al.*, 2000]. Other time scales have not been investigated, but *Reid and Gage* [1996] examined temperature variations at Truk Island in the tropical Pacific and found that both the seasonal cycle and the daily variations at levels above 125 hPa tended to be oppositely correlated with variations at levels below 125 hPa. The reversal between is consistent with rising motion below and sinking motion above anvil top with a crossover at 125 hPa in the tropics as measured in stratiform cloud systems by *Balsley et al.* [1989].

### Interpretation

Near the tropopause (~100 hPa), mechanisms not previously considered may become important. One key difference is that above 150 hPa, the tropical troposphere typically becomes more stable, in contrast to the consistently near-adiabatic profiles between 150 and 300 hPa. This region of the atmosphere is therefore better able to support wave

activity than lower levels, and the waves will have much greater temperature signatures. For example, *Tsuda et al.* [1994] have shown that Kelvin waves can perturb the tropical tropopause temperature by upwards of 4 K; this implies a factor-of-two variation in saturation mixing ratio. Short period gravity waves generated by convection have been observed in the tropopause region [*Pfister*, 1986; *Alexander and Pfister*, 1995]. These gravity waves cause temperature fluctuations that may cause cirrus clouds to form [*Potter and Holton*, 1995]. The effects of these clouds are discussed further below.

A second unique feature of this region is that radiative transfer models predict net radiative heating above 150 hPa in the absence of clouds [e.g., *Folkins et al.*, 1999], in contrast to net cooling that occurs elsewhere in the troposphere. The very dry air observed at the cold tropical tropopause, generally occurs at potential temperatures considerably greater than the equivalent potential temperature of the surface [*Selkirk*, 1993], implying that air at the tropopause has been radiatively heated. Only in the regions of most active deep convection (such as over the warm pool in the western Pacific) does the tropopause reach potential temperatures near the equivalent potential temperature of the surface. The stability and radiative heating of this region, together with trace gas measurements, imply a weakening of vertical mixing and a transition to slow ascent [*Folkins et al.*, 1999]. The ascent should lead to high relative humidity and increased cloud occurrence just below the tropopause. As pointed out by *Robinson* [1980], large-scale ascent would cause thick cirrus decks to form in the upwelling regions. High relative humidity indeed appears in recent satellite vapour measurements [*Jensen et al.*, 1999], as do large sheets of thin cirrus [*Wang et al.*, 1996].

High relative humidity and supersaturation (relative humidity > 100%) are often observed at the tropical tropopause region, with high values above convective regions, but with relative humidity still near 50% in the subtropics [*Jensen et al.*, 1999]. This high humidity indicates that water vapour in the tropical tropopause region is critically dependent on the saturation vapour mixing ratio, and hence the temperature. The seasonal variation in tropical stratospheric water vapour is linked to the seasonal cycle in tropical tropopause temperature [*Weinstock et al.* 1995; *Mote et al.*, 1995]. Temperatures in the tropical tropopause region have important variations in space and time, which have long been known [e.g., *Reed*, 1962; *Staley*, 1962; *Reed and Vlcek*, 1969]. The tropical tropopause temperatures are coldest in boreal winter (December to February) and highest in boreal summer (July-August) [*Newell and Gould-Stewart*, 1981; *Atticks and Robinson*, 1983]. This cycle can also be seen in the temperature of the coldest point in the temperature profile [*Zhou*, 2000b] and satellite observations of upper troposphere/lower stratospheric temperatures [*Yulaeva et al.*, 1994]. The annual cycle in temperatures is evident below the tropopause to 125 hPa [*Reid and Gage*, 1996]. The structure of temperature variations on the tropical tropopause has been discussed as a response to large scale tropospheric heating by *Highwood and Hoskins* [1998], and the interannual variations of the tropical tropopause in response to El Niño and the Southern Oscillation and the Quasi-Biennial Oscillation have been discussed by *Reid and Gage*, [1985], *Gage and Reid*, [1986], and *Reid*, [1994] among others (see section 3.4.2).

At the tropical tropopause (in Figures 3.6 and 3.11) the driest air occurs in the winter hemisphere, in both January and July, whereas the ascent in the Intertropical Convergence Zone is stronger in the summer hemisphere. One explanation of the wintertime dryness is that vertical convection on the winter side of the equator is deeper [*Tuck et al.* 1997], and hence colder and drier. A more comprehensive explanation notes that the dry air in the subtropics is consistent with forced ascent by a wintertime 'dynamical pump' driven by wave forcing driving air poleward at high altitudes and upward in the tropics [*Haynes et al.*, 1991; *Holton et al.*, 1995]. In theory this upwelling occurs more strongly in the winter hemisphere, though there are limitations outlined by *Plumb and Eluszkiewicz* [1999], who

---

argue that tropospheric thermal forcing may also be necessary to explain the observed upwelling in the tropics. The observed upwelling at 100 hPa is centred over the equator, and in the middle stratosphere is in the summer hemisphere [Eluszkiewicz *et al.*, 1996]. This wave-driven circulation is consistent with the annual cycle of temperature and of the sheets of cirrus clouds.

Large sheets of thin cirrus might constitute evidence of slow ascent. Significantly, the areas where thin cirrus are commonly observed [Wang *et al.*, 1996] are also the regions of coldest tropopause temperatures [e.g., Newell and Gould-Stewart 1981]. Thin cirrus is formed both *in situ* and by convective outflow [Winker and Trepte, 1998]. Newell and Gould-Stewart [1981] concluded from monthly-mean 100 hPa temperatures that the tropical tropopause was generally too warm to explain the extremely dry stratosphere unless the ascent was temporally and spatially limited to a “stratospheric fountain” in the coldest regions. The full three-dimensional circulation may be much more complicated. Gage *et al.* [1991] examined vertical velocities in the upper tropical troposphere and proposed that ascent may be occurring in regions of clear sky above the downward branch of the Walker circulation. The downward branch of this “reverse Walker” circulation would be found over convective regions, as noted by Sherwood [2000] and seen in the analysis of Simmons *et al.* [1999]. However, uncertainties in water vapour concentrations and in the temperature and vertical velocities in the region of the tropical tropopause are currently too great to determine whether ascent is predominantly widespread or localised and predominantly slow or fast (see Vömel and Oltmans [1999] and Dessler [1999]).

Cirrus, water vapour, radiation, and temperature undoubtedly interact through a variety of mechanisms that are not yet understood. The formation and maintenance of cirrus clouds involves dynamics, radiation, and microphysics [Jensen *et al.*, 1996b]. These clouds can both moisten the tropopause region by radiatively induced heating [Rosenfield *et al.*, 1998] or radiatively induced upward advection of water vapour “radiative pumping,” [Sherwood, 1999a]. Cirrus clouds may also dehydrate the tropopause region by radiative destabilisation of anvils formed in the stratosphere from penetrating convection Danielsen [1982] or by ice fallout [Jensen *et al.*, 1996a]. Unfortunately, model simulations of cirrus are at present poorly constrained due to lack of good data on cloud composition and water vapour. Observations suggest some degree of supersaturation occurs below the tropical tropopause [Jensen *et al.*, 1999], indicating the potential sensitivity of moisture levels there to microphysical behaviour.

## 3.4 Non-seasonal Variations

In addition to the seasonal variations described in the previous section, which are driven by the seasonal variation in solar forcing, there are a number of variations at other time scales. We describe here interannual variations and intraseasonal variations. We also discuss the variability of water vapour on small temporal and spatial scales.

### 3.4.1 Interannual Variations

In most of the UT/LS, interannual variations in the stratosphere and upper troposphere are almost completely independent: the quasi-biennial oscillation (QBO) in the stratosphere and the ocean-atmosphere interaction known as El Niño-Southern Oscillation (ENSO) in the troposphere. Only at the tropical tropopause are both phenomena evident.

#### The Quasi-Biennial Oscillation

Among the most important transport-related influences on trace constituents in the stratosphere is the quasi-biennial oscillation. The quasi-biennial oscillation is an irregular fluctuation, with average period of 28 months, of the mean zonal wind in the equatorial lower stratosphere and is accompanied by temperature perturbations of a few degrees Kelvin. These perturbations represent a departure from radiative equilibrium and require a diabatic mean meridional circulation to maintain them. Positive vertical shear of westerly momentum ( $du/dz > 0$ ) is associated with above-normal temperatures and below-normal ascent, and vice versa. Through these anomalies in ascent, the quasi-biennial oscillation affects the distribution of trace constituents like water vapour. Because of its relatively long period, however, the quasi-biennial oscillation is difficult to identify in observations even with a record of several years. Two satellite data sets have sufficiently long records to isolate the signature of the quasi-biennial oscillation in stratospheric water vapour: SAGE II and HALOE. SAGE II water vapour data are significantly affected by aerosol contamination in the tropics at about 20 km (see section 1.4.3, and Figure 2.63), making isolation of a quasi-biennial oscillation signal problematic. *Randel et al.* [1998] have described the quasi-biennial oscillation signature using HALOE data and here we show the time series updated through 1999.

Figure 3.18 shows time series of HALOE water vapour anomalies over the equator, at several pressure levels spanning the lower to upper stratosphere. These time series are generated by simply removing the seasonal cycle at each level, following *Randel et al.* [1998]. The dominant component of interannual variability in the middle and upper stratosphere is a QBO signal, approximately out of phase between the 15 hPa and 3 hPa levels. There is an apparent QBO signal in the lower stratosphere, which appears most coherently after 1995, but relatively little QBO variance at 32 hPa. Figure 3.19 shows a vertical section of these equatorial water vapour anomalies, showing the vertical extent and coherence of the QBO variations. Similar variations occur in methane in the upper stratosphere (38-45 km), such that  $2 \times \text{CH}_4 + \text{H}_2\text{O}$  is approximately constant there [*Randel et al.*, 1998]. In contrast, the QBO patterns below 35 km in Figure 3.19 are not observed in methane (which in fact has a small vertical gradient there), and thus represent QBO modulations of water vapour due to other mechanisms.

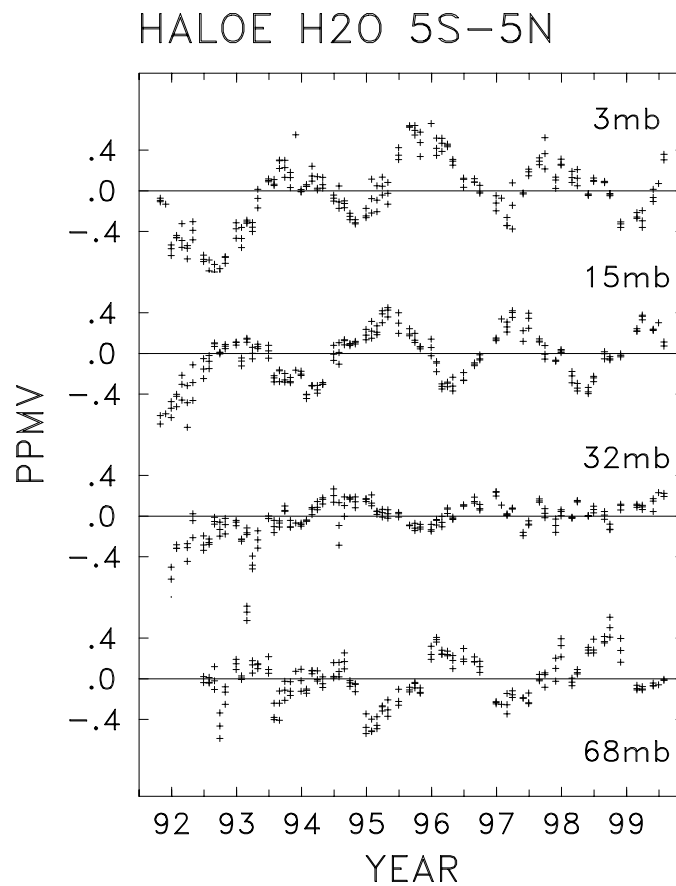


Figure 3.18. Time series of zonal mean deseasonalised HALOE water vapour anomalies at 3, 15, 32 and 68 hPa over the equator, following the method of *Randel et al.* [1998].

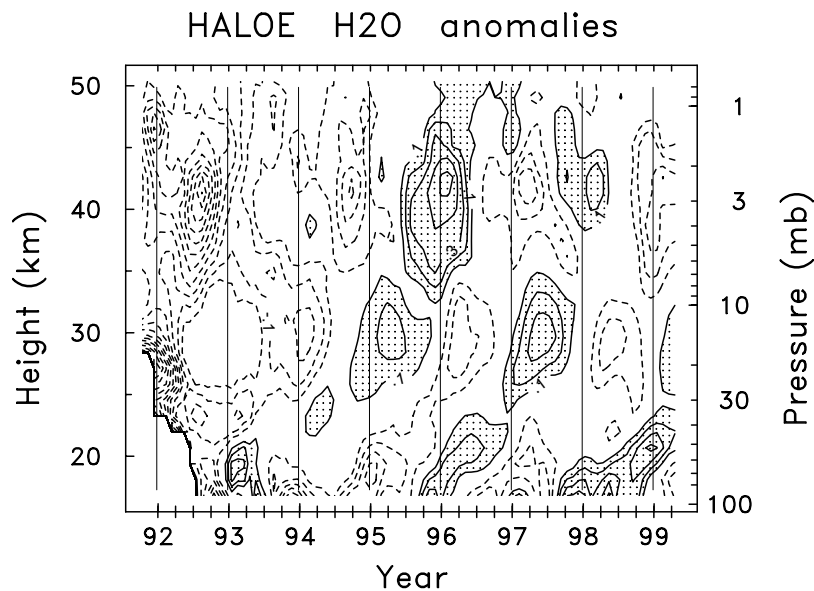


Figure 3.19. Time-height section of interannual water vapour anomalies over the equator. Contour interval of 0.1 ppmv, zero contour omitted. The anomalies are calculated by removing the annual cycle following the method of *Randel et al.* [1998].

Although the QBO is a tropical phenomenon, it affects trace constituents at mid-latitudes. Figure 3.20 shows meridional cross sections of HALOE water vapour measurements when the QBO was in roughly opposite phases: in April 1996 (top panel) and April 1997 (middle panel), and their difference (bottom panel). The extent of the QBO influence outside of the tropics is evident. A comparison of mean fields shows that the QBO induces large changes in meridional gradients in the subtropics [O'Sullivan and Dunkerton, 1997; Gray and Russell, 1999], and furthermore acts to modulate the double-peaked semi-annual oscillation patterns in the upper stratosphere [e.g., Kennaugh et al., 1997]. As was noted above, the large H<sub>2</sub>O anomalies in the upper stratosphere (and mid-latitude lower stratosphere) are mirrored in oppositely signed methane patterns, signifying that these anomalies are due to transport. The global character of the QBO meridional circulation patterns inferred from meteorological analyses are consistent with these mid-latitude patterns [Randel et al., 1999a].

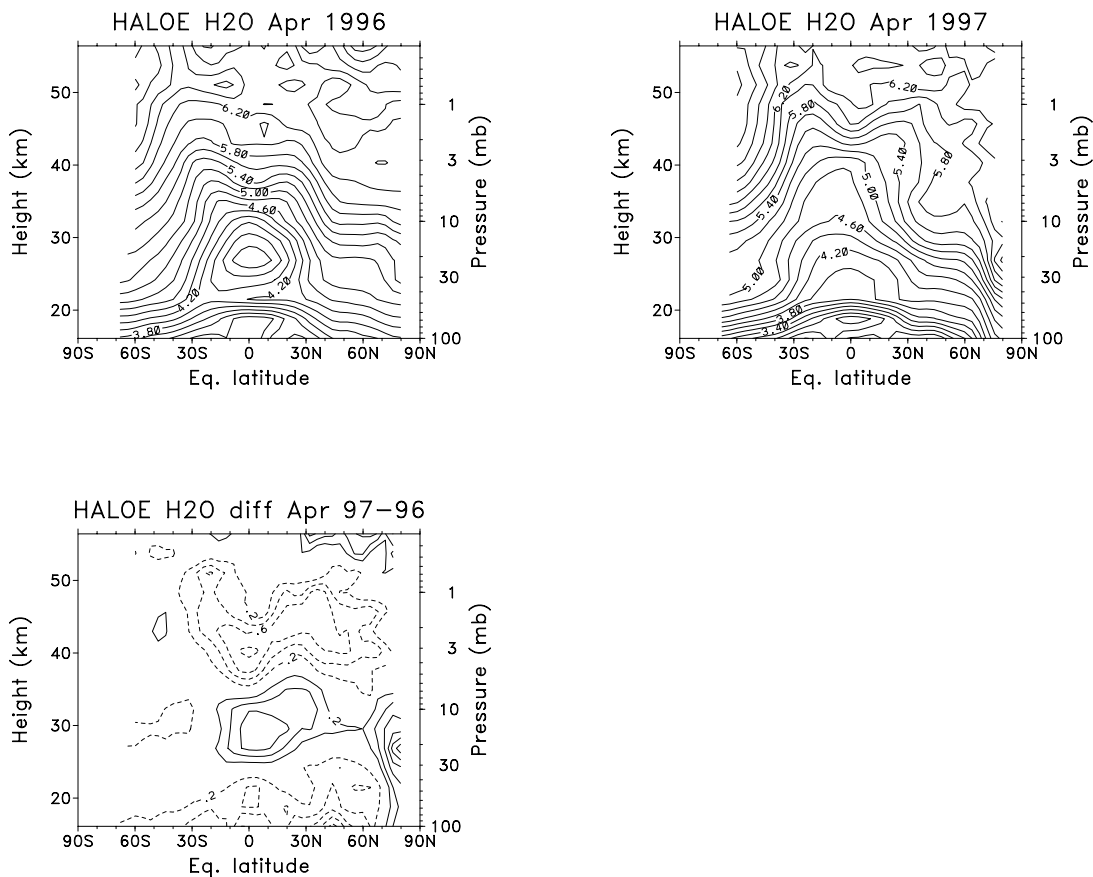


Figure 3.20. Zonal monthly mean equivalent latitude-height water vapour distribution for April 1996, April 1997 and the difference between them. The contour interval is 0.3 ppmv for the first two panels; in the third panel, the contour interval is 0.2 ppmv, the zero contour is omitted, and negative contours are dashed.

Several possible mechanisms are responsible for the water vapour variations in the lower stratosphere associated with the QBO. (1) The zonal mean circulation associated with the QBO, which is stronger in the winter hemisphere than in the summer hemisphere [Jones et al., 1998, Randel et al. 1999a, Kinnersley, 1999]. This mechanism affects water vapour

throughout the stratosphere, particularly in the upper stratosphere, where advection from the summer hemisphere (see Figure 3.4) is significant. (2) The QBO influences planetary-wave propagation and the subtropical mixing barrier (see section 3.2) [O'Sullivan and Dunkerton, 1997; Gray and Russell, 1999; Gray, 2000]. (3) Interannual variations in equatorial ascent rate are associated with the QBO mean meridional circulation [Mote *et al.*, 1996; Seol and Yamazaki, 1998; Randel *et al.*, 1999a]. (4) The QBO affects tropopause temperature and pressure, hence the saturation mixing ratio of water vapour [Reid and Gage, 1985; Giorgetta and Bengtsson, 1999; Randel *et al.*, 2000; Zhou *et al.*, 2000a].

This last mechanism, which probably is the dominant mechanism represented in the tropical time series (Figure 3.19), bears further discussion. As was shown in Figure 3.11, annual variations in tropical tropopause temperature (section 3.3.3) are imprinted on air passing through the tropopause. In a similar manner, it seems plausible that interannual variations in tropical tropopause temperature induced by the QBO could modify the seasonal imprinting. The QBO's contribution to temperature variation near the tropopause is approximately  $\pm 0.5$  K, whereas the annual cycle in this region is about  $\pm 5$  K [e.g., Reed and Vlcek, 1969]. QBO circulation anomalies have associated temperature anomalies [Plumb and Bell, 1982]. Reid and Gage [1985] have shown that the QBO is associated with changes of  $\sim 300$  m in tropopause height, and potential temperature changes as expected from theory [Plumb and Bell, 1982]. These temperature changes can result in significant modifications to the saturation vapour mixing ratio, potentially changing the water vapour concentration of air entering the stratosphere. This effect has recently been simulated in a tropospheric GCM with an assimilated QBO [Giorgetta and Bengtsson, 1999]; the simulated water vapour anomalies in the lower and middle stratosphere are  $\pm 0.2$  ppmv, somewhat smaller than those shown in Figure 3.19.

### El Niño and the Southern Oscillation

The leading pattern of global interannual atmospheric variability in the troposphere [e.g., Rasmusson and Wallace, 1983] is associated with El Niño and the Southern Oscillation (ENSO), an irregular variation of the tropical Pacific Ocean and overlying atmosphere with a return period of 2–7 years. In the cool or La Niña phase of the Southern Oscillation, the warmest water and convection are located in the western Pacific north of Australia. In the warm or El Niño phase, warm water and convection spread eastward, usually over a greater longitudinal range. Upper tropospheric water vapour is profoundly influenced by the Southern Oscillation, and not just in the tropics. In fact, the leading pattern of interannual variability in upper tropospheric water vapour (derived using empirical orthogonal function analysis; see Preisendorfer, [1998]) is also associated with the Southern Oscillation (Figure 3.21). This pattern highlights the tendency for the central and eastern Pacific to vary oppositely from the western Pacific and also has a strong signature in the subtropical Pacific, probably because strong convection in the central and eastern Pacific drives subsidence in the subtropics at those longitudes.

That this mode is associated with the Southern Oscillation is also clear from its temporal characteristics (Figure 3.21, lower panel). The strength and phase of the Southern Oscillation are often measured in terms of the average sea surface temperature anomaly over one of several rectangles in the Pacific Ocean [Trenberth, 1997], one of which is called Niño3 ( $5^{\circ}\text{N}$ - $5^{\circ}\text{S}$ ,  $90^{\circ}$ - $150^{\circ}\text{W}$ ). The time series of the first principal component tracks that of Niño3 strikingly well. The large El Niño events of 1982-1983 and 1997-1998, and the La Niña event of 1998-1999, are clearly visible in both time series. Similar relationships with the Southern Oscillation are evident in the shorter MLS data set [Newell *et al.*, 1997]. Wang and Fu [2000] describe the impacts of the Southern Oscillation on

lower tropospheric water vapour. The mechanisms influencing upper tropospheric water vapour on the time scales of the Southern Oscillation are discussed above in section 3.3.2.

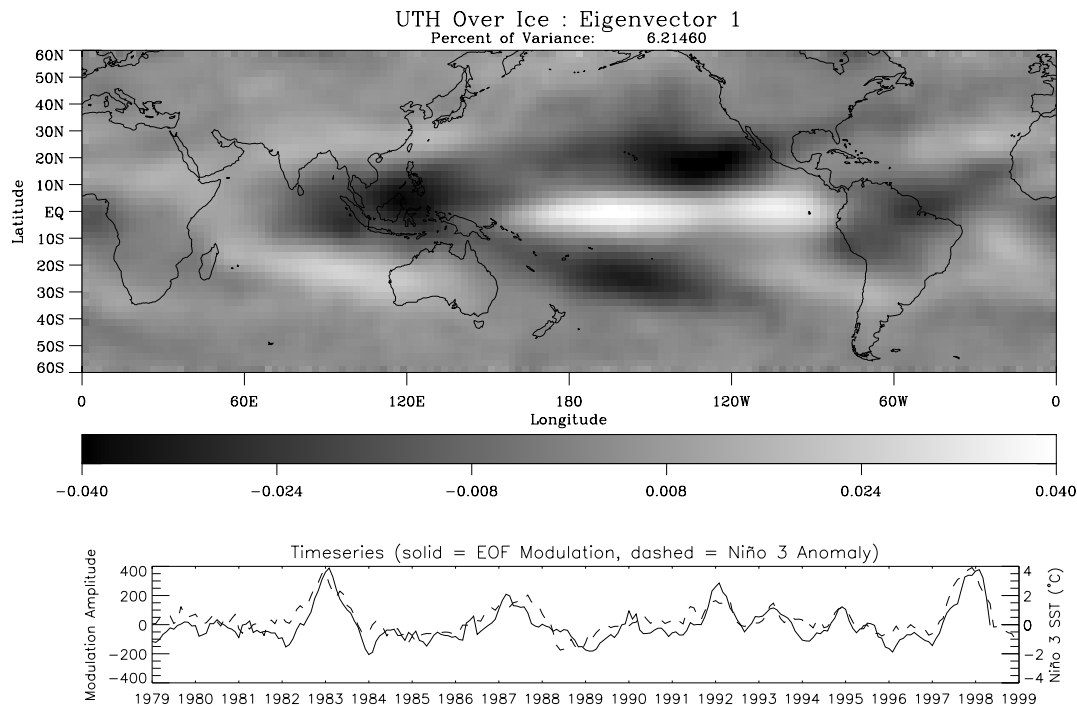


Figure 3.21. Leading global pattern of interannual variations in Upper Tropospheric Humidity over ice (UTHi), 1979-1999, from the HIRS data set (Section 1.4.1). Top panel, the pattern itself; bottom panel, its temporal evolution (solid line, left scale) compared with a normalised time series of average sea surface temperature over the domain  $5^{\circ}\text{N}$ - $5^{\circ}\text{S}$ ,  $90^{\circ}\text{W}$ - $150^{\circ}\text{W}$  (dashed line, right scale).

### 3.4.2 Intraseasonal Variations

In the tropics, where the seasonal cycle in upper tropospheric water vapour is relatively weak [Newell *et al.*, 1997], intraseasonal variations (those with periods of say 10-120 days) have a significant influence on upper tropospheric water vapour. Such variations are associated with the tropical intraseasonal oscillation or Madden-Julian Oscillation (MJO). The MJO is a tropical phenomenon with characteristic period of 30-60 days that has a signature in many tropospheric fields [Madden and Julian, 1971]. Only recently have satellite data been used to show the signature of the MJO in upper tropospheric [Clark *et al.*, 1998] and lower stratospheric [Mote *et al.*, 2000] water vapour. In upper tropospheric water vapour data from MLS, the MJO intraseasonal variability accounts for as much as 35% of total power (with daily time resolution), compared with 19% for the annual cycle [Clark *et al.*, 1998].

Intraseasonal variations are evident in Figure 3.22, which is a longitude-time diagram of tropical water vapour produced with data from the HIRS instrument. Several slow, eastward-moving features appear over the Indian Ocean ( $45^{\circ}$ - $90^{\circ}\text{E}$ ) and travel to the middle of the Pacific before disappearing. For example, one feature can be tracked from  $45^{\circ}\text{E}$  in mid-November to about  $180^{\circ}\text{E}$  in early January, and another can be tracked from  $0^{\circ}\text{E}$  in early January to about  $160^{\circ}\text{E}$  in early March. These features tend to disappear in the central and

eastern Pacific because the convection that generates them fades over the colder water there. The extension of warm water eastward along the equator during El Niño years (see section 3.4.1) allows convection and the associated MJO anomalies to penetrate farther eastward; this can be seen as the 1997-1998 El Niño event develops (top part of Figure 3.22) and was also shown using MLS data by *Clark et al.* [1998].

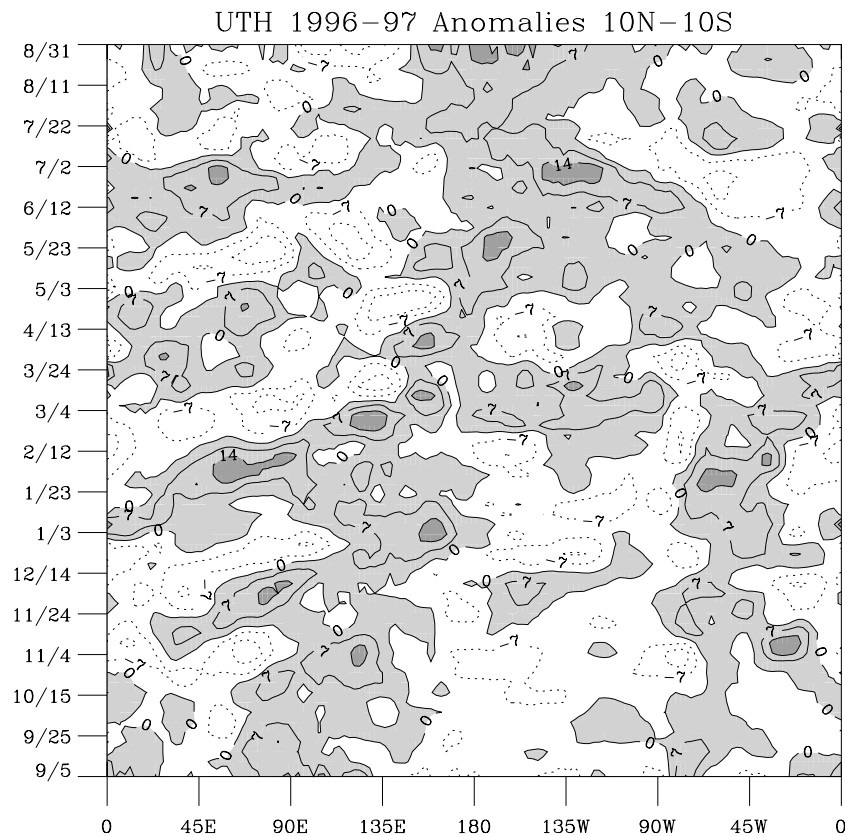


Figure 3.22. Intraseasonal variations in HIRS humidity for five-day average values over the domain 10°N-10°S. Contour interval is 7%, grey shading indicates positive anomalies, and dotted contours indicate negative anomalies.

The influence of the MJO on water vapour appears to extend at least to 100 hPa [*Mote et al.*, 1998a, 2000] with an amplitude of only a few tenths of 1 ppmv (less than 10% variability about the mean), though the true variations may be much larger and could be smeared by the coarse vertical resolution of MLS [*Mote et al.*, 2000]. Variations at the next MLS level up, 68 hPa, also have some spectral power in the intraseasonal band [*Mote et al.*, 1998a], but it has not been shown that those variations are caused by the MJO. The mechanisms influencing upper tropospheric water vapour on these time scales are essentially the same as those for the seasonal cycle, which is discussed above in section 3.3.2.

### 3.4.3 Transient Variability

Though the focus of this document is on variability at large scales, when trying to assess large-scale variability from limited data it is important to recognise that spatial distributions of atmospheric constituents are far from being smooth. This point is especially relevant for water vapour in the upper troposphere and lower stratosphere since many of the most

reliable data sources are point measurements with very limited spatial coverage. The existence of transient small-scale variations also complicates efforts to validate satellite observations against *in situ* data as discussed in Chapter 2.

### Processes producing transient variations, and observed examples

A good overview of the structure present in the water vapour field is provided by geostationary water-vapour imagery (Figure 3.23), indicating significant horizontal structure in upper tropospheric relative humidity. Several processes account for this variability.

First, small-scale tracer structure results naturally from the process whereby air masses having different initial tracer concentrations are combined by fluid motions. Shear in the motion field tends to produce elongated structures which become increasingly sharp and fine-grained as the material surfaces are stretched and folded [Batchelor, 1952, Welander, 1955], before the tracer is eventually homogenised by molecular diffusion. Both chaotic advection (or stirring) and diffusion are essential for final tracer mixing to occur in a reasonable time [Young *et al.*, 1982]. Even a simple, laminar motion field can create complex tracer structure, provided that the field is time varying [Aref, 1984]. Such mixing between moist and dehydrated air masses, performed by large-scale motions, accounts for many of the structures seen at mid-latitudes in Figure 3.23. This process tends to occur on isentropic surfaces [Pierrehumbert, 1991], and was simulated in the upper troposphere by Yang and Pierrehumbert [1994] and in the stratosphere by Pierce and Fairlie [1993] and others. The process is widely believed to lead to fractal tracer distributions (see below).

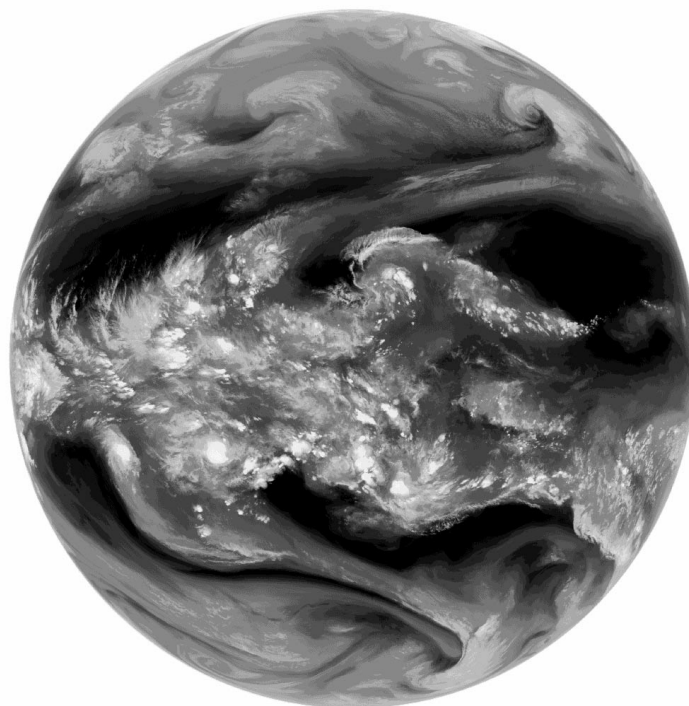


Figure 3.23. Image from GMS IR3 water vapour channel on 5 February 2000. This instrument observes upper tropospheric water vapour with a weighting function similar to HIRS.

Three-dimensional advective effects also add to small-scale structure. Non-turbulent "differential" advection can produce lamination in the vertical by bringing air masses of different origins into the same column at different levels [e.g., *Newman and Schoeberl, 1995*], a process that contributes to vertical tracer mixing [*Haynes, 1997*]. Turbulent events such as wave breaking can produce complicated laminar, roll-like, and/or filamentary structures [e.g., *Bithell et al., 1994*]. Such features have been reported most extensively in ozone [e.g., *Reid and Vaughan, 1991; Appenzeller and Davies, 1992; Appenzeller et al., 1996*], but also appear in water vapour [*Gray et al., 1994*] as would be expected. Horizontal moisture layering is also frequent in the troposphere [e.g., *Mapes and Zuidema, 1996, Newell et al., 1999*].

Vertical advection or convection can also produce horizontal structure in water vapour due to the extreme vertical gradients in the climatological water vapour field, particularly in the troposphere. Vertical transport can occur in association with waves at all scales, from small-scale gravity waves to large-scale wave-like phenomena such as the Madden-Julian oscillation (see also Section 3.4.2). The patterns most evident in the tropics in Figure 3.23 are clearly due to the contrast between near-saturated conditions in the immediate environment of convection and relatively dry surrounding areas. This variability occurs on length scales down to less than 1 km, and is transient in that convection decays and reappears on time scales of less than a day. Of course, variability in the tropics can also be produced by the advective mechanisms described earlier.

The importance of these processes in the troposphere is revealed by a series of profiles taken near Panama (Figure 3.24). Water vapour is again quite variable near and below the tropopause owing to tropospheric weather. In contrast, above the tropopause the vapour levels are low and change little from sounding to sounding. The relatively uniform dryness near the equator at the time of these measurements is also supported by ER-2 observations over the Pacific [*Weinstock et al., 1995*]. Similar conclusions may be drawn from the data presented in *Kelly et al. [1993]*, though in that study somewhat more variability was found in the first few kilometres above the tropopause. Mechanisms leading to variability near the tropical tropopause are still poorly understood (see Section 3.3.3).

Recently, airborne laser hygrometers have begun providing unparalleled section views of the water vapour field that can help illustrate some of the structure that occurs and should lead to further understanding. A mid-latitude example measured by the NASA Lidar Atmospheric Sensing Experiment (LASE) off the East coast of the United States during July 1996 appears in Figure 3.25. Considerable horizontal variability is evident, with mixing ratios at 9 km varying by more than one order of magnitude owing to an intrusion of dry lower stratospheric air in apparent folding events near 69°W and 72°W longitude. Around 74°W, high humidity occurs in association with some clouds (not shown) that indicate prior convection. Small-scale vapour variations all along the flight (particularly evident between 4 and 8 km but noticeable at most altitudes) are likely remnants of earlier mixing events or filamentation, while slower horizontal variations near the tropopause (12-13 km level) shown here are probably related to large-scale vertical advection.

Since molecular diffusion is very slow in eliminating tracer gradients, the latter can become extremely sharp in the atmosphere, regardless of the advective or other mechanisms that create them. An example of this for water vapour near the tropopause is shown in Figure 3.26. Such features are highly problematic for accurate measurement of spatial averages or large-scale variations.

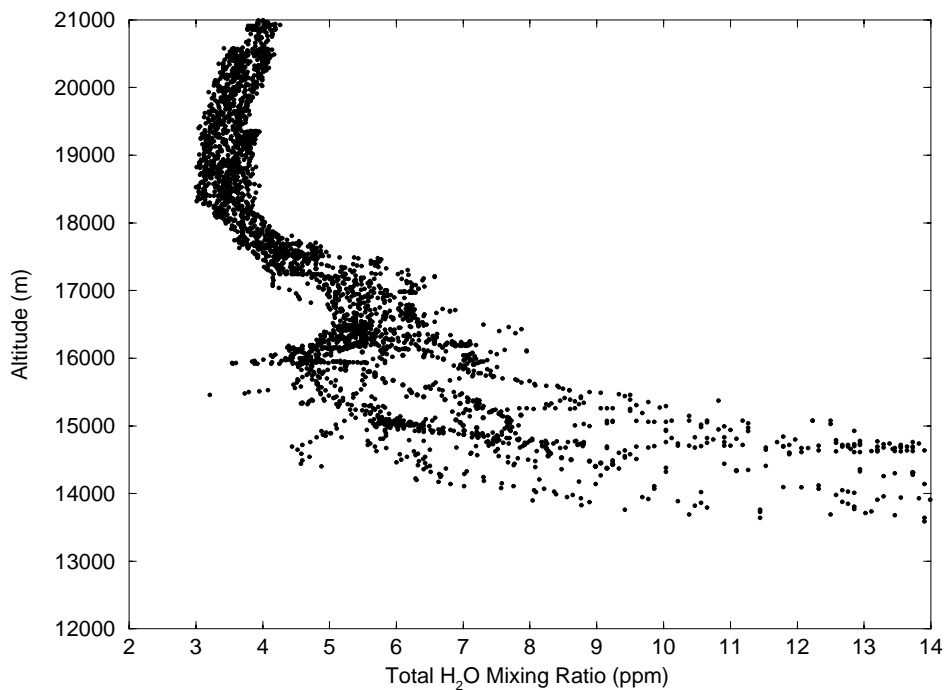


Figure 3.24. Total water vapour mixing ratio profiles obtained by the NOAA Aeronomy Lab. U2 Lyman- $\alpha$  hygrometer in September 1980 during the Water Vapour Exchange Experiment over Howard AFB, Panama. The profiles are from ER2 research aircraft on August 30 and September 7, 9, 11, 12, 13, 15, and 16. Previously published by *Kley et al.* [1982].

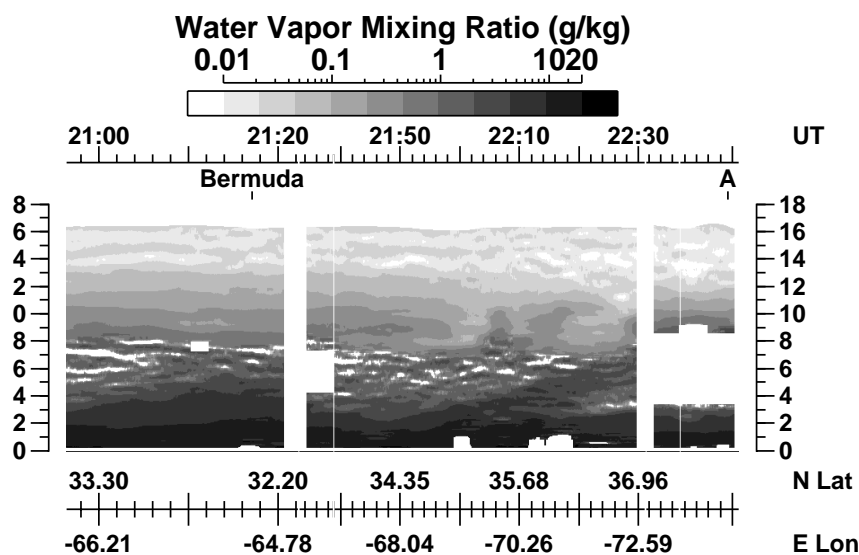


Figure 3.25. Measurements of water vapour mixing ratio during a flight near Bermuda and from Bermuda to Wallops, Virginia, on July 26, 1996 made by the Lidar Atmospheric Sensing Experiment (LASE) as part of the TARFOX campaign. Data provided by Syed Ismail and Edward Browell, NASA Langley Research Center.

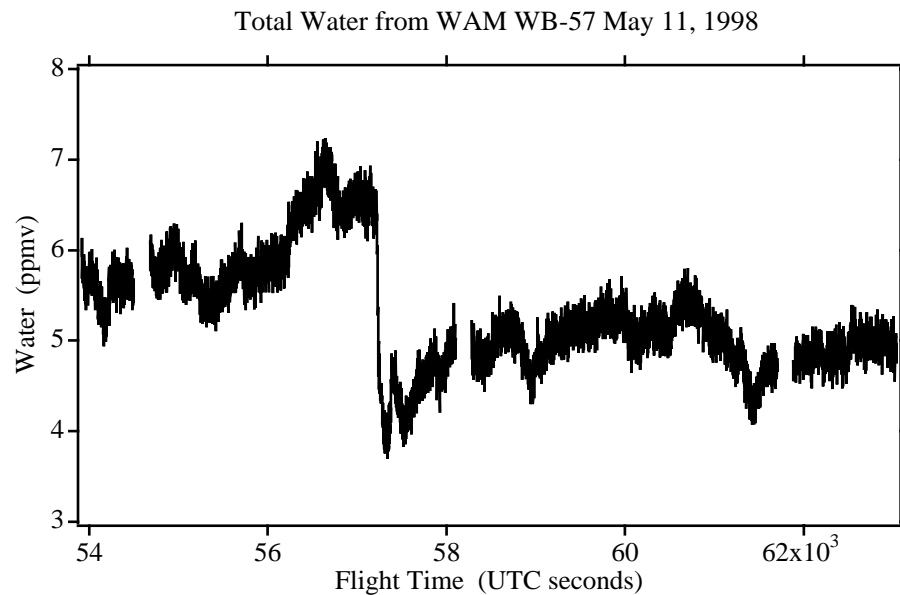


Figure 3.26. Total water observed on 11 May 1998 by the WB57F on a southbound leg from (30°N, 95°W) to (10°N, 95°W) at 120 hPa pressure. 103 seconds correspond to 200 km (figure provided by A. Tuck).

### Statistical description of variability

Strategies for quantifying overall transient variability are not straightforward, and a number of statistical approaches to the modelling of tracer variability have been attempted. We do not attempt to review this active research area here, mentioning only a few recent studies specifically of water vapour in the upper troposphere and lower stratosphere. *Gierens et al.* [1997], analysing data from the MOZAIC program, confirmed that fluctuations of humidity and temperature from their local means are characterised by occasional large fluctuations (i.e. heavy-tailed distributions) in the upper troposphere. *Gierens et al.* [1999] found further that the frequency of occurrence of relative humidity greater than 100% decreased exponentially above ice saturation, and that it decreased exponentially for the entire range of values in the lower stratosphere. They offered a stochastic source-sink model capable of producing such distributions. *Cho et al.* [2000] analysed the scaling properties of the water vapour distribution in the troposphere, finding “anomalous scaling” or multifractality out to scales of 100 km. Similar behaviour was found for other tracers out to larger scales in the upper troposphere and lower stratosphere by *Tuck and Hovde* [1999]. Importantly, *Cho et al.* [2000] note that while vapour increments are statistically stationary (see below), the transient vapour field itself is not. This means that the probability distribution (e.g., variance) of transients cannot be characterised accurately from a finite number of observations. Work continues actively in this area.

To supplement these studies we present here a simple analysis focusing on the practical issue of comparing measurements from imperfectly collocated instruments. Specifically, we consider the increment distribution, or probability distribution of possible difference values  $\delta q$  between water vapour observed at two locations with a given horizontal separation distance  $\delta x$ , and at approximately the same time and height in the atmosphere. This and related measures of variability are discussed by *Bacmeister et al.* [1997] and *Cho et al.* [2000]. Since the variability is produced for the most part by free turbulent motions, it is also possible to convert statistical functions of separation distance at a given time into

functions of time lag at a given location using Taylor's Hypothesis—i.e., by multiplying the time lag by a typical horizontal wind speed.

MOZAIC data serve this purpose well in the upper troposphere. Figure 3.27 shows the distribution of the variable  $\delta RH$ , the difference in moisture between two points 100 km apart. This distribution also is clearly non-Gaussian with a narrow peak near zero and very heavy tails (in fact it is reasonably well fit by decaying exponentials on either side of zero). The heavy tails reflect the existence of large jumps in humidity such as those discussed previously. Since these data are not collected strictly on an isentropic surface, they will contain some variability due to vertical structure in the atmosphere, if this is present, as well as horizontal.

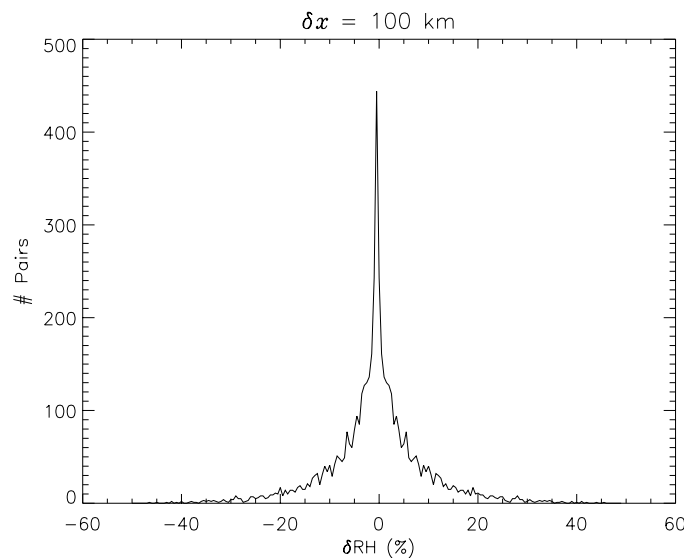


Figure 3.27. Histogram of  $\delta RH$ , the difference in relative humidity at two neighbouring locations in the upper troposphere separated by 100 km. Data are obtained from MOZAIC aircraft measurements at altitudes between 10–12 km. The histogram is symmetric because each pair is counted as a positive and negative difference.

Scaling behaviour [Cho *et al.*, 2000; Tuck and Hovde, 1999] suggests that the properties of this distribution should change in a simple and predictable way with increasing separation distance  $\delta x$ . Distributions for other values of  $\delta x$  (not shown) are indeed qualitatively similar to that shown in Figure 3.27, but become broader with increasing separation distance.

This broadening is shown in Figure 3.28 as a second-order “structure function,” or plot of the root-mean-square (RMS) value of  $\delta RH$  as a function of  $\delta x$ . The RMS difference increases from about 5% relative humidity at a few tens of kilometres, to 25% RH at distances of 1000 km or more. This increase appears roughly log-linear (a hallmark of “scaling” behaviour) until the statistics deteriorate at larger scales. The variability is somewhat greater in the tropics than in the northern mid-latitudes, out to distances of 100 km or less; this is likely due to the more frontal character, and/or greater horizontal shearing, of mid-latitude weather compared with that in the tropics. The difference is particularly apparent in the probability of two adjacent RH values differing by more than 10% (a nominal, modest accuracy level); at distances near 100 km the probability of this is almost twice as high in the tropics as at mid latitudes. Such statistical “heterogeneity” makes any statistical treatment of transient variability more difficult (see also Gierens *et al.*, [1999]).

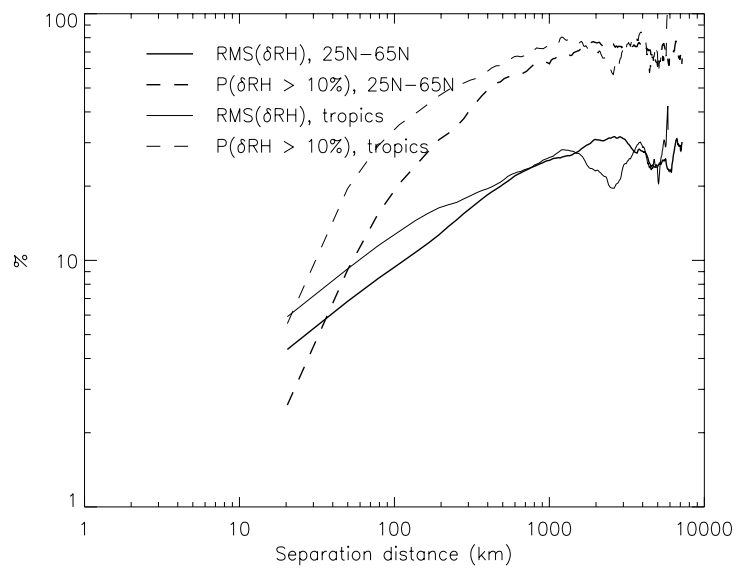


Figure 3.28. Plot of the square root of  $\delta RH^2$  as a function of  $\delta x$ , where  $\delta RH$  is the difference in relative humidity at two neighbouring locations in the upper troposphere separated by distance  $\delta x$  (solid lines); and probability that  $\delta RH$  will exceed 10% (dashed lines). Thick lines are for data north of 25N; thin lines, data between 25S and 25N. Statistical robustness weakens after a few hundred kilometres, where the curves become irregular, since effective sample size varies inversely with separation distance.

Figure 3.29 shows the structure function  $\delta q$  describing vapour variability in the mid-latitude lower stratosphere, as calculated from ER-2 measurements. Flights during the spring and fall seasons show more small-scale variability than flights during summer and winter. The high variability in spring is due to the early spring break-up and equatorward mixing of the relatively dry polar vortex, while that in fall is likely due to the delayed mixing of moist season (July-August) air from near the tropical tropopause [e.g., *Rosenlof et al.*, 1997]. At other times, mixing is relatively inhibited. Significant jumps in mixing ratio (0.5 ppmv) are possible over distances as short as 10 km, especially in spring and fall, though the ratio of RMS variability to the mean (4-5 ppmv) is substantially less than that in the upper troposphere (Figure 3.28).

### Instrument collocation

Plots such as Figure 3.28 and Figure 3.29 may form the basis for a quantitative approach to maximising the effectiveness of instrument intercomparisons. However, to go any further depends on the details of the task at hand, including the sampling characteristics of the instruments and the availability of approximate collocations. The issue of how to model tracer distribution statistics and use these to improve collocation efforts is an ongoing area of research with few results to date. Further quantitative development of this topic would be of great help to instrument validation and data assimilation.

A few things can be said on the basis of the foregoing plots and discussion, however. Large moisture differences are possible over small distances (illustrated in Figures 3.25 and 3.26), so that a reasonable number of instrument collocations is essential to say anything useful about the relative accuracy of any two instruments even when collocation is good. Figures 3.28 and 3.29 can be used as a rough guide to how much of the apparent discrepancy between two instruments can likely be explained by real variability in the moisture field, for a given set of collocation distances. Often, the comparison will be between an

instrument with volumetric sampling (i.e. a satellite) and one with point sampling. In this case a rough idea of the possible natural variations can still be obtained from the given plots, though other statistics (less readily available from aircraft data alone) would be more appropriate. *Gierens et al.* [1997] give further analyses of direct relevance to collocation. Finally, these results also show that some seasons with less variability are considerably more favourable than others for instrument collocation.

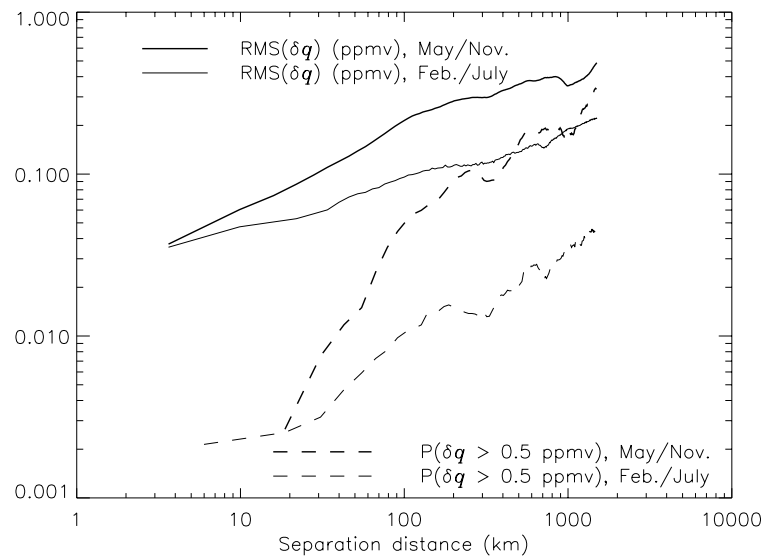


Figure 3.29. Plot of the square root of  $\delta q^2$  as a function of  $\delta x$ , where  $\delta q$  is the difference in mixing ratio at two neighbouring locations in the lower stratosphere separated by distance  $\delta x$  (solid lines); probability that difference will exceed 0.5 ppmv (dashed lines). Thick lines are made using flights during May and November; thin lines, flights during February and July. Data are obtained from Harvard Lyman-A measurements during the STRAT experiment, between latitudes of 25-55°N and potential temperatures of 460-500 K. A small correction has been applied to remove white instrument noise.

## 3.5 Long-term Variations

In this section we shall examine variations in water vapour on time scales longer than the quasi-biennial oscillation. We shall highlight the results from several instruments that have made long-term measurements on a nearly continuous basis and examine their results in some detail. Some of these instruments provide global coverage, and thus show that the evidence for an increase in northern mid-latitude stratospheric water vapour presented in Chapter 2 is not, at least in the 1990s, geographically confined to these regions. Long-term variations in water vapour in the upper troposphere will also be presented. Finally we will discuss some of the mechanisms that might cause the observed changes, and some of the important consequences of significant changes in atmospheric water vapour.

### 3.5.1 Stratospheric Measurements

Chapter 2 presented data from a large number of instruments that have measured water vapour at northern mid-latitudes since the 1950s. In this section we will highlight two specific data sets that have long records of regular measurements of stratospheric water vapour. The oldest data set that has provided quasi-continuous measurements of water vapour has been taken over Boulder, Colorado, since 1981 [Oltmans and Hofmann, 1995]. Since the early 1990s measurements from HALOE and from ground-based microwave instruments have also become available [Russell *et al.*, 1993, Nedoluha *et al.*, 1996]. The HALOE water vapour measurements are of particular value because they provide global coverage and because simultaneous measurements of methane are available.

#### **The water vapour increase over Boulder, Colorado**

Section 1.2.1 describes the operation of the balloon-borne, frost point hygrometer used to obtain vertical profiles of water vapour over Boulder, Colorado (40°N). This nearly 20-year record is unique in describing water vapour in the upper troposphere and lower stratosphere [Oltmans and Hofmann, 1995]. The relatively infrequent soundings (approximately monthly) do not provide adequate information to determine long-term changes in the troposphere because of the high variability of water vapour in this region. However, as has been shown in earlier chapters, the data are of suitable quality to provide information about changes in the lower stratosphere up to normal ceiling altitudes of the balloon of about 28 km.

The time series of water vapour mixing ratio in 2 km layers for three layers in the stratosphere is shown in Figure 3.30. The 16-18 km layer (Figure 3.30a) is the lowest level that is always in the stratosphere. This layer has a significant seasonal cycle and is the lowest altitude at which a linear trend fit to the data shows a significant increase in water vapour concentrations. Numerical increases are seen at altitudes even as low as 10 km but the large variability because of the mixture of tropospheric and stratospheric data makes the trend determination not statistically different from zero. At 20-22 km (Figure 3.30b) the seasonal cycle is small so that variability is a minimum in this region. The increase at 24-26 km (Figure 3.30c) is similar to that at all levels above 16 km (Figure 3.31). The increase of approximately 1%/year is highly significant at all levels above 16 km.

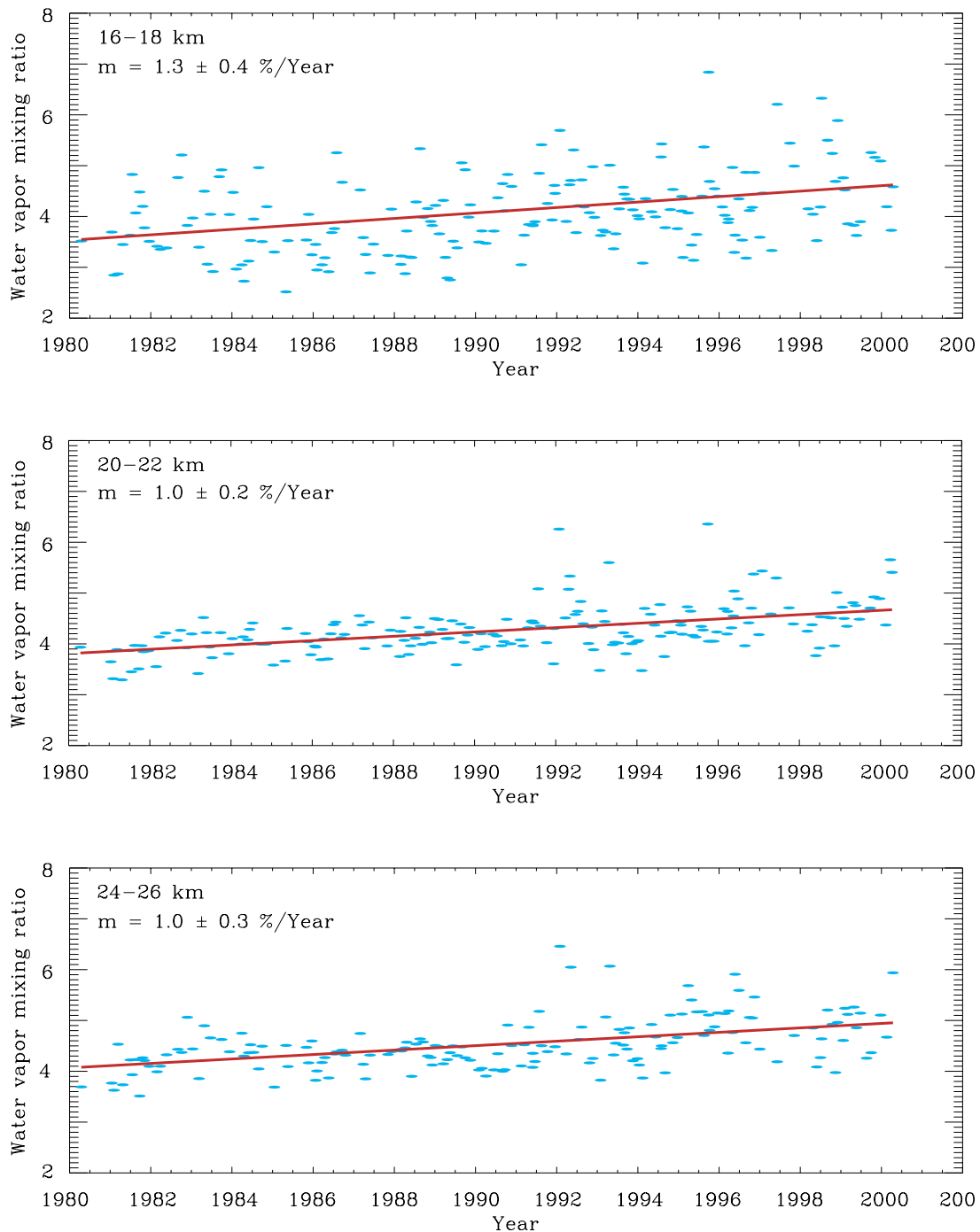


Figure 3.30. Time series of 2 km layer average water vapour mixing ratio in parts per million by volume (ppmv) over Boulder, Colorado, for (Top) 16-18 km which is the lowermost stratosphere over Boulder, (Middle) 20-22 km which is an altitude above the strong seasonal variation, and (Bottom) 24-26 km. The data are obtained from balloon-borne, chilled-mirror hygrometers that are launched approximately monthly. The solid line is a least squares fit to the data and  $m$  is the slope with the 95% confidence interval.

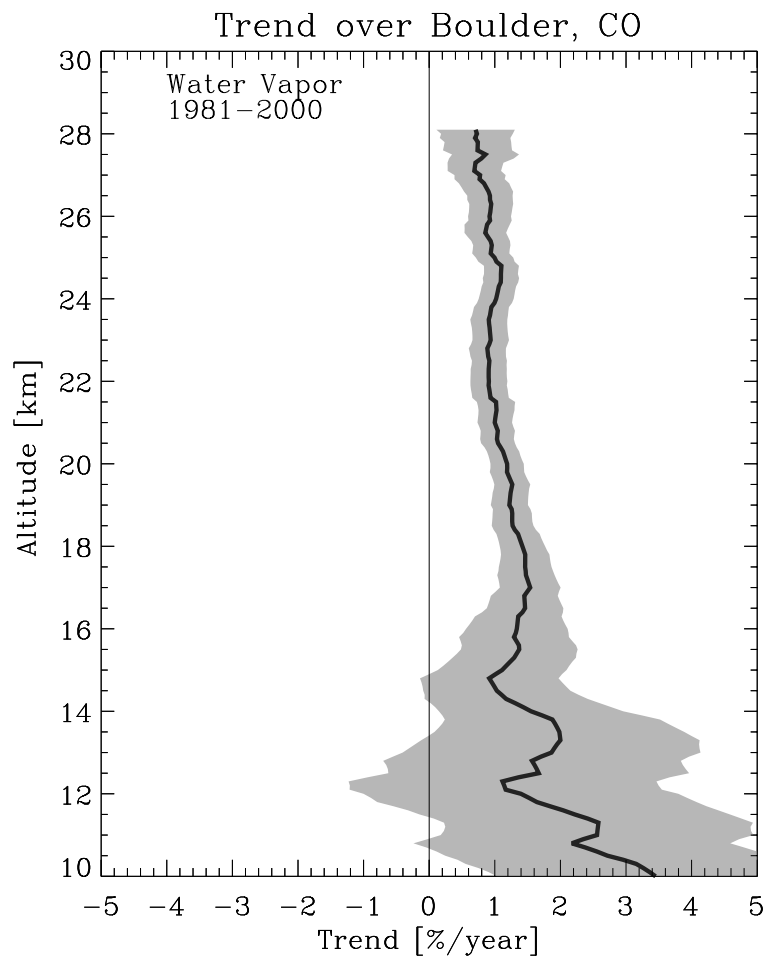


Figure 3.31. The linear trend of water vapour mixing ratio (percent per year) and 95% confidence interval (shaded area) as a function of altitude over Boulder. Significant increases of about 1% per year are found at all altitudes above 16 km.

The computation of seasonal changes does not yield significant linear trends in many instances but may yield some information on the pattern of changes. Figure 3.32 is similar to Figure 3.31, but it shows a linear trend as a function of height over Boulder for two different 4-month periods of the year. Above about 18 km, linear trends for December to March are stronger than linear trends for August to November, exceeding 1%/year. For the remainder of the annual cycle, linear trends still exceed 0.5% year<sup>-1</sup>. Linear trends for the April-July period (not shown) would fall between these lines. The stronger increase during December to March, which is when the water vapour minimum occurs over Boulder (Figure 3.10) has reduced the amplitude of the seasonal variation in the lowermost stratosphere over Boulder. This region of the stratosphere over Boulder has water vapour mixing ratios that can have only the equatorial lower stratosphere as their source. This suggests that an important component of the increase over Boulder is a change in the water vapour content of the source region or a weakening of the transport of air from this region to Boulder.

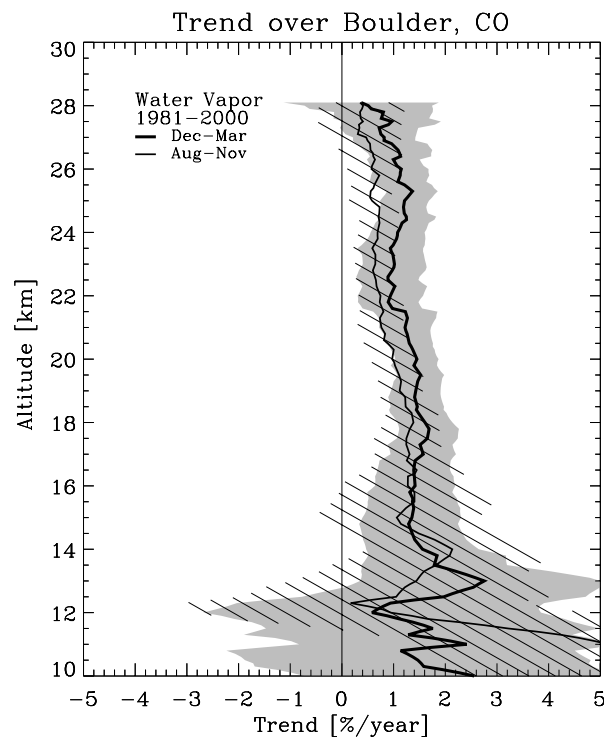


Figure 3.32. Four month averages of the linear trend of water vapour mixing ratio (in percent per year) and 95% confidence interval as a function of altitude over Boulder. Thick solid line and shaded confidence interval for December-March, thin solid line and diagonal hatched confidence interval for August-November. The April-July linear trend would fall between these two lines (not shown).

### Increases in stratospheric water vapour in the 1990s

In addition to the multi-decadal increases in water vapour observed by balloon measurements at 40°N and by aircraft measurements over Southern England (section 2.5.4), a particularly rapid increase was observed globally during the years 1991-1996. This increase was documented with observations from the HALOE instrument, which first made measurements in October 1991 [Nedoluha *et al.*, 1998a; Evans *et al.*, 1998; Randel *et al.*, 1999b]. In Figure 3.33 we show the global increases in water vapour (solid line B) and  $2 \times \text{CH}_4 + \text{H}_2\text{O}$  (solid line A) as measured by HALOE from January 1992 to December 1996. The results in this figure are derived from time series of monthly, zonal, averages of HALOE version 19 H<sub>2</sub>O and  $2 \times \text{CH}_4 + \text{H}_2\text{O}$  profiles starting in January 1992 and extending through December 1996. The HALOE H<sub>2</sub>O data are averaged vertically in 2 km increments over the altitude range 20–70 km and in 10° latitude increments from 70°S to 70°N; i.e. 70°N to 60°N; 60°N to 50°N; and so on. The HALOE CH<sub>4</sub> and H<sub>2</sub>O profiles are first combined on common altitudes to calculate individual  $2 \times \text{CH}_4 + \text{H}_2\text{O}$  profiles and then these profiles are averaged similarly to H<sub>2</sub>O. Each of these monthly zonal averages are then averaged again with area weighting to produce a near-globally averaged time series. To investigate the annual average increase in H<sub>2</sub>O and  $2 \times \text{CH}_4 + \text{H}_2\text{O}$  mixing ratios, multiple linear regression is used to fit the HALOE near-globally averaged time series to a model including a linear trend, an annual, semi-annual, and 27-month harmonic, and an autoregressive noise series of order 1.

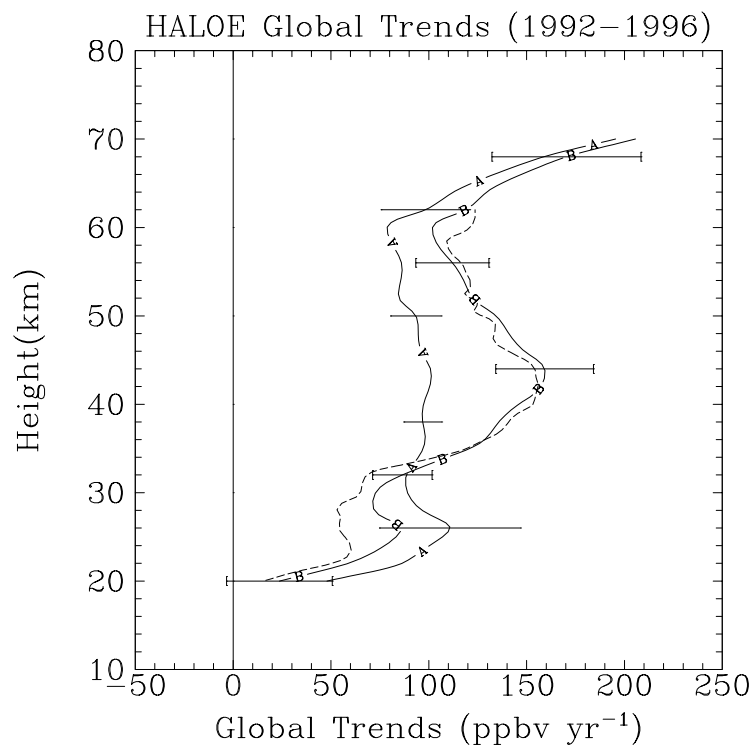


Figure 3.33. Vertical profiles of near global (70°N-S) linear increases in HALOE  $2\times\text{CH}_4+\text{H}_2\text{O}$  (profile A with no ticks on error bars) and  $\text{H}_2\text{O}$  (profile B with ticks on error bars) derived from January 1992 through December 1996. Dashed line is the linear increase in HALOE  $\text{H}_2\text{O}$  (profile B), but with a different fit to the quasi-biennial oscillation (see text). Linear increases are expressed in  $\text{ppbv yr}^{-1}$  and the error bars on each curve represent the  $\pm 2$  standard errors of the derived linear variation.

Since previous analyses of the linear variation in water vapour measured by HALOE during this period have indicated significant differences [WMO, 1999], we have included a second independently calculated linear increase in Figure 3.33. The primary difference between the two calculations is the replacement of the 27-month sinusoid (solid line B in Figure 3.33) with a time series based on zonal wind measurements at Singapore between 70 and 10 hPa (dashed line in Figure 3.33). Other analysis techniques also provide very similar results. We conclude that the details of the analysis technique should not result in significantly different linear variations for this period.

Figure 3.34 shows the change in water vapour detected by HALOE throughout the stratosphere and mesosphere from October 1991 to December 1996. The measurements show that the global increase shown in Figure 3.33 was present at all latitudes. Ground-based microwave instruments at 34.4°N and 45.0°S were therefore able to validate the increase detected by HALOE [Nedoluha *et al.*, 1998a]. A comparison between the increase derived from the ground-based measurements and those from HALOE is given in section 2.5.5. Examination of the HALOE  $2\times\text{CH}_4+\text{H}_2\text{O}$  measurements over a longer period of time (Figure 3.35) shows that the increase observed between 1992 and 1996 has not continued beyond 1996. Linear variations calculated for the period 1996-1999 (not shown) show no significant increases anywhere in the stratosphere. The strong change in low-frequency behaviour demonstrates that the global increases during 1992-1996 are not characteristic of monotonic decadal-scale trends, but rather suggestive of episodic change (possibly linked with the 1991 Mount Pinatubo volcanic eruption). The character of this time series

suggests cautious interpretation of trends derived from short time series with arbitrary beginning and endpoints.

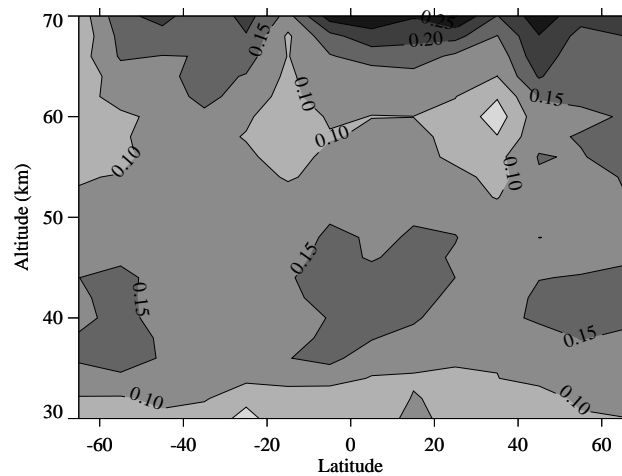


Figure 3.34. The linear increase calculated for the period October 1991 through December 1996 from HALOE  $\text{H}_2\text{O}$  measurements that have been binned in  $10^\circ$  latitude increments. In units of  $\text{ppmv year}^{-1}$ .

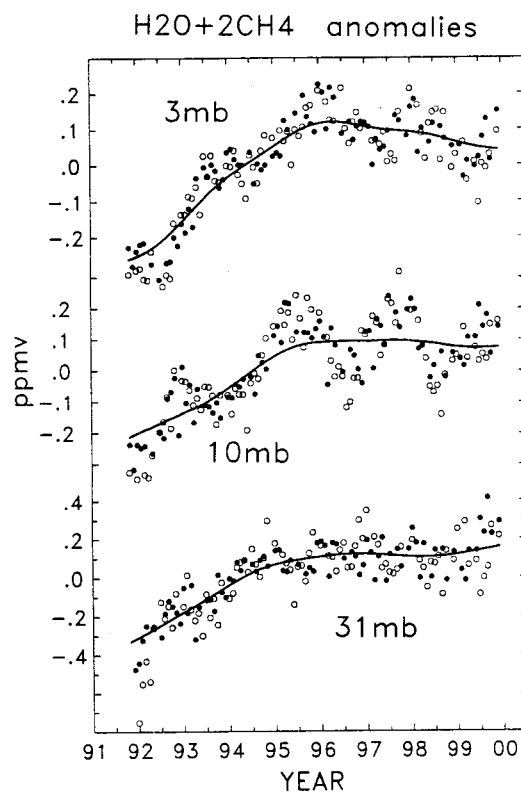


Figure 3.35. Time series of deseasonalised anomalies in  $2\times\text{CH}_4+\text{H}_2\text{O}$  from HALOE measurements. The solid and open circles show anomalies averaged over the southern and northern hemispheres, respectively, and the smooth lines show the global means derived from a running gaussian filter intended to minimise the effects of the quasi-biennial oscillation (clearly seen in the time series at 10 hPa). Taken from *Randel et al.* [2000].

### 3.5.2 Tropospheric Measurements

In this section we shall investigate the long-term variations observed in the troposphere. In considering our ability to detect long-term changes in the troposphere, it is important to note that, with the exception of the MLS measurements, most of the measurements discussed here are taken by instruments that were designed to provide operational weather information. These measurements have therefore not generally put a high priority on the stability required for the study of long-term variations. Changes in instrumentation over time may therefore introduce time-varying biases into these measurements.

#### **MLS observations of the upper troposphere**

Figure 3.36 shows a 7-year time series of daily averaged data for humidity in specific and relative units, percent cloudiness and temperature in low latitudes (between 30°S and 30°N) derived from measurements made by MLS. MLS measures UTH from emission and reports vapour in relative humidity and mixing ratio units. The millimetre signals received by MLS can make observations in cirrus but the received signal will be enhanced by ice emission that is approximately half as strong on a per-mass-density content as vapour. Therefore ice has an impact on the data analysis and needs to be accounted for. Relative humidity values greater than 120% indicate likely presence of cloud and these were counted to derive a percent cloudiness. All measured humidity values exceeding 120% were then adjusted to 100% before analysing for humidity trends. The corresponding specific humidity values are set to ice saturation.

The data at 147 and 215 hPa are considered suitable for an analysis of long-term temporal variations. Daily averages of data taken between 30°S and 30°N were computed. To minimise sampling problems only days having at least 80% of the maximum possible science data are included in the analysis. An analysis of the global data set gives results similar to those found at low latitudes, but the magnitude of the long-term variations is reduced because the higher latitudes are much drier. The daily cloud counts are divided by the total number of observations for that day to give a percent cloudiness. The temperature data are exclusively from daily averaged NCEP reanalyses sampled at the MLS measurements points, and are entirely independent of the MLS measurements themselves. The plots show the daily average (grey dots) and a 12-month smoothed average (thick black line).

The relative humidity and cloudiness fields at both pressure levels show a clear minimum in 1994-1995, while the temperature field shows a maximum at this time. The anti-correlation in the variations of the temperature and relative humidity at 215 hPa produces a water vapour mixing ratio that has a shallow maximum at this level. Qualitatively the curves at 215 hPa seem reasonable. When the atmosphere cools the vapour carrying capacity of the atmosphere declines, hence relative humidity and cloudiness should increase. If cloudiness increases with declining temperature as shown, then more water is partitioned into ice and the vapour mixing ratio declines. At 147 hPa there is also a large decrease in relative humidity from 1991-1995, but this is accompanied by only a small increase in temperature during this period. This results in a clear minimum in water vapour mixing ratio during in 1994-1995. We note that there are several possible mechanisms that could cause variations on multi-year time scales that would not result in a linear trend over this time period, including the Pinatubo eruption that occurred 3 months prior to UARS launch, and ENSO.

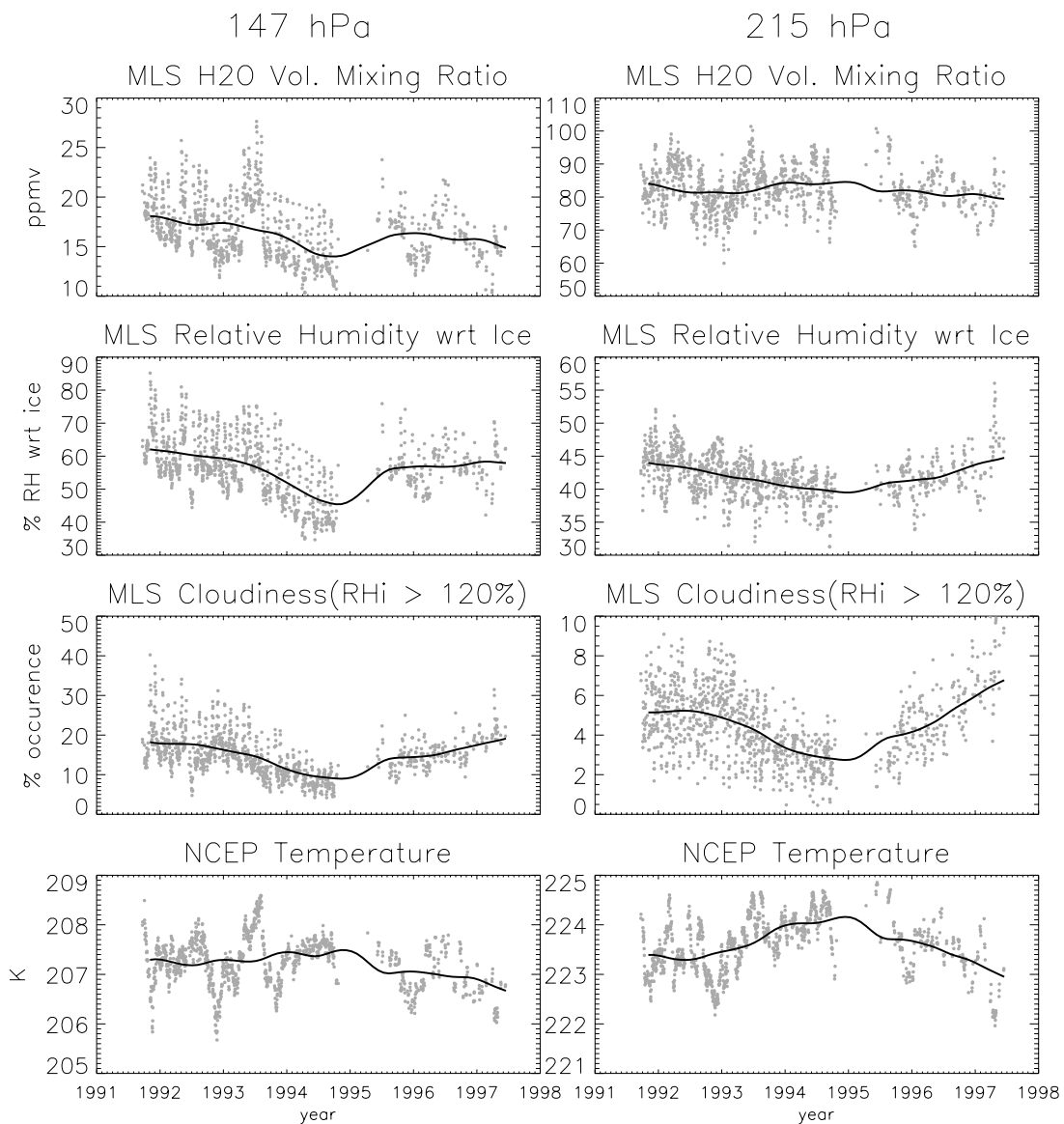


Figure 3.36. Top panel to bottom: MLS volume mixing ratio, MLS relative humidity, MLS % cloudiness and NCEP temperature. Daily averaged data for 7 years between 30S and 30N. The columns represent different altitudes: a 3 km layer around 147 hPa (left column) and 215 hPa (right column). Dots are daily averages, and the black line is a 12-month running mean boxcar filter to remove the annual cycle.

### HIRS observations of the upper troposphere

The HIRS observations provide information on relative humidity over ~200-500 hPa. Because this is a nadir-viewing instrument the vertical resolution is significantly coarser than that of MLS or SAGE. In addition, the level at which the emission is observed can also vary slightly. All of these differences result in decreased variability in the HIRS measurements relative to MLS and SAGE.

For this analysis, data from eight different HIRS instruments were used over a nearly 20-year time period of long-term variations. The intercalibration procedure uses the overlap periods of the different satellites to transfer the calibration from a baseline satellite to all

other satellites [Bates *et al.*, 1996]. The HIRS instruments used to derive UTH are filtered radiometers and slight differences in the filter response functions from one instrument to the next are measured in the laboratory before each instrument launch. Thus, the empirical in-orbit intercalibration can be compared with a physically based intercalibration using the known filter responses, a sample set of atmospheric temperature and moisture profiles, and a forward radiative transfer model [Bates *et al.*, 2000]. In most cases, the agreement between the empirical and forward-modelled intersatellite biases is on the order of only a few tenths of a degree. This excellent agreement lends credibility to the assertion that most of the inter-satellite bias is attributable to known differences in the filter response functions and is removed by empirical inter-satellite calibration.

Although satellite remote sensing has the advantage of complete global coverage from a single instrument, the inversion of the radiometric observations into geophysical variables, such as the specific humidity profile or water vapour mixing ratio, is an ill-conditioned problem that requires the use of additional a priori data. Great care must be exercised to ensure that the use of such a priori data does not lead to systematic biases. The alternative, analysis of the radiances or their close equivalent UTH, reduces the dependence on a priori data, but does not provide information on the water vapour amount independent of temperature.

Assessing long-term variability of UTH for climate change studies is difficult because of the high variability due to the southern oscillation and the competing effects of water vapour and temperature changes on UTH. Figure 3.37 shows the time series for the annual averages of UTH for different regions and the results of a linear fit for each region. The subtropical regions have the lowest relative humidity (28.6% for 10°S-30°S and 33.1% for 10°N-30°N) and the mid-latitudes the highest relative humidity (44.3% for 30°N-60°N and 43.7% for 30°S-60°S). The relative humidity for the deep tropics (10°N-10°S) is 38.9%, and the average for the entire region (60°N-60°S) is 39.7%. None of the calculated linear variations are significant at the 99% level assuming that each year is independent. The linear changes for 60°N-60°S (0.04% year<sup>-1</sup>), 30°S-60°S (-0.1% year<sup>-1</sup>) and 10°N-10°S (0.1% year<sup>-1</sup>) are significant at the 95% level. These values should be viewed with caution because of the short length of the time series. In particular, in the deep tropics significant interannual variability and persistence, hamper the detection of long-term variations. The variability masks longer-term variations, and the persistence reduces the statistical significance of calculated linear changes because temporal autocorrelation reduces the number of independent observations.

The 30°S-30°N UTH variations measured by HIRS are also plotted in Figure 3.37 to provide a comparison with the variations observed by MLS (Figure 3.36). Of particular interest is the minimum in relative humidity that occurs in 1994. This minimum is contemporaneous with the minima observed in the MLS data at 147 hPa and 215 hPa, but is clearly much shallower. The shallower minimum seen in the HIRS data is qualitatively consistent with the shallower minimum seen with decreasing altitude in the MLS data, but care must be taken in comparing the two data sets because of the large differences in vertical resolution and because the HIRS measurements are not always sampling precisely the same pressure levels.

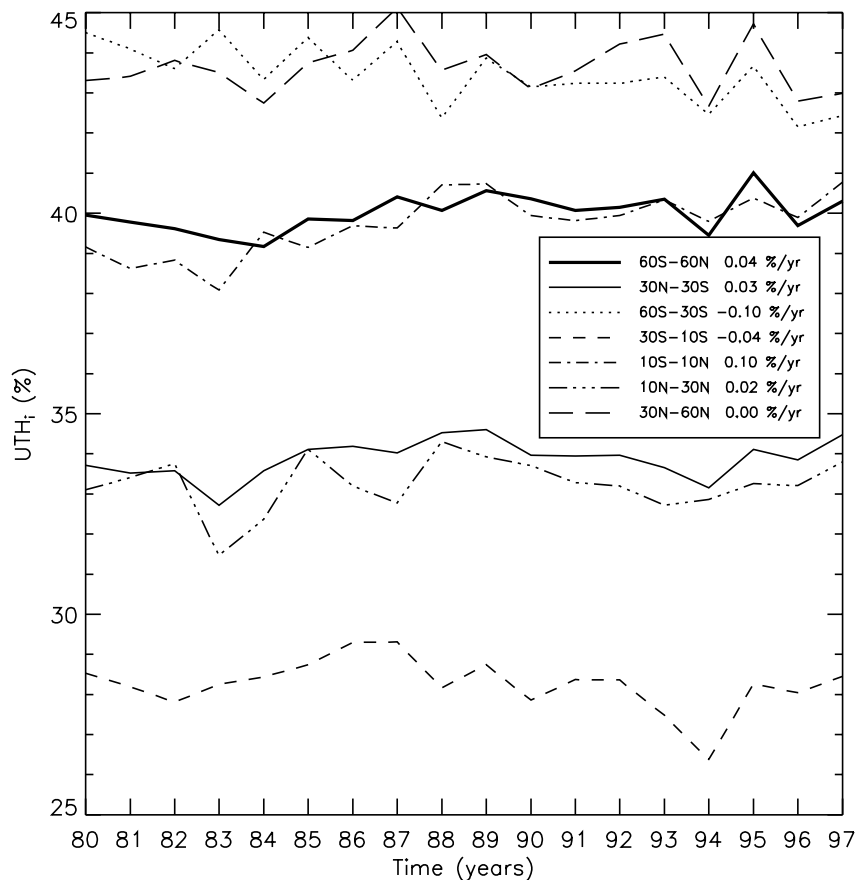


Figure 3.37. Annual mean upper tropospheric humidity over ice from HIRS for various latitude bands and linear fit statistics from 1980 to 1997. 60S-60N (solid line), 60S-30S (dotted line), 30S-10S (dashed line), 10S-10N (dot-dash line), 10N-30N (dash-3dots line) and 30N-60N (long dashed line).

### Lower tropospheric measurements

Because the lower and upper troposphere are dynamically linked, and are not separable in the way the stratosphere and troposphere are, it is appropriate to examine long-term changes in lower tropospheric water vapour. Here we summarise long-term variations determined using *in situ*, meteorological observations and satellite observations, some not presented in the previous Chapters. Multi-decadal changes in water vapour over some Northern Hemisphere land areas have been deduced from surface and radiosonde observations. These observing systems are not research quality systems, nor were they designed for the purpose of monitoring multi-year or multi-decadal changes in water vapour. Changes in instrumentation and observing methods, often not documented, hinder analysis of long-term water vapour changes [Elliott and Gaffen 1991, Elliott 1995, Rind 1998]. Nevertheless, efforts to detect long-term variations of lower-tropospheric water vapour have been made because of the importance of lower-tropospheric moisture in the global energy and water budgets. Lower-tropospheric water vapour increases are expected to accompany increases in global surface temperatures, because of the temperature dependence of both evaporation from the surface and the capacity of the atmosphere to hold moisture. Therefore, monitoring tropospheric water vapour changes is part of the much broader global climate change detection effort.

The most comprehensive analysis of radiosonde-based water vapour variations focused on surface to 500 hPa precipitable water (column-integrated water vapour) at those Northern Hemisphere radiosonde stations with temporally homogeneous records for 1973-95. *Ross and Elliott* [1998] find increases over North America except for Northeast Canada, consistent with an earlier analysis of a shorter record [*Ross and Elliott* 1996]. Over Eurasia, only China and the Pacific islands showed coherent, statistically significant, regional increases. The remainder of Eurasia showed a mix of positive and negative changes with a tendency for decreases in water vapour over Eastern Europe and western Russia.

These results are broadly consistent with the *Gaffen et al.* [1992] analysis of a smaller global station network with shorter records. Other regional analyses are those of *Zhai and Eskridge* [1997], who found increases of about 1-3 % decade<sup>-1</sup> in surface-to-200 hPa precipitable water over China for 1970-90, and *Gutzler* [1992, 1996], who found specific humidity increases of 3 to 9 % decade<sup>-1</sup> at 1000, 700, and 300 hPa from four western tropical Pacific radiosonde stations.

In an attempt to analyse water vapour changes over a longer time period, *Ross and Elliott* [1999] found mostly positive annual variations in lower tropospheric specific humidity and dew point data at 25 Northern Hemisphere stations with temporally homogeneous records for 1961-1995. The increases were smaller than those for the 1973-1995 period and few were statistically significant.

The aforementioned studies are consistent in their findings of tropospheric water vapour increases at individual radiosonde stations over periods during which instrument changes are not believed to contaminate data records. In contrast, *Peixoto and Oort* [1996] reported decreases in zonal-mean relative humidity between 1974 and 1988. The decreases were more marked at 300 hPa, where they are more likely associated with instrument changes than at lower levels, and were more pronounced at higher latitudes than in the tropics.

One of the striking results of global studies of total-column water vapour (most of which resides in the lower troposphere) is the strong correlation with globally averaged tropospheric temperature. This result is found in comparisons between a merged radiosonde, HIRS and Special Sensor Microwave Imager (SSM/I) tropospheric water vapour data set and the global Microwave Sounding Unit (MSU) temperature data [*Randel et al.* 1996] for 1988-1994. A similar result is found in the SSM/I data alone, compared with MSU over oceans [*Wentz and Schabel*, 2000] for 1987-1998. Locally, both radiosonde data and satellite data show correlations between total-column water vapour and sea surface temperature or surface air temperature, although the correlations break down at very high temperatures in tropical locations [*Stephens* 1990; *Gaffen et al.*, 1992; *Bony et al.*, 1995].

An earlier analysis that used HIRS and MSU data to estimate precipitable water for 30°N-30°S, for the period 1979-1995, suggested a 3% average drying of the tropical belt between the two periods 1979-1987 and 1989-1995 [*Schroeder and McGuirk* 1998a, 1998b]. However, the analysis could be influenced by artificial drying signals associated with changes in radiosonde instrument types, because radiosonde data were used in the statistical regression of precipitable water from the HIRS data [*Ross and Gaffen* 1998]. Total-column water vapour data from (SSM/I) for July 1987 through October 1998 show a global (over ocean only) increase of 2.2% per decade [*Wentz and Schabel*, 2000].

In summary, radiosonde humidity measurements show some evidence for increases in lower-tropospheric water vapour over limited regions of the globe during the past one to four decades, at rates of several percent per decade. Satellite data yield better spatial coverage, but analysis of long-term changes has been limited both by shorter data records and

problems merging the data from multiple satellites. A study of SSM/I data from 1987-1998 indicates increases comparable to those found in the radiosonde record.

### 3.5.3 Causes of Long-term Variations

While any long-term changes in upper tropospheric water vapour would be extremely important because of their radiative impact (see 3.5.4), it is not clear whether a significant change has indeed taken place. The long-term increase in water vapour in the stratosphere does, however, seem to be well documented. Several mechanisms that could be important in causing changes in stratospheric water vapour, both on a decadal time-scale and on longer time-scales, will be discussed in this section.

Only since 1991 is a continuous, near-global data set available for water vapour in the stratosphere. Since the quantity  $2\times\text{CH}_4+\text{H}_2\text{O}$  is nearly conserved in the stratosphere (3.2.1) the ability of HALOE to measure both of these molecules is important in distinguishing different mechanisms that can cause an increase in water vapour. Figure 3.33 showed the increase in  $2\times\text{CH}_4+\text{H}_2\text{O}$ . The only other significant reservoir of hydrogen in the stratosphere is  $\text{H}_2$  ( $\sim 0.5$  ppmv), and given the slow reaction rates associated with this species it is unlikely to contribute significantly to the observed changes. Of the three major hydrogen containing species in the stratosphere, only the entry level of  $\text{H}_2\text{O}$  (3.2.1 and 2.5.4) can plausibly vary enough to provide the observed increase in  $2\times\text{CH}_4+\text{H}_2\text{O}$ .

The increase in stratospheric water vapour seems to have stopped about 1996. This suggests that the large increase in the early 1990s might be related to the June 1991 eruption of Mt. Pinatubo [*Nedoluha et al.*, 1998a], but there are certainly other possibilities. The 11-year solar cycle is near solar minimum at the same time that stratospheric water vapour peaks in  $\sim 1995$ -1996. While upper mesospheric water vapour is closely tied to the solar cycle, there is no known mechanism through which the solar cycle should affect stratospheric water vapour. There are many well known decadal scale oscillations which affect tropospheric parameters (e.g., the Arctic Oscillation, the Pacific Decadal Oscillation, etc.), and it is possible that some of the variations in stratospheric water vapour that have been observed are related to these oscillations. As an example, the Pacific Decadal Oscillation may itself help to prolong the period of the southern oscillation [*Barnett et al.*, 1999], and it is possible that the variations in stratospheric water vapour are related to the enhanced El Niño activity of the early 1990s.

While the rapid global increase in water vapour in the early 1990s may be attributable to volcanic events or to decadal scale oscillations, the results shown in Chapter 2 (Figures 2.68 and 2.70) suggest that there is a much longer-term increase in water vapour in the lower stratosphere since the 1950s, across many instruments (Figures 2.70 and 2.72). Average water vapour mixing ratios as low as  $\sim 2$  ppmv were reported for 140-170 hPa in the 1950s over Southern England by the British Meteorological Research Flight frost-point instrument (Figure 2.68e). This is significantly lower than the current entry-level water vapour mixing ratio. Such low mixing ratios are not currently found anywhere in the stratosphere, except in air that has been dehydrated in the extremely cold regions of the Antarctic vortex. Unless these older measurements are seriously in error, we must assume that these extremely low water vapour mixing ratios measured with the British Meteorological Research Flight frost-point instrument in the 1950's and the Naval Research Laboratory frost-point in the middle 1960's (see Figure 2.68d) point toward a very large change in global stratospheric water vapour over the last 50 years.

### Changes in tropical tropopause temperature

Since the amount of water vapour in the stratosphere is very sensitive to the temperature at which air enters the stratosphere, long-term variations in the cold point tropopause temperatures may result in variations in the stratospheric water vapour budget. Even a small change in temperature could have significant effects, since the saturation vapour pressure of water vapour changes by ~15-20% for each 1 K change in temperature near the tropopause (at constant pressure).

The extent to which changes in tropical tropopause temperature affect stratospheric water vapour is dependent upon the saturation level of the air entering the stratosphere, and this is in turn dependent upon where tropospheric air enters the stratosphere. While the tropopause temperature calculated during the recent particularly cold years seems to suggest that the observed water vapour mixing ratios are consistent with tropical air crossing the tropopause uniformly throughout the tropics [Dessler, 1998], such a result is inconsistent with the stratospheric water vapour and tropopause temperature measurements from the 1980s and early 1990s [Vömel and Oltmans, 1999]. Regardless of whether or not air crosses the tropopause uniformly in the tropics, a long-term increase in the tropical tropopause temperature would probably result in an increase in water vapour.

Four studies of temperature trends at 100 hPa are summarised in WMO [1999]. These cover the years 1979-1994 and therefore do not include the particularly cold years of 1996 and 1997. The trends shown range from  $\sim 0.3^\circ\text{K decade}^{-1}$  heating to  $\sim 0.5^\circ\text{K decade}^{-1}$  cooling. Six studies of trends at 50 hPa do, however, all agree that from 1979-1994 there is a cooling trend in the tropical stratosphere, with numbers ranging from  $\sim 0.3$  to  $1.4^\circ\text{K decade}^{-1}$ .

Using analyses of the European Centre for Medium Range Weather Forecasting (ECMWF) from 1979-1998, Simmons *et al.* [1999] calculated a cooling trend of  $\sim 0.6^\circ\text{K/decade}$  in the global means of the 100 hPa temperatures. They also noted that the tropical 100 hPa temperatures for 1996 and 1997 were particularly cold. While there was a change in the ECMWF analysis technique in January 1996, Simmons *et al.* consider it unlikely that this is the cause the very cold temperatures in the final 2 years of the study.

Zhou *et al.* [2000a] examined tropical tropopause temperatures using operational sounding data from 1973-1998. Instead of calculating the global trend at the 100 hPa level as did Simmons *et al.* [1999], they calculated the average temperature at the tropical cold-point tropopause. While the time scale, altitude, and latitude range of their study was different from that of Simmons *et al.*, Zhou *et al.* found a cooling trend of  $0.57^\circ\text{K/decade}$ , in agreement with the trend calculated by Simmons *et al.*

Randel *et al.* [2000] conducted a study of the interannual variability of the tropical tropopause temperature from radiosonde data and from the NCEP reanalyses. They noted that, while the radiosonde data shows a cooling trend of  $0.5 \text{ K/decade}$  from 1979-1997, no such trend is apparent in the NCEP reanalyses. Furthermore, both the radiosonde and NCEP data showed that while the 1996 and 1997 years were relatively cold, they were similar to values in the period 1984-1987 (unlike the ECMWF results of Simmons *et al.* [1999]). They also point out that there is widespread evidence of abrupt temperature changes due to changes in instrumentation and methods, and these changes may significantly impact any long-term analysis, especially for data extending back before the mid-1980s [Gaffen, 1994; Gaffen *et al.*, 2000]. Reanalysis data also contain artificial abrupt changes [Randel *et al.*, 2000], such as discontinuities introduced by satellite data assimilation begun in late 1978.

These problems in both data sources hamper detection of long-term changes in tropopause temperature.

None of these studies of tropopause temperature extend back to the 1950s, but they are roughly coincident with the period of the measurements made in Boulder since 1981. Since observations show that stratospheric water vapour has been increasing over this period, especially during the early 1990s, we cannot make a direct link between long-term changes in tropical tropopause temperatures and increases in stratospheric water vapour. The lack of a relationship, if real, casts doubt on the hypothesis that the temperature of the tropical tropopause (or cold point tropopause) is the major governing process for stratospheric water vapour. As noted in section 3.3.3, other processes such as convection, cloud microphysics or circulation changes may be important.

### Aircraft emissions

Another suggested source of increasing stratospheric water vapour is from aircraft emissions. The contribution of aircraft to atmospheric water vapour is directly from the H in the fuel. For a typical fuel hydrogen mass concentration of  $13.8 \pm 0.02\%$  by mass, aircraft emit with an emission index  $EI(H_2O)$  of  $1.23 \pm 0.02$  kg of water vapour per kg of burned fuel [Schumann, 1996; IPCC, 1999]. Stratospheric emissions from the current world aircraft fleet are concentrated in Northern mid-latitudes as is expected from the air traffic pattern and the latitudinal variation of tropopause height. Depending on the definition of the tropopause, between 18 and 44% of current emissions of water vapour by aircraft are deposited in the stratosphere [Hoinka *et al.*, 1993; Gettelman and Baughcum, 1999]. However, since flight routes are close to the tropopause and reach at most into the lowermost stratosphere, this effluent is rapidly returned to the troposphere with little expected accumulation [Holton *et al.*, 1995].

For the IPCC assessment on the effects of aviation [IPCC, 1999], systematic tracer simulations were carried out with a suite of two-dimensional and three-dimensional atmospheric models to determine upper bounds for the accumulation of aviation aerosol in the atmosphere [Fahey and Schumann, 1999; Danilin *et al.*, 1998]. These tracer simulations strongly suggest that aircraft emissions are not the source of observed decadal  $H_2O$  changes at  $40^\circ N$ . The simulation results can be scaled by  $EI(H_2O)$  to provide an upper bound (neglecting precipitation from the upper troposphere) for the accumulation of water vapour above the tropopause due to aircraft emissions. Taking the model that shows the largest tracer accumulation at  $40^\circ N$ , the computed  $H_2O$  mixing ratio due to subsonic aircraft emissions reaches a maximum of 0.055 ppmv at 10 km altitude decreasing smoothly to 0.012 ppmv at 24 km. These values are small in comparison to current ambient values of 5.9 ppmv at 10 to 12 km and 4.2 ppmv at 22 to 24 km [Oltmans and Hofmann, 1995]. Assuming  $5\% \text{ yr}^{-1}$  growth in fuel consumption, the change in aircraft-produced  $H_2O$  ranges from  $0.0034 \text{ ppmv yr}^{-1}$  at 10 km to  $0.0008 \text{ ppmv yr}^{-1}$  at 24 km. These values represent a change of  $+0.006\% \text{ yr}^{-1}$  at 10 km and  $+0.018\% \text{ yr}^{-1}$  at 24 km. These increases in water vapour are more than a factor of 20 smaller than those found in long-term balloon observations ( $1\text{--}2\%/\text{yr}$ , Figure 3.31 and section 3.5.1).

The current contribution of aircraft emissions to stratospheric water vapour is therefore small, and unlikely to be a significant contributor to the observed increase. Nevertheless, far larger concentration changes and radiative forcing values would result from a large fleet of supersonic aircraft emitting water vapour into the stratosphere [IPCC, 1999].

### Methane oxidation

The only well understood cause of long-term increases in stratospheric water vapour is the increase in anthropogenic methane emission. Increases in methane entering the stratosphere will lead to an increase in stratospheric water as the methane is oxidised. As can be seen in Figure 3.38, the increase in methane during the 1990s is less than  $\sim 0.01$  ppmv  $\text{yr}^{-1}$  [Dlugokencky *et al.*, 1994, Dlugokencky *et al.*, 1998]. This should result in at most a  $\sim 0.02$  ppmv  $\text{yr}^{-1}$  increase in stratospheric water vapour, far below what is observed in the HALOE data. For the period 1951 to 1981 Rinsland *et al.* [1985] derived column methane linear trends of  $1.1 \pm 0.2\%$   $\text{yr}^{-1}$ , while Zander *et al.* [1989] found  $0.7 \pm 0.1\%$   $\text{yr}^{-1}$  for the period 1951 to 1986. A conservative upper limit for the total increase in methane since 1951 is  $\sim 0.5$  ppmv. If all of the methane that entered the stratosphere were oxidised, then this would result in an increase of  $\sim 1.0$  ppmv in water vapour since 1951. In regions, such as the lower stratosphere, where only a fraction of the methane entering the stratosphere has been oxidised this increase will be smaller. In particular, in the northern mid-latitude lower stratosphere regions where long-term measurements are available,  $\sim 1/2$  of the methane will have been oxidised. The long-term increase in water vapour on these measurements due to increased methane entering the stratosphere would therefore be at most  $\sim 0.01$  ppmv/year, which is below the rate of increase estimated from either the British Meteorological Research Flight data or the Boulder balloon data.

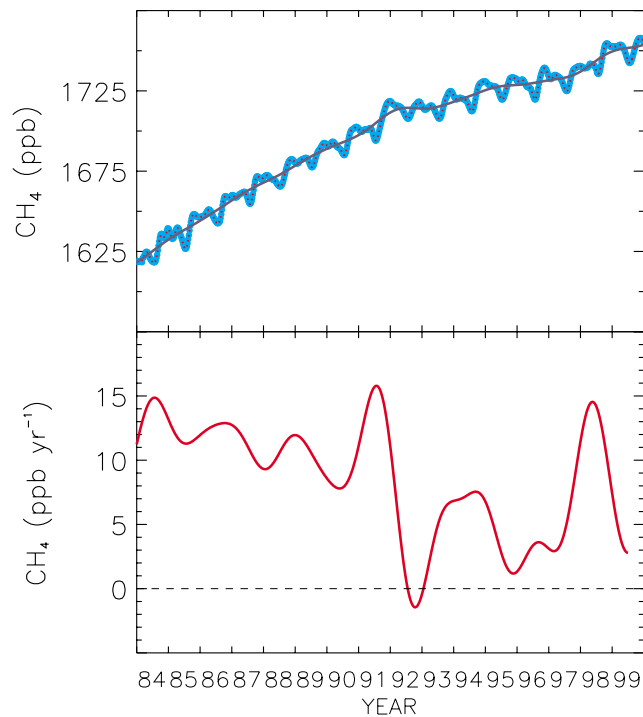


Figure 3.38. Top Panel: Globally averaged CH<sub>4</sub> mole fractions (dots) based on NOAA Climate Monitoring and Diagnostics Laboratory cooperative air sampling network sites [see Dlugokencky *et al.*, 1998]. A smooth curve and deseasonalised trend have been fitted to the global averages. Bottom Panel: The globally averaged instantaneous CH<sub>4</sub> growth rate, calculated as the derivative with respect to time of the trend curve in the top panel.

The rate at which methane is entering the stratosphere is increasing slowly, and thus plays only a minor role during periods of rapid increase such as the early 1990s. Changes in the fraction of methane that is oxidised in a particular region can, however, cause rapid changes

in water vapour at some altitudes. This is best seen in Figure 3.33, where the increase in  $\text{H}_2\text{O}$  alone is, at some altitudes, significantly larger than the increase in  $2\times\text{CH}_4+\text{H}_2\text{O}$ . *Nedoluha et al.* [1998b] found that there were no plausible changes in methane chemistry that could reproduce the observed changes in stratospheric methane in the early 1990s. Using a model, *Nedoluha et al.* [1998b] illustrated that a decrease in the tropical upward transport rate in the stratosphere could, however, cause the observed change in methane. Such a change in transport may, in turn, have been caused by the June 1991 eruption of Mount. Pinatubo.

### Transport

Some of the long-term variations in stratospheric water vapour may be caused by changes in transport. As mentioned in section 3.5.1, the changes in water vapour observed at mid latitude locations (such as Boulder, Colorado or over southern England) may be due to changes in the transport of air from the tropical tropopause. The changes in transport need not be steady or uniform. Water vapour increases could be caused by less transport of dry tropical air, or by more transport of wet tropical air. *Smith et al.*, [2000] found, using a seasonal analysis of the HALOE record, that the increases in HALOE water vapour between 1992 and 1999 may be driven by increases in the upper troposphere in boreal autumn, when water vapour concentrations are high in the tropics. *Smith et al.*, [2000] attribute these changes to changes in the Asian monsoon. Similarly, *Zhou et al.*, [2000a] have proposed that the increases in stratospheric water vapour might be a result of changes in the latitudinal extent of the upwelling in the tropics. If tropical upwelling extended to higher latitudes with warmer tropical tropopause temperatures, water vapour in the stratosphere would increase. Thus changes in the location or rate of transport in either time or space may affect the water vapour distribution in the stratosphere.

### Summary of causes and expected future variations

The mechanisms described here do not, in any combination, offer an explanation of the long-term increase in stratospheric water vapour that is fully consistent with all of the observations. Since water vapour chemistry in the stratosphere is thought to be well understood, and since the increase in stratospheric water vapour is now very well documented, we conclude that there have probably been changes in the process of stratosphere-troposphere exchange especially at the tropical tropopause, a process that is still poorly understood (see section 3.3.3). The increase in water vapour entering the stratosphere is occurring despite an observed decrease in the average tropopause temperature. This suggests that the average tropical tropopause temperature does not fully explain the amount of water vapour entering the stratosphere, and that changes in transport into the stratosphere, or within the stratosphere are important. Such a conclusion is perhaps not surprising, since it has long been argued that the tropical tropopause temperature is too warm to explain the dryness of the stratosphere [*Newell and Gould-Stewart*, 1981].

As noted above, the increase in anthropogenic methane emission from the 1950s through the 1980s is responsible for perhaps one half (0.5 ppmv) of the increase in stratospheric water vapour between the British Meteorological Research Flight measurements and the present suite of measurements described in detail in Chapter 2 (Figure 2.68). IPCC reports from the early 1990s forecast continued increases in anthropogenic methane concentrations in the 21st century, which could result in continued increases in stratospheric water vapour. Figure 3.38 shows, however, that during the 1990s, there were

significant changes in the growth rate of atmospheric methane concentration. If this change in the rate of methane increase is an indication that atmospheric methane is approaching a steady-state value, then any increase in stratospheric water vapour that is caused by increases in methane emission will soon cease. We note, however, that it is possible that recent changes in tropospheric chemistry are causing a decrease in the lifetime of methane, and that this is temporarily masking a continued increase in methane emissions [Dlugokencky, 1998].

Given the uncertainties in the future changes in methane, it is impossible to determine whether water vapour will continue to increase during the 21st century. It is certainly possible that if the positive trend in the amount of methane entering the stratosphere has come to a halt, then the increase in water vapour that has occurred over the last 50 years will also cease. Measurements since the mid-1990s do suggest that there has been no increase in water vapour since that time, and it is therefore possible that water vapour in the stratosphere has now stabilised.

We note, however, that a large fraction of the increase in stratospheric water vapour over the last 50 years cannot be attributed solely to increases in methane concentrations, but is instead probably the result of as yet unidentified changes in the exchange of water vapour from the troposphere. The amount of water vapour in the stratosphere will therefore only approach a steady-state value if the changes resulting from changes in methane concentrations, and the changes resulting from the as yet unidentified exchange mechanism, sum to zero. Since any changes in methane concentration that do occur in the future are likely to cause an increase in water vapour, and since the as yet unidentified mechanism has caused a large increase since the 1950s, it seems likely that some increase in stratospheric water vapour will continue in the 21<sup>st</sup> century. Based on figures such as 3.30 and 3.35, we have more confidence in saying that future increases (or decreases) in the water vapour content of the stratosphere may not be well described by a linear trend.

### 3.5.4 Consequences of long-term variations

#### **Effect of water vapour changes in the stratosphere**

*Forster and Shine* [1999] have shown that a prolonged increase in stratospheric water vapour would cause significant cooling of the stratosphere, and that this could be a significant contribution to the observed cooling of the stratosphere. They found that a fixed 0.7 ppmv increase in stratospheric water vapour mixing ratio would result in a global cooling effect, which is comparable to that caused by stratospheric ozone losses from 1979-1997. The cooling is particularly strong in the Arctic, where they calculate a temperature decrease of 3-7 K in the spring. *Shindell et al.* [1998], in modelling the effect of increasing greenhouse gas concentrations, found that a 5-7 K decrease in springtime Arctic temperatures resulted in ozone column depletions of ~50%. These results were obtained by assuming that chlorine activation takes place whenever temperatures fall below 195 K, an approximate threshold for the formation of polar stratospheric clouds. *Kirk-Davidoff et al.* [1999] combined the *Shindell et al.* [1998] results with the *Forster and Shine* [1999] results and pointed out that these implied that an increase in water vapour could have a significant effect on Arctic ozone depletion. In addition to its indirect effect on stratospheric temperatures, an increase in water vapour would also raise the saturation temperature required for the formation of polar stratospheric clouds. *Kirk-Davidoff et al.* [1999], however, found that the effect of increased saturation temperature on the formation of

polar stratospheric clouds was about an order-of-magnitude smaller than the effect of the reduced Arctic temperature due to increased water vapour.

In addition to its effect on Arctic ozone depletion, a prolonged increase in water vapour at the rate observed in the early 1990s, would also have a significant impact on ozone recovery in the upper stratosphere. (Note, however, that the evidence quoted earlier does not necessarily support the idea of a prolonged, continuous increase in water vapour mixing ratios). Nevertheless, it appears that the changes observed over decadal time-scales are capable of exerting a significant effect on the radiative and chemical balance of the stratosphere. For example, *Jucks and Salawitch [2000]* find that a 2.0 ppmv increase in water vapour in this region would negate the recovery of ozone caused by a 15% reduction of odd chlorine,  $\text{Cl}_y$ . While this portion of the stratosphere does not significantly affect total column ozone amounts, this is the region where ozone recovery could first become apparent: this would be a sensible place to monitor for such evidence.

Furthermore, recent work has shown that stratospheric water vapour changes may contribute significantly to radiative forcing of surface temperature. Using an atmospheric model to simulate the last 20 years, and an increase of stratospheric water vapour consistent with the observations in Figure 3.30, *Shindell [2000]* illustrated that this simulation was consistent with observed changes in stratospheric temperature, and that the radiative forcing from the additional stratospheric water vapour contributed  $0.2 \text{ W m}^{-2}$  (~25 %) to climate forcing over the period. Thus continuing changes in stratospheric water vapour might significantly affect the evolution of climate forcing beyond greenhouse gas emissions. However, *Shindell [2000]* increased stratospheric water vapour concentrations by increasing the tropopause temperatures, which is not in accord with observations.

### **Effect of water vapour changes in the troposphere**

The principal effects of variations of water vapour in the troposphere are expected to be: (i) the effect on the radiative balance, and (ii) the effect on cloudiness (which indirectly influences the radiative field). We will concentrate here on the effect on the radiation balance, since the effects of water vapour on clouds are beyond the scope of this assessment.

Water vapour throughout the troposphere exerts a strong influence over how the Earth loses radiative energy to space to balance the energy received and absorbed from the sun. The water vapour feedback (i.e., the feedback on global temperature caused by changes to water vapour resulting from increases in  $\text{CO}_2$  and other gases) is now almost universally accepted to be positive and strong. *Lindzen [1990]* hypothesised a negative feedback process occurring in the upper troposphere in regions of strong descent near tropical convection, and suggested that general circulation models cannot properly simulate this effect and furthermore that it could overwhelm the direct feedback in the boundary layer. Since that time, however, many observational and modelling studies [e.g., *Rind et al., 1991, Allan et al., 1999*] have indicated that general circulation models broadly (though with poor absolute accuracy at present) capture the essential processes governing upper tropospheric moisture. Hence, a positive water vapour feedback is expected except in quite localised regions of strong descent.

*Doherty and Newell [1984]* and *Clough et al. [1992]* demonstrated that the complex pattern of cooling rates, or energy loss to space, as a function of spectral frequency is considerably influenced by the far infrared pure rotation band of water vapour. *Doherty and Newell [1984]* introduced the use of a height-spectral wave number cross section, on which

cooling rates are displayed. Figure 3.2 is an example of this cross section, taken from the work of *Brindley and Harries* [1998]. This shows, for two model atmospheres, tropical and sub-Arctic, that the pure rotation band of water vapour between about 100 and 500  $\text{cm}^{-1}$  cools strongly to space from the upper and middle troposphere. Cooling rates up to  $10^{-2} \text{ K day}^{-1} (\text{cm}^{-1})^{-1}$  over some 200-300  $\text{cm}^{-1}$  are calculated in the upper troposphere, that is an integrated cooling rate of about  $3 \text{ K day}^{-1}$ . In addition, the continuum bands in the window region between about 800 and 1200  $\text{cm}^{-1}$ , and the  $\nu_2$  vibration-rotation band between about 1200 and 1600  $\text{cm}^{-1}$  also contribute to the cooling, but from deeper layers, near the surface and in the lower and middle troposphere. This is in addition, of course, to the strong cooling concentrated in a relatively narrow band around the 667  $\text{cm}^{-1}$   $\text{CO}_2$  band, extending through the whole depth of the troposphere and stratosphere, together with cooling due to other spectral features, such as the  $\text{CH}_4$  band centred at 1300  $\text{cm}^{-1}$ . With this description in mind, it is possible to discuss how humidity variations might affect the thermal radiation field.

*Sinha and Harries* [1995 and 1997] and *Brindley and Harries* [1998] demonstrated that the peak response to a change in the vertical water vapour mixing ratio distribution occurred at mid-troposphere levels within the atmospheric window for a warm, humid tropical case, and in the far infrared at upper tropospheric levels for a cold, dry sub-Arctic atmosphere. The quantitative effect of changes in upper tropospheric humidity are demonstrated in Figure 3.39 which shows the change in the greenhouse parameter (surface emission minus the outgoing longwave radiation) for +12% increases in water amounts for a tropical model atmosphere in the three layers (a) surface-800 hPa; (b) 800-500 hPa; and (c) 500-0 hPa. Comparing these results with Figure 3.1 shows that this 12% increase in the upper tropospheric humidity leads to a +2% increase, or about  $0.5 \text{ W m}^{-2}$ , in the outgoing longwave radiation to space. The reason for the small % response of outgoing longwave radiation to a given % change in humidity arises because of the competing effects of an increase in humidity (and thus optical depth) which increases the emission, but which also raises the effective height of cooling to space to a higher, colder layer. Being colder, the enhanced emission due to the higher humidity is offset by the effect of the lower temperature [*Harries, 1996, Slingo and Webb, 1997*].

*Slingo and Webb* [1997] analysed the sensitivity of the spectrally resolved outgoing longwave radiation emerging from the top of the atmosphere, as the concentration of atmospheric components and temperature varied as predicted by a climate change calculation using the UK Hadley Centre Climate Model. The modelled stratospheric cooling caused a decrease in outgoing radiation in the  $\text{CO}_2$  and  $\text{O}_3$  bands centred at 667 and 1060  $\text{cm}^{-1}$  and the predicted surface warming causing an increased emission to space in the window region. The response of the outgoing longwave radiation to the modelled increase in humidity was very complex, however, due to the near-cancellation between temperature and humidity effects mentioned above.

Because of this cancellation between increasing humidity and decreasing temperature with height, and because of the current uncertainty over the precise water vapour concentration in the upper troposphere, and even greater uncertainty over trends in upper tropospheric humidity and temperatures, it has not been possible to date to carry out a firm quantitative estimate of the upper tropospheric radiative consequences of long-term changes in upper tropospheric humidity. However, current knowledge indicates that the radiative response to long-term changes in upper tropospheric water vapour will almost certainly be significant.

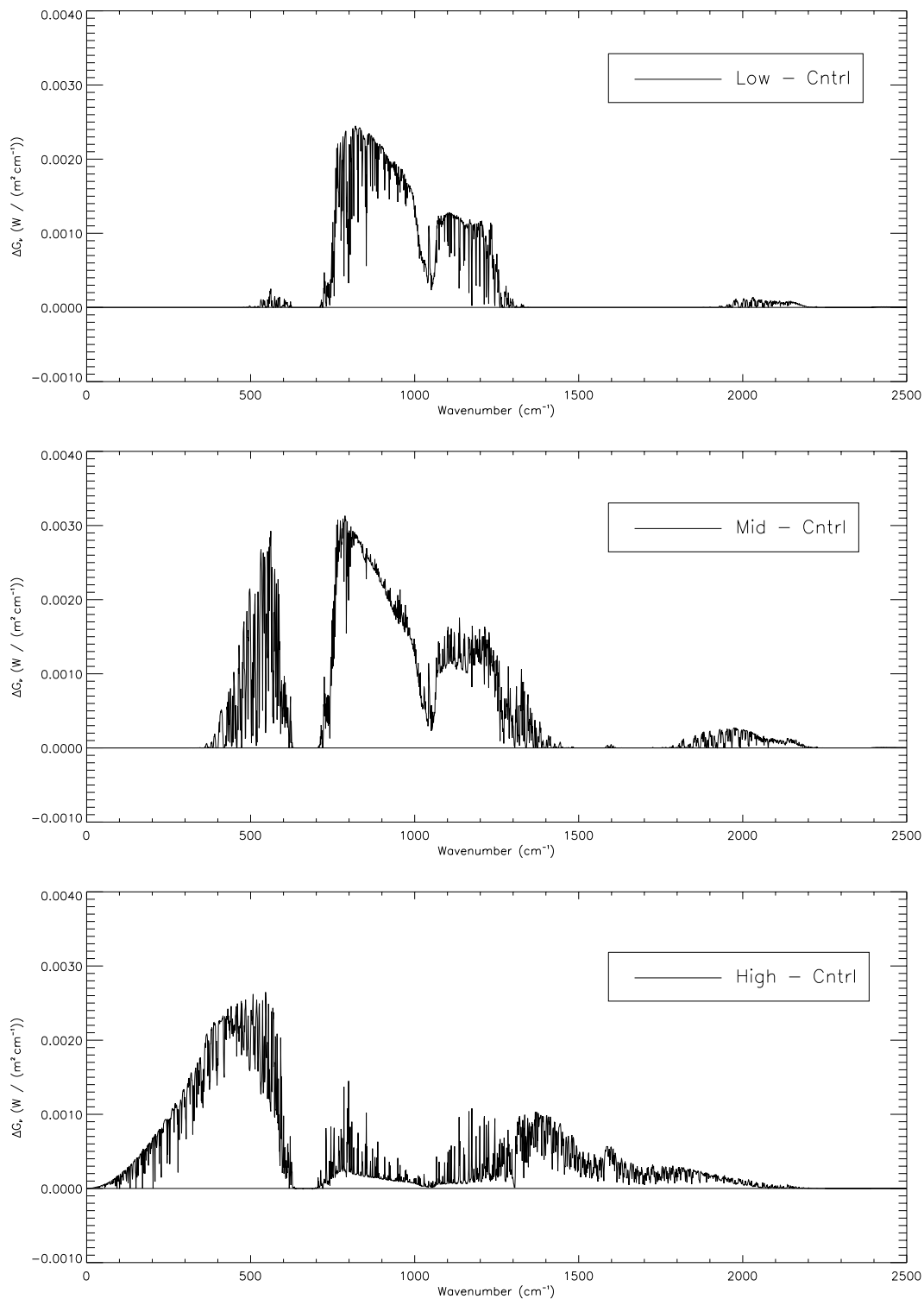


Figure 3.39. Change in greenhouse parameter (surface emission minus outgoing long-wave radiation) for 12% increases in water vapour amounts for a tropical model atmosphere in three layers: Low, surface to 800 hPa (top); Middle, 800–500 hPa (middle) and high, 500–0 hPa (bottom).

### 3.6 Conclusions

Water vapour is unique among atmospheric trace constituents in that conditions for saturation are common in the atmosphere. This property is the most important factor governing the distribution of water vapour in the atmosphere, both in the troposphere, where it varies by as much as four orders of magnitude in a vertical profile, and in the stratosphere, where variations are much smaller but still significant.

The global time-mean distribution and large-scale variations of water vapour are fairly well characterised by satellite data sets, especially HALOE and MLS (in the stratosphere) and MLS and HIRS (in the upper troposphere). *In situ* and ground-based data sets augment satellite information and present a picture consistent with satellite observations. *In situ* and ground-based data sets are also essential for revealing behaviour at smaller spatial scales, for long-term monitoring and for validation of satellite data sets.

In the stratosphere above approximately 100 hPa, the distribution of water vapour can be explained as a balance between dry air entering via the tropical tropopause and a source of water vapour from methane oxidation in the upper stratosphere. The “Brewer-Dobson” circulation then helps determine the distribution, along with wave-induced mixing and (in the lowest few kilometres of the stratosphere) upward extension of tropospheric circulation. Variations in the zonal direction are rapidly mixed so that water vapour is nearly constant following a fluid element. Nearly all air passing from the troposphere to the part of the stratosphere above 100 hPa enters through the tropical tropopause, where the removal of water vapour by low temperatures and a combination of other processes dries the air to around 3.5-4 ppmv in the annual mean. Some of this dry air rises slowly in the tropics, but most spreads poleward, or is mixed with mid-latitude air, especially in the lowest few kilometres of the stratosphere. Consequently, water vapour concentrations increase upward and away from the equator as methane is oxidised. Below approximately 100 hPa, the extratropical lower stratosphere is moistened by leakage from the troposphere, mostly by roughly horizontal transport across the subtropical tropopause. This horizontal transport has a strong seasonal component, being much stronger in the summer hemisphere. There is also a hemispheric asymmetry in the transport, with the South Asian monsoon in boreal summer significantly moistening the Northern Hemisphere, more than similar monsoon circulation in the Southern Hemisphere. Other important seasonal variations in the stratosphere occur in the winter and spring polar vortex, especially the Antarctic, where cold temperatures cause dehydration via the formation of ice clouds (which play a pivotal role in catalytic ozone destruction every spring).

In the tropics and subtropics, upper-tropospheric water vapour is strongly influenced by the three-dimensional time-mean circulation whose meridional projection is the Hadley circulation and whose zonal projection is the Walker circulation. The predominant source for moisture in the tropical and subtropical upper troposphere is convection, so that, on average, moist areas appear in the convective areas over the western Pacific, South America and Africa. Moist areas also appear seasonally in the region of the Asian summer monsoon and along the intertropical and South Pacific convergence zones. The seasonality of surface temperature and of convection, which roughly follow the sun, as well as seasonal variations in monsoon circulation, produce concomitant seasonal changes in water vapour in the troposphere. This relationship between convection and upper tropospheric moisture changes sign near the tropical tropopause, somewhere between 150 hPa and 100 hPa, so that convection dries the tropopause region. Water vapour is also influenced by fluctuations at both shorter and longer time scales, including the quasi-biennial oscillation in

---

the stratosphere, and El Niño and the Southern Oscillation and the Tropical Intraseasonal Oscillation in the troposphere.

In middle to high latitudes in the upper troposphere, water vapour is highly variable and can be supplied by transport from the tropics, by mesoscale convection, or by extratropical cyclones. Dry air can be transported from the subtropics or from the extratropical lower stratosphere. These transport phenomena tend to be episodic rather than steady.

At the tropical tropopause, a complex mix of processes act to remove water vapour from air as it enters the stratosphere. Within the framework of large-scale mean ascent, the dehydration processes probably include smaller-scale ascent (convective and possibly non-convective), radiative and microphysical processes within clouds, and wave-driven fluctuations in temperature. The location, strength, and relative importance of these processes vary seasonally, but the seasonal variation in tropopause-level water vapour is influenced most of all by the seasonal variation in tropical tropopause temperatures. Air rising through the tropopause is marked with seasonally varying mixing ratio, and retains these markings as it spreads rapidly poleward and more slowly upward into the stratosphere.

In the upper troposphere and occasionally near sharp gradients in the stratosphere, filaments of water vapour with scales from tens to thousands of kilometres are prevalent. Sharp transitions between moist and dry air masses are produced naturally in the atmosphere by turbulent processes, and complicate quantitative comparisons between imperfectly collocated observations.

### 3.6.1. Long-Term Variations

Because water vapour is a radiatively active and chemically important gas, its future concentration will have an important influence on future climate. Measurements of water vapour in the lower stratosphere indicate increases over the last 20 years of about 20%. Older measurements imply a 50% increase in water vapour in the lower stratosphere since the 1950s. Unfortunately, projections of future concentrations of water vapour in the UT/LS are hampered by several factors, most notably the lack of definitive understanding of the causes of these long-term changes. Also, as discussed in chapter 2, the instrumental record is not of sufficient quality to combine records across instruments to derive overall long-term changes for water vapour in the lower stratosphere.

In the upper troposphere, long-term relative humidity observations were made as part of routine meteorological soundings, but are of such poor quality as to be unusable for detection of change. Satellite measurements since 1979 show a small but insignificant increase in *relative* humidity. Satellite measurements of *specific* humidity have been made only since late 1991, and show no significant change. Changes of specific humidity can be derived from measurements of relative humidity and of temperature, both of which show small increases since 1979, implying increases of specific humidity, but the combined uncertainty of these two measurements is such that the uncertainty in specific humidity is large and masks any changes of significance to climate. Total column water vapour, which is dominated by the lower troposphere, has increased over much of the Northern Hemisphere in the past 20-30 years.

In the lower stratosphere, satellite measurements of sufficient quality and continuity for detection of long-term variations began much more recently. The longest continuous, reliable data set is at a single location (Boulder, Colorado) and dates back only to 1981. Over this period, variations in stratospheric water vapour are consistently positive with a

value of about  $1\% \text{ year}^{-1}$  at all levels between about 10 and 28 km, and these increases are statistically significant above 16 km. While a linear trend can be fit to this data, increases in the record are neither continuous nor steady. Global variations calculated over a much shorter period using the HALOE data set show an increase of  $2\% \text{ year}^{-1}$  over several years (1993-1996) but also show a change in the sign of the variations around 1996. This underscores the limitations of using data records of this length for studying long-term linear trends.

Our understanding of factors controlling long-term changes in UT/LS water vapour is inadequate to explain the observed variations or to make good projections into the future. In the lower stratosphere, the observed 20-year increase at Boulder (and probably globally) is about twice what would be expected from methane oxidation alone. A simple explanation would be an increase in average saturation mixing ratio at the tropical tropopause; changes in this quantity are difficult to calculate, but appear to be in the opposite direction [e.g., *Simmons et al.*, 1999]. Thus, it is likely that the expected increases in the concentration of atmospheric methane will lead to further increases in stratospheric water vapour, but the inability to explain past changes diminishes our confidence in the projection of future increases in water vapour.

It is fairly clear which processes (transport, convection, and clouds) are involved in determining the distribution of upper tropospheric water vapour, but their influences are very difficult to quantify. Since it is also difficult to predict how these might change in response to natural and human-induced climate change, future changes in the distribution and variability of upper tropospheric water vapour are unknown.

The combination of these uncertainties on the future of the water vapour content of the upper troposphere and lower stratosphere means that using available data we cannot answer fundamental questions about the influence of UT/LS water vapour on future climate.

### 3.6.2. Recommendations

1. Upper tropospheric specific humidity should be monitored with a view to determining long-term variations. It is important to have complementary observations, not relying solely on one instrument or approach.
2. Process studies of upper tropospheric water vapour and convection should be undertaken. These would include joint measurements of water vapour, cloud microphysical properties, and chemical species that can provide a history of the air.
3. More observations of the tropical tropopause region (15-20 km), by both *in situ* and remote sensing methods, are needed in order to improve our understanding of stratosphere-troposphere exchange there.
4. Stratospheric water vapour should be monitored at various latitudes. Maintaining current long-term measurement programs is necessary for any interpretation of long-term change. These measurements would have greater value if methane were simultaneously measured. Monthly balloon measurements like those over Boulder would be extremely useful for validation of satellite instruments in the upper troposphere and lower stratosphere and for measurement of long-term variations. Future satellite instruments should be planned so as to overlap with existing instruments.

- 
5. Further theoretical work is needed to make best use of existing observations. For example, the variations observed in the HALOE data set around 1996 need to be better understood.
  6. All the data used in this Assessment should be kept in a digital archive at the SPARC data centre. The purpose of this archive would not be on-line instant access, but research access to data in the future (e.g., for subsequent assessment activities). Therefore, data sets collected in the future should be added to this archive. Valuable data from the 1940's, 1950's, and 1960's may already be lost, but some could and should be rescued.

---

## References

- Abbas, M. M., *et al.*, Seasonal variations of water vapor in the lower stratosphere inferred from ATMOS/ATLAS-3 measurements of H<sub>2</sub>O and CH<sub>4</sub>, *Geophys. Res. Lett.*, *23*, 2401-2404, 1996a.
- Abbas, M. M., *et al.*, The hydrogen budget of the stratosphere inferred from ATMOS measurements of H<sub>2</sub>O and CH<sub>4</sub>, *Geophys. Res. Lett.*, *23*, 2405-2408, 1996b.
- Abrams, M. C., *et al.*, On the assessment and uncertainty of atmospheric trace gas burden measurements with high resolution infrared solar occultation spectra from space by the ATMOS experiment, *Geophys. Res. Lett.*, *23*, 2337-2340, 1996a.
- Abrams, M. C., M. R. Gunson, L. L. Lowes, C. P. Rinsland, and R. Zander, Pressure sounding of the middle atmosphere from ATMOS solar occultation measurements of CO<sub>2</sub> absorption lines, *Appl. Opt.*, *35*, 2810-2820, 1996b.
- Aellig, C. P., *et al.*, Space-borne water vapor observations in the Arctic stratosphere and mesosphere in the spring of 1992, *Geophys. Res. Lett.*, *23*, 2325-2328, 1996.
- Albritton, D.L., and R.J. Zander, Instrument intercomparisons and assessments, in *Atmospheric Ozone 1985 WMO Report No. 16*, pp. 963-968, World Meteorological Organization, Geneva, 1985.
- Alexander, M.J., and L. Pfister, Gravity wave momentum flux in the lowerstratosphere over convection. *Geophys. Res. Lett.*, *22* (15), 2029-2032, 1995.
- Allan, R.P., K.P. Shine, A. Slingo, and J.A. Pamment, The dependence of clear-sky outgoing long-wave radiation on surface temperature and relative humidity, *Q. J. R. Meteorol. Soc.*, *125*, 2103-2126, 1999.
- Altmann, J., R. Baumgart, and D. C. Weitkamp, Two-mirror multipass absorption cell, *Appl. Opt.*, *20*, 995-999, 1981.
- Andrews, A.E., *et al.* Empirical age spectra for the lower stratosphere from *in situ* observations of CO<sub>2</sub>: implications for stratospheric transport, *J. Geophys. Res.*, *104* (26), 581-595, 1999.
- Angell, J.K., and J. Korshover, Quasi-biennial and long term fluctuations in tropopause pressure and temperature and the relation to stratospheric water vapour, *Mon. Weather Rev.*, *102*, 29-34, 1974.
- Ansmann, A., M. Riebesell, U. Wandinger, C. Weitkamp, E. Voss, W. Lahmann, and W. Michaelis. Combined Raman elastic-backscatter LIDAR for vertical profiling of moisture, aerosol extinction, backscatter and lidar ratio. *Appl. Phys.*, *B55*, 18-28 1992.
- Antikainen, V., and A. Paukkunen, Studies on improving humidity measurements in radiosondes, in *Instruments and observing methods*, pp. 137-141, World Meteorological Organization, Geneva, 1994.
- Appenzeller, C., and H.C. Davies, Structure of stratospheric intrusions into the troposphere, *Nature*, *358*, 570-572, 1992.
- Appenzeller, C., H.C. Davies and W.A. Norton, Fragmentation of stratospheric intrusions, *J. Geophys. Res.*, *101*(D1), 1435-1456, 1996.
- Aref, H., Stirring by chaotic advection, *J. Fluid Mech.*, *143*, 1-21, 1984.
- Atticks, M.G., and G.D. Robinson, Some features of the structure of the tropical tropopause, *Q. J. R. Meteorol. Soc.*, *109* (460), 295-308, 1983.
- Avallone, L.M., and M.J. Prather, Photochemical evolution of ozone in the lower tropical stratosphere, *J. Geophys. Res.*, *101*, 1457-1461, 1996.

- Backus, G. E. and J. F. Gilbert, Uniqueness in the inversion of inaccurate gross Earth data, *Philos. Trans. R. Soc. London, Ser. A*, 266, 123-192, 1970.
- Bacmeister, J.T., S.D. Eckermann, L. Sparling, K.R. Chan, M. Loewenstein, and M.H. Proffitt, Analysis of intermittency in aircraft measurements of velocity, temperature and atmospheric tracers using wavelet transforms, in *Gravity Wave Processes: Their Parameterization in Global Climate Models*, edited by K. Hamilton, *NATO ASI Series, I 50*, 85-102, 1997.
- Balsley, B. B. and D. A. Carter, Mountain waves in the tropical Pacific atmosphere: a comparison of vertical wind fluctuations over Pohnpei and Christmas Island using VHF wind profilers, *J. Atmos. Sci.*, 46(17): 2698-2715, 1989.
- Bannon, J. K., R. Frith, and H. C. Shellard, Humidity of the upper troposphere and lower stratosphere over southern England, *Meteorological Office Geophysical Memoirs, XI*, No. 88, 36pp., U.K. Meteorological Office, London, 1952.
- Barath, F., *et al.*, The Upper Atmosphere Research Satellite Microwave Limb Sounder Instrument, *J. Geophys. Res.*, 98, 10,751-10,762, 1993.
- Barnett, T.P., D.W. Pierce, M. Latif, D. Dommenges, and R. Saravanan, Interdecadal interactions between the tropics and midlatitudes in the Pacific basin, *Geophys. Res. Lett.*, 26, 615-618, 1999.
- Batchelor, G.K., The effect of homogeneous turbulence on material lines and surfaces, *Proc. R. Soc. A*, 213, 349, 1952.
- Bates, J. J., and D. L. Jackson, A comparison of water vapor observations with AMIP I simulations, *Journal of Geophysical Research*, 102, 21,837-21,852, 1997.
- Bates, J. J., X. Wu, and D. L. Jackson, Interannual variability of upper-tropospheric water vapor band brightness temperature, *J. Climate*, 9 (2), 427-438, 1996.
- Bates, J.J., D.L. Jackson, F.M. Breon, and Z.D. Bergen, Variability of Upper Tropospheric Humidity 1979-1998. Submitted to *J. Geophys. Res.*, 2000.
- Bertaux, J.-L., and A. Delannoy, Vertical distribution of H<sub>2</sub>O in the stratosphere as determined by UV fluorescence in situ measurements, *Geophys. Res. Lett.*, 5, 1017-1020, 1978.
- Bertram, A.K., D.D. Patterson, and J.J. Sloan, The mechanisms and temperatures for the freezing of model sulfuric acid aerosols measured by FTIR extinction spectroscopy, *J. Phys. Chem.*, 100, 2376, 1996.
- Betts, A.K., Greenhouse warming and the tropical water budget, *Bull. Amer. Meteorol. Soc.*, 71, 1464-1465, 1990.
- Bevilacqua, R. M., Introduction to the special section: Polar Ozone and Aerosol Measurement (POAM II), *J. Geophys. Res.*, 102, 23,591-23,592, 1997.
- Bevilacqua, R. M. *et al.*, MAS Measurements of the Latitudinal Distribution of Water Vapor and Ozone in the Mesosphere and Lower Thermosphere, *Geophys. Res. Lett.*, 23, 2317-2320, 1996.
- Bevington, P.R., *Data reduction and error analysis for the physical sciences*, 336 pp., McGraw-Hill, New York, 1969.
- Bignell, K., The water vapour infrared continuum, *Q. J. R. Meteorol. Soc.*, 96, 390-403, 1970.
- Bithell, M., L.J. Gray, J.E. Harries, J.M. Russell III, and A.F. Tuck, On the synoptic interpretation of HALOE measurements using PV analysis, *J. Atmos. Sci.*, 51, 2942-2956, 1994.
- Bjerknes, J., Atmospheric teleconnections from the equatorial pacific, *Mon. Weather Rev.*, 97 (3), 163-172, 1969.

- Boering, K.A., *et al.* Measurements of stratospheric carbon dioxide and water vapour at northern midlatitudes: Implications for troposphere-to-stratosphere transport, *Geophys. Res. Lett.*, 22 (20), 2737-2740, 1995.
- Bony, S., J.P. Duvel, and H. Le Treut, Observed dependence of the water vapour and clear-sky greenhouse effect on sea surface temperature: Comparison with climate warming experiments, *Climate Dynamics*, 11, 307-320, 1995.
- Bosenberg, J., A DIAL System for Remote Sensing: Instrumentation and Techniques, *OSA Tech. Digest Series*, 18, 22-25, 1987.
- Bosenberg, J., Ground-based differential absorption LIDAR for water vapor and temperature profiling, *Appl. Opt.*, 37, 3845-3860, 1998.
- Bowman, K.P. Large-scale isentropic mixing properties of the Antarctic polar vortex from analyzed winds, *J. Geophys. Res.*, 98, 23013-23027, 1993.
- Brasseur, G.P., and S. Solomon, *Aeronomy of the Middle Atmosphere*, Second Edition. D. Reidel, Dordrecht, 1984.
- Brewer, A. W., Work carried out on the Fortress Aircraft allotted to H.A.F. for meteorological duties, *MRP #169*, Upper Air Section, Meteorological Research Committee, 14th February, 1944.
- Brewer, A. W, Condensation Trails, *Weather*, 1, 34-40, 1946.
- Brewer, A.W., Evidence for a world circulation provided by the measurements of Helium and Water Vapour distribution in the stratosphere, *Q. J. R. Meteorol. Soc.*, 75, 351-363, 1949.
- Brewer, A. W., B. Cwilong, and G. M. B. Dobson, Measurement of absolute humidity in extremely dry air, *Proc. Phys. Soc.*, 60, 52-70, 1946.
- Briggs, J. and W.T. Roach, Aircraft observations near jet streams, *Q. J. Roy. Met. Soc.* 89, 225-247, 1963
- Brindley, H., An Investigation into the impact of greenhouse gas forcings on the terrestrial radiation field: Sensitivity studies at high spectral resolution, *PhD Thesis*, University of London, London, 1998.
- Brindley, H., and J.E. Harries, The impact of far ir absorption on clear sky greenhouse forcing: Sensitivity studies at high spectral resolution, *J. Quant. Spec. Rad. Trans.*, 60, 151-180, 1998.
- Browell, E. V., T. D. Wilkerson, and T. J. McIlrath, Water Vapor Differential Absorption Lidar Development and Evaluation, *Appl. Opt.*, 18, 3474-3483, 1979.
- Browell, E. V., A. K. Goroch, T. D. Wilkerson, S. Ismail, and R. Markson, Airborne DIAL water Vapor Measurements Over the Gulfstream, Abstracts, 12th Int. Laser Radar Conf., Aix-en-Provence, France, Aug 13-17, 151-155, 1984.
- Browell, E.V., *et al.*, LASE Validation Experiment, in *Advances in Atmospheric Remote Sensing with Lidar*, edited by A. Ansmann, R. Neuber, P. Rairoux, and U. Wandinger, pp. 289-295, Springer-Verlag, Berlin, 1997.
- Brown, L. R., *et al.*, The 1995 Atmospheric Trace Molecule Spectroscopy (ATMOS) line list, *Appl. Opt.*, 35, 2828-2848, 1996.
- Buchart, N. and E. Remsberg, Area of the stratospheric polar vortex as a diagnostic for tracer transport on an isentropic surface, *J. Atmos Sci.*, 43(13): 1319-1339, 1986.
- Buck, A. L., The variable-path Lyman- $\alpha$  hygrometer and its operating characteristics. *Bull. Am. Meteorol. Soc.*, 57, 1113-1118, 1976.
- Burch, D.E, Continuum absorption by atmospheric H<sub>2</sub>O, *Proc. SPIE Atmos. Trans.*, 277, 28-37, 1981.

- Burton, S. P., Thomason, L. W., Sasano, Y., and S. Hayashida, Comparison of aerosol extinction measurements by ILAS and SAGE II. *Geophys. Res. Lett.*, 26, 1719-1722, 1999.
- Busen, R. and A. L. Buck, A high-performance hygrometer for aircraft use: Description, installation and flight data. *J. Atmos. Oceanic Technol.*, 12, 73-84, 1995.
- Butler, J.H., *et al.*, Nitrous Oxide and Halocarbons, in *Climate Monitoring and Diagnostics Laboratory Summary Report*, pp. 91-121, U.S. Dept. of Commerce, Boulder, CO, 1998.
- Cahen, C., G. Megie, and P. Flamant, Lidar monitoring of water vapor cycle in the troposphere, *J. Appl. Meteorol.*, 21, 1506-1515, 1982.
- Chang, A.Y., *et al.*, A comparison of measurements from ATMOS and instruments aboard the ER-2 aircraft: Tracers of atmospheric transport, *Geophys. Res. Lett.*, 23, 2389-2392, 1996.
- Charboureau, J. P., A. Chedin, and N. A. Scott, Remote sensing of the vertical distribution of atmospheric water vapor from TOVS observations: method and validation, *J. Geophys. Res.*, 103, 9743-8752, 1998.
- Chedin, A., N. A. Scott, C. Wahiche, and P. Moliniere, The Improved Initialization Inversion method: a high resolution, physical method for temperature retrievals from satellites of the TIROS-N series, *J. Appl. Meteorol.*, 24, 128-143, 1985.
- Chedin, A., N. A. Scott, C. Claud, B. Bonnet, J. Escobar, S. Dardaillon, F. Cheruy, and N. Husson, Global Scale Observation of the Earth for Climate Studies, *Advances in space research: the official journal of the Committee on Space Research (COSPAR)*, 14 (1), 155-160, 1994.
- Chen, M., R. B. Rood, and W. G. Read, Upper Tropospheric Water Vapor from GEOS Reanalysis and UARS MLS Observations, *J. Geophys. Res.*, 103, 19,587-19,594, 1998.
- Chen M.H., R.B. Rood, and W.G. Read,. Seasonal variations of upper tropospheric water vapour and high clouds observed from satellites, *J. Geophys. Res. Atmos.*, 104 (D6), 6193-6197, 1999.
- Chen, P., Isentropic cross-tropopause mass exchange in the extratropics, *J. Geophys. Res.*, 100 (D8), 16,661-16,673, 1995.
- Chevallier, F., F. Cheruy, N. A. Scott, and A. Chedin, A neural network approach for a fast and accurate computation of longwave radiation budget, *J. Appl. Meteorol.*, 37, 1385-1397, 1998.
- Chiou, E. W., M. P. McCormick, and W. P. Chu, Global water vapor distribution in the stratosphere and upper troposphere derived from 5.5 years of SAGE II observations (1986-1991), *J. Geophys. Res.*, 102, (D15) 19,105-19,118, 1997.
- Chiou, E. W., M. P. McCormick, L. R. McMaster, W. P. Chu, J. C. Larsen, D. Rind, and S. Oltmans, Intercomparison of Stratospheric water vapor observed by satellite experiments: Stratospheric aerosol and gas experiment II versus limb infrared monitor of the stratosphere and atmospheric trace molecule spectroscopy, *J. Geophys. Res.*, 98, 4875-4887, 1993.
- Cho, J., R. E. Newell, and G. W. Sachse, Anomalous scaling of mesoscale tropospheric humidity fluctuations, *Geophys. Res. Lett.*, 27, 377-380, 2000.
- Chu, W. P., M. P. McCormick, J. Lenoble, C. Brogniez, and P. Pruvost, SAGE II inversion algorithm, *J. Geophys. Res.*, 94, 8339-8351, 1989.
- Chu, W. P., E. W. Chiou, J. C. Larsen, L. W. Thomason, D. Rind, J. J. Buglia, S. Oltmans, M. P. McCormick, and L. M. McMaster, Algorithms and sensitivity analyses for stratospheric aerosol and gas experiment II water vapor retrieval. *J. Geophys. Res.*, 98, 4857-4866, 1993.
- Clark, H.L., R.S. Harwood, P.W. Mote, and W.G. Read, Variability of water vapour in the tropical upper troposphere as measured by the Microwave Limb Sounder on UARS, *J. Geophys. Res.*, 103 (31), 695-707, 1998.

- Clough, S.A., M.J. Iacono, and J.L. Moncet, Line-by-line calculations of atmospheric fluxes and cooling rates - application to water-vapor, *J. Geophys. Res.*, *97*, 15,761-15,785, 1992.
- Clough, S.A., *et al.*, Implications for atmospheric state specification from the AERI/LBLRTM quality measurement experiment and the MWR/LBLRTM quality measurement experiment, in *Proceedings of the Sixth Atmospheric Radiation Measurement (ARM) Science Team Meeting*, pp. 45-49, 1996.
- Cluley, A. R., and M. J. Oliver, Aircraft measurements of the humidity in the low stratosphere over Southern England, 1972-1976, *Quart. J. R. Meteorol. Soc.*, *104*, 511-526, 1978.
- Cooney, J., Remote measurement of atmospheric water vapor profiles using Raman component of laser backscatter, *J. Appl. Meteorol.*, *9*, 182-184, 1970.
- Cornejo-Garrido, A.G. and P.H. Stone, On the heat balance of the Walker circulation, *J. Atmos. Sci.*, *34*, 1155-1162, 1977.
- Coudert, L. H., Line frequency and line intensity analyses of water vapor, *Molecular Physics*, *96*, 941-954, 1999.
- Cox, B.D., M. Bithell, and L.J. Grey, A general circulation model study of a tropopause-folding event at middle latitudes, *Q. J. R. Meteorol. Soc.*, *121*, 883-910, 1995.
- Croskey, C.L., *et al.*, The Millimeter-Wave Atmospheric Sounder (MAS): A Shuttle-based Remote Sensing Experiment, *IEEE Trans. on Microwave Theory and Techniques*, *40*, 1090-1100, 1992.
- Daehler, M., *et al.*, Validation of Millimeter-wave Atmospheric Sounder (MAS) Ozone Measurements, *J. Geophys. Res.*, *103*, 19,615-19,639, 1998.
- Danielsen, E.F. A dehydration mechanism for the stratosphere. *Geophys. Res. Lett.*, *9*, 605-608, 1982.
- Danielsen, E F, *In-situ* evidence of rapid, vertical, irreversible transport of lower tropospheric air into the lower tropical stratosphere by convective cloud turrets and by larger-scale upwelling in tropical cyclones, *J Geophys Res.*, *98*, 8665-8681, 1993.
- Danilin, M.Y., D.W. Fahey, U. Schumann, *et al.*, Aviation fuel tracer simulation: Model intercomparison and implications, *Geophys. Res. Lett.*, *25*, 3947-3950, 1998.
- Deepak, A., T. D. Wilkerson, and L. H. Ruhnke, Atmospheric water vapor, *Proc. Intern. Workshop on Atmospheric Water Vapor, Vail, CO, September 11-13, 1979*, Academic Press, 1980.
- Dessler, A.E., A reexamination of the "stratospheric fountain" hypothesis, *Geophys. Res. Lett.*, *25*, 4165-4168, 1998.
- Dessler, A.E., Reply. *Geophys. Res. Lett.*, *26* (17), 2739, 1999.
- Dessler, A.E., E.M. Weinstock, E.J. Hints, J.G. Anderson, C.R. Webster, R.D. May, J.W. Elkins, and G.S. Dutton, An examination of the total hydrogen budget of the lower stratosphere, *Geophys. Res. Lett.*, *21*, 2563-2566, 1994.
- Dessler, A.E., E.J. Hints, E.M. Weinstock, J.G. Anderson, and K.R. Chan, Mechanisms controlling water vapour in the lower stratosphere: A tale of two stratospheres, *J. Geophys. Res.*, *100* (D11), 23,167-23,172, 1995.
- Dessler, A.E., and H. Kim, Determination of the amount of water vapor entering the stratosphere based on Halogen Occultation Experiment (HALOE) data, *J. Geophys. Res.*, *104*, 30605-30607, 1999.
- Dessler, A.E., and S.C. Sherwood, Simulations of tropical upper tropospheric water vapour, *J. Geophys. Res.*, *105*(D15), 20155-20164, 2000.

- Dethof, A., A. O'Neill, J.M. Slingo, and H.G.J. Smit,. A mechanism for moistening the lower stratosphere involving the Asian summer monsoon, *Q. J. R. Meteorol. Soc.*, *125*, 1079-1106, 1999.
- Dlugokencky, E.J., L.P. Steele, P.M. Lang, and K.A. Masarie, The growth rate and distribution of atmospheric methane, *J. Geophys. Res.*, *99*, 17,021-17,043, 1994.
- Dlugokencky, E.J., K.A. Masarie, P.M. Lang, and P.P. Tans, Continuing decline in the growth rate of the atmospheric methane burden, *Nature*, *393*, 447-450, 1998.
- Dobson, G.M.B., The laminated structure of ozone in the atmosphere, *Q. J. R. Meteorol. Soc.*, *99*, 579-607, 1973.
- Dobson, G.M.B, A.W. Brewer, and B. Cwilong. The meteorology of the stratosphere, *Proc. R. Soc. London, Ser. A*, *185*, 144-175, 1946.
- Doherty, G. M. and R. E. Newell, Radiative effects of changing atmospheric water vapour, *Tellus*, *36B*,149-162, 1984 .
- Dunke, K., Untersuchungen der in MOZAIC gemessenen Ozon- und Wasserdampfverteilung im polaren Strahlstrom über dem Nordatlantik, PhD Thesis, Universität Köln, 1998
- Dunkerton, T.J., On the mean meridional mass motions of the stratosphere and mesosphere, *J. Atmos. Sci.*, *35*, 2325-2333, 1978.
- Dunkerton, T.J., Evidence of meridional motion in the summer lower stratosphere adjacent to monsoon regions, *J. Geophys. Res.*, *100*, 16,675-16,688, 1995.
- Ebert, E.E., and G.J. Holland. Observations of record cold cloud-top temperatures in tropical cyclone Hilda-1990, *Mon. Weather Rev.*, *120*, 2240-2251, 1992.
- Ehhalt, D. H., Vertical profiles and transport of HTO in the troposphere, *J. Geophys. Res.*, *76*, 7351-7367, 1971.
- Ehhalt, D. H., Vertical profiles of HTO, HDO and H<sub>2</sub>O in the troposphere, *Tech. Note TN/STR 100*, NCAR, Boulder, 1-131, CO, 1974.
- Ehret, G., C. Kiemle, W. Renger, and G. Simet, Airborne Remote Sensing of tropospheric Water Vapor Using a Near Infrared DIAL System, *Appl. Opt.*, *32*, 4534-4551, 1993.
- Ehret, G., A. Fix, V. Weiß, G. Poberaj, T. Baumert, Diode-laser-seeded optical parametric oscillator for airborne water vapor DIAL application in the upper troposphere and lower stratosphere, *Appl. Phys. B*, *67*, 427-431, 1998.
- Ehret, G., K.P. Hoinka, J. Stein, A. Fix, C. Kiemle, G. Poberaj, Low-stratospheric water vapor measured by an airborne DIAL, *J. Geophys. Res.*, *104*, 31,351-31,359, 1999.
- Eicke, N., *In situ* Messung von Wasserdampf in der unteren Stratosphäre und im Bereich der Tropopause (in German), PhD thesis, Rheinische Friedrich Wilhelms Univ. Bonn, 1999.
- Elliott, W.P., and D.J. Gaffen, On the utility of radiosonde humidity archives for climate studies, *Bull. Amer. Meteorol. Soc.*, *72*, 1507-1520, 1991.
- Elliott, W. P., and D. J. Gaffen, Effects of conversion algorithms on reported upper air dewpoint depression. *Bull. Amer. Meteor. Soc.*, *74*, 1323-1325, 1993.
- Elliott, W.P., On detecting long-term changes in atmospheric moisture, *Climatic Change*, *31*, 349-367, 1995.
- Ellsaesser, H.W., The climatic effect of CO<sub>2</sub>: A different view, *Atmos. Env.* *18*, 431-434, 1984
- Eluskiewicz, J. et al., Residual circulation in the stratosphere and lower mesosphere as diagnosed from microwave limb sounder data, *J. Atmos. Sci.*, *53*(2): 217-240, 1996.
- Engel, A., C. Schiller, U. Schmidt, R. Borchers, H. Ovarlez, and J. Ovarlez, The total hydrogen budget in the Arctic winter stratosphere during the European Arctic Stratospheric Ozone Experiment, *J. Geophys. Res.*, *101*, 14495-14503, 1996.

- Etheridge, D.M., L.P. Steele, R.J. Francey, and R.L. Langenfelds, Atmospheric methane between 1000 A. D. and present: Evidence of antropogenic emissions and climate variability, *J. Geophys. Res.*, *103*, 15979-15993, 1998.
- Evans, S.J., R. Toumi, J.E. Harries, and M.E. Chipperfield, Trends in stratospheric humidity and the sensitivity of ozone to these trends, *J. Geophys. Res.*, *103*, 8715-8725, 1998.
- Fahey, D.W., and U. Schumann, Aviation-produced aerosols and cloudiness, in *Aviation and the Global Atmosphere*, chapter 3, edited by. J.E. Penner, D.H. Lister, D.J. Griggs, D.J. Dokken, and M. McFarland, *A Special Report of IPCC*, pp. 65-120, Cambridge Univ. Press, Cambridge, UK, 1999.
- Farmer, C. B. and O. F. Raper, High resolution infrared spectroscopy from space: A preliminary report on the results of the Atmospheric Trace Molecule Spectroscopy (ATMOS) experiment on Spacelab 3, Spacelab 3 Mission Review, NASA Conf. Proc., CP-2429, May, 1986. (Available from the Natl. Tech. Inf. Serv., Springfield, Va.)
- Farmer, C. B., O. F. Raper, and F. G. O'Callaghan, Final report on the first flight of the ATMOS instrument during the Spacelab 3 mission, April 29 through May 6, 1985, *JPL Publication 87-32*, 1987.
- Ferrare, R.A., S. H. Melfi, D. N. Whiteman, K. D Evans, F. J. Schmidlin and D. O'C. Starr. A comparison of water vapour measurements made by Raman lidar and radiosondes. *J. Atmos. Oc. Tech.*, *12*, 1177-95, 1995.
- Fischer, H., Remote sensing of atmospheric trace gases, *Interdiscip. Sci. Rev.*, *10(3)*, 185-191, 1993.
- Fischer, H., and H. Oelhaf, Remote sensing of vertical profiles of atmospheric trace constituents with MIPAS limb-emission spectrometers, *Appl. Opt.*, *35*, 2787-2796, 1996.
- Fishbein, E. F., *et al.*, Validation of UARS MLS temperature/pressure measurements, *J. Geophys. Res.*, *101*, 9983-10,016, 1996.
- Folkens, I., M. Loewenstein, J. Podolske, S.J. Oltmans, and M. Proffitt, A barrier to vertical mixing at 14 km in the tropics: Evidence from ozonesondes and aircraft measurements, *J. Geophys. Res.*, *104* (D18), 22,095-22,102, 1999.
- Foot, J. F., Aircraft measurements of the humidity in the lower stratosphere from 1977 to 1980 between 45°N and 65°N, *Quart. J. R. Met. Soc.*, *110*, 303-319, 1984.
- Forster, P.M. de F., and K.P. Shine, Stratospheric water vapour changes as a possible contributor to observed stratospheric cooling., *Geophys. Res. Lett.*, *26*, 3309-3312, 1999.
- Frederick, J E and Douglass, A R Atmospheric temperatures near the tropical tropopause:temporal variations, zonal asymmetry and implications for stratospheric water vapor, *Mon. Wea. Rev.* *111*, 1397-1403, 1983.
- Friedl-Vallon, F., G. Maucher, H. Oelhaf, and M. Seefeldner, The new balloon-borne MIPAS-B2 limb emission sounder, in *Proceedings of the 1995 International Geoscience and Remote Sensing Symposium*, IEEE Press, Piscataway, N. J., 242-244, 1995.
- Froidevaux, L., *et al.*, Validation of UARS Microwave Limb Sounder ozone measurements, *J. Geophys. Res.*, *101*, 10,017-10,060, 1996.
- Gaffen, D. J., Historical changes in radiosonde instruments and practices, World Meteorological Organization, Geneva, *Instruments and Observing Methods Report No. 50*, WMO/TD-No. 541, 123, 1993.
- Gaffen, D.J., Temporal inhomogeneities in radiosonde temperature records, *J. Geophys. Res.*, *99*, 3667-3676, 1994.
- Gaffen, D.J., W.P. Elliott, and A. Robock, Relationships between tropospheric water vapour and surface temperature as observed by radiosondes, *Geophys. Res. Lett.*, *19*, 1839-184, 1992.

- Gaffen, D. J. R.D. Rosen and D.A. Salstein, *et al.*, Evaluation of tropospheric water vapor simulations from the Atmospheric Model Intercomparison Project, *J. Clim.*, 10(7): 1648-1661, 1997.
- Gaffen, D. J., M. A. Sargent, R. E. Haberman and J. R. Lazante, Sensitivity of tropospheric and stratospheric temperature trends to radiosonde data quality, *J. Climate* 13:1776-1796, 2000.
- Gage, K.S., and G.C. Reid, Tropical tropopause and the El Nino of 1982-1983, *J. Geophys. Res.*, 91 (D12), 13315-13317, 1986.
- Gage, K.S., J.R. McAfee, D.A. Carter, *et al.*, Long-term mean vertical motion over the tropical pacific: Wind-profiling doppler radar measurements, *Science*, 254, 1771-1773, 1991.
- Gottelman, A., and S.L. Baughcum, Direct deposition of subsonic aircraft emissions into the stratosphere. *J. Geophys. Res.*, 104, 8317-8327, 1999.
- Gottelman, A., A.R. Douglass, and J.R. Holton, Simulations of water vapour in the upper troposphere and lower stratosphere, *J. Geophys. Res.*, 105, 9003-9023, 2000.
- Gierens, K. M., U. Schumann, U., H.G.J. Smit, *et al.*, Determination of humidity and temperature fluctuations based on MOZAIC data and parametrisation of persistent contrail coverage for general circulation models, *Annales Geophysicae.*, 15(8): 1057-1066, 1997.
- Gierens, K., U. Schumann, M. Helten, H. Smit, and A. Marengo, A distribution law for relative humidity in the upper troposphere and lower stratosphere derived from three years of MOZAIC measurements, *Ann. Geophys.*, 7, 1218-1226, 1999.
- Gill, AE., Some simple solutions for heat-induced tropical circulation, *Q. J. R. Meteor. Soc.*, 106, 447-462, 1980.
- Gille, J. C., and J. M. Russell III, The limb infrared monitor of the stratosphere: experiment description, performance, and results, *J. Geophys. Res.*, 89, 5125-5140, 1984.
- Giorgetta, M.A., and L. Bengtsson, Potential role of the quasi-biennial oscillation in the stratosphere-troposphere exchange as found in watervapor in general circulation model experiments, *J. Geophys. Res.*, 104, 6003-6019, 1999.
- Giver, L. P., C. Chackerian, Jr., and P. Varanasi, Water vapor line intensity corrections for HITRAN '96, *J. Quant. Spectrosc. Radiat. Transfer*, 66, 101-105, 2000.
- Glaccum, W., *et al.*, The Polar Ozone and Aerosol Measurement (POAM II) Instrument, The Polar Ozone and Aerosol Measurement (POAM II) Instrument, *J. Geophys. Res.*, 101, 14,479-14,487, 1996.
- Goldmann, A., and R. S. Saunders, Analysis of atmospheric infrared spectra for altitude, distribution of atmospheric trace constituents-I: method of analysis, *J. Q. S. R. T.*, 21, 155-162, 1979
- Goldsmith, J. E. M., F. H. Blair, S. E. Bisson, and D. D. Turner, Turn-key Raman lidar for profiling atmospheric water vapor, clouds, and aerosols, *Appl. Opt.*, 37, 4979-4990, 1998.
- Goody, R., Atmospheric Radiation, Theoretical Basis, Oxford University Press, 1964.
- Goody, R. M., and Y. L. Yung, Atmospheric Radiation--Theoretical Basis, 2<sup>nd</sup> Ed., Oxford Univ. Press, 519, 1989.
- Gordley, L. L., B. T. Marshall, and D. A. Chu, LINEPAK: Algorithms for modeling spectral transmittance and radiance, *J. Quant. Spectrosc. Radiat. Transfer*, 52, 563-580, 1994.
- GossCustard, M., J.J. Remedios, A. Lambert, *et al.*, Measurements of water vapour distributions by the improved stratospheric and mesospheric sounder: Retrieval and validation, *J. Geophys. Res.*, 101, 9907-9928, 1996.
- Graham, N.E., and T.P. Barnett, Sea surface temperature, surface wind divergence, and convection over tropical oceans, *Science*, 238, 657-659, 1987.

- Gray, L.J., A model study of the influence of the quasi-biennial oscillation on trace gas distributions in the middle and upper stratosphere, *J. Geophys. Res.*, *105*, 4539-4551, 2000.
- Gray, L.J., M. Bithell, B.D. Cox, The role of specific-humidity fields in the diagnosis of stratosphere troposphere exchange, *Geophys. Res. Lett.*, *21*, 2103-2106, 1994.
- Gray, L.J., and J.M. Russell, Interannual variability of trace gases in the subtropical winter stratosphere, *J. Atmos. Sci.*, *56*, 977-993, 1999.
- Grossmann, B.E., and E.V. Browell, Spectroscopy of water vapor in the 720-nm wavelength region: Line strengths, self-induced pressure broadenings and shifts, and temperature dependence of line widths and shifts, *J. Mol. Spectrosc.*, *136*, 264-294, 1989a.
- Grossmann, B.E., and E.V. Browell, Water vapor line broadening and shifting by air, nitrogen, oxygen, and argon in the 720-nm wavelength region, *J. Mol. Spectrosc.*, *138*, 562-595, 1989b.
- Gulde, T., Ch. Piesch, C. E. Blom, H. Fischer, F. Fergg and G. Wildgruber, The Airborne MIPAS Infrared Emission Experiment, *Proceedings of the International Airborne Remote Sensing Conference*, Environmental Research Institute of Michigan, Vol. II, p. 301, 1994.
- Gunson, M. R., *et al.*, The Atmospheric Trace Molecule Spectroscopy (ATMOS) experiment: Deployment on the ATLAS Space Shuttle missions, *Geophys. Res. Lett.*, *23*, 2333-2336, 1996.
- Gunson, M. R., C. B. Farmer, R. H. Norton, R. Zander, C. P. Rinsland, J. H. Shaw, and B. C. Gao, Measurements of CH<sub>4</sub>, N<sub>2</sub>O, CO, H<sub>2</sub>O, and O<sub>3</sub> in the middle atmosphere by the Atmospheric Trace Molecule Spectroscopy Experiment on Spacelab 3, *J. Geophys. Res.*, *95*, 13,867-13,882, 1990.
- Gutnik, M., How dry is the sky?, *J. Geophys. Res.* *66*, 2867-2871, 1961
- Gutzler, D., Climatic variability of temperature and humidity over the tropical western Pacific, *Geophys. Res. Lett.*, *19*, 1595-1598, 1992.
- Gutzler, D., Low-frequency ocean-atmosphere variability across the tropical western Pacific, *J. Atmos. Sci.*, *53*, 2773-2785, 1996.
- Haas, M.R., and L. Pfister, A high-altitude site survey for SOFIA, *Pub. Atron. Soc. Pac.*, *110*, 339, 1998.
- Hall, T.M., and R.A. Plumb, Age as a diagnostic of stratospheric transport, *J. Geophys. Res.*, *99*, 1059-1070, 1994.
- Hall, T.M., and D. Waugh, Influence of nonlocal chemistry on tracer distributions: inferring the mean age of air from SF<sub>6</sub>, *J. Geophys. Res.*, *103*, 13327-13336, 1998.
- Hansen, A. R., and G. D. Robinson, Water vapor and methane in the upper stratosphere: an examination of some of the Nimbus 7 measurements, *J. Geophys. Res.*, *94*, 8474-8484, 1989.
- Harries, J.E., The distribution of water vapor in the stratosphere, *Rev. Geophys. Space Phys.*, *14*, 565-575, 1976.
- Harries, J.E., Infrared and submillimetre spectroscopy of the atmosphere, *Infrared and Millimetre Waves*, *6*, 1-64, 1980.
- Harries, J. E., The greenhouse Earth: A view from space, *Q. J. Roy. Meteorol. Soc.*, *122*, 799-818, 1996.
- Harries, J.E., Atmospheric radiation and atmospheric humidity. *Q.J.Roy.Met.Soc.*, *123*, 2173-2186, 1997
- Harries, J.E., *et al.*, Validation of measurements of water vapor from the Halogen Occultation Experiment (HALOE), *J. Geophys. Res.*, *101*, 10205-10216, 1996.

- Harries, J. E., S. Ruth, and J. M. Russell III: On the distribution of mesospheric molecular hydrogen inferred from HALOE measurements of H<sub>2</sub>O and CH<sub>4</sub>, *Geophys. Res. Letts.*, 23, 297-300, 1996b.
- Hartmann, D.L., *Global Physical Climatology*, in *International Geophysics Series*, vol. 56, Academic Press, San Diego, CA, 1994.
- Hartmann, G. K., *et al.*, Measurements of O<sub>3</sub>, H<sub>2</sub>O, and ClO in the middle atmosphere Using the Millimeter-wave Atmospheric Sounder (MAS), *Geophys. Res. Lett.*, 23, 2313-2316, 1996.
- Hartogh, P., G. K. Hartmann and P. Zimmermann, Simultaneous Water Vapor and Ozone Measurements with Millimeterwaves in the Stratosphere and Mesosphere, *International Geoscience and Remote Sensing Symposium 1991, Remote Sensing: Global Monitoring for Earth Management, Vol I*, 227-230, IEEE Catalog Number 91CH2971-0, Espoo, 1991.
- Hartogh, P., G. K. Hartmann, and C. Jarchow, Spurengasmessungen mit Mikrowellen, in *Statusseminar des Ozonforschungsprogramms, Vol. 4*, July 1994, BMFT, pp. 158-164, Wissenschaftszentrum Bonn, Germany, 1994.
- Hartogh, P., and Jarchow. C, Groundbased Detection of Middle Atmospheric Water Vapor, in *Global Process Monitoring and Remote Sensing of the Ocean and Sea Ice*, D.W. Deering and P. Gudmandsen (eds.), *Proc. SPIE*, 2586, 188-195, 1995.
- Haynes, P.H., C.J. Marks, M.E. McIntyre, T.G. Shepherd, and K.P. Shine, On the “downward control” of extratropical diabatic circulations by eddy-induced mean zonal forces, *J. Atmos. Sci.*, 48, 651-679, 1991.
- Haynes, P., and J. Anglade, The vertical-scale cascade in atmospheric tracers due to large-scale differential advection, *J. Atmos. Sci.*, 54, 1121-1136, 1997.
- Helliwell, N. C., Airborne measurements of the latitudinal variation of frost point, temperature and wind, *Publ. by Air Ministry Meteorol. Office, U.K.*, 664, 1-30, 1960.
- Helliwell, N.C., J.K. MacKenzie, and M.J. Kerley, Some further observations from aircraft of frostpoint and tempertaure up to 50,000 ft, *Q. J. R. Meteorol. Soc.*, 83, 257-262, 1957.
- Helten, M., H.G.J. Smit, W. Sträter, D. Kley, P. Nedelec, M. Zöger, and R. Busen, Calibration and performance of automatic compact instrumentation for the measurement of relative humidity from passenger aircraft, *J. Geophys. Res.*, 103, 25643-25652, 1998.
- Helten M., H. G. Smit, D. Kley, J. Ovarlez, H. Schlager, R. Baumann, U. Schumann, P. Nedelec, and A. Marenco, In-flight comparison of MOZAIC and POLINAT water vapor measurements, *J. Geophys. Res.*, 104, 26087-26096, 1999.
- Herman, R.L., D.C. Scott, C.R. Webster, R.D. May, E.J. Moyer, R.J. Salawitch, Y.L. Yung, G.C. Toon, B. Sen, J.J. Margitan, K.H. Rosenlof, H.A. Michelsen, and J.W. Elkins, Tropical entrainment timescales inferred from stratospheric N<sub>2</sub>O and CH<sub>4</sub> observations, *Geophys. Res. Lett.*, 25 (15), 2781-2784, 1998.
- Herriott, D. R., H. Kogelnik, and R. Kompfner, Off-axis paths in spherical mirror resonators, *Appl. Opt.*, 3, 523-526, 1964.
- Hervig, M. E., J. M. Russell III, L. L. Gordley, J. Daniels, S. R. Drayson, and J. H. Park, Aerosol effects and corrections in the Halogen Occultation Experiment, *J. Geophys. Res.*, 100, 1067-1079, 1995.
- Hervig, M. E., J. M. Russell III, L. L. Gordley, S. R. Drayson, K. A. Stone, R. E. Thompson, M. E. Gelman, I. S. McDermid, A. Hauchecorne, P. Keckhut, T. J. McGee, U. N. Singh, and M. R. Gross, Validation of temperature measurements from the Halogen Occultation Experiment, *J. Geophys. Res.*, 101, 10,277-10,285, 1996.
- Hervig, M. E., and M. J. McHugh, Cirrus detection using HALOE measurements, *Geophys. Res. Lett.*, 26, 719-722, 1999.

- Heymsfield, A. J., and L. M. Miloshevich, Relative humidity and temperature influences on cirrus formation and evolution: Observations from wave clouds and FIRE-II. *J. Atmos. Sci.*, 52, 4302-4326, 1995.
- Heymsfield, A.J., L.M. Miloshevich, C. Twohy, G. Sachse, and S. Oltmans, Upper tropospheric relative humidity observations and implications for cirrus ice nucleation, *Geophys. Res. Lett.*, 25, 1343, 1998.
- Higdon, N. S., *et al.*, Airborne differential absorption lidar system for measurements of atmospheric water vapor and aerosols, *Appl. Opt.*, 33, 6422-6438, 1994.
- Highwood, E.J., and B.J. Hoskins, The tropical tropopause, *Q. J. R. Meteorol. Soc.*, 124 (549), 1579-1604, 1998.
- Hints, E.J., E.M. Weinstock, A.E. Dessler, J.G. Anderson, M. Loewenstein, and J.R. Podolske, SPADE H<sub>2</sub>O measurements and the seasonal cycle of stratospheric water vapour, *Geophys. Res. Lett.* 21 (23), 2559-2562, 1994.
- Hints, E. J., E. M. Weinstock, J. G. Anderson, R. D. May and D. F. Hurst, On the accuracy of *in situ* water vapor measurements in the troposphere and lower stratosphere with the Harvard Lyman- $\alpha$  hygrometer, *J. Geophys. Res.*, 104, 8183-8189, 1999.
- Hitchman, M.H., M. McKay, and C. Trepte, A climatology of stratospheric aerosol, *J. Geophys. Res.*, 99, 20,689-20,700, 1994.
- Hoinka, K.P., M.E. Reinhardt, and W. Metz, North Atlantic air traffic within the lower stratosphere: Cruising times and corresponding emissions, *J. Geophys. Res.*, 98, 23113-23131, 1993.
- Holton, J.R., P.H. Harnes, M.E. McIntyre, A.R. Douglass, R.B. Rood, and L. Pfister, Stratosphere-troposphere exchange, *Rev. Geophys.*, 33, 403-439, 1995.
- Hoskins, B.J., Towards a PV- $\theta$  view of the general circulation, *Tellus*, 43 (A-B), 27-35, 1991.
- Houze, R.A., Structure and dynamics of a tropical squall-line system, *Mon. Weather Rev.*, 105, 1540-1567, 1977.
- Houze, R.A., in *Cloud Dynamics*, pp 573, Academic Press, San Diego, 1993.
- Hurst, D.F., G.S. Button, P.A. Romashkin, *et al.*, Closure of the total hydrogen budget of the northern hemisphere extratropical lower stratosphere, *J. Geophys. Res.*, 104 (D7), 8191-8200, 1999.
- IPCC, The IPCC Scientific Assessment. Report prepared by the working group 1. Chapter 3.2.2, 1991
- IPCC, The Supplementary Report to the IPCC Assessment. Report prepared for IPCC by working group 1. Chapter 3.3.2, 1993
- IPCC, The Science of Climate Change. Contribution of working group 1 to the second assessment report of the Intergovernmental Panel on Climate Change. Chapter D 2, 1995
- IPCC, Aviation and the Global Atmosphere, *A Special Report of IPCC* (Intergovernmental Panel on Climate Change), edited by. J.E. Penner, D.H. Lister, D.J. Griggs, D.J. Dokken, and M. McFarland, pp. 373, Cambridge Univ. Press, Cambridge, UK, 1999.
- Iskenderian, H., A 10-year climatology of Northern Hemisphere tropical cloud plumes and their composite flow patterns, *J. Climate*, 8, 1630-1637, 1995.
- Ismail, S. and E. V. Browell, Airborne and Spaceborne Lidar Measurements of Water Vapor Profiles: A Sensitivity Analysis, *Appl. Opt.*, 28, 3603-3615, 1989.
- Jackson, D.R., S.J. Driscoll, E.J. Highwood, *et al.*, Troposphere to stratosphere transport at low latitudes as studied using HALOE observations of water vapour 1992-1997, *Q. J. R. Meteorol. Soc.*, 124, 169-192, 1998.

- Janssen, M. A. (ed.), Atmospheric remote sensing by microwave radiometry, John Wiley & Sons, 1993.
- Jarchow, C., Bestimmung atmosphärischer Wasserdampf- und Ozonprofile mittels bodengebundener Millimeterwellen-Fernerkundung, PhD. thesis, MPAE-W-016-99-06, 1998.
- Jarchow, C. and Hartogh P., Retrieval of data from ground-based microwave sensing of the middle atmosphere: Comparison of two inversion techniques, in Global Process Monitoring and Remote Sensing of the Ocean and Sea Ice, D.W. Deering and P. Gudmandsen (eds.), *Proc. SPIE*, 2586, 196-205, 1995.
- Jarnot, R. F., R. E. Cofield, J. W. Waters, and D. A. Flower, Calibration of the Microwave Limb Sounder on the Upper Atmosphere Research Satellite, *J. Geophys. Res.*, 101, 9957-9982, 1996.
- Jensen, E.J., O.B. Toon, L. Pfister, and H.B. Selkirk, Dehydration of the upper troposphere and lower stratosphere by subvisible cirrus clouds near the tropical tropopause, *Geophys. Res. Lett.*, 23, 825-828, 1996a.
- Jensen, E.J., O.B. Toon, H.B. Selkirk, *et al.*, On the formation and persistence of subvisible cirrus clouds near the tropical tropopause, *J. Geophys. Res.*, 101, 21,361-21,375, 1996b.
- Jensen E.J., O.B. Toon, A. Tabazadeh, *et al.*, Ice nucleation processes in upper tropospheric wave-clouds observed during SUCCESS, *Geophys. Res. Lett.*, 25, 1363-1366, 1998.
- Jensen E.J., W.G. Read, J. Mergenthaler, *et al.*, High humidities and subvisible cirrus near the tropical tropopause, *Geophys. Res. Lett.*, 26, 2347-2350, 1999.
- Johnson, R.H., W.A. Gallus Jr., and M.D. Vescio, Near-tropopause vertical motion within the trailing stratiform region of a midlatitude squall line, *J. Atmos. Sci.*, 47, 2200-2210, 1990.
- Johnson, D. G., K. W. Jucks, W. A. Traub, and K. V. Chance, Smithsonian stratospheric far-infrared spectrometer and data reduction system, *J. Geophys. Res.*, 100, 3091-3106, 1995.
- Johnson, D. G., J. Orphal, G. C. Toon, K. V. Chance, W. A. Traub, K. W. Jucks, G. Guelachvili, and M. Morillon-Chapey, Measurement of chlorine nitrate using the  $\nu_4$  and  $\nu_5$  bands, *Geophys. Res. Lett.*, 23, 1745-1748, 1996.
- Johnston, H.S., and S. Solomon, Thunderstorms as a possible micrometeorological sink for stratospheric water, *J. Geophys. Res.*, 84, 3155-3158, 1979.
- Jones, D.B.A., H.R. Schneider, and M.B. McElroy. Effects of the quasi-biennial oscillation on the zonally averaged transport of tracers, *J. Geophys. Res.*, 103 (D10), 11,235-11,249, 1998.
- Jones, R. L., J. A. Pyle, J. E. Harries, A. M. Zavody, J. M. Russell III, and J. C. Gille, The water vapor budget of the stratosphere studied using LIMS and SAMS satellite data, *Q. J. R. Meteorol. Soc.*, 112, 1127-1143, 1986.
- Jucks, K. W., D. G. Johnson, K. V. Chance, W. A. Traub, J. J. Margitan, G. B. Osterman, R. J. Salawitch, and Y. Sasano, Observations of OH, HO<sub>2</sub>, H<sub>2</sub>O, and O<sub>3</sub> in the upper stratosphere: Implications for HO<sub>x</sub> photochemistry, *Geophys. Res. Lett.* 25, 3935-3938, 1998.
- Jucks, K.W., and R.J. Salawitch, Future changes in upper stratospheric ozone, 2000: Chapman Monograph on Atmospheric Science Across the Stratopause, *Amer. Geophys. Union*, in press, 2000.
- Kämpfer, N., Microwave remote sensing of the atmosphere in Switzerland, *Opt. Eng.*, 34(8), 2413-2424, 1995.
- Kanzawa, H., Y. Kondo, C. Camy-Peyret, and Y. Sasano, Balloon campaigns at Kiruna-Esrange planned in ILAS Correlative Measurements Program. Proc. 12th ESA Symp. European Rocket and Balloon Programmes and Related Research (Lillehammer, Norway, 29 May - 1 June 1995), ESA SP-370 (September 1995), 345-349, 1995.

- Kanzawa, H., C. Camy-Peyret, Y. Kondo, and N. Papineau, Implementation and first scientific results of the ILAS validation balloon campaign at Kiruna-Esrange in February - March 1997. Proc. 13th ESA Symp. European Rocket and Balloon Programmes and Related Research (Oland, Sweden, 26-29 May 1997), ESA SP-397 (September 1997), 211-215, 1997.
- Kanzawa, H., Ed.: ILAS Correlative Measurements Plan. National Institute for Environmental Studies, F-105-97-NIES, 178pp., 1997.
- Kaye, J. A., and T. L. Miller, The ATLAS series of shuttle missions, *Geophys. Res. Lett.*, **23**, 2285-2288, 1996.
- Kelly, K.K., A.F. Tuck, D.M. Murphy, *et al.*, Dehydration in the lower Antarctic stratosphere during late winter and early spring 1987, *J. Geophys. Res.*, **94** (D9), 11317-11357, 1989.
- Kelly, K.K., A.F. Tuck, L.E. Heidt, *et al.*, A comparison of ER-2 measurements of stratospheric water vapour between the 1987 antarctic and 1989 arctic airborne missions, *Geophys. Res. Lett.*, **17** (4), 465-468, 1990.
- Kelly, K.K., A.F. Tuck, and T. Davies, Wintertime asymmetry of upper tropospheric water between the Northern and Southern Hemispheres, *Nature*, **353**, 244, 1991.
- Kelly, K.K., M.H. Proffitt, K.R. Chan, *et al.*, Water vapour and cloud measurements over Darwin during the STEP 1987 Tropical mission, *J. Geophys. Res.* **98**, 8713-8723, 1993.
- Kennaugh R., S.L. Ruth, and L.J. Gray, Modeling quasi-biennial variability in the semi-annual double peak, *J. Geophys. Res.*, **102**, 16,169-16,187, 1997.
- Kerley, M.J., High-altitude observations between the United Kingdom and Nairobi, *Meteorol. Mag.*, **90**, 3-18, 1961.
- Kerridge, B. J., and E. E. Remsberg, Evidence from the limb infrared monitor of the stratosphere for nonlocal thermodynamic equilibrium in the nu<sub>2</sub> mode of mesospheric water vapour and the nu<sub>3</sub> mode of stratospheric nitrogen dioxide, *J. Geophys. Res.*, **94**, 16,323-16,342, 1989.
- Khaplanov, M., J. Gumbel, N. Wilhelm, and G. Witt, Hygrosonde - A direct measurement of water vapor in the stratosphere and mesosphere, *Geophys. Res. Lett.*, **23**, 1645-1648, 1996.
- Khattatov V., V. Yushkov, M. Khaplanov, I. Zaitcev, J. Rosen, N. Kjome, Some results of water vapor, ozone and aerosol balloon borne measurements during EASOE, *Geophys. Res. Lett.*, **21**, 1299-1302, 1994.
- Kiladis, G.N., Observations of Rossby waves linked to convection over the eastern tropical Pacific, *J. Atmos. Sci.*, **55**, 321-339, 1998.
- Kinnersley, J.S., Seasonal asymmetry of the low- and middle latitude QBO circulation anomaly, *J. Atmos. Sci.*, **56**(9), 1140-1153, 1999.
- Kirk-Davidoff, D.B., E.J. Hints, J.G. Anderson, and D.W. Keith, The effect of climate change on ozone depletion through changes in stratospheric water vapour, *Nature*, **402**, 399-401, 1999.
- Kley, D., Ly  $\alpha$  absorption cross section of H<sub>2</sub>O and O<sub>2</sub>, *J. Atmos. Chem.*, **2**, 203-221, 1984.
- Kley, D., and E. J. Stone, Measurement of water vapor in the stratosphere by photodissociation with Ly- $\alpha$  (1216 Å) light, *Rev. Sci. Instrum.*, **49**, 691-697, 1978.
- Kley, D., E. J. Stone, W. R. Henderson, J. W. Drummond, W. J. Harrop, A. L. Schmeltekopf, T. L. Thompson, and R. H. Winkler, *In situ* measurements of the mixing ratio of water vapor in the stratosphere, *J. Atmos. Sci.*, **36**, 2513-2524, 1979.
- Kley, D., A.L. Schmeltekopf, K. Kelly, *et al.*, Transport of water through the tropical tropopause, *Geophys. Res. Lett.*, **9** (6), 617-20, 1982.

- Kley, D., *et al.*, The U-2 Lyman- $\alpha$  hygrometer: Results from the 1980 Panama experiment in the 1980 Stratospheric-Tropospheric Exchange Experiment, A. P. Margozzi (ed.), NASA Techn. Memo., *NASA TM-842297*, 85-125, 1983.
- Kley, D., H. G. J. Smit, H. Vömel, H. Grassl, V. Ramanathan, P. J. Crutzen, S. Williams, J. Meywerk, S. J. Oltmans, Tropospheric water-vapour and ozone cross-sections in a zonal plane over the central equatorial Pacific Ocean, *Q. J. R. Meteorol. Soc.*, *123*, 2009-2040, 1997.
- Koike, M., *et al.*, A comparison of Arctic HNO<sub>3</sub> profiles measured by the Improved Limb Atmospheric Spectrometer and balloon-borne sensors, *J. Geophys. Res.*, *105*, 6761-6771, 2000.
- Koop, T., H.P. Ng, L.T. Molina, and M.J. Molina, A new optical technique to study aerosol phase transitions: The nucleation of ice from H<sub>2</sub>SO<sub>4</sub> aerosols, *J. Phys. Chem.*, *102*, 8924, 1998.
- Lahoz, W. A., *et al.*, Validation of UARS Microwave Limb Sounder 183 GHz H<sub>2</sub>O measurements, *J. Geophys. Res.*, *101*, 10,129-10,149, 1996.
- Langford, A. O., and S.J. Reid, Dissipation and mixing of a small-scale stratospheric intrusion in the upper troposphere, *J. Geophys. Res.*, *103*, 31,265-31,276, 1998.
- Larsen, J. C., Inversion and analysis of remotely sensed atmospheric water vapor measurements at 940 nm, Ph.D. thesis, Old Dominion University, 1998.
- Lee, K.-M., J. M. McInerney, Y. Sasano, J. H. Park, W. Choi, and J. M. Russell III, Intercomparison of ILAS and HALOE ozone at high latitudes, *Geophys. Res. Lett.*, *26*, 835-838, 1999.
- LeTexier, H., S. Solomon, and R.R. Garcia, The role of molecular hydrogen and methane oxidation in the water vapour budget of the stratosphere, *Q. J. R. Meteorol. Soc.*, *114*, 281-295, 1988.
- Liebe, H. J., G. A. Hufford, and M. G. Cotton, Atmospheric propagation effects through natural and man-made obscurants, *AGARD conference proceedings 542*, 1993.
- Lin, X., and R.H. Johnson, Kinematic and thermodynamic characteristics of the flow over the western Pacific warm pool during TOGA COARE, *J. Atmos. Sci.*, *53*, 695-715, 1996.
- Lindzen, R.S., Some coolness concerning global warming, *Bull. Am. Meteorol. Soc.*, *71*, 288-289, 1990.
- Lindzen, R. S. and S. Nigam, On the role of sea surface temperature gradients in forcing low-level winds and convergence in the Tropics, *J. Atmos. Sci.*, *44*(17): 2418-2436, 1987.
- List, R.J., *Smithsonian Meteorological Tables*, 527 pp., Smithsonian Institution Press, Washington, D.C., 1949.
- Lohmann, U., J. Feichter, C.C. Chuang, *et al.*, Prediction of the number of cloud droplets in the ECHAM GCM, *J. Geophys. Res.*, *104*, 9169-9198, 1999.
- Lucke, R. L., *et al.*, The Polar Ozone and Aerosol Measurement (POAM III) instrument and early validation results, *J. Geophys. Res.*, *104*, 18,785-18,799, 1999.
- Ludlam, F.H., *Clouds and Storms : The behavior and effect of water in the atmosphere*, Penn State University Press, 1980.
- Lueb, R. A., D. H. Ehhalt, and L. E. Heidt, Balloon-borne low temperature air sampler, *Rev. Sci. Inst.*, *46*, 702-705, 1975.
- Lumpe, J. D., *et al.*, POAM II Retrieval Algorithm and Error Analysis, *J. Geophys. Res.*, *102*, 23,593-23,614, 1997.
- Madden, R.A., and P.R. Julian, Detection of a 40-50 day oscillation in the zonal wind in the tropical Pacific, *J. Atmos. Sci.*, *28*, 702-708, 1971.

- 
- Manabe, S. and R.T. Wetherald, Thermal equilibrium of the atmosphere with a given distribution of relative humidity, *J. Atmos. Sci.*, 24, 241-259, 1967
- Manney, G. L., H. A. Michelsen, M. L. Santee, M. R. Gunson, F. W. Irion, A. E. Roche, and N. J. Livesey, Polar vortex dynamics during spring and fall diagnosed using trace gas observations from the Atmospheric Trace Molecule Spectroscopy instrument, *J. Geophys. Res.*, 104, 18,841-18,866, 1999.
- Manney, G.L., R.W. Zurek, A. O'Neill, and R. Swinbank, On the motion of air through the stratospheric polar vortex, *J. Atmos. Sci.*, 51, 2973-2994, 1994.
- Mapes, B.E., and P. Zuidema, Radiative-dynamical consequences of dry tongues in the tropical troposphere, *J. Atmos. Sci.*, 53, 620-638, 1996.
- Marengo, A., *et al.*, Measurement of ozone and water vapor by AIRBUS in-service aircraft: The MOZAIC airborne program, An overview, *J. Geophys. Res.*, 103, 25631-25642, 1998.
- Marshall, B. T., L. L. Gordley, and D. A. Chu, BANDPAK: Algorithms for modeling broadband transmission and radiance, *J. Quant. Spectrosc. Radiat. Transfer*, 52, 581-599, 1994.
- Marti, J., and K. Mauersberger, A survey and new measurements of ice vapor pressure at temperatures between 170 and 250 K, *Geophys. Res. Lett.*, 20, 363-366, 1993.
- Mastenbrook, H. J., The vertical distribution of water vapor over Hyderabad, India, and comparison with mid-latitude distribution, *U.S. Naval Research Lab. Rep. 5817*, Washington DC, 13 Aug 1962.
- Mastenbrook, H. J., vertical distribution of water vapor over Kwajalein Atoll, Marshall Islands, *U.S. Naval Research Lab. Rep. 6367*, Washington DC, 30 Dec 1965.
- Mastenbrook, H. J., Water vapor observations at low, middle and high latitudes during 1964 and 1965, *U.S. Naval Research Lab. Rep. 6447*, Washington DC, 13 Sept 1966.
- Mastenbrook, H.J. Water vapour distribution in the stratosphere and high troposphere, *J. Atmos. Sci.*, 25, 299-311, 1968.
- Mastenbrook, H.J., The variability of water vapor in the stratosphere, *J. Atmos. Sci.*, 28, 1495-1501, 1971
- Mastenbrook, H.J., Water-vapor measurements in the lower stratosphere, *Can. J. Chem.*, 52 (2), 1527-31, 1974.
- Mastenbrook, H. J., Measurements of stratospheric water vapor from the NASA C141 aircraft, *U.S. Naval Research Lab. Rep. 7960*, Washington DC, 18 Feb 1976.
- Mastenbrook, H. J., and J. E. Dinger, The measurement of water vapor distribution in the stratosphere, *U. S. Naval Research Lab. Rep. 5551*, Washington DC, Nov 1961.
- Mastenbrook, H.J. and R.E. Daniels, Measurements of stratospheric water vapor using a frost point hygrometer, in: *Atmospheric Water Vapor*. Edited by Adarsh Deepak, Thomas D. Wilkerson and Lothar H. Ruhnke. Academic Press, 1980
- Mastenbrook, H.J., and S.J. Oltmans, Stratospheric water vapor variability for Washington D.C./Boulder, CO.: 1964-1982, *J. Atmos. Sci.*, 40, 2157-2165, 1983.
- Mathews, D. A.: Review of the lithium chloride radiosonde hygrometer. Humidity and Moisture: Measurement and Control in Science and Industry, I - Principles and Methods of Measuring Humidity in Gases, R. Ruskin, ed., Reinhold Publishing Corp., New York, 219-227, 1965.
- Mattis, I., U. Wandinger, D. Muller, A. Ansmann, D., Althausen, Routine dual-wavelength Raman lidar observations at Leipzig as part of an aerosol lidar network in Germany, *Proc. 19<sup>th</sup> Int. Laser Radar Conf., NASA/CP-1998-207671/PT1*, 29-32, 1998.

- 
- Mauldin, L. E. III, N. H. Zaub, M. P. McCormick, J. H. Guy, and W. R. Vaughn, Stratospheric aerosol and gas experiment II instrument: A functional description, *Opt. Eng.*, *24*, 307-312, 1985.
- May, R. D., and C. R. Webster, Data processing and calibration for tunable diode laser harmonic absorption spectrometers, *J. Quant. Spectrosc. Radiat. Transfer*, *49*, 335-347, 1993.
- May, R. D., Open-path, near-infrared tunable diode laser spectrometer for atmospheric measurements of H<sub>2</sub>O, *J. Geophys. Res.*, *103*, 19,161-19,172, 1998.
- McCormick M. P., E. W. Chiou, L. R. McMaster, W. P. Chu, J. C. Larsen, D. Rind, and S. Oltmans. Annual Variations of water vapor in the stratosphere and upper troposphere observed by the Stratospheric Aerosol and Gas Experiment II, *J. Geophys. Res.*, *98*, 4867-4874, 1993.
- McGuirk, J.P., A.H. Thompson, and J.R. Schaefer, An eastern Pacific tropical plume, *Mon. Weather Rev.*, *116*, 2505-2521, 1988.
- McNally, A.P., and M. Vesperini, Variational analysis of humidity from the TOVS radiances, *Quarterly Journal of the Royal Meteorological Society*, *122*, 1521-1544, 1996.
- Mecikalski, J.R., and G.J. Tripoli, Inertial available kinetic energy and the dynamics of tropical plume formation, *Mon. Weather Rev.*, *126*, 2200-2216, 1998.
- Melfi, S., J. D. Lawrence, M. P. McCormick, Observations of Raman scattering by water vapor in the atmosphere, *Appl. Phys. Lett.*, *15*, 295-297, 1969.
- Melfi, S., and D. Whiteman, Observations of lower-atmospheric moisture structure and its evolution using a Raman lidar, *Bull. Am. Meteorol. Soc.*, *66*, 1288-1292, 1985.
- Michelsen, H.A., G.L. Manney, M.R. Gunson, and R. Zander, Correlations of stratospheric NO<sub>y</sub>, O<sub>3</sub>, N<sub>2</sub>O, and CH<sub>4</sub> derived from ATMOS measurements, *J. Geophys. Res.*, *103*, 28347-28359, 1998.
- Michelsen, H.A., *et al.*, Intercomparison of ATMOS, SAGE II, and ER-2 observations in Arctic vortex and extra-vortex air masses from spring 1993, *Geophys. Res. Lett.*, *26*, 291-294, 1999a.
- Michelsen, H.A., *et al.*, Maintenance of high HCl/Cl<sub>y</sub> and NO<sub>x</sub>/NO<sub>y</sub> in the Antarctic vortex: A chemical signature of confinement during spring, *J. Geophys. Res.*, *104*, 26419-26436, 1999b.
- Michelsen, H. A., *et al.*, ATMOS Version 3 water vapor measurements: Comparisons with ATMOS Version 2 retrievals and observations from two ER-2 Lyman- $\alpha$  hygrometers, MkIV, MAS, HALOE, and MLS, *J. Geophys. Res.*, submitted, 2000a.
- Michelsen, H.A., F.W. Irion, G.L. Manney, G.C. Toon, and M.R. Gunson, Features and trends in ATMOS Version 3 water vapor and methane measurements, *J. Geophys. Res.*, *in press*, 2000b.
- Miloshevich, L.M., H. Vömel, A. Paukkunen, A.J. Heymsfield, and S.J. Oltmans, Characterization and correction of relative humidity measurements from Vaisala RS80-A radiosondes at cold temperatures, *J. Atmos. Oceanic Technol.*, *in press*, 2000.
- Minschwaner, K. *et al.* The bulk properties of isentropic mixing into the tropics in the lower stratosphere, *J. Geophys. Res.*, *101*, 9433-9349, 1996.
- Morrey, M.W., and R.S. Harwood, Interhemispheric differences in stratospheric water vapour during late winter, in version 4 MLS measurements, *Geophys. Res. Lett.*, *25* (2), 147-150, 1998.
- Mote, P.W., J.R. Holton, and B.A. Boville, Characteristics of stratosphere-troposphere exchange in a general circulation model, *J. Geophys. Res.*, *99*, 16,815-16,829, 1994.

- 
- Mote, P.W., Reconsideration of the cause of dry air in the southern middle latitude stratosphere, *Geophys. Res. Lett.*, 22(15), 2025-2028, 1995.
- Mote, P.W., K.H. Rosenlof, J.R. Holton, *et al.*, Seasonal variations of water vapour in the tropical lower stratosphere, *Geophys. Res. Lett.*, 22, 1093-1096, 1995.
- Mote, P.W., K.H. Rosenlof, M.E. McIntyre, *et al.*, An atmospheric tape recorder: The imprint of tropical tropopause temperatures on stratospheric water vapour, *J. Geophys. Res.*, 101, 3989-4006, 1996.
- Mote, P.W., T.J. Dunkerton, and H.C. Pumphrey, Sub-seasonal variations in lower stratospheric water vapour, *Geophys. Res. Lett.*, 25, 2445-2448, 1998a.
- Mote, P.W., T.J. Dunkerton, M.E. McIntyre, *et al.*, Vertical velocity, vertical diffusion, and dilution by midlatitude air in the tropical lower stratosphere, *J. Geophys. Res.*, 103 (D8), 8651-8666, 1998b.
- Mote, P.W., H.L. Clark, T.J. Dunkerton, *et al.*, Intraseasonal variations of water vapor in the tropical upper troposphere and tropopause region, *J. Geophys. Res.*, 105, 17,457-17,470, 2000.
- Murcray *et al.*, Intercomparison of stratospheric water vapor profiles obtained during the balloon intercomparison campaign, *J. Atmos. Chem.*, 10, 159-179, 1990.
- Murgatroyd, R. J., Ozone and water vapour in the upper troposphere and lower stratosphere, in *Meteorological Aspects of Atmospheric Radioactivity*, edited by W. Bleeker, *World Meteorological Organization*, pp. 68-94, 1965.
- Murgatroyd, R.J., P. Goldsmith, and W.E.H. Hollings, Some recent measurements of humidity from aircraft up to heights of about 50,000 ft over southern England, *Q. J. R. Meteorol. Soc.*, 81, 533-537, 1955.
- Murgatroyd, R.J., and F. Singleton, Possible meridional circulations in the stratosphere and mesosphere, *Q. J. R. Meteorol. Soc.* 87, 125-135, 1961.
- Murphy, D. M. *et al.*, Reactive nitrogen and its correlation with ozone in the lower stratosphere and upper troposphere *J. Geophys. Res.*, 98, 8751-8773, 1993
- Nakamura, N., and J. Ma, Modified Lagrangian-mean diagnostics of the stratospheric polar vortices 2. Nitrous oxide and seasonal barrier migration in the cryogenic limb array etalon spectrometer and SKYHI general circulation model, *J. Geophys. Res.*, 102, 25,721-25,735, 1997.
- Nedoluha, G. E., R. M. Bevilacqua, R. M. Gomez, D. L. Thacker, W. B. Waltman, and T. A. Pauls, Ground-based measurements of water vapor in the middle atmosphere, *J. Geophys. Res.*, 100, 2927-2939, 1995.
- Nedoluha, G. E., R. M. Bevilacqua, R. M. Gomez, W. B. Waltman, B. C. Hicks, D. L. Thacker, and W. A. Matthews, Measurements of water vapor in the middle atmosphere and implications for mesospheric transport, *J. Geophys. Res.*, 101, 21183-21193, 1996.
- Nedoluha, G. E., *et al.*, A comparative study of mesospheric water vapor measurements from the ground-based water vapor millimeter-wave spectrometer and space-based instruments, *J. Geophys. Res.*, 102, 16,647-16,661, 1997.
- Nedoluha, G.E., R.M. Bevilacqua, R.M. Gomez, D.E. Siskind, B.C. Hicks, and J.M. Russell III, Increases in middle atmospheric water vapor as observed by the Halogen Occultation Experiment (HALOE) and the ground-based Water Vapor Millimeter-wave Spectrometer from 1991-1997, *J. Geophys. Res.*, 103, 3531-3542, 1998a.
- Nedoluha, G.E., D.E. Siskind, J.T. Bacmeister, *et al.*, Changes in upper stratospheric CH<sub>4</sub> and NO<sub>2</sub> as measured by HALOE and implications for changes in transport, *Geophys. Res. Lett.*, 25, 987-990, 1998b.

- Nedoluha, G.E., R.M. Bevilacqua, R.M. Gomez, B.C. Hicks, and J.M. Russell III, Measurements of middle atmospheric water vapor from low latitudes and midlatitudes in the Northern Hemisphere, 1995-1998, *J. Geophys. Res.*, *104*, 19257-19266, 1999.
- Newell, R.E., Transfer through the tropopause and within the stratosphere, *Q. J. R. Meteorol. Soc.*, *89* (380), 167-204, 1963.
- Newell, R. E. Stratospheric temperature change from the Mt Agung volcanic eruption of 1963. *J. Atmos. Sci.* *27*(6):977-978, 1970.
- Newell, R.E., and S. Gould-Stewart, A stratospheric fountain ? *J. Atmos. Sci.*, *38*, 2789-2796, 1981.
- Newell, R. E., Y. Zhu, E. V. Browell, S. Ismail, W. G. Read, J. W. Waters, K.K. Kelly, and S.C. Liu, Upper tropospheric water vapor and cirrus: Comparison of DC-8 Observations, preliminary UARS microwave limb sounder measurements and meteorological analyses, *J. Geophys. Res.*, *101*, 1931-1941, 1996a.
- Newell, R. E., Y. Zhu, E. V. Browell, W. G. Read, and J. W. Waters, Walker circulation and tropical upper tropospheric water vapor, *J. Geophys. Res.*, *101*, 1961-1974, 1996b.
- Newell, R.E., Y. Zhu, W.G. Read, and J.W. Waters, Relationship between tropical upper tropospheric moisture and eastern tropical Pacific sea surface temperature at seasonal and interannual timescales, *Geophys. Res. Lett.*, *24*, 25-28, 1997.
- Newell, R.E., V. Thouret, J.Y.N. Cho, P. Stoller, A. Marengo, and H.G. Smit, Ubiquity of quasi-horizontal layers in the troposphere, *Nature*, *398*, 316-319, 1999.
- Newman, P.A., and M.R. Schoeberl, A reinterpretation of the data from the NASA Stratosphere Troposphere Exchange Project, *Geophys. Res. Lett.*, *22*, 2501-2504, 1995.
- Normand, C.W.B., On instability from water vapour, *Q. J. R. Meteorol. Soc.*, *64*, 47-70, 1938.
- Norton, R. H., and C. P. Rinsland, ATMOS data processing and science analysis methods, *Appl. Opt.*, *30*, 389-400, 1991.
- NRC Report, Reconciling observations of global temperature change, National Academy Press, Washington, D.C., 104 pp., 2000.
- Oelhaf, H., *et al.*, Remote sensing of the Arctic stratosphere with the new balloon-borne MIPAS-B2 instrument, in *Polar Stratospheric Ozone, Proceedings of the 3rd European Workshop 18 to 22 September 1995*, edited by J. A. Pyle, N. R. P. Harris, and G.T. Amanatidis, Eur. Comm., Brussels, Luxembourg, 270-275, 1996.
- Oliver, M.J., and A.P. Cluley, A systematic error in the measurement of frostpoint using a Meteorological Office Mk 3 hygrometer, *Q. J. R. Meteorol. Soc.*, *104*, 503-509, 1978.
- Oltmans, S. J., Measurements of water vapor in the stratosphere with a frost point hygrometer, in: *Measurement and Control in Science and Industry, Proc. 1985 International Symposium on Moisture and Humidity, Washington, D. C.*, pp. 251-258, *Instrument Society of America*, 1985.
- Oltmans, S.J., and D.J. Hofmann, Increase in lower-stratospheric water vapor at a mid-latitude Northern Hemisphere site from 1981 to 1994, *Nature*, *374*, 146-149, 1995.
- Oltmans, S.J., H. Vömel, D.J. Hofmann, K.H. Rosenlof and D. Kley, The increase in stratospheric water vapor from balloon-borne, frostpoint hygrometer measurements at Washington, D.C. and Boulder, Colorado, *Geophys. Res. Lett.*, accepted for publication, 2000.
- Orlando, J. J., G. S. Tyndall, K. E. Nickerson, and J. G. Calvert, The temperature dependence of collision-induced absorption by oxygen near 6 $\mu$ m, *J. Geophys. Res.*, *96*, 20,755-20,760, 1991.
- O'Sullivan, D., and T.J. Dunkerton, The influence of the quasi-biennial oscillation on global constituent distributions, *J. Geophys. Res.*, *102*, 21,731-21,743, 1997.

- 
- Ovarlez, J., A two temperature calibration system, Measurement and Control in Science and Industry, *Proc. 1985 International Symposium on Moisture and Humidity*, Washington, D. C., Instrument Society of America, 235-241, 1985.
- Ovarlez, J., Stratospheric water vapor measurement in the tropical zone by means of a frost-point hygrometer on board long-duration balloons, *J. Geophys. Res.*, *96*, 15,541-15,545, 1991.
- Ovarlez, J., and H. Ovarlez, Stratospheric water vapor content evolution during EASOE, *Geophys. Res. Lett.*, *21*, 13, 1235-1238, 1994.
- Ovarlez, J., and H. Ovarlez, Water vapour and aerosols measurements during SESAME, and the observation of low water vapour content layers, *Air Pollution report N°56*, Polar Stratospheric Ozone, CEC Publ., 205-208, 1995.
- Ovarlez, J., and H. Ovarlez, Water vapour and aerosol measurements during SESAME, and the observation of low water vapour content layers, European Commission Bruxelles, 1996.
- Ovarlez J., H. Ovarlez and H. Teitelbaum, *In situ* water vapour measurement, a case study of the drying mechanism of the tropical stratosphere, *Quart. J. Roy. Meteorol. Soc.*, *122*, 1447-1458, 1996.
- Ovarlez, J., and P. van Velthoven, Comparison of water vapor measurements with data retrieved from ECMWF analyses during the POLINAT experiment, *J. Appl. Meteorol.*, *36*, 1329-1335, 1997.
- Ovarlez J., P. van Velthoven, and Hans Schlager, Water vapor measurements from the troposphere to the lowermost stratosphere : Some signature of troposphere to stratosphere exchanges, *J. Geophys. Res.*, *104*, 16,973-16,978, 1999.
- Ovarlez, J., P. van Velthoven, G. Sachse, S. Vay, H. Schlager, H. Ovarlez, Comparison of water vapor measurements from POLINAT2 with ECMWF analysis humidity conditions, *J. Geophys. Res.*, *105*, 3737-3744, 2000.
- Pan, L., S. Solomon, W. Randel, *et al.*, Hemispheric asymmetries and seasonal variations of the lowermost stratospheric water vapour and ozone derived from SAGE II data, *102* (D23), 28,177-28,184, 1997.
- Paukkunen, A., Sensor heating to enhance reliability of radiosonde humidity measurement. Preprints. 11th International Conference on Interactive Information and Processing Systems for Meteorology, Oceanography, and Hydrology, Dallas, Texas, January 15-20, 1995, 103-106, 1995.
- Pedlosky, J., in *Geophysical Fluid Dynamics*, Springer-Verlag, New York, Heidelberg, Berlin, pp. 624, 1979.
- Peixoto, J.P., and A.H. Oort, *Physics of Climate*, American Institute of Physics, New York, 1992.
- Peixoto, J.P., and A.H. Oort, The climatology of relative humidity in the atmosphere. *J. Climate*, *9*, 3443-3463, 1996.
- Peppler, R.A., and P.J. Lamb, Tropospheric static stability and central North American growing season rainfall, *Mon. Weather Rev.*, *117*, 1156-1180, 1989.
- Peter, R., Latitude-altitude cross-sections of middle atmospheric water vapour obtained by airborne millimeter-wave spectroscopy, *Adv. Space Res.*, *21* (10), 1413-1416, 1998a.
- Peter, R., Stratospheric and mesospheric latitudinal water vapor distributions obtained by an airborne millimeter-wave spectrometer, *J. Geophys. Res.*, *103*, 16,275-16,290, 1998b.
- Peter, R., K. Künzi and G. K. Hartmann, Latitudinal survey of water vapor in the middle atmosphere using an airborne millimeter-wave sensor, *Geophys. Res. Lett.*, *15*, 1173-1176, 1988.

- Peter, R. and N. Kämpfer, Stratospheric and mesospheric water vapor distribution over northern Europe measured with an airborne mm-wave sensor, *Proc. of IGARSS 94*, Pasadena, 1350-1353, 1994.
- Pfister, L., Small-scale motions observed by aircraft in the tropical lower stratosphere: evidence for mixing and its relationship to large-scale flows, *J. Atmos. Sci.*, 43 (24), 3210-3225, 1986.
- Pickett, H. M., R. L. Poynter and E. A. Cohen, Submillimeter, millimeter and microwave spectral line catalog, *JPL tech report 8033 Rev. 3*, JPL, 1992.
- Pickett, H. M., *et al.*, Submillimeter, millimeter, and microwave spectral line catalog, *JQSRT*, 60, 883-890, 1998.
- Pierce, R.B., and T.D., Fairlie, A chaotic advection in the stratosphere - implications for the dispersal of chemically perturbed air from the polar vortex, *J. Geophys. Res. Atmos.*, 98 (D10), 18589-18595, 1993.
- Pierce, R.B., T.D. Fairlie, W.L. Grose, *et al.*, Mixing processes within the polar night jet, *J. Atmos. Sci.*, 51, 2957-2972, 1994.
- Pierrehumbert, R.T., Large-scale horizontal mixing in planetary-atmospheres, *Phys. Fluids A-Fluid*, 3 (5) 1250-1260 Part 2, 1991.
- Pierrehumbert, R.T., and R. Roca., Evidence for control of Atlantic subtropical humidity by large scale advection, *Geophys. Res. Lett.*, 25, 4573-4540, 1998.
- Plumb, R.A., and R.C. Bell, A model of the quasi-biennial oscillation on an equatorial beta plane, *Q. J. R. Meteorol. Soc.*, 108, 335-352, 1982.
- Plumb, R.A., and J. Eluszkiewicz, The Brewer-Dobson circulation: Dynamics of the tropical upwelling, *J. Atmos. Sci.*, 56, 868-890, 1999.
- Pollock, W., L. E. Heidt, R. Lueb, and D. H. Ehhalt, Measurement of stratospheric water vapor by cryogenic collection, *J. Geophys. Res.*, 85, 5555-5568, 1980.
- Ponsardin, P. L., and E. V. Browell, Measurements of H<sub>2</sub><sup>16</sup>O Linestrengths and Air -induced Broadenings and Shifts in the 815-nm Region, *J. Mol. Spectrosc.*, 185, 58-70, 1997.
- Potter B.E., and J.R. Holton, The role of monsoon convection in the dehydration of the lower tropical stratosphere, *J. Atmos. Sci.*, 52 (8), 1034-1050, 1995.
- Poulida, O., R.P. Dickerson, and A. Heymsfield, Stratosphere-troposphere exchange in a midlatitude mesoscale convective complex 1 observations, *J. Geophys. Res.*, 101, 6823, 1996.
- Pratt, R. W., Review of radiosonde humidity and temperature errors. *J. Atmos. Ocean. Tech.*, 2, 404-407, 1985.
- Preisendorfer, R.W., *Principal Components Analysis in Meteorology and Oceanography*, Elsevier, 425, 1988.
- Press, W.H., S.A. Teukolsky, W.T. Vetterling, and B.P. Flannery, *Numerical Recipes in Fortran 77 : The Art of Scientific Computing*, 933 pp., Cambridge University Press, Cambridge England, 1996.
- Pruvost, P., J. Ovarlez, J. Lenoble, and W.P. Chu, Comparison of Stratospheric Aerosol and Gas Experiment II and balloon-borne stratospheric water vapor measurements, *J. Geophys. Res.*, 98, 4889-4896, 1993.
- Pumphrey, H. C., Validation of a new prototype water vapour retrieval for the UARS Microwave Limb Sounder, *J. Geophys. Res.*, 104, 9399-9412, 1999.
- Pumphrey, H. C., D. Rind, J. M. Russell III, and J. E. Harries, A preliminary Zonal mean climatology of water vapour in the stratosphere and mesosphere, *Adv. Space Res.*, 21, 1417-1420, 1998.

- Pumphrey, H. C., and S. Buehler, Instrumental and spectral parameters: their effect on and measurement by microwave limb sounding of the atmosphere, *JQSRT*, 64, 421-437, 2000.
- Pyle, J.A., A.M. Zavody, J.E. Harries, and P.H. Moffat, Derivation of OH concentration from satellite infrared measurements of NO<sub>2</sub> and HNO<sub>3</sub>, *Nature*, 305, 690-692, 1983.
- Randel, D.L., T.H. Vonder Haar, M.A. Ringerud, *et al.*, A new global water vapour dataset, *Bull. Amer. Meteorol. Soc.*, 77, 1233-1246, 1996.
- Randel, W.J., F. Wu, J.M. Russell III, A. Roche, and J.W. Waters, Seasonal cycles and QBO variations in stratospheric CH<sub>4</sub> and H<sub>2</sub>O observed in UARS HALOE data, *J. Atmos. Sci.*, 55, 163-185, 1998.
- Randel, W.J., F. Wu, R. Swinbank, *et al.*, Global QBO circulation derived from UKMO analyses, *J. Atmos. Sci.*, 56, 457-474, 1999a.
- Randel, W.J., R. Wu, J.M. Russell III, and J. Waters, Space-time patterns of trends in stratospheric constituents derived from UARS measurements, *J. Geophys. Res.*, 104, 3711-1727, 1999b.
- Randel, W.J., F. Wu, and D.J. Gaffen, Interannual variability of the tropical tropopause derived from radiosonde data and NCEP reanalyses, *J. Geophys. Res.*, in press, 2000.
- Rasmusson, E.M., and J.M. Wallace, Meteorological aspects of the El Nino/Southern oscillation, *Science*, 222, 1195-1202, 1983.
- Ray, E.A., F.L. Moore, J.W. Elkins, G.S., *et al.*, Transport into the northern hemisphere lowermost stratosphere revealed by *in situ* tracer measurements, *J. Geophys. Res.* 104, 26,565-26,580, 1999.
- Read, W.G., J.W. Waters, L. Froidevaux, D.A. Flower, R.F. Jarnot, D.L. Hartmann, and R.S. Harwood, Upper-Tropospheric Water Vapor from UARS MLS, *Bull. Amer. Met. Soc.*, 76, 2381-2389, 1995.
- Reed, R.J., A study of a characteristic type of upper-level frontogenesis, *J. Meteorol.*, 12, 226-237, 1955.
- Reed, R.J., Some features of the annual temperature regime in the tropical stratosphere. *Mon. Weather Rev.*, 90 (6), 211-215, 1962.
- Reed, R.J., and E.F. Danielsen, Fronts in the vicinity of the tropopause, *Archiv. Meteorol. Geophys. Bioklimat., Ser. A*, 11 (1), 1-17, 1959.
- Reed, R.J., and C.L. Vlcek, The annual temperature variation in the lower tropical stratosphere, *J. Atmos. Sci.*, 26, 163-167, 1969.
- Reid G.C., and K.S. Gage, Interannual variations in the height of the tropical tropopause, *J. Geophys. Res.*, 90 (D3), 5629-5635, 1985.
- Reid, G.C., Seasonal and interannual temperature variations in the tropical stratosphere, *J. Geophys. Res.*, 99 (D9), 18,923-18,932, 1994.
- Reid, G.C., and K.S. Gage, The tropical tropopause over the western Pacific: Wave driving, convection, and the annual cycle, *J. Geophys. Res.*, 101 (D16), 21,233-21,241, 1996.
- Reid S.J., and Vaughan G., Lamination in ozone profiles in the lower stratosphere, *Q. J. R. Meteorol. Soc.*, 117 (500), 825-844 Part A, 1991.
- Remsberg, E. E., J. M. Russell III, L. L. Gordley, J. C. Gille, and P. L. Bailey, Implications of the stratospheric water vapor distribution as determined from the NIMBUS 7 LIMS experiment, *J. Atmos. Sci.*, 41, 2934-2945, 1984.
- Remsberg, E. E., and J. M. Russell III, The near global distributions of middle atmospheric H<sub>2</sub>O and NO<sub>2</sub> measured by the Nimbus 7 LIMS experiment, in *Transport Processes in the Middle Atmosphere*, edited by G. Visconti and R. Garcia, Reidel, 87-102, 1987.

- Remsberg, E.E., P.P. Bhatt, and J.M. Russell, III, Estimates of the water vapor budget of the stratosphere from UARS HALOE data, *J. Geophys. Res.*, *101*, 6749-6766, 1996.
- Renaut, D., J. C. Pournay, and R. Captini, Daytime Raman-lidar measurements of water vapor, *Opt. Lett.*, *5*, 233-235, 1980.
- Rennó, N. O., K.A.Emanuel and P. H. Stone, Radiative-convective model with an explicit hydrologic cycle. 1: Formulation and sensitivity to model parameters *J. Geophys. Res.*, *99*(D7): 14429-14441, 1994.
- Riehl, H., and Malkus, J.S., On the heat balance in the equatorial trough zone, *Geophys.*, *6*, 503-537, 1958.
- Rind, D., Just add water vapour, *Science*, *281*, 1152-1153, 1998.
- Rind D., E.W Chiou., W. Chu, *et al.*, Positive water-vapor feedback in climate models confirmed by satellite data, *Nature*, *349* (6309), 500-503, 1991.
- Rind, D., E. W. Chiou, W. Chu, S. Oltmans, J. Lerner, J. Larsen, M. P. McCormick, and L. McMaster, Overview of the stratospheric aerosol and gas experiment II water vapor observations: Method, validation, and data characteristics, *J. Geophys. Res.*, *98*, 4835-4856, 1993.
- Rind, D. and P. Lonergan, Modeled impacts of stratospheric ozone and water vapour perturbations with implications for high speed civil transport aircraft, *J. Geophys. Res.*, *100*, 7381-7396, 1995
- Rinsland, C.P., J.S. Levine, and T. Miles, Concentration of methane in the troposphere deduced from 1951 infrared solar spectra, *Nature*, *318*, 245-249, 1985.
- Rinsland, C. P., *et al.*, ATMOS observations of H<sub>2</sub>O+2CH<sub>4</sub> and total reactive nitrogen in the November 1994 Antarctic stratosphere: Dehydration and denitrification in the vortex, *Geophys. Res. Lett.*, *23*, 2397-2400, 1996.
- Roach, W. T., Aircraft observations in the lower Sub-Arctic stratosphere in winter, Rep. by Air Ministry Meteorol. Office, U.K., 121, 1-7, 1962.
- Roach, W.T., An analysis of eight flights by U-2 aircraft over severe storms in oaklahoma. U.S. Dept. of Commerce, Environmental Sciences Services Administration, Tech. Report NSSL-29, 23-51, 1966.
- Robinson, G.D., Transport of minor atmospheric constituents between troposphere and stratosphere, *Q. J. R. Meteorol. Soc.*, *106*, 227-253, 1980.
- Robinson G.D., and M.G. Atticks-Schoen, The formation and movement in the stratosphere of very dry air, *Q. J. R. Meteorol. Soc.*, *113*, 653-679, 1987.
- Rodgers, C. D., Retrieval of atmospheric temperature and composition from remote measurements of thermal radiation, *Rev. Geophys. and Space Phys.*, *14*, 609-624, 1976.
- Rodgers, C. D., Characterization and error analysis of profiles retrieved from remote sounding measurements, *J. Geophys. Res.*, *95*, 5587-5595, 1990.
- Rood, R. B., A. R. Douglass, M. C. Cerniglia, and W. G. Read, Synoptic-Scale Mass Exchange from the Troposphere to the Stratosphere, *J. Geophys. Res.*, *102*, 23,467-23,485, 1997.
- Rosenfield, J.E., P.A. Newman, and M.R. Schoeberl, Computations of diabatic descent in the stratospheric polar vortex, *J. Geophys. Res.*, *99* (D8), 16677-16689, 1994.
- Rosenfield, J.E., D.B. Considine, M.R. Schoeberl, and E.V. Browell, The impact of subvisible cirrus clouds near the tropopause on stratospheric water vapour, *Geophys. Res. Lett.*, *25* (11), 1883-1886, 1998.
- Rosenlof, K.H., Seasonal cycle of the residual mean meridional circulation in the stratosphere, *J. Geophys. Res.*, *100*, 5173-5191, 1995.

- Rosenlof, K.H., A.F. Tuck, K.K. Kelly, *et al.*, Hemispheric asymmetries in water vapour and inferences about transport in the lower stratosphere, *J. Geophys. Res.*, *102* (D11), 13,213-13,234, 1997.
- Ross, R.J., and W.P. Elliott, Tropospheric water vapour climatology and trends over North America: 1973-93, *J. Climate*, *9*, 3561-3574, 1996.
- Ross, R.J., and W.P. Elliott, Northern hemisphere water vapour trends, paper presented at Ninth Symposium on Global Change Studies, Phoenix, Arizona, 11-16 January 1998, American Meteorological Society, Boston, 39-41, 1998.
- Ross, R. J., and D. J. Gaffen, Comment on "Widespread tropical drying from 1979 to 1995" by Schroeder and McGuirk, *Geophys. Res. Lett.*, *25*, 4357-4358, 1998.
- Ross, R.J., and W.P. Elliott, A search for tropospheric water vapour trends: 1948-1995, paper presented at Tenth Symposium on Global Change Studies, Dallas, Texas, 11-15 January 1999, American Meteorological Society, Boston, 126-128, 1999.
- Rothman, L. S., AFGL atmospheric absorption line parameters compilation: 1980 version, *Appl. Opt.*, *20*, 791-795, 1981.
- Rothman, L. S., R. R. Gamache, R. H. Tipping, C. P. Rinsland, M. A. H. Smith, D. C. Benner, V. M. Devi, J.-M. Flaud, C. Camy-Peyret, A. Perrin, A. Goldman, S. T. Massie, L. R. Brown, and R. A. Toth, The HITRAN molecular database: editions of 1991 and 1992. *J. Quant. Spectrosc. Rad. Transf.*, *48*, 469-507, 1992.
- Rothman, L. S., *et al.*, The HITRAN molecular spectroscopic database and HAWKS (HITRAN Atmospheric WorkStation): 1996 edition, *J. Quant. Spectrosc. & Rad. Transfer*, *60*, 665-710, 1998.
- Russell, JM, J.C. Gille, E.E. Remsberg, *et al.*, Validation of water-vapor results measured by the limb infrared monitor of the stratosphere experiment on Nimbus-7, *J. Geophys. Res.*, *89*, 5115-5124, 1984.
- Russell, J. M., III, L. L. Gordley, J. H. Park, S. R. Drayson, A. F. Tuck, J. E. Harries, R. J. Cicerone, P. J. Crutzen, and J. E. Frederick, The Halogen Occultation Experiment, *J. Geophys. Res.*, *98*, 10,777-10,797, 1993.
- Sachse, G. W., G. F. Hill, L. O. Wade, and M. G. Perry, Fast-response, high-precision carbon monoxide sensor using a tunable diode laser absorption technique, *J. Geophys. Res.*, *92*, 2071-2081, 1987.
- Sachse, G. W., J. E. Collins, Jr., G. F. Hill, L. O. Wade, L. G. Burney, and J. A. Ritter, Airborne tunable diode laser sensor for high precision concentration and flux measurements of carbon monoxide and methane, *Proc. SPIE*, 1991.
- Salathé E.P., D. Chesters, and Y.C. Sud, Evaluation of the upper-tropospheric moisture climatology in a general-circulation model using TOVS radiance observations, *J. Climate*, *8* (10), 2404-2414, 1995.
- Salathé, E.P., and D.L. Hartmann, A trajectory analysis of tropical upper-tropospheric moisture and convection, *J. Climate*, *10*, 2533-2524, 1997.
- Sandor, B. J., W. G. Read, J. W. Waters, and K. H. Rosenlof, Seasonal Behavior of Tropical to Mid-Latitude Upper Tropospheric Water Vapor from UARS MLS, *J. Geophys. Res.*, *103*, 25,935-25,947, 1998.
- Sasano, Y., Suzuki, M., Yokota, T., and Kanzawa, H., Improved Limb Atmospheric Spectrometer (ILAS) for stratospheric ozone layer measurements by solar occultation technique. *Geophys. Res. Lett.*, *26*, 197-200, 1999a.
- Sasano, Y., *et al.*, Validation of ILAS Version 3.10 ozone with ozonesonde measurements. *Geophys. Res. Lett.*, *26*, 831-834, 1999b.

- Sasano, Y., Suzuki, M., Yokota, T., and Kanzawa, H., ILAS for stratospheric ozone layer monitoring: Outline of data processing (Version 3.00 and 3.10) and validation experiments. *IEEE Transactions Geoscience Remote Sensing*, 37, 1508-1516, 1999c.
- Schiller, C., O. Bujok, N. Eicke, D. S. McKenna, M. Zöger, H. Fischer, F. Wienhold, A. Engel, H<sub>2</sub>O in the lowermost stratosphere: seasonal and regional variability, AGU spring meeting, Boston, USA, 1998.
- Schiller, C., *et al.*, Ice particle formation and sedimentation in the tropopause region: A case study based on in situ measurements of total water during POLSTAR 1997, *Geophys. Res. Lett.*, 26, 2219-2222, 1999.
- Schmidlin, F. J., and A. Ivanov: Radiosonde relative humidity sensor performance: The WMO intercomparison-Sept. 1995. Preprint volume. 10th Symposium on Meteorological Observations and Instrumentation, Amer. Meteor. Soc., 68-71, 1998.
- Schmidt, U., G. Kulesa, E. Klein, E.-P. Röth, P. Fabian, and R. Borchers, Intercomparison of balloon-borne cryogenic whole air samplers during the Map/Globus 1983 Campaign, *Planet. Space Sci.*, 35, 647-656, 1987.
- Schoeberl, M.R., *et al.*, Reconstruction of the constituent distribution and trends in the Antarctic polar vortex from ER-2 flight observations, *J. Geophys. Res.*, 94, 16,815-16,846, 1989.
- Schoeberl, M.R., M. Luo, and J.E. Rosenfield, An analysis of the Antarctic Halogen Occultation Experiment trace gas observations, *J. Geophys. Res.*, 100, 5159-5172, 1995.
- Scholz, T.G., D.H. Ehhalt, L.E. Heidt, and E.A. Martell, Water vapour, molecular hydrogen, methane and tritium concentrations near the stratopause, *J. Geophys. Res.*, 75, 3049-3054, 1970.
- Schotland, R. M., Some Observations of the Vertical Profile of Water Vapor by Means of a Ground Based Optical Radar, Proc. 4th Symposium on Remote Sensing of Environment, U. Michigan, Ann Arbor, 12-24 Apr., 1966.
- Schroeder, S.R., and J.P. McGuirk, Widespread tropical drying from 1979 to 1995, *Geophys. Res. Lett.*, 25, 1301-1304, 1998a.
- Schroeder, S.R., and J.P. McGuirk, Reply, *Geophys. Res. Lett.*, 25, 4359-4360, 1998b.
- Schumann, U., On conditions for contrail formation from aircraft exhausts, *Meteorologische Zeitschrift*, 5, 4-23, 1996.
- Schumann, U., H. Schlager, F. Arnold, R. Baumann, P. Haschberger, and O. Klemm, Dilution of aircraft exhaust plumes at cruise altitudes, *Atmos. Environ.*, 32, 3097-3103, 1998.
- Schwab, J. J., E. M. Weinstock, J. B. Nee, and J. G. Anderson, In situ measurement of water vapor in the stratosphere with a cryogenically cooled Lyman alpha hygrometer, *J. Geophys. Res.*, 95, 13,781-13,796, 1990.
- Scott, N., A. Chedin, A. Armante, J. Francis, C. Stubenrauch, J. Chaboureaud, F. Chevallier, C. Claud, and F. Cheruy, Characteristics of the TOVS Pathfinder PATH-B dataset, *Bull. Amer. Meteorol. Soc.*, 80, 2679-2701, 1999.
- Seele, C and P. Hartogh, Water vapor of the polar middle atmosphere: Annual variation and summer mesosphere conditions as observed by ground-based microwave spectroscopy, *Geophys. Res. Lett.*, 26, 1517-1520, 1999.
- Selkirk, H.B., The tropopause cold trap in the Australian monsoon during STEP/AMEX 1987, *J. Geophys. Res.*, 98, 8591-8610, 1993.
- Seol, D.I., and K. Yamazaki, QBO and Pinatubo signals in the mass flux at 100 hPa and stratospheric circulation, *Geophys. Res. Lett.*, 25, 1641-1644, 1998.

- 
- Sherlock, V. J., A. Garnier, A. Hauchecorne and P. Keckhut, Implementation and validation of a Raman backscatter lidar measurement of mid and upper tropospheric water vapour, *Appl. Optics*, 38, 5816-5837, 1999a.
- Sherlock, V. J., J. Lenoble and A. Hauchecorne, Methodology for the independent calibration of Raman backscatter water vapour lidar systems, *Appl. Opt.*, 38, 5838-5850, 1999b.
- Sherwood, S.C., Maintenance of the free-tropospheric tropical water vapour distribution, Part I: Clear regime budget, *J. Climate*, 9, 2903-2918, 1996a.
- Sherwood, S.C., Maintenance of the free-tropospheric tropical water vapour distribution, Part II: Simulation by large-scale advection, *J. Climate*, 9, 2919-2934, 1996b.
- Sherwood, S.C., On cirrus moistening of the tropical troposphere, *J. Geophys. Res.*, 104, 11949-11960, 1999a.
- Sherwood, S.C., Feedbacks in a simple prognostic tropical climate model, *J. Atmos. Sci.*, 56, 2178-2200, 1999b.
- Sherwood, S.C., A stratospheric "drain" over the maritime continent, *Geophys. Res. Lett.*, 27, 677-680, 2000.
- Shindell, D.T., Climate and ozone response to increased stratospheric water vapor, *Geophys. Res. Lett.*, in press, 2000
- Shindell, D.T., D. Rind, and P. Lonergan, Increased polar stratospheric ozone losses and delayed eventual recovery owing to increasing greenhouse-gas concentrations, *Nature*, 392, 589-592, 1998.
- Showalter, A. K., State-of-the-art survey on the application of hygrometry to meteorology. *Humidity and Moisture: Measurement and Control in Science and Industry, Volume Two - Applications*, E. J. Amdur, ed., Reinhold Publishing Corp., New York, 441-445, 1965.
- Simmons, A.J., A. Untch, C. Jakob, *et al.*, Stratospheric water vapour and tropical tropopause temperatures in ECMWF analyses and multi-year simulations, *Q. J. R. Meteorol. Soc.*, 125, 353-386, 1999.
- Sinha, A., Relative influence of lapse-rate and water-vapor on the greenhouse-effect, *J. Geophys. Res.*, 100, 5095-5103, 1995
- Sinha, A., and M.R. Allen, Climate sensitivity and tropical moisture distribution, *J. Geophys. Res.*, 99, 3707-3716, 1994.
- Sinha A., and J.E. Harries, Water-vapor and greenhouse trapping - the role of far-infrared absorption, *Geophys. Res. Lett.*, 22, 2147-2150, 1995.
- Sinha, A, and J.E. Harries, The earth's clear-sky radiation budget and water vapour absorption in the far infrared, *J. Climate*, 10, 1601-1614, 1997.
- Sissenwine, N., D.D. Grantham and H.A. Salmela, Midlatitude humidity to 32 km, *J. Atmos. Sci.*, 25, 1129-1140 1968
- Slingo, A., and M.J. Webb, The spectral signature of global warming, *Q. J. R. Meteorol. Soc.*, 123, 293-307, 1997.
- Smit, H. G. J., W. Sträter, D. Kley, and M. H. Profitt, The evaluation of ECC-ozone sondes under quasi flight conditions in the environmental simulation chamber at Jülich, in *Proc. EUROTRAC Symposium 1994*, P. M. Borrell (ed.), pp. 349-353, Academic, San Diego, Calif., 1994.
- Smith, C. A., R. Toumi and J. D. Haigh. Seasonal trends in stratospheric water vapour, *Geophys. Res. Lett.*, 27, 1687-1690, 2000.
- Smith, W. L., H. M. Woolf, C. M. Hayden, D. Q. Wark, and L. M. McMillin, The TIROS-N operational vertical sounder, *Bull. Amer. Meteorol. Soc.*, 60, 1177-1187, 1979.

- Soden, B. J., and F. P. Bretherton, Upper tropospheric relative humidity from the GOES 6.7 micrometer channel: method and climatology for July 1987, *J. Geophys. Res.*, 98, 16,669-16,688, 1993.
- Soden, B.J., and F.P. Bretherton, Evaluation of water-vapor distribution in general-circulation models using satellite-observations, *J. Geophys. Res.*, 99, 1187-1210, 1994.
- Soden, B.J. and R. Fu., A satellite analysis of deep convection, upper tropospheric humidity, and the greenhouse effect, *J. Climate*, 8, 2333-2351, 1995.
- Soden, B. J., and J. R. Lanzante: An assessment of satellite and radiosonde climatologies of upper-tropospheric water vapor. *J. Climate*, 9, 1235-1250, 1996.
- Soden, B. J., *et al.*, An intercomparison of radiation codes for retrieving upper tropospheric humidity in the 6.3 micrometer band: a report from the first GVaP workshop, *Bull. Amer. Meteorol. Soc.*, 81, 797-808, 2000.
- Sonntag, D., Advancements in the field of hygrometry, *Meteorol. Zeitschrift, N. F.* 3, 51-44, 1994.
- SPARC, *SPARC/IOC/GAW Assessment of Trends in the Vertical Distribution of Ozone*, Edited by N. Harris, R. Hudson and C. Phillips. SPARC Report No. 1, WMO-Ozone research and Monitoring Project Report No. 43, 1998.
- Spencer, R. W., and W. D. Braswell, How dry is the tropical free troposphere? Implications for global warming theory, *Bull. Amer. Meteor. Soc.*, 78, 1097-1106, 1997.
- Spyers-Duran, P. A., An airborne cryogenic frost-point hygrometer. *Proceedings of 7<sup>th</sup> Symp. On Meteorol. Observations and Instrumentation*, Amer. Meteorol. Soc., 303-306, 1991.
- Staley, D.O., On the mechanism of mass and radioactivity transport from stratosphere to troposphere, *J. Atmos. Sci.*, 19, 450-467, 1962.
- Steele, H. M., and R. P. Turco, Separation of aerosol and gas components in the Halogen Occultation Experiment and the Stratospheric Aerosol and Gas Experiment (SAGE) II extinction measurements: Implications for SAGE II ozone concentrations and trends, *J. Geophys. Res.*, 102, 19,665-19,681, 1997.
- Stephens, G.L., On the relationship between water vapour over the oceans and sea surface temperature, *J. Climate*, 3, 634-645, 1990.
- Stephens, G. L., D. L. Jackson, and I. Wittmeyer, Global observations of upper-tropospheric water vapor derived from TOVS radiance data, *J. Climate*, 9 (2), 305-326, 1996.
- Stiller, G. P., *et al.*, Stratospheric and mesospheric pressure-temperature profiles from the rotational analysis of CO<sub>2</sub> lines of ATMOS/ATLAS-1 observations, *J. Geophys. Res.*, 100, 3107-3117, 1995.
- Stommel, H., Entrainment of air into a cumulus cloud, *J. Meteorol.*, 4, 91-94, 1947.
- Stone, E. M., W. J. Randel, J. L. Stanford, W. G. Read, and J. W. Waters, Baroclinic wave variations observed in MLS upper tropospheric water vapor, *Geophys. Res. Lett.*, 23, (21) 2967-2970, 1996.
- Stone, E.M., L. Pan, B.J. Sandor *et al.*, Spatial distribution of upper tropospheric water vapour measurements from the UARS Microwave Limb Sounder, *J. Geophys. Res.*, 105(D10), 12149-12162, 2000.
- Stowasser, M., H. Oelhaf, G. Wetzel Simultaneous measurements of HDO, H<sub>2</sub>O and CH<sub>4</sub> with MIPAS-B: Hydrogen budget and indication of dehydration inside the polar vortex, *J. Geophys. Res.*, 104, 19125-19225, 1999.
- Stowasser, M., *et al.*, Simultaneous measurements of HDO, H<sub>2</sub>O and CH<sub>4</sub> with MIPAS-B: Hydrogen budget and indication of dehydration inside the polar vortex, *J. Geophys. Res.*, 104, 19213-19225, 1999.

- Strom, J., and J. Heintzenberg, Water-vapor, condensed water, and crystal concentration in orographically influenced cirrus clouds, *J. Atmos. Sci.*, *51*, 2368-2383, 1994.
- Sun, D.Z., and R.S. Lindzen, Distribution of tropical tropospheric water vapour, *J. Atmos. Sci.*, *50*, 1643-1660, 1993.
- Suzuki, M., A. Matsuzaki, T. Ishigaki, N. Kimura, N. Araki, T. Yokota, and Y. Sasano: ILAS, the Improved Atmospheric Spectrometer, on the Advanced Earth Observing Satellite. IEICE Trans. Commun., E78-B, 1560-1570, 1995.
- Thibault, F., V. Menoux, R. LeDoucen, L. Rosenmann, J.-M. Hartmann, and C. Boulet, Infrared collision-induced absorption by O<sub>2</sub> near 6.4 mm for atmospheric applications: Measurements and empirical modeling, *Appl. Opt.*, *36*, 563-567, 1997.
- Tillman, J. E., Water vapor density measurements utilizing the absorption of vacuum ultraviolet and infrared radiation, in: A. Wexler and R. E. Ruskin (eds.), Humidity and Moisture, I: Principles and methods of measuring humidity in gases, *Proc. 1963 Int. Symp. on Humidity and Moisture, Washington, D.C.*, Reinhold Publishing Corporation, New York, 428-443, 1965.
- Timofeyev, Y. M., and M. V. Tonkov, Effect of the induced oxygen absorption band on the transformation of radiation in the 6  $\mu$ m region in the earth's atmosphere, *Isvest. Atmos. Ocean. Phys.*, *14*, 437-441, 1978.
- Tompkins, A.M., and K.A. Emanuel, The vertical resolution sensitivity of simulated equilibrium tropical atmosphere and water vapour profiles, *Q. J. R. Meteorol. Soc.*, *126*:565,1219-1238, 2000.
- Toon, G. C., The JPL MkIV Interferometer, *Optics and Photonics News*, *2*, 19-21, 1991.
- Toon, G.C., *et al.*, Comparison of MkIV balloon and ER-2 aircraft measurements of atmospheric trace gases, *J. Geophys. Res.*, *104*, 26779-26790, 1999.
- Traub, W. A., K. W. Jucks, D. G. Johnson, M. T. Coffey, W. G. Mankin, and G. C. Toon, Comparison of column abundances from three infrared spectrometers during AASE II, *Geophys. Res. Lett.*, *21*, 2591-2594, 1994.
- Trenberth, K.E., The definition of El Nino, *Bull. Amer. Meteorol. Soc.*, *78*, 2771-2777, 1997.
- Trepte, C.R., R.E. Viega, and M.P. McCormick, The poleward dispersal of the Mt. Pinatubo volcanic aerosol, *J. Geophys. Res.*, *100*, 18,562-18,573, 1993.
- Tsuda, T., Y. Murayama, H. Wiryosumarto, *et al.*, Radiosonde observations of equatorial atmosphere dynamics over Indonesia, 1: Equatorial Waves and Tides, *J. Geophys. Res.*, *99*, 10491-10506, 1994.
- Tuck, A. F. Synoptic and chemical evolution of the Antarctic vortex in late winter and early spring, 1987. *J. Geophys. Res.*, *94* (D9), 11687-11737, 1989.
- Tuck, A. F., and M. H Proffitt, Comment on "On the magnitude of transport out of the Antarctic polar vortex" by M. F. Wiel *et al.*, *J. Geophys. Res.*, *102*, 28,215, 1997.
- Tuck, A., D. Baumgardner, K.R. Chan, *et al.*, The brewer-dobson circulation in light of high altitude *in situ* aircraft measurements, *Q. J. R. Meteorol. Soc.*, *123*, 1-69, 1997.
- Tuck, A.F., and S.J. Hovde, Fractal behavior of ozone, wind and temperature in the lower stratosphere, *Geophys. Res. Lett.*, *26* (9), 1271-1274, 1999.
- Turner, D. D., R. A. Ferrare, L. A., Heilman, J. E. M. Goldsmith, and T. P. Tooman, Raman lidar profiles (RL OROF) family of value added procedures, *DOE Techn. Memo. TR-xxx*, in press, 1999.
- Udelhofen, P.M., and D.L. Hartmann, Influence of tropical cloud systems on the relative humidity in the upper troposphere, *J. Geophys. Res.*, *100*, 7423-7440, 1995.

- U.S. Standard Atmosphere, 1976, National Oceanic and Atmospheric Administration, National Aeronautics and Space Administration, United States Air Force. Washington, D.C., 1976
- Vaughan, G., D. P. Wareing, L. Thomas, and V. Mitev, Humidity measurements in the free troposphere using Raman backscatter, *Q. J. R. Meteorol. Soc.*, *114*, 1471-1484, 1988.
- Vaughan, G. and C. Timmis, Transport of near-tropopause air into the lower midlatitude stratosphere, *Q. J. R. Meteorol. Soc.*, *124*(549 Part A): 1559-1578, 1998.
- Vay, S., *et al.*, DC-8-based observations of aircraft CO, CH<sub>4</sub>, N<sub>2</sub>O, and H<sub>2</sub>O<sub>(g)</sub> emission indices during SUCCESS, *Geophys. Res. Lett.*, *25*, 1717-1720, 1998.
- Vay, S.A., *et al.*, Tropospheric water vapor measurements over North Atlantic during Subsonic Assessment Ozone and Nitrogen Oxide Experiment (SONEX), *J. Geophys. Res.*, *105*, 3745-3756, 2000.
- Volk, C.M., *et al.*, Quantifying transport between the tropical and mid-latitude lower stratosphere, *Science*, *272*, 1763-1768, 1996.
- Vömel, H., S.J. Oltmans, D.J. Hofmann, T. Deshler, and J.M. Rosen, The evolution of the dehydration in the Antarctic stratospheric vortex, *J. Geophys. Res.*, *100* (D7), 13919-13926, 1995a.
- Vömel, H., S.J. Oltmans, D. Kley, and P.J. Crutzen, New evidence for the stratospheric dehydration mechanism in the equatorial Pacific, *Geophys. Res. Lett.*, *22* (15) 3235-3238, 1995b.
- Vömel, H., and S.J. Oltmans, Comments on A reexamination of the 'stratospheric fountain' hypothesis by A. E. Dessler, *Geophys. Res. Lett.*, *26*, 2737-2738, 1999.
- Von Clarmann, T., *et al.*, Determination of the stratospheric organic chlorine budget in the spring arctic vortex from MIPAS-B limb emission spectra and air sampling experiments, *J. Geophys. Res.*, *100*, 13,979-13,997, 1995.
- Wade, C. G., An evaluation of problems affecting the measurement of low relative humidity on the United States radiosonde. *J. Atmos. Ocean. Tech.*, *11*, 687-700, 1994.
- Wade, C. G., Calibration and data reduction problems affecting national weather service radiosonde humidity measurements. Preprints, Ninth AMS Symposium on Meteorological Observations and Instrumentation, Charlotte, North Carolina, March 27-31, 37-42, 1995.
- Wang, J., S. H. Melfi, P. Racette, D. Whiteman, L. Chang, R. Ferrare, K. Evans and F. Schmidlin. Simultaneous measurements of atmospheric water vapour with MIR, Raman lidar and rawinsondes. *J. Appl. Met.*, *34*, 1595-1607, 1995.
- Wang, P.H., P. Minnis, M.P. McCormick, G.S. Kent, and K.M. Skeens, A 6-year climatology of cloud occurrence frequency from Stratospheric Aerosol and Gas Experiment II observations (1985-1990), *J. Geophys. Res.*, *101* (D23), 29,407-29,429, 1996.
- Wang, H., and R. Fu, Influences of ENSO SST anomalies and winter storm tracks on the interannual variability of upper troposphere water vapour over the northern hemisphere extratropics, *J. Clim.*, *13*(1),59-73, 2000.
- Waters, J. W., Microwave limb sounding, in Atmospheric Remote Sensing by Microwave Radiometry, J. A. Janssen, Ed., John Wiley and Sons, 383-496, 1993.
- Waters J.W., W.G. Read, L. Froidevaux, *et al.*, The UARS and EOS Microwave Limb Sounder (MLS) experiments, *J. Atmos. Sci.*, *56*, 194-218, 1999.
- Watterson, I.G., and A.F. Tuck, A comparison of the longitudinal distributions of polar stratospheric clouds and temperatures for the 1987 Antarctic spring, *J. Geophys. Res.*, *94* (D14), 16511-16525, 1989.
- Wayne, R.P., Chemistry of Atmospheres, Oxford University Press, 1985.

- Webster, C. R., R. T. Menzies, and E. D. Hinkley, Infrared laser absorption: theory and applications, in *Laser Remote Chemical Analysis*, Chapter 3, edited by R. M. Measures, John Wiley, New York, 1988.
- Webster, C.R., R.D. May, C.A. Trimble, R.G. Chave, and J. Kendall, Aircraft (ER-2) Laser Infrared Absorption Spectrometer (ALIAS) for *in situ* stratospheric measurements of HCl, N<sub>2</sub>O, CH<sub>4</sub>, NO<sub>2</sub>, and HNO<sub>3</sub>, *Appl. Opt.*, *33*, 454-472, 1994.
- Weinstock, E. M., J. J. Schwab, J. B. Nee, M. J. Schwab, and J. G. Anderson, A cryogenically cooled photofragment fluorescence instrument for measuring stratospheric water vapor, *Rev. Sci. Instrum.*, *61*, 1413-1432, 1990.
- Weinstock, E. M., E. J. Hints, A. E. Dessler, J. F. Oliver, N. L. Hazen, J. N. Demusz, N. T. Allen, L. B. Lapson and J. G. Anderson, New fast response photofragment fluorescence hygrometer for use on the NASA ER-2 and the Perseus remotely piloted aircraft, *Rev. Sci. Instrum.*, *65*, 3544-3554, 1994.
- Weinstock E.M., E.J Hints, A.E. Dessler, *et al.*, Measurements of water-vapor in the tropical lower stratosphere during the CEPEX campaign - results and interpretation, *Geophys. Res. Lett.*, *22* (23), 3231-3234. 1995.
- Weitkamp, M. Riebesell, E. Voss, W. Lahmann, W. Michaelis, Raman lidar for the measurement of height profiles of water vapor and carbon dioxide, GKSS-Forschungszentrum Geesthacht GmbH, 1986.
- Welander, P., Studies on the general development of motion in a two-dimensional, ideal fluid, *Tellus*, *7*, 141-156, 1955.
- Wennberg, P.O., *et al.*, Removal of stratospheric O<sub>3</sub> by radicals: In situ measurements of OH, HO<sub>2</sub>, NO, NO<sub>2</sub>, ClO and BrO, *Science*, *266* 398-404, 1994.
- Wentz, F.J., and M. Schabel, Precise climate monitoring using complementary satellite data sets, *Nature*, *403*, 414-416, 2000.
- Wetzel, G. *et al.*, Vertical profiles of N<sub>2</sub>O<sub>5</sub>, HO<sub>2</sub>NO<sub>2</sub>, and NO<sub>2</sub> inside the Arctic vortex, retrieved from nocturnal MIPAS-B2 limb emission measurements in February 1995, *J. Geophys. Res.*, *102*, 19,177-19,186, 1997.
- Wexler, A., and R. E. Ruskin (eds.), Humidity and Moisture, I: Principles and methods of measuring humidity in gases, *Proc. 1963 Int. Symp. on Humidity and Moisture*, Washington, D.C, Reinhold Publishing Corporation, New York, 1965.
- Wexler, A., and W. A. Wildhack (eds.), Humidity and Moisture, III: Fundamentals and Standards, *Proc. 1963 Int. Symp. on Humidity and Moisture*, Washington, D.C, Reinhold Publishing Corporation, New York, 1965.
- Whiteman, D. N., S. H. Melfi and R. A. Ferrare, Raman lidar system for the measurement of water vapour and aerosols in the Earth's atmosphere, *Applied Optics* *31*, 3068-3082, 1992.
- Whiteman, D. N., and S. H. Melfi, Cloud liquid water, mean droplet radius and number density measurements using a Raman lidar, *J. Geophys. Res.*, *104*, 31411-31419, 1999.
- Wiederhold, P. R., Water vapor measurement, Marcel Dekker Inc., New York, ISBN 0-8247-9319-6, 1997.
- Winker, D.M., and C.R. Trepte, Lamina cirrus observed near the tropical tropopause by LITE, *Geophys. Res. Lett.*, *25*, 3351-3354, 1998.
- WMO, Measurements of upper air temperature, pressure, and humidity. Guide to Meteorological Instruments and Methods of Observation, Chapter 12. WMO-No.8, sixth edition, Geneva, I.12-1 - I.12-32, 1996.
- WMO, Scientific Assessment of Ozone Depletion: 1998, *WMO Report 44*, Geneva, 1999.
- Woodberry, K, K. Tanaka, H. Hendon, and M. Salby, An interactive system for analysis of global cloud imagery, *J. Am. Ocean. Tech.*, *8*, 627-638, 1991.

- Wu, X., J. J. Bates, and S. J. S. Khalsa, A climatology of the water vapor band brightness temperatures from NOAA operational satellites, *J. Climate*, 6 (7), 1282-1300, 1993.
- Wulfmeyer, V., and J. Bosenberg, Ground-based differential Absorption Lidar for Water Vapor Profiling: Assessment of Accuracy, resolution, and Meteorological Applications, *Appl. Opt.*, 37, 3825-3844, 1998.
- Wylie, D.P., and W.P. Menzel, Two years of cloud cover statistics using VAS, *J. Climate*, 2, 380-392, 1989.
- Yang, H., and R.T. Pierrehumbert, Production of dry air by isentropic mixing, *J. Atmos. Sci.*, 51, 3437-3454, 1994.
- Yokota, T., M. Suzuki, O. V. Dubovik, and Sasano, Y., ILAS (Improved Limb Atmospheric Spectrometer) /ADEOS data retrieval algorithms. *Adv. Space Res.*, 21, 393-396, 1998.
- Young, W. R., P.B. Rhines and C.J.R. Garrett, Shear-flow dispersion, internal waves, and horizontal mixing in the ocean, *Journal of Physical Oceanography*, 12(6): 515-527, 1982.
- Yulaeva, J., R. Holton, and J.M. Wallace, On the cause of the annual cycle in tropical lower- E. stratospheric temperatures, *J. Atmos. Sci.*, 51 (2), 169-174, 1994.
- Yushkov V., A. Lukyanov, S. Merkoulov, M. Khaplanov, L. Shyshatzkaya, J. Gumbel, Optical fluorescent hygrometer for water vapor low concentration measurements, in: P. Fabian, M. Tacke, K. Weber and C. Werner (eds), Air pollution and visible measurements, *Proc SPIE*, 2506, 783-794, 1995.
- Yushkov V., V. Dorokhov, V. Khattatov, A. Lukyanov, I. Zaitcev, N. Zvetkova, H. Nakane, H. Akiyoshi, and T. Ogawa, Evidence of ozone depletion over Yakutsk, Eastern Siberia, in 1995. R.Bojkov and G.Visconti (eds.), *Proc. XVIII Quadr. Ozone Symp., l'Aquila, Italy, 1996*, 241-244, 1998.
- Zander, R., P. Demoulin, D.H. Ehhalt, and U. Schmidt, Secular increase of the vertical column abundance of methane derived from IR solar spectra recorded at the Jungfraujoch station, *J. Geophys. Res.*, 94, 11029-11039, 1989.
- Zhai, P., and R.E. Eskridge, Atmospheric water vapour over China, *J. Climate*, 10, 2643-2652, 1997.
- Zhang, C., On the annual cycle in highest, coldest clouds in the tropics, *J. Climate*, 6, 1987-1990, 1993.
- Zhou, X., M.A. Geller, and M. Zhang, The cooling trend of the tropical cold point tropopause temperatures and its implications, *J. Geophys. Res.*, in press, 2000a.
- Zhou, X., M.A. Geller, and M. Zhang, Tropical cold point tropopause characteristics derived from ECMWF reanalyses and soundings, *J. Climate*, in press, 2000b.
- Zhu, Y., R.E. Newell and W.G. Read, Factors controlling upper tropospheric water vapor, *J. Clim.* 13, 836-848, 2000
- Zöger, M., C. Schiller, O. Bujok, N. Eicke, A. Engel, and D. S. McKenna, Measurements of water vapour at the tropopause for investigation of stratosphere troposphere exchange, Proc. 1st SPARC Assembly, Melbourne, Australia, 2.-6.12.1996, *Rep. WMO/TD 814*, 413-416, 1997.
- Zöger, M., *et al.*, Fast *in situ* stratospheric hygrometer: A new family of balloon-borne and airborne Lyman-alpha photofragment fluorescence hygrometers, *J. Geophys. Res.*, 104, 1807-1816, 1999a.
- Zöger, M., A. Engel, D. S. McKenna, C. Schiller, U. Schmidt, and T. Woyke, Balloon-borne *in situ* measurements of stratospheric H<sub>2</sub>O, CH<sub>4</sub> and H<sub>2</sub> at midlatitudes, *J. Geophys. Res.*, 104, 1817-1825, 1999b

---

## Appendix I

---

### Co-chairs, Authors, Contributors and Reviewers

---

#### Co-Chairs

Dieter Kley	Forschungszentrum Jülich	Germany
James M. Russell III	Hampton University	USA

---

#### Introduction

---

#### Co-authors

Dieter Kley	Forschungszentrum Jülich	Germany
James M. Russell III	Hampton University	USA

---

#### Chapter 1

---

#### Lead Authors

Ellis E. Remsberg	NASA Langley Research Center	USA
Cornelius Schiller	Forschungszentrum Jülich	Germany

#### Co-authors

John J. Bates	NOAA Environmental and Technology Laboratory	USA
Richard M. Bevilacqua	Naval Research Laboratory	USA
Ed Browell	NASA Langley Research Center	USA
Er-Woon Chiou	NASA Science Applications International Corporation	USA
William P. Chu	NASA Langley Research Center	USA
Gerhard Ehret	Deutsches Zentrum für Luft und Raumfahrt	Germany
Dietrich Feist	University of Bern	Switzerland
Diane Gaffen	NOAA Aeronomy Laboratory	USA
Larry Gordley	G & A Technical Software, Inc.	USA

---

Michael R. Gunson	NASA Jet Propulsion Laboratory	USA
Paul Hartogh	Max-Planck-Institut für Aeronomie	Germany
Manfred Helten	Forschungszentrum Jülich	Germany
Robert Herman	NASA Jet Propulsion Laboratory	USA
Eric J. Hints	Woods Hole Oceanographic Institution	USA
F. W. Irion	NASA Jet Propulsion Laboratory	USA
Syed Ismail	NASA Langley Research Center	USA
David G. Johnson	SAO Smithsonian Center for Astrophysics	USA
Niklaus Kämpfer	University of Bern	Switzerland
Hiroshi Kanzawa	National Institute for Environmental Studies	Japan
Ken Kelly	NOAA Aeronomy Laboratory	USA
Dieter Kley	Forschungszentrum Jülich	Germany
Randy May	NASA Jet Propulsion Laboratory	USA
Marty McHugh	NASA Science Applications International Corporation	USA
Hope A. Michelsen	Sandia National Laboratories	USA
Larry Miloshevish	NOAA Aeronomy Laboratory	USA
Gerald E. Nedoluha	Naval Research Laboratory	USA
Hermann Oelhaf	Forschungszentrum Karlsruhe	Germany
Samuel Oltmans	NOAA Climate Monitoring and Diagnostics Laboratory	USA
Joëlle Ovarlez	Laboratoire de Météorologie Dynamique du CNRS	France
Hugh Pumphrey	University of Edinburgh	UK
William G. Read	NASA Jet Propulsion Laboratory	USA
Glenn Sachse	NASA Langley Research Center	USA
Vanessa Sherlock	Service d'Aéronomie du CNRS, France, now at UK Meteorological Office	UK
Herman Smit	Forschungszentrum Jülich	Germany
Geoffrey Toon	NASA Jet Propulsion Laboratory	USA
Holger Vömel	NOAA Climate Monitoring and Diagnostics Laboratory	USA
Joe W. Waters	NASA Jet Propulsion Laboratory	USA
Elliot M. Weinstock	Harvard University	USA
Dave Whiteman	NASA Goddard Space Flight Center	USA

### Contributors

Alain Chedin	Laboratoire de Météorologie Dynamique du CNRS	France
Dieter H. Ehhalt	Forschungszentrum Jülich	Germany
Vladimir Yushkov	CAO Moscow	Russia

---

**Reviewers**

Linnea Avallone	Laboratory for Atmospheric and Space Physics	USA
Bruno Carli	IROE-CNR	Italy
Herbert Fischer	Forschungszentrum Karlsruhe	Germany
Howard Roscoe	British Antarctic Survey	UK
Adrian Tuck	NOAA Aeronomy Laboratory	USA
Geraint Vaughan	University College of Wales	UK

---

**Chapter 2**


---

**Lead Authors**

Samuel J. Oltmans	NOAA Climate Monitoring and Diagnostics Laboratory	USA
Karen H. Rosenlof	NOAA Aeronomy Laboratory	USA

**Authors**

Hope A. Michelsen	Sandia National Laboratories	USA
Gerald E. Nedoluha	Naval Research Laboratory	USA
Liwen Pan	National Center for Atmospheric Research	USA
William G. Read	NASA Jet Propulsion Laboratory	USA
Ellis E. Remsberg	NASA Langley Research Center	USA
Cornelius Schiller	Forschungszentrum Jülich	Germany

**Co-authors**

John J. Bates	NOAA Environmental and Technology Laboratory	USA
Richard M. Bevilacqua	Naval Research Laboratory	USA
Marie-Lise Chanin	Service d'Aéronomie du CNRS	France
Er-Woon Chiou	NASA Science Applications International Corporation	USA
William P. Chu	NASA Langley Research Center	USA
Herbert Fischer	Forschungszentrum Karlsruhe	Germany
Larry L. Gordley	G & A Technical Software, Inc.	USA
Paul Hartogh	Max-Planck-Institut für Aeronomie	Germany
Manfred Helten	Forschungszentrum Jülich	Germany
Robert L. Herman	NASA Jet Propulsion Laboratory	USA
Eric J. Hints	Woods Hole Oceanographic Institution	USA

---

Syed Ismail	NASA Langley Research Center	USA
David G. Johnson	Harvard-Smithsonian Center for Astrophysics, now at NASA Langley Research Center	USA
Hiroshi Kanzawa	National Institute for Environmental Studies	Japan
Kenneth K. Kelly	NOAA Aeronomy Laboratory	USA
Dieter Kley	Forschungszentrum Jülich	Germany
Randy D. May	Spectra Sensors, Inc.	USA
Larry M. Miloshevich	National Center for Atmospheric Research	USA
Hermann Oelhaf	Forschungszentrum Karlsruhe	Germany
Joëlle Ovarlez	Laboratoire de Météorologie Dynamique du CNRS	France
Hugh C. Pumphrey	University of Edinburgh	UK
Patrick N. Purcell	NASA Science Applications International Corporation	USA
James M. Russell III	Hampton University	USA
Glen W. Sachse	NASA Langley Research Center	USA
Vanessa Sherlock	Service d'Aéronomie du CNRS, France, now at UK Meteorological Office	UK
Herman G.J. Smit	Forschungszentrum Jülich	Germany
Geoffrey C. Toon	NASA Jet Propulsion Laboratory	USA
Stephanie A. Vay	NASA Langley Research Center	USA
Holger Vömel	University of Colorado	USA
Elliot M. Weinstock	Harvard University	USA

### Reviewers

Jens Boesenberg	MPI für Meteorologie Hamburg	Germany
Bruno Carli	IROE-CNR	Italy
Dale Hurst	NOAA Climate Monitoring and Diagnostics Laboratory	USA
Rod Jones	University of Cambridge	UK
Danny McKenna	Forschungszentrum Jülich	Germany
Gérard Mégie	Service d'Aéronomie du CNRS	France
John Pyle	University of Cambridge	UK
Howard Roscoe	British Antarctic Survey	UK
Darin Toohey	PAOS University of Colorado	USA
Adrian Tuck	NOAA Aeronomy Laboratory	USA

---

## Chapter 3

---

### Lead Authors

Andrew Gettelman	National Center for Atmospheric Research	USA
John E. Harries	Blackett Laboratory, Imperial College	UK
Philip W. Mote	Climate Impacts Group, Joint Institute for the Study of the Atmosphere and Oceans, University of Washington	USA

### Co-authors

J. Anderson	Hampton University	USA
John J. Bates	NOAA Environmental and Technology Laboratory	USA
Richard M. Bevilacqua	Naval Research Laboratory	USA
Andrew E. Dessler	Joint Center for Earth System Science, University of Maryland	USA
R. Fu	University of Arizona	USA
Dian J. Gaffen	NOAA Aeronomy Laboratory	USA
E. J. Jensen	NASA Ames Research Center	USA
Dieter Kley	Forschungszentrum Jülich	Germany
Gerald E. Nedoluha	Naval Research Laboratory	USA
Samuel J. Oltmans	NOAA Climate Monitoring and Diagnostics Laboratory	USA
Liwen Pan	National Center for Atmospheric Research	USA
Leonhard Pfister	NASA Ames Research Center	USA
Hugh C. Pumphrey	University of Edinburgh	UK
William J. Randel	National Center for Atmospheric Research	USA
Ellis E. Remsberg	NASA Langley Research Center	USA
E. P. Salathe	University of Washington	USA
Ulrich Schumann	DLR Oberpfaffenhofen	Germany
Steven C. Sherwood	NASA Goddard Space Flight Center	USA
Herman G. Smit	Forschungszentrum Jülich	Germany
D. C. Smith		
E. M. Stone	NASA Jet Propulsion Laboratory	USA
R. Toumi	Imperial College	UK
Holger Vömel	NOAA Climate Monitoring and Diagnostics Laboratory	USA
Elliot M. Weinstock	Harvard University	USA
Xuelong Zhou	University of Washington	USA

---

**Reviewers**

Bruno Carli	IROE-CNR	Italy
Lesley Gray	Rutherford Appleton Laboratory	UK
Richard H. Johnson	Colorado State University	USA
James R. Holton	University of Washington	USA
Rod Jones	University of Cambridge	UK
G�rard M�gie	Service d'A�ronomie du CNRS	France
Reginald E. Newell	Massachusetts Institute of Technology	USA
William J. Randel	National Center for Atmospheric Research	USA
Howard Roscoe	British Antarctic Survey	UK
Ulrich Schmidt	Johann Wolfgang Goethe Universit�t Frankfurt	Germany
Adrian Tuck	NOAA Aeronomy Laboratory	USA

---

## Acronyms and Abbreviations

ADEOS	Advanced Earth Observing Satellite
AFGL	Air Force Geophysics Laboratory
AL	Aeronomy Laboratory of NOAA, USA
AMSU-B	Advanced Microwave Sounding Unit
ARC	NASA Ames Research Center, USA
ARM	Atmospheric Radiation Monitoring
ATLAS	Atmospheric Laboratory for Applications and Science (Spacelab Shuttle Missions)
ATMOS	Atmospheric Trace Molecule Spectroscopy
CCR	Clear Column Radiance
CLAES	Cryogenic Limb Array Etalon Spectrometer (on UARS)
CMDL	NOAA Climate Monitoring and Diagnostics Laboratory, USA
CNRS	Centre National de la Recherche Scientifique, France
DAAC	Distributed Active Archive Center, NASA LaRC, USA
DIAL	Differential Absorption LIDAR
DLH	Diode Laser Hygrometer
DLR	Deutsches Zentrum für Luft- und Raumfahrt, Germany
DMSP	Defence Meteorological Satellite Program
DOE	Department of Energy, USA
ECMWF	European Centre for Medium-Range Weather Forecasts
EI	Emission Index
ENSO	El Niño and the South Oscillation
EOS	Earth Observing System (of NASA's global satellite system)
ERBE	Earth Radiation Budget Experiment
FIRS	Far-Infrared Spectrometer
FISH	Fast In-situ Stratospheric Hygrometer
FTIR	Fourier Transform Infra-Red
FWHM	Full Width Half Maximum
GOES	Goddard Positioning System
GSFC	Goddard Space Flight Center, NASA, USA
HALOE	Halogen Occultation Experiment (on UARS)
HITRAN	HIgh-resolution TRANsmission

---

HIRS	High Resolution Infrared Sounder
ILAS	Improved Limb Absorption Spectrometer
IPCC	Intergovernmental Panel on Climate Change
ISAMS	Improved Stratospheric and Mesospheric Sounder
LASE	LIDAR Atmospheric Sensing Experiment
LIDAR	LIght Detection And Ranging
LIMS	Limb Infrared Monitor of the Stratosphere
LS	Lower Stratosphere
MAS	Microwave Atmospheric Sounder
MIPAS	Michelson Interferometer for passive Atmospheric Sounding
MJO	Madden-Julian Oscillation
MLS	Microwave Limb Sounder (on UARS)
MOZAIC	Measurement of Ozone by Airbus In-Service Aircraft
MPAE	Max-Planck-Institut für Aeronomie, Germany
MSU	Microwave Sounding Unit
NASA	National Aeronautics and Space Administration, USA
NASDA	National Space Development Agency, Japan
NCEP	National Center for Environmental Prediction, USA
NDSC	Network for the Detection of Stratospheric Change
NESDIS	National Environmental Satellite, Data and Information Service (NOAA)
NIST	National Institute for Standards and Technology, USA
NOAA	National Oceanic and Atmospheric Administration, USA
NRL	Naval Research Laboratory, USA
POAM	Polar Ozone and Aerosol Measurements
POLARIS	Photochemistry of Ozone Loss in the Arctic Region in Summer
POLINAT	Pollution from Aircraft Emissions in the North Atlantic Flight Corridor
ppmv	parts per million (by volume), i.e. $10^{-6}$
PV	Potential Vorticity
QBO	Quasi-Biennial Oscillation
RH	Relative humidity
RMS	Root-Mean-Square
SAGE	Stratospheric Aerosol and Gas Experiment
SAMS	Stratospheric And Mesospheric Sounder

---

SAO	Smithsonian Astrophysical Observatory, USA
SPADE	Stratospheric Photochemistry Aerosols and Dynamics Expedition
SPARC	Stratospheric Processes And their Role in Climate
SSB	Single sideband
SSM/I	Special Sensor Microwave Imager
SSMT2	Special Sensor Microwave / Temperature 2 parameter of the Defense Meteorological Satellite Program microwave instrument
SSU	Stratospheric Sounding Unit
TDL	Tuneable Diode Laser
TIGR	TOVS Initial Guess Retrieval
TIO	Tropical Intraseasonal Oscillation
TOVS	TIROS Operational Vertical Sounder
UARS	Upper Atmosphere Research Satellite
UKMO	United Kingdom Meteorological Office, UK
UT	Upper Troposphere
UTH	Upper Tropospheric Humidity
VUV	Vacuum Ultra Violet
WASPAM	Wasserdampf und Spurengasmessungen mit Mikrowellen
WCRP	World Climate Research Programme
WMO	World Meteorological Organisation
WVMS	Water Vapour Millimetre-wave Spectrometer

---

**LIST OF REPORTS**

- WCRP-1      VALIDATION OF SATELLITE PRECIPITATION MEASUREMENTS FOR THE GLOBAL PRECIPITATION CLIMATOLOGY PROJECT (Report of an International Workshop, Washington, D.C., 17-21 November 1986) (WMO/TD-No. 203) (out of print)
- WCRP-2      WOCE CORE PROJECT 1 PLANNING MEETING ON THE GLOBAL DESCRIPTION (Washington, D.C., 10-14 November 1986) (WMO/TD-No. 205) (out of print)
- WCRP-3      INTERNATIONAL SATELLITE CLOUD CLIMATOLOGY PROJECT (ISCCP) WORKING GROUP ON DATA MANAGEMENT (Report of the Sixth Session, Fort Collins, U.S.A., 16-18 June 1987) (WMO/TD-No. 210) (out of print)
- WCRP-4      JSC/CCCO TOGA NUMERICAL EXPERIMENTATION GROUP (Report of the First Session, Unesco, Paris, France, 25-26 June 1987) (WMO/TD-No. 204) (out of print)
- WCRP-5      CONCEPT OF THE GLOBAL ENERGY AND WATER CYCLE EXPERIMENT (Report of the JSC Study Group on GEWEX, Montreal, Canada, 8-12 June 1987 and Pasadena, U.S.A., 5-9 January 1988) (WMO/TD-No. 215) (out of print)
- WCRP-6      INTERNATIONAL WORKING GROUP ON DATA MANAGEMENT FOR THE GLOBAL PRECIPITATION CLIMATOLOGY PROJECT (Report of the Second Session, Madison, U.S.A., 9-11 September 1988) (WMO/TD-No. 221) (out of print)
- WCRP-7      CAS GROUP OF RAPPORTEURS ON CLIMATE (Leningrad, U.S.S.R., 28 October-1 November 1985) (WMO/TD-No. 226) (out of print)
- WCRP-8      JSC WORKING GROUP ON LAND SURFACE PROCESSES AND CLIMATE (Report of the Third Session, Manhattan, U.S.A., 29 June-3 July 1987) (WMO/TD-No. 232) (out of print)
- WCRP-9      AEROSOLS, CLOUDS AND OTHER CLIMATICALLY IMPORTANT PARAMETERS: LIDAR APPLICATIONS AND NETWORKS (Report of a Meeting of Experts, Geneva, Switzerland, 10-12 December 1985) (WMO/TD-No. 233) (out of print)
- WCRP-10     RADIATION AND CLIMATE (Report of the First Session, JSC Working Group on Radiative Fluxes, Greenbelt, U.S.A., 14-17 December 1987) (WMO/TD-No. 235) (out of print)
- WCRP-11     WORLD OCEAN CIRCULATION EXPERIMENT - IMPLEMENTATION PLAN - DETAILED REQUIREMENTS (Volume I) (WMO/TD-No. 242) (out of print)
- WCRP-12     WORLD OCEAN CIRCULATION EXPERIMENT - IMPLEMENTATION PLAN - SCIENTIFIC BACKGROUND (Volume II) (WMO/TD-No. 243) (out of print)
- WCRP-13     RADIATION AND CLIMATE (Report of the Seventh Session of the International Satellite Cloud Climatology Project (ISCCP) Working Group on Data Management, Banff, Canada, 6-8 July 1988) (WMO/TD-No. 252) (out of print)
- WCRP-14     AN EXPERIMENTAL CLOUD LIDAR PILOT STUDY (ECLIPS) (Report of the WCRP/CSIRO Workshop on Cloud Base Measurement, CSIRO, Mordialloc, Victoria, Australia, 29 February-3 March 1988) (WMO/TD-No. 251) (out of print)

- 
- WCRP-15      MODELLING THE SENSITIVITY AND VARIATIONS OF THE OCEAN-ATMOSPHERE SYSTEM (Report of a Workshop at the European Centre for Medium Range Weather Forecasts, 11-13 May 1988) (WMO/TD-No. 254) (out of print)
- WCRP-16      GLOBAL DATA ASSIMILATION PROGRAMME FOR AIR-SEA FLUXES (Report of the JSC/CCCO Working Group on Air-Sea Fluxes, October 1988) (WMO/TD-No. 257) (out of print)
- WCRP-17      JSC/CCCO TOGA SCIENTIFIC STEERING GROUP (Report of the Seventh Session, Cairns, Queensland, Australia, 11-15 July 1988) (WMO/TD-No. 259) (out of print)
- WCRP-18      SEA ICE AND CLIMATE (Report of the Third Session of the Working Group on Sea Ice and Climate, Oslo, 31 May-3 June 1988) (WMO/TD-No. 272) (out of print)
- WCRP-19      THE GLOBAL PRECIPITATION CLIMATOLOGY PROJECT (Report of the third Session of the International Working Group on Data Management, Darmstadt, FRG, 13-15 July 1988) (WMO/TD-No. 274) (out of print)
- WCRP-20      RADIATION AND CLIMATE (Report of the Second Session of the WCRP Working Group on Radiative Fluxes, Geneva, Switzerland, 19-21 October 1988) (WMO/TD-No. 291) (out of print)
- WCRP-21      INTERNATIONAL WOCE SCIENTIFIC CONFERENCE (Report of the International WOCE Scientific Conference, Unesco, Paris, 28 November-2 December 1988) (WMO/TD-No. 295) (out of print)
- WCRP-22      THE GLOBAL WATER RUNOFF DATA PROJECT (Workshop on the Global Runoff Data Set and Grid estimation, Koblenz, FRG, 10-15 November 1988) (WMO/TD-No. 302) (out of print)
- WCRP-23      WOCE SURFACE FLUX DETERMINATIONS - A STRATEGY FOR IN SITU MEASUREMENTS (Report of the Working Group on In Situ Measurements for Fluxes, La Jolla, California, U.S.A., 27 February-3 March 1989) (WMO/TD-No. 304) (out of print)
- WCRP-24      JSC/CCCO TOGA NUMERICAL EXPERIMENTATION GROUP (Report of the Second Session, Royal Society, London, U.K., 15-16 December 1988) (WMO/TD-No. 307) (out of print)
- WCRP-25      GLOBAL ENERGY AND WATER CYCLE EXPERIMENT (GEWEX) (Report of the First Session of the JSC Scientific Steering Group for GEWEX, Pasadena, U.S.A., 7-10 February 1989) (WMO/TD-No. 321) (out of print)
- WCRP-26      WOCE GLOBAL SURFACE VELOCITY PROGRAMME (SVP) (Workshop Report of WOCE/SVP Planning Committee and TOGA Pan-Pacific Surface Current Study, Miami, Florida, U.S.A., 25-26 April 1988) (WMO/TD-No. 323) (out of print)
- WCRP-27      DIAGNOSTICS OF THE GLOBAL ATMOSPHERIC CIRCULATION (Based on ECMWF analyses 1979-1989, Department of Meteorology, University of Reading, Compiled as part of the U.K. Universities Global Atmospheric Modelling Project) (WMO/TD-No. 326) (out of print)
- WCRP-28      INVERSION OF OCEAN GENERAL CIRCULATION MODELS (Report of the CCCO/WOCE Workshop, London, 10-12 July 1989) (WMO/TD-No. 331) (out of print)

- 
- WCRP-29 CAS WORKING GROUP ON CLIMATE RESEARCH (Report of Session, Geneva, 22-26 May 1989) (WMO/TD-No. 333) (out of print)
- WCRP-30 WOCE - FLOW STATISTICS FROM LONG-TERM CURRENT METER MOORINGS: THE GLOBAL DATA SET IN JANUARY 1989 (Report prepared by Robert R. Dickinson, Eddy Statistics Scientific Panel) (WMO/TD-No. 337) (out of print)
- WCRP-31 JSC/CCCO TOGA SCIENTIFIC STEERING GROUP (Report of the Eighth Session, Hamburg, FRG, 18-22 September 1989) (WMO/TD-No. 338) (out of print)
- WCRP-32 JSC/CCCO TOGA NUMERICAL EXPERIMENTATION GROUP (Report of the Third Session, Hamburg, FRG, 18-20 September 1989) (WMO/TD-No. 339) (out of print)
- WCRP-33 TOGA MONSOON CLIMATE RESEARCH (Report of the First Session of the Monsoon Numerical Experimentation Group, Hamburg, FRG, 21-22 September 1989) (WMO/TD-No. 349) (out of print)
- WCRP-34 THE GLOBAL PRECIPITATION CLIMATOLOGY PROJECT (Report of the Fourth Session of the International Working Group on Data Management, Bristol, U.K., 26-28 July 1989) (WMO/TD-No. 356) (out of print)
- WCRP-35 RADIATION AND CLIMATE (Report of the Third Session of the WCRP Working Group on Radiative Fluxes, Fort Lauderdale, U.S.A., 12-15 December 1989) (WMO/TD-No. 364) (out of print)
- WCRP-36 LAND-SURFACE PHYSICAL AND BIOLOGICAL PROCESSES (Report of an ad-hoc Joint Meeting of the IGBP Co-ordinating Panel No. 3 and WCRP Experts, Paris, France, 24-26 October 1989) (WMO/TD-No. 368) (out of print)
- WCRP-37 GLOBAL ENERGY AND WATER CYCLE EXPERIMENT (Report of the Workshop to Evaluate the Need for a Rain Radar in Polar Orbit for GEWEX, Greenbelt, U.S.A., 25-26 October 1989) (WMO/TD-No. 369) (out of print)
- WCRP-38 GLOBAL ENERGY AND WATER CYCLE EXPERIMENT (Report of the First Session of the WCRP-GEWEX/IGBP-CP3 Joint Working Group on Land-Surface Experiments, Wallingford, U.K., 25-26 January 1990) (WMO/TD-No. 370) (out of print)
- WCRP-39 RADIATION AND CLIMATE (Intercomparison of Radiation Codes in Climate Models, Report of Workshop, Paris, France, 15-17 August 1988) (WMO/TD-No. 371) (out of print)
- WCRP-40 GLOBAL ENERGY AND WATER CYCLE EXPERIMENT (Scientific Plan), August 1990 (WMO/TD-No. 376) (out of print)
- WCRP-41 SEA-ICE AND CLIMATE (Report of the Fourth Session of the Working Group, Rome, Italy, 20-23 November 1989) (WMO/TD-No. 377) (out of print)
- WCRP-42 PLANETARY BOUNDARY LAYER (Model Evaluation Workshop, Reading, U.K., 14-15 August 1989) (WMO/TD-No. 378) (out of print)
- WCRP-43 INTERNATIONAL TOGA SCIENTIFIC CONFERENCE PROCEEDINGS (Honolulu, U.S.A., 16-20 July 1990) (WMO/TD-No. 379) (out of print)
- WCRP-44 GLOBAL ENERGY AND WATER CYCLE EXPERIMENT (Report of the 2nd Session of the JSC Scientific Steering Group, Paris, France, 15-19 January 1990) (WMO/TD-No. 383) (out of print)

- 
- WCRP-45 SEA ICE NUMERICAL EXPERIMENTATION GROUP (SINEG) (Report of the First Session, Washington, D.C., 23-25 May 1989) (WMO/TD-No. 384) (out of print)
- WCRP-46 EARTH OBSERVING SYSTEM FOR CLIMATE RESEARCH (Report of a WCRP Planning Meeting, Reading, U.K., 2-3 July 1990) (WMO/TD-No. 388) (out of print)
- WCRP-47 JSC/CCCO TOGA SCIENTIFIC STEERING GROUP (Report of the Ninth Session, Kona, Hawaii, U.S.A., 23-25 July 1990) (WMO/TD-No. 387) (out of print)
- WCRP-48 SPACE OBSERVATIONS OF TROPOSPHERIC AEROSOLS AND COMPLEMENTARY MEASUREMENTS (Report of experts meeting at Science and Technology Corporation, Hampton, Virginia, U.S.A., 15-18 November 1989) (WMO/TD-No. 389) (out of print)
- WCRP-49 TOGA MONSOON CLIMATE RESEARCH (Report of the Second Session of the Monsoon Numerical Experimentation Group, Kona, Hawaii, U.S.A., 26-27 July 1990) (WMO/TD-No. 392) (out of print)
- WCRP-50 TOGA NUMERICAL EXPERIMENTATION GROUP (Report of the Fourth Session, Palisades, New York, U.S.A., 13-14 June 1990) (WMO/TD-No. 393) (out of print)
- WCRP-51 RADIATION AND CLIMATE (Report of the First Session, International Working Group on Data Management for WCRP Radiation Projects, New York City, U.S.A., 21-23 May 1990) (WMO/TD-No. 398) (out of print)
- WCRP-52 THE RADIATIVE EFFECTS OF CLOUDS AND THEIR IMPACT ON CLIMATE (Review prepared by Dr. A. Arking at request of IAMAP Radiation Commission) (WMO/TD-No. 399) (out of print)
- WCRP-53 CAS/JSC WORKING GROUP ON NUMERICAL EXPERIMENTATION (Report of the Sixth Session, Melbourne, Australia, 24-28 September 1990) (WMO/TD-No. 405) (out of print)
- WCRP-54 RADIATION AND CLIMATE (Workshop on Implementation of the Baseline Surface Radiation Network, Washington, D.C., 3-5 December 1990) (WMO/TD-No. 406) (out of print)
- WCRP-55 GLOBAL CLIMATE MODELLING (Report of First Session of WCRP Steering Group on Global Climate Modelling, Geneva, Switzerland, 5-8 November 1990) (WMO/TD-No. 411) (out of print)
- WCRP-56 THE GLOBAL CLIMATE OBSERVING SYSTEM (Report of a meeting convened by the Chairman of the Joint Scientific Committee for the WCRP, Winchester, U.K., 14-15 January 1991) (WMO/TD-No. 412) (out of print)
- WCRP-57 GLOBAL ENERGY AND WATER CYCLE EXPERIMENT (Report of the 3rd Session of the JSC Scientific Steering Group, Hamilton, Bermuda, 21-25 January 1991) (WMO/TD-No. 424) (out of print)
- WCRP-58 INTERCOMPARISON OF CLIMATES SIMULATED BY 14 ATMOSPHERIC GENERAL CIRCULATION MODELS (CAS/JSC Working Group on Numerical Experimentation, prepared by Dr. G.J. Boer et al) (WMO/TD-No. 425) (out of print)
- WCRP-59 INTERACTION BETWEEN AEROSOLS AND CLOUDS (Report of Experts Meeting, Hampton, Virginia, U.S.A., 5-7 February 1991) (WMO/TD-No. 423) (out of print)

- 
- WCRP-60 THE GLOBAL PRECIPITATION CLIMATOLOGY PROJECT (Report of the Fifth Session of the International Working Group on Data Management, Laurel, Maryland, U.S.A., 20-21 May 1991) (WMO/TD-No. 436)
- WCRP-61 GLOBAL ENERGY AND WATER CYCLE EXPERIMENT (Report of the Second Session of the WCRP-GEWEX/IGBP Core Project on BAHC Joint Working Group on Land-Surface Experiments, Greenbelt, Maryland, U.S.A., 3-4 June 1991) (WMO/TD-No. 437)
- WCRP-62 SEA-ICE AND CLIMATE (Report of a Workshop on Polar Radiation Fluxes and Sea-Ice Modelling, Bremerhaven, Germany, 5-8 November 1990) (WMO/TD-No. 442)
- WCRP-63 JSC/CCCO TOGA SCIENTIFIC STEERING GROUP (Report of the Tenth Session, Gmunden, Austria, 26-29 August 1991) (WMO/TD-No. 441)
- WCRP-64 RADIATION AND CLIMATE (Second Workshop on Implementation of the Baseline Surface Radiation Network, Davos, Switzerland, 6-9 August 1991) (WMO/TD-No. 453)
- WCRP-65 SEA-ICE AND CLIMATE (Report of the Fifth Session of the Working Group, Bremerhaven, Germany, 13-15 June 1991) (WMO/TD-No. 459)
- WCRP-66 GLOBAL ENERGY AND WATER CYCLE EXPERIMENT (Report of the First GEWEX Temperature/Humidity Retrieval Workshop, Greenbelt, U.S.A., 23-26 October 1990) (WMO/TD-No. 460) (out of print)
- WCRP-67 GEWEX CONTINENTAL SCALE INTERNATIONAL PROJECT (Scientific Plan, December 1991) (WMO/TD-No. 461) (out of print)
- WCRP-68 SIMULATION OF INTERANNUAL AND INTRASEASONAL MONSOON VARIABILITY (Report of Workshop, Boulder, CO, U.S.A., 21-24 October 1991) (WMO/TD-No. 470)
- WCRP-69 RADIATION AND CLIMATE (Report of Fourth Session of the WCRP Working Group on Radiative Fluxes, Palm Springs, U.S.A., 24-27 September 1991) (WMO/TD-No. 471)
- WCRP-70 CAS/JSC WORKING GROUP ON NUMERICAL EXPERIMENTATION (Report of the Seventh Session, Boulder, CO, U.S.A., 24-29 October 1991) (WMO/TD-No. 477)
- WCRP-71 GLOBAL CLIMATE MODELLING (Report of Second Session of WCRP Steering Group on Global Climate Modelling, Bristol, U.K., 18-20 November 1991) (WMO/TD-No. 482)
- WCRP-72 SCIENTIFIC CONCEPT OF THE ARCTIC CLIMATE SYSTEM STUDY (ACSYS) (Report of the JSC Study Group on ACSYS, Bremerhaven, Germany, 10-12 June 1991 and London, U.K., 18-19 November 1991) (WMO/TD-No. 486) (out of print)
- WCRP-73 TOGA NUMERICAL EXPERIMENTATION GROUP (Report of the Fifth Session, San Francisco, California, U.S.A., 9-11 December 1991) (WMO/TD-No. 487)
- WCRP-74 GLOBAL ENERGY AND WATER CYCLE EXPERIMENT (Report of the Fourth Session of the JSC Scientific Steering Group for GEWEX, Tokyo, Japan, 27-31 January 1992) (WMO/TD-No. 490)
- WCRP-75 HYDROLOGY AND SURFACE RADIATION IN ATMOSPHERIC MODELS (Report of a GEWEX Workshop, European Centre for Medium-range Weather

- 
- Forecasts, Reading, U.K., 28 October-1 November 1991) (WMO/TD-No. 492) (out of print)
- WCRP-76 REVIEWS OF MODERN CLIMATE DIAGNOSTIC TECHNIQUES - Satellite data in climate diagnostics, (A. Gruber and P.A. Arkin, November 1992) (WMO/TD-No. 519) (out of print)
- WCRP-77 INTERNATIONAL SATELLITE CLOUD CLIMATOLOGY PROJECT (Radiance Calibration Report, December 1992) (WMO/TD-No. 520) (out of print)
- WCRP-78 GLOBAL OBSERVATIONS, ANALYSES AND SIMULATION OF PRECIPITATION (Report of Workshop, National Meteorological Center, Camp Springs, Maryland, U.S.A., 27-30 October 1992) (WMO/TD-No. 544) (out of print)
- WCRP-79 INTERCOMPARISON OF TROPICAL OCEAN GCMS (TOGA Numerical Experimentation Group, prepared by T. Stockdale et al., April 1993) (WMO/TD-No. 545)
- WCRP-80 SIMULATION AND PREDICTION OF MONSOONS - RECENT RESULTS (TOGA/WGNE Monsoon Numerical Experimentation Group, New Delhi, India, 12-14 January 1993) (WMO/TD-No. 546)
- WCRP-81 ANALYSIS METHODS OF PRECIPITATION ON A GLOBAL SCALE (Report of a GEWEX Workshop, Koblenz, Germany, 14-17 September 1992) (WMO/TD-No. 558) (Out of print)
- WCRP-82 INTERCOMPARISON OF SELECTED FEATURES OF THE CONTROL CLIMATES SIMULATED BY COUPLED OCEAN-ATMOSPHERE GENERAL CIRCULATION MODELS (Steering Group on Global Climate Modelling, September 1993) (WMO/TD-No. 574)
- WCRP-83 STRATOSPHERIC PROCESSES AND THEIR ROLE IN CLIMATE (SPARC): INITIAL REVIEW OF OBJECTIVES AND SCIENTIFIC ISSUES (SPARC Scientific Steering Group, December 1993) (WMO/TD-No. 582) (out of print)
- WCRP-84 PROCEEDINGS OF THE INTERNATIONAL CONFERENCE ON MONSOON VARIABILITY AND PREDICTION (Trieste, Italy, 9-13 May 1994) (WMO/TD-No. 619) (Out of print)
- WCRP-85 INITIAL IMPLEMENTATION PLAN FOR THE ARCTIC CLIMATE SYSTEM STUDY (ACSYS) (September 1994) (WMO/TD-No. 627) (out of print)
- WCRP-86 CLOUD-RADIATION INTERACTIONS AND THEIR PARAMETERIZATION IN CLIMATE MODELS (Report of international workshop, Camp Springs, Maryland, U.S.A., 18-20 October 1993) (WMO/TD-No. 648)
- WCRP-87 PROCEEDINGS OF THE WORKSHOP ON GLOBAL COUPLED GENERAL CIRCULATION MODELS (La Jolla, California, USA, 10-12 October 1994) (WMO/TD-No. 655)
- WCRP-88 INTRASEASONAL OSCILLATIONS IN 15 ATMOSPHERIC GENERAL CIRCULATION MODELS (Results from an AMIP diagnostic subproject) (WMO/TD-No. 661)
- WCRP-89 CLIMATE VARIABILITY AND PREDICTABILITY (CLIVAR) Science Plan (August 1995) (WMO/TD-No. 690) (out of print)

- 
- WCRP-90      WORKSHOP ON CLOUD MICROPHYSICS PARAMETERIZATIONS IN GLOBAL ATMOSPHERIC CIRCULATION MODELS (Kananaskis, Alberta, Canada, 23-25 May 1995) (WMO/TD-No. 713)
- WCRP-91      PROCEEDINGS OF THE INTERNATIONAL SCIENTIFIC CONFERENCE ON TOGA (Melbourne, Australia, 2-7 April 1995) (WMO/TD-No. 717)
- WCRP-92      PROCEEDINGS OF THE FIRST INTERNATIONAL AMIP SCIENTIFIC CONFERENCE (Monterey, California, USA, 15-19 May 1995) (WMO/TD-No. 732)
- WCRP-93      PROCEEDINGS OF THE WORKSHOP ON ACSYS SOLID PRECIPITATION CLIMATOLOGY PROJECT (Reston, VA, USA, 15-15 September 1995) (WMO/TD-No. 739) (out of print)
- WCRP-94      PROCEEDINGS OF THE ACSYS CONFERENCE ON THE DYNAMICS OF THE ARCTIC CLIMATE SYSTEM (Göteborg, Sweden, 7-10 November 1994) (WMO/TD-No. 760) (out of print)
- WCRP-95      WCRP WORKSHOP ON AIR-SEA FLUX FIELDS FOR FORCING OCEAN MODELS AND VALIDATING GCMS (Reading, UK, 24-27 October 1995) (WMO/TD-No. 762) (out of print)
- WCRP-96      NORTHERN HEMISPHERE ATMOSPHERIC BLOCKING AS SIMULATED BY 15 ATMOSPHERIC GENERAL CIRCULATION MODELS IN THE PERIOD 1979-1988 (Results from an AMIP Diagnostic subproject) (WMO/TD-No. 784) (out of print)
- WCRP-97      INTERNATIONAL WORKSHOP ON RESEARCH USES OF ISCCP DATASETS (NASA Goddard Institute for Space Studies, New York, NY, USA, 15-18 April 1996) (WMO/TD-No. 790) (out of print)
- WCRP-98      PROCEEDINGS OF THE WORKSHOP ON THE IMPLEMENTATION OF THE ARCTIC PRECIPITATION DATA ARCHIVE (APDA) AT THE GLOBAL PRECIPITATION CLIMATOLOGY CENTRE (GPCC), (Offenbach, Germany, 10-12 July 1996) (WMO/TD-804)
- WCRP-99      PROCEEDINGS OF THE FIRST SPARC GENERAL ASSEMBLY (Melbourne, Australia, 2-6 December 1996) (WMO/TD-No. 814) (2 volumes)
- WCRP-100     MONSOON PRECIPITATION IN AMIP RUNS (Results from an AMIP diagnostic subproject) (WMO/TD-No. 837)
- WCRP-101     CLIVAR - A RESEARCH PROGRAMME ON CLIMATE VARIABILITY AND PREDICTABILITY FOR THE 21ST CENTURY, 1997 (WMO/TD-No. 853)
- WCRP-102     ORGANIZATION OF INTERNATIONALLY CO-ORDINATED RESEARCH INTO CRYOSPHERE AND CLIMATE (Proceedings of a meeting of experts on cryosphere and climate) (WMO/TD-No. 867)
- WCRP-103     CLIVAR INITIAL IMPLEMENTATION PLAN (WMO/TD-No.869)
- WCRP-104     PROCEEDINGS OF THE FIRST WCRP INTERNATIONAL CONFERENCE ON REANALYSES (Silver Spring, Maryland, USA, 27-31 October 1997) (WMO/TD-No. 876)
- WCRP-105     SPARC IMPLEMENTATION PLAN (WMO/TD-No. 914)

- 
- WCRP-106 PROCEEDINGS OF THE ACSYS CONFERENCE ON POLAR PROCESSES AND GLOBAL CLIMATE (Rosario, Orcas Island, WA, USA, 3-6 November 1997) (WMO/TD-No. 908)
- WCRP-107 COARE-98: PROCEEDINGS OF A CONFERENCE ON THE TOGA COUPLED OCEAN-ATMOSPHERE RESPONSE EXPERIMENT (COARE) (Boulder, CO, USA, 7-14 July 1998) (WMO/TD-No. 940)
- WCRP-108 PROCEEDINGS OF THE INTERNATIONAL CLIVAR CONFERENCE (Paris, France, 2-4 December 1998) (WMO/TD No. 954)
- WCRP-109 PROCEEDINGS OF THE SECOND WCRP INTERNATIONAL CONFERENCE ON REANALYSES (Wokefield Park, nr Reading, UK, 23-27 August 1999) (WMO/TD-No. 985)
- WCRP-110 WORKSHOP ON CLOUD PROCESSES AND CLOUD FEEDBACKS IN LARGE-SCALE MODELS (ECMWF, Reading, Berkshire, UK, 9-13 November 1999) (WMO/TD-No. 993)
- WCRP-111 PALEOCLIMATE MODELLING INTERCOMPARISON PROJECT (PMIP) (Proceedings of workshop, La Huardière, Canada, 4-8 October 1999) (WMO/TD-NO. 1007)
- WCRP-112 INTERCOMPARISON AND VALIDATION OF OCEAN-ATMOSPHERE ENERGY FLUX FIELDS (Final report of the Joint WCRP/SCOR Working Group on Air-Sea Fluxes) (November 2000) (WMO/TD-No. 1036)
- WCRP-113 SPARC ASSESSMENT OF UPPER TROPOSPHERIC AND STRATOSPHERIC WATER VAPOUR (WMO/TD-No. 1043) (limited distribution only)